

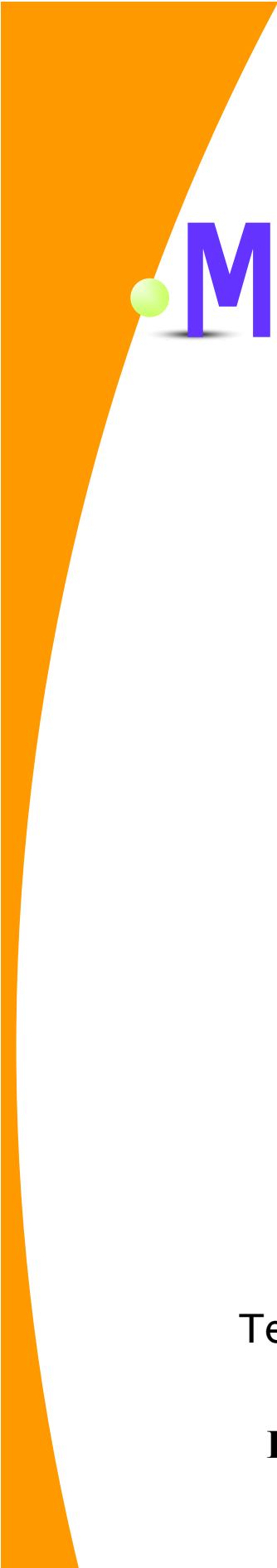
MST 12

**Proceedings of
the Twelfth International Workshop on
Technical and Scientific Aspects of MST Radar**

London (Ontario), Canada

**Radar School 12—16 May 2009
Workshop 17—23 May 2009**

Edited by N. Swarnalingam and W. K. Hocking



MST12 Twelfth International

WORKSHOP

On Technical and Scientific Aspects of MST Radar

17—23 May 2009

&

Radar School

12—16 May 2009

London (Ontario), Canada.

Proceedings of the Twelfth Workshop on
Technical and Scientific Aspects of MST Radar

Edited by N. Swarnalingam and W. K. Hocking

Proceedings of the Twelfth International Workshop on Technical and Scientific Aspects
of MST Radar

Editors: N. Swarnalingam and W. K. Hocking

Published 2010

ISBN: 978-0-9867285-0-1



Distributed by

Canadian Association of Physicists (CAP)
Ottawa, Ontario
Canada

For hard copies contact

Canadian Association of Physicists
Suite 112, MacDonald Building
University of Ottawa
150 Louis Pasteur Priv.
Ottawa, Ontario
Canada K1N 6N5
<http://www.cap.ca>

Hard copies will require reimbursement of shipping costs, packaging and preparation of the book. Prices will be negotiated on an individual basis at the time of request.

This work is subject to copyright. All rights are reserved, whether the whole or part of the material is concerned, specifically the rights of translation, reprinting, reuse of illustrations, recreations, reproduction on microfilm or in any other way.

Acknowledgements

The International Steering Committee of MST-12 consisted of W. K. Hocking and T. Tsuda (co-chairs), W. Singer, J. Chau, D. Hooper, P. Chilson, E. Kudeki, and I. Reid. The ISC would like to sincerely thank the support of the following sponsors:

- STELab (Solar-Terrestrial Environment Laboratory, Nagoya University), Japan
- RISH (Research Institute for Sustainable Humanity of Japan), Japan
- Mardoc Inc., Canada.
- Research Services, University of Western Ontario, Canada.
- Faculty of Science, University of Western Ontario, Canada.
- SCOSTEP (Scientific Committee on Solar-Terrestrial Physics), especially through CAWSES, USA.
- Vaisala, USA.
- CRESS (Centre for Research in Earth and Space Science) /York University, Canada.
- URSI (International Union of Radio Science), especially commissions F and G, Belgium
- Genesis Software Pty. Ltd., Australia.

Many thanks go to the Local Organization Committee of MST-12 comprising of W. Hocking (chair), A. Hocking, N. Swarnalingam, A. Farag, I. Beres, M. Osman, A. Dehghan and R. Wing.

Special thanks go to Adam Farag for setting up the MST-12 website and for taking care of online registrations. The support of Anna Hocking in many aspects of conference organizing is greatly appreciated, as is the invaluable support of Nimalan Swarnalingam throughout the workshop. Also, thanks to R. Sukara for valuable support during the radar school and workshop. Thanks to the London Convention Centre for its handling of the conference, and to the Canadian Association of Physicists (CAP) for acting as the publisher and distribution centre for this publication. Finally, thanks to all who contributed in any way to the MST-12 workshop and the radar school.

W. K. Hocking
On behalf of the ISC.



Some of the attendees at MST12, during a visit to the Negro Creek Radar. More photographs may be found at the end of the booklet.

The MST12 Workshop – Introduction and Overview.

The MST series of workshops are held roughly every 2-3 years, each time at a different venue. Formally, the workshops are referred to as “International Workshops on Technical and Scientific Aspects of MST Radar”, where “MST” refers to “Mesosphere, Stratosphere and Troposphere”. The twelfth in the series, MST12, was held in London, Ontario, Canada, from May 17 to May 23, 2009, at the London Convention Centre. London is home to the University of Western Ontario.

The workshop was also preceded by an international school on atmospheric radar (12 to 16 May, 2009), the details of which will be discussed later in this book.

The workshop itself was formally opened by Dr. Gerry Kidder, representing the University of Western Ontario Office of Research Services.

Approximately 131 participants attended, with countries of origin as shown in table 1. In all, 197 oral and poster papers were submitted (128 oral and 69 poster), covering a wide range of topics and interests.

However, these numbers do not tell the whole story. Due to the last-minute appearance of the H1N1 virus, many scientists who had intended to attend the workshop could not do so. The number of participants (131) would unquestionably have been higher under any other circumstances. In addition, the non-attendance of these scientists resulted in a substantial rearrangement of the program at the last minute. It is really quite difficult to say how many papers were actually presented – some scientists who could not attend asked colleagues to present their findings on their behalf, others withdrew their papers. In all it can be said that about 180 oral and poster presentations were discussed, although a few were only summaries. Nevertheless, the overall quality was good, as will be seen from the extended abstracts appearing in this booklet.

The workshop was sponsored by the following organizations and individuals, many of whom provided significant financial support. In all, about \$35,000 was provided by these sponsors, allowing support of needy scientists from various countries, support of students, and reduced registration fees.

Australia	7
Belgium	2
Canada	34
China	2
Costa Rica	1
Finland	1
France	3
Germany	10
India	21
Japan	9
Peru	4
South Korea	2
Sweden	2
Taiwan	4
United Kingdom	8
United States of America	21
TOTAL	131

Table 1.
Attendance at MST12 by country.

Table 2. Sponsors for MST12

STELab (Solar-Terrestrial Environment Laboratory, Nagoya University), Japan
RISH (Research Institute for Sustainable Humanity of Japan), Japan
Mardoc Inc.
University of Western Ontario Research Services
University of Western Ontario Individual Grant (W. Hocking)
University of Western Ontario Faculty of Science
SCOSTEP (Scientific Committee on Solar-Terrestrial Physics), especially through CAWSES
Vaisala
CRESS (Centre for Research in Earth and Space Science) /York University
URSI (International Union of Radio Science), especially commissions F and G.
Genesis Software Pty. Ltd.

The successful preparation of the workshop resulted from the hard work of several key committees and individuals.

Preliminary organization was implemented by the **International Steering Committee (ISC)**, comprising *W.K. Hocking and T. Tsuda (co-chairs), W. Singer, J. Chau, D. Hooper, P. Chilson, E. Kudeki, and I. Reid*. This committee also had the responsibility to oversee all aspects of the conference organization.

Local organization was the responsibility of the **Local Organizing Committee (LOC)**, comprising *W. Hocking (chair), A. Hocking, N. Swarnalingam, A. Farag, I. Beres, M. Osman, A. Dehghan and R. Wing*. Additional valuable support was provided by *R. Sakura*. This committee arranged the conference venue and the banquet, planned the timing of the presentations, organized excursions and attended to all local matters. Thanks are also due to the London Convention Centre for its handling of the conference.

The conference itself comprised 7 main sessions, and reports about these sessions will be given later in this book. Table 3 briefly summarizes the sessions. “MSO” refers to “Main Session Organizer”. Each session was overseen by a member of the ISC, but invitation of guest speakers and organization of session order was left to the MSOs, who reported back to the appropriate member of the ISC, as listed in the table. Some difference in presentation style existed between sessions, such as the length of talks, the number of invited speakers, and the division between oral and poster sessions. These differences reflect the preferences of the MSO’s. The MSO’s were also free to chair the sessions themselves, and/or to enlist the help of additional chairs. The personal involved in all these aspects are listed in table 3. A new element was added to the sessions this time –a 20 minute slot (typically) was added to the end of each session, to allow discussion of the preceding papers. Some of the session summaries will report on these discussions.

Table 3. Sessions, Organizers and chairs.

Session	ISC representative(s)	MSO: Main Session Organizer(s)	Additional Chairs
1. Scattering, Calibration and Microscale processes.	David Hooper	Andreas Muschinski, Ralph Latteck	
2. New instruments, signal processing, and quality control	Iain Reid	D. Narayana Rao, Iain Reid	
3. Meteors studied with MST radar.	Wayne Hocking	Geetha Ramkumar, Diego Janches	Ray Morris
4. Plasma irregularities	Jorge Chau, Erhan Kudeki	Mamuro Yamamoto, Amit Patra	Micheal Nicolls Gerald Lehmacher
5. Meteorology and forecasting/nowcasting	Phillip Chilson	William (Bill) Brown, Edwin Campos	
6. Middle Atmosphere Dynamics and Structure	Werner Singer	Peter Hoffman, S. Gurubaran	Iain Reid William Ward Nick Mitchell
7. Tropopause processes and Stratospheric/Tropospheric Exchange	Toshitaka Tsuda	David Tarasick, Masayuki Yamamoto	Hubert Luce

I would like to thank all of these organizers, and all of the conference attendees, for making MST12 a memorable event. This book contains summaries of various events that took place during the workshop, and also contains extended abstracts of a subset of the papers presented. Not all authors elected to present extended abstracts, however. For this reason we also include, as an appendix, a listing of all of the papers presented.

Despite the complications of the H1N1 virus, the workshop turned out to be a successful event. A special issue of the Journal of Atmospheric and Terrestrial Physics is currently under preparation which will include key papers from this workshop.

Thank you to all who attended, and all who contributed in any way to this event.

Wayne Hocking
ISC co-chair.

Contents

Awards	1
Report on the International School on Atmospheric Radar	3
Session Summaries	9
Summary of Session 1	11
Summary of Session 2	13
Summary of Session 3	15
Summary of Session 4	17
Summary of Session 5	19
Summary of Session 6	21
Summary of Session 7	23
The initial decade of MST radars: looking back 30 - 40 years 1971 - 1981 by J. Röttger	27

Session 1: Scattering, Calibration and Microscale Processes	67
Fine structure of wintertime mesospheric radar echoes - a comparison between high and low latitudes	
by E. Belova, S. Kirkwood, T. Sergienko, H. Nilsson, S. Satheesh Kumar, and T. Narayana Rao	69
Discrimination between lightning-generated RF and radar reflections from lightning	
by I. Beres, W. K. Hocking, and R. Thomas	73
Evaluation of absolute radar calibration using cosmic noise (QDC) and simulated signals	
by G. Stober, W. Singer, and C. Jacobi	77
Frequency dependence of PMSE: results from simulta- neous and common volume measurements with EISCAT radars	
by Q. Li, M. Rapp, J. Röttger, R. Latteck, M. Zecha, and C. Hall	81
Longitudinal differences of PMSE strength at high arctic latitudes	
by W. Singer, N. Swarnalingam, J.M. Wissing, R. Latteck, C. Meek, M.-B. Kallenrode, A. H. Manson, J. Drummond, and W. K. Hocking	85
A Decade-long PMSE aspect-sensitivity study at Res- olute Bay	
by N. Swarnalingam and W. Hocking	89

Session 2: New Instruments, Signal Processing and Quality Control	93
The new MST radar on Andøya/Norway by R. Latteck, W. Singer, M. Rapp, and T. Renkwitz	95
What is the optimal level of time-averaging for radar-derived wind-profiles? by D. Hooper and C. Gaffard	99
Radars measured errors in spectral-width turbulence determination by A. Dehghan and W. Hocking	103
Improvement of vertical resolution of RASS measurements by applying frequency-domain interferometric imaging by J. Furumoto, T. Shinoda, T. Tsuda, and A. Matsugatani	107
Continuous observations of temperature profiles by 443 MHz wind profiling radar with RASS in Okinawa by T. Shinoda, J. Furumoto, T. Tsuda, S. Satoh, and Y. Murayama	111
Design of a digital radar receiver: increasing the bandwidth of aeronomy observations at Arecibo Observatory by M. Sunderland, J. Urbina, M. Sulzer, and S. González	115
The effects of almost 20 years of operation on the performance of the Aberystwyth MST radar by J. Eastment, W. Bradford, D. Hooper, Z. Olewicz, O. Davies, and L. Dean	119

The diagnosis of a range gating problem suffered by the Aberystwyth MST radar	
by D. Hooper, O. Davies, J. Nash, T. Oakley, and M. Turp . . .	123
Study of multibeam ability for the VHF MST ALWIN radar system	
by T. Renkwitz, W. Singer, and R. Latteck	127
Pulse coding to reduce the influence of man-made noise on MF radar observations of winds	
by D. Keuer , P. Hoffmann, and W. Singer	131
Procedure to extract boundary-layer wind measurements using relatively long pulses	
by W. Hocking and A. Hocking	135
Correlation between vertical and horizontal winds in the troposphere as seen by the O-QNET	
by A. Farag and W. Hocking	139
Session 3: Meteors Studied with MST Radar	143
Development and initial measurements of a digital receiver for networked meteor radar applications	
by C. Vaudrin and S. Palo	145
A curious feature in meteor trail 3-D wind analysis	
by C. Meek and A. Manson	150
Signatures of the ionization trail of a fireball observed in the HF, and VHF range above Middle-Europe on January 17, 2009	
by D. Keuer, W. Singer, and G. Stober	154

Session 4: Plasma Irregularities 159

**Coupling processes in the equatorial atmosphere (CPEA):
a new feature of plasma irregularities revealed over the
Indonesian Equator**

by S. Fukao, Y. Otsuka, M. Yamamoto, and The CPEA Science
Group 161

**Multi-frequency radar studies of the equatorial 150-km
region**

by J. Chau, M. Milla, and E. Kudeki 165

Hydroxyl optical emissions by high-power radiowaves

by L. Kagan 169

**On the relation between MF radar scatterers and equa-
torial sporadic E**

by R. Dhanya, S. Gurubaran, and K. Emperumal 173

Session 5: Meteorology, Forecasting and Nowcasting 177

**Progress report on the O-QNET, a new Canadian wind-
profiler network**

by W. Hocking, P. Taylor, N. Swarnalingam, P. S. Argall, D.
Tarasick, I. Zawadzki, F. Fabry, J. Barron, R. Mercer, G. Klaassen,
G. McBean, R. Sica, and H. Hangan 179

**Refinement of 3D doppler velocity using 3D windprofiler
data**

by Y. Zhang, J. Barron, and R. Mercer 183

Dynamical structure of tropical cyclones revealed by atmospheric radars	
by S. Fukao, M. Teshiba, and Y. Shibagaki	187
Detecting and tracking severe storms in 3D doppler radar images	
by R. Mercer, J. Barron, and P. Joe	191
Identifying monsoon dynamics using wind profiler	
by S. Vanukuru, M. Rao, and M. Kalapureddy	195
Meso-γ-scale convective systems observed by a 443 MHz wind-profiling radar with RASS in the Okinawa subtropical regions	
by A. Mikami, J. Furumoto, T. Tsuda, S. Satoh, S. Nagai, Y. Murayama, and T. Kawabata	199
Modelling the outer scale of turbulence to improve temperature profile measurements with a VHF radar	
by V. Klaus	203
MU radar and lidar observations of clear-air turbulence and mammatus underneath cirrus	
by H. Luce, T. Nakamura, M. K. Yamamoto, M. Yamamoto, and S. Fukao	213
Exchange processes of energy and matter between the surface and the atmosphere	
by A. Serafimovich, S. Schier, F. Meixner, and T. Foken	217
Boundary layer wind profiler observations over the north atlantic gulf stream	
by W. Brown, J. Edson, and H. McIntyre	221

Skeleton based hook echo detection in radar reflectivity data	
by H. Wang, J. Barron, R. Mercer, and P. Joe	225

Mammatus and turbulence observations with the VHF MU radar and a Ka-band radar during the Tanuki 2008 campaign	
by H. Luce, M. K. Yamamoto, T. Mega, M. Yamamoto, H. Hashiguchi, S. Fukao, T. Tajiri, M. Nakazato, T. Ichiyama, and Y. Ohigashi	229

Characteristics of kelvin-helmholtz instabilities in the troposphere (up to 11 km) seen by the mu radar in range imaging mode by	
H. Luce, S. Fukao, M. K. Yamamoto, T. Mega, M. Yamamoto, H. Hashiguchi, T. Tajiri, M. Nakazato, T. Ichiyama, and Y. Ohigashi	233

Session 6: Middle Atmosphere Dynamics and Structure 237

Intraseasonal variations of 6-day wave in the tropical middle atmosphere	
by R. Kondala Rao, S. Gurubaran, S. Sathishkumar, S. Sridharan, T. Nakamura, T. Tsuda, H. Takahashi, P. Batista, R. Buriti, D. Riggin, D. V. Pancheva, and N. Mitchell	239

The AXONMET a pole to pole chain of atmospheric meteor radars	
by W. Hocking, A. Hocking, N. Mitchell, P. Batista, B. Clemesha, R. Buriti, A.H. Manson, C. Meek, M. Taylor, D. Janches, D. Riggin, D. Fritts, J. Drummond, and R. Hibbins	243

Long-term variations of low latitude mesospheric mean winds observed using Indian MST radar, MF radar, M-100 rocketsondes and HRDI measurements	
by G. Kishore Kumar, M. Venkat Ratnam, A. K. Patra, K. Kishore Kumar, G. Ramkumar, S. Gurubaran, and S. Vijaya Bhaskara Rao	247
Tidal and planetary wave coupling of the low latitude mesosphere lower thermosphere ionosphere (MLTI) region	
by S. Gurubaran, R. Dhanya, S. Sathishkumar, and P. T. Patil	251
Diurnal and seasonal variability of D-region electron densities at 69N	
by W. Singer, R. Latteck, and M. Friedrich	255
On the viability of lagrangian theories of internal wave spectra: implications for Doppler-Spread theory and radar measurements	
by G. Klaassen	259
Mesosphere lower thermosphere turbulence over Bear Lake, Utah, 1999-2002	
by R. Roper and F. Berkey	266
Hi-resolution radar observations of KH-billows at upper-tropospheric heights	
by R. Woodman and F. Villanueva R	269
Characteristics of atmospheric waves in the upper troposphere observed with the Gadanki MST radar RASS	
by T. Chandrasekhar Sarma and T. Tsuda	273

Latitudinal variability in the middle atmosphere (30-90 km) winds during the major stratospheric warm- ing event in 2005/2006	
by S. Sathishkumar, R. Kondala Rao, S. Gurubaran, D. Riggan, W. Singer, A. Manson, and C. Meek	277
Gravity wave momentum fluxes in the mesosphere / lower thermosphere at high- and mid-latitudes	
by M. Placke, C. Jacobi, P. Hoffmann, W. Singer, E. Becker, M. Rapp, and G. Stober	281
CAWSES INDIA: an overview	
by P. B. Rao, R. Sridharan, S. C. Chakravarty, K. G. Rao, G. Beig, R. S. Dabas, S. Gurubaran, P. K. Manoharan, T. K. Pant, and S. Ravindran	285
Session7: Tropopause Processes and Stratospheric/Tropospheric Exchange	289
Stratospherictropospheric exchange of ozone during Feb- ruary April 2008, Eureka	
by M. Osman, W. Hocking, D. Tarasick, H. He, and J. Drummond	291
High resolution measurements of stratosphere-troposphere exchange using radar windprofilers and balloon-borne ozonesondes	
by D. Tarasick, T. Carey-Smith, W. Hocking, P. S. Argall, O. Cooper, H. He, G. Liu, and Y. Rochon	295
A study of tropical tropopause variation at GADANKI (13.46N, 79.17E) using a long-term MST radar data-base	
by T. Chandrasekhar Sarma and T. Tsuda	299

Range-imaging observation of turbulence around tropical tropopause by equatorial atmosphere radar	
by T. Mega, M. Yamamoto, M. Abo, H. Luce, H. Hashiguchi, Y. Tabata, M. Yamanaka, and S. Fukao	302
Large-scale studies of STE using trajectory modeling, satellite and ozonesonde measurements	
by H. He, D. Tarasick, T. Carey-Smith, W. Hocking, Y. Rochon, M. Moran, P. S. Argall, K. Strawbridge, J. McConnell, D. Jones, and M. Bourqui	306
Appendices	311
Appendix A	313
Appendix B	337
Author Index	341

AWARDS

Several awards were made at MST12.

First, Dr. Juergen Roettger was rewarded for his many years of service to the MST community. He was one of the earliest developers and users of MST radar, and wrote many key papers. He was an important force behind development of the MST workshops, and was always a motivator and contributor at all of them. In addition he was a key activist in bringing the importance of MST radar to the attention of other communities, such as the meteorological community and the ionospheric community,

Dr. Roettger was given a plaque reading

“To Juergen Roettger:

For over 30 years of exemplary leadership of the MST community

Awarded at MST12, May 2009.”

Dr. Roettger gave a talk on the history of the development of MST radar, which was well received. An expanded version of this talk can be found in these proceedings.

STUDENT AWARDS

The following students (MSc, Ph D and early post-doctoral) were congratulated for the quality of talks and posters presented at MST12, receiving a certificate and a \$50 reward. However, we hasten to add that the quality of talks by all young scientists was high, and this bodes well for the future of the MST community. Choosing these awardees was very difficult for the judges. Special thanks are offered to Drs. David Hooper and Phil Chilson for their role as chairs of the student talks evaluation committee.

Awardees were (no special order)

Matthew Sunderland (USA)

Joel Younger (Australia)

Emily McCullough (Canada)

Gunter Stober (Germany)

Yong Zhang (Canada)

Francis Verbeek (Belgium)

Ildiko Beres (Canada)

Report on the International School on Atmospheric Radar held at The University of Western in May 2009, prior to MST12.

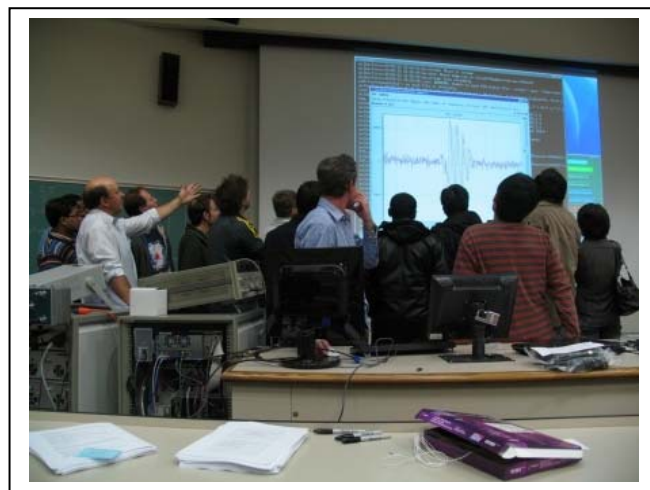
An international school on atmospheric radar was held on the campus of the University of Western Ontario, prior to the MST12 workshop (17-23 May 2009). Almost 50 students attended, with 15 from Canada, 10 from India, 7 from the USA, 6 from Germany, 3 from China, 2 from Peru, 1 from Belgium, 1 from Ethiopia, and 1 from Costa Rica.

The instructor team comprised Wayne Hocking (University of Western Ontario, Canada), David Hooper (Rutherford-Appleton Labs, UK), Margaret Campbell-Brown (University of Western Ontario, Canada), Diego Janches (Colorado Research Associates, USA), Phillip Chilson (University of Oklahoma, USA), Jun-Ichi Furumoto (Kyoto University, Japan), Werner Singer (Institute of Atmospheric Physics, Germany) and Juergen Roettger (Germany). Toru Sato (Japan), Stephen Eckermann (USA) and Catherine Gaffard (UK) were also invited, but needed to withdraw at the last minute due to travel restrictions associated with the H1N1 virus. Their lectures were substituted by Hocking (Eckermann and Sato) and Hooper (Gaffard).

The lecture schedule is shown at the end of this discussion.

The first day dealt with radar design and scattering mechanisms, with talks by Hocking, Hooper Campbell-Brown and Janches pertaining to these issues. An additional talk by Chilson on measurement techniques was also given. Such a set of talks is typical of many similar schools.

However, the second day of the school diverged substantially from traditional schools. It was the intent from the start to make the school a “hands-on” experience, and we had planned to have students visit a variety of radars on the Thursday of the school. But an additional opportunity presented itself which truly made the school special, and this opportunity made the Wednesday afternoon of the school something that all students will remember for a long time. A new Genesis-built transmitter and receiver system had recently been purchased by a London company, Mardoc Inc., and they loaned the system to the school for the day. Therefore, the afternoon of the Wednesday (day 2) was set aside to build all the additional components required to construct a complete radar. This involved making antennas, matching boxes and cables from scratch, plus tuning the system. A set of four Uda-Yagi antennas was *created by the students*, under the guidance of the teaching staff. The students had to cut all cables to length, connectorize them, create matching units, and tune the antennas. When finally complete, the system was fired up, and within seconds a strong echo from a meteor trail was seen. The students really seemed to enjoy this opportunity, and some photographs of the construction period are shown below.



Pictures showing students at work building the radar. Upper pictures show cable and matching unit assembly, middle pictures show antenna construction, and the picture at lower right shows the first meteor seen with the radar (displayed on the screen behind the students).



*Students and Instructors at the school
flanked by the antennas that they assembled and installed.*

The third day of the workshop was set aside for visits to various radars in the surrounding area. The University of Western Ontario, in partnership with York University and McGill University, were in the process of building a network of windprofiler radars in Ontario and Quebec, and four of these radars were accessible within a 3-hour drive of London, Ontario. Buses were rented and used to take students to the radars. In addition, some students visited the CMOR (Canadian Meteor Orbit Radar), which is also within a 2-hour drive of London. Two shifts of bus-trips were planned, so that group-sizes could be kept to 5-6 people per group, allowing all students good level of access to the radars.

At the radars, students had to perform a variety of tasks. One antenna was deliberately disabled by an instructor in advance, and students had to isolate and fix the antenna. They then had to plan an experiment, alter the software to implement the experiment, and collect the data for subsequent analysis on the following days.

On day 4 (Friday), the format of the school returned to a more traditional one, with a series of lectures. This time the focus was not on instruments, but atmospheric phenomena which could be measured with radar. Topics included gravity waves, meteorology, and turbulence. In addition, there was a lecture on radio Acoustic Sounding, and a second lecture on meteors and radio-meteor science.

Towards the end of the days, the format changed to a tutorial-type one, and students were given the data that they had collected on their trips to the radar, and asked to analyze it. Topics included searches for gravity waves, and correlation between wind motions at the various radar sites. Students

had a wide variety of skills, and were asked to collaborate with other students in the class so that data-analysis procedures could be shared between participants. Instructors could also be consulted for advice.

The final day of the school was Saturday the 16th of May. Again a lecture format was adopted in the morning, and an analysis session was held in the afternoon. A preliminary analysis for the data collected on the Thursday was completed, and some students volunteered to present their findings. In general only a preliminary analysis was possible since time was short, but the process of performing the data analysis was the focus of the session. There was no expectation that any scientifically publishable results would arise from such a short analysis, but students were able to become familiar with reading the data, performing various types of spectral and correlative analyses, and develop some understanding of the complexity of atmospheric motions.

A questionnaire related to the school was distributed to the students on the last day. Responses from the students were overwhelmingly positive. The students especially appreciated radar-building session and the opportunity to visit the radar sites. A summary of the questionnaire responses was presented to the organizers of the next MST Workshop for their consideration when planning the next radar school.

Financial Issues

Financial contributions to the school were provide by Scostep, Mardoc Inc, and the University of Western Ontario, and totalled about \$3,500. Expenditures were as follows (all in Ca\$):

Lecture room rental – 5 days at \$300 per day = \$1500

Morning coffee and juices - \$10 x 50 = \$500

Students paid for their own lunches.

Lecturers received a modest per-diem. Total spent on these per diems was \$2700. Accommodation for the lecturers was also covered, amounting to \$1972.

Bus rental for the Thursday (radar visits) was \$80 per van per day, and we rented 4 vans for 2 days, giving \$640. Van drivers volunteered their time free of charge.

Raw material for the antenna construction was provided by Mardoc Inc., and amounted to over \$500.

Free pizza was provided on the last day.

Registration fees were modest, being \$140 for students from developed countries and \$110 for students from developing or underdeveloped countries. Total income from this source was close to \$4000 (some students from developing countries had their registration fees waived).

In all, total expenditures were over \$7,500, while net income from registration fees was close to \$4,000, leaving a shortfall of over \$3,500. This was covered from contributors like Scostep, University contributions, and contributions from private industry.

In addition, several students were awarded scholarships to help them to attend the school, but it is hard to place a monetary value on these because they also helped in allowing students to attend the MST12 workshop that followed. Over \$10,000 was spent on travel scholarships, spread across the school and workshop.

Questionnaire

A *questionnaire* related to the school was distributed to the students on the last day. Responses from the students were overwhelmingly positive. The students especially appreciated the radar-building session and the opportunity to visit the radar sites. Some student responses appear on the next page.

Here are some student comments about the school

About the notes

“Great to have such detailed lecture notes to take home. Just right.”

About the radar construction

“The team building along with the radar building effort was appreciated.”

“Brilliant. Helps to show to a theoretical guy it’s not such a big deal getting your hands ‘dirty’”

“Best part of conference”

“I was amazed how well it worked – good fun.”

“This was an excellent idea. I learned a lot and had fun”

About the visits to the radars

“It was the first radar I had seen”

“This is one of the main reasons I enrolled.”

“Yes. It was also nice to get out of the lecture theatre and see some of Canada”

“Meteor radar visit was very useful, informative and gave me an understanding of where I get my data. Really enjoyed it”

Overall comments

“The diversity of fields and speakers helped me to get the big picture.”

“Dedication and energy of Prof. Hocking”

“Interacting with so many learned and experienced teachers and students from the field from all over the world made it a very unique experience. I am impressed by the enthusiasm and motivation of the teachers in the school.”

“Discussion with the lecturers as well as the students about the different interests in MST.”

“If you are working or planning to work with radars this school is a must have.”

“Absolutely brilliant would definitely go again.”

“Quite useful it is nice to be able to discuss topics with students from different research groups and backgrounds.”

“Great atmosphere, putting all these people together, learning a lot about each others fields. A big “thank you” to the organizers for running this so smoothly and for the vast amounts of time you invested to make this pay off big time.”

“The university environment was a comfortable setting for the school.”

“Brilliant. Would recommend it for other students”

School Program

The actual program of lectures, travel and practical classes for the school is presented below.

Tuesday 12 May, 2009

- 08.30 to 09.00 Introductory remarks
 - 09.00 to 10.15 Hocking: Radar types, design principles, part I.
 - 10.15 to 10.30 Short Break
 - 10.30 to 11.45 Hooper: scattering mechanisms, part I.
 - 11.45 to 13.00 Lunch
 - 13.00 to 14.15 Campbell-Brown and Janches: Meteor radars - basic principles
 - 14.15 to 15.30 Hocking: Radar Design principles, part II.
 - 15.30 to 16.00 Coffee Break
 - 16.00 to 17.00 Chilson: measurement techniques - Doppler, spaced antenna, etc - part I.
 - 17.00 to 17.45 Hocking: pulse-coding.
 - 17.45 to 18.00 Wrap-up session for day 1. Discussion of outstanding issues.
-

Wednesday 13 May, 2009

- 08.30 to 09.45 Chilson: Spaced antenna methods, including interferometry (continued in more detail)
 - 09.45 to 11.00 Hooper: data storage
 - 11.00 to 12.15 Hocking: overview of radars to be visited, capabilities. Discussion of plans for Thursday.
Introduction of necessary software.
 - 12.15 to 13.00 Lunch
 - 13.00 to 19.00 Radar Construction.
-

Thursday 14 May, 2009

Visits to radars. Each student to be assigned to a radar. Groups of about 6-7 people per radar-group. Students to gain some experience with radars. Some experiments to be performed, partly defined and set up by students. Data analysis to take place later. Some selected students may visit the meteor radars too.

Friday 15 May, 2009

- 08.30 to 09.45 Hocking (replacing Eckermann) Gravity waves
 - 09.45 to 11.00 Hooper (replacing Gaffard) Meteorology with radar
 - 11.00 to 12.15 Jun-Ichi Furumoto RASS, more advanced scattering.
 - 12.15 to 13.00 Lunch
 - 13.00 to 14.15 Hocking Turbulence
 - 14.15 to 15.30 Janches, Cambell-Brown - Meteors, part II.
 - 15.30 to 15.45 Coffee Break
 - 15.45 to 18.00 Analysis workshop - analysis of data collected Thursday.
-

Saturday 16 May, 2009

- 08.30 to 09.45 Hocking (replacing Sato) Antenna theory
- 09.45 to 11.00 Singer MF methods, Differential Absorption
- 11.00 to 12.15 Roettger - Ionospheric and Atmospheric Research with radars.
- 12.15 to 13.15 Lunch
- 13.15 to 15.30 Analysis of data - workshop style
- 15.30 to 15.45 Coffee Break
- 15.45 to 17.30 General discussions, questions, comparisons of results from radar analyses.

Session Summaries

Summary of Session 1: Scattering, Calibration and Microscale Processes

ISC representative: David Hooper <david.hooper@stfc.ac.uk>

Session Organizers: Andreas Muschinski <muschinski@ecs.umass.edu>
 Ralph Latteck <latteck@iap-kborn.de>

Session Chairs: Andreas Muschinski <muschinski@ecs.umass.edu>
 Ralph Latteck <latteck@iap-kborn.de>

This session encompassed 14 oral and 4 poster presentations. Two invited talks were given: "The spatial distribution of Cn₂ in the convective boundary layer: a LES analysis" by Cheinet, and "Intermittent clutter echoes in radar wind profilers: Signal characteristics and filtering" by Lehmann.

Several presentations considered the refractive index structure at scale sizes considerably smaller than the vertical extent of the radar observation volume. Two modelling studies achieved this with significantly different approaches. One (Fritts) looked at the evolution of the temperature structure parameter in response to the shear instabilities associated with a monochromatic gravity wave in the mesosphere. The second (Cheinet) considered both the temperature and humidity structure parameters generated by convective plumes in the planetary boundary layer. The first of these studies suggests that radar returns will be predominantly from the edges rather than from the centre of the turbulent layers. This will lead to the magnitude of the velocity variability being underestimated. Another study (Muschinski) suggested that the value of the mean vertical velocities can be biased owing to the strong weighting of signals from regions of high reflectivity. Moreover, care must be taken to exclude the contributions from non-clear-air radar returns (including those from precipitation, birds, and ground-clutter) before an attempt is made to derive atmospheric data products from radar return signals (Lehmann). One presentation (Balsley) emphasised the need for in-situ measurements to be made at intervals as small as a metre. Richardson numbers of less than 0.25 are significantly more-commonly seen at these scales than they are at scales of many tens of metres. Such measurements can be made using radiosondes with under-filled balloons, which have a reduced ascent rate. Instrumented model aircraft offer an alternative platform for making small-scale measurements. Another presentation (Lee), which used in-situ turbulence measurements made from a manned aircraft, emphasised the difficulty of determining the largest scale size to consider when comparing with radar-derived spectral widths. In particular it can be difficult to determine at what scale size the transition from turbulence to gravity waves occurs. A consideration of the role of turbulence layer thickness on scattered power was used in one study (Singh) to understand radar height coverage. Another study (Housley) took a statistical approach to relate the refractive index structures seen at the small-scale to those seen at the radar observation volume scales.

Many presentations which considered radar returns from the mesosphere made use of observations made by more than one radar. One (Belova) compared the nature of (non-summer) VHF returns observed above northern-Scandinavia and those observed above southern-India. Although turbulent scatter could explain some of the northern-Scandinavian returns, an alternative mechanism was required to explain the south-Indian returns. A second presentation (Singer) examined the reason for the lower strength of Polar Mesosphere Summer Echoes (PMSEs) observed above northern Canada compared to those observed above northern-Scandinavia. This was attributed to the different sources of electrons within the polar cap and within the auroral oval. This study relied upon compensating the radar return strengths for the differences in peak transmitted power and sensitivity of the radars used. Another study (Strober) specifically considered the use of a calibrated noise source to perform absolute calibrations of individual radars. A third multi-radar study (Li) used calibrated 53.5 MHz and 500 MHz radar returns, from Svalbard, to derive the microphysical properties of mesospheric ice clouds. Another study (Swarnalingam) examined the aspect sensitivity of PMSEs from a decade of observations made at Resolute Bay. Amongst other things, this demonstrated that large aspect sensitivity tended to be associated with high signal power and small aspect sensitivity with low signal power. A final study of the mesosphere (Meek) involved an MF rather than a VHF radar and looked at the angle of arrival of echoes. Lightning generates ionisation trails through the atmosphere which are, in some respects, similar to those caused by meteors. One study (Beres) looked for the signatures of the radar echoes from these trails in the in-phase and quadrature samples. This study also made use of data from a passive Lightning Mapping Array, which give an accurate indication of the location of the lightning.

The discussion session emphasised the fact that despite several decades of research, the question of precisely what we are seeing with VHF radars remains difficult to answer. It was generally agreed that the simplistic idea of homogeneous, isotropic irregularities of refractive index uniformly filling the radar observation was seldom (if ever) applicable. The current attempts to model scatter from shear-induced turbulence generation were seen by many as being too simplistic. For example, it was felt that they should include the contributions of humidity and electron density to refractive index and that they should consider the effects of multiple rather than single gravity waves. Nevertheless, it was recognised that Kelvin-Helmholtz billow structures, similar to those produced by the model, were commonly seen in radar returns. The fact was raised that relatively little attention paid to the aspect sensitivity of radar returns in recent years. There were conflicting views as to whether specular reflection and isotropic scatter were entirely separate phenomena. For example, could temperature sheets arise from the top and bottom boundaries of a turbulent layer after thorough mixing? Or could spectral broadening arise from corrugations in a temperature sheet? With regards to mesospheric echoes, it was recognised that there was currently a strong emphasis on studies of northern hemisphere PMSEs. More attention needs to be given to mesospheric echoes observed during non-summer months and at other latitudes.

Summary of Session 2: New Instruments, Signal Processing and Quality Control

ISC representative:	Iain Reid	< iain.reid@adelaide.edu.au >
Session Organizer:	D. Narayana Rao	<profdnrao2001@yahoo.com>
	Iain Reid	< iain.reid@adelaide.edu.au >
Session Chair:	Iain Reid	< iain.reid@adelaide.edu.au >

In this session, 22 oral papers and 14 posters were presented. No invited talks were given. Topics focused on a few main areas.

Design and construction of digital receivers was an area of considerable interest. One or two papers on this topic appeared at MST11, but the number has increased here, with papers by Urbina et al., Sunderland et al., and McLaughlin et al. being presented. No fully operational system seems to have been yet developed, but the enhanced flexibility of a fully digital system was discussed, and no doubt this will be an area of even greater interest at later MST workshops.

The second area of focus was development of new radars, and results there-from. Nicolls et al. discussed the new AMISR-type radars, and especially the PFISR (Poker Flat Incoherent Scatter Radar). These radars use large numbers of small sub-antennas, each with their own small transmitter (typically 1 or 2 kW), to produce flexible beam steering and large power-aperture product. Other such radars of interest include the new MST radar under development at Andoya, Norway (Latteck et al.), the Japanese Pansy radar at Syowa in Antarctica, and a multiple-beam system for Mesospheric observations (Renkwitz et al.). Cohn et al. presented plans for a deployable modular radar especially for tropospheric studies. Lindseth et al. discussed engineering aspects of the 449 MHz profilers. Other new, but more traditional, radar designs were presented e.g. MST radars in China (Li Chen et al.) and India (Viswanathan et al. (200 MHz), Srinivasulu et al (UHF)). Bhattacharjee et al. discussed the problems involved in building a radar in the Himalayan mountains, where flat land is not available. Their current plan is to place the radar on the roof of a building.

An interesting variation on the theme of radar development was the presentation of papers concerning radar degradation. Eastment et al., and Hooper et al. looked at effects of physical degradation and in-built software errors associated with a traditional radar that had been active for many years. Other hard-ware-related projects included development of new beam-steering and beam-forming equipment (Aryal et al.).

Signal processing was another area of considerable interest, with a variety of areas of interest. New processes and filters were applied to the raw data and raw spectra (e.g. Anandan and Jagannatham, Kumar et al., Palo, and Pillai et al). Keuer et al. looked at implementation of pulse coding at MF to reduce the effects of man-made noise on MF radar data, Khandare looked at

monopulse systems for atmospheric tracking, and Hooper and Gaffard examined the optimum data lengths and temporal averaging required to produce the best wind data information.

Several papers discussed errors and impact of beam-broadening in spectral measurements, either in relation to its impact on the mean wind through shear effects (Chen and Chu, as well as Scipion et al. – one oral, one poster), or its impact on estimates of turbulence (Dehghan and Hocking) . In a different, but related aspect, Farag and Hocking used correlation between the vertical and horizontal winds to deduce information about the pointing angle of the nominally “vertical” beams used in VHF radar studies.

Another group of papers considered measurements of backscattered power, and presented methods to improve or calibrate radar backscattered powers (Jenn-Shyong Chen et al; Prakash et al.), to observe specific layers (especially the tropopause e.g. Kuyeng et al.) or to better visualize regions of turbulence in 3 dimensions (Nishimura et al.). The latter study is one of great interest for future developments of radar, and was also a topic of keen interest in the session on scattering processes.

Finally, further developments in Radio Acoustic Sounding, and associated measurements of temperature, were presented (Furumoto et al., Shinoda et al.).

Summary of Session 3: Meteors studied with MST radar

ISC representative: Wayne Hocking <whocking@uwo.ca>
 Session Organizers: Geetha Ramkumar <geetha_ramkumar@vssc.gov.in>
 Diego Janches <diego@cora.nwra.com>
 Session Chair: Ray Morris <ray.morris@aad.gov.au >

In this session, 14 oral papers (2 of which were invited), and 7 posters were presented. Meteor studies can broadly be divided into two main components: studies of the meteors themselves (generally considered as “astronomical studies”) and studies of the manner and consequences of their interaction with the atmosphere. The latter class is generally considered as “atmospheric studies”. Astronomical studies include such things as determination of fluxes, calculation of orbits, and determination of their origin. Atmospheric studies includes studies of the rate of expansion of the trail (relating to atmospheric temperature and pressure), the drift of the trails (leading to determination of atmospheric wind vectors), and chemistry.

The two invited talks were by Brown et al (wavelet algorithm for meteor identification) and Fritts et al. (the SAAMER radar). The second talk considered details for a new radar in southern Argentina which is designed to not only be usable as an all-sky radar, but can also be used to detect head echoes and other effects normally only possible with very large and powerful radars. Astronomical studies presented included studies of meteor shower radiants in the southern hemisphere (Younger et al.), calculation of meteoroid flux density for the Geminids (Verbeek and Ryabova), and a study of the Perseid meteor stream with the Gadanki radar (Reddy and Yellaiah). Galindo and Chau studied head-echoes with the large Jicamarca radar. Hibit et al. examined the seasonal and diurnal variability of both specular and non-specular meteor echoes. A few studies involved meteor deceleration, the nature of the meteor trails, and their rates of expansion. Janches et al. discussed differential ablation of micrometeors, and Younger et al. presented a paper on the evaporation, ionization and deceleration of the trails. Better knowledge of the rate of expansion is important for deriving atmospheric temperatures, and a second paper by Younger et al. looked at the effect of aerosols on meteor trail expansion. Keuer et al. presented details of the signatures of a fireball observed with both MHF and VHF radar over Europe.

Most of the rest of the papers discussed either meteor-atmosphere interactions, or measurement of atmospheric parameters from measurements of meteor characteristics, with the exception of Vaudrin and Palo, who discussed a new digital receiver for meteor studies.

Selvamurugan et al. concentrated on interactions between meteors and the E-region plasma, especially looking at E-region irregularities over Gadanki in two papers. Chilson et al. looked at the effect of charged aerosols on both PMSE and meteor decay times, hinting at the possibility that meteors detected in PMSE layers might produce biases in temperature estimations. Cheng et al. also looked at mesospheric temperatures deduced from meteor decay times. Meek and Manson studied reasons why the mean vertical wind determined with multi-meteor fits to mean wind field often produced apparent “vertical velocities” of tens of metres per second. Finally, several papers used the meteor echoes as tracers to determine atmospheric parameters, particularly winds (Antonita et al., Xiong et al., and Selvamurugan). Chu and Cheng examined gravity waves in the atmosphere, but unlike the other papers, which concentrated on underdense meteors, they used long-lived meteor trails for their studies.

Overall, the session produced a nice mixture of different types of meteor studies, from astronomical to atmospheric, and demonstrated the new capabilities to be found in this revamped field. At the end of the session about 20 minutes we spent discussing key topics. One point special note was the need to better understand the physics and chemistry of meteor trail expansion, especially as it relates to determination of temperature by meteor radar.

Summary of Session 4: Plasma Irregularities

ISC representatives:	Jorge Chau	<chau@geo.igp.gob.pe>
	Erhan Kudeki	<erhan@illinois.edu>
Session Organizers:	Mamuro Yamamoto	<yamamoto@rsh.kyoto-u.ac.jp>
	Amit Patra	<akpatra@narl.gov.in>
Session Chairs:	Micheal Nicolls	<michael.nicolls@sri.com>
	Gerald Lehmacher	<glehmac@clemson.edu>

This session was aimed to include reports and studies using MST-like radars to study mesospheric and ionospheric irregularities with special emphasis on:

1. PMSE (multifrequency, heating, interhemispheric comparisons)
2. Using radar echoes from plasma irregularities (EEJ, ESF, QP, 150-km echoes) to diagnose the ionosphere/atmosphere with coherent scatter radars (densities, temperatures, winds, electric fields)
3. 2D and 3D radar imaging of plasma irregularities

Two weeks before the workshop started, we had more than 24 scheduled presentations (15 oral and more than 9 posters), including 4 invited talks, covering the aforementioned topics. However, due to the swine flu, most of our Asian participants (India, Japan, and Taiwan) cancelled their trips. The final program consisted of 8 oral talks and 2 posters. The oral talks were divided into four for the ionospheric sub-session chair by Dr. Michael Nicolls, and four for the mesosphere sub-session chair by Dr. Gerald Lehmacher. Although the number of presentations was reduced, most of the topics were covered: ionospheric irregularities by the EAR radar (Fukao et al.), 150-km echoes using multi-beam and multi-frequency observations (Chau et al.), radar cross sections of equatorial mesospheric echoes (Kudeki et al.), optical emissions by high-power radiowaves (Kagan), multi-frequency studies of PMSE (Latteck et al. and La Hoz et al.), PMSE studies using the new AMISR radar in Poker Flat (Nicolls and Kelley), auroral E region echoes using SuperDarn (Koustov), MF and E region echoes (Ramani and Guruban) and PMSE Interhemispheric differences and similarities (Kirkwood et al.). This session ended with a short discussion around the following questions:

1. What is the relevance of this session for MST?
2. For PMSE, are low frequencies (MF, HF?) necessary?
3. How are PMSEs influenced by ionization, temperature, chemistry?
4. Is there a connection to the climate discussion?
5. Which other sites can contribute to PMSE studies?
6. Which other sites can contribute to 150-km echoes?

Summary of Session 5: Meteorology, Forecasting and Nowcasting

ISC Representative:	Phillip Chilson	<chilson@ou.edu>
Session Organizers:	William Brown	<wbrown@ucar.edu>
	Edwin Campos	<Edwin.Campos@ec.gc.ca>
Session Chairs:	William Brown	<wbrown@ucar.edu>
	Edwin Campos	<Edwin.Campos@ec.gc.ca>

The session dedicated to meteorology, forecasting, and nowcasting included a wide variety of topics focusing on wind profilers as both stand-alone and complementary instruments for weather observations. There were 21 oral and 9 posters presentations. The session commenced with an invited talk given by Taylor and Hocking, which described the implementation of the Canadian O-QNet and the impact it is having on forecasting in Canada. The O-QNet is a network of VHF wind profilers in Ontario and Quebec. Clearly wind profilers offer many benefits for the meteorological community and this presentation nicely set the stage for the remainder of the talks. It is exciting to consider the variety of uses of wind profiler data in meteorology; however, it is still somewhat frustrating that wind profilers are not used more widely in this capacity. It is incumbent on MST radar community to help promote the integration of wind profiler data into operational meteorology. It is difficult to find common themes, which can be used to describe the content of the many different presentations in this session. It is also difficult to outline the result of each presentation in this summary. Therefore, what follows is a brief overview highlighting some of the more prevalent research foci and some of the presentations that addressed them. It is followed by a summary of the moderated open discussion that followed the presentations.

Several of the talks and posters described studies and experiments in which observations from wind profilers and weather radars are integrated or the wind profiler is seen as a validation tool for other instruments (e.g., Argall, Barron, Caccia, Chilson, Mercer, and Zhang). It was shown during the session how these instruments complement and add value to one another. For example, wind profilers can be used to refine three-dimensional wind field analysis and dual-polarimetric weather radar can be used in conjunction with wind profilers to retrieve better height profiles of the vertical wind field and parameters associated with the drop size distributions. We will likely see even more collaborative uses of observational data sets such as these as the weather services move more towards a "network of networks" approach. Applying multiple sensors to address a particular forecasting goal could also become more prevalent as data assimilation techniques continue to improve. Other presentations focused more on the utility of wind profilers on their own merits for atmospheric studies (e.g., Brown, Cohn, Fukao, Williams, and Tabata). These presentations primarily spotlighted the utility of wind profiler observations for studies of the boundary layer and lower free atmosphere. These included measurements of rotors from a collection of boundary layer radars, studies of the marine boundary using a shipboard wind profiler, and dual frequency (UHF and VHF) wind profiler observations for the retrieval of precipitation parameters. Another theme during the session was the integration of wind profiler data into models (e.g., Gaffard, Kalia, Kirkwood, Mikami, and Tabata). It will be necessary to

demonstrate the utility of integrating wind profiler data into models if they are to have any significant impact on weather forecasting. Here a variety of models and data integration approaches were discussed. In one study, data from a wind profiler were compared against results from the Weather Research and Forecasting (WRF) model for the case of mountain induced waves. In another study, results from UHF and VHF wind profilers, together with other data sources such as surface stations were studied in conjunction with output from the Global Environmental Multiscale (GEM) model.

Other presentations concentrated more directly on the role of wind profilers for mesoscale forecasts (e.g., Campos, Mikami, and White). For example, wind profilers are being used to support weather forecasts for the Vancouver 2010 Olympic and Paralympic Winter Games. Also, it was shown how data from a network of UHF wind profilers was used on the island of Okinawa to observe meso-gamma-scale convective systems. Finally, there were a few presentations focusing on the use of wind profilers to study the relationship between meteorological phenomena and atmospheric dynamics (e.g., Klaus, Luce, and Serafimovich). One presentation revisited the retrieval of temperature data from wind profiler observations based on outer-scale turbulence considerations. It was also shown how range imaging data collected with the MU radar in Japan could be used to investigate Kelvin-Helmholtz instabilities up to an altitude of 16 km.

After the formal presentations by the speakers, an informal discussion of the key points from the session was conducted by the conveners. There were two extended discussions, one on the integration of wind profiler observations into forecasts from the weather services and one pertaining to the need for more measurements that offer good vertical resolution. Regarding the former, the discussion focused on the Japanese, UK, and US meteorological offices. Some points of the discussion were: 1) more work is needed in order to address the impact of wind profilers on forecasts; 2) it should be recognized that quality control of the data that is sent to the meteorological offices is very important, 3) not surprisingly wind profilers have the greatest potential for impacting forecasts at the mesoscale - the UK is pulling wind profiler data into the mesoscale forecasts; 4) progress in the area of data assimilation with respect to wind profilers has been slow; 5) wind profiler parameters offer other parameters besides just wind, which could be assimilated into models; and 6) stronger connections from the wind profiler community are needed within the meteorological schools. It was felt that more atmospheric observations with good vertical resolution (10s of meters or less) are needed in order to investigate the roles of different scattering mechanisms under various meteorological conditions. Range imaging was seen as a viable means of improving range resolution, but more fine-scale, in-situ comparisons are needed for validation and comparison. Range imaging could also be used to address the filling factor issue (see presentation by Klaus on the modeling of the outer scale of turbulence). The SOUSY radar at Jicamarca can make observations with a resolution of about 30 m and we are expecting interesting results along these lines with this system. Some of the other discussion points (in no particular order) include 1) vertical velocity biases in VHF wind profilers attributed to persistent tilted layers in the atmosphere; 2) the advantages of operating wind profilers at 50 MHz compared to 40 MHz on account of the background sky noise; 3) the utility of coupling wind profiler and lidar data when observing clouds; and 4) the utility of using wind profiler data (especially in connection with other observations such as weather radars) to retrieve drop size distributions aloft.

Summary of Session 6: Middle Atmosphere Dynamics and Structure

ISC Representative: Werner Singer <singer@iap-kborn.de>
 Session Organizers: S. Gurubaran <gurubara@iigs.iigm.res.in>
 Peter Hoffman <hoffmann@iap-kborn.de>
 Session Chairs: Iain Reid <iain.reid@adelaide.edu.au >
 William Ward <wward@unb.ca>
 Nick Mitchell <n.j.mitchell@bath.ac.uk>

Section 6 was a well attended session with 26 oral presentations and 11 posters. Topics were diverse and innovative, covering new complex measurement campaigns, planetary waves and tides, gravity waves and turbulence as well as long-term trends of mesospheric dynamics.

New Observations and measurement techniques

A new radar chain for mesospheric science from close to the North Pole to Antarctica was presented by Hocking et al. with a spacing of 10-15 degree in latitude. During the CAWSES Global Tidal Campaign five measurement campaigns were performed during the last four years. Ward et al. discussed first results and future investigations. Of special significance is the establishment of the equivalence of satellite and meteor radar observations of tides. Temperature and wind measurements in the MLT region using meteor radar and airglow in South Australia were presented by Reid et al. including a discussion of the diffusion of meteor trails sorted by echo strength, by height, and by radar frequency in respect of a correct data interpretation. D-region electron densities at 69°N have been derived from differential absorption and phase measurements using a narrow beam 3-MHz Doppler radar (Singer et al.). The ground-based electron densities are in good agreement with co-located simultaneous insitu measurements and both observations show during the occurrence of polar mesosphere summer echoes an electron biteout at PMSE-altitudes.

Planetary waves and tides

The impact of the low latitude 2-day wave on austral mesopause temperatures has been shown by Morris et al. by a January diminution in PMSE above Davis, Antarctica. Gurubaran et al. studied the tidal and planetary wave coupling in the low latitude MLTI region and showed that tides and planetary waves play a large role in ionospheric variability. The short-term variability of quasi 2-day waves and their interaction with tides in the MLT region using meteor radar observations was discussed by K. K. Kumar et al. Intraseasonal variations of 6 day waves in the low latitude middle atmosphere were investigated by R.K. Rao on the basis of meteor radar and MF radar zonal winds. Interference between tidal components are proposed by Ward et al. as possible explanation of the short-term variations in equatorial tides on the basis of results of the extended Canadian Middle Atmosphere model.

Gravity waves and turbulence

Meteor radar wind measurements were the main basis to establish characteristics of gravity waves in the MLT region (climatologies of gravity wave activity, propagation parameters, etc.). Snively et al. assessed gravity wave propagation characteristics with

simultaneous airglow imager and meteor radar winds. Climatologies of gravity wave activity observed by meteor radars were presented by Mitchell et al. for the Arctic and Antarctic mesosphere with increasing wave activity above 87 km in summer with modulation at tidal periods. The seasonal variation of wind variances and momentum fluxes has been examined by Placke et al. for high and mid-latitudes. In summer the strongest positive flux values are found along the line of the zonal wind reversal which shifts from higher to lower latitudes. The results are compared with model simulations. High frequency gravity waves generated at a tropical Indian station by deep convection are characterised by a dominant vertical wavelength of about 1.8 km in the lower stratosphere and wave periods between 8 and 80 minutes (M.C.A. Kumar et al.). Gravity wave variances during the passage of deep convective system were also studied by K.K. Kumar et al. where the gravity wave activity has been studied in terms of dynamical and convective instability using TIMED/SABER temperature observation.

Klaassen presented an important theoretical study to improve our incomplete understanding of the physical dissipation processes within an internal gravity wave field using a Lagrangian wave model rather than the common Eulerian formulation. Kelvin-Helmholtz instabilities (KHI) were observed in the equatorial mesosphere with the Jicamarca 50-MHz radar (Lehmacher et al.). The horizontal wavelength of the KH waves was in the order of 10 km. Various cases of the development of turbulence within the vortex rolls were observed, vortex centers of high reflectivity as well as centers of low reflectivity were found. Woodman presented hi-resolution radar billows in the upper troposphere (8-10 km) obtained with the SOUSY radar (37.5 m mode) at Jicamarca. The upper and lower boundaries of the “eye” were resolved with a calmer region in between.

Long term trends

G. Kishor Kumar et al. investigated long-term variations of low latitude mesospheric mean winds observed with the Indian MST radar, MF radars, M-100 rocket sondes and with the UARS/HRDI experiment. They found a clear semi-annual oscillation (SAO) in zonal winds with maxima during equinoxes and decreasing eastward directed winds in winter with time. The SAO shows a strong modulation by the mesospheric quasi-biennial oscillation. The long-term variability of mesospheric winds observed with MF radar (since 1984) and nightglow emissions from 87 and 97 km (since 1995) near Adelaide, Australia was presented by Reid and Woithe. Wind strength and nightglow intensity showed clear annual, semi-annual, and quasi-biennial oscillations. Talaat et al. studied the inter-annual variability of mesospheric waves (tides and planetary waves) derived from meteor wind observations by the HF SuperDARN network for periods up to more than a solar cycle. Possible relations to sudden stratospheric warmings and to the quasi-biennial oscillation were found.

Main points of the discussion are:

- Importance of observational networks that contribute to identifying and understanding large-scale features
- Necessity to understand conditions favouring regions of instabilities and their implications for dynamics – perhaps networks will help in this regard
- It is important to coordinate observations and collaboration between instrumental groups for proper interpretation of airglow data that inherently contain information on small as well as large-scale structures

Summary of Session 7: Tropopause processes and Stratospheric / Tropospheric Exchange

ISC Representative:	T. Tsuda	<tsuda@rish.kyoto-u.ac.jp>
Session Organizers:	David Tarasick	<david.tarasick@ec.gc.ca>
	Masayuki Yamamoto	<m-yamamo@rish.kyoto-u.ac.jp>
Session Chairs:	David Tarasick	<david.tarasick@ec.gc.ca>
	Hubert Luce	<luce@lseet.univ-tln.fr>

This session was an interesting mix of theory, observation (via radar and other instruments) and data interpretation. Many aspects of STE processes were discussed: transport of chemical species (ozone), synoptic-scale dynamics as seen in models, small-scale processes such as short-period gravity waves and shear instability, and “direct” STE by convective storms. There is still much room to discuss how the MST radar capability (high time and vertical resolution monitoring of wind and turbulence) can be used for validating and/or improving numerical models. The session successfully brought together researchers from different areas of atmospheric science. This cross-pollination was invigorating and will likely prove fruitful. More cross-communication in future is recommended.

T 7.1: The tropopause is a fundamental structure of the atmosphere. Pan examined models of the extratropical tropopause, particularly differences between the thermal, dynamical and chemical tropopause, as well as the “extratropical transition layer (ExTL)”, in which the air changes from tropospheric to stratospheric in character over a finite altitude. This may be a transport pathway. Pan showed results from the recent Stratosphere-Troposphere Analyses of Regional Transport Experiment 2008 (START2008), including examples of isentropic intrusions of subtropical tropospheric air into the extratropical stratosphere, a major mechanism for creating “double tropopauses”, and possibly related to other STE processes. Pan’s presentation highlighted the importance of chemical and dynamical processes in the upper troposphere and lower stratosphere (UTLS) region.

T 7.2: Using wind profiling radar and ozonesondes, Osman examined stratospheric intrusion events in February-April 2008 at Eureka, Canada. Intrusions of high ozone and low humidity air from stratosphere to troposphere were observed by ozonesondes, while radar echo power data showed a weakly defined tropopause. Vertical and horizontal wind variations were further investigated using radar data.

T7.3: Tarasick discussed combined ozonesonde and windprofiler studies of stratosphere-troposphere exchange (STE) in Ontario and Quebec. A strong relationship with discontinuities in the tropopause was found. Trajectory modeling with FLEXPART is able to reproduce the observations fairly well. Where the radar-determined tropopause differs from the thermal tropopause, the radar is typically responding to the sharp gradients of potential temperature and humidity at the lower edge of a stratospheric intrusion. This may explain the radar's success at finding STE events, and be used to follow the descent of stratospheric layers in the troposphere.

T7.4: Bourqui introduced some of the meteorological features leading to STE, and results using his LAGRANTO Lagrangian particle dispersion model (similar to FLEXPART). His analysis examined the dynamic behaviour of intrusions: some are coherent, with trajectories remaining close together over many hours or days, while others disperse rapidly. Coherence seems to depend on the existence of a stable layer underneath the intrusion.

T7.9: Using MST radar at a tropical station, Dutta showed that the likely source of short period (< 2 hour) gravity wave activity is convective activity, as short-period gravity wave activity is well-correlated with cumulus clouds as seen in outgoing longwave radiation and Tropical Rainfall Measurement Mission (TRMM) satellites. Dutta also showed that wind shear in the UTLS region also is an expected source of short period gravity waves. The results presented emphasized the ability of MST radars to reveal generation mechanisms and make quantitative observations of gravity waves in the UTLS region, which play a role in energy transport between the troposphere and the stratosphere.

T7.10: Using the range-imaging mode of the 47 MHz Equatorial Atmosphere Radar at Sumatra, Indonesia, Mega showed an upward-propagating wisp-like structure of Kelvin-Helmholtz billows with vertical resolution of several tens of meters and time resolution of about 16.4 s. The K-H instability occurred due to the decrease of the upper tropospheric easterly jet that commonly prevails over Indonesia. These results indicate that the range-imaging technique using multiple carrier frequencies is a promising tool for observing the fine structure of turbulence and associated wind disturbances by wave breaking.

The poster session offered many interesting observations of radar observations of gravity waves and related phenomena. Some highlights: Srivastava et al. (P7.2) showed reports of combined radar and lidar observations in the tropical UTLS region. Such observations can reveal quantitative links between cirrus cloud formation/maintenance/dissipation and turbulence. Using the MST radar in India, Siddarth (P7.4) and Kumar (P7.5) examined cases

of intense turbulence and air mass exchange in the UTLS region that occurred via convective storms reaching the tropopause altitude or above. Wave activity can affect tropopause height. Huixia He (P7.9) modeled stratospheric intrusions over Canada with the aid of a Lagrangian particle dispersion model (FLEXPART) and compared with profile observations from ozonesondes and the Tropospheric Emission Spectrometer (TES), as well as ground-based radar. During the ARC-IONS 2008 campaign in Canada, stratospheric intrusions were more frequent in summer than in spring.

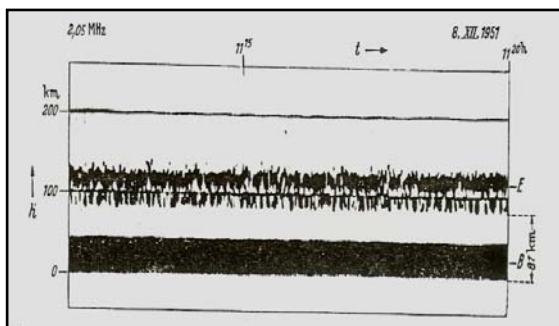
The Initial Decade of MST Radars: Looking back 30 - 40 Years 1971 - 1981

Jürgen Röttger <roettger@mps.mpg.de>
Max-Planck-Institute and
EISCAT-CAWSES-Copernicus, Germany

In the past 40 years the MST radar technique has established itself as an important tool to study the structure and dynamics of the lower and middle atmosphere. In this paper, presented at the 12th Workshop on Technical and Scientific Aspects of MST Radar in London, Ontario in May 2009, the early initial history of the development of the MST radar technique and some atmospheric science highlights, obtained from experiments, and meteorological applications will be summarized. When compiling the material for this paper it turned out that there is a very large amount of publications. It was tried to screen these objectively to present some highlights, but, admittedly, some selection criteria base on the author's memory and interpretations. In order to minimize the length of this paper, which is not considered to be a review paper, the developments presented cover only the first decade of this research area, namely the decade December 1971 to December 1981 with little overlap to earlier and later years.

The Very Early History

Scatter and reflection of electro-magnetic waves from irregularities in the refractive index of the Earth's atmosphere has been a very essential research subject in radio science. Total reflection of high-frequency radio waves as the major mechanism to study the ionosphere since the 1920s – 1930s using the traditional instruments, such as the ionosondes. Forward- and backscattering from atmospheric and ionospheric irregularities was also found at higher frequencies after the invention of the radar technique during the second world war, and have become most effective means to study the ionosphere and atmosphere. In the 1950s the so-called incoherent scatter technique (Gordon, 1958) was introduced for advanced ionospheric research and first observations of electron density profiles of the ionospheric F-region were performed at the University of Illinois in USA by Bowles (1958) using a VHF radar on 41 MHz. Subsequently two major facilities were constructed, one at the Earth magnetic dip equator in Jicamarca near Lima in Peru and another one at the subtropical location of Arecibo on Puerto Rico. Whereas Jicamarca used a phased array consisting of rows of coaxial-collinear dipoles, Arecibo uses a spherical dish which was illuminated by a feed in the focal area.



Actually, some of the first radar observations of the ionospheric D-region/mesosphere were done in the MF band in the early 1950s when studying ionospheric absorption.

Fig. 1 First radar observations of partial reflection on 2.05 MHz from 87 km height on 8 Dec. 1951 (Dieminger, 1952).

Dieminger (URSI Progress in Radio Science 1966-1969) claimed that the increase of absorption coincides with the occurrence of partial reflections related to an increase in ionization at heights below 100 km, which is controlled by the structure of the atmosphere (stratospheric warming) rather than by variation of solar radiation.

The two early incoherent scatter radars in Jicamarca and Arecibo have since proved to contribute essentially to the understanding of complex plasma processes in the Earth ionosphere and near-space environment. They had been the fore-runners of several of such radars, particularly set up in high auroral latitudes. More essentially for our applications, the Jicamarca radar was substantial for initializing the mesosphere-stratosphere-troposphere radar technique. Although Bowles (1957) was the first to report “ionospheric scattering of the turbulence variety” from altitudes of 75 km - 90 km measured with the Illinois VHF radar in USA (Fig. 2), and Flock and Balsley (1967) detected similar kind of echoes with the Jicamarca radar, it were R.F. Woodman and A. Guillen (1974), who substantially improved the technique by implementing coherent detection in order to measure velocities (Fig. 3). They also reported echoes from the stratosphere and recognized the great potential of this VHF radar technique for studying the mesosphere, stratosphere and the troposphere as well, introducing also velocity measurements.

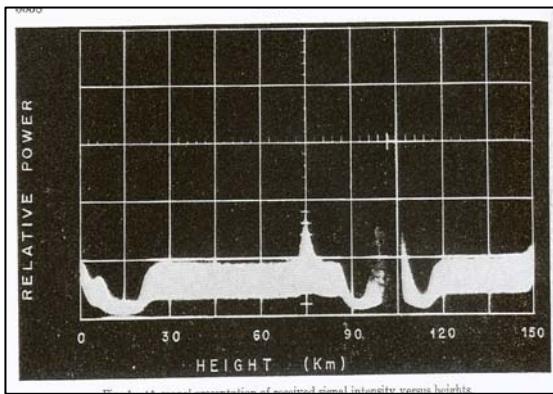


Fig. 2 A-scope presentation of signal intensity received with the Jicamarca VHF radar, showing echoes from 80 km altitude (Flock and Balsley, 1967).

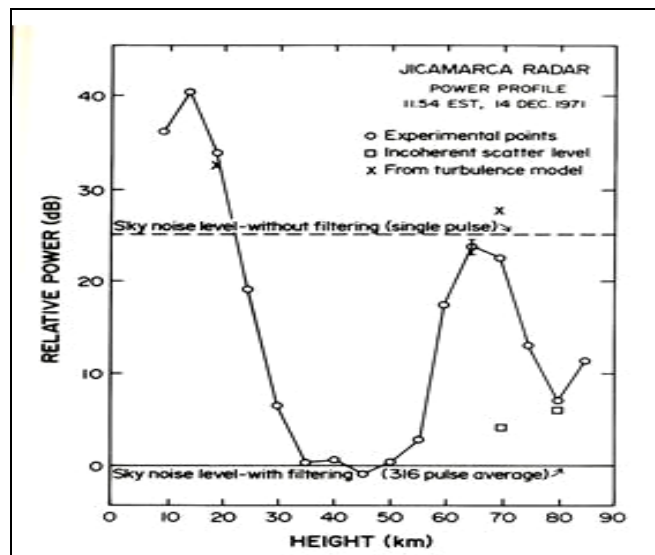


Fig. 3 First backscatter power profile obtained from fluctuations of the refractive index in the mesosphere, stratosphere and troposphere measured on 14 December 1971 with the 50 MHz radar at Jicamarca, Peru (Woodman and Guillen, 1974).

The observations with the Jicamarca radar showed that the relative echo power of this newly detected type of backscatter from altitudes below 100 km was significantly stronger than the underlying incoherent scatter from the ionospheric D-region and that the echo signals were much more coherent than the incoherent scatter signals. A coherent signal is defined here to exhibit long temporal persistency over many interpulse periods. That means, the coherent signals do not substantially change amplitude and phase over one millisecond. This is significantly dissimilar to the incoherent scatter signals.

The coherency of this new type of radar signals from altitudes below 100 km allowed application of novel radar coding and data pre-processing techniques such as the so-called pulse-to-pulse coding and coherent integration and filtering techniques. It then was already shown that the echoes from the mesosphere are caused by scatter from irregularities of the radio refractive index, which are caused by neutral atmosphere turbulence mixing the electron density distribution of the lower ionosphere. This not only opened a possibility to measure mean and fluctuating wind velocities from the Doppler frequency shift and spread, but also yield information on atmospheric turbulence. Whereas the scattering irregularities in the mesosphere are electron density disturbances, in the stratosphere these are caused by temperature variations and in the troposphere by temperature and humidity variations, respectively.

The Development of MST Radar System Concepts and New Radars

Following these striking observations with the Jicamarca radar (Fig. 4 shows part of the large coaxial-collinear antenna array) a fairly explosive growth and development in coherent backscatter radars for studying the structure and dynamics of the troposphere and stratosphere had subsequently occurred. These radars were all operating in the low VHF band at frequencies around 50 MHz and their name **MST radars** (standing for **M**esosphere – **S**tratosphere – **T**roposphere radars) was casted during a small radar workshop at the University of Utah in December 1977. Because these all operate in the lower VHF band between 40 MHz and 55 MHz, they are also called VHF radars.

In the middle of the 1970s two new radars were developed almost in parallel, the Sunset VHF radar (operated on 40.5 MHz) near Boulder in Colorado and the SOUSY VHF radar (53.5 MHz) in Germany. They both used the basic novel, but enhanced data processing techniques introduced in Jicamarca. The Sunset radar applied a coaxial cable version of the Jicamarca antenna array (Fig. 4) and the SOUSY (**S**ounding **S**ystem) radar applied a new approach combining a large array set of Yagi antennas (Figures 5 and 6).



Fig. 4 Part of the coaxial-collinear phased array antenna of the Jicamarca radar.

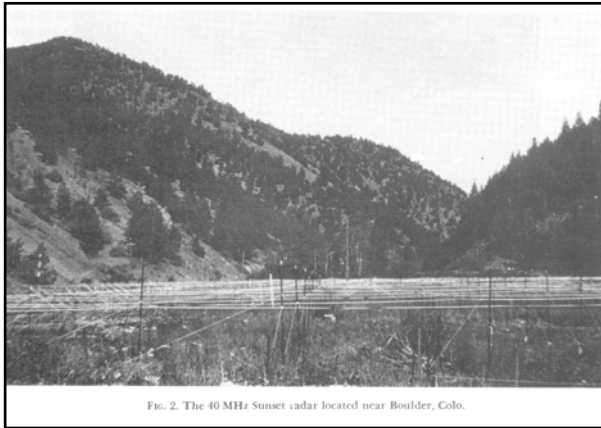


FIG. 2. The 40 MHz Sunset radar located near Boulder, Colo.

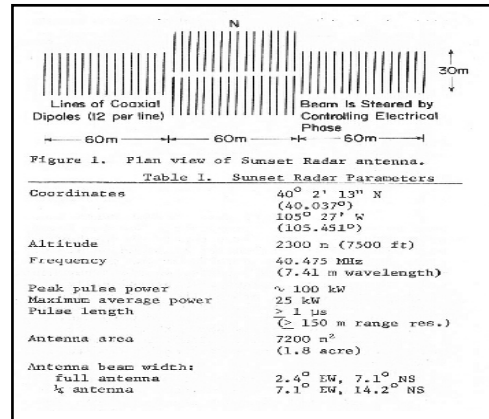


Fig. 5 The Sunset VHF radar coaxial-collinear antenna array (from Gage and Balsley, 1978 and Green et al., 1975).

COHERENT PULSED VHF RADAR
53.5 MHz, 600 kW (24 kW av.)

ANTENNAS (QUASI-VERT. BEAM):
196 YAGIS (STEERABLE), 31 dB
3x32 YAGIS (DRIFT), 3x22 dB

OPT. HEIGHT RESOLUTION ~50 m

INVESTIGATIONS OF THE
STRUCTURE AND DYNAMICS OF
TROPOSPHERE, STRATOSPHERE,
AND MESOSPHERE



SOUSY-VHF-RADAR
MAX-PLANCK-INSTITUT FÜR AERONOMIE



Fig. 6 SOUSY VHF Radar in the German Harz mountains showing the basements of the Yagi antenna forming the arrays (after Röttger et al. 1978).

All the MST radars are applying antenna beams pointing to or close to the zenith direction. Their beam widths in the order of a few degrees require their antenna array diameter to be at least ten wavelengths. The wavelengths of the VHF radars are between 7.5 and 5.5 m. This leads to antenna arrays of the VHF radars between at least 50 m and more than 100 m diameter. This leads to antenna gains in the order of 30 dB or more (30 dB correspond to a power increase of 3 orders of magnitude). In order to enhance the signal-to-noise ratio of the backscattered signals further, the VHF radars apply peak transmitter powers of some 100 kW up to some 1000 kW.

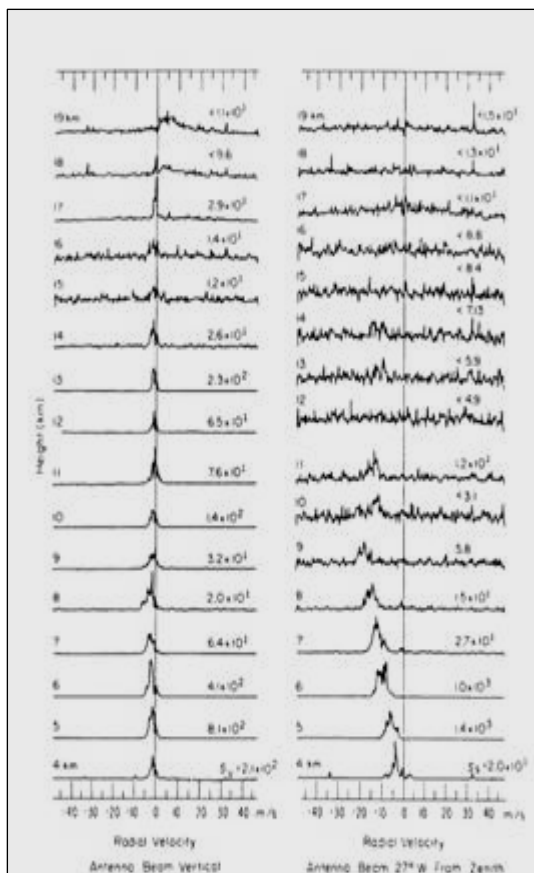


Fig. 7 Doppler spectra received by the 40.5 MHz Sunset radar with vertically pointing (left panel) and off-vertical beams (right panel); from Gage and Green, 1978.

velocity), can well be recognized in the Figure 7, which shows the first spectra of tropospheric and lower stratospheric backscatter from altitudes of 4 km to 19 km observed in early 1977 with the Sunset VHF radar (Gage and Green, 1978). The left-hand panel shows the spectra measured with the vertically pointing antenna beam, and the right-hand panel shows those measured with the off-vertical beam. Since the vertical wind velocity is usually much weaker than the horizontal wind velocity, the Doppler frequency shift of the spectra of the former is much smaller than that of the latter. It could immediately be shown that the horizontal wind velocities which were measured by VHF radar are similar to wind velocities observed by the standard operational radiosondes used by national weather services.

Whereas signals in Figure 7 can be recognized up to 19 km height with the vertical beam, they disappear already around 10 km when one observes with the off-vertical beam. These initial observations of the lower stratosphere and troposphere altitudes, thus, show that the echo power from the zenith direction is stronger than the one from the off-zenith directions. This angular dependence of the echo power points to a so-called aspect sensitivity, which means that the backscattering irregularities have a larger extent in the horizontal than in the vertical direction, i.e. they are anisotropic.

The Sunset Radar, located in a narrow Rocky Mountain canyon to shield for scatter returns from distant mountains, operated with vertical and off vertical beams in order to measure vertical and horizontal wind velocities, which are deduced from the Doppler frequency shift of the received echo. This is a simple principle as well, since the Doppler frequency shift of the echo signal from the vertical beam is directly resulting from the vertical wind velocity component. Thus, measuring Doppler frequency shift can immediately yield the velocity with the precautions which are described in the later literature. The off-vertical beam directions, usually in the order of 10-15 degree zenith angle, are used to measure the combination of the components of the vertical and horizontal wind velocity. By suitably combining these velocities, the three-dimensional wind velocity components are deduced. The Doppler frequency shift, which results from the bulk velocity of scattering irregularities (the bulk velocity corresponds to the wind

The observations with the Jicamarca and Sunset radar were at range (height) resolutions in the order of one kilometer, the SOUSY VHF radar was from the beginning designed for a much finer height resolution of < 150 m. This turned out to be an essential component of this atmospheric radar research, which was an additional new finding in atmospheric VHF radar science.

Some Important Characteristics of Atmospheric Radar Echoes

First observations with the SOUSY VHF Radar showed that there are very thin sheets and layers of irregularities, which required studies with at least a height resolution of 150 m (corresponding to range gating at 1 micro-second). Fig. 8 shows an example which proves that the Doppler frequency spectra of range gates separated by only 150 m have quite a different characteristic.

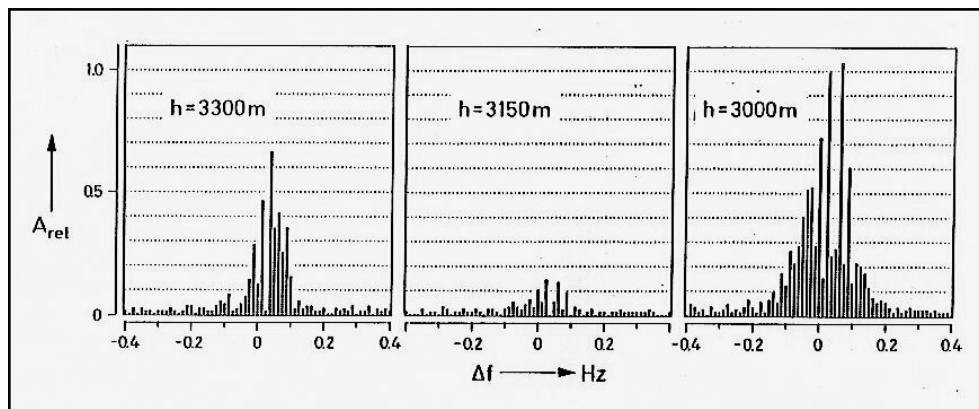
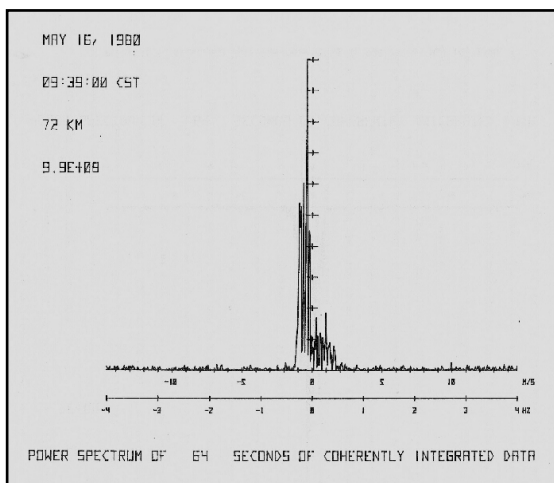


Fig. 8 Spectra of tropospheric echoes measured with 150m height resolution with the SOUSY VHF Radar in August 1977 (from Röttger and Liu, 1978)



First of all, Figure 8 shows that the mean signal power, which is the integral over the spectra, differs substantially over 150 m. This is an indication that there are thin layers of less than 150 m thickness, which comprise a large difference in scatter cross section. Further, the spectra indicate a very spiky nature, which means that the scattering irregularities are quite inhomogeneous. This was also observed in mesospheric echoes observed with the Urbana radar. So far these characteristics were mainly investigated with MF radars (Hocking, 1979).

Fig. 9 Non-Gaussian spectrum of a mesospheric echo described in angular and temporal characteristics of partial reflection from the D-region of the ionosphere observed with the 40-MHz radar in Urbana, Illinois, USA (from Gibbs and Bowhill, 1983).

The partial specular-type reflection observed by the MF and VHF radars as well are connected to a dedicated aspect sensitivity as was clearly noticed in the early experiments. Figure 10 shows an example. It also proves the existence of thin layers of reflectivity range-squared correction of the received echo power).

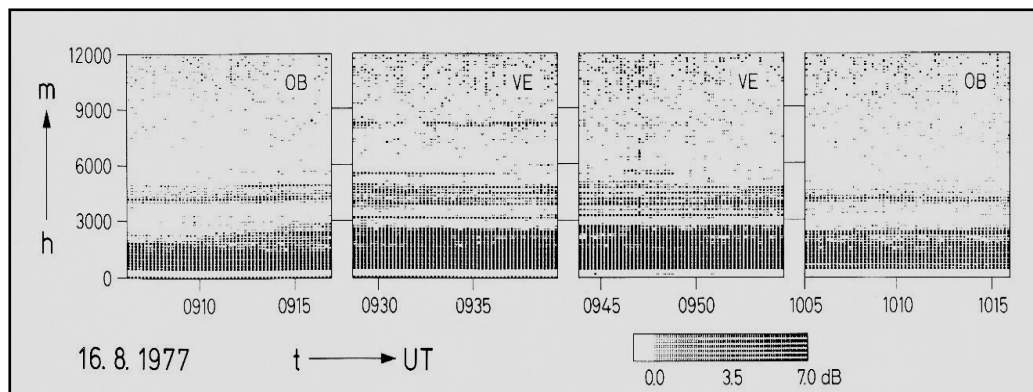


Fig. 10 Structure of VHF radar reflectivity observed with the SOUSY VHF radar antenna pointing into vertical direction (VE) and into oblique direction (OB) at an angle of 12.5 degrees off the zenith direction (Röttger and Liu, 1978).

Scattering and Partial Specular Reflection

In early theories (Ottersten, 1969) the so-called turbulence refractive index structure constant had been derived which assumes that radar backscatter is essentially caused by turbulent fluctuations of the radio refractive index of the clear air, such as humidity and temperature variations in the lower troposphere. The backscatter results from the spatial refractive index variations at half the radar wavelength for monostatic radars (i.e. where transmitter and receiver antennas are at the same location). This is the so-called Bragg-condition, namely that scattered signals constructively interfere for those irregularity spatial spectral components at half a radar wavelength. The turbulence refractive index structure constant then determines the scatter cross section of the Bragg-scale irregularities causing the radar echoes.

A comparison of the scatter cross section deduced theoretically for reasonable turbulence intensity conditions demonstrated that the measured cross sections in the troposphere and lower stratosphere are much larger than the theory allowed. Since this was particularly pronounced when the antenna beams were pointing vertically, the intention was investigated whether these vertical radar echoes are caused by some kind of partial reflection from horizontally stratified refractive index variations. It actually could be shown that such kind of partial, specular-type reflection can actually occur provided that there are vertical steps in the refractive index which are less than or in the order the radar wavelength. This had been debated since, because such steps have to have considerable horizontal extent just like a thin sheet and there must be some, yet unknown atmospheric phenomena to create these steps. It had, though, been adopted as the only viable explanation and was called Fresnel reflection or Fresnel scattering, presuming that there are several of such thin sheets of horizontal size close to the horizontal size of a Fresnel zone superimposing (Fig. 11). A Fresnel zone is the plane area perpendicular to

the wave propagation over which the distance to the transmitting antenna is one-half the wavelength. It was also reasonably assumed, by interpreting the spikes in the Doppler frequency spectra (Figures 8 and 9), that these sheets must exhibit

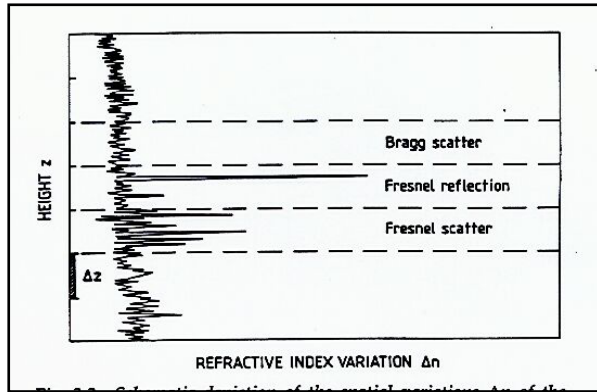


Fig. 11 Schematic depiction of spatial variations of the refractive index variations introduced by Gage and Balsley, 1980 and Röttger, 1980. This graph was published in Röttger and Larsen (1990).

some roughness (as suggested by Beckman and Spizzichino, 1963), i.e. they are vertically and horizontally corrugated surfaces of refractive index

structures. We need to note here that this type of Fresnel scatter can explain the echoes from the troposphere and in particular from the more stratified stratosphere, but that turbulence scatter is mostly the dominating factor in the mesosphere, except of the special kind of Polar Mesosphere Summer Echoes, which were detected at the of the 1970s and discussed here later.

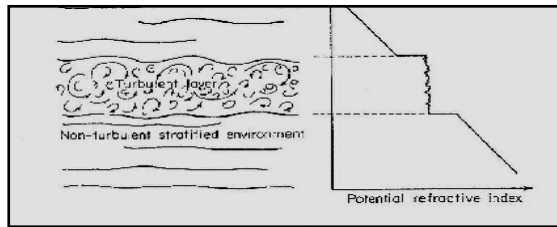


Fig. 12 Gradient mixing proposed by Bolgiano (1968).

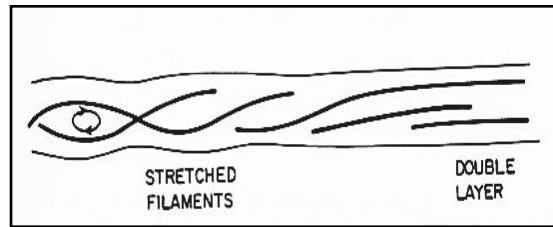


Fig. 13 Development of a Kelvin-Helmholtz-Instability, by Browning (1970).

In Fig. 12 the basic idea of Bolgiano of 1966 is sketched showing a turbulent layer in the environment of a stably stratified environment, as it develops from KHI (Fig. 13). Due to the mixing in the turbulent layer any passive tracer, such as the potential refractive index, is mixed homogeneously. This results in steps of refractive index at the bottom and top of the turbulent layer. These are the “sheets” noted in VHF radar observations. In the ocean thermocline they are steps in temperature. It was suggested by Röttger (1980) that one can learn from high-resolution observations of the ocean, and that such temperature steps are the reason for the aspect sensitive VHF radar echoes from the stratosphere as well as in the troposphere, but there also steps in humidity have to be considered, and in the mesosphere these are induced steps in electron density. It is regarded as self-evident that these horizontally stratified sheets are corrugated by the corresponding turbulence layers or their fossil remnants (Fig. 13). They are in a stable environment, which explains their large horizontal coherence (aspect sensitivity) and temporal coherence (Fig. 14, left). The shorter correlation time would correspond to a wider spectrum (Fig. 14, right).

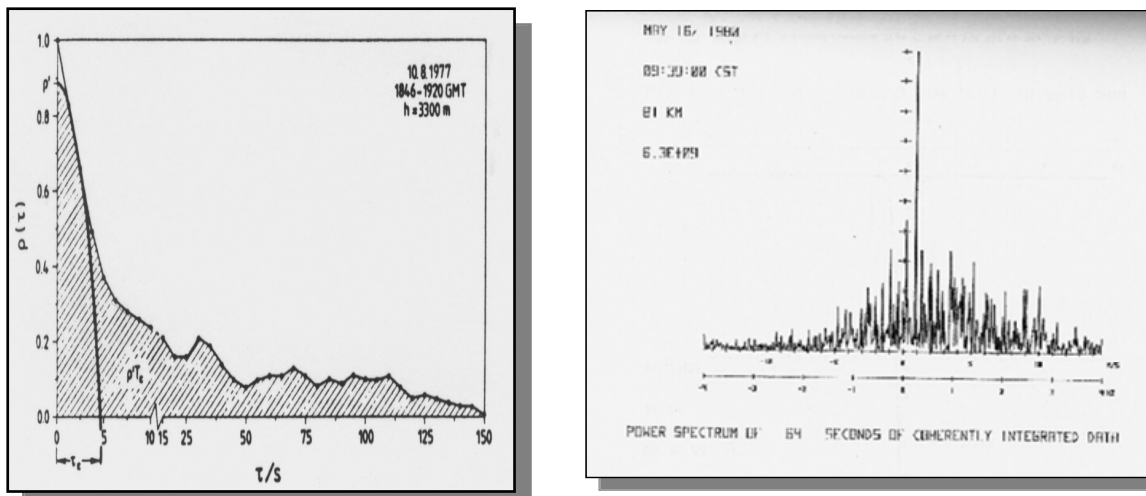


Fig.14 *Left: Autocorrelation function of a tropospheric VHF radar echo showing micro-scale and integral-scale correlation times denoting Fresnel scatter and partial reflection, respectively (from Röttger and Liu, 1978). Right: Broad spectrum of mesospheric echoes showing individual clusters of spikes (see also Fig. 9) consistent with a longer than micro-scale correlation time. (from Gibbs and Bowhill, 1983).*

Consequences of Aspect Sensitivity, Stability and Surface Roughness of Reflectivity Sheets

In this context of Fresnel reflection and scattering the finding of the aspect sensitivity was also further studied, since it is a clear sign of an anisotropic structure of the irregularities. We see in Figure 15 some early profiles observed with 150 m height resolution and vertically and oblique antenna beam pointing, which proves the great difference in received echo power in these two directions, which is attributed to the anisotropy of the irregularities responsible for the radar echoes. We note highest anisotropy in the stratosphere (above about 10-12 km), which is expected since, due to its positive gradient of temperature, the stratosphere is very stable and stratified, as its name expresses. The increase in vertical echo power at about 12 km is due to the very steep gradient of temperature above the tropopause, and thus is used to determine the height of the tropopause. Since the troposphere is usually not as stable as the stratosphere, the anisotropy is less, as we note in the Figure 15. On the 20 June 1978, when the echoes from vertical and oblique directions were almost equal below 9 km, the scatter cross section in the troposphere were almost homogeneous, which occurred during strong isotropic clear air turbulence conditions.

The enhanced echo power characteristic for vertical beam observations and the existence of corrugated refractive index structures, drifting overhead the VHF radar led to the application of the spaced antenna method for the measurement of horizontal velocities as described in the next chapter.

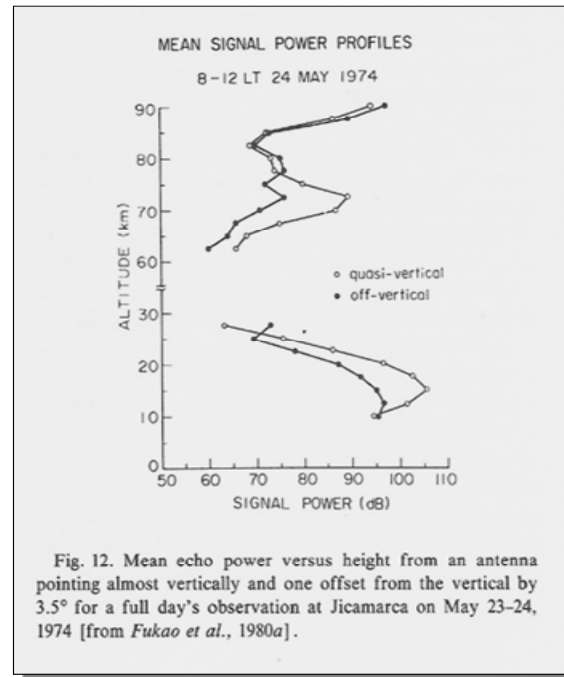
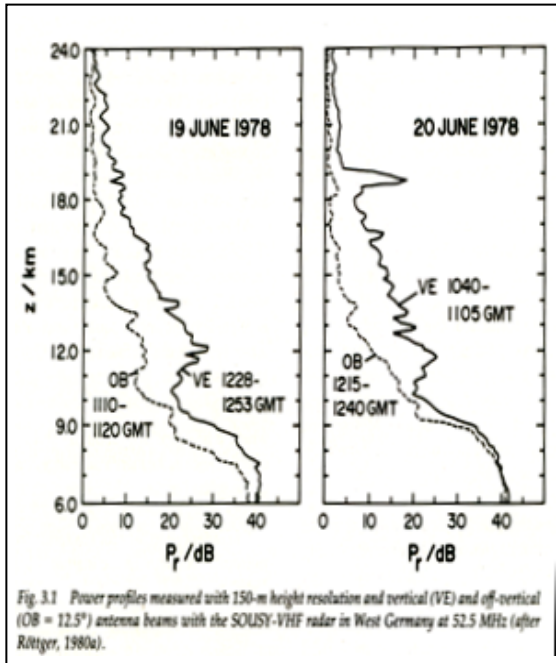
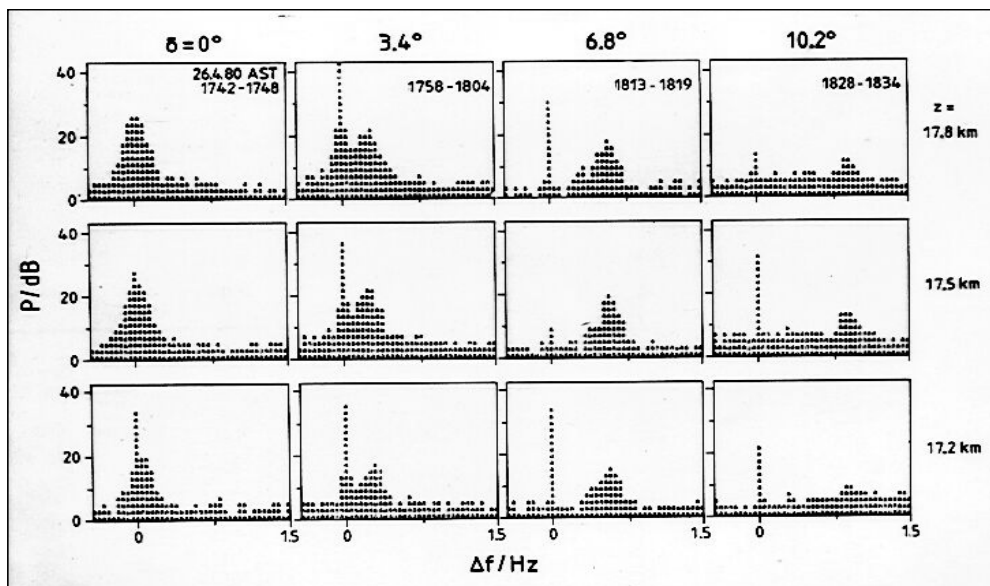


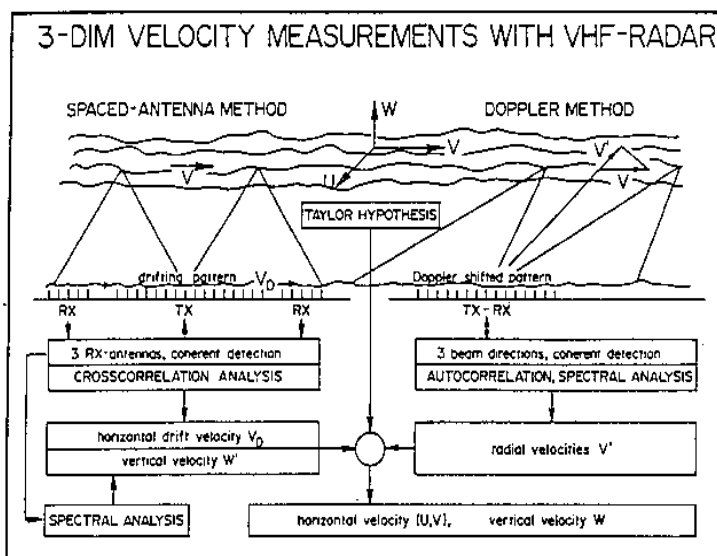
Fig. 15 Left: Power profiles measured with the SOUSY VHF Radar pointing into vertical (VE) and oblique (OB = 12.5 degrees zenith angle) direction (after Röttger, 1980).

Right: Power profiles measured with the Jicamarca VHF radar showing aspect sensitivity at 3.5° zenith angle, even in the lower mesosphere (from Fukao et al., 1980).



Two VHF Radar Methods for Measuring the Horizontal Wind velocity

As described, the three wind velocity components can be measured by pointing the radar antenna beam into several directions close to the zenith. Resulting from the discovery of aspect sensitivity and Fresnel scatter/reflection from corrugated refractive index layers, another method was introduced to measure the horizontal wind components. This is the so-called spaced antenna drift method, which makes use of the fact that the corrugated refractive index surfaces are moving with the background wind. For the application of this method three co-planar receiving antennas are employed, which measure the electro-magnetic field pattern of the backscattered signals on the ground.



When the scattering entities are move with the wind, the pattern on the ground moves as well. Cross correlating the signals from these three (or more antennas) yield the drift velocity, which was shown to be the horizontal wind velocity (Röttger and Vincent, 1978).

Fig. 17a outlines these two methods, which became known as the Spaced Antenna Drift (SA) method and the Doppler Beam Swinging (DBS) method after Röttger, 1981).

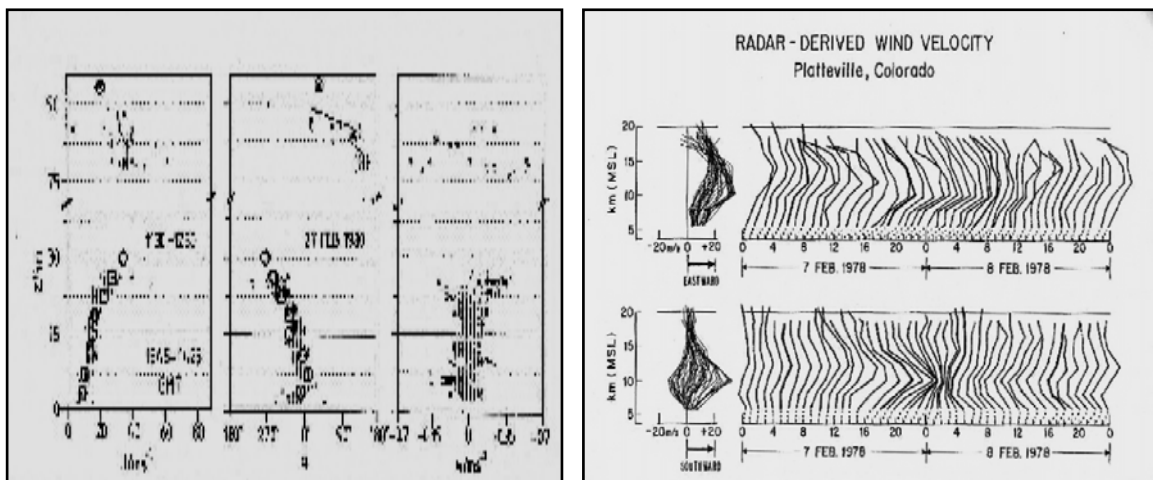


Fig. 17b Left (from Röttger and Czechowsky, 1980.): Profiles of horizontal (and vertical) winds in the troposphere measured with the SA method of the SOUSY VHF Radar (the circles denote radiosonde winds) and the right-hand panel shows the vertical velocity Right (from Ecklund and Balsley., 1979); Wind profiles measured with the DBS method of the Platteville VHF radar, showing the a jet-stream development around 10 km height.

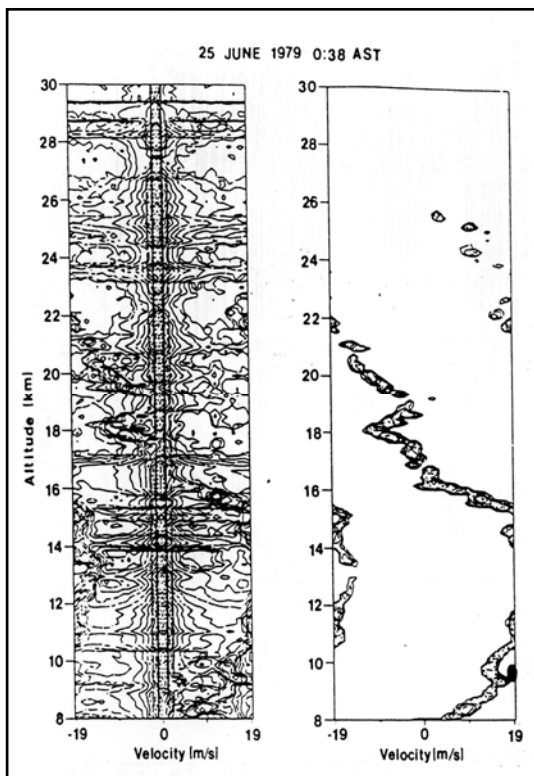


Fig. 18 Velocity contour plots measured with the Arecibo 430 MHz radar under strong ground clutter conditions (left) and after its removal (right), from Sato and Woodman, 1982.

The Arecibo radar, operating on 430 MHz with a very high average power of 120 kW, was also used in the end of the 1970s for observations of the stratosphere and troposphere. The peculiar configuration of the feed system this radar, located high above the spherical dish antenna, caused strong ground clutter echoes to dominate the echoes from the atmosphere at these short ranges of the lower atmosphere (as compared to those at a few hundred kilometers of concern for the primary ionospheric observations with that system). To reduce these clutter effects Sato and Woodman (1982) developed a non-linear parameter estimation technique, which included removing also the fading clutter (causing a widening of the spectral line at zero Doppler frequency shift) and the instrumental biases. Fig. 18 shows the original spectra and the cleaned ones resulting from the application of this algorithm.

The Middle Atmosphere Program and Radar Meteorology

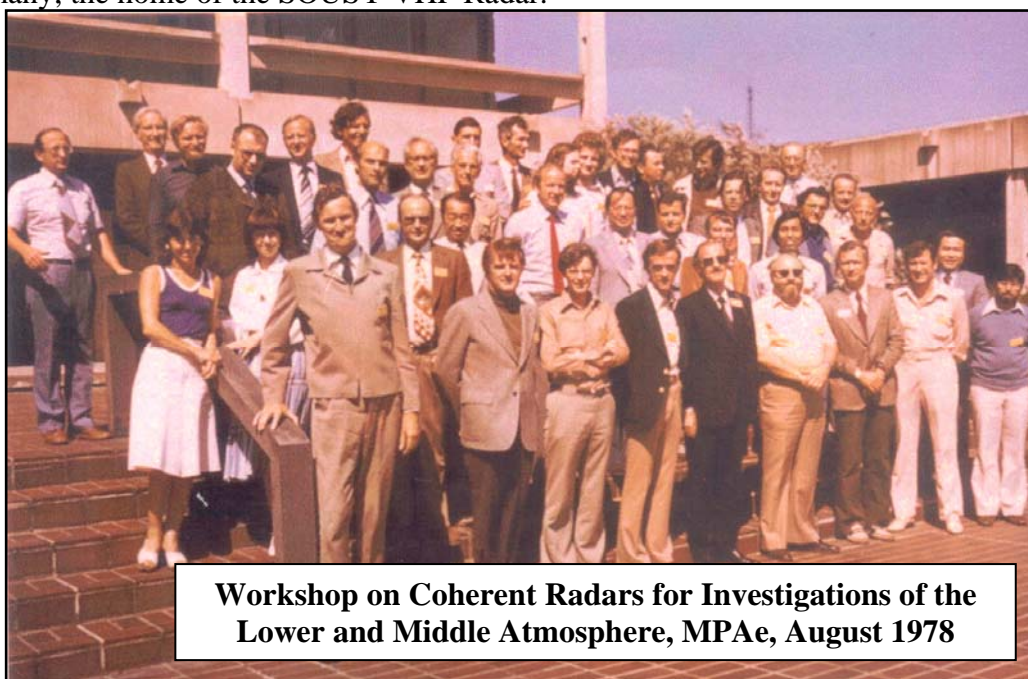
During the middle and late 1970s a major international program was established: The Middle Atmosphere Program (MAP), since it was recognized that the altitude region between the tropopause and the lower thermosphere (called the middle atmosphere) was the most unexplored region of the Earth's atmosphere. This program, installed under the Scientific Committee on Solar Terrestrial Physics (SCOSTEP), boosted the funding for further MST radar systems, which were regarded as substantial for the research during MAP. Also the International Union of Radio Science (URSI) had recognized the importance of these new radar systems already in 1975 at the URSI General Assembly in Lima, Peru.

18th URSI General Assembly in Lima, Peru. Session on VHF radar with Ben Balsley, Tom VanZandt, Jules Fejer, Prabhat Rastogi, Jürgen Röttger, Rüdiger Rüster et al.



The goals of MAP were intensively established during the International Symposium on Middle Atmosphere Dynamics and Transport 28 July – 1 August 1980 at Urbana, Illinois, USA. The contributions to these workshops, symposia and conferences were meticulously collected and published in the MAP Handbooks, edited and published by the Aeronomy Laboratory at the University of Illinois in Urbana.

Since the late 1970s also regular workshops were held, which brought together the radar designing engineers and the scientific user community. These workshops on technical and scientific aspects of MST radar were substantial for the mutual understanding of the engineering and the scientific community, which was another benefit observed during the historical development of the MST radars. The first one (MST-0) was held in August 1978 at the Max-Planck-Institute for Aeronomie in Lindau, Germany, the home of the SOUSY VHF Radar.



Workshop on Coherent Radars for Investigations of the Lower and Middle Atmosphere, MPAe, August 1978

This early workshop was attended by distinguished MST radar representatives, such as Sid Bowhill, Ben Balsley, Bob Vincent, Don Farley, Phil McClure, Bob Hunsucker, Prabhat Rastogi, Susumu Kato, Sho Fukao, K.C. Yeh, Earl Gossard, Bob Crane, Tom VanZandt, Adolf Ebel, Francoir Bertin, Bill Gordon, Ron Woodman, Jules Fejer, Lance Thomas, the MPI SOUSY group members and many others.



SOUSY-VHF Radar with K. Meyer and K.D. Preschel



K.C. Yeh, R.K. Crane, R.F. Woodman in the SOUSY array

Further workshops of this kind followed at the University of Illinois in Urbana-Champaign, USA (“MST-1” in 1983), and at several other places. All these MST Radar Workshops were documented in Proceedings, the early ones were edited under Sidney A. Bowhill by Belva Edwards and later published as MAP Handbooks. (The 12th MST radar workshop MST-12 was held in London, Ontario/Canada in May 2009). At the end of the 1970s special journal issues were published containing highlights of MST radar research. The original one was published in *Radio Science*, volume 15.2, in March-August 1980 under the guest editors Earl E. Gossard and K.C. Yeh. This special issue on “Radar Investigations of the Clear Air” contained the first review of MST radar studies of the middle atmosphere by Bob M. Harper and Bill E. Gordon, the description of the MST radar in Pokerflat by Ben B. Balsley, Warner L. Ecklund, Dave A. Carter and Paul E. Johnston, the initial design concept of the middle and upper atmosphere radar (MUR) by Shoichiro Fukao, Susumu Kato, Takehiko Aso, M. Sasada and T. Makihira, a coherent integrator-decoder preprocessor by R.F. Woodman, R.P. Kugel and J. Röttger, scattering and reflection mechanisms of clear air echoes from the troposphere, stratosphere and mesosphere by Ken S. Gage and Ben B. Balsley, reflection and scattering of VHF radar signals from atmospheric refractivity structures by J. Röttger, scattering of VHF and UHF signals from the turbulent air by C.H. Liu and K.C. Yeh, spaced antenna VHF radar observations of tropospheric velocities and irregularities by Bob A. Vincent and J. Röttger, VHF radar measurements during a jet stream passage by Rüdiger Ruster and Peter Czechowsky, observations of stable layers in the troposphere and stratosphere by John L. Green and Ken S. Gage, use of Doppler radar for the measurement of atmospheric turbulence parameters from the intensity of clear air echoes by Ken S. Gage, John L. Green and Tom E. VanZandt, high resolution stratospheric measurements with the Arecibo 430-MHz radar as well as the Arecibo 2380-MHz radar by Ron F. Woodman, measurements of short-period gravity waves and related scattering properties at 13-25 km over Jicamarca by S. Fukao, K. Wagasuki and S. Kato, depolarization of 50-MHz radar waves backscattered from the middle atmosphere by Wagasuki, S. Kato and S. Fuka and radio wave scattering from the tropical mesosphere observed with the Jicamarca 50-MHz radar by Sho Fukao, Toru Sato, Robert M. Harper and Susumu Kato.



**International Symposium on
Middle Atmosphere
Dynamics and Transport**
28 July – 1 August 1980
Urbana, Illinois.
MAP Handbook Vol. 2

**URSI/SCOSTEP Workshop
on Technical Aspects of
MST Radar MST - 1**
23 – 27 May 1983
Urbana, Illinois.
MAP Handbook Vol. 9

Up to the time when these first MST radar measurements were done, merely radars at higher frequencies up to the range of several 1000 MHz were used, which are sensitive to backscatter from precipitation (Battan, 1973). Some of these radars could also observe clear air turbulence, when they were using very high power and large antenna gain. Questions then came up why one needs to operate radars at such low frequencies around 50 MHz and whether there would be a scientific or operational merit in their applications. The atmospheric radar community, generally using these weather radars, was represented in the regular Conferences on Radar Meteorology of the American Meteorological Society (AMS) and it took until about the end of the 1970s and early 1980s to convince this community about the merits of the MST radars. A break-through occurred in the 19th and 20th Conferences on Radar Meteorology in Miami and Boston, respectively, when special sessions were introduced on VHF/UHF radar technique and such a progress that reviews in the Bulletin of the American Meteorological Society, published by Gage and Balsley (1978) and Larsen and Röttger (printed in 1990 by the American Meteorological Society), were accepted. A strong proponent of this development was David Atlas. It also turned out that the MST radar technique, applied with lower power and smaller antennas and thus covering only the troposphere and lower stratosphere (then called ST radars), is quite suitable for meteorological applications for continuous wind profiling (Röttger, 1981). An initial attempt was done with the SOUSY VHF Radar to produce profiles in real-time (Fig. 19). Although the SOUSY VHF Radar was never really employed as wind profiler, several special-purpose radars were built and operated thereafter for meteorological operations (Strauch et al., 1982).

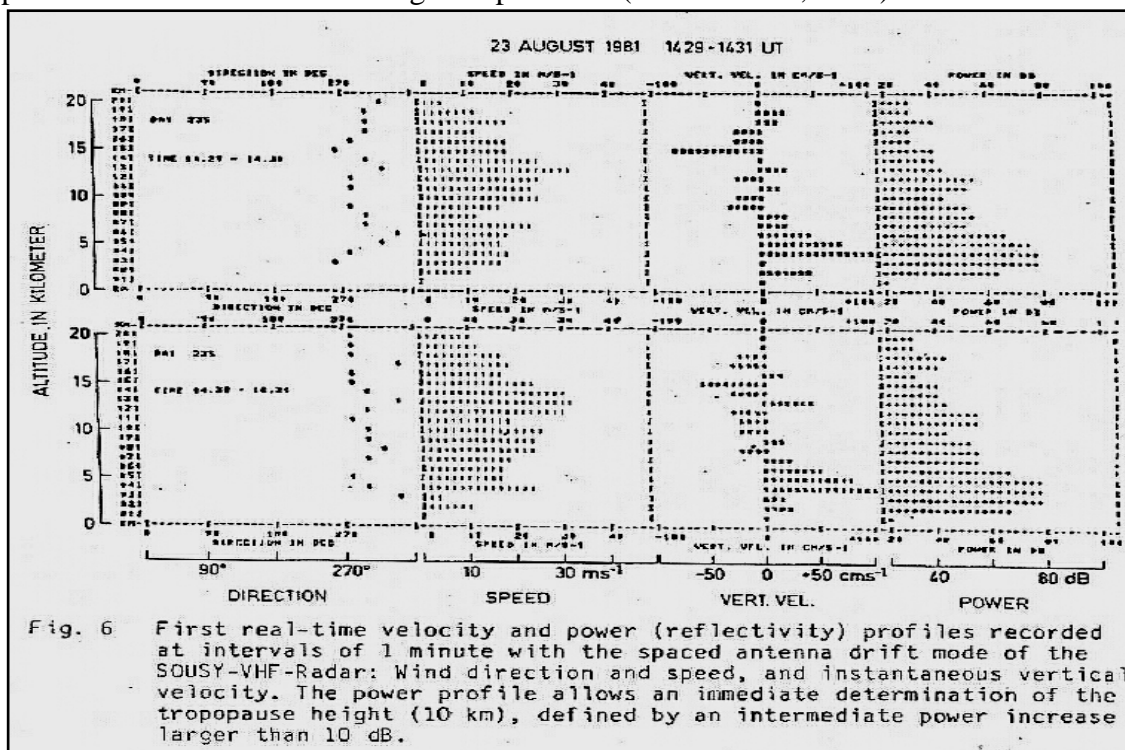


Fig. 19 Real-time profiling of the troposphere and lower stratosphere obtained with the SOUSY VHF Radar in the Harz mountains, Germany, on 23 August 1981 (published by Röttger in 1984, PolarFront).

Some New Technical Developments

To apply the VHF radar technique some new developments were necessary, such as Yagi phased array design with electronic beam steering, wide-band transmitters to allow high range resolution, fast transmit-receive switches, coherent detection and integration as well as binary phase coding, and special digital pre-processors, etc.

The application of complementary coding was novel (published by Schmidt et al., 19xx). It is applicable to VHF MST radars due to the long coherence time of the radar echoes. Fig. 20 shows an A-scope display of the RF output of a complementary coded transmitted signal and the sketch of a block diagram of a digital integrator-decoder.

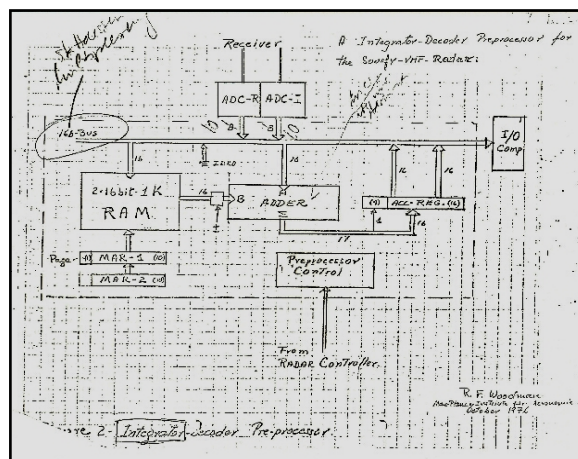
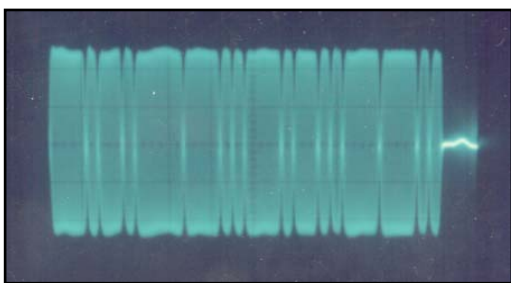
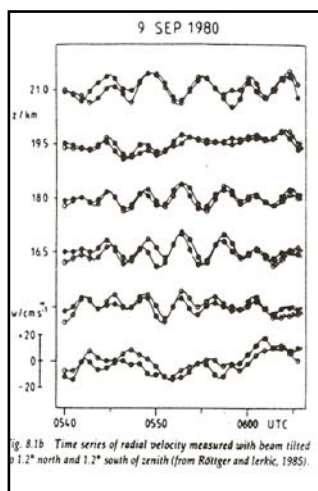
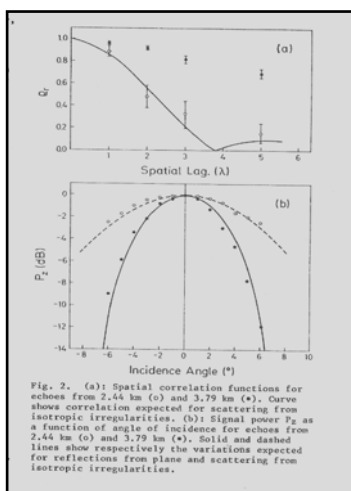


Fig. 20 A-scope display of one pair part of a 32-bit complementary code and block-diagram (right) of pre-processor (Woodman et al., 1980).



The application of the spaced-antenna technique did, besides its usage to measure horizontal wind velocities, yield another important complement to study atmospheric structures and dynamics, namely the interferometry and digital beam forming. The first results were obtained with the SOUSY VHF Radar in 1978 as shown in Fig. 21. The pointing angle was changed by off-line insertions of phase differences to the digital data.

Fig. 21 Left: First measurements of the aspect sensitivity by spaced antenna off-line digital beam forming with the SOUSY-VHF Radar in 1978 (Röttger and Vincent, 1978). Right: Pointing the antenna beam digitally into two directions and deducing the phase difference of radial velocities allowed for the first time to deduce horizontal phase velocities and other parameters of atmospheric gravity waves as well as to track turbulence patches and correct velocities (published by Röttger, 1984, and Röttger and Ierick, 1985).

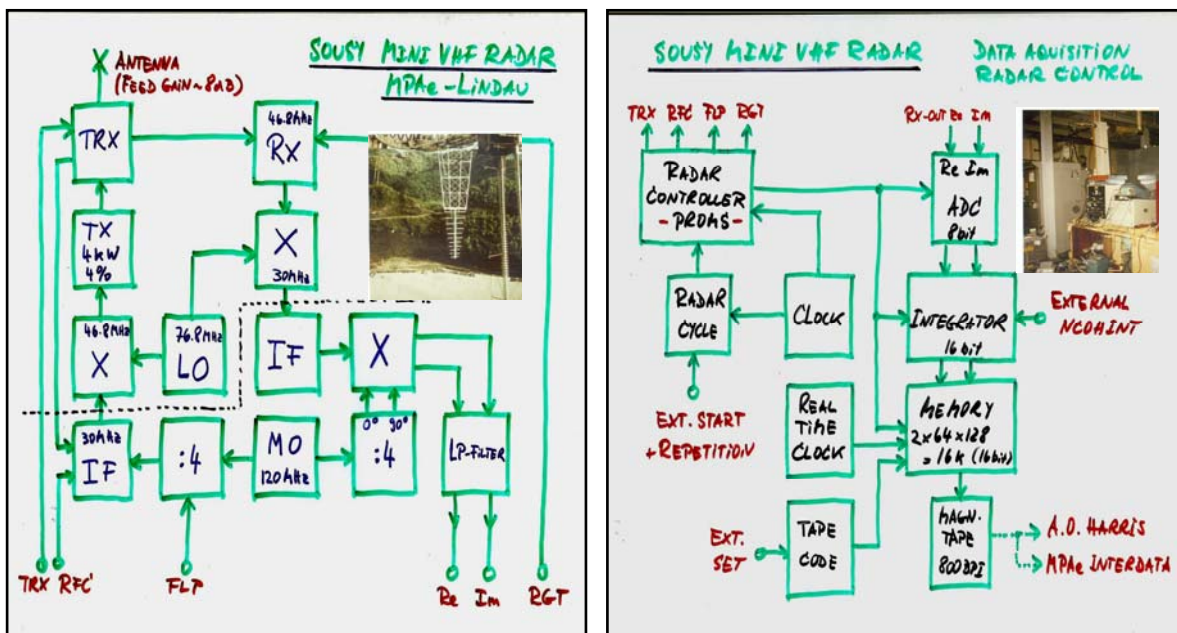


Fig. 22 The block-diagram of the SOUSY Mini VHF radar (4 kW peak power and 4% duty cycle at 46.8 MHz) which was used around 1980 at the Arecibo Observatory with a special broad-band feed illuminating the 305m spherical reflector (left-hand photo inset) and its stand-alone radar control and data acquisition unit (right-hand photo inset).

The large effective aperture of the Arecibo dish of 13000 m, deduced for the 46.8-MHz radar configuration, provided an excellent sensitivity despite the low average transmitter power of 160 W (Röttger et al., 1981). Figure 22 shows wind profiles measured with this configuration which compared very well with wind measurements with the Arecibo 430-MHz radar even up to 20 km altitude. This mini-radar was thereafter replaced by the mobile SOUSY radar running at 150 kW peak power. This allowed high sensitivity observations further up into the stratosphere and the mesosphere as well (these latter ones were possible already with the 4 kW mini-system).

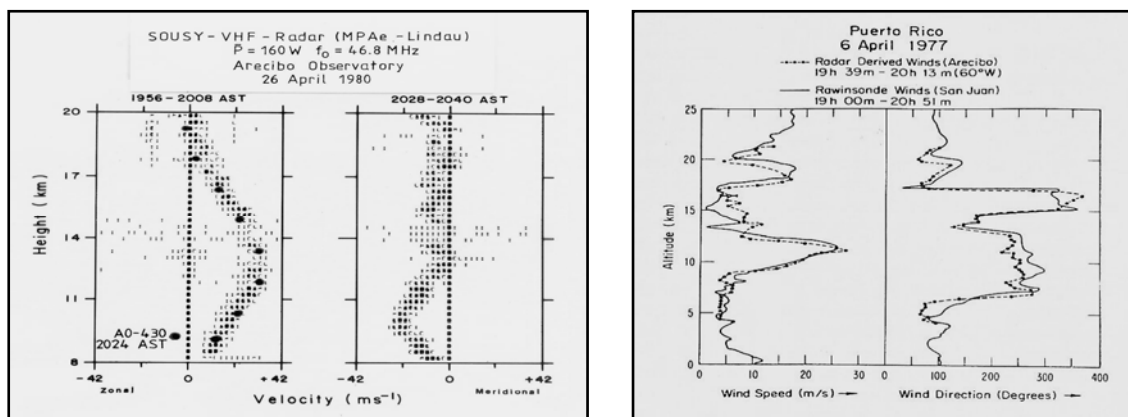


Fig. 23 Left: Wind velocity profiles obtained at Arecibo with the low power SOUSY VHF radar on 46.8- MHz and the high power (> 1 MW) UHF radar on 430 MHz, both using the Arecibo 300 m dish. Right: Wind velocity with 430-MHz radar and radiosonde profiles (Farley et al., 1979).

VHF Radar Observations of the Mesosphere

The maximum stratospheric height of the just presented 430 MHz observations is about 26 km, which is essentially given by decrease of refractive index variations on given turbulence Bragg scatter scale (0.35 m for this radar) with altitude. The high frequency of 430 MHz also prevents to use this radar for observations of turbulence scatter from the mesosphere as observed with the 50-MHz radar of Jicamarca (see Fig. 3). The radio refractive index in the mesosphere is inversely proportional to the square of the radar frequency, since it depends on the dispersion by the electron density at those altitudes. This means, the lower the radar frequency the better is the chance to observe mesospheric echoes. For this purpose, the 46.8 MHz SOUSY VHF radar was operated at the Arecibo observatory around the years 1979-1981 (Röttger et al., 1981, Czechowsky et al., 1983). It allowed to measure tropospheric, stratospheric and mesospheric echoes. The latter are shown in Fig. 23. This plot, presenting continuous observations over 3 days, clearly demonstrates the occurrence of mesospheric echoes during day time only, i.e. when the electron density was sufficiently high. However, the echoes were also confined to 60 to 85 km, where the lower height is given by the diminishing electron density and the upper height by the disappearance of turbulence at the Bragg scale of this radar (i.e. 3,2 m). The echoes occurring between 90 km and 110 km are from meteor trails (mainly in the morning hours), which were later used for wind and temperature deductions. Figure 24 shows the intermittency and persistency of thin sheets and layers, which needs high range resolution measurements (<300 m), and is typical for many mesosphere observations.

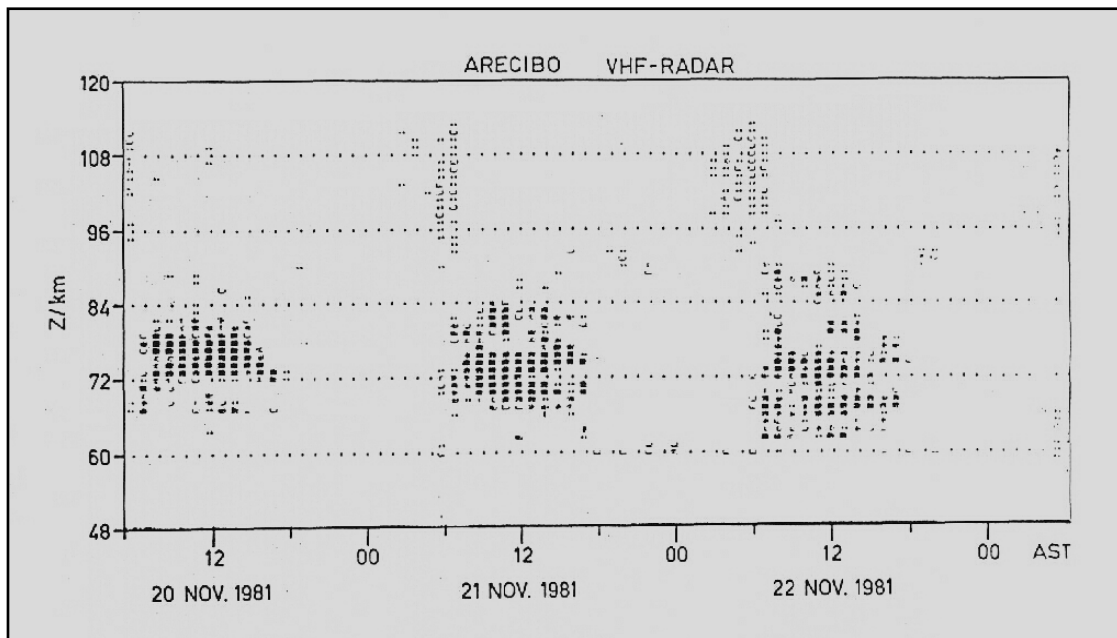


Fig. 24 Diurnal and day-to-day occurrence of mesospheric echoes VHF radar echoes measured with the mobile SOUSY VHF radar at Arecibo Observatory. The diurnal variation of VHF radar echoes is very clearly seen here, which results from the D-region ionization minimum during nighttime (from Röttger, 1984).

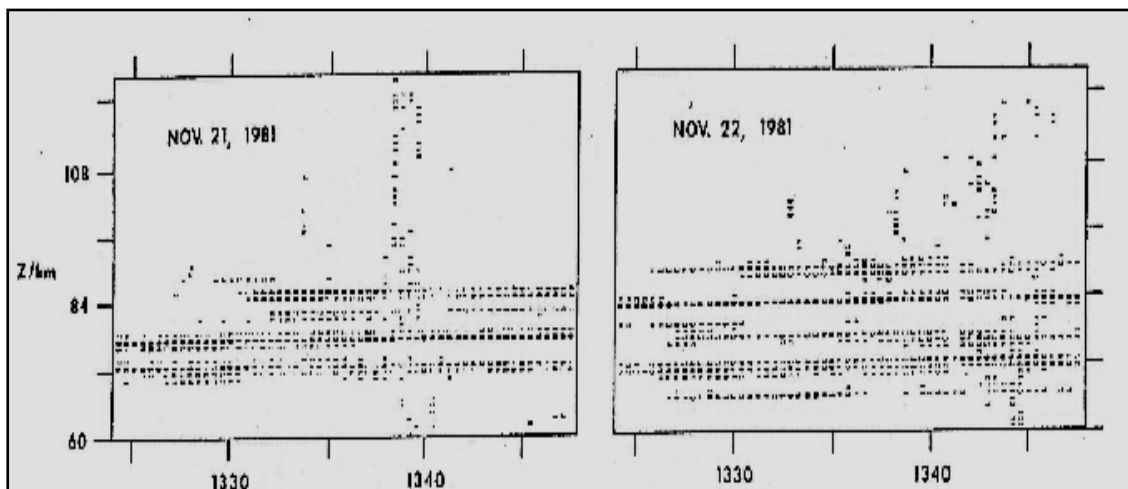


Fig. 25 Typical mesospheric VHF radar echoes as measured at the Arecibo Observatory in November 1981 (published by Röttger, 1987) showing the evident thin layering of mesospheric reflectivity structures.

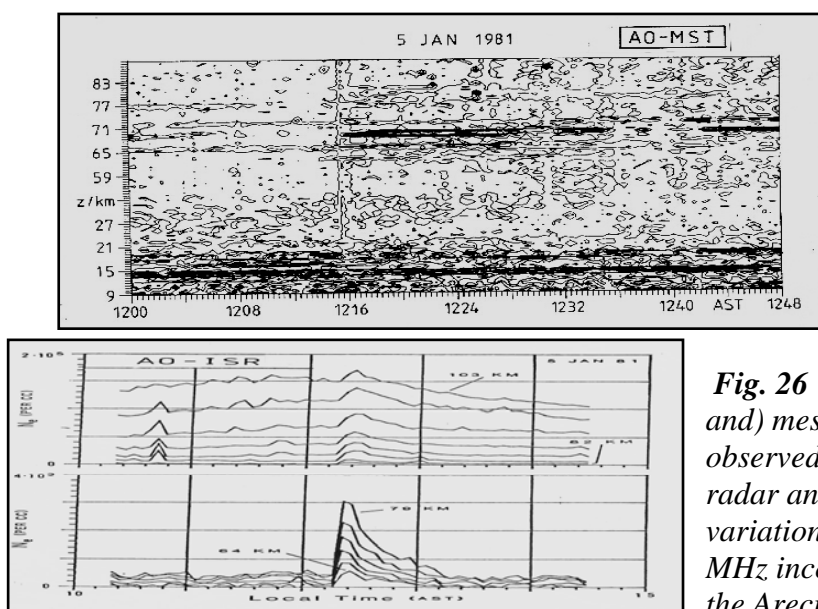


Fig. 26 Graph of (stratospheric and) mesospheric layers observed by the 46.8 MHz MST radar and electron density variations observed by the 430-MHz incoherent scatter radar at the Arecibo Observatory.

An impressive proof for the dependence of VHF mesosphere echoes on the electron density was obtained by simultaneous operations of the SOUSY VHF radar (46.8 MHz) in the MST mode and the UHF radar (430 MHz) at the Arecibo Observatory. On 5 January 1981 a burst of solar x-rays increased the electron density (lower graph of Fig. 25) and simultaneously the reflectivity of mesospheric layers increased (upper graph of Fig. 25). This was described in detail by Röttger et al. (1983) and Rastogi et al. (1986). Stratospheric and tropospheric turbulence structures and their thickness, intensity and intermittency were also studied with radar, however, care has to be taken here due to the involvement of specular-type reflection, which is particularly important at the longer

wavelength VHF (50 MHz) radars. It does not seem to appear at shorter wavelengths, such as the Arecibo 430-MHz and 2380-MHz radar (Woodman, 1980a, b).

Incoherent scatter radar reflectivity is very much weaker than the MST radar reflectivity as it was shown by Woodman and Guillen (1974); see Fig.3. This dependence and the scattering mechanism was investigated quite deeply already using the Jicamarca VHF radar in collaboration with the Aeronomy Laboratory at the University of Illinois in Urbana-Champaign during the 1970 decade. K.P. Gibbs and S.A. Bowhill elaborated this in the Aeronomy Report No. 110 “An Investigation P.K. Rastogi and S.A. Bowhill have meticulously described the features of mesospheric returns, namely their intermittency, their estimated vertical thickness of a few tens of meters and horizontal extent of several kilometers etc. This is published 1975 in the Aeronomy Report No. 68 “Remote Sensing of the Mesosphere Using the Jicamarca Incoherent-Scatter Radar”, and by Rastogi and Woodman (1976). Rastogi and Bowhill (1975) had for instance already shown a correlation between signal correlation time and

relative signal power by analyzing Jicamarca mesosphere data of 1972 (see Figure 26).

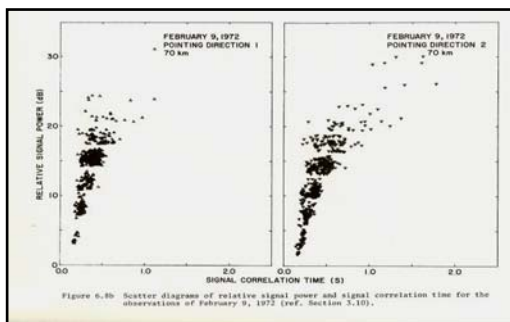


Fig. 27 Jicamarca radar signal correlation time and mesospheric signal power (Rastogi and Bowhill, 1975).

Also the Urbana VHF radar, operating on 40.92 MHz, was used for this purpose. This was described in 1979 in the Aeronomy Report No. 90 “The Urbana Coherent-Scatter Radar: Synthesis and First Results” by K.P. Gibbs and S.A. Bowhill (1979). It was shown that there is a clear day-to-day variability and velocity measurements were done as well, although with a fairly coarse height resolution of 1-2 km only.

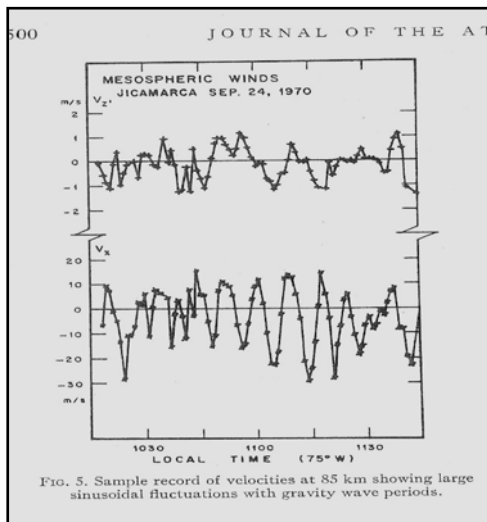


Fig. 28 Early velocity measurements of the mesosphere with the Jicamarca radar (from Woodman and Guillen, 1974)

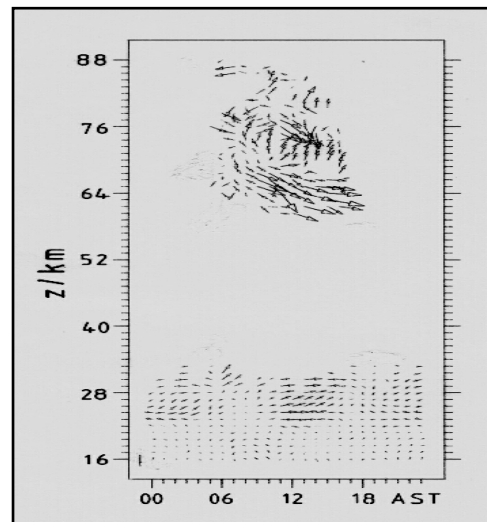


Fig. 29 Mesosphere-stratosphere-troposphere measurements of horizontal velocities with Arecibo VHF radar.

Velocity measurements had also been done with the Jicamarca VHF radar. These showed distinct sinusoidal oscillations (Figure 27). It turned out that such velocity data are eminent for studies of atmospheric gravity waves, their propagation, breaking and momentum transfer. Also tidal oscillations of winds in the mesosphere were noticed with these radars (Figures 28 and 29).

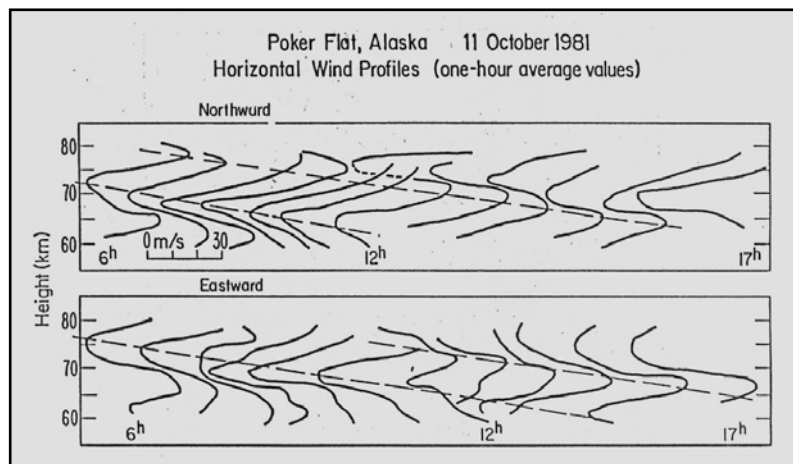


Fig. 30 Meridional and zonal wind in the mesosphere over Poker Flat in the Arctic, showing downward phase progression, likely due to tides. (from Ecklund and Balsley, 1981).

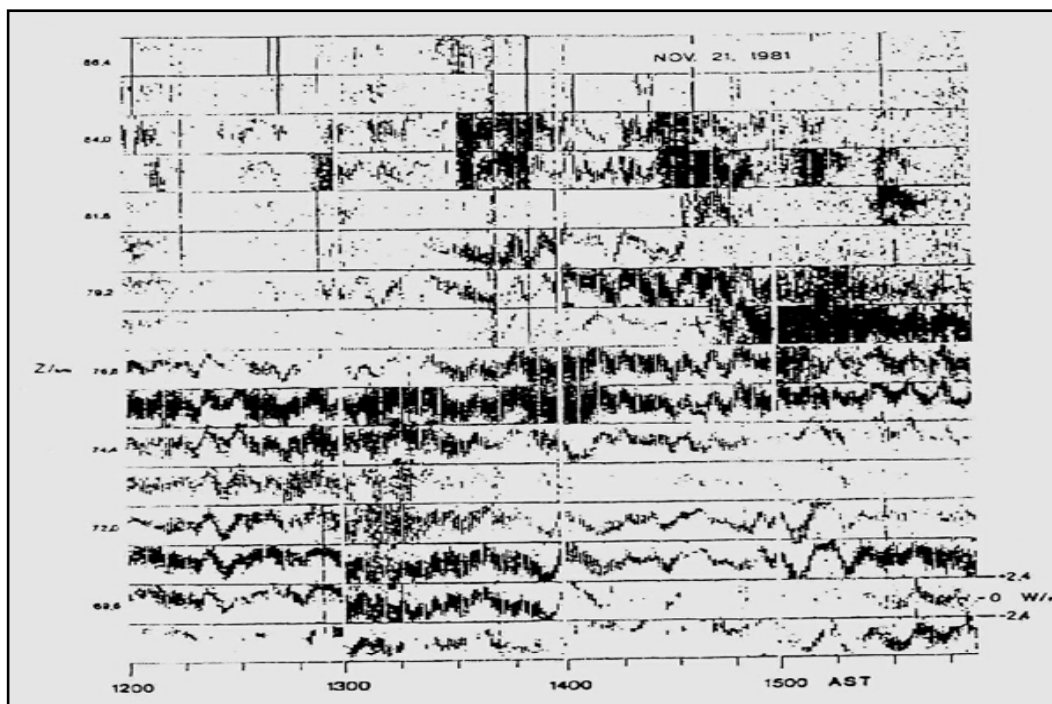


Fig. 31 Intensity plots of spectra showing mesospheric wave and turbulence structures measured on 21 November 1981 with the SOUSY VHF radar at Arecibo; published by Röttger (1987).

It was also detected that there is an immense shorter-period atmospheric gravity wave and turbulence activity in the mesosphere over Arecibo. We notice in Fig. 30 waves with different periods from 4 minutes upwards. It was conjectured that wave breaking (manifested by intensity and spectrum width increase) occurred only in some upper heights. The intermittency in space and time is clearly visible in this plot but it is not obviously related to the wave oscillations. Evidence of wave steepening and short-period waves superimposed on low-period waves was found.

As just described, the main initial radar observations of the mesosphere, stratosphere and troposphere were done in low (Jicamarca, Peru) and subtropical (Arecibo, Puerto Rico) latitudes. The first high latitude MST radar was built end of the 1970s in Poker Flat, Alaska. It was a super-power radar on 49.9 MHz which consisted of 64 phase-coherent transmitters with a total specified peak power of 6400 kW feeding a coaxial-collinear antenna array of 40000 m² aperture (Balsley et al., 1980).

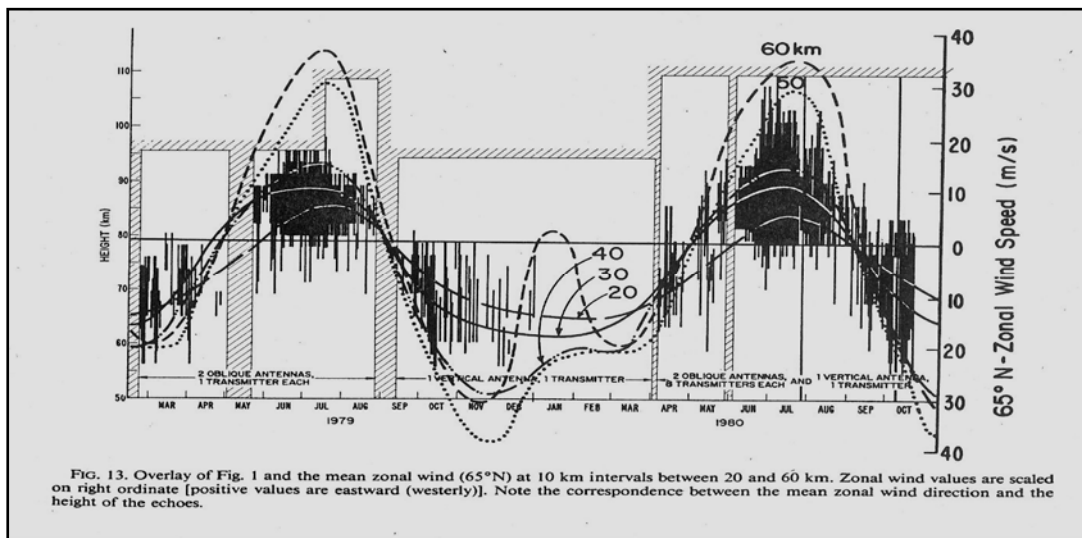


Fig. 32 Polar mesosphere summer echoes were first observed with the Poker Flat VHF radar in 1979. These echoes are much stronger than the echoes observed during winter. Their occurrence is related to the mean zonal wind as measured with the same radar (from Ecklund and Balsley, 1981).

This radar started up with another surprise, which is shown in Figure 32. As compared to the mesospheric echoes observed in low and mid-latitudes, the echoes observed at high latitudes were extremely stronger in summer than in winter. Due to their particular seasonal, regional and altitude occurrence, they were later called Polar Mesosphere Summer Echoes (PMSE). They attracted very broad attention, since it was impossible to explain them by the conventional turbulence scatter theory. It was also not possible to explain these echoes by enhanced reflection. Ecklund and Balsley (1981) considered them to be related to the cold polar summer mesopause. It was later confirmed that the scatter cross section of the PMSE-generating irregularities is resulting from the existence of small ice particles which form in the cold polar mesopause region and interact with the ionization of the mesosphere.

VHF Radar Observations of Atmospheric Gravity Waves, their Velocity Spectra and Turbulence

The clearly detectable spectrum of atmospheric gravity waves (e.g., Figure 31) extends over the troposphere, stratosphere and mesosphere. Many VHF radar observations of these waves were done as early as MST radars were operated. Here only a very few examples are shown here. These concentrate on the main generation mechanisms, Kelvin-Helmholtz-Instability (KHI) in wind shears, penetrative convection due to Rayleigh-Taylor-Instability (RTI) and due to mountain lee waves.

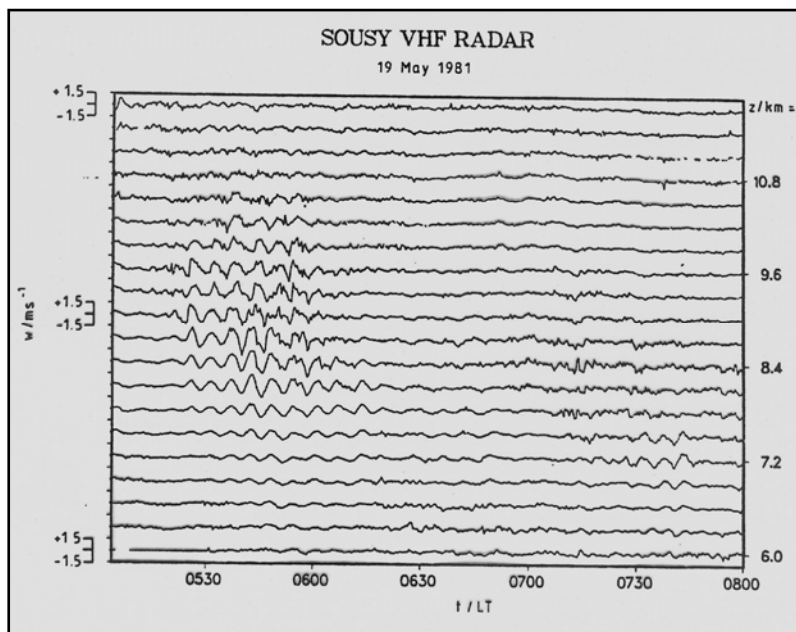


Fig. 33a shows periodic oscillations observed in the upper troposphere over Arecibo. These were proved by Klostermeyer and Ruster (1981) to be generated by wind shear in a jetstream, i.e. by a KHI. The oscillations, which occur during a limited time period and limited altitude range indicate a phase difference above and below 9 km height, which was measured to be the region of the mean strongest wind shear.

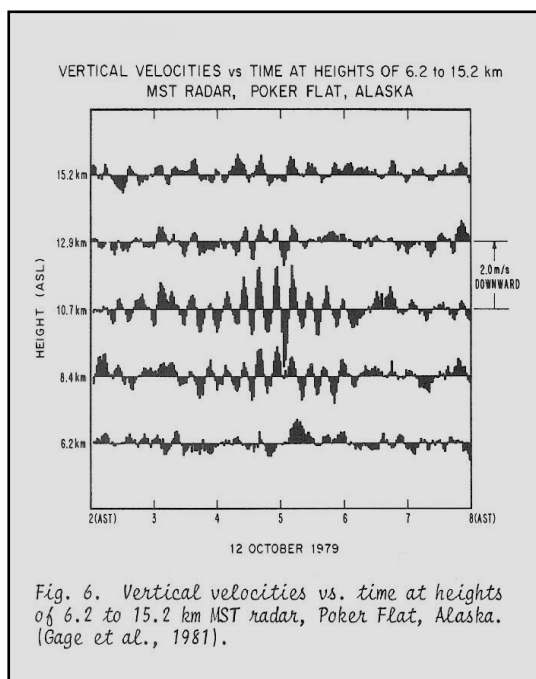


Fig. 33b Such vertical velocity oscillations, which are evidently generated by atmospheric gravity waves, were observed with all MST radars in the troposphere, stratosphere and mesosphere at all latitudes from tropical to polar regions (see here another example from Poker Flat, Alaska, from Gage et al., 1981). A relation of velocities and radar reflectivity was considered due to tilting of atmospheric structures in the presence of gravity waves. It was also proposed by VanZandt (1982) to introduce a universal spectrum of gravity waves, i.e. the spectrum of vertical and horizontal velocities in the MST altitudes due to atmospheric gravity waves. It turned out that MST radars are most valuable tools for this purpose of studying middle and lower atmosphere dynamics.

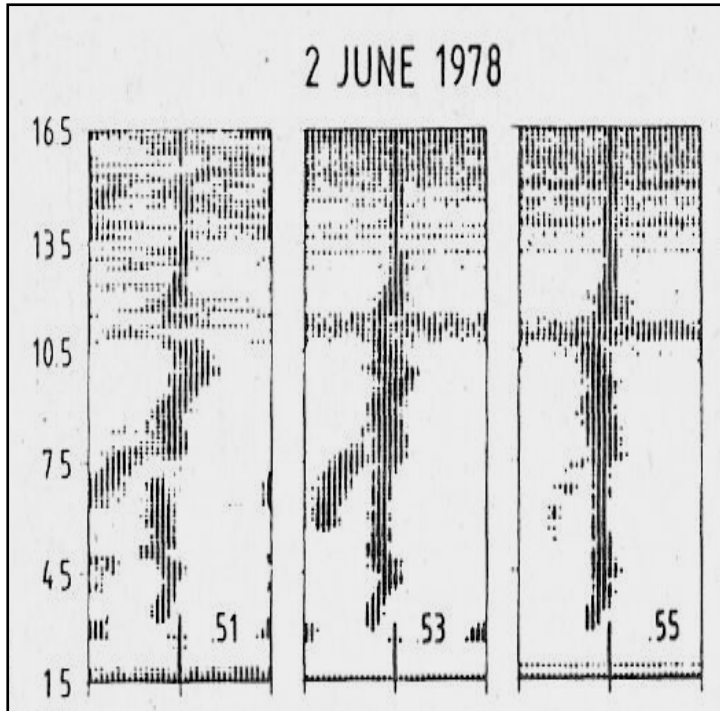


Fig. 34a shows dynamic spectra of VHF radar echoes during a thunderstorm. The convective activity (RTI) was changing velocity with height and was penetrating into the lower stratosphere around 12-13 km (from Larsen and Röttger, 1987). Noticed is also a spectral component separating from the inner low-velocity spectral part, which was attributed to backscatter from precipitating rain drops, which was later used to determine the rain drop size distribution.

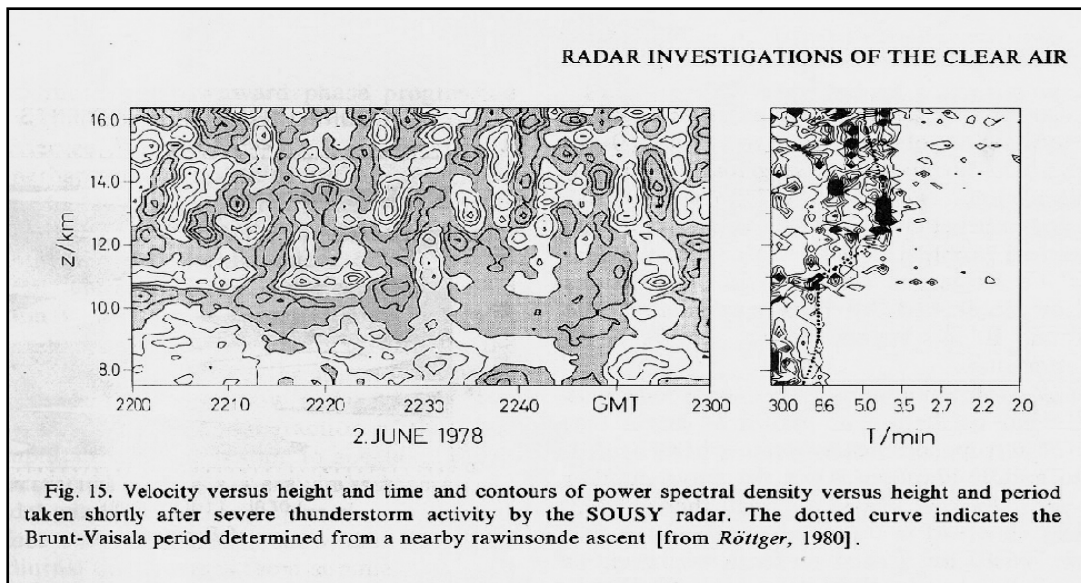
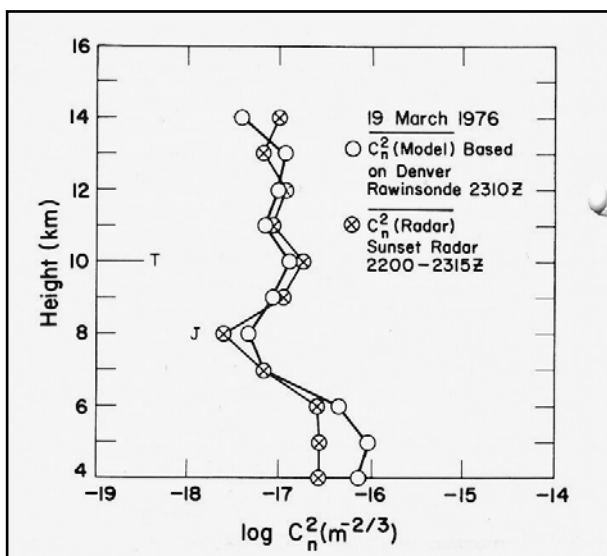


Fig. 15. Velocity versus height and time and contours of power spectral density versus height and period taken shortly after severe thunderstorm activity by the SOUSY radar. The dotted curve indicates the Brunt-Väisälä period determined from a nearby rawinsonde ascent [from Röttger, 1980].

Fig. 34b Contour plots of vertical velocity in the upper troposphere and lower stratosphere (left-hand panel) and the corresponding power spectrum of the velocities (right-hand panel). These quasi-periodical oscillations were observed after the passage of a thunderstorm (Fig. 34a). There is a clear cut-off in the short period part of the spectra. This is equivalent to the Brunt-Väisälä period (given by the straight line), which is the limit of atmospheric gravity wave existence in a stably stratified atmosphere. It actually was observed that there is an peak in the gravity wave oscillation amplitude very close to the Brunt-Väisälä period, which can be recognized well in the stratospheric altitudes 12.5-13.5 km (from Röttger, 1980).

Under certain conditions the gravity waves break into turbulence, which is one of the components for radar backscatter. Ottersten (1969) had introduced the so-called turbulence refractive index structure constant C_n^2 , which assumed that radar backscatter is essentially caused by isotropic turbulent fluctuations of the radio refractive index of the clear air, such as humidity and temperature variations. VanZandt et al. (1978) had used a more elaborate approach to determine C_n^2 from rawinsonde/radiosonde profiles and compared this with VHF radar observations (Figure 35). Both methods could compare well, provided that the reflected component in the VHF radar signal power is removed.



There were several possibilities introduced to allow this. The mostly applied method is to point the antenna beam at 10-20 degrees off the vertical direction to assure that scatter is only from isotropic turbulence. Nastrom et al. (1981) started to use radar data for obtaining the climatology of the refractive index constant.

Fig. 35 Vertical profiles of potential turbulence refractive index structure constant C_n^2 measured by the Sunset VHF radar and deduced by a model (from VanZandt et al., 1978).

We have to note that C_n^2 does not directly provide the turbulence intensity, since it depends also on mean temperature and humidity profiles. A more better approach to deduce turbulence and the corresponding turbulence transport coefficient is either using the Doppler spectrum width or the so-called flux method was developed by Rastogi and Woodman (1983). They obtained an empirical transport coefficient from Arecibo 430 MHz radar observations (Figure 36), which also took into account the intermittency of turbulence layers as clearly noticed by many radar observations.

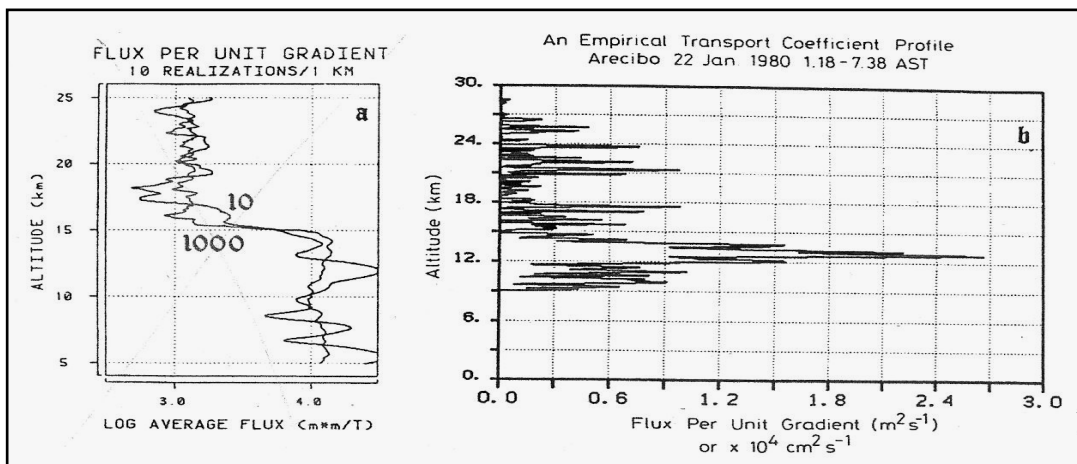


Fig. 36 Turbulent flux and empirical transport coefficient from radar observations

Atmospheric Stability, Tropopause and Fronts

The aspect sensitivity due to specular-type reflection from horizontally stratified rough refractivity surfaces in the troposphere and stratosphere has the advantage to create stronger radar echoes from directions close to the zenith. This not only allows easier application of the spaced antenna method (Figure 16) but also to determine atmospheric stability, which is determined by the temperature lapse rate. A clear indication of this effect is the enhancement of VHF radar signal power (measured with vertically pointing antenna beam) in the tropopause altitudes (e.g., Figure 15, left at 11-12 km). Gage et al. (1979) had developed a Fresnel scattering model which showed the direct relationship between the intensity of specular-type VHF radar echoes and atmospheric stability. Gage and Green (1979) showed that this allows the determination of the tropopause height (Fig. 37), and even the determination of the tropospheric temperature profile (Figure 38).

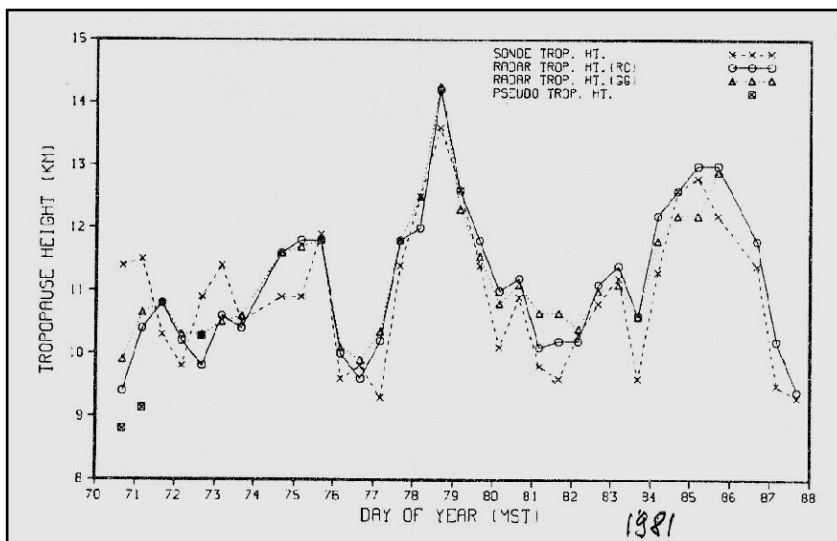


Fig. 37 Three weeks of tropopause height observations in 1981 by radiosondes and using the Gage and Green method as well as a radar reflectivity method of Westwater et al. (1983). This proves that VHF radar is well capable to determine the tropopause height accurately.

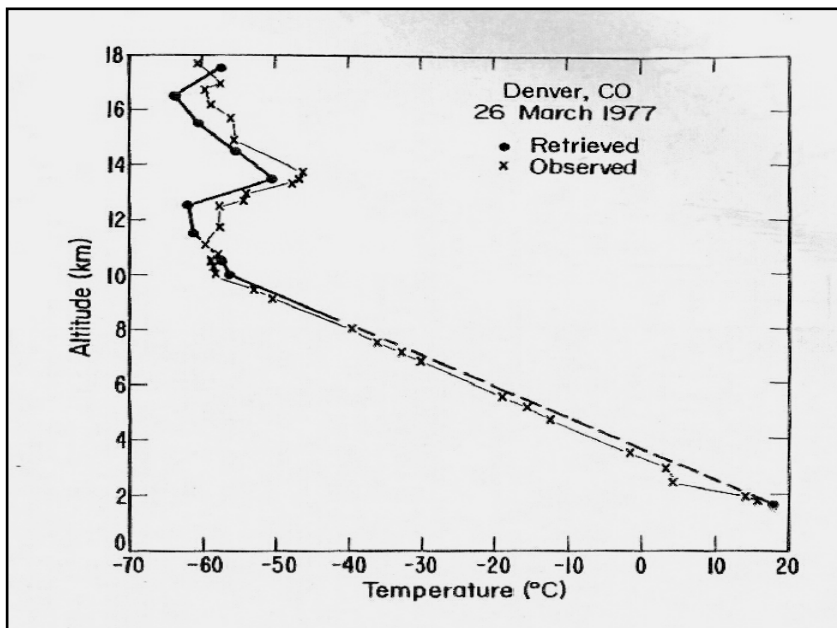


Fig. 38 Gage and Green (1982) and Gage and Balsley (1983) used stability deductions from VHF radar to reconstruct the temperature profile. This needs the surface temperature as starting point and assuming a constant lapse rate in the troposphere and also includes the increase of VHF radar echo power above the tropopause.

Whereas the tropopause height can usually be determined quite well, it was often difficult to decide whether an increase in reflectivity in the lower troposphere was due to a vertical gradient in temperature (inversion layer) or a vertical gradient in humidity. Figure 39 shows an example of a very early film record of signal power measured with the test set-up of the SOUSY VHF Radar, which shows such a layer below 3 km height.

A longer record with this set-up (Figure 40) showed particularly long-lasting echoes below about 3 km, which were attributed to humidity dominating the scattering/reflection process, and some structures moving downward within many hours. An analysis of synoptic weather conditions proved that the downward progression of a reflectivity structure was due to the passage of a warm front of an extra-tropical cyclone over the SOUSY radar (Röttger, 1977 and Röttger, 1979). The frontal zone separates warm air from cold air and, thus, forms a vertical gradient of temperature (inversion layer) which enhances the radar reflectivity. Such warm and cold front passages were quite frequently observed by VHF radar in mid and high latitudes (see Figure 41). Besides frontal surfaces also wind field was observed.

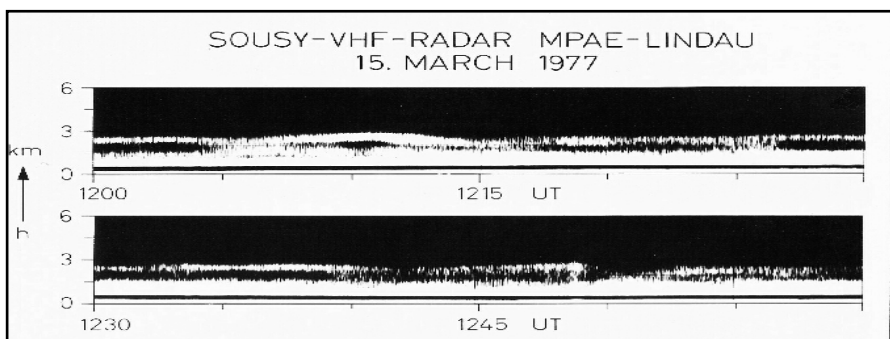


Fig. 39 Film record of one hour SOUSY VHF radar test operation (80 kW and 8 Yagi antennas) showing a discrete layer around 2-3 km altitude.

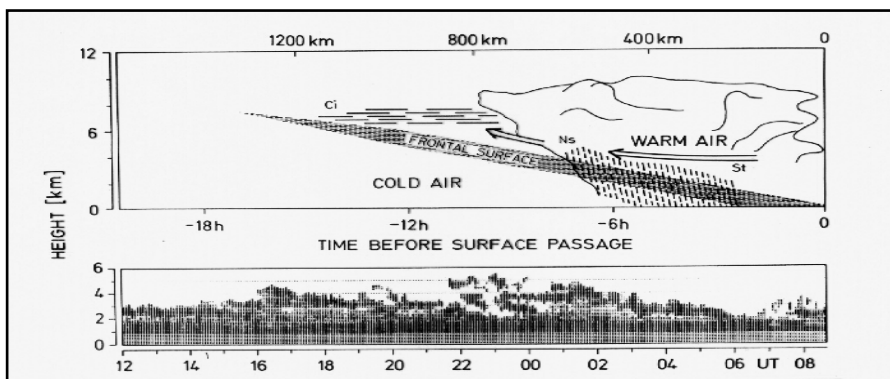


Fig. 40 Passage of a warm front of an extra-tropical cyclone (mid-latitude synoptic scale disturbance) over the SOUSY VHF radar on 15-16 March 1977.

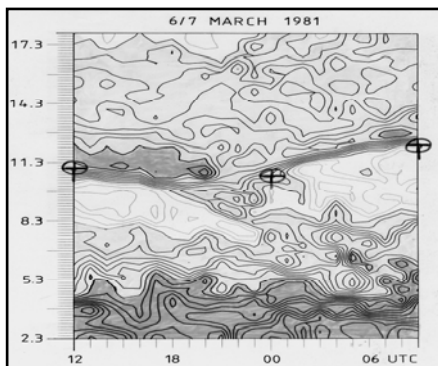
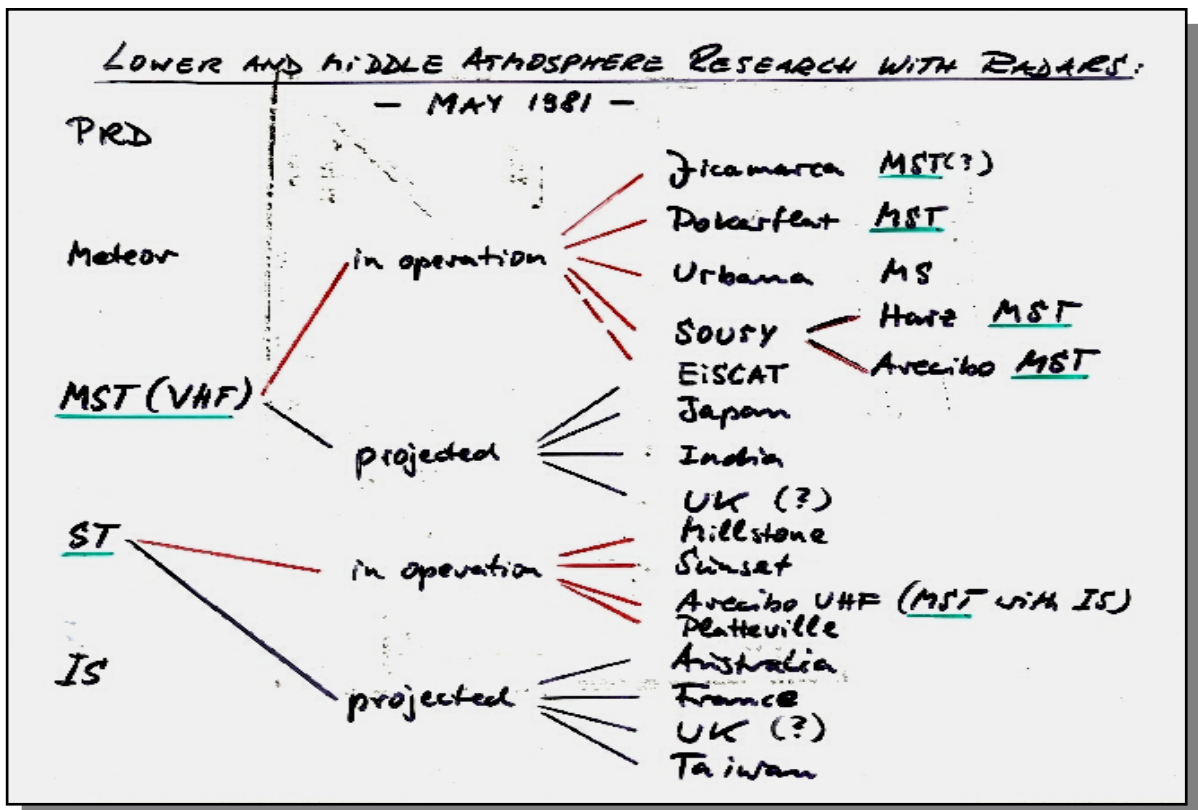
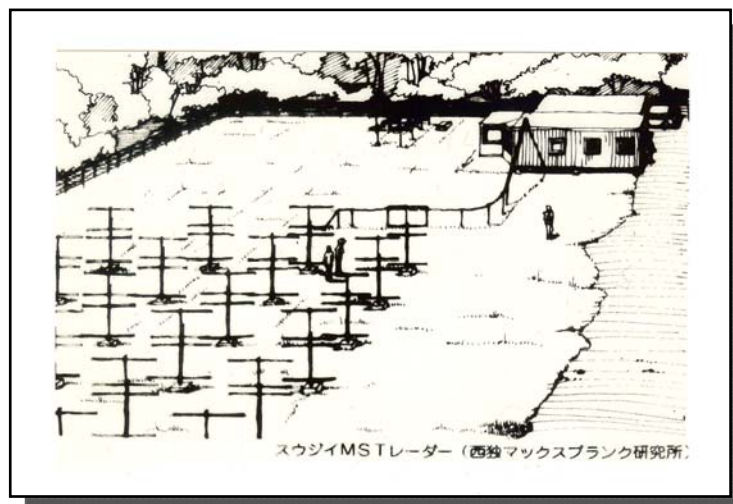


Fig. 41 Frontal passages are often connected with tropopause breaks/foldings as noticed in this record of VHF radar reflectivity (Röttger and Schmidt, 1981). The circled crosses show the height of the tropopause determined with radiosonde. The downward sloping reflectivity is due to a passage of a warm front. After midnight strong jet stream winds were measured with the radar measured with the radar between 8 km and 11 km height.



The status of MST radars in May 1981 (from an oral presentation of Jürgen Röttger), mainly showing the ST and MST radars in operation (red arrows) and projected (i.e. in planning or early construction phases, black arrows). Meteor, partial reflection (PRD) and incoherent scatter (IS) radars, which are also used for mesosphere studies, are not included here. Within the following years, the MU radar in Japan (see artist's cartoon of 1980 (?) at the end, which bases on the lay-out of the SOUSY VHF radar in the Harz mountains in Germany), the NMRF radar in India, the Buckland Park radar in Australia, wind profilers in France and the USA, the Aberystwyth radar in the UK and the NCU VHF radar in Taiwan became operational.



Final remarks and acknowledgement:

This publication can only contain some of the highlights, which I remembered taking place during the first decade following the break-through of this research direction after the special experiments at the Jicamarca VHF radar by R.F. Woodman and A. Guillen in December 1971. I apologize if I had not mentioned several further important designs and findings due to the limited space for publishing this paper. Searching through the large amount of papers published on the experimental results and their initial interpretations it appears to me that this first decade was a major highlight leading the way for many further decades.

I want to thank Wayne Hocking and the MST radar workshop steering committee for inviting me to present this historical summary during the MST-12 workshop and honoring me by the award for over 30 years of exemplary leadership of the MST community. I also appreciate the patience of the editor, Wayne Hocking, allowing me really ample time and excessive pages for the publication of this paper.

References:

Here mainly those references are summarized, which relate to figures or particular highlights chosen in the context of this paper. There exists a very much larger number of further publications in journals, books, proceedings and reports, as well as some unpublished results presented at workshops or meetings, which were performed during the decade 1971-1981. To allow a general overview, part of these are included in this list without mentioning them in the text of the paper. Several corresponding publications were in the years after 1981; these are cited here as well, when the results were obtained before end of 1981. To get information on further papers **some review and tutorial papers are cited at the end of this list**, to find where this information is accessible.

Aso, T. and S. Kato, Arecibo middle atmosphere experiment, *Geophys. Res. Lett.*, vol. 4, 10-12, 1977.

Balsley, B.B., N. Cianos, D.T. Farley and M.J. Baron, Winds derived from radar measurements in the arctic troposphere and stratosphere, *J. Appl. Met.*, vol. 16, 1235-1239, 1977.

Balsley, B.B., The use of sensitive coherent radars to examine atmospheric parameters in height range 1-100 km, *Proc. 18th Conf. on Radar Meteor.*, Mar. 28-31, Atlanta, GA, 190, 1978.

Balsley, B.B. and J. Green, Coherent radar systems for probing the troposphere, stratosphere and mesosphere, *4th Sympos. Met. Obs. Instr.*, *Amer. Met. Soc.*, 2-5, 1978.

Balsley, B.B., W.L. Ecklund, C.A. Carter and P.E. Johnston, The Poker Flat MST radar: First results, *Geophys. Res. Lett.*, vol. 6, 921-924, 1979.

Balsley, B.B., W.L. Ecklund, D.A. Carter, and P.E. Johnston, The MST radar at Poker Flat, Alaska, *Radio Sci.*, vol. 15(2), 213-224, 1980.

Balsley, B. B., and K. S. Gage, On the vertical-incidence VHF backscatter power profile from the stratosphere, *Geophys. Res. Letts.*, 8, 1173, 1981.

Balsley, B.B. and K.S. Gage, On the use of radars for operational wind profiling, *Bull. Amer. Met. Soc.*, vol. 63, 100-1018, 1982.

Balsley, B.B., D.A. Carter and W.L. Ecklund, On the relationship between electrojet intensity fluctuations and the wind field near the mesopause, *Geophys. Res. Lett.*, vol. 9(3), 219-222, 1982.

Beckman, P., and A. Spizzichino, The scattering of electro-magnetic waves from rough surfaces, Pergamon Press, 503 pp., 1963.

Bolgiano, R., Structure of turbulence in stratified media, *J. Geophys. Res.*, vol. 67, 3015-3023, 1962.

Bolgiano, R., The general theory of turbulence in the atmosphere, *Proc. NATO Advanced Study Inst.*, 371-398, 1968.

Bowles, K.L., Observations of vertical incidence scatter from the ionosphere at 41 Mc/sec, *Phys. Rev. Lett.*, 1, 454-455, 1958.

Bowles, K.L., Incoherent scattering by free electrons as a technique for studying the ionosphere and exosphere: Some observations and theoretical considerations, *J. Res. NBS, D*, vol. 65D(1), 1-14, 1961.

Bowles, K. L., Radio waves scattering in the ionosphere, *Advances in Electronics and Electron Physics*. Academic Press, 19, 55-176, 1964.

Browning, K.A., and C.D. Watkins, Observations of clear air turbulence by high power radar, *Nature*, vol. 227, 260-263, 1970.

Czechowsky, P., R. Rüster and G. Schmidt, Variations of mesospheric structures at different seasons, *Geophys. Res. Lett.*, vol. 6, 459-462, 1979.

Czechowsky, P., G. Schmidt and R. Rüster, The mobile SOUSY Doppler radar: Technical design and first results, *Radio Sci.*, vol. 19(1), 441-450, 1984.

Czechowsky, J. Klostermeyer, J. Röttger, R. Rüster, G. Schmidt and R.F. Woodman, The SOUSY VHF Radar for tropo-, strato- and mesospheric sounding, Proc. 17th Conf. Radar Met., Amer. Met. Soc., 349-353, 1976.

Dieminger, W., On the causes of excessive absorption in the ionosphere on winter days, J. Atm. Terr. Phys., vol.2, 340-349, 1952.

Ecklund, W.L., D.A. Carter and K.S. Gage, Sounding of the lower atmosphere with a portable 50-MHz coherent radar, J. Geophys. Res., vol. 82, 4969-4971, 1978.

Ecklund, W.L. and B.B. Balsley, Continuous measurements of upper atmosphere winds and turbulence using a VHF Doppler radar, J. Atmos. Terr. Phys., vol. 41, 983-994, 1979.

Ecklund, W.L. and B.B. Balsley, Long-term observations of the Arctic mesosphere with the MST radar at Poker Flat, Alaska, J. Geophys. Res., vol. 86, 7775-7780, 1981.

Ecklund, W.L., K.S. Gage and A.C. Riddle, Gravity wave activity in vertical winds observed by the Poker Flat MST radar, Geophys. Res. Lett., vol. 8, 285-288, 1981.

Ecklund, W.L., B.B. Balsley, R.G. Strauch, and J.L. Green, Vertical wind variability observed by VHF radar in the lee of the Colorado Rockies, Month. Weath. Rev., vol. 110, 1451-1457, 1982.

Farley, D.T., B.B. Balsley, W.E. Swartz, and C. LaHoz, Tropical winds measured by the Arecibo radar, J. Appl. Met., vol. 18, 227-230, 1979.

Flock, W. L. and Balsley, B. B.: VHF radar returns from the D- region of the equatorial ionosphere, J. Geophys. Res., 72, 5537-5541, 1967.

Fukao, S., S. Kato, S. Yokoi, R. M. Harper, R. F. Woodman, and W. E. Gordon, One full-day radar measurement of lower stratospheric winds over Jicamarca, J. Atmos. Terr. Phys., 40, 1331, 1978.

Fukao, S., T. Sato, I. Hirota, and S. Kato, A preliminary radar observation of long-period waves in the tropical mesosphere over Jicamarca, J. Geophys. Res., 85, 1955, 1980.

Fukao, S., T. Sato, R. M. Harper, and K. Kato, Radio wave scattering from the tropical mesosphere observed with the Jicamarca radar, Radio Sci., 15, 447, 1980.

Fukao, S., K. Aoki, K. Wakasugi, T. Tsuda, S. Kato, and D. A. Fleisch, Some further results on the lower stratospheric winds and waves over Jicamarca, J. Atmos. Terr. Phys., 43, 649, 1981.

Gage, K.S., and B.B. Balsley, Doppler radar probing of the clear atmosphere, Bull. Amer. Met. Soc., vol. 59.9, 1074-1093, 1978.

Gage, K.S. and J.L. Green, Evidence for specular reflection from monostatic VHF radar observations of the stratosphere, *Radio Sci.*, vol. 13, 991-1001, 1978.

Gage, K.S. and J.L. Green, Tropopause detection by partial specular reflection using VHF radar, *Science*, vol. 203, 1238-1240, 1979.

Gage, K.S. and B.B. Balsley, On the scattering and reflection mechanisms contributing to clear air echoes from the troposphere, stratosphere and mesosphere, *Radio Sci.*, vol. 15, 243-257, 1980.

Gage, K.S. and T.E. VanZandt, Wind measuring techniques available for the middle atmosphere program, *J. Geophys. Res.*, vol. 86, 9591-9598, 1981.

Gage, K.S., D.A. Carter, and W.L. Ecklund, The effect of gravity waves on specular echoes observed by the Poker Flat MST radar, *Geophys. Res. Lett.*, vol. 8, 599-622, 1981.

Gage, K.S., B.B. Balsley and J.L. Green, A Fresnel scattering model for the specular echoes observed by VHF radar, *Radio Sci.*, vol. 16, 1447-1453, 1981.

Gage, K.S. and J.L. Green, A technique for determining the temperature profile from VHF radar observations, *J. Appl. Meteor.*, vol. 21, 1146-1149, 1982.

Gage, K.S. and J.L. Green, An objective method for the determination of tropopause height from VHF radar observations, *J. Appl. Met.*, vol. 12, 1159-1163, 1982.

Gage, K.S. and B.B. Balsley, Advances in remote sensing of the atmosphere, *Rev. Geophys. Space Phys.*, vol. 21, 955-965, 1983.

Gage, K.S. and T.W. Schlatter, VHF/UHF radar and its application for nowcasting, *Nowcasting Symp. Norrköping, Sweden*, 1-8, 1984.

Gibbs, K.P. and S.A. Bowhill, The Urbana coherent-scatter radar: Synthesis and first results, *Aeronomy Laboratory Report 90*, Univ. Illinois, Urbana, IL, pp.90, 1983.

Gordon, W.E., Incoherent scattering of radio waves by free electrons with applications to space exploration by radar, *Proc. IRE*, vol. 46, 1824-1829, 1958.

Green, J., J.M. Warnock, R.H. Winkler, and T.E. VanZandt, A sensitive radar for the studies of winds, waves and turbulence in the troposphere, stratosphere and mesosphere, *Proc. 16th AMS Radar Met. Conf.*, 313-315, 1975.

Green, J., J.M. Warnock, R.H. Winkler, and T.E. VanZandt, Studies of winds in the upper troposphere with a sensitive VHF radar, *Geophys. Res. Lett.*, vol. 2, 19-21, 1975.

Green, J.L., R.H. Winkler, J.M. Warnock, W.L. Clark, K.S. Gage and T.E. VanZandt, Observation of enhanced clear air reflectivity associated with convective clouds, Proc. 18th AMS Radar Meteor. Conf., 8-93, 1978.

Green, J.L., K.S. Gage and T.E. VanZandt, Atmospheric measurements by VHF pulsed Doppler radar, IEEE Trans. Geosci. Electron. GE-17, 262-280, 1979.

Green, J.L. and K.S. Gage, Observations of stable layers in the troposphere and stratosphere using VHF radar, Radio Sci., vol. 15, 395-405, 1980.

Green, J.L., K.S. Gage, W.L. Clark, T.E. VanZandt and P.H. Hildebrand, Joint instrumented aircraft and VHF Doppler radar measurements of winds near Boulder, Colorado, Proc. 19th AMS Radar Meteor. Conf, Amer. Meteor. Soc., 624-628, 1980.

Hocking, W.K., Angular and temporal characteristics of partial reflections from the D-region of the ionosphere, J. Geophys. Res., vol. 84, 845, 1979.

Klostermeyer, J. and R. Rüster, Further study of a jet stream generated Kelvin-Helmholtz-Instability. J. Geophys. Res., vol. 86, 6631-6637, 1981.

Larsen, M.F. and J. Röttger, Comparison of tropopause height and frontal boundary locations based on radar and radiosonde data, Geophys. Res. Lett., vol. 10, 325-328, 1983.

Larsen, M.F. and J. Röttger, Observations of thunderstorm reflectivities and Doppler velocities measured at VHF and UHF, J. Atmos. Ocean. Technol., vol. 4, 151-159, 1987.

Little, C.G., Ground-based remote sensing for meteorological nowcasting,, in Nowcasting, ed. K. Browning, Academic press, London, 65-85, 1982.

Leppänen, P., On complementary code pairs and matched filters for them, Inst. Telcom., Uni. Oulu, Finland, 1976.

Maekawa, Y., T. Aso, J. Röttger, P. Czechowsky, R. Rüster, G. Schmidt, I. Hirota, R.F. Woodman and S. Kato, A cooperative synchronous observation of winds and tides in the tropical lower stratosphere and mesosphere using VHF radars at Jicamarca and Arecibo, J. Geomag. Geoelectr., vol. 38, 81-97, 1986.

Nastrom, G.D., K.S. Gage and B.B. Balsley, Variability of Cn₂ at Poker Flat, Alaska, from mesosphere, stratosphere, troposphere (MST) Doppler radar observations, SPIE, Atmospheric Transmission, vol. 277, 10-15, 1981.

Ottersten, H., Radar backscattering from the clear atmosphere, Radio Sci., vol. 4, 1251-1255, 1969.

Rastogi, P. K., and S. A. Bowhill, Remote Sensing of the Mesosphere Using the Jicamarca Incoherent-Scatter Radar, Aeronomy Laboratory Report 68, Dept. of Electrical Engineering, Univ. of Illinois, Urbana, pp. 41, 1975.

Rastogi, P. K., and S. A. Bowhill, Scattering of radio waves from the Mesosphere-1. Theory and observations, *J. Atmos. Terr. Phys.*, vol. 38, 399-411, 1976.

Rastogi, P. K., and S. A. Bowhill, Scattering of radio waves from the Mesosphere-2: Evidence for intermittent mesospheric turbulence, *J. Atmos. Terr. Phys.*, vol. 38, 51-60, 1976.

Rastogi, P.K. and R.F. Woodman, Mesospheric studies using the Jicamarca incoherent scatter radar, *J. Atm. Terr. Phys.*, vol. 36, 1217-1231, 1974.

Rastogi, P.K. and R.F. Woodman, Vertical transport in the tropo-stratosphere by intermittent turbulence: A simulation study, 6th Symp. Turbulence and Diffusion, *Amer. Met. Soc.*, 265-268, 1983.

Rastogi, P.K., J.D. Mathews, W.-P. Ying and J. Röttger, Simultaneous VHF and UHF radar observations of the mesosphere at Arecibo during a solar flare: A check on the gradient-mixing hypothesis, *Radio Sci.*, vol. 23, 97-105, 1988.

Royrvik, O., VHF radar signals scattered from the equatorial mesosphere, *Radio Sci.*, vol. 18(6), 1325-1335, 1983.

Röttger, J. and P. Czechowsky, Clear-air turbulence and tropospheric refractivity variations observed with a new VHF-radar, *Naturwissenschaften*, vol. 64, 580, 1977.

Röttger, J., Evidence for partial reflection of VHF radar signals from the troposphere, *J. Geophys.*, vol. 44, 393-394, 1978.

Röttger, J. and C.H. Liu, Partial reflection and scattering of VHF radar signals from the clear atmosphere, *Geophys. Res. Lett.*, vol. 5, 357-360, 1978.

Röttger, J. and R.A. Vincent, VHF radar studies of tropospheric velocities and irregularities using spaced antenna techniques, *Geophys. Res. Lett.*, vol. 5, 917-920, 1978.

Röttger, J., J. Klostermeyer, P. Czechowsky, R. Rüster, and G. Schmidt, Remote sensing of the atmosphere by VHF radar experiments, *Naturwissenschaften*, vol. 65, 285-296, 1978.

Röttger, J., VHF radar observations of a frontal passage, *J. Appl. Meteor.*, vol. 18, 85-91, 1979.

Röttger J., P. K. Rastogi, and R. F. Woodman, High-resolution VHF radar observations of turbulence structures in the mesosphere, *Geophys. Res. Lett.*, vol. 6, 617-620, 1979.

Röttger, J. and G. Schmidt, High resolution VHF radar sounding of the troposphere and stratosphere, *IEEE Transact. Geosc. Electr.*, vol. GE-17(4), 182-189, 1979.

Röttger, J., Reflection and scattering of VHF radar signals from atmospheric refractivity structures, *Radio Sci.*, vol. 15, 259-276, 1980.

Röttger, J., and P. Czechowsky, Tropospheric and stratospheric wind measurements with the spaced antenna drifts technique and the Doppler beam swinging technique using VHF radar, *Proc. 19th Radar Meteor. Conf.*, Amer. Meteor. Soc., 577-584, 1980.

Röttger, J., Investigations of lower and middle atmosphere dynamics with spaced antenna drifts radars, *J. Atmos. Terr. Phys.*, vol. 43, 277-292, 1981.

Röttger, J., The capabilities of VHF radars for meteorological observations, *ESA SP-165, IAMAP Third Scientific Assembly*, European Space Agency, Paris, 143-148, 1981.

Röttger, J. and G. Schmidt, Characteristics of frontal zones determined from spaced antenna VHF radar observations, *Proc. 20th Radar Meteorology Conf.*, Boston, Amer. Meteor. Soc., 30-37, 1981.

Röttger, J., P. Czechowsky and G. Schmidt, First low-power VHF radar observations of tropospheric, stratospheric and mesospheric winds and turbulence at the Arecibo Observatory, *J. Atmos. Terr. Phys.*, vol. 43, 789-800, 1981.

Röttger, J., P. Czechowsky, R. Rüster and G. Schmidt, VHF radar observations of wind velocities at the Arecibo Observatory, *J. Geophys.*, vol. 52, 34-39, 1983.

J. Röttger, The potential of VHF radars for meteorological applications, *Polarfront*, *Medlemsblad SMHI*, Sweden, vol. 11(41), 6-11, 1984.

J. Röttger, Potential advantages of the spaced antenna method for operational wind profiling, *Publication Series WMO*, No. 5, 97-102, 1984.

Röttger, J. and H.M. Ierkic, Postset beam steering and interferometer applications of VHF radars to study winds, waves and turbulence in the lower and middle atmosphere, *Radio Sci.*, vol. 20, 1461-1480, 1985.

Rüster, R., J. Röttger and R.F. Woodman, Radar measurements of waves in the lower stratosphere, *Geophys. Res. Lett.*, vol. 5, 555-558, 1978.

Rüster, R., and R. F. Woodman, Digitale Filterung, Kalibrierung and Korrelations-analyse von Radarechos aus der Tropo-und Stratosphäre, *Kleinheubacher Berichte, Proc.*, vol. 21, 239-246, 1978.

Rüster, R., P. Czechowsky and G. Schmidt, VHF radar measurements of dynamical processes in the stratosphere and mesosphere, *Geophys. Res. Lett.*, vol. 7, 999-1001, 1980.

Sato, T. and S. Fukao, Altitude smearing due to instrumental resolution in MST radar measurements, *Geophys. Res. Letts.*, vol. 9, 72, 1982.

Sato, T. and R.F. Woodman, Spectral parameter estimation of CAT radar echoes in the presence of fading clutter, *Radio Sci.*, vol. 17, 817-826, 1982.

Strauch, R.G., M.T. Decker and D.C. Hogg, An automatic profiler of the troposphere, 20th AIAA Aerospace Sciences Meeting, AIAA-82-0014, 1982.

Schmidt, G., R. Rüster and P. Czechowsky, Complementary code and digital filtering for detection of weak VHF radar signals from the mesosphere, *IEEE Trans. Geosci. Electr.*, vol. GE-17, No 4, 154-161, 1979.

VanZandt, T.E., J.L. Green, K.S. Gage and W.L. Clark, Vertical profiles of refractivity turbulence structure constant: Comparison of observations with the Sunset radar with a new theoretical model, *Radio Sci.*, vol. 13, 819-829, 1978.

VanZandt, T.E., A universal spectrum of buoyancy waves in the atmosphere, *Geophys. Res. Lett.*, vol. 9, 575-578, 1982.

Vincent, R.A. and J. Röttger, Spaced antenna VHF radar observations of tropospheric velocities and irregularities, *Radio Sci.*, vol. 15, 319-335, 1980.

Wakasugi, K., S. Kato, and S. Fukao, Depolarization of a 50-MHz radio wave backscattered from the middle atmosphere, *Radio Sci.*, vol. 15, 439, 1980.

Westwater, E.R., M.T. Decker, A. Zachs and K.S. Gage, Ground-based remote sensing of temperature profiles by a combination of microwave radiometry and radar, *J. Clim. Appl. Met.*, vol. 32, 126- 133, 1983.

Woodman, R.F. and A. Guillen, Radar observations of winds and turbulence in the stratosphere and mesosphere, *J. Atmos. Sci.*, vol. 31, 493-505. 1974.

Woodman, R.F., High-altitude-resolution stratospheric measurements with the Arecibo 430-MHz radar, *Radio Sci.*, vol. 15(2), 417-422, 1980a.

Woodman, R.F., High-altitude-resolution stratospheric measurements with the Arecibo 2380-MHz radar, *Radio Sci.*, vol. 15(2), 423-439, 1980b.

Woodman, R.F., R.P. Kugel and J. Röttger, A coherent integrator-decoder preprocessor for the SOUSY-VHF-Radar, *Radio Sci.*, 15, 233-242, 1980.

Books, reviews, tutorials and special journal and handbook issues:

Atlas, D. (editor), Radar in Meteorology: Battan Memorial and 40th Anniversary Radar Meteorology Conference, American Meteorological Society, Boston, 806 p.p., 1990.

Battan, L.J., Radar observations of the atmosphere, The University of Chicago Press, 323 pp., 1973.

Balsley, B. B., and K. S. Gage, The MST radar technique: Potential for middle atmospheric studies, Pure and Applied Geophys., vol. 118, 452, 1980.

Balsley, B. B., The MST technique - a brief review, J. Atmos. Terr. Phys., vol. 43, 495, 1981.

Balsley, B.B. and K.S. Gage, On the use of radars for operational wind profiling, Bull. Amer. Met. Soc., vol. 63, 100-1018, 1982.

Balsley, B., R.B. Chadwick, W.L. Clark, W.L. Ecklund, D.T. Farley, S. Fukao, J.L. Green, M.F. Larsen, J. Röttger, R.G. Strauch, R.A. Vincent, B.J. Watkins and R.F. Woodman, Panel Report, in Radar in Meteorology (ed. D. Atlas), Amer. Met. Soc., Boston, Mass., U.S.A., 235-281, 1990.

Bowhill, S.A., and B. Edwards, URSI/SCOSTEP Workshop on Technical Aspects of MST Radar 1983, Handbook for MAP, vol. 9, pp. 579, publ. by SCOSTEP Secretariat, Univ. of Illinois, Urbana, Ill., USA, 1983.

Bowhill, S.A., and B. Edwards, URSI/SCOSTEP Workshop on Technical Aspects of MST Radar 1984, Handbook for MAP, vol. 14, pp. 368, publ. by SCOSTEP Secretariat, Univ. of Illinois, Urbana, Ill., USA, 1984.

Bowhill, S.A., and B. Edwards, URSI/SCOSTEP Workshop on Technical Aspects of MST Radar 1985, Handbook for MAP, vol. 20, pp. 505, publ. by SCOSTEP Secretariat, Univ. of Illinois, Urbana, Ill., USA, 1986.

Czechowsky, P., Principles of wind profilers, in COST 74 Final Report Utilization of UHF/VHF radar wind profiler networks for improving weather forecasting in Europe, ed. L. Lafaysse, EUR 15450, 21-43, 1994.

Gage, K.S., and B.B. Balsley, Doppler radar probing of the clear atmosphere, Bull. Amer. Meteor. Soc., vol. 59(9), 1074-1093, 1978.

Gage, K., Radar observations of the free atmosphere: Structure and dynamics, in Radar in Meteorology (ed. D. Atlas), Amer. Meteor. Soc., Boston, Mass., U.S.A., 534-565, 1990.

Gossard, E.E. and K.C. Yeh, Guest Editors, Radar investigations of the clear air, Special issue Radio Science, vol 15(2), 147-457, 1980.

Harper, R.M., and W.E. Gordon, A review of radar studies of the middle atmosphere, Radio Sci., vol. 15(2), 195-211, 1980.

Larsen, M.F. and J. Röttger, VHF and UHF Doppler radars as tools for synoptic research, Bull. Amer. Meteor. Soc., 63, 996-1008, 1982.

Liu, C.H., and S. Kato, Guest Editors, Technical and scientific aspects of MST radar, Special issue Radio Science, vol. 20(6), 1139-1517, 1985.

Rastogi, P. K., Radar studies of gravity waves and tides in the middle atmosphere: A review, J. Atmos. Terr. Phys., vol. 43, 511, 1981.

Rastogi, P.K., Data processing techniques used with MST radars, a review, , Handbook for MAP, vol. 9, SCOSTEP Secretariat, Univ. of Illinois, Urbana, Ill., USA, 477-488, 1983.

Röttger, J., Structure and dynamics of the stratosphere and mesosphere revealed by VHF radar investigations, Pure and Appl. Geophys., vol. 118, 494-527, 1980.

Röttger, J., The capabilities of VHF radars for meteorological observations, ESA SP-165, IAMAP Third Scientific Assembly, European Space Agency, Paris, 143-148, 1981.

Röttger, J., The MST radar technique, Handbook for MAP, vol. 13, ed. R.A. Vincent, SCOSTEP Secretariat, Univ. of Illinois, Urbana, Ill., USA, 187-232, 1984.

Röttger, J., VHF radar measurements of small-scale and meso-scale dynamical processes in the middle atmosphere, Phil. Trans. Roy. Soc. London, A, vol. 323, 611-628, 1987.

Röttger, J., Studies of the Middle Atmosphere, Proceedings of a Royal Society Discussion Meeting, held on 4 and 5 December 1986 in London; ed. J.A. Pyle, L. Thomas and R. Wilson, F.R.S., publ. by The Royal Society, London, 91-108, 1987.

Röttger, J., The relation of gravity waves and turbulence in the mesosphere, Adv. Space Res., vol. 7, (10)345-(10)348, 1987.

Röttger, J., The instrumental principles of MST radars and incoherent scatter radars and the configuration of radar system hardware, Handbook for MAP, vol. 30, International School on Atmospheric Radar; ed. S. Fukao, 54-113, publ. by SCOSTEP Secretariat, Univ. of Illinois, Urbana, Ill. U.S.A., 54-113, 1989.

Röttger, J. and M.F. Larsen, UHF/VHF radar techniques for atmospheric research and wind profiler applications, Radar in Meteorology (ed. D. Atlas), Amer. Meteor. Soc., Boston, Mass., U.S.A., 235-281, 1990.

Vincent, R.A., Ground-based techniques, Handbook for MAP, vol. 13, publ. by SCOSTEP Secretariat, Univ. of Illinois, Urbana, Ill., USA, pp. 261, 1984.

Walker, J.C.G., Radar measurements of the upper atmosphere, Science, vol. 206, 180-189, 1979.

Woodman, R.F., Mesospheric winds at equatorial latitudes: a review on observational aspects, J. Atmos. Terr. Phys., vol. 39, 941-958, 1977.

Woodman R.F., Turbulence in the Middle Atmosphere: a review, MAP Handbook, vol. 2, SCOSTEP Secretariat, Univ. of Illinois, 1406, W. Green St., Illinois 61801, 293-300, 1981.

**Session 1:
Scattering, Calibration
and Microscale Processes**

FINE STRUCTURE OF WINTERTIME MESOSPHERIC RADAR ECHOES - A COMPARISON BETWEEN HIGH AND LOW LATITUDES

E. Belova¹, S. Kirkwood¹, T. Sergienko¹, H. Nilsson¹, S. Satheesh Kumar², T. Narayana Rao²

¹ Swedish Institute of Space Physics, Kiruna, Sweden

² National Atmospheric Research Laboratory, Gadanki, India

1. Introduction.

Polar mesosphere winter echoes (PMWE), between 55-80 km altitude, are seen by high latitude radars when excess ionization is produced by energetic particle precipitation (Kirkwood et al, 2006). Using FCA technique for the ESRAD MST radar located in Kiruna, Northern Sweden it has been found that PMWE can move horizontally at very high speeds, up to 500 m/s and they are strongly aspect sensitive. PMWE spectra measured with E(uropean) I(ncoherent) SCAT(atter) (EISCAT) radar have the same widths as standard incoherent ion-acoustic spectra from adjacent altitudes. On the basis of all characteristics an interpretation of PMWE was proposed in terms of generation of diffusion waves (Hocking, 2003) by partial reflection of incident infrasound from a region of strong gradient of temperature or wind shear (Kirkwood et al., 2006). At low latitudes, mesospheric echoes (LLME) are a common daytime phenomenon occurring throughout the year as shown by climatological studies with the Indian MST radar, located at Gadanki (Kishor Kumar et al, 2007). Most strong and frequently occurring echoes were observed in preferred height regions (70-75 km) and seasons (equinox). No conclusive evidence has been obtained on the aspect sensitive nature of these echoes. So, some similarities can be seen between LLME and PMWE. When echoes are particularly strong, fine structure can be resolved in both cases. The purpose of the present work was to compare mesospheric echoes between the polar and low latitudes and propose an explanation for the observed features.

2. Observations.

PMSE observations were made with the ESRAD 52 MHz radar located near Kiruna (68°N, 21°E), Sweden and the EISCAT 224 MHz radar located near Tromsø (69°N, 19°E), Norway. On November 9-13, 2004 there was strong solar proton event when precipitating energetic protons ionized additionally the ionospheric D layer. This made it possible to detect PMSE with both radars (Figure 1). The EISCAT radar ran the arc_dlayer experiment with vertical beam and 300 m altitude and 5 s time resolutions. At the same time ESRAD ran the fca_4500 experiment with 600 m altitude resolution and 20 ms time resolution. On November 11 the EISCAT echo was particularly strong allowing us to distinguish regular perturbations with a period ~60 s in echo power and dynamic spectra (Figure 2). For comparison with LLME we have chosen November 23, when the Indian MST radar located at Gadanki (14°N, 80°E), India detected a backscattering layer at about 72 km which lasts more than 5 hours (Figure 3). In this experiment the vertical beam was used, altitude resolution was 600 m and we used 8.2 s integration for calculation of dynamical spectra shown in Figure 3 (the bottom panels). The spectra at four altitudes clearly show pulsations with a period ~20 min.

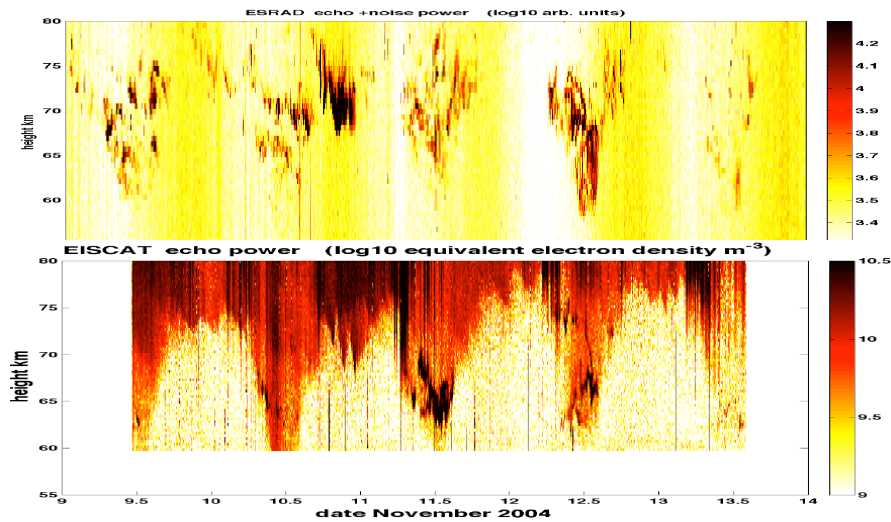


Figure 1. (Top panel) ESRAD backscattered power in arbitrary units. (Bottom panel) EISCAT backscattered power in units of equivalent electron density per m^{-3} .

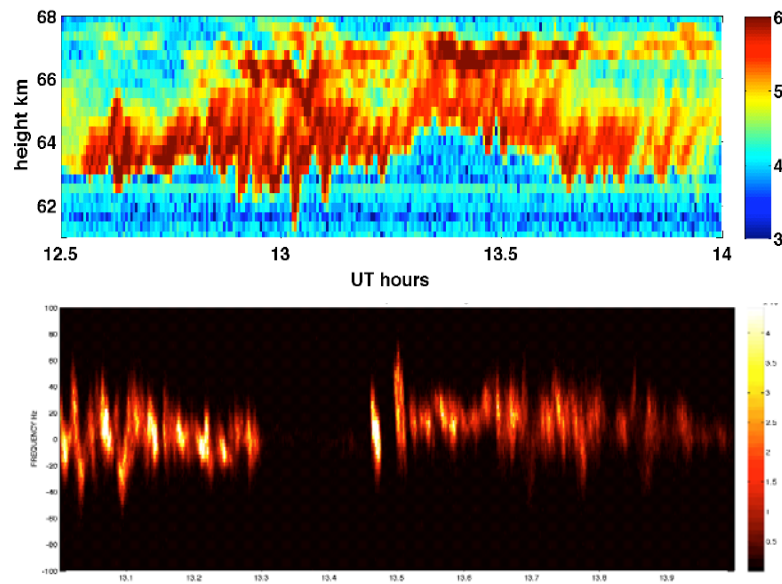


Figure 2. (Top panel) EISCAT backscattered power (equivalent electron density per m^{-3}) on November 11, 2004. (Bottom panel) Dynamic spectra from 13 UT to 14 UT at altitude 64 km.

3. Discussion.

For PMWE measured with ESRAD and EISCAT radars during 10-12 November 2004 the spectral widths were derived from the computed spectra and then were corrected for gradients in Doppler in height and time. The latter correction considers the presence of waves with periods comparable to integration time and the former one compensates for spectral broadening due to integration of these waves over each altitude range. Half maximum half widths (hmmw) for PMWE heights together with those for incoherent spectra ion line for EISCAT measurements without PMWE are presented in Figure 4 on the left panel. The right panel shows theoretical spectral widths calculated for incoherent spectra (IS) ion line (Mathews, 1984) and for turbulent spectra assuming different turbulence dissipation rates (Hocking, 1982) and 0.02 rad/s buoyancy frequency.

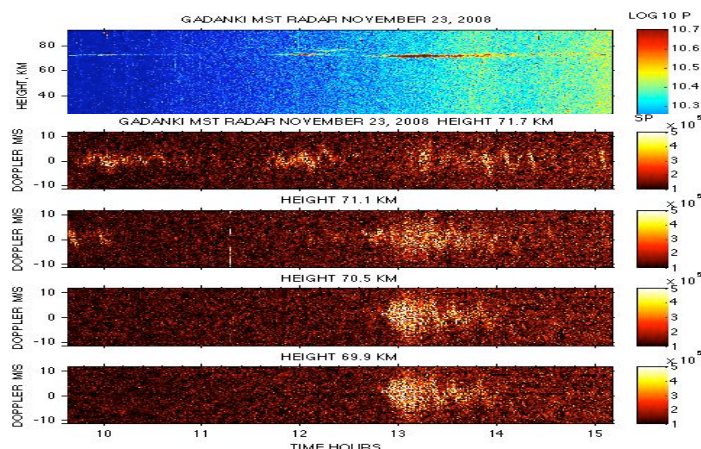


Figure 3. (Top panel) The Indian radar backscattered power in arbitrary units. The next panels show dynamical spectra at four altitudes 69.9 km, 70.5 km, 71.1 km and 71.7 km.

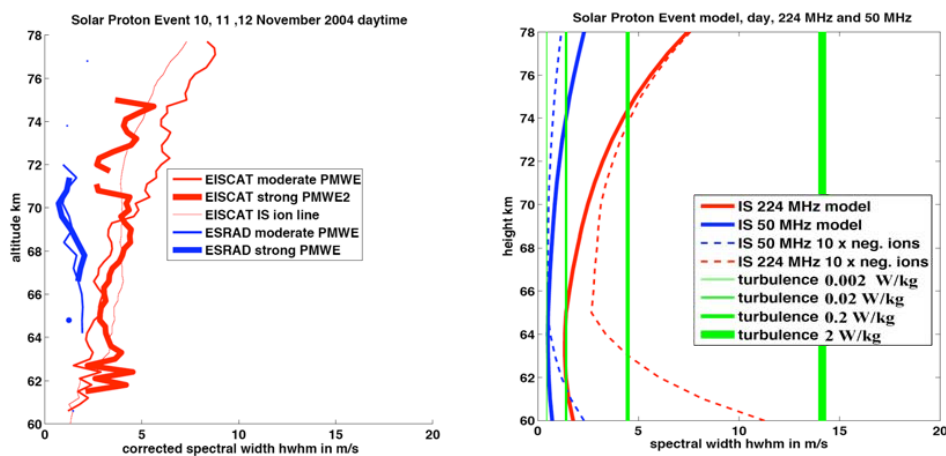


Figure 4. (Left panel) The profiles of the half spectral widths for PMWE and ion line derived from EISCAT and ESRAD radar measurements 10-12 November 2004. (Right panel) The profiles of the theoretical half spectral widths

From Figure 4 we can see that the experimental spectral widths for both EISCAT and ESRAD radars do not show dependence on PMWE strength. PMWE spectral widths at 224 MHz are the same as spectral widths for the IS ion-line for the diffusion limit. Spectral widths at 52 MHz are about 4 times less than at 224 MHz (in m/s). The height profile of PMWE spectral widths is close to theoretical expectations for the IS ion line, for normal molecular/cluster ions, at both 224 MHz and 52 MHz.

We calculated spectral widths for LLME on November 23, 2008 and plotted them versus echo power in Figure 5. Experimental spectral widths do not need to be corrected as those for PMWE because only long period of waves (20 min) with large vertical wavelength (> 2 km) modulated LLME, as seen from Figure 3.

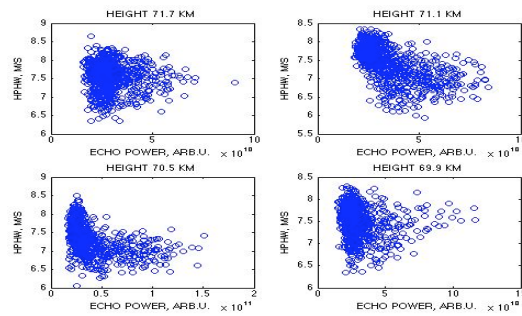


Figure 5. Half maximum half widths of LLME on November 23, 2008 versus echo power for four altitudes.

Estimated half maximum half spectral width for LLME is 6.5-8.5 m/s (correction for beam broadening is negligible). It is too large to be considered as an incoherent spectra ion line (as is the case for PMWE) and requires high turbulence dissipation rate of 0.4 W/kg to be explained by turbulent scatter. For LLME the spectral width decreases with growth of backscattered power in the middle of the layer and either does not change or increases at the layer edges. Sheth et al. [2006] detected similar layers with the 50 MHz Jicamarca radar which they identified as thin turbulent sheets of anisotropic aspect-sensitive scatters.

4. Summary.

When the signal is strong both PMWE and LLME show signatures of waves. PMWE were modulated with a wave period of about 1 min, and LLME with period of about 20 min. We suggest that such waves have no relation to generation of echoes, they just modulate them. PMWE corrected spectral widths are likely determined by the same process as for the IS ion-line, i.e. diffusion of positive and negative molecular ions and cluster ions. This is consistent with the proposal that PMWE are due to ‘evanescent diffusion waves’ resulting from partial reflection of infrasound (Kirkwood et al., 2006). We have not enough data for drawing conclusions on the LLME generation mechanism. There is some similarity with thin turbulent sheets observed with the Jicamarca radar in the SH tropics, however the echo spectral widths are more than 3 times larger than there (Gue et al., 2007) indicating stronger turbulence.

Bibliography.

- Gue, L., G. Lehmacher, E. Kudeki, A. Akgiray, R. Sheth, J. Chau, Turbulent kinetic energy dissipation rates and eddy diffusivities in the tropical mesosphere using Jicamarca radar data, *Adv. Space Res.* 40, 744-750, 2007.
- Hocking, W.K., Evidence for viscosity, thermal conduction and diffusion waves in the Earth's atmosphere", *Review of Scientific Instruments*, 74(1), 420-426, 2003.
- Kirkwood, S., P. Chilson, E. Belova, P. Dalin, I. Häggström, M. Rietveld and W. Singer, Infrasound – the cause of strong Polar Mesosphere Winter Echoes? *Ann. Geophys.* , 24, 475-491, 2006.
- Kumar, G. K., M. V. Ratnam, A. K. Patra, V. V. M. J. Rao, S. V. B. Rao, and D. N. Rao, Climatology of lowlatitude mesospheric echo characteristics observed by Indian mesosphere, stratosphere, and troposphere radar, *J. Geophys. Res.*, 112, D06109, doi:10.1029/2006JD007609, 2007.
- Mathews, J.D., The incoherent scatter radar as a tool for studying the ionospheric D region, *J. Atmos. Terr. Phys.* 11, 975-986, 1984.
- Sheth, R., E. Kudeki, G. Lehmacher, M. Sarango, R. Woodman, J. Chau, L. Guo, and P. Reyes, A high-resolution study of mesospheric fine structure with the Jicamarca MST radar, *Ann. Geophys.*, 24, 1281-1293, 2006.

DISCRIMINATION BETWEEN LIGHTNING-GENERATED RF AND RADAR REFLECTIONS FROM LIGHTNING.

I. Beres¹, W.K. Hocking¹ and R. Thomas²

1. University of Western Ontario, London, Ont., N6A 3K7 Canada.
2. New Mexico Institute of Mining and Technology

1. Introduction

Lightning can be a serious contaminant for many MST studies, since it produces short bursts of strong electromagnetic radiation, with a corresponding broad frequency range. Fourier components cover the range from MF and HF up through to UHF and higher. Emissions at VHF are particularly strong.

On the other hand, because of its impact on human activities, lightning is also a topic worthy of study in its own right. Radio waves can be used to study lightning by two methods. The first uses the radio emissions produced by the lightning itself, while the second uses radio wave pulses generated by a transmitter. In the latter case, the radio pulses are reflected from lightning channels and local variations in refractivity. We will refer to the first method as a “passive” mode of study, since it requires only receivers, while the second mode will be called an “active” mode, since it requires the observer to produce RF radiation and actively probe the lightning region.

A variety of preliminary investigations of lightning were undertaken using active methods in the middle and later parts of the 20th century (e.g. Ligda, 1950; Browne, 1951; Hewitt, 1957; Pawsey, 1957; Dawson, 1972; Proctor, 1981; Mazur et al., 1985; Roettger et al., 1985). Interesting studies were made, but in the 1990’s the passive technique came to the fore as the method of choice. By using multiple receivers at various points spread out by distances of typically kilometers and more across the ground, and using fast timing methods to compare times of arrival of lightning-generated RF bursts, the sources of the RF could be located in 3 dimensions to accuracies of tens of metres and better. The sources could be tracked on time-scales of milliseconds. The method requires highly computer-intensive algorithms for identification of common RF burst, since in any time interval of a second or so there could be many thousands of RF sources, and the signals from these multiple bursts need to be untangled and cross-correlated.

Time-of-arrival Methods for Lightning Studies.

The first use of TOA (Time-of-arrival) measurements for lightning studies, using passive methods, was undertaken by Proctor in South Africa (Proctor, 1971). Oetzel and Pierce (1969) examined the possibility of using VHF radio signals emitted by lightning to map the structure of individual discharges, and in time, this procedure was used to develop a viable research instrument. Examples of such systems include the Lightning Detection and Ranging (LDAR) system (Poehler and Lennon, 1979) and the Lightning

Mapping Array (LMA), developed and operated by The New Mexico Institute of Mining and Technology.

As an example, the LMA consists of 10-15 stations set up in a network over an area from 50 to 80 km in diameter. The arrival of impulsive VHF events is detected and accurately timed by each station in a 6 MHz passband centered at 63 MHz. A received power threshold value is set, and if the received power of the VHF source events exceeds this value, the time and received power of the event is recorded as frequently as once every 80 μ s. As many as 12,500 events can be recorded per second. Data collected from each station are combined with all the other stations and post-processing involves using the time-of-arrival values to generate solutions for the locations of the source events. A more complete discussion of the system can be found in Thomas et al., (2004), and references there-in.

Radar applications.

As powerful as the TOA methods are, they do require the existence of rapid electron acceleration in order to produce the radio frequency emissions. Hence these methods usually give source-positions associated with the leading tip of the lightning channel, as it forces its way through the atmosphere. The trailing regions of the channel may still exist in plasma form, but often do not radiate RF. It is in studies of such “radio-quiet” regions that radar may still play a role. In addition, within a typical cloud there can also be regions of variation in dielectric permittivity which can also produced radio reflections.

Proctor (1981) undertook radar studies with wavelengths of 5.5, 50, and 111 cm. The radars with wavelengths of 50 and 111 cm produced strong lightning echoes. At 5.5 cm the echoes were weak and smaller in number due to masking by hydrometeors. Echoes appeared to behave in one of two ways. Occasionally strong echoes appeared individually and moved rapidly in range; Proctor ascribed these to the tips of underdense channels. Stationary echoes that extended in range to become multiple echoes similar to those observed at VHF were ascribed to reflections by many channel segments that happened to be overdense at 5.5 GHz. A plot of amplitude versus range showed that these echoes were seen to grow in strength and then decay. Along with Holmes et al. (1980), it was concluded that radar echoes received from lightning in the cloud are due to many reflectors that are distributed throughout a volume of cloud, rather than being arrayed along a tortuous path that is mostly one dimensional.

These observations suggest that active methods still have an important role to play. It still needs to be unambiguously determined where the most prominent lightning reflectors occur. Once determined, there is important physics to be determined in association with these reflectors, such as determination of their lifetimes and the mechanisms of decay. The lifetimes may also give information about diffusion within the cloud, and associated ambipolar diffusion coefficients.

However, often a problem exists in discriminating the reflected radio pulses from the lightning-generated RF bursts. An example is seen in fig. 1, covering about 0.5 seconds. In regions “A” and “C”, the signal is dominated by RF emissions from the lightning, while in regions B and D, evidence exists of more temporally coherent signal. Where the

RF emissions dominate, the phase is variable and largely erratic. In extreme cases, it can be completely random from pulse to pulse.

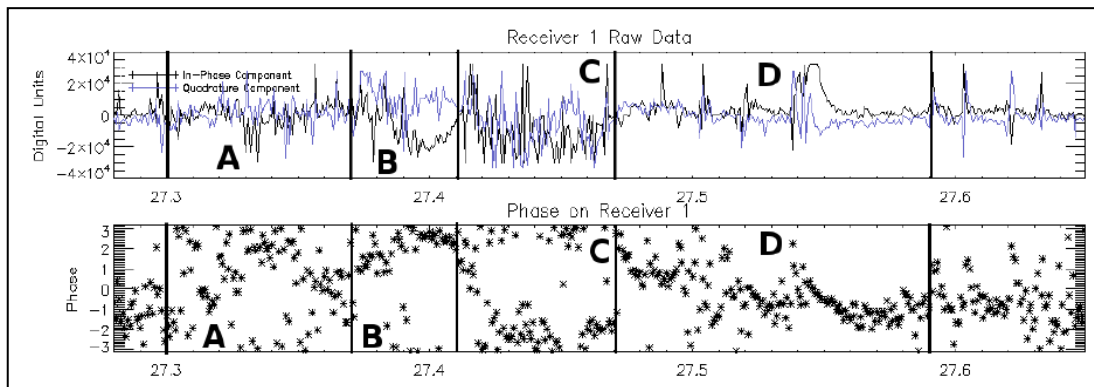
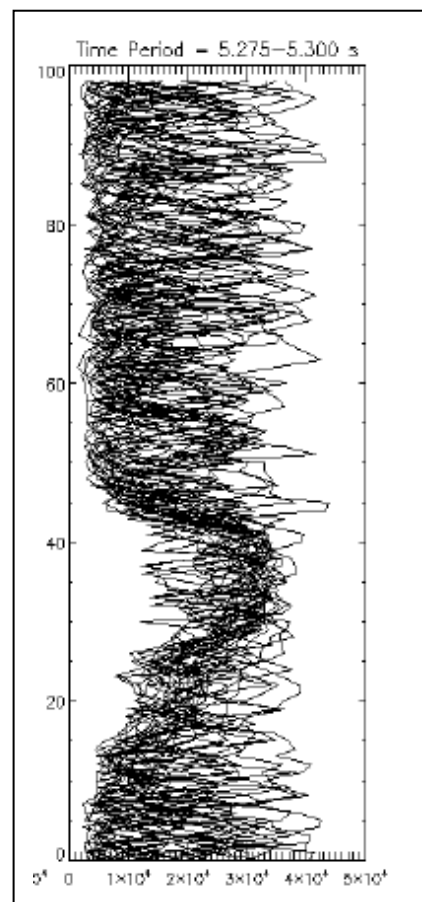


Fig.1. Plots of the in-phase and quadrature components (upper graph) and the phase (lower graph) of radar detections during a lightning episode. Time (abscissa) is in seconds.

The fact that some level of coherence does exist in fig.1, at least in the regions like B and D, suggests that useful radar studies can be extracted from these data, even though they are contaminated by RF emissions. If events like this can be found, it is possible to perform interferometry and determine the location of the reflecting regions. This has been done by, for example, Roettger et al., (1995). We have also been able to perform interferometry, using a small transmit-receiver with 3 separated antennas comprising groups of 4 Yagis (see Fig. 2 of Hocking and Hocking, this issue). We have also employed a 5-element interferometer like the systems commonly used for meteor studies (e.g. Hocking et al., 2001).

Fig 2. Successive height profiles recorded and overlaid during an lightning event. The abscissa shows amplitude, ordinate shows range-bin number.



However, often the signal is dominated by RF emissions. A major objective of our current work was to develop a method to remove the effects of this RF.

Because lightning echoes are very strong, we were able to sacrifice the usual condition that the transmitter pulse and the receiver should be “matched”. Pulse lengths

are usually 1 or 2 km, due to frequency allocation limitations, so the matching filter width should have width of the order of 75 or 150 kHz. However, we used a much wider filter-width – in our case, 400 kHz. Because lightning is broadband, pulses from RF lightning emissions were narrow – typically 350-400 metres or so. The reflected pulse is about 5 times broader. Successive profiles have been overlaid in fig. 2, and a smooth variation is seen embedded in the much choppier background from range-gates 25 to 45. The rapidly varying signal is due to lightning emissions, while the smoother variation is due to the reflected pulse.

Now that the pulse can be identified, it can be further cleaned by application of averaging, or even the application of median filters, within user-specified time-intervals and over user-specified gates. For example, if a histogram is formed within a time interval of say 10 ms, and over 5 successive height-gates, the histogram will have a median which will be close to the true reflected pulse value, and multiple outliers which are due to the RF, allowing rejection of the outliers. Further averaging then reveals the true reflected pulse profile, and interferometry can now be applied. The use of wider receiver filters, and higher pulse repetition frequencies, will improve the method further.

References:

- Browne, I. , “A radar echo from lightning”. *Nature*, 167, 438, 1951.
- Dawson, G., “Radar as a diagnostic tool for lightning”, *J. Geophys. Res.*, 77, 4518, 1972.
- Hewitt, F., “Radar echoes from interstroke processes in lightning”, *Proc. Phys.Soc. of London*, Section B, 70, 961–979, 1957.
- Hocking, W.K., B. Fuller and B. Vandeppeer, "Real-time Determination of Meteor-related Parameters Utilizing Modern Digital Technology", *J. Atmos. Solar-Terr. Physics*, 63, 155-169, 2001.
- Holmes, C., Szymanski, E., Szymanski, S., and Moore, C.,”Radar and acoustic study of lightning”, *J. Geophys. Res.*, 85, 7517–7532, 1980.
- Ligda, M. (1950). “Lightning detection by radar”, *Bull. Amer. Meteorol. Soc.*, 31, 279–283, 1950.
- Mazur, V.,D. Zrnica, and W. Rust, “Lightning channel properties determined with vertically pointing Doppler radar”, *J. Geophys. Res.*, 90, 6165–6174, 1985.
- Pawsey, J., “Radar observations of lightning on 1.5 meters”, *J. Atmos. Terr. Phys.*, 11, 289–290, 1957.
- Oetzel, G. and E. Pierce, “VHF technique for locating lightning”, *Radio Sci.*, 4, 199–202, 1969.
- Poehler, H. and C. Lennon, “Lightning detection and ranging system, LDAR, system description and performance objectives. Technical Report 741005, NASA, 1979.
- Proctor, D., “ Radar observations of lightning”, *J. Geophys. Res.*, 86, 12109–12114, 1981.
- Roettger, J., Liu, C., Pan, C., and Su, S. (1995). Characteristics of lightning echoes observed with vhf ST radar. *Radio Science*, 30:1085–1097.
- Thomas, R. J., P.R. Krehbiel, W. Rison, S.J. Hunyady, W. P. Winn, T., Hamlin and J. Harlin,, “Accuracy of the lightning mapping array”, *J. Geophys. Res.*, 109, doi:10.1029/2004JD004549, 2004.

EVALUATION OF ABSOLUTE RADAR CALIBRATION USING COSMIC NOISE (QDC) AND SIMULATED SIGNALS

Gunter Stober^{1,2}, Werner Singer² and Christoph Jacobi¹

¹University Leipzig, Institute of Meteorology, Leipzig, Germany

²Leibniz-Institute of Atmospheric Physics, Kühlungsborn, Germany

1. Introduction

Calibrated radars have been used, among others, to investigate PMSE events on both hemispheres (Latteck et al., 2008). This possibility was achieved by developing improved calibration methods, which were also applied to standard all-sky meteor radars. Swarnalingam et al., 2009 used calibrated radars to analyse PMSE strength and to compute the backscatter cross sections. Singer et al., 2008 used calibrated meteor observations and separated them into weak and strong meteor echoes, which lead to a significant improvement of the temperature estimates of the meteor radars.

In this paper we are going to compare the different calibration techniques to point out the advantages and disadvantages of the different methods. Therefore, we did apply three calibration methods to the Collm meteor radar (51.3° N, 13° E), which are more less different from each other, to investigate the impact of the antenna pattern and system parameters.

2. Radar calibration methods

A classical approach to calibrate a radar is the use of a well-defined noise source. Meteor radars operating in the VHF frequency range are also sensitive to cosmic radio emissions, which can be taken as such a well-defined noise source. However, this method requires a detailed knowledge of the employed antenna pattern, which can be difficult to estimate in the presence of side lobes, and a reference noise map for the same frequency. For the calibration of the Collm meteor radar, the sky noise map of Cane, 1978 was used.

Figure 1 presents the calibration methods, which are described in detail by Latteck et al., 2008. During both calibration procedures the receiving antennas remained disconnected and the cable losses and antenna impedances were checked separately.

The delay line method is a more sophisticated method to calibrate a radar (figure 1a). This procedure uses a directional coupler to extract the in the ASU/Transmitter generated signal and feed it into the delay line. During the calibration the entrance power is monitored. Applying a proper attenuation in the range between 30-110 dB and a delay of 100 μ s to the original coherent signal ensures that a well-defined power enters into the receivers and the A/D converter.

The noise generator method works similar to the cosmic noise calibration procedure. However, in this case the receiving antenna array is still disconnected and therefore the generated signal can be directly related to the digitized output in the A/D converter.

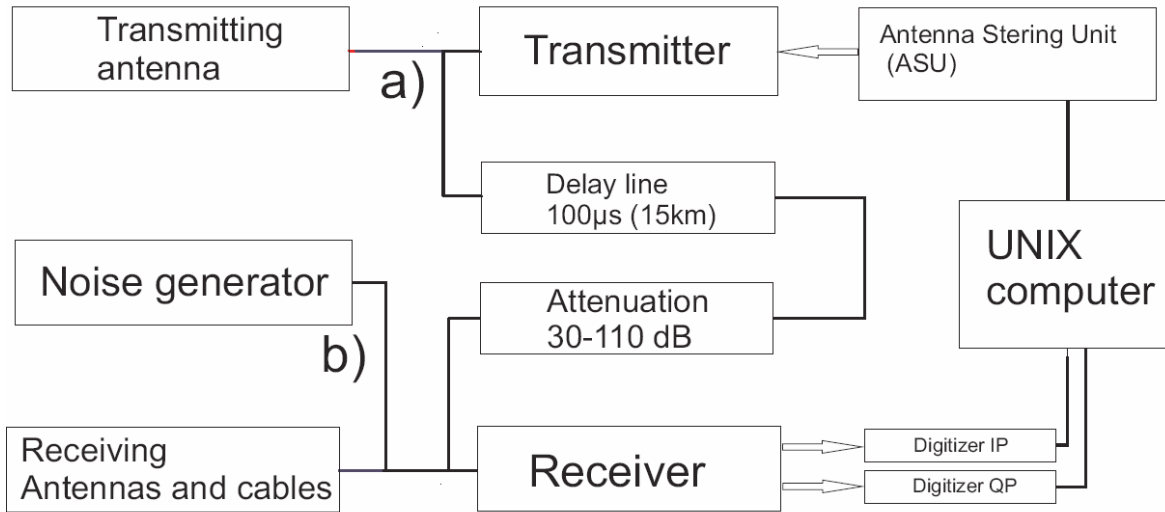


Figure 1: Scheme of the radar calibration of a VHF radar as applied to the Collm meteor radar site. a) Calibration circuit for the delay line method. b) Calibration circuit for the noise generator method.

The difference between the noise generator and the delay line method are given by the signals types for the calibration. The delay line uses a coherent signal, in the contrast to the noise generator that employs an incoherent Gaussian noise. Hence, each method leads to a different calibration coefficient. The conversion between the two coefficients depends on the number of coherent integrations and the digitization resolution.

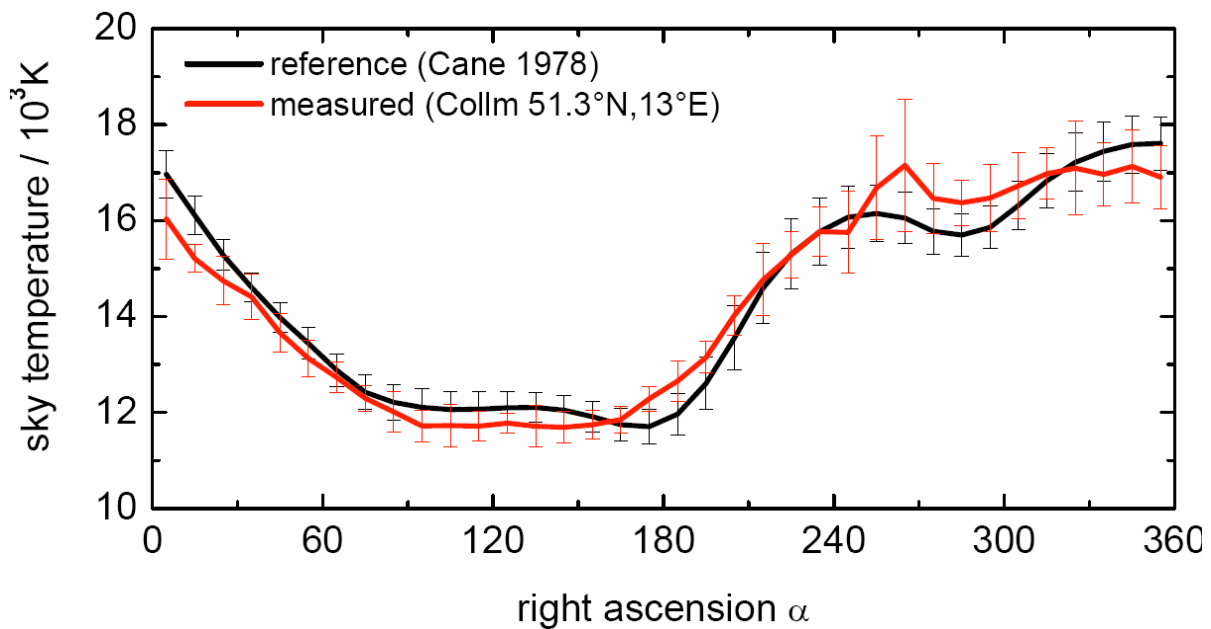


Figure 7: QDC defined by the cosmic radiation measurements during January 2008/2009 at Collm (51.3° N, 13° E).

One critical aspect in calibrating a radar are the antenna gains, in particular, if the sky noise calibration method is applied to the system. The impact of the antenna pattern on observing sky noise has to be considered. Friedrich et al., 2002 investigated the impact of the antenna beam width for isotropic antenna pattern on the resultant noise curves. To this aim, the antenna pattern was fitted to a sky noise map and the received noise power for a specific sidereal time was computed to receive a noise quiet day curve (QDC). These QDCs are a characteristic feature for each radar and depend on the beam properties as well as the geographic latitude. However, the determination of a QDC requires an undisturbed cosmic radiation that is not modified due to absorption or other ionospheric effects.

In figure 7 a computed QDC based on the sky noise map of Cane, 1978 considering the Collm antenna pattern, is compared to the QDC determined for the Collm meteor radar. The QDC was calculated using preferably data recorded during January 2008/2009. Days with low geomagnetic indices of K_p and A_p as well as low solar activity in the F10.7 flux were selected. For the measurement the calibration coefficient of the delay line method was used and all cable losses as well as the antenna gains were considered.

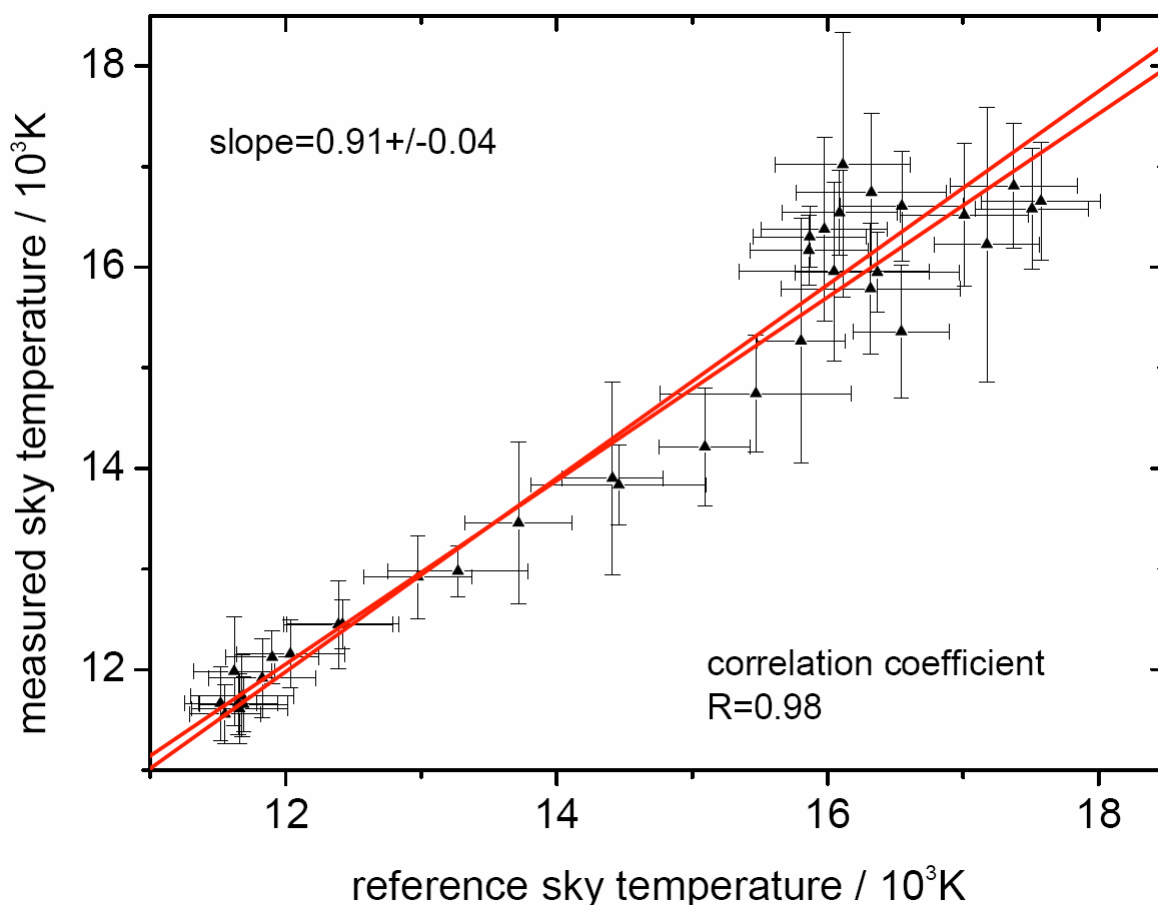


Figure 3: QDC-measurement during January 2008 and 2009 at Collm vs. reference sky temperature after Cane (1978).

Figure 3 shows the scatter plot of the measured vs. the computed reference sky noise temperature. The correlation coefficient of 0.91 demonstrates the good coincidence between the two QDCs. The error bars of the reference QDC shown in figure 2 and 3 were computed by integrating the fluctuation over the complete beam width of the sky noise map from Cane, 1978. The errors of the measured QDC represent the standard deviation of all meteor observations with the 10° bin in right ascension. The QDC was determined with an accuracy of approximately 650K.

The sky noise measurements deliver also the basis to investigate the detection threshold for the meteor observation. This can be used to improve the meteor fluxes as well as to estimate the ablated mass in the specular point (Stober, 2009).

3. Conclusion

In this paper we evaluated existing radar calibration methods and applied them successfully to the Collm meteor radar. The comparison of a computed reference QDC from a sky noise map considering the antenna pattern is in agreement with the determined QDC. This demonstrates the capability of meteor radar to observe cosmic noise and to use this data to calibrate the radar. Additionally, this data is useful for meteor science and to improve the measurements of meteor fluxes, due to the development of a method to quantify the noise threshold for the meteor detection.

References

Cane, H., 1978. A 30 MHz map of the whole sky. *Australian Journal of Physics* (31), 561.

Friedrich, M., Harrich, M., Torkar, K., Stauning, P., 2002. Quantitative measurements with wide-beam riometers. *J. Atmos. Solar-Terr. Phys.* 64 (3), 359 – 365.

Latteck, R., Singer, W., Morris, R., Hocking, W., Murphy, D., Holdsworth, D., Swarnalingam, N., 2008. Similarities and differences in polar mesosphere summer echoes observed in the arctic and antarctica. *Ann. Geophys.* 26, 2795–2806.

Singer, W., Latteck, R., Millan, L., Mitchell, N., Fiedler, J., 2008. Radar backscatter from underdense meteors and diffusion rates. *Earth Moon and Planets* 102 (1-4), 403 – 409.

Stober, G., 2009. Astrophysical studies on meteors using a SKiYMET all-sky meteor radar. *Ph.D. thesis*, Institute of Meteorology, University Leipzig.

Swarnalingam, N., Hocking, W., Argall, P., 2009. Radar efficiency and the calculation of decade-long PMSE backscatter cross-section for the resolute bay VHF radar. *Ann. Geophys.* (27), 1643–1656.

Swarnalingam, N., Hocking, W., Singer, W., Latteck, R., 2009. Calibrated measurements of PMSE strengths at three different locations observed with SKiYMET radars and narrow beam VHF radars. *J. Atmos. Solar-Terr. Phys.* doi:10.1016/j.jastp.2009.06.014.

FREQUENCY DEPENDENCE OF PMSE: RESULTS FROM SIMULTANEOUS AND COMMON VOLUME MEASUREMENTS WITH EISCAT RADARS

Qiang Li¹, M. Rapp¹, J. Röttger², R. Latteck¹, M. Zecha¹, and C. Hall³

¹Leibniz Institute of Atmospheric Physics, Kühlungsborn, Germany

²Max-Planck Institute of Solar System Research, Katlenburg-Lindau, Germany

³Tromsø Geophysical Observatory, University of Tromsø, Tromsø, Norway

1. Introduction

Polar mesosphere summer echoes (or PMSE) are very strong radar echoes scattering from the extremely cold polar mesosphere in summer seasons. Since the first observation around 50 MHz (*Ecklund and Balsley, 1981*), further measurements of PMSE have been carried out using various radars operating within a wide frequency range between 2.78 MHz and 1.29 GHz (see *Rapp and Lübken, 2004*, for a review). One of the most striking properties of PMSE is the fact that their absolute volume reflectivities depend significantly on the frequencies of the radars. I.e. the observed volume reflectivities decrease extremely with increasing frequencies (or decreasing Bragg wavelengths). According to the theory with the common acceptance in the community, PMSE are created by turbulent scatter in combination with an enhanced Schmidt number caused by the presence of charged ice particles, the radar scattering should either come from a spectral range dominated by a k^{-3} -dependence (the so-called viscous-convective subrange) or from a spectral range dominated by an exponential decay at the smallest spatial scales (the so-called viscous-diffusive subrange). As a consequence, the expected ratio of the volume reflectivities obtained by two radars should be equal to or larger than a minimum value, which is the ratio of the radar frequencies to the third power. This provides the unique possibility for a direct experimental test of the theory.

2. Experimental details and observations

The observations described in this manuscript were obtained with two pairs of common-volume radars, i.e., the EISCAT Svalbard Radar (ESR, 500 MHz) and the SOUSY Svalbard Radar (SSR, 53.5 MHz) collocated near Longyearbyen on Svalbard (78°N, 16°E) and the EISCAT VHF (224 MHz) and UHF (930 MHz) radars collocated at Ramfjordmoen near Tromsø, Norway (69°N, 19°E). Detailed descriptions of these four radars can be found in *Wannberg et al. (1997)*, *Röttger (2001)*, *Baron [1986]* and *Folkestad et al. (1983)*, respectively.

The ESR/SSR measurements were obtained in June 2006. During this period, the SSR was run continuously, whereas the ESR was run for 1-4 hours during 18 days around noon. Details regarding these measurements have recently been presented by *Li et al. (2009)*. The measurements by EISCAT VHF/UHF radars were performed for 2-6 hours in July 2004 and 2005 while the RF Heating facility was also operated (*Rietveld et al., 1993*). The heating parts of the observations hence have been removed before the data were integrated over 1 minute interval. Technical and physical parameters relevant to our study are summarized in Table 1.

In order to compare the strength of PMSE obtained by different radars, we should convert the absolute volume reflectivity, i.e. the radar backscatter cross section per unit volume, which is a system independent parameter.

Table 1 Radar system parameters.

	ESR	SSR	EISCAT-VHF	EISCAT-UHF
Frequency (MHz)	500	53.5	224	930
Wavelength (m)	0.60	5.61	1.34	0.32
Antenna gain (dBi)	42.5	30.0	46	48.1
Half-power beam width (°)	1.23	5	0.7	1.2×1.6
Peak power (MW)	0.8	0.004	1.2	1.2
Baud length (s)	2	2	2	2
Range resolution (m)	300	300	300	300
Number of coherent integration	4×2	16×2×2	29	29
System temperature (k)	60	3000	250-350	110

In the case of the ESR, this was done on the basis of a noise calibration, i.e., a well known calibration noise source was switched on during each pulse reception interval and fed into the receiver system (see *Wannberg et al.*, 1997). Whereas in the case of SSR, a delay line calibration was performed and verified against an additional noise calibration as described in detail in *Latteck et al.* (2008). For the delay line calibration, the transmitter output itself is fed into the receiver input using a directional coupler and delaying the transmitted pulse by 100 μs (corresponding to a range of 15 km) using an ultra-sonic delay line. As for the case of the EISCAT VHF/UHF radars, incoherent scatter measurements are routinely analyzed in terms of electron number densities (or ‘apparent’ electron number density in the case of PMSE) by comparing measured power values to measurements of a calibration source of known brightness temperature and by using IS theory. Such derived apparent electron number densities can be converted to volume reflectivities using the well known relation

$$\eta = \sigma \cdot N_e \quad (1)$$

Where $\sigma = 5 \times 10^{-29} \text{ m}^2$ is half the scattering cross section σ_e of an electron and N_e is the (apparent) electron density (e.g., *Röttger and LaHoz*, 1990).

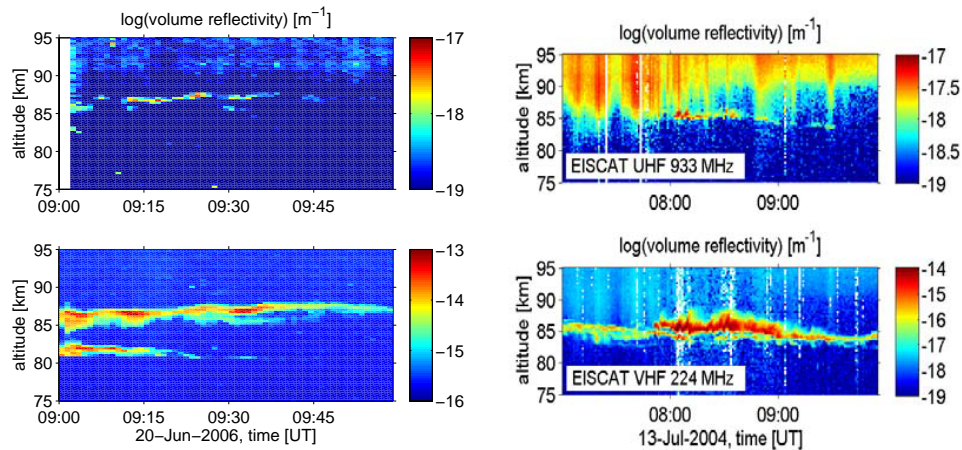


Figure 1. Height-Time-Intensity plots of the radar echoes observed by the ESR/SSR (left panel) and the EISCAT VHF/UHF radars (right panel), respectively.

Figure 1 presents two typical examples of simultaneous PMSE observations with the ESR/SSR (left panel) and the EISCAT VHF/UHF radars (right panel), respectively. Both pairs of radars have observed prominent echoes in approximately the same altitude range. The VHF-echoes (by the SSR and EISCAT VHF radar) generally extend over a larger altitude range than the UHF-echoes (by the ESR and EISCAT UHF radar) and show more variations in the morphology (sometimes appearing with double-layers or even multi-layer structures).

3. Discussion and conclusions

We now proceed with the comparison of the volume reflectivities obtained at different radar frequencies. Following the work by *Rapp et al. (2008)*, which is based on the classical formulation for pure turbulent scatter by *Hocking (1985)* and using the results of *Batchelor (1959)* for the case of tracers with Schmidt numbers larger than 1, the theoretical expression of the radar volume reflectivity for the case of the turbulent scatter aided by a large Schmidt number is given by:

$$\eta = 8\pi^3 \cdot \frac{f_\alpha \cdot q \cdot Ri}{Pr^t} \cdot \frac{\sqrt{\varepsilon v}}{N^2} \cdot \tilde{M}_e^2 \cdot r_e^2 \cdot \frac{1}{k^3} \cdot \exp\left(-\frac{2\eta_K^2}{Sc} \cdot k^2\right) \quad (2)$$

where ε is the turbulent energy dissipation rate, v is the kinematic viscosity, N is the buoyancy frequency, $k = 4\pi/\lambda$ is the Bragg wavenumber of the radar, $\eta_K = (v^3/\varepsilon)^{1/4}$ is the Kolmogorow microscale, r_e is the classical electron radius, and $Sc = v/D_e$ is the Schmidt number. The reduced potential refractive index gradient is give by

$$\tilde{M}_e = \frac{n_e N^2}{g} - \frac{dn_e}{dz} - \frac{n_e}{H_n} \quad (3)$$

It depends on the electron number density n_e , the buoyancy frequency, and the density scale height H_n . Finally, f_α , q , Ri and Pr^t are all ‘constants’ derived from either theory or by comparison with observations (see Appendix A in *Rapp et al. (2008)* for more details).

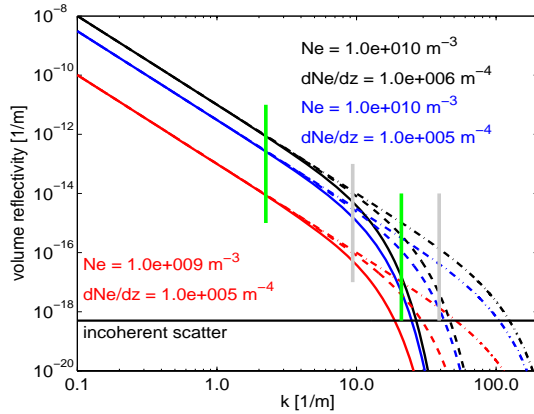


Figure 2. Simulated volume reflectivities for turbulent scatter for a turbulent energy dissipation rate of 0.1 W/kg and electron number density Ne and its gradient dNe/dz indicated in the insert. The solid, dashed and dashed-dotted lines were calculated for $Sc = 650, 1600$ and 41600 , respectively (corresponding to radii $r_A = 10, 20,$ and 80 nm, respectively). The four vertical bars indicate the Bragg Wavelengths of the SSR, EISCAT VHF radar, the ESR and EISCAT UHF radar (from left to right).

In Figure 2, we have plotted various theoretical curves $\eta(k)$ for different combinations of the electron number density and its gradient and the Schmidt number. This figure shows two interesting things (for convenience, focus on the ESR/SSR): if the Schmidt number is large, then the ratio between $\eta(\text{SSR})$ and $\eta(\text{ESR})$ should be a constant value, i.e., the three curves of $\log(\eta(k))$ are parallel to each other. Going back to Equation 2 we see that in this case $\eta(k) \propto k^{-3}$, i.e., for large Sc both η -values fall into the viscous-convective subrange such that the ratio $\eta(\text{SSR})/\eta(\text{ESR})$ is given by $(k_{\text{ESR}}/k_{\text{SSR}})^3 = (500 \text{ MHz}/53.5 \text{ MHz})^3 = 816$. If, however, the Schmidt number is not very large, then $\eta(\text{SSR})$ would fall into a part of $\eta(k)$ where the latter is dominated by the k^{-3} -dependence whereas $\eta(\text{ESR})$ would already fall into the part where $\eta(k)$ is dominated by the exponential term. In consequence, the ratio should be larger than the minimum value of 816 in those cases. For the case of the EISCAT VHF/UHF radars, the ratio $\eta(\text{VHF})/\eta(\text{UHF})$ should be larger than the minimum value of $(k_{\text{UHF}}/k_{\text{VHF}})^3 = (930 \text{ MHz}/224 \text{ MHz})^3 = 72$.

We then investigate this further with the radar observations. The histograms of the ratio $\eta(\text{SSR})/\eta(\text{ESR})$ (left panel) and $\eta(\text{VHF})/\eta(\text{UHF})$ (right panel) are shown in Figure 3. For the

ESR/SSR, the ratios vary between ~ 400 and 100000 . Importantly, however, more than 94% are larger than a value of 816, i.e., the ratio of the radar frequencies to the third power. This means that the large majority of our data is consistent with the expectations based on the here considered theory. The remaining 6% which lie to the left of 816 can likely be explained by the uncertainty of the calibrations as well as by the fact that the radar volume of the ESR is significantly smaller (beamwidth of 1.2°) than the radar volume of the SSR (beamwidth of 5°). This argument can be supported by the independent results from the EISCAT VHF/UHF observations, which have near identical beam widths and hence observing volumes. The ratio $\eta(\text{VHF})/\eta(\text{UHF})$ shows that more than 99% are larger than a value of 72, which is the corresponding ratio of the radar frequencies to the third power. These results give strong support that PMSE are indeed created by turbulent scatter in the presence of a large Schmidt number.

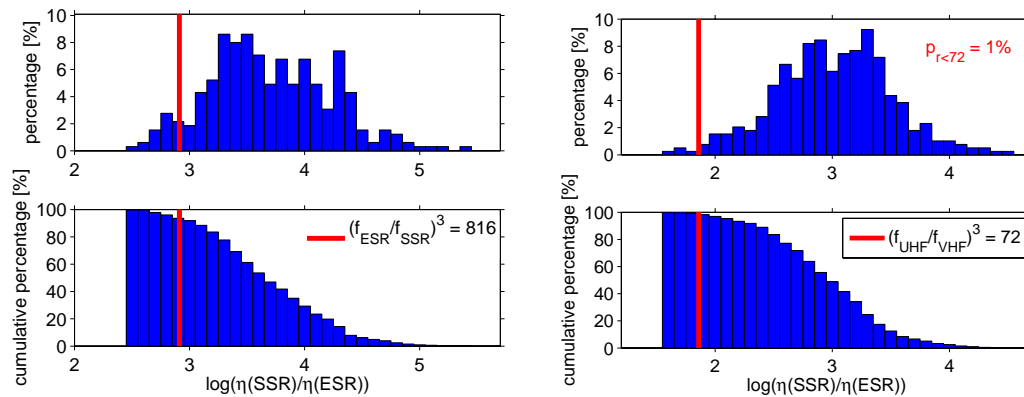


Figure 3. Distribution (upper panels) and the cumulative percentage (lower panels) of the ratio of the volume reflectivities observed by the ESR/SSR (left panels) and the EISCAT VHF/UHF radars (right panels). Red vertical bars show the corresponding ratio of the radar frequencies to the third power.

Bibliography

- Ecklund, W.L., B.B. Balsley, Long-term observations of the arctic mesosphere with the MST radar at Poker Flat, Alaska, *J. Geophys. Res.*, *86*, 7775-7780, 1981.
- Hocking, W.K., Measurements of turbulent energy dissipation rates in the middle atmosphere by radar techniques: A review, *Radio Sci.*, *20* (6), 1403-1422, 1985.
- Latteck, R., W. Singer, R.J. Morris, W.K. Hocking, D.J. Murphy, D.A. Holdsworth, and N. Swarnalingam, Similarities and differences in polar mesosphere summer echoes observed in the Arctic and Antarctica, *Ann. Geophys.*, *26*, 2795-2806, 2008.
- Li, Q., M. Rapp, J. Röttger, R. Latteck, M. Zecha, I. Strelnikova, G. Baumgarten, M. Hervig, C. Hall, and M. Tsutsumi, Microphysical parameters of mesospheric ice clouds derived from calibrated observations of polar mesosphere summer echoes at Bragg wavelengths of 2.8 m and 30 cm, *J. Geophys. Res.*, 2009JD012271, revised, 2009.
- Rapp, M., F.-J. Lübken, Polar mesosphere summer echoes (PMSE): review of the observations and current understanding, *Atmos. Chem. Phys.*, *4*, 2601-2633, 2004.
- Rapp, M., I. Strelnikova, R. Latteck, P. Hoffmann, U.-P. Hoppe, I. Häggström, and M.T. Rietveld, Polar mesosphere summer echoes (PMSE) studied at Bragg wavelengths of 2.8 m, 67 cm, and 16 cm, *J. Atmos. Sol. Terr. Phys.*, *70*, 947-961, 2008.
- Röttger, J., Observations of the polar D-region and the mesosphere with the EISCAT Svalbard Radar and SOUSY Svalbard Radar, *Mem. Nat. Inst. Pol. Res.*, *54*, 9-20, 2001.
- Wannberg, U. G., I. Wolf, L. G. Vanhernen, K. Koskeniemi, J. Röttger, The EISCAT Svalbard Radar: A case study in modern incoherent scatter radar design, *Radio Sci.*, *32*, 2283-2307, 1997.

LONGITUDINAL DIFFERENCES OF PMSE STRENGTH AT HIGH ARCTIC LATITUDES

W. Singer¹, N. Swarnalingam², J.M. Wissing³, R. Latteck¹, C. Meek⁴,
M.-B. Kallenrode³, A.H. Manson⁴, J. Drummond⁵, and W.K. Hocking²

¹ Leibniz-Institute of Atmospheric Physics, 18225 Kuehlungsborn, Germany

² University of Western Ontario, London, Ontario, Canada, N6A 3K7

³ Dept. of Physics, University of Osnabrueck, 49076 Osnabrueck, Germany

⁴ ISAS, University of Saskatchewan, Saskatoon, Saskatchewan, Canada, S7N 5E2

⁵ Dalhousie University, Halifax, Nova Scotia, Canada, B3H 4J1

1. Introduction

Polar Mesosphere Summer Echoes (PMSE) have been observed with VHF radars at high polar latitudes on both hemispheres as well as at mid-latitudes to study their properties in relation to the background atmosphere. The relative strengths of PMSE at different radar sites and their latitudinal and longitudinal variations are still an open question. Selected operational radar sites are depicted in Fig. 1.

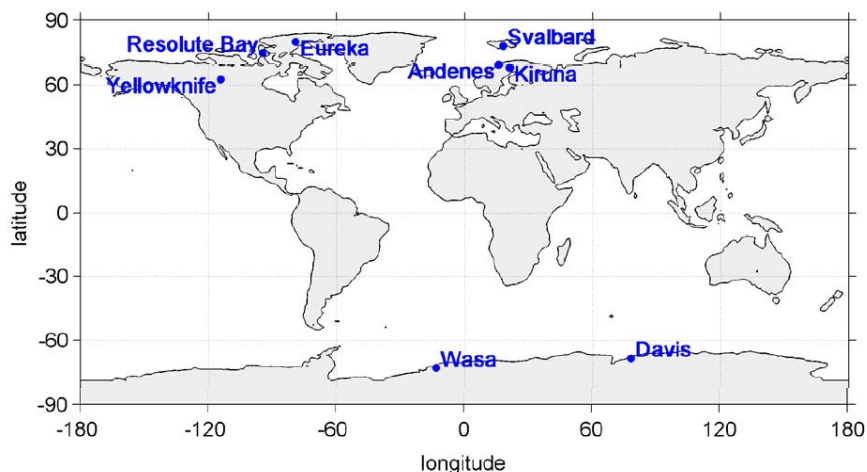


Figure 1. MST VHF radars and meteor radars observing PMSE.

PMSE observations with calibrated VHF radars at high arctic latitudes but well separated in longitude, namely at Andenes (69°N, 16°E) and Resolute Bay (75°N, 95°W), resulted in less PMSE strength and lower occurrence rate above Resolute Bay compared to Andenes (Latteck et al., 2008). Basing on decade-long PMSE backscatter cross-sections for the Resolute Bay VHF radar Swarnalingam et al. [2009a] concluded that the observed longitudinal difference to Andenes is related to geophysical reasons as Resolute Bay is located nearby the magnetic pole. But the different radar hardware and antennas applied at Andenes and Resolute Bay still represent a cause for concern.

A case study of calibrated PMSE observations at Yellowknife (62°N, 114°W) away from the magnetic pole and at Andenes using identical SKiYMET meteor radars indicated that the strengths of PMSE at both sites are comparable and both are significant stronger than at Resolute Bay (Swarnalingam et al., 2009b). The installation of the meteor radar at Eureka (80°N, 86°W) offered the possibility to perform PMSE observations with identical radars inside of the polar cap and in the auroral oval (Andenes) to confirm the assumption of Swarnalingam et al. [2009b].

2. PMSE observations with meteor radars in Eureka and Andenes

To detect coherent radar backscatter from PMSE structures and specular reflections from meteor trails the meteor radars are operated with a peak power of 12 kW, a pulse repetition frequency of 1072 Hz and a pulse width of 13.3 μ s. The meteor count rate is reduced by about 30-40 % compared to the normally used pulse repetition frequency of 2144 Hz. Continuous raw data sampling is done for 30 minutes for 60 range gates from 6 to 126 km in steps of 2 km. For PMSE detection power profiles are estimated in real time with an integration time of 20 s. The received signals of the five antennas of the interferometer are combined in software to produce a about 10° wide receiving beam with sidelobes 20°-25° apart from zenith.

The co-located meteor and VHF radar in Andenes observe PMSE at the same altitudes taking the different vertical resolution (VHF radar: 300m; meteor radar: 2000 m) and sensitivity of both systems into consideration as shown in Fig. 2.

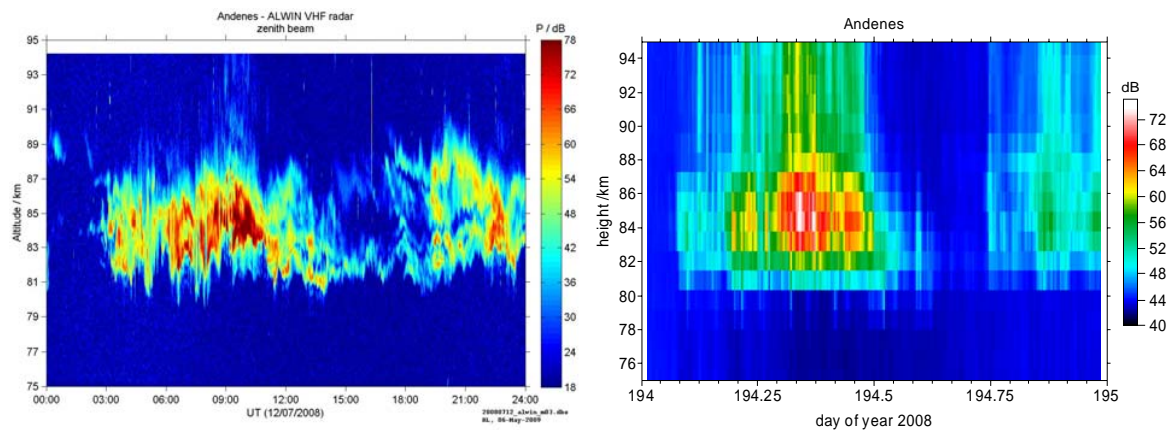


Figure 2. PMSE echoes (relative echo power) observed by co-located VHF radar and meteor radar in Andenes on July 12, 2008.

Simultaneous observations of PMSE using identical meteor radars at Eureka and Andenes are performed between July 11 and August 18 in 2008. The Eureka observations are influenced by high man made background noise preventing the detection of weak PMSEs. Fig. 3 shows the observations obtained on July 12. The echo power relative to the background noise level (5-minute median values) is presented after gain adjustment.

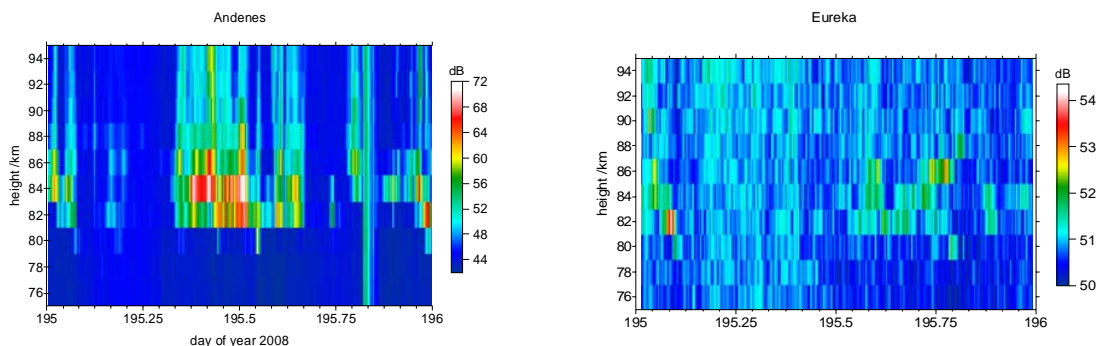


Figure 3. PMSE observations at Andenes and Eureka on July 13, 2008.

Both radars were carefully calibrated using cosmic noise variations with additional help of a commercially available calibrated noise source (Swarnalingam et al., 2009b). The sky noise variation at the radar site was calculated by a convolution process between the radar polar

diagram and the equivalent sky noise power. A linear regression fit between the recorded sky noise and the actual sky noise values obtained from a sky survey map provides the radar efficiency which is needed to estimate radar volume reflectivities for the comparison of PMSE strengths on an absolute level. Examples of the variation of the recorded sky noise and the actual sky noise are shown for both sites in Fig. 4.

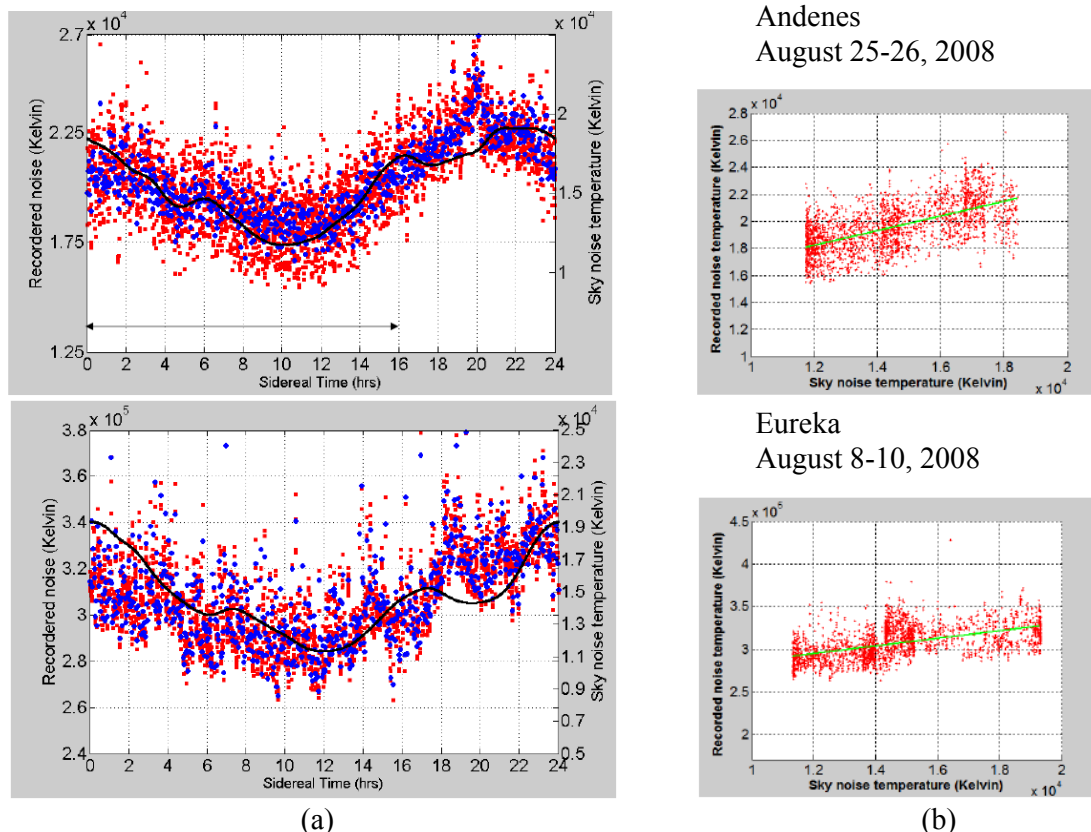


Figure 4. (a) Comparison of 2-min recorded sky noise (red dots) with sky survey map values (black line), Blue dots refer the mean values in each time bin. (b) Linear regression fit between the recorded sky noise temperatures and actual sky noise values for a sidereal day.

3. Results and discussion

PMSE radar reflectivities are calculated from the maximum echo powers observed between 80 and 90 km in every 2-min interval of the campaign. Distributions are presented in Fig. 5.

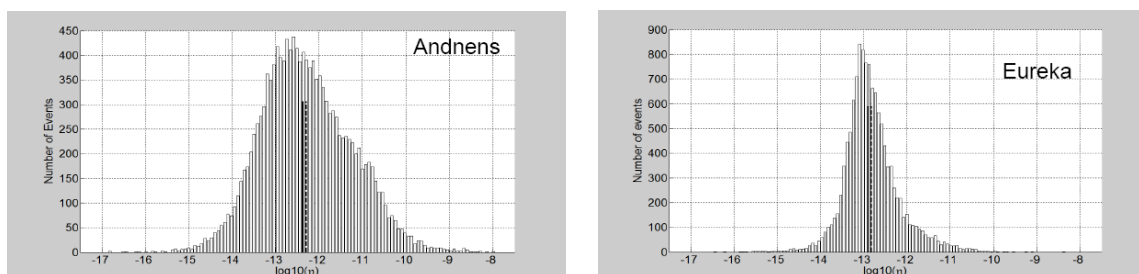


Figure 5. Distributions of PMSE volume reflectivity at Andenes and Eureka in summer 2008.

The median values of the distributions for Andenes/Eureka are $4.2 \cdot 10^{-13} / 1.2 \cdot 10^{-13} \text{ m}^{-1}$, the 10th and 90th percentiles are $2.9 \cdot 10^{-14} / 3.4 \cdot 10^{-14} \text{ m}^{-1}$ and $1.3 \cdot 10^{-11} / 8.8 \cdot 10^{-13} \text{ m}^{-1}$. Comparison of two meteor radar volume reflectivities shows that the PMSE strength at Eureka is significantly

lower than at Andenes. It confirms the comparison of the two MST radars at Andenes and Resolute Bay by *Latteck et al.* [2008] and the assumption that the difference is caused by geophysical reasons most likely due to differences of the background ionization as the radar reflectivity is proportional to the square of the background electron density.

The 3D numerical model AIMOS (**A**tmospheric **I**onization **M**odule **O**Snabrück) of atmospheric ionization due to precipitating particles with high spatial resolution has been used to estimate the ionization by precipitating particles. It is basing on the background atmosphere of the HAMMONIA model and the observations from two polar orbiting satellites (GOES 10/11, NOAA 15/16; time period 2002-2005) which are assigned to horizontal precipitation cells in dependence on geomagnetic activity (Wissing et al., 2008, 2009). During quiet times, the major contribution to ionospheric ionization is from electrons in both the polar cap (solar electrons) as well as in the auroral oval (magnetospheric electrons) whereas the ionization in the auroral oval exceeds that in the polar cap. Fig. 6 presents mean ionization rates in northern summer 2005 which are characterised by enhanced ionization rates in auroral oval (Andenes, Yellowknife) and lower rates in the polar cap (Resolute Bay, Eureka) in agreement with the observed weaker PMSE strengths at Resolute Bay and Eureka.

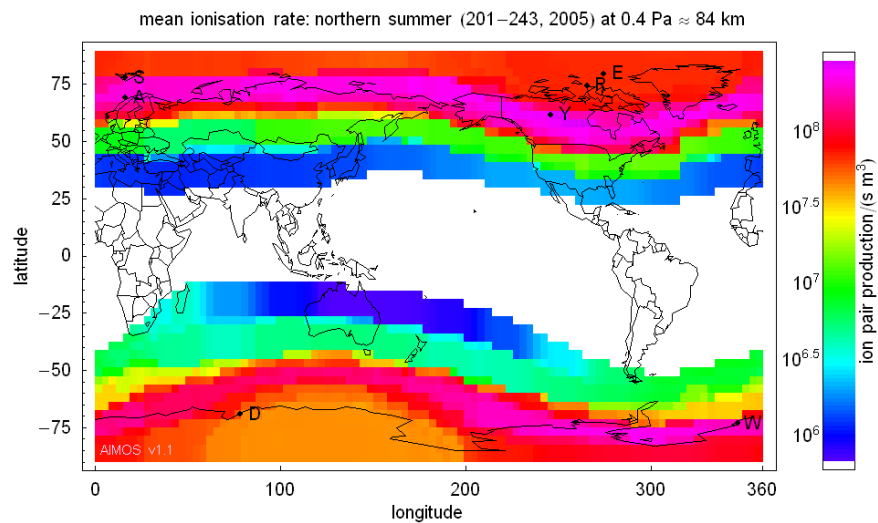


Figure 6. Mean ionization rates by alpha particles, energetic protons, and energetic electrons under quiet geomagnetic conditions in northern summer 2005 from AIMOS. The radar sites are abbreviated by the first character of their names (see also Fig. 1).

References

- Latteck, R., Singer, W., Morris, R.J., Hocking, W.K., Murphy, D.J., Holdsworth, D.A., and Swarnalingam, N.: Similarities and differences in polar mesosphere summer echoes observed in the Arctic and Antarctica, *Ann. Geophys.*, 26, 2795-2806, 2008.
- Swarnalingam, N., Hocking, W.K., and Argall, P.S., Radar efficiency and the calculation of decade-long PMSE backscatter cross-section for the Resolute Bay VHF radar, *Ann. Geophys.*, 27, 1643-1656, 2009a.
- Swarnalingam, N., Hocking, W.K., W. Singer, and R. Latteck, Calibrated measurements of PMSE strengths at three different locations with SKiYMET radars and narrow beam VHF radars, *J. Atmos. Sol.-Terr. Phys.*, doi:10.1016/j.jastp.200906.014, 2009b.
- Wissing, J.M., Bornebusch, J.P., and Kallenrode, M.-B., Variation of energetic particle precipitation with local magnetic time, *Adv. Space Res.*, 41, 1274-1278, 2008.
- Wissing, J.M., and Kallenrode, M.-B., Atmospheric Ionization Module Osnabrück (AIMOS) 1: A 3D Model to Determine Atmospheric Ionization by Energetic Charged Particles from Different Populations, *J. Geophys. Res.*, 2009, in press.

A Decade-long PMSE aspect-sensitivity study at Resolute Bay

N. Swarnalingam and W. K. Hocking

Department of Physics and Astronomy, University of Western Ontario, Canada

Introduction

A 51.5 MHz VHF radar system at Resolute Bay (75.0°N, 95.0°W) has been observing Polar Mesosphere Summer Echoes (PMSE) since 1997. PMSE are a unique form of strong coherent radar echoes from the cold summer mesosphere at high latitudes. Although PMSE are now a well recognized summer phenomenon in the polar regions, debate still exists on the physical mechanism that causes such a strong radar backscattering on the ground. In this paper, we present a long term aspect-sensitivity study for PMSE scatterers observed at Resolute Bay. Aspect-sensitivity studies can provide information about the shape of scatterers, and hence distinguish between the possible scattering processes. Over the years, many PMSE experiments were carried out, but only few were involved with aspect-sensitivity measurements (e.g Reid et al., 1988; Czechowsky et al., 1988).

The radar system consists a total of 128 2-element Yagi antennas. It uses an array in the form of a cross, with four separate arms such that the north arm is aligned 19 deg anti-clockwise from true north. The antenna array setup produces a narrow polar diagram with only 2 deg half-power-half width (HPHW). The beam not only points vertical, but also can be steered from vertical to 10.9 deg (off-zenith) along north arm, east arm, south arm and west arm. The system is operated at 51.5 MHz with 12 kW peak pulse power (Hocking et al., 2001). Recently this radar system was carefully calibrated using cosmic noise variations with the additional help of a commercially available calibrated noise source (Swarnalingam and Hocking, 2006) and (Swarnalingam et al., 2009), which allowed to compare the PMSE absolute strengths at this location with other locations. In order to observe PMSE, 8-bit complementary coded signals are transmitted with the Pulse Repetition Frequency (PRF) of 1200 Hz. The received signals are sampled using 750 m pulse and also are averaged using 16-point coherent integrations.

Method

A method to investigate the aspect-sensitivity in VHF radar was described by Hocking et al. (1986) (and references there-in), which subsequently has been applied to study the aspect-sensitivity of the PMSE. In their method, they expressed the aspect-sensitivity parameter θ_s as the 1/e half-width angular polar diagram of the scatterers which were assumed to be on average oblate spheroids, with a Gaussian increase or decrease in refractive index from the edge towards the center. Based on this, the polar diagram of the backscattered signal as a function of off-zenith angle θ is given by

$$P_\theta = \exp\left(-\frac{\sin^2\theta}{\sin^2\theta_s}\right) \quad (1)$$

where P_θ is the return power for the off-vertical direction, and P_v is the return power in the vertical direction. This means that small values of θ_s indicate a larger level of aspect-sensitivity, whereas larger values of θ_s indicate a lower level of aspect-sensitivity (meaning a more isotropic

nature of the scatterers). Under this assumption, the aspect-sensitivity parameter (θ_s) can be determined as

$$\theta_s = \arcsin \sqrt{\frac{\sin^2 \theta_s}{\ln(P_v/P_\theta)} - \sin^2 \theta_o} \quad (2)$$

Where P_v/P_θ is the ratio of the power on the vertical beam to that on an off-zenith beam at the direction of θ . θ_o is the 1/e beam width of the antenna polar diagram (Hooper and Thomas, 1995; Hobbs and Reid, 2001). Based on the above concept, several short term aspect-sensitivity studies have been conducted on PMSE at high latitudes, especially in the European sector (e.g. Reid et al., 1988; Czechowsky et al., 1988). (Zecha et al., 2001) used space antenna technique to estimate aspect sensitivity of PMSE. The results of these studies showed that θ_s has a value 5 - 6° especially in the lower altitude PMSE layers. At higher altitudes θ_s has larger values. A four year study in the North American sector was conducted by Huaman and Balsley (1998), and they also found an increase of θ_s with increasing height. These results support the speculation that PMSE could be associated with two different scattering mechanisms.

Data Presentation and Discussion

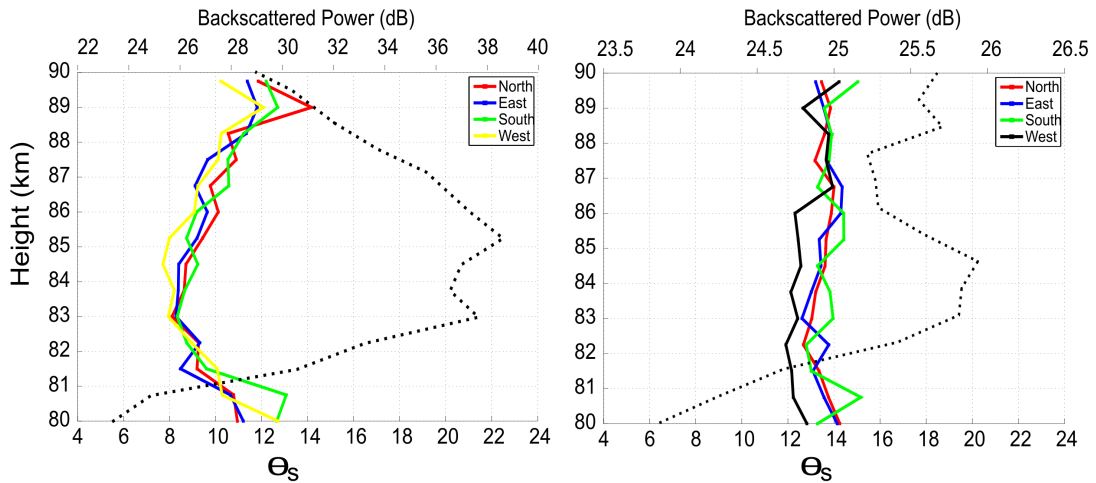


Figure 1: An example of PMSE aspect-sensitivity profile when PMSE were strong in strength at Resolute Bay in July 2000 (left panel). The same for the case when PMSE were relatively weak in strength at the same location in July 2006 (right panel). The dot-dot line represent the PMSE backscatter power in the vertical beam.

The examination of long-term aspect angle of PMSE scatterers at Resolute Bay was conducted with the two major aims. The first aim was to compare the aspect nature among the four off-zenith beams, and the second aim was how they various from year to year. In order to check this, we have used PMSE data collected during the period from year 1998 to 2008. In the calculation process of aspect angle, first the background noise in all beams were removed. The absolute PMSE backscattered powers were then determined using our radar calibration results. Following this, the absolute PMSE backscattered power ratio between vertical beam and off-zenith beams were estimated separately for each off-zenith beam. The relative efficiencies of each beam were taken into account in this comparison. Using Eq: 2, a distributions of θ_s were produced for a given range-height for each off-zenith beam. From the estimated

distributions the median values were considered as the aspect angle for that range-height. Eq: 2 is too sensitive whenever the power ratio between vertical beam and off-zenith beam is close to one. Due to this reason, we have avoided the cases in which the powers in vertical and off-zenith beams are nearly equal. However, such occurrences are in very low.

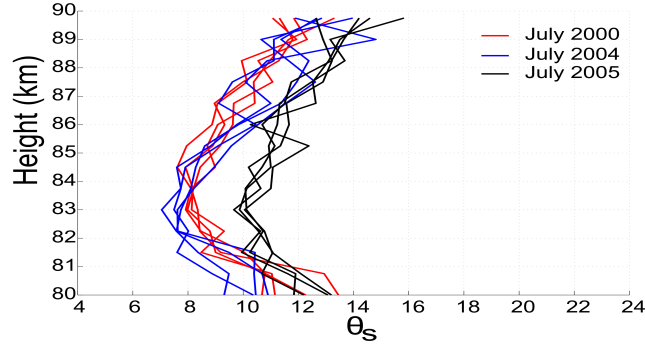


Figure 2: Estimated PMSE aspect-sensitivity profiles for each off-zenith beam for the month of July in 2000, 2004 and 2005. While four red profiles represent the aspect angle values for July 2000, blue and black lines represent July 2004 and July 2005, respectively.

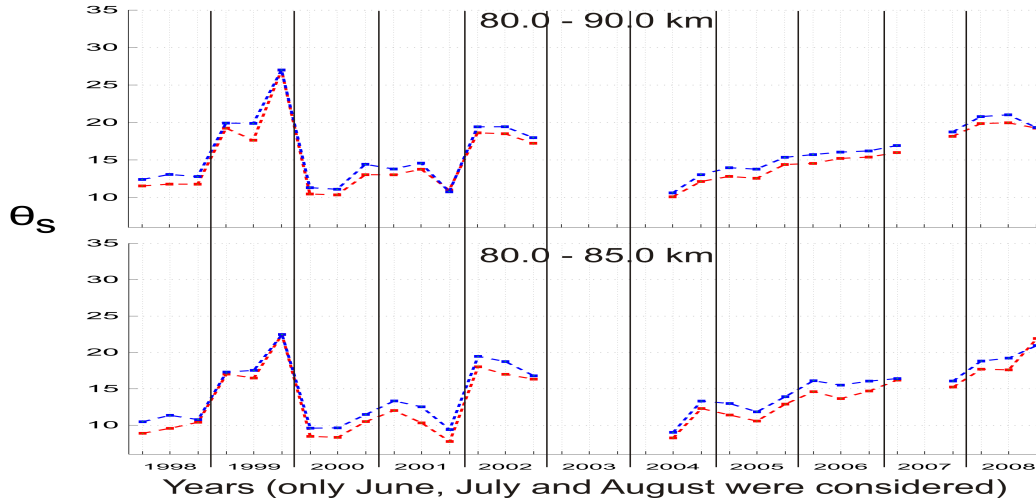


Figure 3: Mean monthly aspect-sensitivity values for height ranges 80 - 85 km and 80 - 90 km.

Figure 1 shows the estimated hourly averaged aspect angle height profiles for all four off-zenith beams for month July in 2000 (left panel) and 2006 (right panel). As it can be seen in figure that the profile takes two different shapes. Over the years, it has been noticed that PMSE strength at Resolute Bay shows great level of inter annual variability Swarnalingam et al. (2009). It is therefore apparat that the two different shapes in aspect angle profile are associated with the PMSE signal strengths and the occurrence rates (black dot-dot line refers the PMSE backscattered power profile). Note that the calculated aspect angles and their variations with height show a good agreement in all four beam, especially when PMSE are strong at Resolute Bay. This implies the existence of the stable PMSE layering structures extending to several km in the time scales of hours.

It also noticed that when PMSE are strong at Resolute Bay, the shape of the aspect angle

height profile takes the same shape. This can be seen from Fig 2, which contains data from July 2000, July 2004 and July 2005. While the aspect angle is in range 7 - 11 deg at 83 km, it takes 10 - 13 deg at 88 km meaning that upper PMSE layers are more isotropic in nature than lower ones. This feature of PMSE have been already observed by several researchers. Our calculated aspect angle values show a reasonable agreement with the calculated mean aspect angles for Poker Flat radar by Huaman and Balsley (1998). They found While the aspect angle at around 84 km is on average 10° , the aspect angle at around 88 km is about 13° .

Finally, Fig 3 shows the variation of aspect angle during 1998 - 2008. Note that figure contains aspect angle from both strong as well as weak PMSE activities at Resolute Bay (see Fig.4 in Swarnalingam et al. (2009) for strong and weak seasons at Resolute Bay).

References

- Czechowsky, P., Reid, I. M., and Rüster, R. (1988). VHF radar measurements of the aspect sensitivity of the summer polar mesopause echoes over Andenes (69° N, 16° E), Norway. *Geophys. Res. Lett.*, 15(11):1259–1262.
- Hobbs, B. G. and Reid, I. M. (2001). A comparison of tropospheric VHF Doppler beam steering and full correlation analysis measurements of aspect sensitivity. *Radio Sci.*, 36(5):955–964.
- Hocking, W., Rüster, R., and Czechowsky, P. (1986). Absolute reflectivities and aspect sensitivities of VHF radio wave scatterers measured with the SOUSY radar. *J. Atmos. Terr. Phys.*, 48:131–144.
- Hocking, W. K., Kelley, M., Rogers, R., Maurice, J.-P. S., and Moorcroft, D. (2001). Resolute Bay VHF radar: A multi-purpose tool for studies of tropospheric motions, middle atmosphere dynamics, meteor physics and ionospheric physics. *Radio Sci.*, 36:1839–1857.
- Hooper, D. A. and Thomas, L. (1995). Aspect sensitivity of VHF scatterers in the troposphere and stratosphere from comparisons of powers in off-vertical beams. *J. Atmos. Terr. Phys.*, 57:655–663.
- Huaman, M. M. and Balsley, B. B. (1998). Long-term-mean aspect sensitivity of PMSE determined from Poker Flat MST radar data. *Geophys. Res. Lett.*, 25:947–950.
- Reid, I. M., Rüster, R., Czechowsky, P., and Schmidt, G. (1988). VHF radar measurements of momentum flux in the summer polar mesosphere over Andenes (69° N, 16° E). *Geophys. Res. Lett.*, 15:1263–1266.
- Swarnalingam, N. and Hocking, W. K. (2006). Calibration and calculation of absolute backscatter cross-section using sky noise and calibrated noise source for Resolute Bay radar. *The Eleventh Workshop on Technical and Scientific Aspects of MST Radar - December 2006*, Tirupati, India.
- Swarnalingam, N., Hocking, W. K., and Argall, P. S. (2009). Radar efficiency and the calculation of decade-long PMSE backscatter cross-section for Resolute Bay VHF radar. *Ann. Geophys.*, 27(4):1643–1656.
- Zecha, M., Röttger, J., Singer, W., Hoffmann, P., and Keuer, D. (2001). Scattering properties of PMSE irregularities and refinement of velocity estimates. *J. Atmos. Terr. Phys.*, 63(2-3):201–214.

Session 2:
**New Instruments, Signal
Processing and Quality
Control**

THE NEW MST RADAR ON ANDØYA/NORWAY

Ralph Latteck, Werner Singer, Markus Rapp, Toralf Renkwitz

Leibniz-Institut für Atmosphärenphysik, Schloss-Str. 6, 18225 Kühlungsborn, Germany

Introduction

In October 1998 the Leibniz-Institute of Atmospheric Physics in Kühlungsborn, Germany installed the *ALWIN*-VHF radar on the island Andøya (69.30°N, 16.04°E) as a successor of the former *ALOMAR SOUSY* radar Singer et al. (1995). The *ALWIN* radar (Latteck et al., 1999) was designed for unattended and continuous observations of the tropo- and lower stratosphere but especially for observations of the mesosphere during summer time. The radar operated at a frequency of 53.5 MHz with a peak power of 36 kW and a minimum range resolution of 150 m. The antenna array consisted of 144 Yagi antennas arranged in 36 squared subsystems of four antennas. The system allowed operation in spaced antenna (SA) or in Doppler beam swinging (DBS) configuration with a 6.6° radar beam (half power full width) but with a fixed number of beam directions.

After 10 years of nearly continuous operation the *ALWIN* radar was switched off in September 2008 to be replaced by a new more powerful and more flexible radar. The major requirements for the new systems are (1) classical DBS observation with improved temporal and spatial resolution and free beam steering capability, (2) multiple beam observation and (3) multi-receiver and multi-frequency operation for modern interferometry applications (e.g. FDI).

The goal of the new system is the investigation of horizontal structures of Polar Mesosphere Summer Echoes (PMSE) caused by mesospheric ice clouds. Three-dimensional structures of the wind field and turbulent parameters determined from the radar data will be used to compare the detected PMSE distribution in detail with wind and turbulence variations caused by wave activity.

System description

The new *ALWIN* radar is a monostatic radar with an active phased array antenna. Its operational frequency is 53.5 MHz and the maximum peak power is approximately 800 kW. The system is composed of an active phased antenna consisting of 433 array elements and an identical number of transceiver modules. The basic parameters of the new *ALWIN* radar are given in Table 1, Figure 1 shows a photograph of the antenna array during its installation in July 2009.



Figure 1: Photograph of the new *ALWIN* site during the installation of the antenna array in July 2009.

Table 1: Basic parameters of the new ALWIN radar. The statements in brackets indicate later upgrades

Location	Andenes, Norway 69.30°N, 16.04°E
Operating Frequency	53.5 MHz
Peak power	~800 kW
Allocated bandwidth	4 MHz
Maximum duty cycle	5%
Pulse length	$\geq 0.33\mu s$
Sampling resolution	25 m
Transmitted waveforms	Single pulse, Complementary code, Barker code
Pulse shapes	Square, Gaussian, Shaped Trapezoid
Antenna array	433 three-element (crossed) Yagi
Effective antenna area	$\sim 6300m^2$
Half power beam width	3.6°
Directive gain	33.5 dBi
Beam directions	arbitrary pointing directions for zenith angles $< 30^\circ$
Receiving channels	16 (64)

The antenna array consists of three-element linear polarized Yagi antennas arranged in an equilateral triangle grid structure with a spacing of 4 m ($= 0.71\lambda$). A sketch of the antenna array is shown in Figure 2. The 433 antennas are indicated by crosses, the small quadrates below the crosses represent the antenna footings made of massive concrete. At first stage the NW-SE oriented Yagi antennas will be mounted on the poles only, the SW-NE oriented antennas will be installed in the near future. The nearly circular array with a diameter of approximately 90 m corresponding to an aperture of $\sim 6300 m^2$ results in a very symmetric antenna radiation pattern (Figure 2) with a half power beam width of 3.6°, an directive gain of 33.5 dBi and an almost symmetric first sidelobe with more than 17 dB suppression with respect to the main lobe. The equilateral triangle grid structure of the array allows the beam steering down to an off-zenith angle of 30° without grating lobes.

The antenna array is divided in 61 subarrays, 55 of them are identical hexagons consisting of 7 antennas each, 6 subgroups consisting of 8 antennas each are located at the perimeter of the array making it nearly circular. The theoretical beam width is approximately 30° for a single hexagon subarray consisting of 7 individual antennas, and 11° for a combination of 7 adjacent hexagonal subarrays ("anemone" antenna patch).

Each antenna is connected to its own transceiver with independent phase control and a scalable output up to 2 kW. This arrangement allows very high flexibility of beam forming and beam steering with a symmetric radar beam and arbitrary beam pointing directions. The transceivers are accommodated in six 20-ft office containers located in equal distance at the perimeter of the antenna array. The transceivers are state of the art VHF solid state pulsed transmitters and down converters with widely programmable

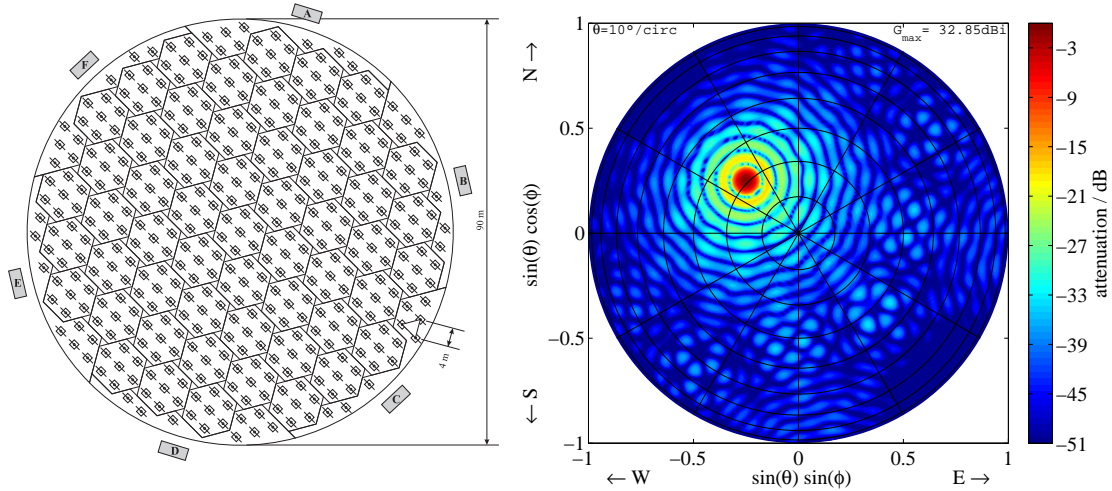


Figure 2: Left: Sketch of the new ALWIN antenna array. Each cross represents crossed three-element Yagi antennas mounted on a concrete block (small boxes). The six rectangles outside the array, indicated as A-F, represent containers accommodating the transmit-receive modules. Right: Computed radiation pattern of the new ALWIN antenna for an antenna beam pointed to 21° to the NW direction.

operating parameters, such as frequency, phase and amplitude. The innovative design incorporates vector RF detection circuitry allowing continuous monitoring of output power, phase and load impedance on a pulse-to-pulse basis. The radar hardware is designed and manufactured by Genesis Software Pty Ltd.

On reception the IF signals of each with 7 transceivers connected to each with 7 antennas arranged in a hexagon structure are combined to 61 receiving channels. The combined IF signals are led by coaxial cables of equal length to the data acquisition hardware in the nearby located radar control house. On the first expansion stage the radar will have 16 baseband receivers and 32 digitizers for the corresponding numbers of I and Q channels only. Therefore controllable multifunction combiners will be used to either combine the IF signals of 7 adjacent hexagonal antenna substructures ("anemone" antenna patch) or select one of them to the input of one of the 16 base band converters. Overall 9 multifunction combiners will be in use to connect the IF signals of 7 anemone patches, 6 single hexagons, and 6 remaining antenna patches along the perimeter of the array to the 16 base band receivers as shown in Figure 3. These combining unit allows a wide range of receiving arrangements with different antenna configurations for interferometric or multi-receiver applications. Additionally a 16 channel antenna interface unit with down conversion to IF is used to feed 16 additional RF signals from separate receiving antennas used for e.g. interferometer observations of meteors or for boundary layer observations.

A second output of the multifunction combiner will provide the 9 combined signals to a 9-to-1 combiner whose output is permanently connected to base band receiver one. This receiving setup in combination with the 433 phased controlled transmitters will be used for classical Doppler beam swinging. It will remain in the new ALWIN system also after an upgrade to 61 analog or digital receiving channels.

The individual phase control of each transceiver module allows also multiple beam operations. During the first expansion stage of the radar the maximum number of separated beams is limited to 7 due to the number of available detection channels and the associated "anemone" antenna patches.

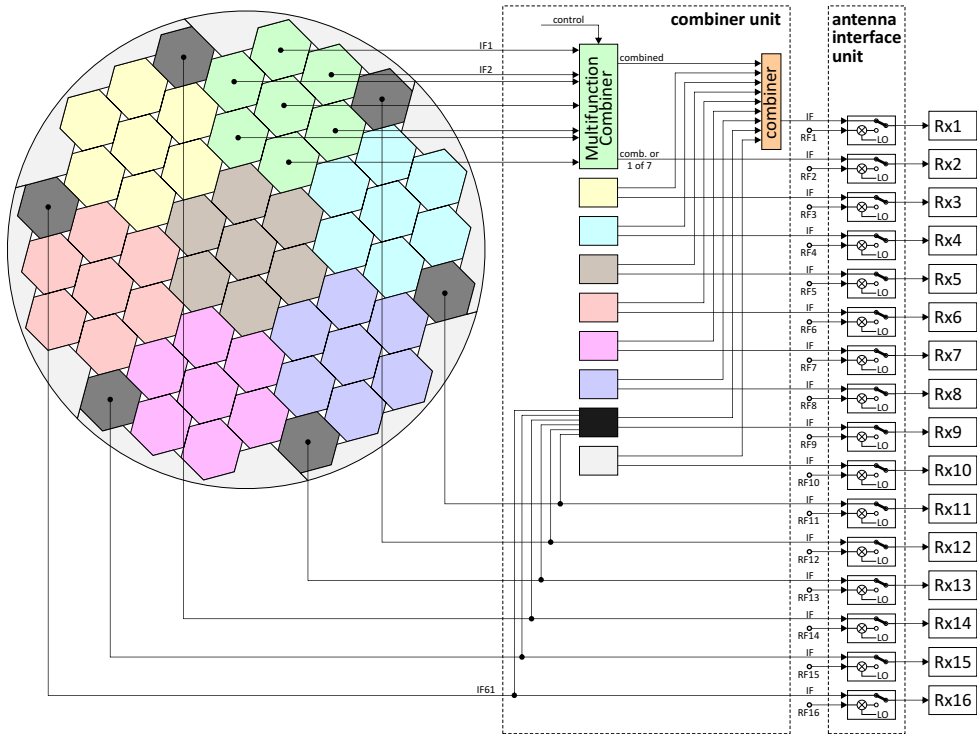


Figure 3: Block diagram of receiving channel structure of the new ALWIN radar .

Installation schedule

To this date the installation of the antenna array is completed and the RF cables between the 433 antennas and the six containers accommodating the transceivers as well as the 61 IF cables from the containers to the radar control house are laid. The radar control and data acquisition hardware as well as 145 transceiver modules will be installed in November 2009. The initial expansion stage will use the inner 19 hexagons of the array and additional 6 antennas to form a circular aperture. The antenna beam will be comparable to the old ALWIN system but with symmetrical sidelobes and without grating lobes. The second expansion stage is scheduled for spring 2010 with the goal to observe the upcoming PMSE saison with full power.

References

- R. Latteck, W. Singer, and H. Bardey. The ALWIN MST radar – technical design and performances. In B. Kaldeich-Schürmann, editor, *Proceedings of the 14th ESA Symposium on European Rocket and Balloon Programmes and Related Research, Potsdam, Germany (ESA SP-437)*, pages 179–184, 1999.
- W. Singer, D. Keuer, P. Hoffmann, P. Czechowsky, and G. Schmidt. The ALOMAR SOUSY radar: Technical design and further developments. In *Proceedings of the 12th ESA Symposium on European Rocket and Balloon Programmes and Related Research, Lillehammer, Norway (ESA SP)*, pages 409–415, 1995.

WHAT IS THE OPTIMAL LEVEL OF TIME-AVERAGING FOR RADAR-DERIVED WIND-PROFILES?

D. A. Hooper¹ and C. Gaffard²

¹STFC Rutherford Appleton Laboratory, Chilton, Didcot, OX11 0QX, UK

²Met Office, Department of Meteorology, University of Reading, Reading, RG6 6BB, UK

1. Introduction

The (UK) Met Office currently assimilates wind-profile data from a number of European radars. The quality of the data for an averaging period of 30 minutes can be comparable to that of radiosonde-derived winds, i.e. with random measurement errors of up to a few m s^{-1} (e.g. *Dibbern et al.*, 2003). As ever-increasing computing power allows numerical weather prediction models to be run at increasingly-high resolutions, there is a corresponding need to increase the resolution of the assimilated data. However, by reducing the period over which radar-derived wind-profiles are averaged, the effects of random measurement errors will become more significant. This is demonstrated in the left panel of Figure 1, which shows the root mean square (RMS) differences between the eastward wind components, derived from Doppler Beam Swinging (DBS) observations made by the MST Radar at Aberystwyth, at adjacent times. The RMS differences represent a combination of the random measurement error and of the natural degree of variability of the wind. The latter is expected to increase with increasing time separation between the estimates. Note that the RMS differences between wind components estimated from just a single cycle of observation (orange line), i.e. at separations of 4.7 minutes, are considerably larger than those estimated for 30 minute averages (blue line). This suggests that the variability between single cycle estimates is dominated by the random measurement error. Moreover, as will be shown here, much of this random measurement error can be attributed to geophysical effects which fundamentally limit the accuracy of single cycle measurements.

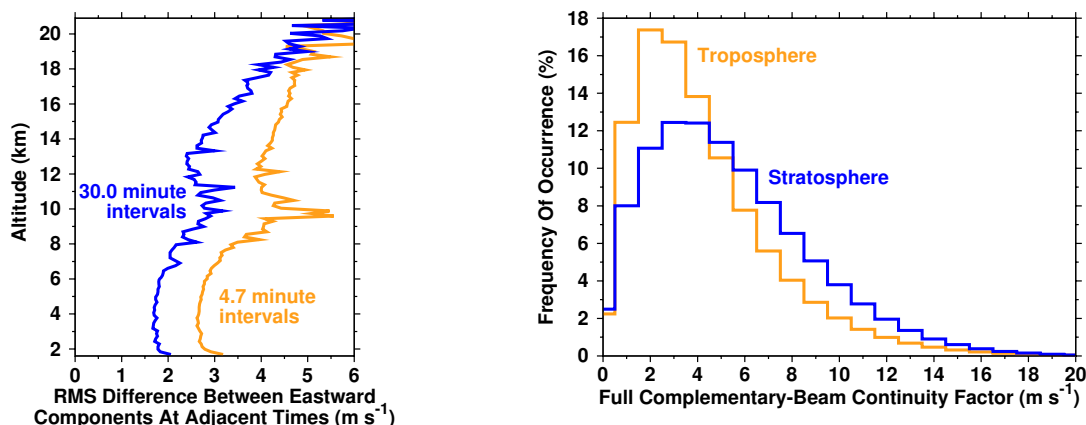


Figure 1: The results of statistical analyses which show (left panel) that the RMS difference between wind components at adjacent times is greater for single cycle data than it is for 30 minute averaged data, and (right panel) that the distribution of the full complementary-beam continuity factor is shifted to larger values for the stratosphere compared to the troposphere.

2. The Complementary-Beam Continuity Factor

The statistics shown in Figure 1 relate to observations made by the Aberystwyth MST Radar during the period 1st July 2006 - 31st January 2007. Each cycle of observation followed an enhanced five-beam sequence, i.e. one which includes dwells in the Vertical direction and at four off-vertical directions which share the same zenith angle, θ , and which have azimuth angles, ϕ , at intervals of 90° . The radial velocity derived from the Vertical beam dwell is interpreted as representing the

upward wind component, w (the convention used here is for a positive radial velocity to represent motion away from the radar). This allows the horizontal wind component along the azimuth of each of the off-vertical beams, $v_H(\phi)$, to be inferred from its radial velocity, $v_R(\theta, \phi)$:

$$v_H(\phi) = \frac{v_R(\theta, \phi) - w \cos \theta}{\sin \theta} \quad (1)$$

The availability of complementary (off-vertical) beam pointing directions, i.e. those separated in azimuth by 180° , allows two quasi-independent estimates (albeit with opposite signs) to be made of the horizontal wind component along each of two orthogonal azimuths. These are averaged in order to give a single estimate along each of the two orthogonal azimuths. What is of particular interest here is the use of the difference between the two estimates (after taking the change of sign into account) to give a measure of the reliability of the averaged value. The complementary-beam continuity factor, $\Delta v_{HC}(\phi)$, is defined as:

$$\Delta v_{HC}(\phi) = v_H(\phi) + v_H(\phi + 180^\circ) \quad (2)$$

Attention will be confined here to the full complementary-beam continuity factor, $\Delta v_{HC}(full)$, which is defined as the root of the sum of the squares of the values for the two orthogonal azimuths.

The details of the enhanced five-beam sequence are as follows: NE6.0°, Vertical, SW6.0°, Vertical, SE6.0°, Vertical, NW6.0°, Vertical, W4.2°, Vertical, Mesospheric-Vertical, Vertical. The names for off-vertical beam directions represent first the azimuth and then the zenith angle. Each dwell represents almost 21 s worth of observations made at 300 m range resolution, albeit sampled at 150 m intervals. Note that every other dwell is in the Vertical direction, which provides estimates of the upward wind component every 48 s (taking the 3 s gaps between dwells into account). This was originally introduced for studies of convection, which can give rise to absolute changes in the upward wind in excess of 1 m s^{-1} over this time scale (*Hooper et al.*, 2005). Nevertheless, as will be demonstrated shortly, such an observation strategy is desirable for regular wind-profiling activities. For each off-vertical beam dwell, the upward wind velocity from the Vertical beam dwell which is closest to it in time is used in deriving the corresponding horizontal wind component. Note that complementary (6° off-vertical) beams are grouped together, albeit separated by a single Vertical beam observation. The total cycle time was 4 minutes 43 s.

The right panel of Figure 1 shows the probability distributions of $\Delta v_{HC}(full)$ values for single cycle data at tropospheric (orange line) and stratospheric (blue line) altitudes. The altitude of the tropopause, which is predominantly between 8.0 and 12.5 km, is derived from the profile of Vertical beam signal power. Values of $\Delta v_{HC}(full)$ are calculated only where all four 6° off-vertical beam observations have passed radial- and time-continuity quality control tests, as described by *Hooper et al.* (2008). Nevertheless, values in excess of 10 m s^{-1} occur for a significant proportion of the time. Such large values are inconsistent with the fundamental DBS assumption of the wind field being stationary over the time scale required to make a full cycle of observation and over the horizontal scale separating the different radar observation volumes.

It seems likely that discrepancies between complementary-beam estimates of a horizontal wind component are primarily caused by variations in the upward wind over the time scale separating the dwells. Atmospheric oscillations which are close to the Brunt-Väisälä period (around 10 minutes in the troposphere and around 5 minutes in the lower stratosphere) are predominantly evident in the vertical direction. However, it is possible that some apparent variations are caused by roughness in the nominally-horizontal scattering layers and are not related to changes in the upward velocity. Moreover, actual variations in the horizontal wind, e.g. caused by turbulent motions (which will be evident at time scales of less than the Brunt-Väisälä period), cannot be ruled out as

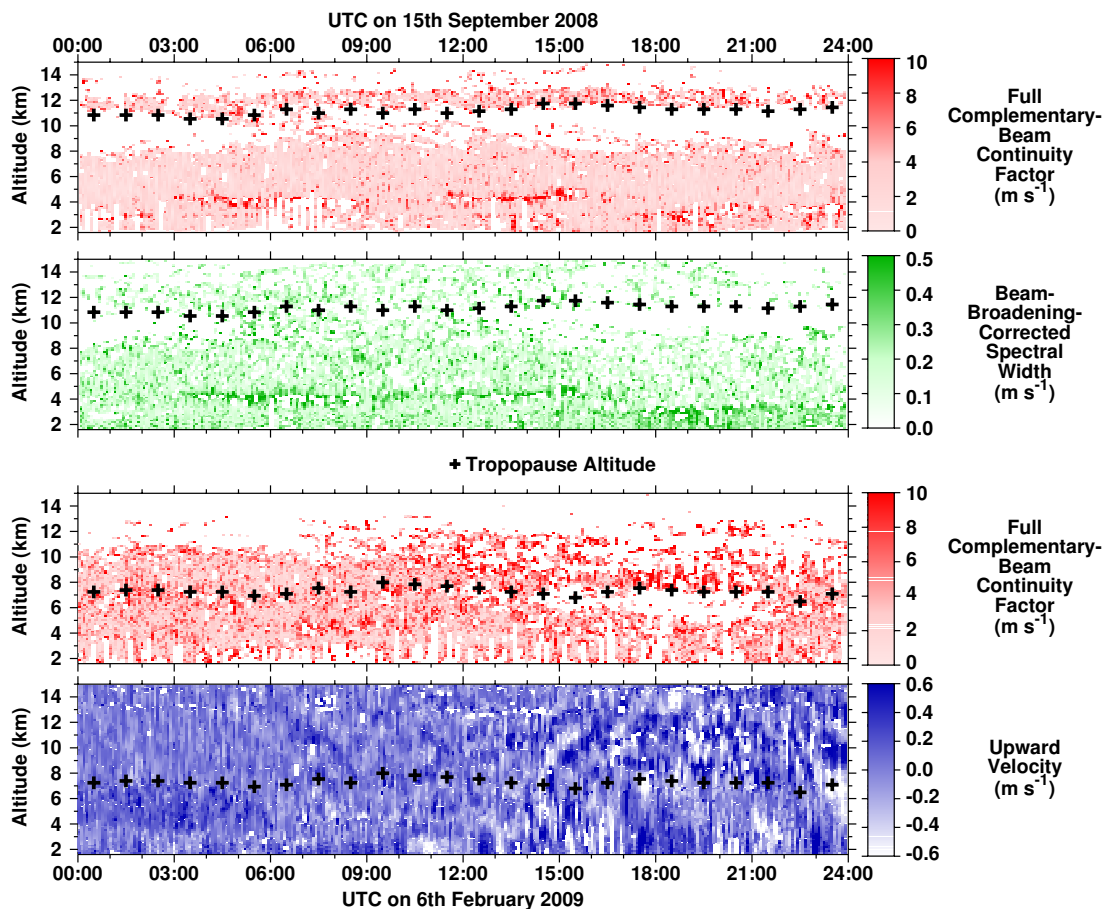


Figure 2: Examples of enhancements in the value of the full complementary-beam continuity factor associated with (upper panels) turbulent layers, and (lower panels) mountain wave activity.

a cause.

3. Case Studies Of Reduced Complementary-Beam Continuity

The top panel of Figure 2 shows the (single cycle) values of $\Delta v_{HC}(full)$ for a day characterised by low wind speeds ($< 10 \text{ m s}^{-1}$) over most of the troposphere. There is a weak background of upward wind velocity activity (not shown), which is typical at Aberystwyth owing to its close proximity to mountains. Enhanced values of $\Delta v_{HC}(full)$, at altitudes of around 3 and 4, clearly correspond to enhanced values of the beam-broadening-corrected (Vertical beam) spectral width (second panel). The expectation that these layers are turbulent is supported by the the accompanying large values of vertical wind shear (not shown). Correlations between large values of $\Delta v_{HC}(full)$ and large values of corrected spectral width have been seen in a number of similar situations.

The lower two panels of Figure 2 relate to a day characterised by moderate mountain wave activity. It can be seen that enhanced values of $\Delta v_{HC}(full)$ (third panel) are more-widely-spread in the troposphere than they are in the first case study (top panel). Moreover they become particularly prevalent in the lower stratosphere after 12:00 UT, when the amplitude of the upward wind velocity activity (bottom panel) becomes well-established at these altitudes. Enhanced values of $\Delta v_{HC}(full)$ are commonly associated with mountain wave activity. However they are not obviously correlated with any particular characteristic of the waves, e.g. their amplitude, their apparent period of oscillation, or their phase.

The probability distributions shown in the right panel of Figure 1 indicate that, unsurprisingly, large values of $\Delta v_{HC}(full)$ are more common in the stratosphere than in the troposphere. Complementary-beam observation volumes for a zenith angle of 6.0° are separated by a horizontal distance of only 1 km at an altitude of 5 km but by over 3 km at an altitude of 15 km. Consequently there is greater potential for spatial variations in the three-dimensional wind field to become apparent in the stratosphere. The horizontal wavelength of convectively-generated gravity waves can be just 10 km (e.g. *Hauf*, 1993) and that of mountain waves tends to be just a few 10s of km. Moreover, the Brunt-Väisälä period approaches the interval encompassing two complementary beam dwells (1 minute 13 s) much more closely in the stratosphere (5 minutes) than it does in the troposphere (10 minutes).

4. Discussion and Conclusions

The short-term variations between upward wind components are expected to be more-reliable than those between horizontal wind components. This is partly owing to the fact, mentioned above, that the highest-frequency oscillations are predominantly in the vertical direction. Moreover, the upward wind components are derived from observations made during a single dwell. This minimises the potential for the measurements to be affected by spatial or temporal variations in the three-dimensional wind field. Nevertheless, no attempt has yet been made to fully exploit the availability of the Vertical beam observations at every other dwell (i.e. at intervals of 48 s) in the Aberystwyth dataset. For example, a test needs to be made as to how the values of the complementary-beam continuity factor will vary if the upward wind values used to derive horizontal wind components are not taken from a Vertical beam dwell which is adjacent in time to the off-vertical beam dwells. Data from a recent set of special observations, during April 2009, suggest that they will increase. However, this was based on a comparison between 150 m resolution observations, which followed the dwell sequence described in Section 2, and 300 m resolution observations, which made use of a restricted 5-beam sequence for which only a single Vertical beam dwell was available. Incidentally, Met Office monthly model-comparison statistics for April 2009 (see “*The diagnosis of a range gating problem suffered by the Aberystwyth MST Radar*” in these proceedings for more details about the use of such statistics) do not suggest any degradation in the quality of the 30 minute averages of the 300 m resolution data. This is in spite of the fact that only 3 single cycle wind-profiles were available for each 30 minute period, as opposed to 6 for standard observations.

In conclusion, geophysical phenomena, including mountain wave activity and turbulence, can reduce the reliability of single DBS cycle wind-profile estimates. The optimal level of time averaging needed to minimise the random measurement error remains to be determined.

5. References

- Dibbern, J., D. Engelbart, U. Goersdorf, N. Latham, V. Lehmann, J. Nash, T. Oakley, H. Richner, and H. Steinhagen, Operational aspects, in *EUR 20614 - COST Action 76 - Development of VHF/UHF wind-profilers and vertical sounders for use in European observing systems - Final report*, edited by J. Dibbern, W. Monna, J. Nash, and G. Peters, pp. 133–224, European Commission, Luxembourg, 2003.
- Hauf, T., Aircraft observation of convection waves over southern Germany - a case study, *Mon. Wea. Rev.*, 121, 3282–3290, 1993.
- Hooper, D. A., A. J. McDonald, E. Pavelin, T. K. Carey-Smith, and C. L. Pascoe, The signature of mid-latitude convection observed by VHF wind-profiling radar, *Geophys. Res. Lett.*, 32, L04808, doi:10.1029/2004GL020,401, 2005.
- Hooper, D. A., J. Nash, T. Oakley, and M. Turp, Validation of a new signal processing scheme for the MST radar at Aberystwyth, *Ann. Geophys.*, 26, 3253–3268, 2008.

Radars Measured Errors in Spectral-width Turbulence Determination

Armin Dehghan and Wayne K. Hocking

Department of Physics and Astronomy, University of Western Ontario, London, Ontario

Introduction

Turbulent energy dissipation rates, ε have been measured using radar. In order to estimate energy dissipation rate, the spectral-width method has been used which utilizes the difference between the square of a measured spectral width and a “beam-broadening” component. The turbulent contributor is small and very sensitive to statistical fluctuations of measurements, which can lead to occasional negative values for turbulent energy dissipation rate. Negative values are physically unrealistic, however they could arise from observational errors (i.e., beam broadening) or from geophysical effects like anisotropic scatter. The beam-broadening term can be affected by the mean wind, the wind shear, the curvature of the wind profile and signal to noise ratio. In this paper, we will study some of these effects using data from radars located in Southwestern Ontario.

Methods

The main radars used in this study are located at Walsingham and Harrow, all in Ontario, Canada. The antenna system at Walsingham radar has a large cross-structure (see fig.3 from Hocking et al., 2007; Walsingham is type I). The Harrow radar has a similar layout to the Walsingham radar, but has a greater concentration of antenna in the centre (Hocking et al., 2007, fig 3, type II). However, the Walsingham radar (44.5 MHz, one way half-width 2.3°) has a narrower main beam than the Harrow radar (40.68 MHz, one way half-width 2.75°). The radars are operated in five beam positions (four in off vertical and then one in vertical), typically every 5 minutes. Data of 20-40 seconds in duration are collected and then the corresponding spectra and spectral widths are determined. Once the spectral width due to non-turbulent effects has been calculated, the spectral width due to turbulence can be estimated from the following equation:

$$f_{turb}^2 = f_e^2 - f_{nt}^2 \quad (1)$$

Where f_{turb}^2 , f_e^2 and f_{nt}^2 are the squares of the spectral half power half-widths due to turbulence, experimental measurements and non-turbulent (or “beam-broadened”) effects respectively. Therefore, energy dissipation rate is given by (Hocking, 1983):

$$\varepsilon = C \langle v^2 \rangle \omega_B = C \langle \lambda / 2 \rangle^2 f_{turb}^2 \omega_B / 2 \ln(2) \quad (2)$$

Where $\langle v^2 \rangle$ is the mean square fluctuating vertical velocity of the scatterers, ω_B is Brunt-Vaisala frequency, λ is the radar wavelength and $C \approx 0.49$. If it is assumed that only beam broadening contributes to the width due to non-turbulent effects, then the beam-broadened spectral width, f_{nt}^2 is approximately given by (Hocking, 1985, equation 45).

In order to estimate f_{nt}^2 , Nastrom (1997) gave an expression which includes both beam and wind shear broadening (see Nastrom, 1997, equation 16).

Hocking (1983) used a model which uses the full wind profile to estimate the beam-shear broadening (see Hocking, 1983, equation 35). Hocking (2003) discusses this model in

some detail. Therefore, the spectral width can be estimated for any given range, wind speed and direction. In order to consider the wind shear, the layer of interest is divided into thin sub-layers with constant wind speed and direction. The spectrum expected due to non-turbulent effects is obtained by adding all the spectra due to the full wind profile. Here we compare these different methods mentioned above. It should be noted that we used only data recorded with an off-vertical beam (south) to decrease the contribution of specular reflections in our measurements. Other beams (to the north, east and west) revealed similar results to the south beam.

Results

If the measured spectral half-power half-width is narrower than the expected non-turbulent one, the calculated “turbulent contribution” f_{turb}^2 will be negative. This is unphysical, but can occur due to different reasons, including turbulence anisotropy and statistical effects. Fig. 1 shows vertical profiles of monthly averaged values of ε from 2 to 9.5 km for only positive values of ε and for all measured values of ε (both positive and negative) for February and July 2007 for the Walsingham radar. It can be seen that from 2 to around 4-5 km, profiles of “positive” and “all” values have a somewhat similar pattern and magnitude. However, above approximately 5 km, the energy dissipation rate decreases significantly with increasing height when we include all values of ε .

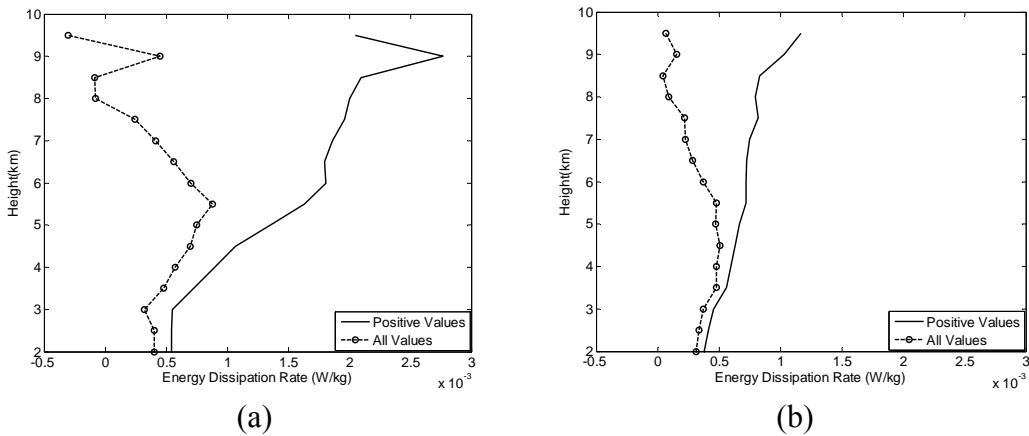


Fig. 1. Vertical profiles of energy dissipation rate for (a) February and (b) July 2007 at Walsingham. The solid line shows the profile of only positive values of ε and dashed line with o marker shows the profile of all measured values of ε .

Fig. 2 shows the monthly-average of received mean power recorded by the Walsingham radar as a function of height. It can be seen that power decreases with increasing height. However, the signal-to-noise ratio exceeds 10 dB even at 5-6 km altitude and above. So while the signal-to-noise ratio may contribute to negative ε , it is not the only reason.

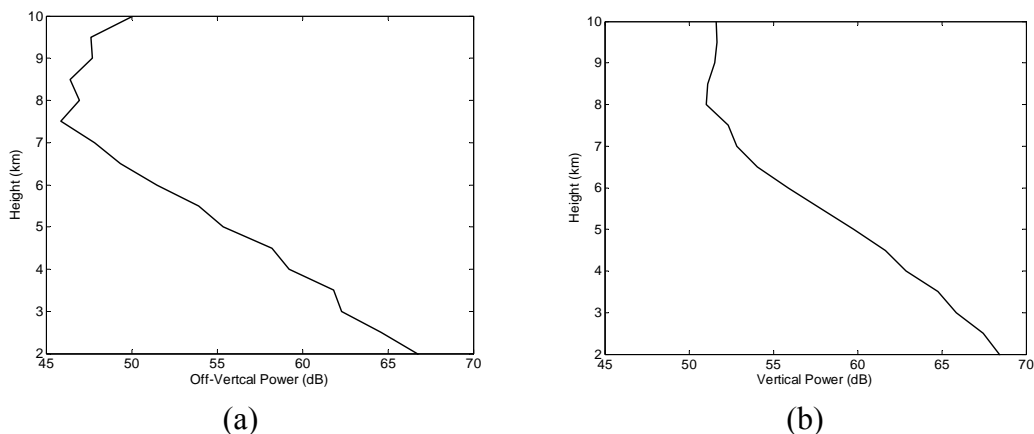


Fig. 2. Vertical profiles of (a) off-vertical power and (b) vertical power measured by the Walsingham radar for February 2007. The noise level is typically around 40 (dB), although of course it varied as a function of sidereal time.

Fig. 3 shows the vertical profile of wind speed for a warm and a cold month at Walsingham. Clearly the wind speeds increase significantly with increasing height and it is expected to be more difficult to measure turbulence when the mean wind is larger. These results suggest that the increase of wind speed is an important factor in the increase of negative ε at the upper heights.

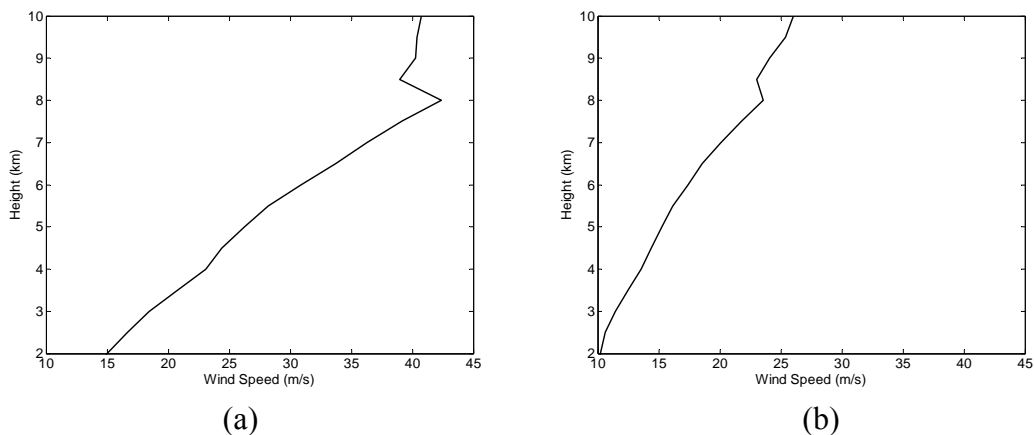


Fig. 3. Vertical profiles of wind speed for the Walsingham radar for (a) February and (b) July 2007.

In order to study the contribution of wind shear in turbulence measurements, we have estimated the strength of turbulence using the Harrow radar for the month of July in 2007. We used 3 different methods. The first method is the simple constant wind model (equation 45 of Hocking, 1985), the second one is the model which uses a constant wind plus wind shear (equation 16 of Nastrom, 1997), and the third one is the full model (equation 35 of Hocking, 1983 and Hocking, 2003). The results are seen in the in figs. 4. It can be seen that the case of a uniform wind gives a high percentage of negative values for ε , and this has been reduced with the other two models, especially with the full numerical model. It should be noted that since the increasing wind speed with height

reduces f_{nt} , the full model helps us to estimate turbulence more precisely at greater heights.

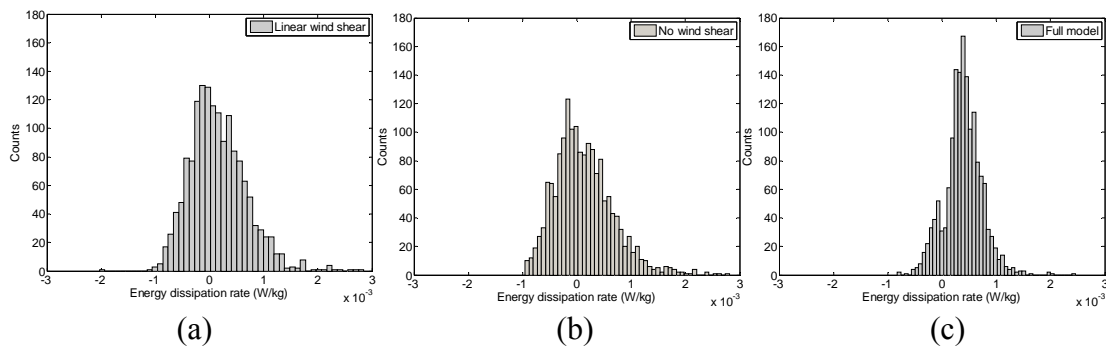


Fig. 4. Histograms of turbulence strengths deduced when the non-turbulent contribution is calculated by using (a) a constant mean wind, (b) beam-broadening plus wind-shear and (c) the full spectral model, for the altitude interval of 2-5 km at Walsingham for wind speeds of 10-15m/s.

Conclusions

The spectral-width method can produce negative values of the turbulent energy dissipation rate. An increasing wind speed with increasing height produces narrower theoretical spectra than those measured with an assumed uniform wind speed with height, allowing estimates of turbulence strengths at wind speeds (and heights) where such measurements could not normally be made if a uniform wind is assumed. Determination of theoretical spectral widths must include full representation of the wind profile, and properly integrate over the profile, in order to help us to estimate turbulence more precisely. The number of negative ϵ values reduces significantly when the full model has been used.

References

- Hocking, W.K., 1983. On the extraction of atmosphere turbulence parameters from radar backscatter Doppler spectra- Theory, *J. Atmos. Terr. Phys.*, 45, 89-102.
- Hocking, W.K., 1985. Measurements of turbulent energy dissipation rates in the middle atmosphere by radar techniques, *Radio Science.*, 20, 1403-1422.
- Hocking, W.K., 2003. Fast and accurate calculation of spectral beam-broadening for turbulence studies, *Proceeding of the Tenth International Workshop on Technical and Scientific Aspect of MST Radar*, Piura, Peru, May 13-20, 2003, 214-217.
- Hocking, W.K., Taylor, P., Zawadzki, I., Argall, S., Fabry, F., McBean, G., Sica, R., Hangan, H., Klaassen, G., Barron, J., Mercer, R., 2007. "A New 40-55 MHz Windprofiler Network in Ontario and Quebec, Canada – The O-Qnet", *Proceeding of the Eleventh International Workshop on Technical and Scientific Aspects of MST Radar*, Gadanki, India, Dec 11-15, 2006, 377-380.
- Nastrom, G.D., 1997. Doppler radar spectral width broadening due to beamwidth and wind shear, *Ann. Geophysics*, 15, 786-796.

IMPROVEMENT OF VERTICAL RESOLUTION OF RASS MEASUREMENTS BY APPLYING FREQUENCY-DOMAIN INTERFEROMETRIC IMAGING

Jun-ichi Furumoto, Tomonori Shinoda, Toshitaka Tsuda, and Atsushi Matsugatani

Research Institute for Sustainable Humanosphere, Kyoto University, JAPAN

1. Introduction.

Atmospheric temperature is one of the most important meteorological parameters in the thermodynamics of meteorological disturbances. The measurement of temperature profiles with good vertical and temporal resolutions is seriously taken in investigation and prediction of severe meteorological phenomena.

Radio Acoustic Sounding System (RASS) is a radar remote sensing technique to monitor temperature profiles with good temporal and height resolutions, regardless weather conditions. RASS measurements with the MU radar (MU radar-RASS) can provide temperature profiles from the height of 1.5 km to the lower stratosphere with temporal and height resolutions of several minutes and 150 m, respectively (e.g, Tsuda et al., 1994).

Radar interferometric imaging techniques are an array processing technique. Signals received by different receivers are weighted and combined in order to focus the receiver sensitivity in directions or ranges. Coherent Radar Imaging (CRI) is a technique to overcome the angular resolution limitation of conventional method by combining data obtained by spatially separated elements (Palmer et al., 1998). Frequency domain Interferometric Imaging (FII) is the adaptation of CRI to the operational frequency array processing for improving range resolution (e.g., Luce et al. 2006).

The height resolution of conventional RASS measurements is restricted to the radar pulse width. To overcome this limitation, in the this study, we apply the radar interferometric imaging technique to the MU radar-RASS observation for improving the vertical resolution of RASS experiment. The technique is applied to the MU radar-RASS measurement, and evaluated by comparisons of the retrieval results with the simultaneous *in-situ* measurements.

2. Basic Principle of RASS Measurements.

Acoustic waves transmitted upward from ground-based speakers produce a sinusoidal perturbation of the atmospheric refractive index, which backscatters the transmitted radio waves. From the Doppler velocity of acoustic wave, the atmospheric virtual temperature can be derived since the acoustic velocity depends on the atmospheric virtual temperature. Note that the observed acoustic velocity is the sum of the true acoustic velocity and radial wind velocity. The effect of radial wind velocity should be carefully subtracted from observed acoustic velocity using simultaneous wind observations.

Strong RASS echoes are obtained if the Bragg condition is satisfied between the acoustic and radar wavenumbers. However, the wavenumber of acoustic wave increases with height in the troposphere, since temperature generally decreases with height. Wider height coverage is expected if an FM-chirped acoustic wave is used to fulfill the Bragg condition throughout the observation height range. For the RASS measurements with a chirped acoustic wave, the transmitted radiowave is backscattered only from a part of the chirped acoustic pulse, where the Bragg condition is approximately satisfied (hereafter, referred as the Bragg area). The effective scattering range (L_{fm}) of RASS echo is propotional to the $1/\sqrt{|\Delta F|}$, where ΔF is the chirp sweep ratio (Masuda et al, 1998).

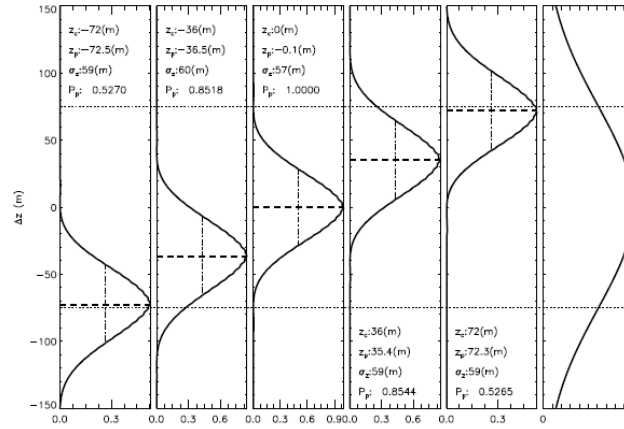


Figure 1. The five left-most panels show the range sensitivity profiles of the RASS-FII results using the parameters listed in Table 2. From left-hand to right, the results for the scanning heights of -72, -36, 0, 36, and 72 m are shown. The dashed and dot-dashed lines show the heights of the peak sensitivity and the HPHW of the FII results. The right-most panel shows the radar range function approximated by the Gaussian distribution function with a HPHW of 75 m.

The overview of FII analysis for RASS echo (RASS-FII) is now explained. The amplitude of RASS echo intensity varies with height because the sensitivity of radar range weighting has its maximum at the center of the radar range gate. This effect should be compensated before applying FII. However, detailed temperature variation within the radar range gate is required for the precise compensation, since the location of propagating acoustic pulse is determined by the temperature profile. To solve this problem, we have developed an algorithm to apply the temperature profile of RASS-FII results to compensate the Doppler bias in the next iteration step until the number of the iteration reaches its maximum. In the first step of the iteration, the model temperature profile with a constant lapse ratio of 1/150 (K/m) is used for the compensation.

After this compensation, the timeseries of FII output is extracted into an adequate partial timeseries to suppress the RASS scattering from the unexpected height. Then, the FII is applied to the extracted timeseries. Note that the apparent sound speed is derived from the least-squared Gaussian fitting method applied to the power spectral density of the RASS-FII result.

For removing the effects of radial wind velocity from apparent acoustic speed derived with RASS-FII analysis, the wind velocity data with comparable vertical resolution with that of RASS-FII results are obtained from the FII analysis of turbulence echo.

3. The Performance of the MU radar RASS Imaging Method

The MU radar-RASS imaging experiment was conducted in the daytime on October 29-31, 2006. In FII observational mode, the complex timeseries have been collected without interruption for 22.5 minutes. A total of 26 receiver channel was used; one was dedicated to detect RASS echo combined for 25 sub-arrays with the offset of 103 Hz for the receiver Intermediate Frequency (IF) frequency, and the other were employed to detect turbulence echo received by each subarray of the MU radar. Five operational frequencies of 46.00, 46.25, 46.50, 46.75 and 47.00 MHz were switched every IPP. The wind velocity data within the radar range gate were obtained from FII analysis of the turbulence echo. In order to suppress interferences and ground clutters, the turbulence signals independently obtained by 25 subarrays were combined by CRI before FII was applied.

An FM-chirped sound wave swept from 110 Hz down to 85 Hz was employed. One radar beam was always steered to the vertical direction, considered the vertical resolution of FII imaging is smallest in the vertical beam direction. For FII analysis, only the data from the vertical beam direction was used. During the campaign period, radiosondes were launched

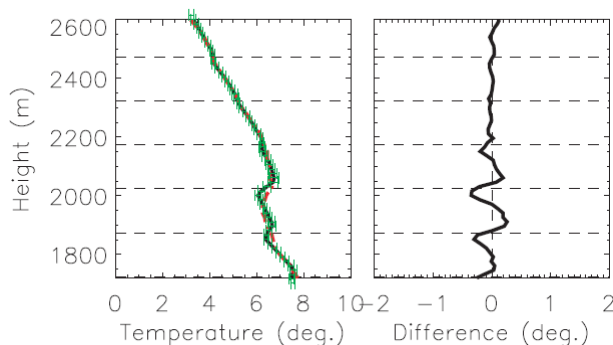


Figure 2. The left-hand panel shows the temperature profiles (solid black line) and standard error (error bar) retrieved from the MU radar-RASS imaging data for 08:53-09:19 LT on October 29. The simultaneous radiosonde result is shown as the dashed line. The profile of the temperature discrepancy between the RASS-FII and radiosonde results is shown in the right-hand panel.

every three hours from 09 LT to 18 LT, and temperature profiles derived by RASS-FII imaging technique are compared with those obtained from the simultaneous radiosonde measurements.

The performance of the RASS-FII technique was evaluated by applying the technique to the simulated timeseries, focused on, in particular, the effective height resolution and the precision of range selectivity. The simulated complex timeseries was calculated for the actual radar and acoustic parameters.

The complex timeseries calculated for the constant lapse ratio of $-1/150$ (K/m) was used as the input of FII technique, and the temporal extraction for the period are conducted for suppressing scatterings at unexpected height. Figure 1 shows the height variation of range sensitivity for the scanning height of -72 , -36 , 0 , 36 and 72 m apart from the range gate center. Note that the range sensitivities are normalized by the maximum value of the simulation results for the scanning height of the range gate center. The normalized peak power (P_p) at 72 m apart from the center of radar range gate is attenuated to about 0.52 , due to the effect of the range gate function. The range resolution of FII result defined by the HPFW of range pattern (σ_x) was between 57 m and 60 m.

In this analysis, data of the continuous observation with the MU radar/RASS-FII on November 11-14, 2008 is also used. In this campaign, the smaller sweep ratio of -50 Hz/s was used to accomplish the excellent vertical resolutions of 50 m.

4. Temperature retrieval results with RASS-FII algorithm.

Detailed temperature profiles were derived by combining the RASS- and turbulence-imaging data obtained with the MU radar-RASS measurements. Left panel of Figure 1 shows a typical temperature retrieval result averaged for 08:53-09:19 LT on October 29, 2006. The radar-derived virtual temperature (T_{vR}) has the clear inversion structure with the minimum temperature at 1.95 km and the positive lapse ratio at 1.95 - 2.10 km, which well agrees with the virtual temperature of simultaneous radiosonde result (T_{vS}). The standard error calculated for 26 minutes (error bars) is less than 0.05 K throughout the height range, which shows the statistical dispersion of RASS-FII estimation seems to be very small. The discrepancy between T_{vR} and T_{vS} was within the error bar except at the height of 1.83 - 1.85 , 1.95 - 2.02 km. The right panel shows the differences between FII- and radiosonde-derived virtual temperatures. The difference was smaller than 0.4 K throughout the entire height range, which shows the excellent precision of the RASS-FII retrieval. The discrepancy is seen around the boundary of the radar range gate, which suggests the effect of amplitude phase

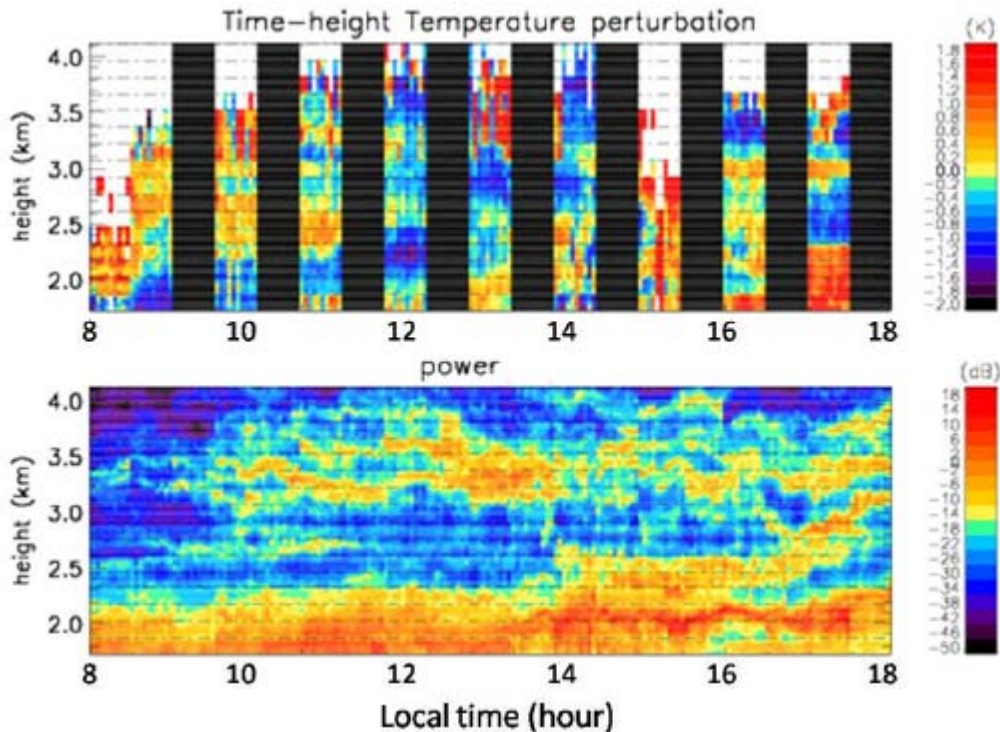


Figure 3. (Top) Time-height distribution of virtual temperature perturbation and (Bottom) time-height distribution of turbulence power obtained by RASS-FII observation with MU radar between 0800LT and 1820LT on November 14, 2008.

rotation due to the range gate function seems to be not fully removed.

The top panel of Figure 3 shows the time-height distribution of virtual temperature perturbation after subtracting the mean virtual temperature profile during 0800LT and 1820LT on November 14, 2008 at each height. The FII results were averaged for 2.5 minutes. The black dashed lines show the reference of the radar range gate width. In the period shown by black rectangle, we could not obtain temperature profile due to weak RASS echoes since the FM chirped acoustic wave with the sweep ratio of -80 dB was used for the RASS-FII observation. In spite of data missing, the detailed temporal variation of the radar-derived virtual temperature with the temporal scale of a few minutes was recognized. The detailed vertical variation of virtual temperature with the amplitude of 1 K is revealed within 1.5 hours in RASS-FII results. The bottom panel shows the time-height distribution of turbulence echo power intensity obtained with the FII analysis for turbulence echo. Strong turbulence echo regions seem to concern with larger temperature regions at 13:00-16:30 LT at the height of 2-2.25 km.

Bibliography

Luce, H., Hassenpflug, G., Yamamoto, M., and Fukao, S.: High-resolution vertical imaging of the troposphere and lower stratosphere using the new MU radar system, *Annales Geophysicae*, 24, 791-805, 2006.

Masuda, Y., Awaka, J., Nakamura, K., Adachi, T., and Tsuda, T.: Analysis of the radio acoustic sounding system using a chirped acoustic-wave, *Radio Science*, 27, 681-691, 1992.

Palmer, R. D., Gopalam, S., Yu, T. Y., and Fukao, S.: Coherent radar imaging using Capon's method, *Radio Science*, 33, 1585-1598, 1998.

Tsuda, T., Adachi, T., Masuda, Y., Fukao, S. and Kato, S.: Observations of tropospheric temperature fluctuations with the MU radar/RASS, *J. Atmos. Oceanic Technol.*, 11, 50-62, 1994.

CONTINUOUS OBSERVATIONS OF TEMPERATURE PROFILES BY 443 MHZ WIND PROFILING RADAR WITH RASS IN OKINAWA

Tomonori Shinoda¹, Jun-ichi Furumoto¹, Toshitaka Tsuda¹,
Shinsuke Satoh², and Yasuhiro Murayama²

¹ Research Institute for Sustainable Humanosphere, Kyoto University, JAPAN

² National Institute of Information and Communications Technology, JAPAN

1. Introduction.

Severe meteorological phenomena such as a heavy rainfall accompanying with the Baiu front, a typhoon sometimes and so on causes serious disasters to damage our properties. For the mitigation of disasters due to hazardous weather, it is very important to elucidate the mechanism of such an anomalous event. Continuous monitoring of wind velocity, temperature and humidity profiles with good temporal and height resolutions regardless weather conditions is very important for the research on the thermodynamics and prediction of such severe phenomena.

A wind profiling radar enables us to observe the three components of wind velocity with good temporal and height resolution. Temperature profile is monitored with Radio Acoustic Sounding System (RASS), which is a radar remotesensing technique by combining a wind profiling radar and acoustic transmitters (e.g., Tsuda et al. 1989; 1994). Humidity profiles are also available by using the wind profiling radar with RASS measurement (e.g., Furumoto et al., 2007).

National Institute of Communication Technology (NICT) operates the 443 MHz wind profiling radar (443 MHz-WPR) at the Ogimi wind profiler facility (hereafter, called as Ogimi observatory) in the northern part of Okinawa island (26.68°N, 128.16°E). This study is devoted to monitoring continuous temperature profiles with a good temporal resolution regardless weather conditions by 443 MHz-WPR with RASS (hereafter, called as 443 MHz-WPR/RASS). The continuous temperature data with 443 MHz-WPR/RASS will be very useful to understand and predict the behavior of subtropical meteorological disturbances.

2. Outline of 443 MHz-WPR/RASS System

The 443 MHz-WPR is a mono-static pulse Doppler atmosphere radar, and three dimensional components of wind velocity with a time resolution of four minutes are continuously obtained from turbulence scattering of radio waves with the 443 MHz-WPR. Wind velocity data are averaged for 10 minutes, and are transferred to the Japan Meteorological Agency (JMA) within a latency of two hours for a real-time data assimilation into a numerical weather prediction (NWP) model. Thus, the 443 MHz-WPR is one of Wind Profiler Network and Data Acquisition System (WINDAS) of JMA, which is very useful to improve prediction accuracy of weather forecast.

Kyoto University and NICT are collaborating on application of the RASS technique to the 443 MHz-WPR since 2006. Left panel of Figure 1 shows the photo of the portable horn speaker, designed to effectively transmit the acoustic frequency range to satisfy the Bragg condition in the entire observation height range. An acoustic driver (RADIANT PB-950) with the maximum input and efficiency of 100 W and 111 dB sound pressure level per W (hereafter, called as SPL/W), respectively, is installed inside the horn box, and connected to the high directional horn with the aperture of 30 degrees.

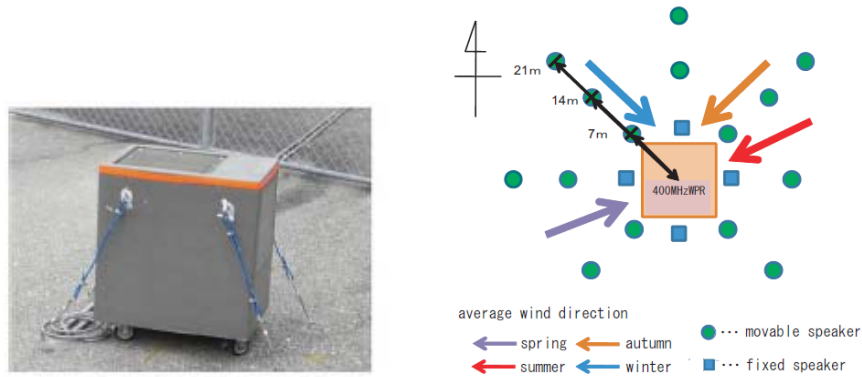


Figure 1. (Left) The photo of a portable speaker. (Right) Speaker position of a 443 MHz-WPR/RASS system. Squares and circles show the position of fixed speakers and portable speakers, respectively.

Since the Doppler velocity for RASS echoes is about -300 m/s, the spectral window should be wide enough to detect the acoustic velocity without frequency aliasing. However, a frequency resolution is decreased when the wide spectral window is used. In order to save the frequency band width, we can shift the Intermediate Frequency (IF) for the receiver (RX-IF) so as to the Doppler velocity of RASS echoes appear near the center of the spectrum window. We have attached an external circuit to shift RX-IF by 1 kHz during RASS observations, by providing RX-IF with 24.001 MHz as LO from a signal generator.

A strong RASS echo can be obtained when acoustic source is located in the windward of the radar antenna. Since the dominant azimuth direction of background wind velocity below the height of 4 km varies with season at the observatory, a number of acoustic sources were installed around the 443 MHz-WPR antenna. It is noteworthy that, when 443 MHz-WPR was installed at the Ogimi observatory in 2001, four high directional horn (hereafter, referred as fixed horn) were attached to the north, east, south, and west side of the radar antenna. These horn speakers did not show a good performance in the previous study, but we have re-operated them for our RASS observations. In this study, in order to connect two water proof acoustic drivers (UNI-PEX P-700) with the maximum continuous output and efficiency of 70 W and 110 dB SPL/W, respectively. The location of the 15 portable acoustic sources and four fix horn was determined from the result of ray-tracing for the acoustic wavefront, in which we used the seasonal averaged wind velocity obtained with 443 MHz-WPR.

3. Remote control and monitoring system for continuous operation

It is very important to continuously operate the RASS observation to monitor sporadic severe weather phenomena with a short lifetime which is often occurred in Okinawa subtropical region. In this study, we developed a remote control and monitoring system for 443 MHz-WPR/RASS observation to achieve the unpeopled continuous observation.

Figure 2 shows the block diagram of the remote control and monitoring system. This system consists of (a) a control personal computer (hereafter, called as PC) with digital input-and-output card (hereafter, called as DIO card), (b) multi-channel input/output audio devices, (c) stereo audio power amplifiers (hereafter, called as PA), (d) a RASS control box consisted of relays, current sensors, a temperature-and-moisture sensor, and a fan (e) water proofed microphone, and (f) RF switch for RX-IF offset. The detailed descriptions for the function of this system are shown in the followings.

To suppress noise pollution to the neighboring villages, it is very important to use only the speakers that are efficient to obtain strong RASS echo. Since speakers located leeward from the radar antenna are not so efficient to obtain strong RASS echo (Masuda,

1988), these speakers should be turned off in the RASS observation. In the control system, the output of each acoustic source can be controlled individually by using a mechanical relay. In order to control a relay, the DIO card with the response time of $11 \mu\text{s}$ was used for the relay control of 19 speakers.

It is very important for the remote control and monitoring system to notice speaker failures as soon as possible. For checking the status of speakers and guidewire malfunction in diaphragms, a current fed to each speaker is monitored using the current sensor. The output voltage of the current sensor is in proportional to the instantaneous current. Multi-channel input-and-output audio devices (Roland UA-101) are connected to the output of current sensor. Three sets of UA-101 are used to detect the current of 19 speakers, because one UA-101 has 8 analog input terminals. A water proof microphone was also installed on the roof of the observatory building to monitor the acoustic wave transmitted by speakers.

The offset of RX-IF is also controlled by the new control and monitoring system. Two interruption channel of the DIO card are used to monitor the start and finish timings of 443 MHz-WPR observation and timings of RASS observations is detected. Another DIO port is used to control RF switch to control RX-IF frequency.

We have developed a Windows-based application to control the above functions with Microsoft Visual C++ 2005. Acoustic wave transmission is automatically stopped in nighttime by setting the local-time for start and end of transmission. The software can be operated by the remote computer using Transmission Communication Protocol / Internet Protocol (TCP/IP) connection. Operation history of the software and status of RASS observation are automatically recorded in a log file. E-mail is also automatically sent in the case of fatal error.

3. Real-time Temperature Data Processing

To obtain a real time temperature data with 443MHz-WPR/RASS, the data processing system was constructed. NICT is operating a data distribution system to transfer the L1 data processed in Ogimi observatory to the data server at NICT headquarter office in Tokyo (NICT Koganei) every hour. The L1 data in NICT Koganei are automatically downloaded to the data server in Research Institute for Sustainable Humansphere (RISH) of Kyoto University, and the virtual temperature data are processed within the latency of 2.25 hours.

Continuous observation of the 443 MHz-WPR/RASS has been operated since May 23, 2007, except during October 11, 2007 and February 3, 2008 for developing the remote control and monitoring system and evaluating noise pollution to neighboring villages.

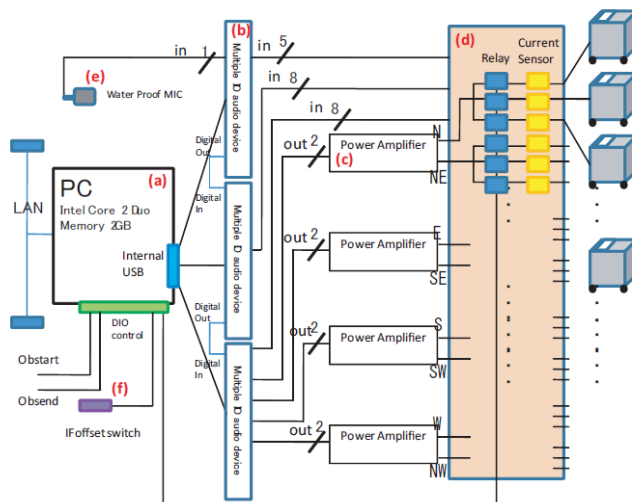


Figure 2. Block diagram of the remote control and monitoring system of 443 MHz-WPR/RASS observation.

From February 4, RASS observations are continuously operated at 7:00-20:00 LT every day with an operating ratio of 85 %. Two turbulence echo observations with the pulse width of $1.33\mu\text{s}$ and $2.00\mu\text{s}$ and one RASS observation are repeatedly conducted, and it takes four minutes for a entire cycle.

Figure 3 shows virtual temperature profiles averaged for 40 minutes at 2030LT on June 8, 9, and 10, 2007. We also plot the radiosonde data launched at JMA Naha weather station located by 80 km SSW from the Ogimi observatory in dashed lines. Virtual temperature profiles with 443 MHz-WPR/RASS show a good agreement well with the simultaneous radiosonde results. The difference between the RASS and radiosonde results were less than 1 K on June 8-9. Although the difference on June 10 has the difference of 2 K at 2.8 km, this difference seems to be due to the horizontal difference of the observation place.

Now, our data processing system is also ready to transfer virtual temperature profiles to meteorological agency for assimilating into the operational NWP model. Although the data processing system developed in this study can derive virtual temperature data with the latency of 2.25 hours, it is expected that the temperature data is generated faster by installing the data processing system in Ogimi observatory.

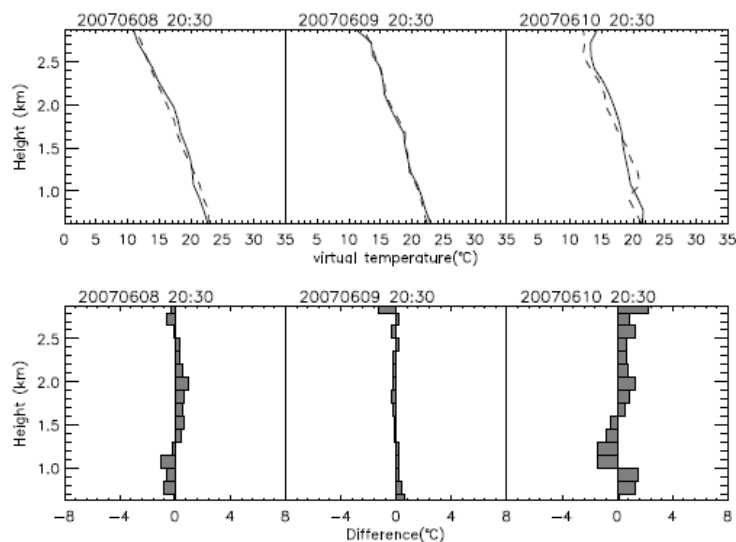


Figure 3. (Top) Successive virtual temperature profiles averaged for 40 minutes at 2030 LT on June 8, 9, and 10, 2007 (solid lines). The simultaneous radiosonde results launched at Naha are also plotted in the dashed lines. (Bottom) The difference profile of virtual temperature obtained with the RASS and radiosonde results.

Bibliography

Tsuda, T., Masuda, Y., Inuki, H., Takahashi, K., Takami, T. and Sato, T.: High time resolution monitoring of tropospheric temperature with a radio acoustic sounding system (RASS), *Pure Appl. Geophys.*, 130, 497–507, 1989.

Tsuda, T., Adachi, T., Masuda, Y., Fukao, S. and Kato, S.: Observations of tropospheric temperature fluctuations with the MU radar/RASS, *J. Atmos. Oceanic Technol.*, 11, 50–62, 1994.

Furumoto, J., Imura, S., Tsuda, T., Seko, H., Tsuyuki, T. and Saito, K.: The Variational Assimilation Method for the Retrieval of Humidity Profiles with the Wind-profiling Radar, *J. Atmos. Oceanic Technol.* 24, 1525–1545, 2007.

Masuda, Y.: Influence of wind and temperature on the height limit of a radio acoustic sounding system, *Radio Sci.*, 23, 647–654, 1988.

DESIGN OF A DIGITAL RADAR RECEIVER: INCREASING THE BANDWIDTH OF AERONOMY OBSERVATIONS AT ARECIBO OBSERVATORY

Matthew Sunderland, Julio Urbina, Mike Sulzer, Sixto González

The Pennsylvania State University, 121 Electrical Engineering East,
University Park, PA, USA 16802

1 Introduction

Ionospheric plasma-density irregularities are typically observed with pulsed backscatter radars that operate at twice the wavelength of ionospheric density fluctuations. These plasma irregularities are studied extensively since they affect the propagation of electromagnetic waves and radio communications. Only very large power/aperture product radars, known as incoherent scatter radars (ISRs), can detect these returns from fluctuations in a stable ionosphere, namely, its temperature and density, as well as ion-composition and charged particle drifts. Less than a dozen of ionospheric research radars operated around the globe have the size and sensitivity to count as ISRs -one of such instruments is the Arecibo radar. The Arecibo ISR transmits a peak power value of 2.5 MW. It has a spherical dish antenna with a diameter of 305 m and its operation frequency is 430 MHz.

Until recently, the capabilities have not been such that in cases of strong ionization the entire backscatter spectra could be captured during a single observation and with a single receiver. The bandwidth limitations of existing systems have prevented obtaining the entire spectra. In events of a highly active ionosphere, the plasma lines may be shifted in frequency by as much as 16 MHz. In these cases, a receiver must be capable of recording at least 32 MHz to capture both the up-shifted and down-shifted plasma lines. The existing analog acquisition system is capable of recording only 5 MHz of bandwidth of incoherent backscatter [Isham, 2000]. Though provisional attempts at receiving multiple band segments mixed to different center frequencies were capable of capturing the entire bandwidth, no single dataset contained the entire scattering spectra. This limitation prompted the development of a new, digital receiver system aimed at, among other things, increasing the available bandwidth of plasma line observations. Based on a commercially available digitizing PCI card (the Echotek-GC214), *Seal* [2008] developed a new digital receiver system that increased radar observation bandwidth to 10 MHz. Nevertheless, obtaining the full 32 MHz bandwidth required the development of a newer and even more capable system. The digital radar receiver presented in this report, uses reconfigurable hardware developed for Pulsar detection—a substantially different scientific goal than ionospheric studies—to implement the newer digital radar receiver. Nevertheless, modest adaptation of the pulsar system (a digital FPGA-based receiver) proves to be suited for aeronomy observations [Sunderland, 2008]. Such hardware versatility is a major advantage of reconfigurable digital-based systems.

2 Receiver Design

2.1 System Overview

Originally designed for the astronomy group at Arecibo Observatory, the pulsar detection (PDEV) system features an FPGA-based signal processor interfacing to four 170 MHz ADCs and an embedded PowerPC processor supporting a Gigabit Ethernet to a host PC. The FPGA houses the Signal Processor, memory interface for buffering the stream of incoming data from the ADC, and the interface to the PowerPC embedded processor. The PowerPC processor runs a version of the Linux operating system and provides TCP/IP networking over Gigabit Ethernet to which one or more PC's are attached. Several applications on the host computer configure and run an observation, receive and store the data, and display the data in real time [Mock, 2007].

This work has focused on the development of a new signal processing block implementing pulsed radar functionality, and the development of host applications which store the data using more conventional file structures and a real-time oscilloscope view of the received data. Figure 1 shows the logical flow of the received radar signal as it is converted to a digital signal and subsequently processed by the signal processor FPGA block and host computer software.

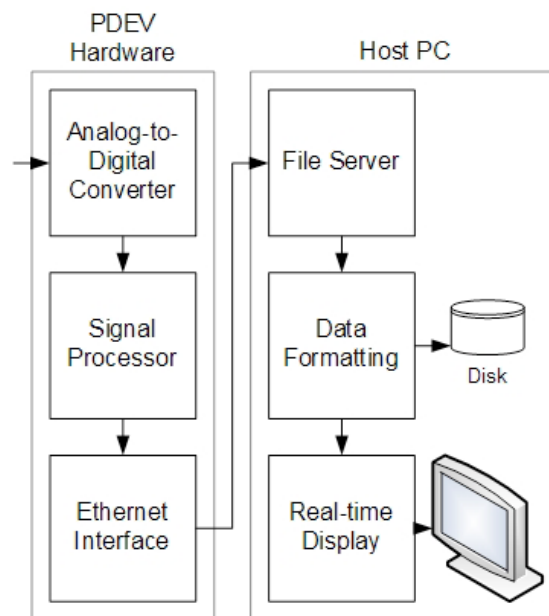


Figure 1: PDEV Pulsed Radar Receiver System

2.2 Signal Processor

By changing the signal processing performed by the FPGA, it's possible to implement experiments differing from the original intentions of the system. Indeed, a receiver for Pulsar detection is being simply reprogrammed to perform aeronomy measurements. It is the flexibility and performance of FPGA devices that enables digital receivers to perform such varied tasks.

The signal processor implements a digital quadrature downconverter, polyphase decimating filters, and supporting logic to control operation. Effort has been put into the

digital downconverter design to maximize the Spurious Free Dynamic Range (SFDR, a limiting factor in mixer designs) by the use of a pseudo-random dither noise source [Vankka, 1996]. Tests comparing various optimization techniques for digital synthesis have revealed a 4.55 dB gain in SFDR when using a dither source versus a basic test case. Polyphase filter implementations further reduce FPGA resource usage by time-sharing expensive logic elements such as multipliers and adders.

2.3 First Results

The first results are promising as the ionospheric return is visible in the data spectra. The first test was configured to capture 52 MHz of bandwidth, exceeding the goal of 32 MHz. Figure 2 shows the backscatter return centered around zero MHz and the effect of the 30 MHz bandpass filter used during the experiment. However, the test also revealed a synchronization issue in the host software which has caused spurious signals to corrupt the data. Improvements to the host software should eliminate the artificial signals and allow useful data to be collected with the new system.

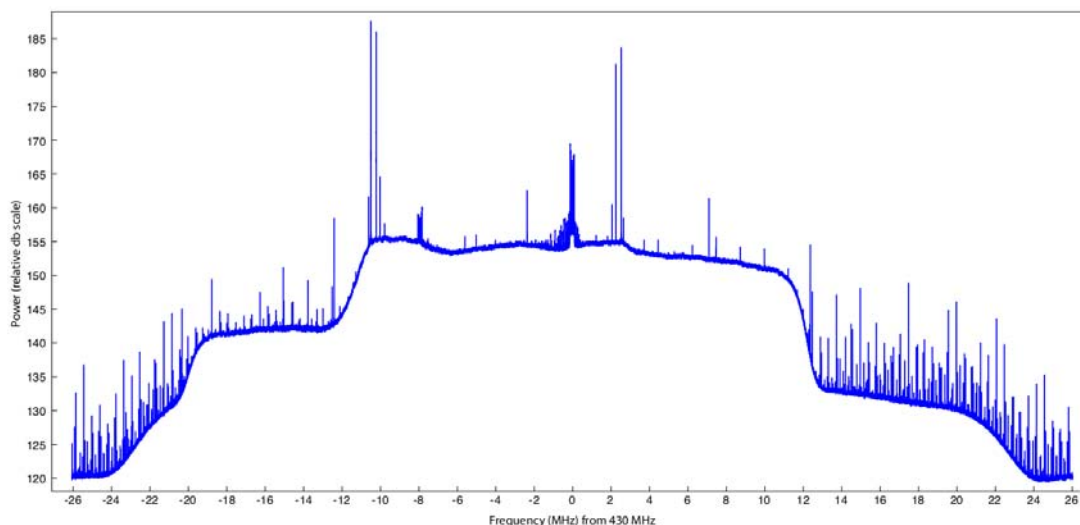


Figure 2: Initial results, shows both the ionospheric return near zero MHz and the presence of the artificial signals at 2 and -10 MHz.

3 Capabilities

The purpose of developing this system has been to increase the overall bandwidth of observations. The PDEV spectrometer hardware provides ample performance by offering eight high-speed ADCs and two high-performance FPGAs. However, the gigabit Ethernet interface, capped to a practical limit of around 70 MB/s, limits the overall system performance. Without performing significant real-time processing on the FPGA or using both Ethernet ports simultaneously, this limit determines the maximum range–bandwidth product which can be recorded to disk.

To illustrate the decimation rate–altitude range tradeoff, Figure 3 plots the maximum recordable altitude range as a function of the maximum signal bandwidth. The figure assumes that the internal ADC clock of 156.25 MHz is used with an IPP of 10 ms.

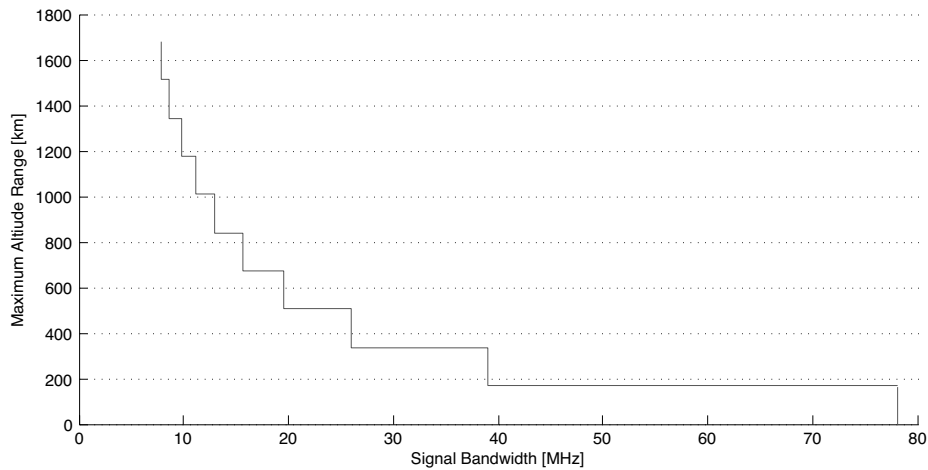


Figure 3: Maximum recordable altitude range versus signal bandwidth. ($CLK_{ADC} = 156.25 \text{ MHz}$ and IPP Length = 10 ms .)

4 Conclusion

By leveraging the inherent flexibility of digital design, we are able to reprogram existing hardware to perform a completely different task than for which it was originally designed. And, this reprogrammed system is capable of performing the new task with greater capability than existing systems designed specifically for the task of aeronomy observations. Though the first results are corrupted by spurious signals, the test confirmed that a majority of the new system is working. After improving the software controlling the data acquisition, the problems with the new receiver should be eliminated. Such a demonstration points to the future of radar system design and the possibilities of such digital implementations.

References

- Isham, et. al. Upper Atmospheric Observations at Arecibo Observatory. *J. of Geophys. Res.* 108. 18,609-18,637. 2000.
- Mock, J., PDEV Users Guide. 2007.
- Seal, R., Multi-channel Digital Receiver Data Acquisition System for the Arecibo Radar System. *University of Arkansas. M.S. Thesis.* 2008.
- Sunderland, M., Software Defined Radar Receiver Implementation for Pulsed Radar Applications. *The Pennsylvania State University. B.S. Thesis.* 2008.
- Vankka, J., Spur Reduction Techniques in Sine Output Direct Digital Synthesizers. *IEEE, International Frequency Control Symposium.* 1996.

THE EFFECTS OF ALMOST 20 YEARS OF OPERATION ON THE PERFORMANCE OF THE ABERYSTWYTH MST RADAR

J. D. Eastment¹, W. J. Bradford¹, D. A. Hooper¹, Z. A. K. Olewicz², O. T. Davies¹, and L. Dean³

¹STFC Rutherford Appleton Laboratory, Chilton, Didcot, OX11 0QX, UK

²formerly of the NERC MST Radar Facility, Capel Dewi, Aberystwyth, SY23 3HU, UK

³Institute of Mathematics and Physics, Aberystwyth University, Aberystwyth, SY23 3BZ, UK

1. Introduction

The MST Radar at Aberystwyth, a 46.5 MHz Doppler Beam Swinging instrument, was constructed in 1989/1990. The hardware has remained virtually unchanged ever since. For the first few years the radar was operated on a campaign basis, i.e. for up to a few days at a time (using one of a number of different observation formats) and with gaps of up to a few days in-between. Since late 1997 it has been operated on a quasi-continuous basis with a typical down-time of no more than 2%, i.e. an accumulation of less than 8 days in a year. Although it is still a powerful system, the performance has noticeably decreased over the past few years. As can be seen in Figure 1, whereas the typical maximum useful altitude for wind-profiling purposes (using an off-vertical angle of 6.0°) was around 20 km in 1999 (top panel), it is now closer to 15 km almost a decade later (bottom panel). Consequently a detailed review of the entire system was undertaken in late 2008 with a view to renovating the system. This extended abstract focuses on those components of the system which have degraded significantly over the lifetime of the radar.

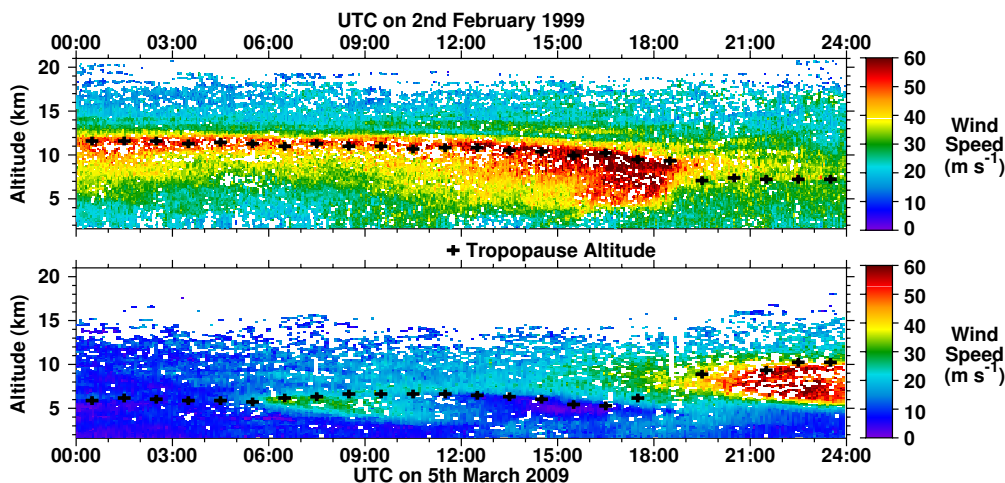


Figure 1: An illustration of how the maximum useful altitude for wind-profiling purposes has reduced from nearly 20 km in 1999 (top panel) to around 15 km a decade later (bottom panel).

2. System Overview

Figure 2 shows the principal functional components of the Aberystwyth radar. The design is fairly typical for an instrument of late-1980s vintage. Owing to the relatively limited computer power available, dedicated hardware units were designed to carry out the high speed functions. The Radar Control Unit generates all of the control signals needed by the other radar components in order to automatically acquire the necessary data for a single dwell. The principal role of the Pre-Processor Unit is to carry out coherent integration.

3. Transmitters

The 5 valve-based transmitters are of type WPT-50, manufactured by Tycho Technologies. Each has a peak power of 32 kW and a maximum duty cycle of 5%. They were designed for operation

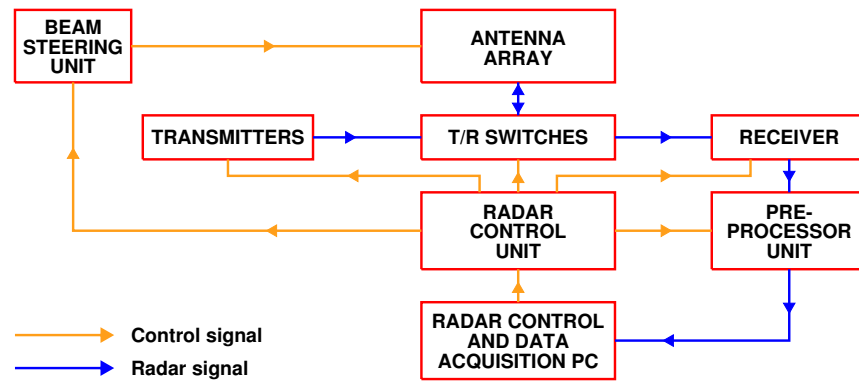


Figure 2: The principal functional components of the Aberystwyth MST radar.

from a mains supply of 110 V and 60 Hz. Although they were modified for the UK standard of 240 V and 50 Hz, the difference in mains frequency led to the valve heater voltages being too low. This resulted in the valves initially suffering from cathode poisoning. The heater circuits were subsequently modified and the valves no longer suffer from this problem.

Although the reduction in radar altitude cover had initially been attributed to a degradation in transmitter performance, these units appear to still be in a good working condition. Their reliability has increased considerably since a 3 kVA Uninterruptible Power Supply unit was installed for each one in 2007. The Aberystwyth radar is located in a rural location where mains fluctuations, as opposed to complete losses of power, are relatively common. Such fluctuations have proved to be the principal cause of transmitter component failure.



Figure 3: Examples of vermin damage to RG 213 cables.

4. Antenna Array

The antenna of the Aberystwyth radar is composed of a 20 by 20 array of 4-element Yagis at 0.85λ spacing, where λ is the radar wavelength. From a control point of view the antenna is configured as a 10 by 10 array of Quads, i.e. 2 by 2 sub-arrays of Yagis which act collectively as single units. Each Quad has an associated Phasing Unit, which allows the radar beam to be steered off-vertical - see next Section. Each Quad belongs to one of five variable-sized sectors and each sector is powered by one of the five identical transmitters. The signal from each transmitter is distributed equally to each Quad within the sector using a cascade of power splitters. Most of the interconnecting cables are of type LCF 7/8" or LCF 1/2". They are primarily routed underground, but those sections which are visible appear to be in a good condition. The final sections of cable are of type RG 213. Some of these shown signs of mild vermin damage and the outer PVC jackets of all of those inspected show signs of degradation due to solar UV light and leaching of plasticiser.

5. Beam Steering Unit and Phasing Units

The Phasing Units are composed of three electro-mechanical Relay Units, which can switch equivalent cable lengths of $\lambda/2$, $\lambda/4$, and $\lambda/8$ in to or out of the signal feed. The Relay Units (top-left panel of Figure 4) are N-type, DPDT transfer relays, part number R 563703230, manufactured by Radiall of France. They are designed to switch from a dc control voltage of between 24 and 30 V.

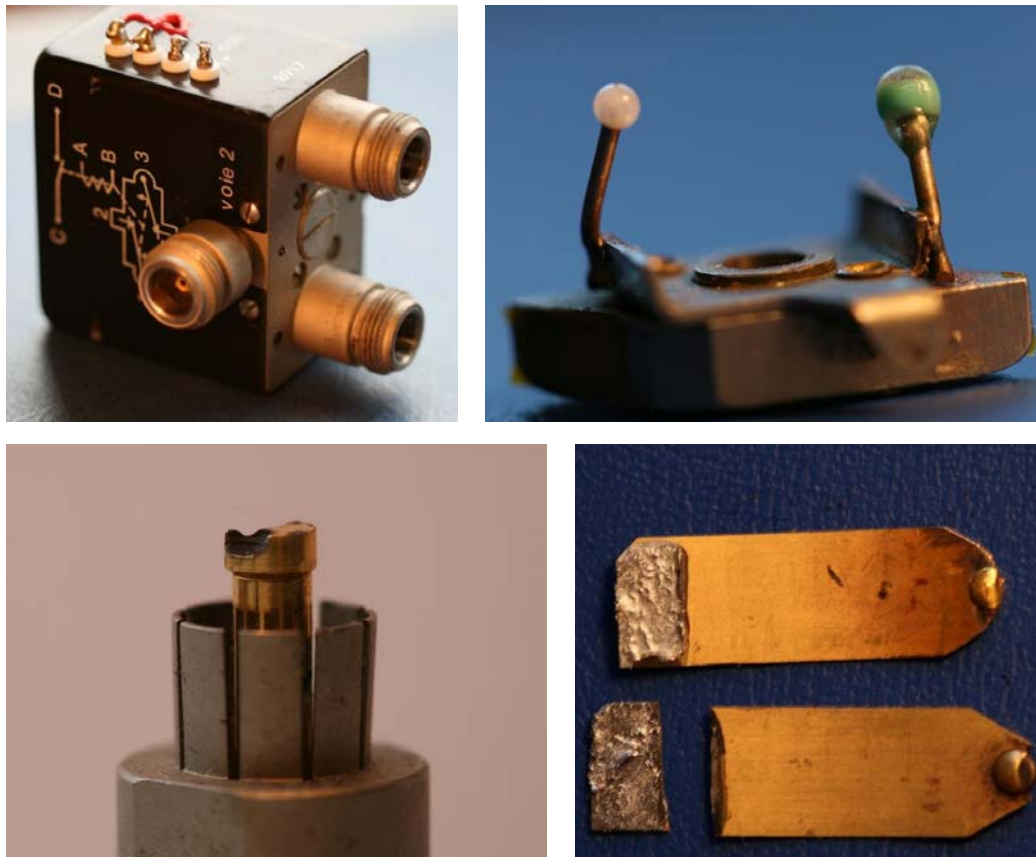


Figure 4: (top left) A complete relay unit; (top-right) the rotor mechanism; (bottom-left) an RF cable connector contact pin which has suffered from severe contact erosion; (bottom-right) an intact and a snapped contact blade.

The Relay Units in use today are all from the original stock, which included a number of spare units. They each perform approximately a million switching operations a year. Consequently they are subject to continuous, albeit gradual, degradation. The most common problem is an increase in the mechanical resistance experienced by the rotor mechanism (top-right panel of Figure 4). This can be solved by simply removing the accumulated debris (principally metal filings) from around the mechanism. Occasionally the rotor pins snap off. A new pin, which uses the plastic bead from a child's toy necklace as an insulator, can be welded back on as a replacement. The pin with a white bead seen in the top-right panel of Figure 4 is an original, whereas the one with a green bead is a replacement.

A more serious problem is that Relay Unit contacts are prone to erosion. RF arcing, which leads to evaporation of the contact metal, is believed to be responsible. As shown in the bottom-left panel of Figure 4, this is a particular problem for the contact pins at the back of the RF connectors. The degree of erosion can range from being superficial through to the loss of material to a depth of over 1 mm (the contact pins are approximately 3 mm in diameter). The lifetime of a connector can typically be extended by rotating it slightly so as to present a more-robust portion of the pin

to the contact blade. Nevertheless, a number of connectors have become so badly eroded that they have had to be removed from service. The contact blades (bottom-right panel of Figure 4) are also prone to contact erosion, albeit to a lesser degree. Nevertheless, they also have a finite lifetime and must be removed from service when they snap (as in the lower example).

The role of the Beam Steering Unit is to energise the appropriate Relays Units in order to achieve each of the pre-programmed beam pointing directions. Power is supplied from four 28 V dc, 10 A units. It appears that an allowance of 0.4 A has been made for each Phasing Unit, i.e. 0.13 A per Relay Unit. Although the Beam Steering Unit is in a good working condition, virtually no documentation is available for it. This will make it time-consuming to repair in case of a failure. It has twice suffered from extensive damage after lightning struck in the close vicinity of the radar site.



Figure 5: Examples of (left) a vermin-damaged relay control cable and (right) one of the probable culprits.

A single 18-core control cable connects each of the 100 Phasing Units to the Beam Steering Unit. They are primarily routed underground but are visible in the vicinity of their destination Phasing Units. Many of these sections show signs of vermin damage. In mild cases only the braiding wire is exposed. However, in a few severe cases, such as the one shown in the left panel of Figure 5, the copper of the individual wires is exposed. Most of this type of damage appears to be confined to the NE quadrant of the array. Rabbits (see right panel of Figure 5), which are plentiful on the site, are thought to be the primary culprits. No active steps have been taken to control the on-site population owing to fact that it would be difficult to prevent re-colonisation at this rural location.

Some of the longest relay control cables, which run over 100 m to the western side of the antenna array, have been found to significantly attenuate the voltage (28 V) generated by the Beam Steering Unit. The Relay Units have a specified minimum of 24 V for switching to take place, whereas some of the measured voltages are as low as 21 V. It is not clear as to how much this is a result of the vermin damage. Regardless, such low voltages are likely to result in sub-optimal contact pressure of the Relay Units and so could be aggravating the problems described above.

6. Conclusions

In conclusion, after twenty years of operation, the Relay Units, the Relay Control Cables, and all RG-213 RF cables have reached the end of their useful working lives and are in urgent need of replacement. Moreover, it would be highly desirable to replace the Relay Control Unit since its almost-complete lack of documentation will make it difficult to repair in the case of a failure.

THE DIAGNOSIS OF A RANGE GATING PROBLEM SUFFERED BY THE ABERYSTWYTH MST RADAR

D. A. Hooper¹, O. T. Davies¹, J. Nash², T. Oakley², and M. Turp²

¹STFC Rutherford Appleton Laboratory, Chilton, Didcot, OX11 0QX, UK

²Observations Division - Upper Air Team, Met Office, Exeter, EX1 3PB, UK

1. Introduction

When the Doppler Beam Swinging MST Radar at Aberystwyth (UK) began operations in 1989, the data acquisition was handled by a PDP-11 computer. Rapid increases in available computing power meant that this task could be transferred to a desktop (Windows NT) PC in 1999. When it became necessary to upgrade the PC a few years later, the decision was made to rewrite the software (under Linux) in order to increase the flexibility with which the radar could be operated. Unfortunately the new system, which began operations on 6th February 2007, introduced a range gating error of -4 ($1 \mu s$ interval) gates. This led to the wind-profile data, which are operationally assimilated by the (UK) Met Office for the purposes of numerical weather prediction, being reported at altitudes of almost 600 m lower than they should have been. Thanks to the monthly model-comparison statistics provided by the Met Office, it soon became apparent that the new system had introduced an undesirable change. Nevertheless, they did not indicate the source of the problem, which, owing to the lack of documentation for the previous acquisition system, was extremely difficult to identify. The aim of this extended abstract is to highlight the usefulness of such monitoring statistics as well as to describe the symptoms of the range gating problem.

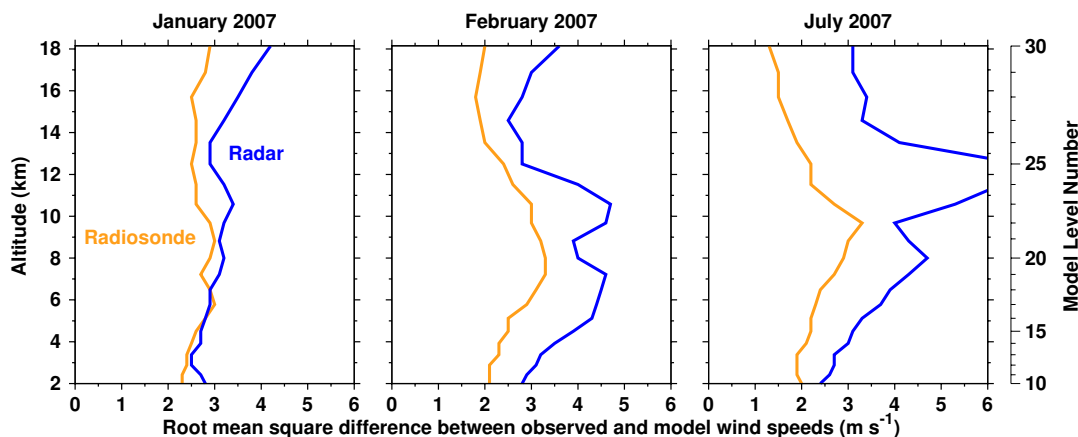


Figure 1: Met Office monthly model-comparison statistics, which are used for evaluating the accuracy of Aberystwyth MST radar wind-profile data.

2. Met Office Monthly Model-Comparison Statistics

The Met Office assimilate data from a wide variety of sources and produce a set of monthly model-comparison statistics, courtesy of Colin Parrett, for each of these. In the case of wind-profile data, the statistics include the average and the root mean square differences between the observed and model values of speed, direction, northward velocity component, and eastward velocity component. These differences should not be regarded as solely representing errors in the observed values, since the model itself is not perfect. Nevertheless, two data sources which have similar model-comparison statistics can be regarded as having similar accuracies (*Dibbern et al.*, 2003). A composite of all simultaneously-measured radiosonde wind-profiles from across the British Isles is used to generate reference model-comparison statistics for UK-based wind-profiling radars. This is a consequence of the fact that such radars are intentionally located within gaps in the radiosonde

network and so no single station provides an ideal reference.

The left panel of Figure 1 shows the root mean square differences between the observed and model wind speeds for January 2007, i.e. for the month before the new data acquisition system began operations. As is typical, the profiles are closely matched for the radar and for the composite radiosonde data, indicating that the radar data are of good quality. The slight increase in the radar values compared to the radiosonde values at the higher model levels is attributed to the decreasing availability of useful radar returns with increasing altitude in the lower stratosphere. By contrast to the case for January 2007, the radar values are significantly larger than the radiosonde values at all model levels for February 2007 (middle panel). This gave an unambiguous indication that the new data acquisition system has introduced an undesirable change.

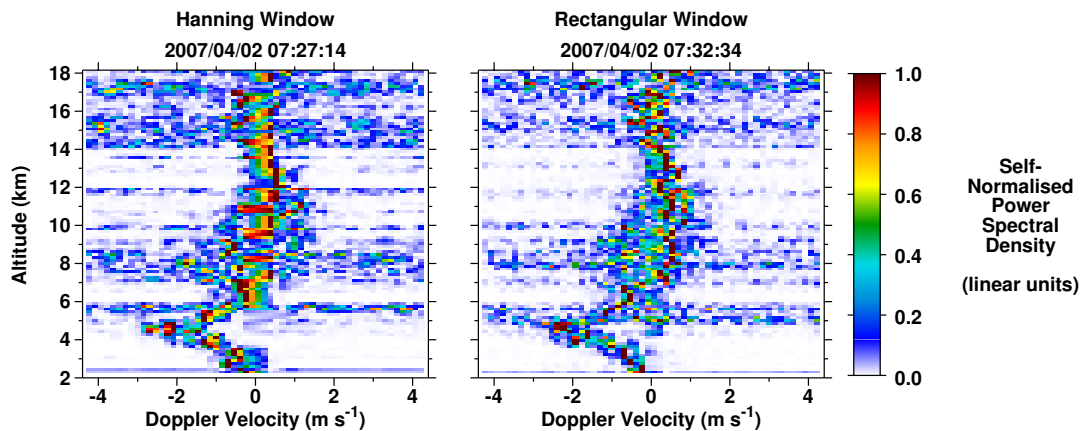


Figure 2: The central halves of two Vertical beam Doppler spectra for observations made just over 5 minutes apart.

The only obvious change between the old and new systems was the choice of data weighting window used in deriving the Doppler spectra (e.g. *Hooper*, 1999). The old system allowed only a Rectangular window to be used. This requires correction of the power spectral density (PSD) for only the central velocity bin (with a value linearly interpolated between the PSDs for the adjacent velocity bins) in order to remove the effects of dc biases in the raw data. A Hanning window was initially used with the new system. This requires correction of the PSDs for the central three velocity bins. As can be seen from Figure 2, use of the Hanning window leads to a more-obvious correction-artefact for signal components which are characterised by near-zero Doppler velocities compared with use of the Rectangular window. It was speculated that this might lead to greater variability in the Vertical beam radial velocities and that this in turn led to a reduction in the accuracy of the horizontal wind components. However, there was no improvement in the model-comparison statistics following a switch to use of the Rectangular window in April 2007.

The jet stream was located much further south during July 2007 than is typical for summer months. Consequently peak upper-tropospheric wind speeds in excess of 50 m s^{-1} were relatively-common above Aberystwyth (the tropopause altitude was predominantly in the range 8 - 11 km). Since wind speeds tend to decrease much more rapidly as a function of altitude above the jet peak than below it, the effects of the range gating error are particularly noticeable in the former region. This explains the exceptionally large differences between the radar and radiosonde model-comparison statistics at altitudes of around 12 km in the right panel of Figure 1.

3. Alternative Methods For Revealing The Range Gating Error

The ability to detect a range gating error is highly-dependent upon the presence of a sharp change in a radar parameter value as a function of altitude. It is unfortunate that such a feature did not

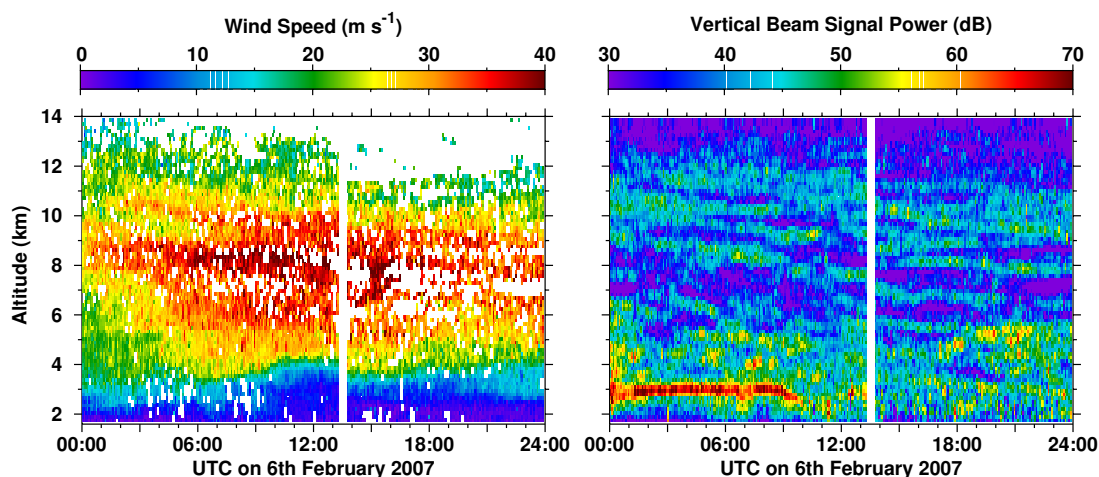


Figure 3: MST radar data for the day when the switch was made between the old and the new data acquisition systems (at around 13:30 UT). No correction has been made for the range gating error.

exist for the day when the switch was made between the old and new data acquisition systems. As can be seen in the left panel of Figure 3, the upper-tropospheric maximum in wind speed is broad and relatively featureless. The data acquired with the new system are shown without correction for the range gating error. They fail to unambiguously suggest that an altitude offset of -600 m has been introduced. Moreover, comparably-plausible visual fits can be obtained for any range gate correction of between 0 and 8 gates. The same is true of the Vertical beam signal power data, shown in the right panel of Figure 3.

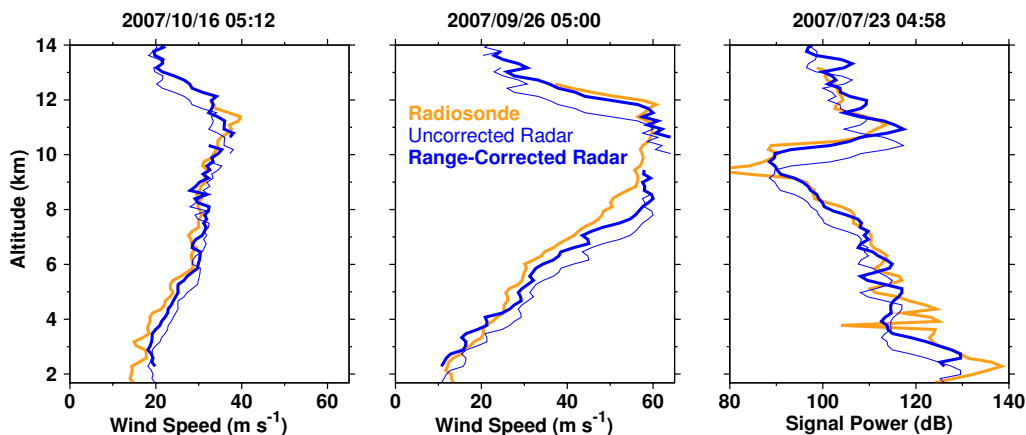


Figure 4: Comparisons between data acquired simultaneously by the MST radar and by radiosondes launched from Aberporth, which is located 45 km to the south-west of the radar site.

Figure 4 compares data from radiosondes launched from Aberporth, which is 45 km to the south-west of the radar site, with MST radar data which are averaged over 1 hour starting from the time of the launch. In the absence of a well-defined peak in the wind speed profile (left panel), the fit between the radiosonde and radar data is comparably-plausible irrespective of whether or not a range gate correction (of $+600$ m) has been applied. However, within the sharp shear layer at the top of the jet shown in the middle panel, it is clear that the range-corrected radar data provide a much better agreement. A sharp change in Vertical beam signal power at the tropopause (right panel) is a more-common radar feature than a sharp wind shear. Consequently it offers an alternative and often-clearer method for identifying a range gating problem. The Vertical beam signal power is predicted from high-resolution radiosonde measurements of temperature, pressure and

relative humidity, as described by *Hooper et al.* (2004) and references therein.

As seen above, a single radar-radiosonde comparison can be highly misleading. A statistical approach is needed in order to reach a meaningful conclusion. The left panel of Figure 5 shows how the correlation coefficient between radar and radiosonde wind speeds varies as a function of the number of range gates by which the radar data are corrected. This is based on 147 radiosondes launched from Aberporth during the period between June and December 2007. It is not clear how much significance should be attached to the fact that the peak value occurs at +5 rather than +4 range gates.

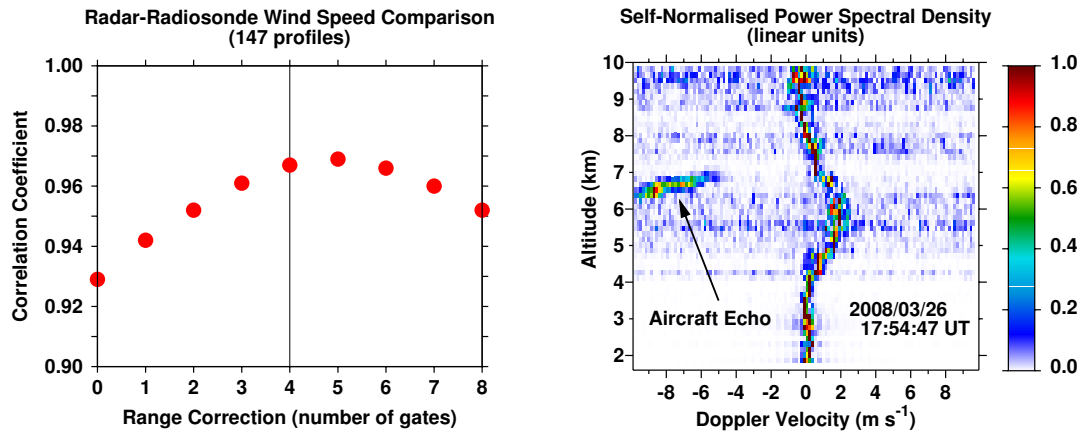


Figure 5: (left) A statistical comparison of radar and radiosonde wind speeds and (right) radar Doppler spectra showing an aircraft echo.

During March 2008, an aircraft flew level paths over the radar at known altitudes. The Doppler spectra shown in the right panel of Figure 5 were observed by a radar beam directed 6° off-vertical towards the north-east. However, given that the aircraft was known to be flying at an altitude of 3.66 km, it must be assumed that the aircraft echo, at an apparent altitude of 6.5 km, was observed through a side-lobe. In the following observation (made 23 s later at 6° off-vertical towards the south-west, but not shown), the aircraft echo is at an apparent altitude of 8.0 km, despite the fact that the aircraft remained at the same level. Clearly aircraft echoes are of no value for validating a radar's range gating.

4. Conclusions

As demonstrated here, monitoring statistics can provide an invaluable indication of degradations in data quality. Nevertheless, their significance can be difficult to interpret until the source of the problem is known. The range gating issue was finally fixed on 8th April 2008.

5. References

- Dibbern, J., D. Engelbart, U. Goersdorf, N. Latham, V. Lehmann, J. Nash, T. Oakley, H. Richner, and H. Steinhagen, Operational aspects, in *EUR 20614 - COST Action 76 - Development of VHF/UHF wind-profilers and vertical sounders for use in European observing systems - Final report*, edited by J. Dibbern, W. Monna, J. Nash., and G. Peters, pp. 133–224, European Commission, Luxembourg, 2003.
- Hooper, D. A., Signal and noise level estimation for narrow spectral width returns observed by the Indian MST radar, *Radio Sci.*, 34, 859–870, 1999.
- Hooper, D. A., J. Arvelius, and K. Stebel, Retrieval of atmospheric static stability from MST radar return signal power, *Ann. Geophys.*, 22, 3781–3788, 2004.

STUDY OF MULTIBEAM ABILITY FOR THE VHF MST ALWIN RADAR SYSTEM

Toralf Renkwitz, Werner Singer, Ralph Latteck
Leibniz Institute of Atmospheric Physics, Kühlungsborn, Germany

1. Introduction

The Leibniz-Institute of Atmospheric Physics in Kühlungsborn is operating the ALWIN MST radar system at 53.5 MHz on the North-Norwegian island Andoya. The ALWIN MST radar has been described by Latteck et al. [1999]. The antenna array of 144 Yagi antennas has been used to form a 6 degree wide beam on transmission and reception. The characteristics of Polar Mesospheric Summer Echoes (PMSE) have been studied with high time resolution using vertical and fixed oblique beams. Investigations of the horizontal structure were limited to 5 or 9 fixed beam positions with sequential data sampling. Investigation of horizontal PMSE structures have been performed sequentially with a single beam either directed to zenith or tilted to 7° or 14° zenith angle.

The aim of this study is to analyze a potential structure for the generation of multiple beams in azimuth/zenith angles for simultaneous observations of the horizontal structure of PMSE layers in a larger area.

For this purpose the use of a Butler matrix is evaluated.

2. Experimental details

The ALWIN successor system will have a phased array of 433 individual 3-element Yagi antennas arranged in an equilateral grid structure. In the first step approximately 150 Yagi antennas and transceiver modules will be operational.

64 Yagi antennas of the former ALWIN antenna array are still available for reception (ALWIN64).

On reception the Butler matrix will be used to form 16 beams in hardware, while for transmission an equal illumination with the ALWIN successor array will be generated. The 16 beams will also be generated in software for comparison with the beams formed by the Butler matrix.

A Butler matrix is a reciprocal structure and is composed of half-power 90° hybrid couplers and phase shifters, first described by Butler [1961].

In this structure the total number of available beams is determined by the amount of independent receivers and antenna feeds. A 4-Port Butler matrix simultaneously generates 4 individual in- and outputs. The structure of a 4-Port matrix is depicted in Figure 1.

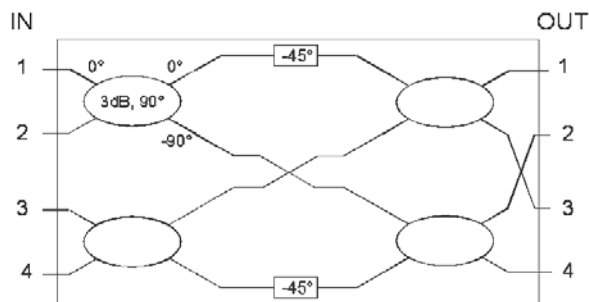


Figure 1. 4-Port Butler matrix

Table 1. Resulting phase table for a 4-port Butler matrix using 45° phase shifter

	OUT1	OUT2	OUT3	OUT4
IN1 = 0°	-45°	-90°	-135°	-180°
IN2 = 0°	-135°	0°	-225°	-90°
IN3 = 0°	-90°	-225°	0°	-135°
IN4 = 0°	-180°	-135°	-90°	-45°

Applying the phases of the 4-Port Butler matrix shown in Table 1 to an array of 4x 4 Yagi antennas, 4 individual main beams are generated at zenith angles of approximately +/-5° and +/-14°.

Radiation pattern for a 4-port Butler matrix using an array of 4x 4 Yagi antennas have been calculated with NEC (Numerical Electromagnetic Code) and are shown in Figure 2.

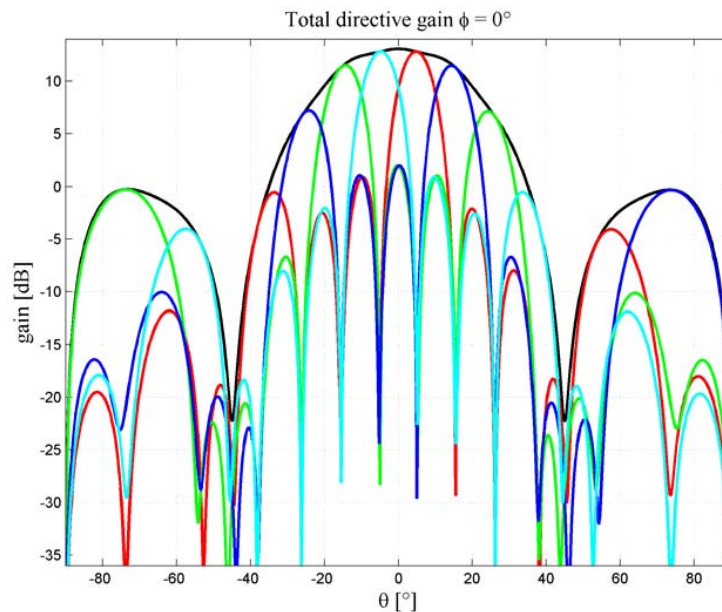


Figure 2. Radiation pattern of a 4-Port Butler matrix

For the evaluation of the theoretical properties of a 4-Port Butler matrix two prototypes have been designed and built. The prototype in strip-line technique and surface mounted hybrid couplers has shown the best performance in terms of phase and amplitude error.

To generate 16 individual beams spread in azimuth and zenith angles a concatenation of 8x 4-Port Butler matrices is needed. The diagram in Figure 3 illustrates a 16-Port Butler matrix.

Using a 16-Port Butler matrix with the ALWIN64 array (16x 4 Yagi antennas) 16 beams with a beam width of approximately 9° are generated. For the height of PMSE-layers the beam width results in a target area of roughly 14km diameter for each single beam.

Radiation pattern in top view of 16 individual beams generated by using the ALWIN64 array with a 16-Port Butler matrix have been calculated with NEC and are presented in Figure 4.

The beams close to the zenith (1, 4, 13, 16) show the best pattern with a clear maximum and good side lobe suppression. Further 8 beams have fair quality, however 4 beams (6, 7, 10, 11) show rather poor side lobe suppression.

A 16-Port Butler matrix has been built and will be implemented to the ALWIN64 radar receiving chain. First measurements are planned for the winter 2009/2010.

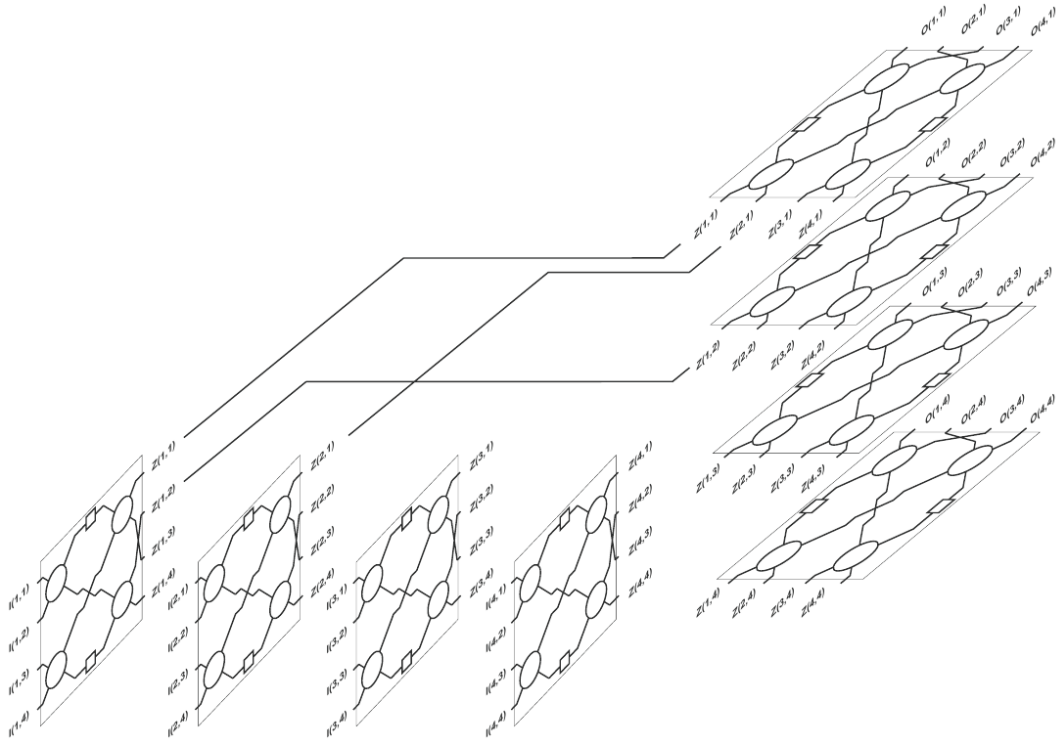


Figure 3. Chart of a 16-Port Butler matrix

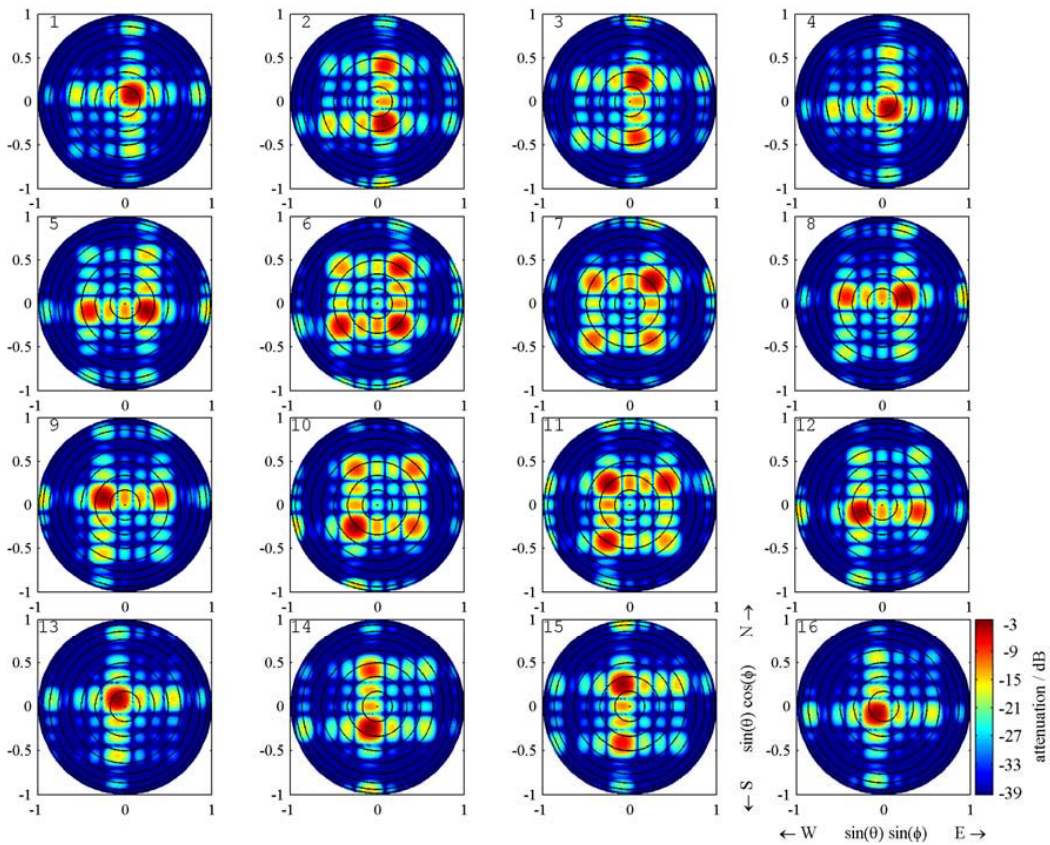


Figure 4. Radiation pattern of ALWIN64 antenna array using a 16-Port Butler matrix

Bibliography

Butler et al., Beam Forming Matrix Simplifies Design of Electronically Scanned Antennas, *Electronic Design*, volume 9, pp. 170-173, April 12, 1961

Latteck et al., The ALWIN MST radar - Technical design and performances, *Proceedings of the 14th ESA Symposium on European Rocket and Balloon Programmes and Related Research*, 1999

PULSE CODING TO REDUCE THE INFLUENCE OF MAN-MADE NOISE ON MF RADAR OBSERVATIONS OF WINDS

D. Keuer , P. Hoffmann, W. Singer

Leibniz-Institute of Atmospheric Physics Kühlungsborn, Schlosstr. 6, D-18225 Kühlungsborn, Germany

1. Introduction

MF-Radar observations of mesospheric winds at Juliusruh (55°N, 13°E) have continuously been carried out at a frequency of 3.18 MHz since 1990 (Singer et al., 1992). Due to an increasing noise level, the operation times were mainly limited to daytime conditions centered at local noon, varying between about 13 hours in winter and about 16 hours in summer. The man-made noise is dominated by interferences generated by communication lines working at the same frequency within our baseband of 50 kHz.

During spring 2003 the formerly used FM-CW radar has been substituted by a radar, working at the same frequency, but using a normal pulse technique also allowing the estimation of the electron density. Figure 1 describes the new antenna design used for the estimation of winds with the spaced antenna method. The technical parameters are described in Table 1. Data are sampled in the altitude range from 50 to 100 km.

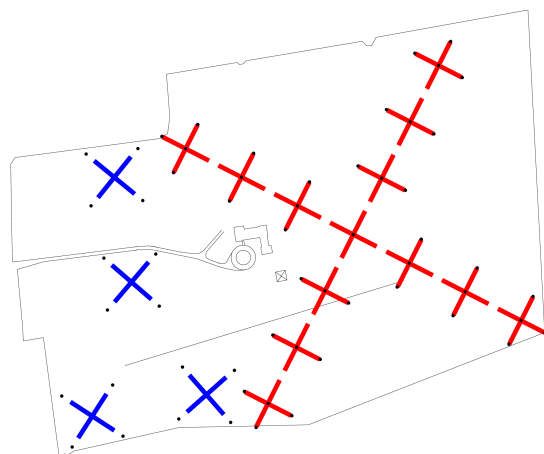


Figure 1: Mills-Cross antenna (red) and the receiving antennas of the MF radars Juliusruh

Table 1. Technical parameter

Frequency:	3.18 MHz
Peak power:	128 kW
Pulse length:	27 μ s
Dipoles:	13 crossed
Rec. antennas:	4 (for FCA)
Rec. channels:	4
Temp. resol.:	120s - 180s
Range resolution:	1 - 4 km
Results:	Winds (1h avr)

The data are used to study the seasonal variation of mean winds and tides (e.g. Keuer et al, 2007). Figure 2a describes the mean zonal wind at Juliusruh during 2008, which is characterized by the typical summer-winter pattern with strong westward directed wind during summer at altitudes below 85 km and eastward winds above 85 km as well as during the winter months where short term wind reversals are observed due to stratospheric warmings (e.g., Hoffmann et al. 2007). The seasonal variation of the amplitudes of semi diurnal tides is presented in Fig. 2b. This tidal mode with enhanced amplitudes around the fall transition is the dominating mode at mid and high latitudes.

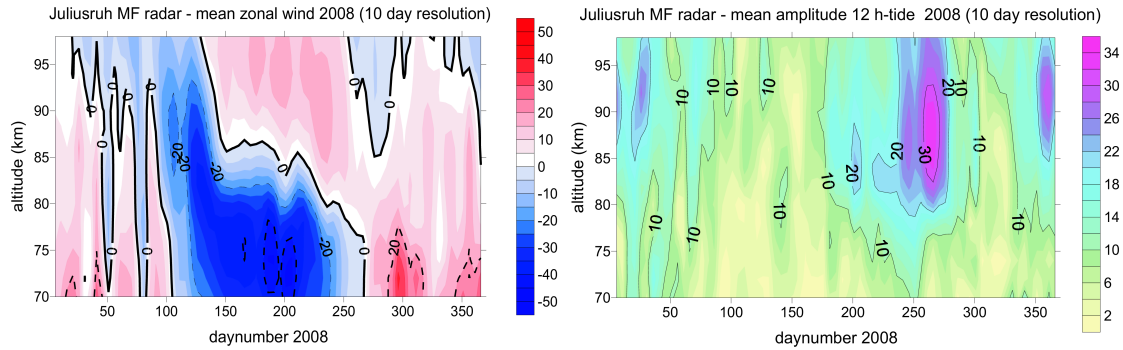


Figure 2: Seasonal variation of zonal winds (a,left) and amplitudes of the semi diurnal tides (b,right) in m/sec derived from observations with the MF radar Juliusruh during 2008.

2. Possible improvements by the application of codes

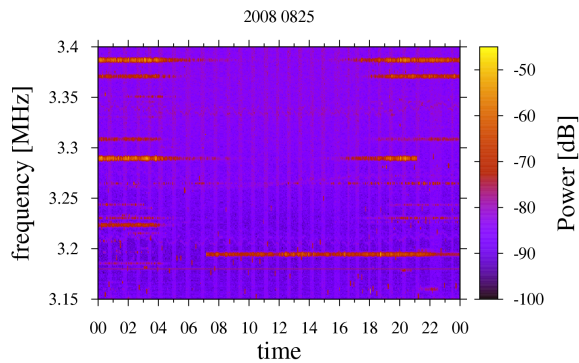


Figure 3: Typical frequency plot during August, 25, 2008. The thin red line indicates the working frequency. A strong disturbance at a frequency of 3.195 MHz starts at 07:00 UT

However, the obtained results are still limited in altitude and time so that, for example, a statistically significant estimation of the diurnal tidal wave is only possible with additional assumptions. Reasons for these constraints are mainly interferences with radio waves from communication lines working with frequencies near the frequency band of the MF radar. Such disturbances are detected by measurements of the RF band around our working frequency with a spectrum analyzer. The frequency time plot in Fig.3

shows a typical situation for Juliusruh. The thin red line indicates the measuring frequency of the MF Radar at 3.18 MHz. Strong interference starts at 7:00 UT with a frequency of about 3.195 MHz. Due to the weaker signal at lower range gates, especially altitudes below 70 km are influenced by these disturbances.

Various coded signals as Barker codes and short complementary codes were used to improve the signal-to-noise ratio. An example is presented in Fig. 4a, where the application of a 2-bit-Barker code leads to an improvement of the dynamical range by about 6 db at lower altitudes (green,dashed) in comparison with the uncoded power profile (red,solid) during disturbed conditions. The application of a 4-bit-Barker code (magenta,dotted) results in an additional improvement by 2-3 dB, but it leads to unwanted side lobes. Therefore, the application of a 2-bit-Barker code seems to be the preferred method. In the case without interference, Figure 4b clearly illustrates that the application of the 2-bit-Barker code

does not produce significant changes of the power profiles.

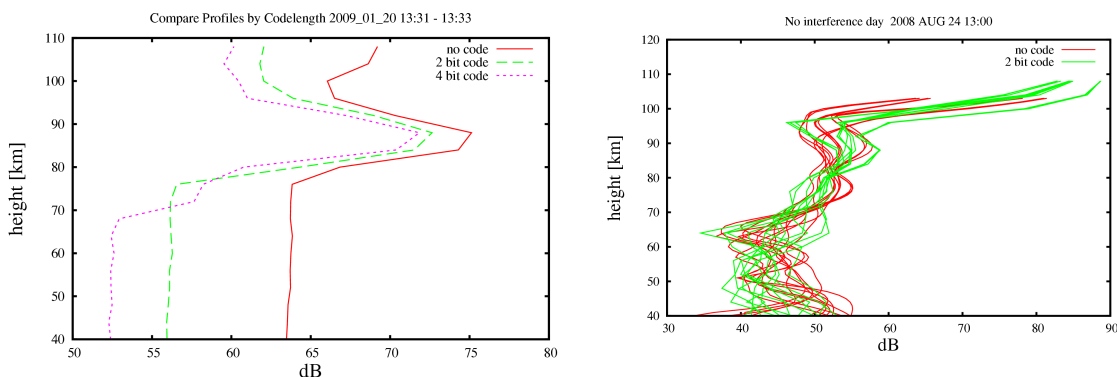


Figure 4: The influence of different codes on the power profiles (dB) during disturbed (a,left) and undisturbed (b,right) conditions.

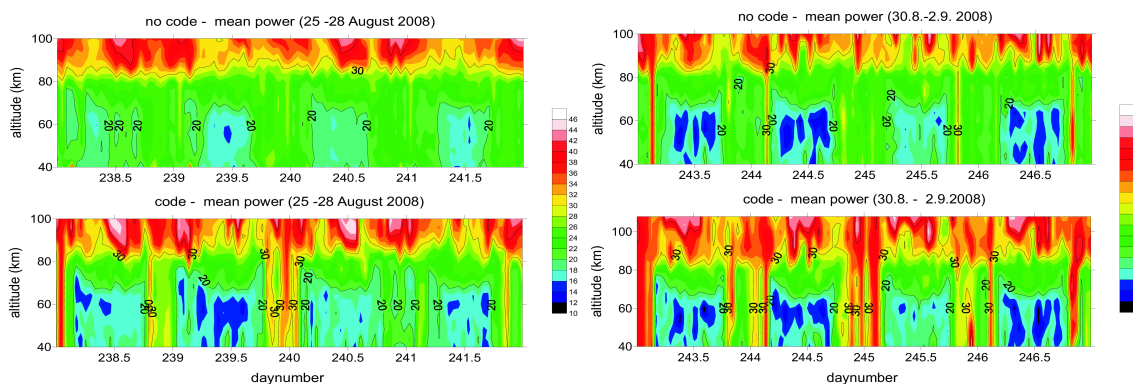


Figure 5: Mean reflected power (dB) during 4 day periods with interference (a,left panels) and without interference (b,right panels). The influence of the 2-bit-Barker code is shown in the lowermost panels

The influence of coded signals on the reflected power during a period with enhanced interference from 25.-28. August 2008 is presented in Figure 5a. The application of a 2-bit-Barker code leads to an extension of the dynamical range during daytime. During an undisturbed period (Fig. 5b), there are no changes of the reflected power during daytime. However, in both case studies, strong disturbances during nights cannot be removed.

Finally, we tested the influence of the 2-bit-Barker code on the acceptance rate and the mean wind profiles during disturbed conditions (Fig.6). As result, we found an enhanced percentage rate of evaluable wind values and furthermore improved vertical profiles of zonal and meridional winds. At altitudes between 75-95 km where the signal to noise ratio is reasonable sufficient, no influences on the mean wind profiles were found due to the use of coded signals.

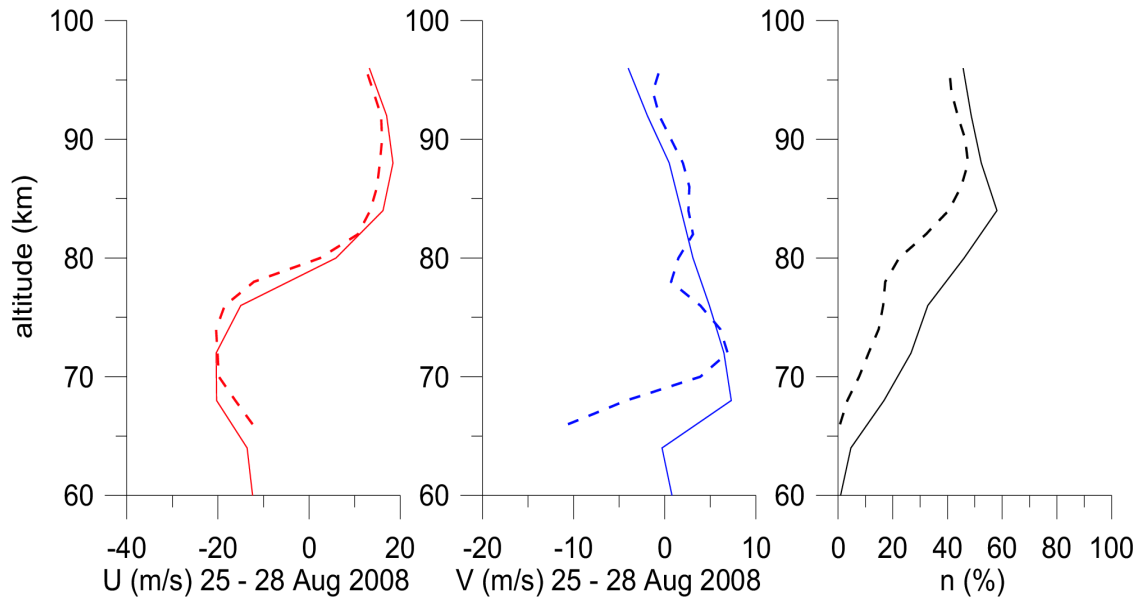


Figure 6: Mean altitude profiles of zonal and meridional winds and the percentage rate of accepted wind data during disturbed conditions. Dashed lines indicates measurements with uncoded pulses, solid lines are measurements with coded pulses.

References

- Hoffmann, P., W. Singer, D. Keuer, W. K. Hocking, M. Kunze, and Y. Murayama, Latitudinal and longitudinal variability of mesospheric winds and temperatures during stratospheric warming, *J. Atmos. Sol. Terr. Phys.*, 69, 2355-2366, 2007.
- Keuer, D., P. Hoffmann, W. Singer, and J. Bremer, Long-term variations of the mesospheric wind field at mid-latitudes, *Ann. Geophys.*, 25, 1779-1790, 2007.
- Singer, W., P. Hoffmann, D. Keuer, R. Schminder, and D. Kürschner, Wind in the middle atmosphere with partial reflection measurements during winter and spring in middle Europe, *Adv. Space Res.* 12(10), 299-302, 1992.

PROCEDURE TO EXTRACT BOUNDARY-LAYER WIND MEASUREMENTS USING RELATIVELY LONG PULSES

W.K. Hocking¹ and A. Hocking²

1. University of Western Ontario, London, Ont., N6A 3K7 Canada.
2. Mardoc Inc., London, Ont., Canada

1. Introduction

VHF wind measurements are possible to heights as low as 400m (e.g. Vincent et al., 2001), but generally this requires short pulse lengths, often as short as 150m or even 75m. A bandwidth of the order of 1-2 MHz is needed (~4-5% of the carrier frequency). It is often impossible to obtain a radio licence for such a broad frequency range.

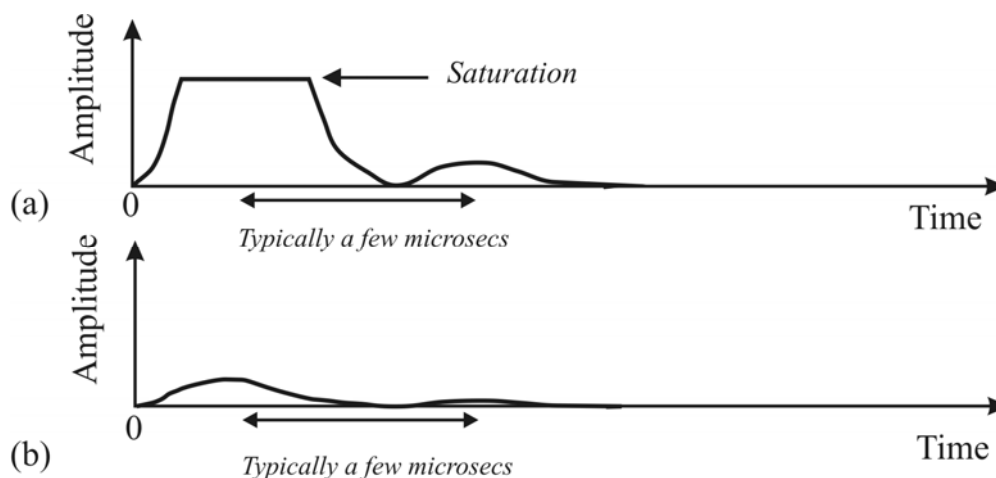


Fig. 1. (a) Typical signal seen on a receiver with a monostatic radar. Note the flat top, indicating saturation. (b) Ground pulse seen by a properly configured bistatic system.

Hocking (2007) discussed a variety of experimental configurations which could lead to the measurement of low altitude winds using relatively long pulses, but despite some interesting specialized applications (including oblique beams and loop antennas), it was concluded that the optimal arrangement was a bistatic system employing 3-element Uda-Yagi antennas.

2. Radar Design.

Fig. 1 shows the signal detected by a receiver when a monostatic radar is used and signal is recorded through a transmit-receive switch. Each antenna within the array detects ground-pulses from every other antenna, leading to a relatively strong signal returned to the TR switch when the pulse is transmitted. This signal saturates the receiver, as shown in fig.1(a). Secondary ground echoes (the second bump in fig. 1(a) may arise due to reflections from nearby bodies (“ground echoes”) and due to multiple pulse reflections between the antenna and the transmit-receive switch. These echoes often

change slowly with time (“fade”). It is generally not possible to allow the receiver to accept signal until the transmitter pulse has died out, for fear of receiver damage during pulse transmission.

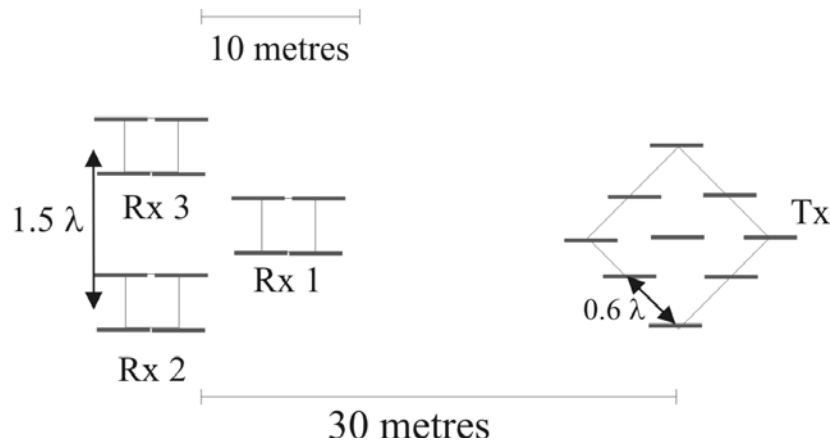


Fig. 2. Configuration of the bistatic system generally used in the O-QNet in Canada.

Fig. 2 shows a bistatic system. The transmitter array is shown on the right, comprising 9×3 -element Yagis, and three groups of four receiver antennas (quartets) are shown on the left, spaced by 1.5 wavelengths. By orientating the antennas so that the receiver antennas point to the transmitter antenna, and conversely, the direct pickup of the ground echo by the receiver antennas is substantially reduced. Furthermore, each receiver quartet is a group of 4 antennas with sides of one half wavelength in length, further suppressing signal received along the ground. The result is that the direct pickup of the transmitter signal by the receivers can be reduced below receiver saturation, as shown in fig. 1(b). This allows the system to start digitization before the pulse has finished transmission, since the receiver is no longer stressed during pulse transmission. Signal scattered from altitudes below one pulse length can therefore be recorded, although ground echoes are mixed in as well.

3. Analysis Procedure.

Normally a spaced-antenna algorithm might be used to determine the winds, but this does not work well here. Special steps are required to separate the true atmospheric echoes from ground-clutter and after-pulse-ringing. While it might be expected that the ground pulse is relatively pure, there are invariably effects which cause some level of fading. These include impurities in the power amplifiers, non-linearities in the amplification process, receiver ringing and temperature drifts in the transmitter and receivers. Therefore the preferred method of analysis is an IDI-type procedure.

A record of typically 30s of data is first acquired, and then a polynomial fit of seventh order is fitted to the data to remove slow oscillations (often associated with temperature drifts). The polynomial fit is then removed, and cross-spectra are formed between signals received by each pair of receiver quartets. A 3-point running mean is calculated across the cross-spectra. The largest peaks are then chosen for subsequent analysis. Generally we use the largest 90% of the spectral amplitudes, but the user may select this percentage. Phase-differences for each receiver pair are determined for each accepted spectral peak in

the frequency range from typically -4 to 4 Hz, and the phase differences on the 3 sets of receivers may be used to determine the position of the scatterer assumed to be associated with this spectral peak. However, the procedure also needs to recognize the possible positional ambiguities associated with the scatterers. Fig. 3 shows the effect. A particular set of phase differences between receivers 1-2, 2-3 and 1-3 can correspond to multiple angles in the sky, due to 2π ambiguities – in this case, 4 possible positions can be seen.

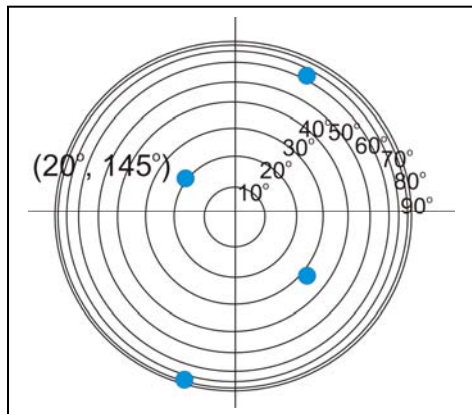


Fig. 3. Illustration of ambiguity.

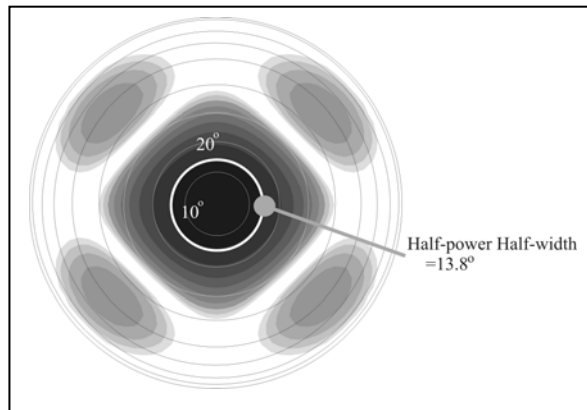


Fig. 4. Polar Diagram of the transmitter antenna

The most likely contributor is one of the two options closest to overhead in fig. 3, since the polar diagram of the transmitter antenna has a half-power half-width of approximately 14° (fig. 4). At 30° off-zenith, the combined effect of the transmitter polar diagram and the receiver polar diagrams, plus the polar diagram of the Yagi antennas themselves, means that the gain is weaker by more than 20 dB than the overhead gain.

Fig. 5 shows a display of the radial velocities and phase differences. Rather than plotting phases, we plot the possible positions of the scatterers (including ambiguous partners), and also plot a line from this point either back towards the origin (for negative Doppler frequency offsets) or away from the origin (for positive frequencies). The length of the line is proportional to the Doppler offset of the scatterer. The location of the scatterer is at the end of the line which has an adjacent number (1, 2, 3 or 4). The numbers refer to ambiguity-level. If a point is part of an ambiguous pairing, triplet or quartet, it is labeled with a 2 (for a pair), 3 or 4. If labeled with a 1, it means it is unambiguous within 30° of overhead. In fig 5(a), the points within the regions labeled “A” and “B” are consistent with the wind vector “W”, with negative radial velocities in “B” and positive in “A”. Even the points at P are consistent with this wind, since here the radial wind component is weak, being close to perpendicular to the wind. Fig 5(b) shows good examples of ambiguous pairs (see the clusters containing labels of “2” in the regions C and D, and E and F. In fig 5(b), there are clearly two main clusters of scatterers in regions A and B, which mainly define the wind vector “W”. In other situations, scatters can be distributed more uniformly in azimuth.

Returning to fig. 5(a), we highlight the points in the shaded section “S”. These are not consistent with the wind vector “W”, having the completely wrong direction, but in this case are a minority. Investigation of many plots like this often reveal clusters of such anomalous points which repeat from record to record. These seem associated with the transmitted pulse, and once identified can be flagged and ignored in subsequent analyses.

Correct identification of artifacts associated with the pulse, and exclusion of them from subsequent fitting, improves the wind-velocity algorithm substantially.

The procedure for analysis is as follows. First, a wind speed and direction is assumed. Then the positions of the various potential scatterers found from the cross-spectra are determined (including ambiguous ones, but ignoring cases beyond 30° off-zenith, and excluding regions in phase/frequency space which are suspected of being contaminated by direct transmitter-pulse effects). For each scatterer location, the expected (model) radial velocity is found from the assumed wind speed, and compared to the measured radial velocity. The scatterer within each ambiguous group which has the closest agreement with the model radial velocity is selected, and the radial velocity is subtracted from the model radial velocity. The quantity is squared, and stored. This is repeated for each spectral peak, and the squared differences summed. The procedure is then repeated for a new estimate of the mean wind speed and direction. The true wind is then the one with the lowest sum. The “correct” scatterer position within any ambiguous sets may change from one initial selected velocity to the next. Proper fitting also requires compensation for instrumental phase differences between the receivers. This is left as a free parameter, and optimum values are determined as part of the fitting process. Other subtleties need to be considered, but this describes the basic procedure, which has proven to give good wind data down to 400 and even 300m, even when using a 300m pulse.

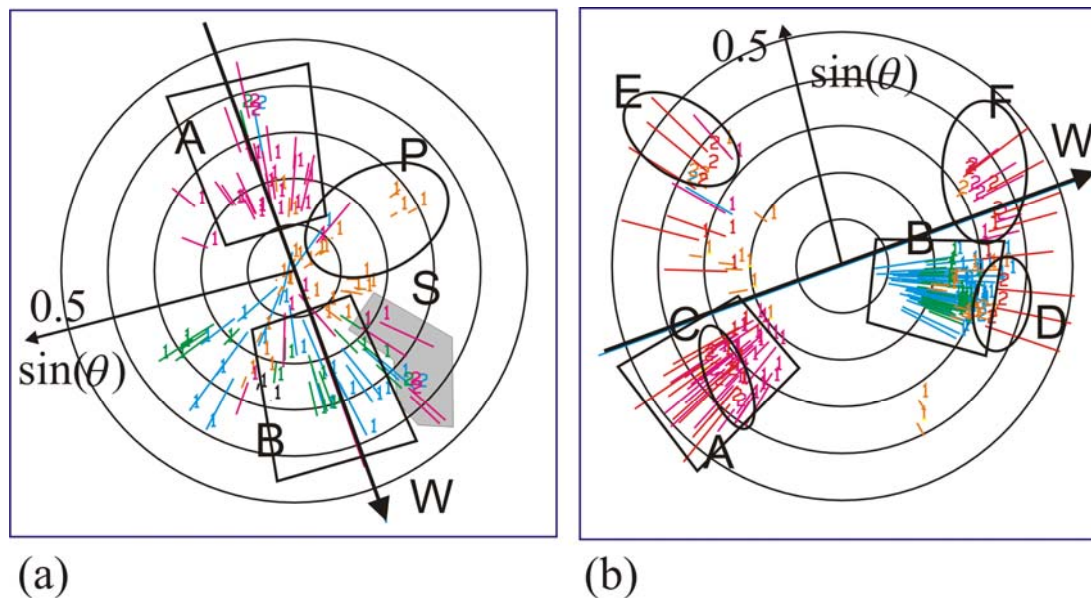


Fig. 5. Sample results of IDI scatterer location determinations.

References:

- Hocking, W.K., “Boundary Layer Winds with 50 MHz Radars – Comparison of Different Approaches”, Proc. of the Eleventh International Workshop on Technical and Scientific Aspects of MST Radar, Gadanki, India, Dec 11-15, 2006, ed. V.K. Anandan, pp 284-287, publ. Macmillan India Inc., 2007.
- Vincent, R.A., S. Dullaway, A. D. MacKinnon, I. M. Reid, F. Zink., P. T. May, and B.H. Johnson, “A VHF boundary layer radar: First Results”, *Radio Science* , 33, 845- 860, 1998.

CORRELATION BETWEEN VERTICAL AND HORIZONTAL WINDS IN THE TROPOSPHERE AS SEEN BY THE O-QNET

A. Farag¹ and W. K. Hocking¹

1. University of Western Ontario, London, Ont., N6A 3K7 Canada.

1. Introduction

Windprofiler radars can, in principle, measure the vertical component of the wind, provided that the vertical beam is correctly aligned. In this paper, we investigate this vertical alignment for the O-QNet radars in Canada (Hocking et al., 2007) by cross-correlating the vertical wind with the horizontal wind component in a variety of directions. Such a cross-correlation should reveal any tilt in the vertical alignment of the radar beam, and should be independent of height and time. Results do show a correlation, but the correlation is not independent of either height or time, suggesting some deeper, more fundamental atmospheric physics is also affecting the vertical velocities seen with the radar.

2. Method

Averaged over a time of typically a month, the vertical velocity should be close to zero. If the (nominally) vertical beam of an atmospheric radar is used to measure the vertical wind w , and the beam is not truly vertical, then the measured vertical velocity will contain a component of the horizontal wind, which will bias the mean vertical wind. If the nominally vertical beam is aligned at an angle θ from vertical, in the azimuthal direction ϕ_0 clockwise from north, then the contribution of the horizontal wind to the vertical wind will be

$$w_u = u \sin\theta \cos(\phi+180-\phi_0) \quad (1)$$

where u is the magnitude of the wind, ϕ is the angle from which the wind blows, and angles are in degrees. The horizontal wind vector \underline{u} can be found from Doppler radar measurements using off-vertical radar beams, while the vertical beam measures w .

By preparing scatter plots of simultaneously measured vertical velocities and horizontal velocity components in the direction ϕ_0 (given by $u \cdot \cos(\phi+180-\phi_0)$), and plotting a least-square best fit line, it is possible to use the slope of the best fit line to determine θ , since the slope will equal $\sin\theta$. By varying ϕ_0 to determine the value with the largest correlation coefficient, it is possible to find the azimuthal direction of tilt.

Examples of such scatter plots are shown in fig. 1(a), taken for the month of April, 2008, with the Walsingham radar, where each point is a simultaneous hourly average in each component. In this case, we have arbitrarily chosen the value for ϕ_0 to be 250° . A standard linear regression is applied, with the abscissa being the horizontal wind – there is no need to apply a fit which allows for the fact that there are errors on both axes, since the horizontal wind is known to have much higher precision than the vertical wind. The first figure (for 7 km altitude) clearly shows wide scatter, but a best-fit line can be seen with slope of -0.019 (± 0.004). The second figure, taken for data from 4 km altitude,

shows a slope of -0.006 ± 0.003 , where the error is one standard deviation. Hence in this case the non-zero slope is not significant at the 95% confidence level.

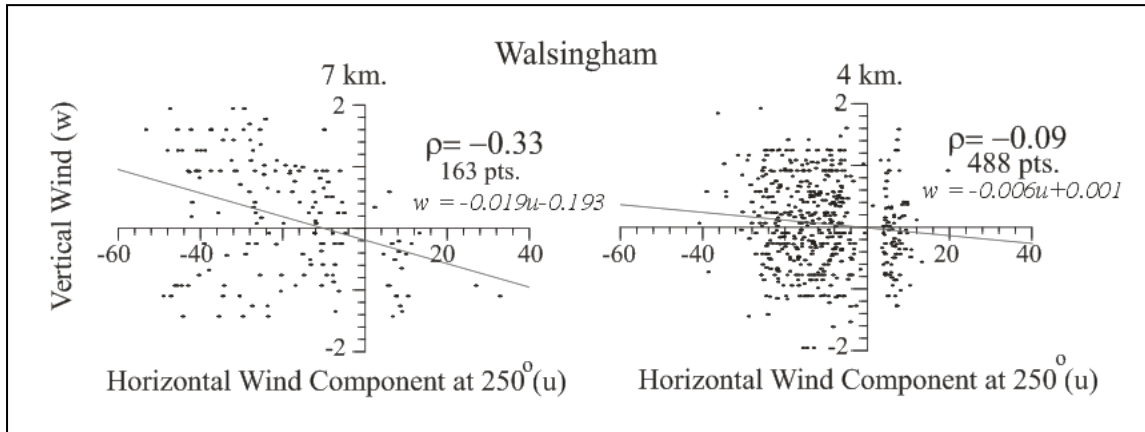


Fig. 1. Scatter plots of vertical hourly mean winds vs. horizontal wind component in the direction 250° clockwise from North for the Walsingham radar for April 2008.

The choice of 250° corresponds approximately to a component of the wind along the off-vertical west beam of the radar, since for horizontal wind determinations the radar uses 4 off-vertical beams pointed 10.9° off zenith in the azimuthal directions $-19, 71, 161,$ and 251 degrees clockwise from north, due to the alignment of the array. In both graphs it can be seen that there are a dearth of horizontal wind components between -3 and 3 m/s – this arises simply because when the wind is blowing directly along one of the radar beam directions, the wind component in the orthogonal beams are zero, so that often a spectrum cannot be isolated and so no wind component found in that direction. Hence the radar is “blind” when wind directions are along any of the beams. The cases of missing data in fig. 1 correspond to cases when the wind was blowing almost directly along the nominal “north” and “south” beams. The fact that there are missing data there does not impact our studies.

Fig.1 immediately demonstrates a problem – the correlations and best-fit slopes are not consistent between the two data sets. This might indicate that there is simply insufficient data for reliable measurements, but the best-fit slope in the first case is significantly non-zero. An alternative explanation is that the correlation may not in fact be due to a tilted beam, but rather due to geophysical effects. We therefore need to repeat these measurements for a more complete set of heights, azimuthal angles, and times of year.

3. A larger data set.

In order to examine the variability of slope and correlation coefficient, we have repeated scatter plots like those in fig. 1 for heights from 2 to 12 km, and for different azimuthal directions ϕ_0 from 0 to 360° . We have then plotted the correlation coefficients and slopes for each of these cases as density-plots, as shown in figs. 2 and 3. The graphs show a sinusoidal variation in slope and correlation coefficient at any one height, as may be expected from equation (1). However, it is quite clear that there is a strong height dependence. The optimum value of ϕ_0 at 7 km is around 0° , while at 12 km

altitude is closer to 50° . The slopes at maxima are close to 0.02, indicating an off-vertical tilt of about 1° .

Fig.2. Plot of the correlation coefficients of vertical velocity vs. horizontal wind component for azimuthal “look-angles” from 0 to 360 degrees, and as a function of height.

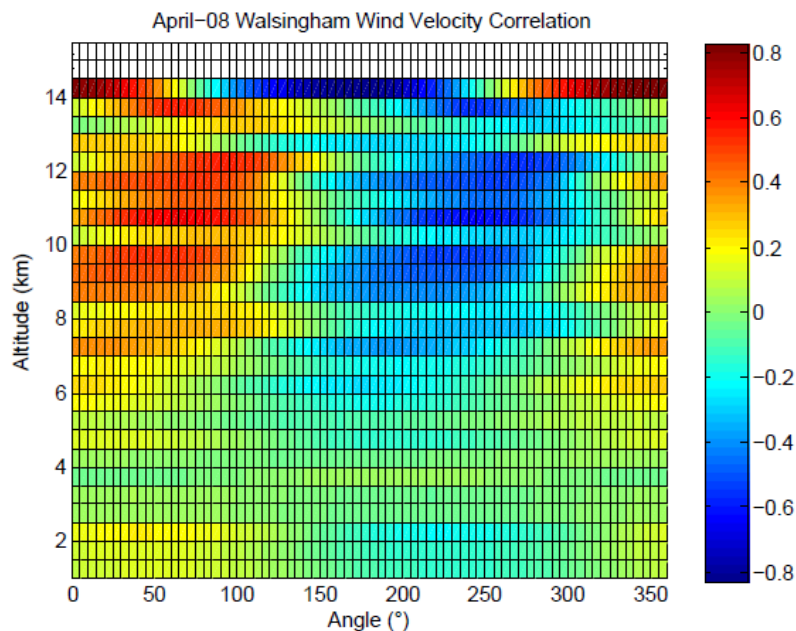
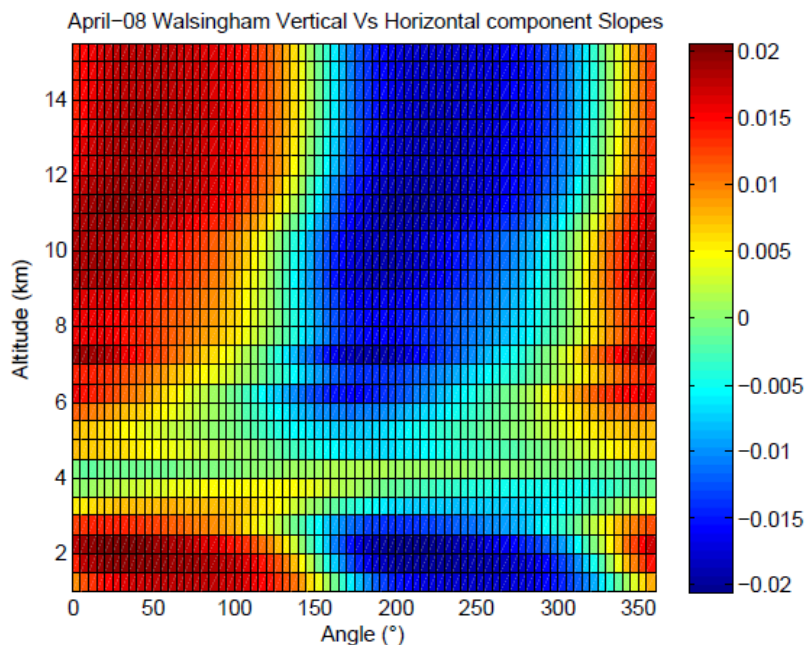


Fig.3. Plot of the slopes deduced from scatter plots of vertical velocity vs. horizontal wind component for azimuthal “look-angles” from 0 to 360 degrees, and as a function of height.



Similar studies at other times of the year show even different values for ϕ_0 ; for example, in August the preferred value is 100° at 6 km altitude. Studies at another site in the O-Net (Harrow) shows similar behaviour, but different values for ϕ_0 yet again\ with values of typically 0° in April and 60° in August.. Importantly, at 3 to 5 km, there is weak or zero correlation, and this is true at both Harrow and Walsingham, in both April and August, indicating that at these heights the beam is truly vertical.

These results suggest that the effect is not due to the radar, but to geophysical effects. Possibilities include a true correlation between vertical wind and horizontal wind. This might arise due to lake breeze effects, for example, since the radar is close to a Lake Erie in the Great Lakes Complex, and perhaps air flowing from the west/south-west over the lake tends to be rising as it transits over the radar. Alternatively, it is possible that the scattering entities themselves are anisotropic and have slight tilts. This could perhaps arise due to land-lake pressure differences, as are known to occur during lake breezes, which may lead to tilted scattering layers. Tilted scatterers would bias the effective pointing direction of the beam.

The fact that there is generally no correlation at 3-5 km is especially important. This is a region of high data quality, so the effect cannot be ascribed to poor data. It seems most likely that the beam is truly vertical, and that the effects at other heights are geophysical. The alternative is to assume that the effects at the heights above 5 km and below 3 km are due to the beam, and that geophysical effects just happen to conveniently null them out at 3-5 km, which seems a less likely scenario.

4. Modeling Studies.

The beam-pointing unit that directs the radar beam comprises 144 relays and multiple lengths of delay cables. The switches are not 50 ohm switches, and due to the different delays involved, impedance adjustments occur so that the transmitter does not see exactly 50 ohms input. In order to compensate, additional capacitors are placed in the paths, so that all SWRs seen by the transmitter are less than 1.4 on all beams, and generally less than 1.2. However, inclusion of these capacitors introduces additional delays. We have measured all delays introduced by this tuning, and included them in a numerical computer model which simulates their effect on the beam directions. The results of our calculations show that the errors in beam direction introduced by these effects is about 0.2° for the vertical beam, and even less for the off-vertical beams. Therefore this effect cannot explain the pointing offsets observed.

5. Future work and Conclusions

The study is not yet complete. We intend to repeat our calculations at other sites in the network, and during all months of the year. We will also deduce vertical velocities using the dual-beam method, rather than using the vertical beam directly. This method is less sensitive to the effects of anisotropic scatterers. These studies should help clarify the reasons for the correlations observed. We will also examine the results in the context of current theories about vertical velocities measured by radar (e.g. Muschinski 1996, among others).

References:

1. Hocking et al "A New 40-55 MHz Windprofiler Network in Ontario and Quebec, Canada—The O-Qnet," Proc. of the 11th International Workshop on Technical and Scientific Aspects of MST Radar, Gadanki, India, Dec 11-15, 2006, ed. V.K. Anandan, pp 377-380, publ. Macmillan India Inc., 2007.
2. Muschinski, A.,J., Possible effect of Kelvin-Helmholtz instability on VHF radar observations of the mean vertical wind Appl. Meteorol., 35, 2210-2217, 1996.

**Session 3:
Meteors Studied with
MST Radar**

DEVELOPMENT AND INITIAL MEASUREMENTS OF A DIGITAL RECEIVER FOR NETWORKED METEOR RADAR APPLICATIONS

Cody Vaudrin
Scott Palo

University of Colorado
UCB 431
ECNT 323
Boulder, CO 80309-0431

Deployment of digital receivers for use in radar remote sensing applications is slowly gaining acceptance within the atmospheric remote sensing community. Some of the justifiable reasons motivating hesitation concerning widespread use of digital receivers are summarized and addressed. Expense, complexity and a falsely perceived lack of scientific value all contribute to some reluctance in the use of digital receivers. Most commercially available digital receivers are both costly in terms of money and in the mandatory time investments required to learn a new cutting-edge technology. Furthermore, wideband digital reception can easily tax high performance workstations, requiring additional knowledge of lower-level programming languages and optimization techniques for efficiently dealing with high bandwidth data. Finally, the need for a digital receiver is sometimes called into question because scientifically relevant observations are commonly made using conventional radar receivers. Cost, complexity and unspecific scientific goals all contribute to a healthy skepticism in using digital receiver systems as the heart of small-scale scientific radars.

The system in development at CU aims to address these usability concerns. Utilizing all commercial off the shelf (COTS) components, a system that is competitive with many more expensive commercial products is constructed for less than \$5000. Much of the complexity involving digital receivers involves the coding of reprogrammable logic devices (FPGAs). Requiring an end user to have extensive knowledge of the receiver's logic devices is prohibitively time consuming. Our system utilizes a framework for data handling and control that is transparent to the user and accessible through a well-defined host API. Digital filtering functionality performed on the receiver's FPGA is designed using the Matlab filter design tools and ported to the FPGA using a set of logic synthesis tools thereby completely eliminating the need for a user to have any familiarity with the FPGA's complex lower-level interconnects and primitives. System portability is addressed by the choice of using USB 2.0 for the receiver's general-purpose computer (GPC) interface. From a scientifically philosophical perspective, having new tools capable of increased time and spatial resolution inevitably leads to the observation of previously undetected geophysical phenomenon. A vacillating power structure as seen in Figure 4, and unobserved with previous instruments is presented in the initial results section.

Reconfigurability supporting new experiments yet to be imagined is the primary advantage of a software-defined digital receiver. This low cost digital receiver system also paves the way for experiments involving multistatic networked arrays of receivers. Data acquired with a geographically separated array of science instruments could be processed long after collection, where the actual science measurements are defined in software on a GPC. [1]. Sharing of computational resources and real-time reconfigurable sensors are both realizable with the software defined radar approach.

Pulsed Doppler radar systems employ a number of digital synchronization signals used in gating the transmit waveform and triggering various system components. Specific reconfigurable radar parameters, programmable over the receiver's USB 2.0, include PRF,

transmit pulse width, frequency, shape and encoding. Similar to a controller in use at Arecibo by Seal [2] but integrated as one component of a complete receiver. Modular host software allows for demodulation of a wide range of signals simply by changing the frequency of the numerical IF and replacing the software-defined matched filter. Changing the modular detection algorithm modifies how signals of interest are identified. Many computational operations of the software radar receiver such as matched filtering and IQ demodulation are well suited for parallel computer architectures. If additional processing speed is needed, use additional inexpensive GPCs. Currently, the upper atmospheric remote sensing community has yet to take advantage of digital receivers for use in taking measurements using distributed arrays for many of the reasons already mentioned. A receiver architecture outlined in this paper eliminates previous roadblocks in the adoption of distributed arrays of small instruments for atmospheric observations.

Hardware

Digital receivers traditionally cover a large range of devices, all containing those common elements shown in the shaded blocks of Figure 1. Additional hardware components necessary for integration as a digital receiver for the COBRA meteor radar are shown as the unshaded blocks. In-phase and quadrature components are generated digitally using an arbitrary and exact (no imbalance) numerical IF on the GPC from a sampled real signal [3].

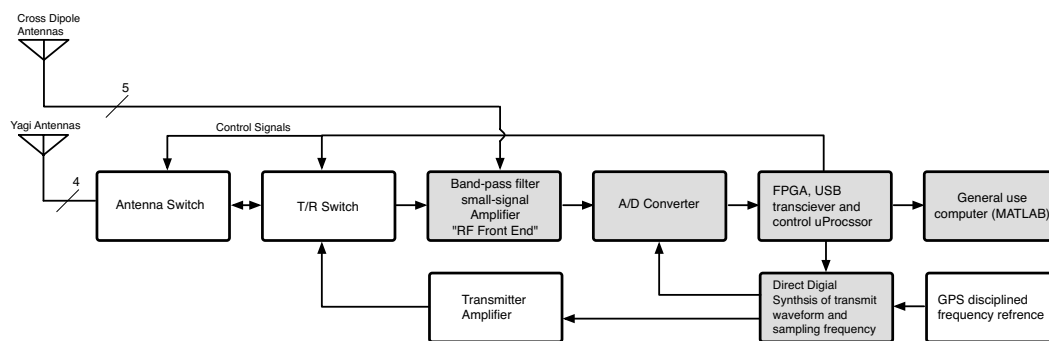


Figure 1 : Software Radar System Architecture

In contrast to the fixed signal processing circuitry of conventional analog receivers, the signal processing algorithms of digital receivers are implemented in software defined digital logic. Because the signal conversion process is software defined, a digital receiver can process the incoming signal in a virtually limitless variety of ways. Digital receivers are made possible by an electrical device called a “Field Programmable Gate Array” or FPGA. FPGAs contain a “fabric” of logical primitives (gates, flip-flops etc.) over which the user will impose an interconnect strategy. Think of a massively parallel, very fast N-dimensionally configurable computer. On initialization, the FPGA is configured according to a binary file encoding the FPGA’s pre-programmed primitive interconnections. Thus, the FPGA can perform any signal processing algorithms within the capabilities of the device.

Modification of the signal processing algorithms is fundamentally accomplished by editing the interconnect description file. A main benefit of this system is that the complexities of directly modifying the interconnect file are hidden from the user provided the system is deployed in the basic radar framework of Figure 1. An extensive knowledge of FPGA programming techniques is unnecessary to perform experiments and successfully acquire data.

Sampling Strategy

sinusoids derived from a master oscillator with the received echoes to generate in-phase and quadrature components. Because of set component values and frequency bands, the classic heterodyning receiver utterly fails with respect to ease of reconfigurability. Figure 3 depicts the second major component of the digital receiver system: a software radar processor. Similar to, but much simpler than processing chain of the Millstone Hill software radar, the receiver hardware of Figure 1 modestly transmits samples of a real signal to a GPC where all traditional radar signal processing tasks take place in the digital domain using a series of transformation elements [1]. Memory managed languages with highly optimized atomic operations such as Matlab are ideal for use in the software radar system. The real samples are read from the receiver by the host PC using a simple, well-defined protocol. Unlike the digital receiver hardware, most GPC operating systems are not real-time, so the possibility of sporadic data loss due to processing bottlenecks on the host is of some concern. A simple transmission protocol imposed on the data samples taken by the receiver hardware allows the GPC software to compensate for any data loss that may have occurred. IQ demodulation is then performed digitally, at any desired intermediate frequency with, of course, perfect channel balance resulting in the total elimination of image frequencies. Radar pulse locations are identified, and an efficient matched filtering algorithm operates on each pulse in parallel. The hardware is completely agnostic to the prospect of modifying the transmit waveform allowing for rapid experimental customizations.

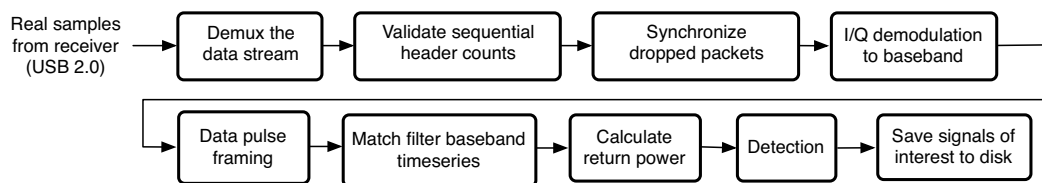


Figure 3 : Software Radar Processing Chain

Again, a modular and reconfigurable detection algorithm looks for power spikes at the radar's carrier frequency and pulse width, saving any signals to disk identified at a set threshold above an estimated noise floor. The saved signals are then read and further processed by subsequent signal processing algorithms, running on any network-enabled GPC.

Conclusions

A complete software defined radar system is presented. The numerous improvements of such a system over conventional analog receivers eclipse all complexity and usability concerns, especially with our HDL and FPGA abstracted system integration flow. Figure 4 displays some meteor echoes processed using the presented system, along with the associated SNR and radial wind velocities. With the system development effort nearing completion, next steps include performing an error analysis, collecting data over a long continuous period of time and performing a comparison analysis against the existing analog receiver.

The echoes shown in Figure 4 were extracted from a data set taken on 9/22/2009 in Platteville, Colorado. On the order of 7000 meteor trails were seen looking in a single cardinal direction over a 24-hour time period, signifying a significant increase in detection rates over that of the previous generation system.

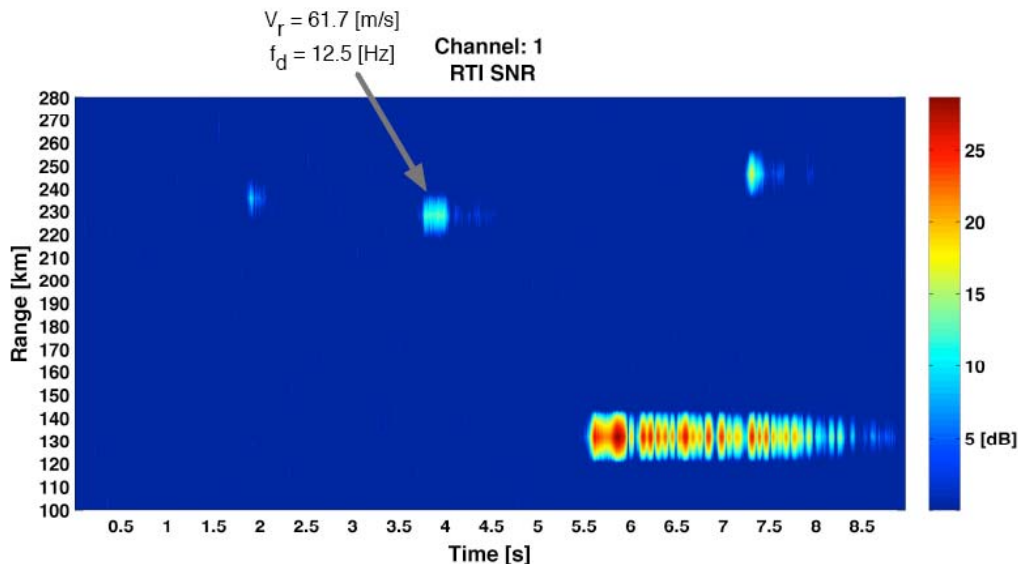


Figure 4 : Example measurement showing three underdense trails and one overdense (lower right) meteor trail with a proof of concept Doppler and radial velocity measurement. Notice the strong power vacillations on the overdense trail.

The digital receiver presented is easily reconfigurable, requiring a minimum knowledge of the underlying HDL code. The hardware mainly serves as a gateway for real samples for further processing on the GPC. Both the host software and receiver HDL code are modular, thereby creating a straightforward reconfiguration path. Simply by modifying the RF front end, this system is easily adopted for use in any situation requiring high-speed data acquisition and processing. Finally, this system's small size and reliance on industry-standard protocols and software result in a low-cost, portable high-speed data acquisition system adaptable to a wide variety of experimental situations.

- [1] T. Grydeland, F. D. Lind, P. J. Erickson, and J. M. Holt, "Software Radar Signal Processing", *Annales Geophysicae*, pp. 109-121, 2005.
- [2] R. Seal and J. Urbina, "Design and Implementation of Multi-Purpose Radar Controller using open-source tools", *RADAR'08*, IEEE, 2008.
- [3] M. Yearly and R. Kelley, "Compact Digital Receiver Development for Radar Based Remote Sensing", in *IEEE International Instrumentation and Measurement Technology Conference*, 2008.

A CURIOUS FEATURE IN METEOR TRAIL 3-D WIND ANALYSIS

Chris Meek and Alan Manson

Institute of Space and Atmospheric Studies University of Saskatchewan, Saskatoon, Canada S7N 5E2

Abstract

Repetition of an earlier seasonal medium frequency radar (MFR) vertical velocity (V_Z) analysis (Meek and Manson, J. Atmos. Sci., 46, 849-858, 1989.) with Eureka (80N,86W) VHF SKiYMET meteor wind radar data has led to strange results. 24 hour averages of wind fits to composite monthly, hourly, 3 km layer sets of trails show a strong upward V_Z , increasing with height, with a maximum of ~ 20 -30 m/s in the summer late morning hours, at the greatest usable height layer (97 km). Divided according to median decay time (per layer/month), the shorter duration trails show the biggest V_Z effect (and also stronger 2D/3D horizontal wind on the average). A cursory look at monthly-hour horizontal wind components finds significant, but not strong, differences between 2D/3D horizontal wind values, with the 2D more physically reasonable, though more detailed study is required. These differences occur at the upper heights. Differences increase if short duration trails are selected. So the question is: what causes the strong V_Z ? Trail distribution? Mathematical fitting effect? Echo point sliding up/down as trail moves horizontally? Physics (e.g. hot air buoyancy)?

1 Introduction

If a simple situation, point scatterers all moving with the same velocity, is assumed, the radial velocity of the reflection point is

$$V_{Rad} = \vec{V} \cdot \hat{r}$$

or

$$V_{Rad} = V_N \sin \alpha \cos \beta + V_E \sin \alpha \sin \beta + V_Z \cos \alpha$$

which if vertical velocity is assumed to be zero, reduces to the well known 2D version:

$$V_{Rad} = V_N \sin \alpha \cos \beta + V_E \sin \alpha \sin \beta$$

where V_{Rad} is the radial velocity in the echo direction, \hat{r} (zenith angle α and azimuth East of North β), +ve if outward, and V_N , V_E , V_Z are the components of wind velocity, \vec{V} , northward, eastward, upward respectively.

The 2D and 3D versions are linear equations, and therefore suitable for a standard least squares fit (which minimizes the sum of squared differences between fitted and measured radial velocities), where the measured data are V_{Rad_i} , α_i , β_i for the i^{th} meteor trail, and the parameters to be found are the three (or two) wind components.

2 Meteor trails

For meteor trails the situation is a little different. For underdense trails the model is one of an ionized line of any orientation in space carried along (without distortion, rotation, etc.) by a constant wind. A specular echo occurs if and where the trail is perpendicular to the line-of-sight from the radar. Depending on the trail orientation and background wind, the reflection point may slide in the vertical and/or horizontal relative to the initial "point scatterer" location on the trail (which is moving with the wind) to maintain perpendicularity as the trail moves. That is, the effective reflection point is not necessarily moving with the wind and a fit might not produce the correct wind vector.

Figure 1 shows a simple example in which the trail is moving horizontally but the reflection point moves vertically up or down depending on whether the trail is respectively downwind or upwind. A 3D fit will translate this apparent motion as a vertical component and modify the horizontal component accordingly, whereas a 2D fit would get the correct result. Now assume that both trails are horizontal and perpendicular to the wind direction. Here the reflection points don't slide up or down, and again the 2D fit gets the correct result.

Added to these considerations is the non-uniform distribution of echoes in azimuth and zenith. Also, from the above discussion, even if the distribution were uniform, the sliding effect still has a dependence on the (unknown) trail orientation. To take a simple case: if more meteors are upwind than downwind, then V_Z will tend to have a negative value. If these distributions were known, a first-pass fit could be used to get the approximate wind, and a second pass with weighting per meteor to correct for the effects of a non-uniform distribution. We know the echo location distribution, but the trail orientation is unknown.

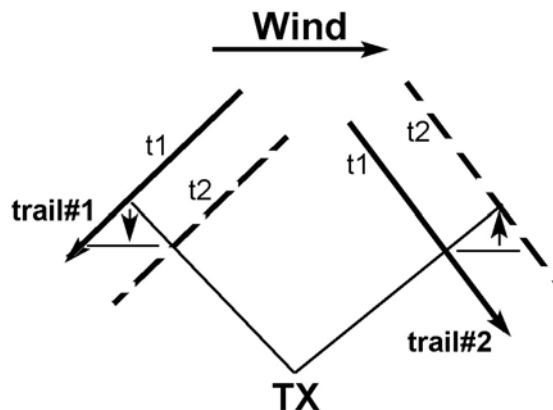


Figure 1: Illustration of reflection point sliding.

3 Monthly mean day profiles

After some preliminary 3D fit analyses which indicated strong vertical components, the complete set of trails was divided into hour-of-day, month, year, height layer; and after some more preliminary analyses, into short and long duration echoes (relative to their medians in corresponding long term month, hour-of-day data sets). One 3D and 2D fit to each set is done, viz. there is one value of V_N , V_E , V_Z per hour-of-day, per month, per height layer.

Figure 2 and Figure 3 show 24 hour average height profiles for each month, for tau less its median, and for tau greater than its median. Significant differences can be seen between the 3D and 2D values of V_N and V_E , with 2D being larger and looking more climatologically reasonable; but the striking feature is the strongly positive V_Z at the upper heights in summer, more obvious for small tau.

4 Vertical velocity results

Figure 4 shows contours of V_Z versus hour-of-day and month for almost 3 years at 94 km. V_Z is seen to vary from near zero in the early evening (0 UT) to very large positive (upward) in the late morning (15-16 UT) of summer. (The effect is greater at 97Km and less at 91Km, not shown.)

Climatologically, e.g. over a month, vertical motions should be the order of cm/s not m/s, and certainly not 10-30 m/s.

5 Discussion

From the above discussions about echo sliding we know that the echo location cannot automatically be assumed to be a point scatterer moving with the wind.

If the usual climatology is accepted then we need to ask: is vertical velocity actually very small and the large calculated V_Z just an artifact of the 3D analysis? In this case 2D is the preferred analysis. Does a non-uniform (in some sense) meteor distribution in echo location (azimuth, zenith) and/or orientation create a bias, viz. a strong positive V_Z ?

There is a last question: given that V_Z seems spurious in long term fits, are the results of 3D analyses on shorter, e.g. 1 - 2hr, data sets meaningful? If a non-uniform meteor distribution is responsible then a 3D analysis on shorter intervals is expected to produce even more spurious results.

Finally we would like to determine the cause of the large V_Z values [even if it's only a mathematical quirk], and why they vary with tau.

6 Conclusions

If the strong V_Z is not due to atmospheric motions, there must be a bias to positive (outward) Doppler velocities, either due to physical cause - e.g. buoyancy effect of hot air in the trail; or in the determination of average Doppler over the receiving antennas by fitting, stronger for short trails. In a 2D fit upwind and downwind trails would tend to cancel each other's bias. The 2D/3D speed bias (not discussed here) at 97Km depending on decay time, tau, seems to be peculiar to Eureka or the Eureka SKiYMET, not to MWRs in general or other SKiYMETs. The +ve V_Z effect is not limited to Eureka. The V_Z bias does not appear to apply in model tests (not shown) with real trail distributions and different assumed wind vectors: then V_Z is small, signs are +ve and -ve.

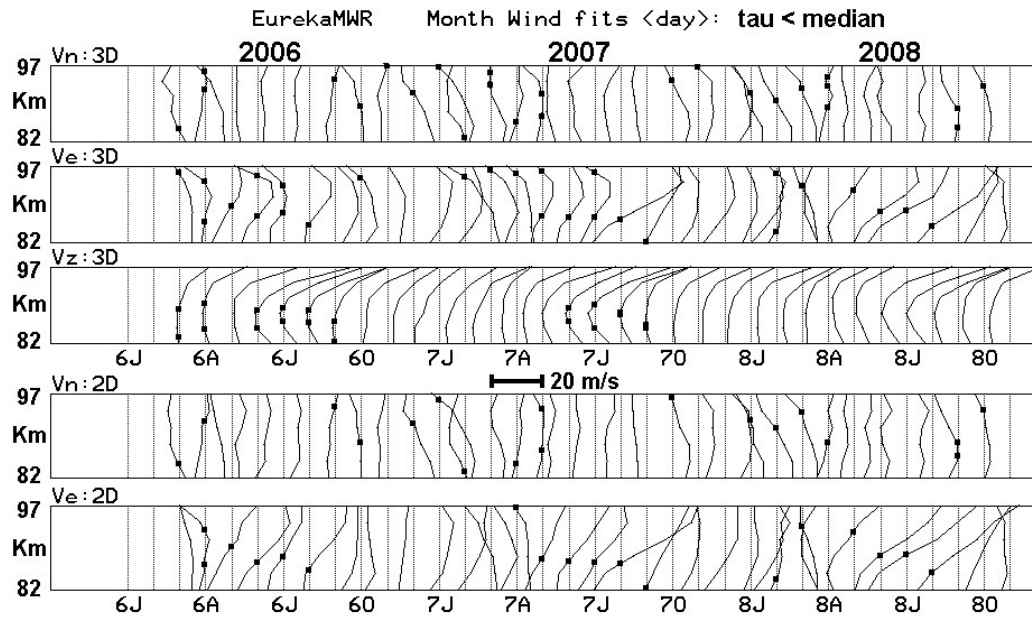


Figure 2: Average of 24 hour-of-day composite-monthly-fit 3D and 2D profiles for τ less than its median. Zero crossings are marked to facilitate profile identification.

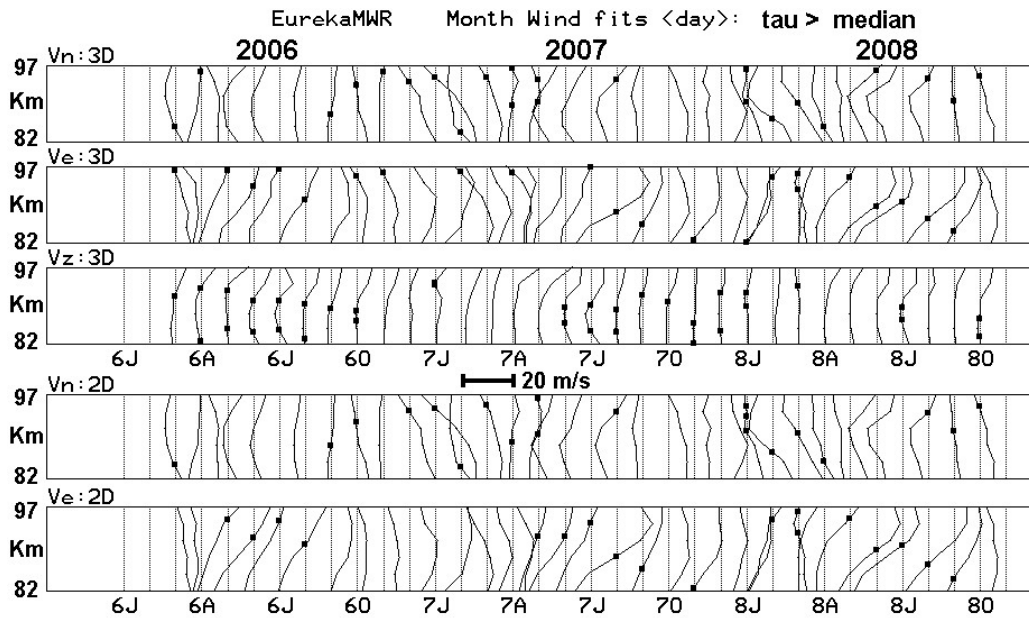


Figure 3: Average of 24 hour-of-day composite-monthly-fit 3D and 2D profiles for τ greater than its median. Zero crossings are marked to facilitate profile identification.

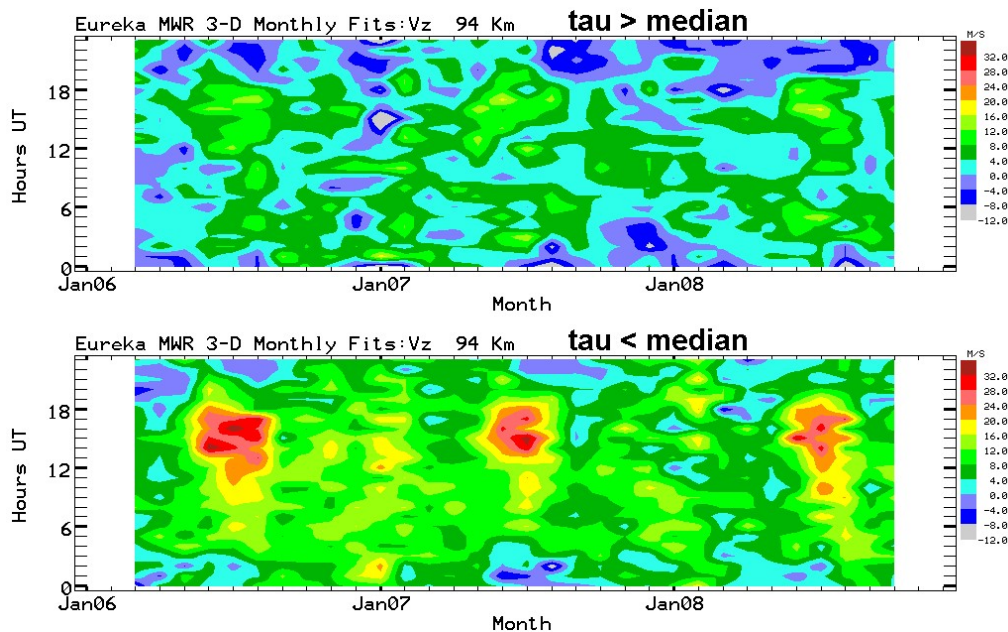


Figure 4: Vz from 3D fits to composite monthly, hour-of-day, height sets of trails divided according to relative time duration, tau.

Factors which may have a signed Doppler bias are the scattering process: e.g. a shock wave in background high electron density (i.e. summer noon); radiowave propagation through decaying trail ionization; and a rising hot air effect. But even if this last elementary physics argument applies, the maximum acceleration is g . In this case a speed of 4m/s is attained in 1/2 sec, much smaller than the measured 10-30 m/s.

It is also possible that the fitting process (unknown) for very short trails may affect speeds.

Regarding the wind values in general, for Eureka the following is noted for heights above 90km, increasingly at 97km, and especially in summer-centred months:

- 1) The range of tau included in the 2D and 3D fits is important, as there are significant changes in these fitted velocities, and V_N/V_E components, for tau less than or greater than the median value.
- 2) Although the horizontal wind vectors are generally similar for 2D and 3D fits, using all tau, the vectors do differ significantly above 90km in summer. Differences increase for choice of tau less than the median. The 2D fits provide the most physically reasonable values.
- 3) The azimuthal distributions of meteors, the departures from symmetry with height and month, and the numbers of meteors are likely of importance in the above.

SIGNATURES OF THE IONIZATION TRAIL OF A FIREBALL OBSERVED IN THE HF, AND VHF RANGE ABOVE MIDDLE-EUROPE ON JANUARY 17, 2009

D. Keuer (1), W. Singer (1), G. Stober (2)

(1) Leibniz-Institute of Atmospheric Physics Kühlungsborn,
Schlossstr. 6, D-18225 Kühlungsborn, Germany

(2) Institute of Meteorology, University of Leipzig, 04103 Leipzig, Germany

1. Introduction

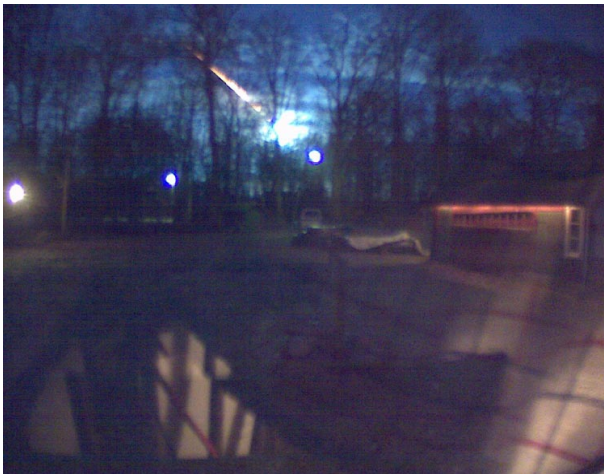
A fireball passed the upper atmosphere above Middle-Europe from south-west towards north-east on January 17, 2009 around 19:00 UT. Remaining parts of the fireball are found on the island Lolland in southern Denmark [Grau, 2009] in March 2009. Signatures of the ionization of the fireball are observed by active radio wave propagation experiments in the HF and VHF frequency range at latitudes between about 51° N and 55° N at altitudes between about 120 km and 60 km.

The experiments used are:

- meteor radar observations on 36.2 MHz (51.3° N, 13.0° E),
- meteor radar observations on 53.5 MHz (54.1° N, 11.8° E and 54.6° N, 13.4° E),
- meteor radar observations on 32.5 MHz (54.6° N, 13.4° E),
- vertical and oblique radar soundings on 3.18 MHz (54.6° N, 13.4° E)

A first guess of the fireball velocity of about 25 - 30 km/s could be obtained from the observations on 32.5 MHz and 3.18 MHz where the center of the ionization trail was located at 54.1° N, 11.8° E, and 54.6° N, 13.4° E at altitudes between about 120 km and 70 km. The ongoing detailed analysis of all observations will provide more data for the radiant estimation of the fireball.

2. Visual observations



A photo, of the fireball (Figure 1), was taken from south Sweden by *Svensson* [2009]. The camera is installed in the village Svensköp, province Skåne. 55.9° N, 13.9° E about 150 km northward from Juliusruh. The sky above northern Germany was illuminated by green diffuse light for a few seconds.

Figure 1. View from Sweden



Figure 2. Individual visual observations of the fireball

Figure 2. summarizes the visual observations made in the southern Baltic Sea region on January 17 (courtesy by *Sorenson*,[2009]). The red lines describe areas where the different observes have seen the trail. of the fireball or listen the sound event.

3. Observations by the Juliusruh MF Radar and Ionosonde

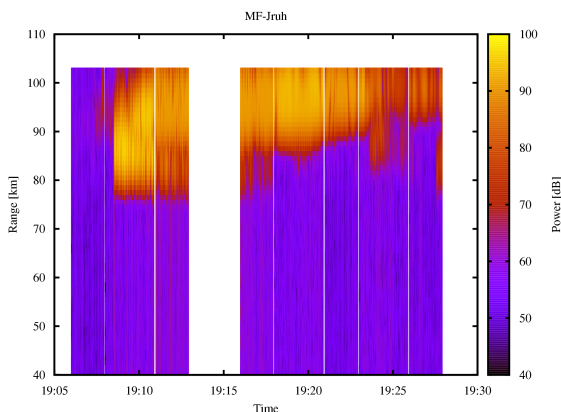


Figure 3. MF-Radar:echo power around the fireball event

The MF radar (3.18 MHz) at Juliusruh observed strongly enhanced echo power between 76 and 104 km just on 19:08:30 UT lasting for about 10 minutes (Figure 3). The radar was operated in Doppler mode and a sequence of vertical and oblique beam observations is presented in Figure 3. White areas represent times when the radar off and the ionosonde was in operation.

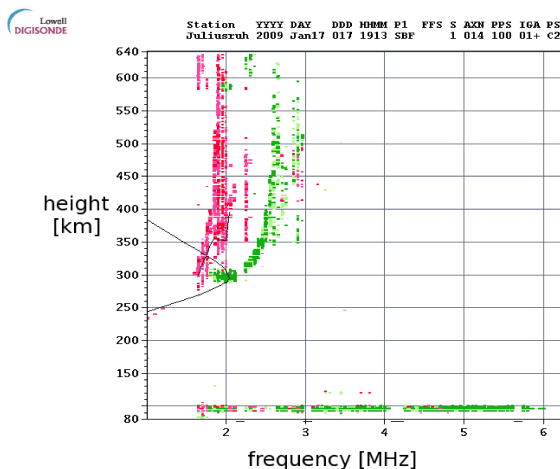


Figure 4. Ionogram 19:15 UT

During the gap in the MF radar echo power around 19:15 UT (Figure 3) the co-located ionosonde detected an unusual sporadic E-layer between 90 and 100 km with a blanketing frequency up to 6 MHz as shown in Figure 4.

4. First results obtained with the Juliusruh Meteor Radar

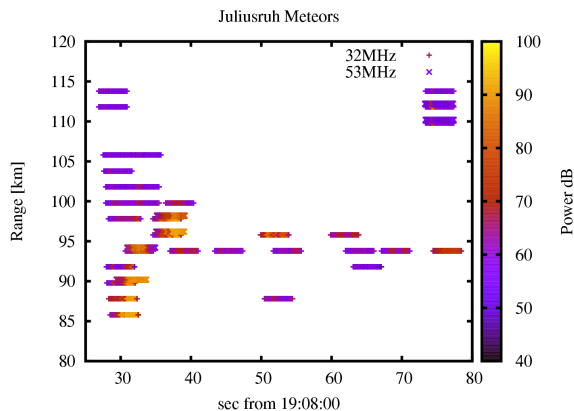


Figure 5. SKiYMET echo trails

SKiYMET radar observations from other locations did not show any data related to the fireball.

5. Meteor trajectory

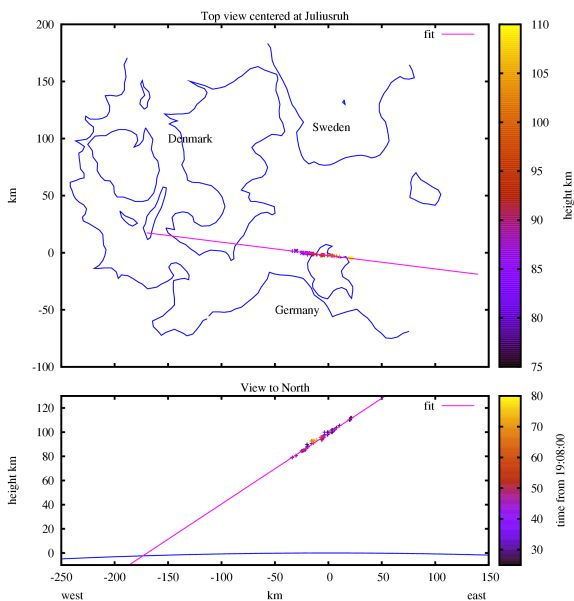


Figure 6. Estimated meteor trajectory

Echo power, derived from four second raw data records of the SKiYMET meteor radar (Hocking et al 2001), are shown in Figure 5.

Trail echoes are observed up to 50 seconds after the initial event. The disturbances caused by this heavy overdensed meteor give a considerable echo power. Positions are estimated using the complex amplitude records of the five receiver interferometer (Jones et al., 1998)

All derived positions are plotted in Figure 6. The fit gives a reasonable trajectory. All echoes sampled during 50 seconds after the event are close to the trajectory, so it seems reasonable that the plotted echo locations are from the fireball. The upper panel shows a top view onto the region around Juliusruh. The coast lines of Sweden, Germany and Denmark are illustrated. The height is indicated by the color of the points. A better view to the height variation of the echoes gives the lower panel, which shows a side view with west on the left hand side and east at right. The occurrence time of the echoes after 19:08:00 UT is depicted by color coded crosses.

Notable is, that reasonable echo power is observed even if the radar beam is not perpendicular to the meteor trail. The perpendicular point was reached when the fireball was fallen down to a height of 74 km, from where we received no echoes at all. As the ballistic curve is not computed, remaining parts of the fireball could roughly reach the ground about 120 km westward from Juliusruh. Left over parts of the fireball were found nearby Hared on the island

Lolland in southern Denmark in March 2009 by Grau [2009].

6. Velocity estimation

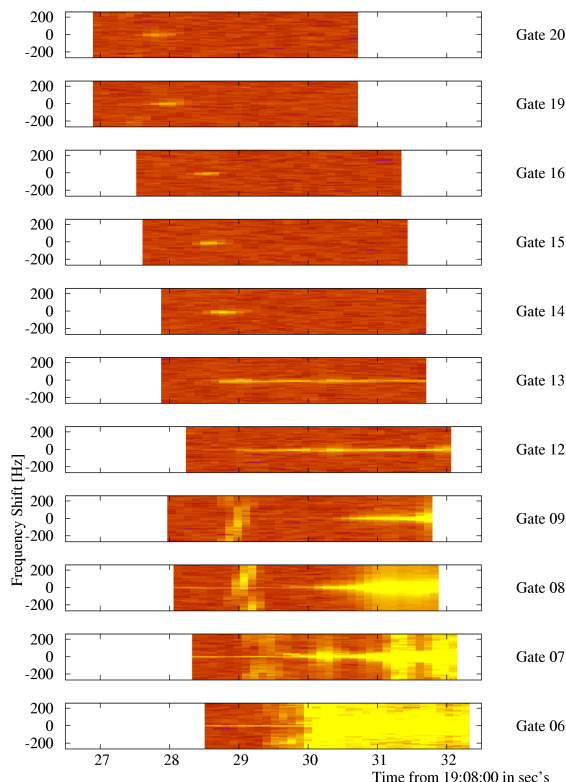


Figure 7. Spectrograms of the range gates

The spectral view makes it possible to distinguish between head and tail echoes due to the Doppler shift. Quite weak head echoes are visible in range gate 20 and 19 (range gate 20 corresponds to 114 km, step size is 2 km). The Doppler shifted echoes are barely detectable. As an effective PRF of only 536 Hz is used, the frequencies are folded into a range of ± 218 Hz, which prevents an unambiguous velocity estimation. The fireball velocity can be estimated in good approximation to 27.5 km s^{-1} using echo location and time of appearance. But as we have the coordinates and the time of appearance of the head echoes we can easily compute an average velocity. Only the head echoes are usable for the velocity computation. Figure 7 shows the head echoes and the delayed ionospheric echoes.

The origin of the meteor was observed with an azimuth of 96° and an elevation of 30° which corresponds to a radiant with a right ascension of $08^{\text{h}}19^{\text{m}}$ and a declination of $20^\circ48'$ in the constellation Cancer.

7. References

- Hocking W.K., Fuller B., Vandepier B., Real-time determination of meteor-related parameters utilizing modern digital technology, *J. Atmos. Sol. Terr. Phys.*, 63, 155-169, 2001.
- Jones, J., Webster R.A., Hocking W.K., An improved interferometer design for use with meteor radars, *Radio Science*, 33, 1, 55-65, 1998.
- Sorenson, Anton Norup, <http://www.astronomie-heute.de/artikel/979148&z=798889>, 2009.
- Svensson, Roger, <http://sydsvenskan.se/webbtv/article406633/Trolig-meteor-lyste-upp-himlen.html>, 2009.

Session 4:
Plasma Irregularities

COUPLING PROCESSES IN THE EQUATORIAL ATMOSPHERE (CPEA): A NEW FEATURE OF PLASMA IRREGULARITIES REVEALED OVER THE INDONESIAN EQUATOR

Shoichiro Fukao¹, Yuichi Otsuka², Mamoru Yamamoto³ and
The CPEA Science Group

¹Fukui University of Technology, Fukui, Japan,

²STELAB, Nagoya University, Nagoya, Japan,

³Research Institute for Sustainable Humanosphere, Kyoto University, Kyoto, Japan

1. Introduction

Solar radiation is most intense in the tropics and active cumulus convections generate a variety of atmospheric waves. They become sources for stratospheric QBO and mesospheric SAO, and are supposed to influence generation of ionospheric irregularities that feature the equatorial ionosphere. The equatorial atmosphere is closely coupled in the vertical direction through these atmospheric waves. Also, exchange of air mass between the troposphere and stratosphere occurs at the tropopause in the tropics. However, details of these processes remain unclear yet.

To investigate these processes a research project called Coupling Processes in the Equatorial Atmosphere (CPEA) was conducted for six years September 2001 to March 2007. CPEA is an observational project conducted in the Indonesian Maritime Continent (IMC) for elucidation of the vertical coupling of the equatorial atmosphere, primarily by means of ground-based observations (Fukao, 2006, 2009).

2. EAR and the EAR Observatory in Indonesia

The Equatorial Atmosphere Radar (EAR; Figure 1) was established at Kototabang, West Sumatra, Indonesia (0.20°S, 100.32°E) close to the geographic equator in March 2001. EAR consists of the same active phased array system as the MU radar in Japan, which allows pulse-to-pulse beam steering (Fukao et al., 2003). The frequency is 47.0 MHz, and the antenna is a near-circular array with a diameter of 110 m. The peak power, however, is only one tenth to that of the MU radar. As shown in Figure 2, during the six-year experimental period of CPEA, a variety of instruments have been installed to the EAR site and its periphery; for instance, sophisticated lidars, meteorological radars, VHF radars, airglow imagers etc. Although the altitude coverage of individual instruments is limited, the whole atmosphere up to several hundred km altitude is complementally covered by operating all instruments at the same time. Varieties of new facts have been found by CPEA, and the

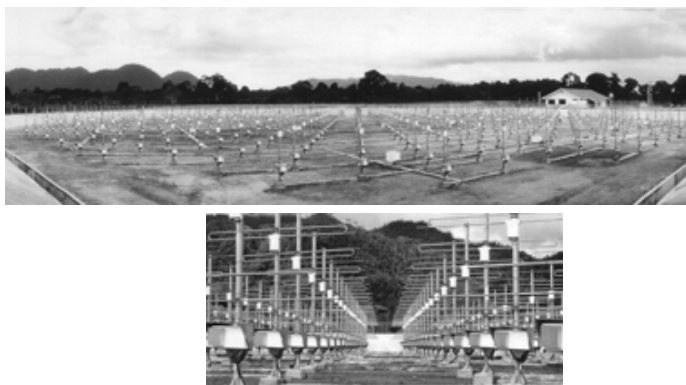


Figure 1. The Equatorial Atmosphere Radar (EAR) in Kototabang, West Sumatra, Indonesia (top) and its 560 three-element Yagi antennas, each with a transmitter-receiver module mounted near the ground (bottom). The operational frequency is 47.0 MHz. The antenna is a near-circular array with a diameter of 110 m, and the peak transmit power is 100 kW (Fukao et al., 2003).

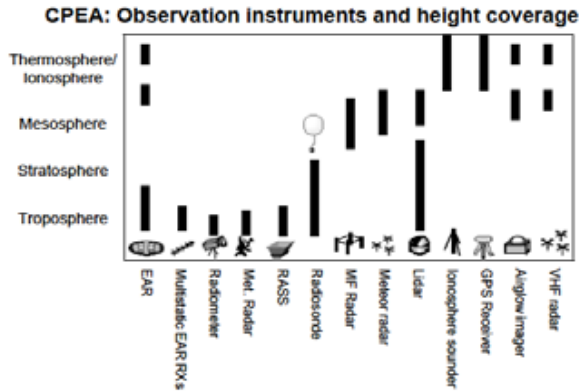


Figure 2. Main instruments of CPEA installed at the Equatorial Atmosphere Observatory (EAO) and its periphery in Kototabang, West Sumatra, Indonesia (0.20°S, 100.32°E). The vertical bars show height coverage (Fukao, 2006).

present paper briefly describes one of them; a possible coupling of the ionospheric irregularities between middle and equatorial latitudes.

3. A new feature revealed by CPEA

One of the most remarkable phenomena in the equatorial ionosphere is the equatorial spread *F* or equatorial plasma bubbles (e.g., Woodman and LaHoz, 1976). Large scale depletion of plasma density originally occurs at bottom side of the ionosphere and rises through the equatorial ionosphere up to one thousand kilometers. They are considered to be generated by the Rayleigh-Taylor instability, but the

rapid growth rate observed is not simply explicable by the theory.

A huge plasma bubble was photographed simultaneously by all-sky airglow imagers located at Sata and Darwin, conjugate sites, at midlatitudes (Otsuka et al., 2002). Their shapes are identical even to structures as small as 50 km. This suggests that the plasma bubbles have the same cross section wherever they are cut, justifying the observation from the single location outside the geomagnetic equator.

It is well known that the scintillation near the Indonesian longitudes occurs before midnight in equinoctial months as shown in the top panels of Figure 3. The occurrence is decreasing year by year due to the decline of solar activity.

EAR has the fast beam steerability, and can steer antenna beam on a pulse-to-pulse basis in a wide azimuth angle almost simultaneously. Occurrence location and zonal distance of plasma bubbles were determined by this multi-beam observation (Fukao et al., 2004). In general, plasma bubbles appeared first at the west beam and successively moved to the eastern beams, being consistent with the conventional result that they propagated eastward. The 30-MHz radar installed for exclusive use to ionospheric irregularity observations a couple of years ago show similar eastward propagation of plasma bubbles (Otsuka et al., 2009).

Occurrence frequency of 30-MHz radar echoes is plotted in the bottom panels of Figure 3. A good correlation is seen between bubble and scintillation occurrences before midnight in the top panels. This indicates that the scintillation is caused by plasma bubbles. On the other hand, the scintillation that occurred after midnight during summer time did not accompany any scintillation as shown in the top panels. This indicates that the spread *F* is of the frequency type. The occurrence increases with decreasing solar activity. In addition, the multi-beam observations indicated that the post midnight echoes propagate westward, opposite to the bubbles. These features recall the plasma plumes observed at midlatitudes.

4. Similarity to midlatitude plasma plumes

The midlatitude plasma plumes are quite dynamic and extensive but occurrence is limited only to summer nights and during solar minimum period (Fukao et al., 1991). It is accompanied by frequency-type spread *F*. They are consistent with the horizontal band structure that is elongated from the NW to the SE and propagates to the SW. The intense plumes are collocated with high velocities of 100-200 m/s perpendicular to the geomagnetic field, and the direction is upward and/or northward. Based upon these features, it is

considered that the plumes are generated by the Perkins instability, and that its smallest growth rate is possibly enhanced by seeding of gravity waves at the bottom side. The 3-m radar backscatter is caused by secondary instabilities on the edges of the dome region (Kelley and Fukao, 1991).

Saito et al. (2002) found that the band structure of the plumes shows an excellent correspondence with that of the medium-scale TIDs (MSTID) detected by the GPS network of Japan. They traveled to the SW at the same propagation velocity. The direction is more or less oriented parallel to the most unstable wave direction for the Perkins instability.

MSTID bands of airglow were compared with the polarization electric fields concurrently observed by the DMSP satellite over Shigaraki (Shiokawa et al., 2003). The electric fields were almost perpendicular to the MSTID bands. The electric field variations look quite consistent with the MSTID band structure, and this correspondence is expected from the Perkins instability mechanism.

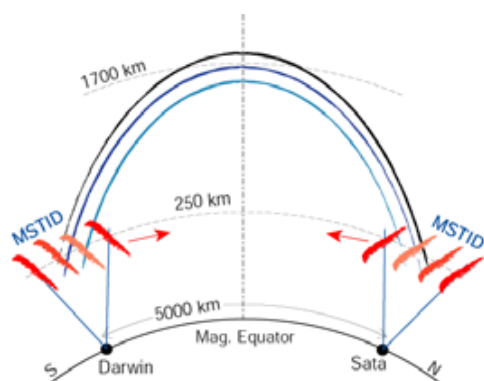


Figure 4. This cartoon schematically shows that the mirrored MSTID images are obtained at Darwin, Australia and Sata, Japan at the same time on the same day. The distance between the two sites is ~5000 km (courtesy of T. Ogawa).

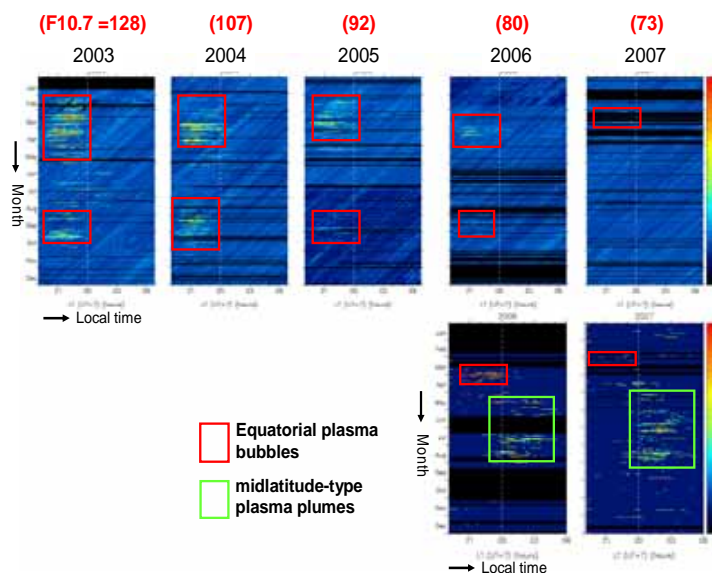


Figure 3. Seasonal and local time variations of GPS scintillation index (S_4) observed in the period 2003 - 2007 (top) and radar backscatter plumes observed with the on-site 30.8-MHz radar between 2006 and 2007 (bottom) at Kototabang, Indonesia (dip latitude 10.4°S) (courtesy of Y. Otsuka).

It was found from simultaneous observations at two conjugate points, Sata Japan and Darwin Australia that the MSTIDs are closely coupled between the hemispheres (Otsuka et al., 2004). Figure 4 schematically shows this feature. It is strongly suggested that MSTIDs are not caused only by atmospheric gravity waves propagating from below, but also by polarization electric field along the geomagnetic field.

On the other hand, long distance propagation of MSTIDs has been recently made using a long baseline of instruments of HF radar, airglow imagers, and TEC observations over Japan. MSTIDs generated at high-latitudes have been demonstrated to propagate a long distance of more than 6,000 km (e.g., Ogawa et al., 2009). It is expected that they will reach over EAR at 10° dip latitudes and cause post midnight irregularities over the equator during summer time.

5. Concluding remarks

Many observational studies on various types of dynamical and electrodynamical coupling in the equatorial atmosphere over the IMC were conducted as a part of CPEA. It has been clearly demonstrated that the equatorial atmosphere is much more closely coupled on multiple temporal and spatial scales in the vertical direction than previously expected. More details on the individual topics and other new areas of achieved progress of CPEA should be referred to the more than 200 papers that have been published in international peer-reviewed journals. Especially, a bunch of papers are contained in the special issues edited by the Journal of Meteorological Society of Japan in 2006 and by *Earth, Planet and Space* in 2009.

REFERENCES

- Fukao, S., Coupling Processes in the Equatorial Atmosphere (CPEA): A Project Overview, *J. Meteor. Soc. Japan*, 84A, 1-18, 2006.
- Fukao, S., What we have learnt from CPEA (Coupling Processes in the Equatorial Atmosphere): A review, *Climate and Weather of the Sun-Earth System (CAWSES): Selected Papers from the 2007 Kyoto Symposium*, (Eds. T. Tsuda, R. Fujii, K. Shibata, and M. A. Geller), 295-336, TERRAPUB, Tokyo, 2009.
- Fukao, S., M. C. Kelley, T. Shirakawa, T. Takami, M. Yamamoto, T. Tsuda, and S. Kato, Turbulent upwelling of the mid-latitude ionosphere, 1. Observational results, *J. Geophys. Res.*, 96, 3725-3746, 1991.
- Fukao, S., H. Hashiguchi, M. Yamamoto, T. Tsuda, T. Nakamura, M. K. Yamamoto, T. Sato, M. Hagio, and Y. Yabugaki, Equatorial Atmosphere Radar (EAR): System Description and First Results, *Radio Sci.*, 38, 1053, doi:10.1029/2002RS 002767, 2003.
- Fukao, S., Y. Ozawa, T. Yokoyama, M. Yamamoto, and R. T. Tsunoda, First observations of the spatial structure of F region 3-m-scale field-aligned irregularities with the Equatorial Atmosphere Radar in Indonesia, *J. Geophys. Res.*, 109, A02304, doi:10.1029/2003JA010096, 2004.
- Kelley, M. C. and S. Fukao, Turbulent Upwelling of the Mid-Latitude Ionosphere, 2. Theoretical Framework, *J. Geophys. Res.*, 96, 3747-3753, 1991.
- Ogawa, T., N. Nishitani, Y. Otsuka, K. Shiokawa, T. Tsugawa, Medium-scale traveling ionospheric disturbances observed with the SuperDARN Hokkaido radar, all-sky imager and GPS network, and their relation to concurrent sporadic-E irregularities, *J. Geophys. Res.*, 114, A03316, doi:10.1029/2008JA013893, 2009.
- Otsuka, Y., K. Shiokawa, T. Ogawa, and P. Wilkinson, Geomagnetic conjugate observations of equatorial airglow depletions, *Geophys. Res. Lett.*, 29, 10.1029/2002GL015347, 2002.
- Otsuka, Y., K. Shiokawa, T. Ogawa, and P. Wilkinson, Geomagnetic conjugate observations of medium-scale traveling ionospheric disturbances at midlatitude using all-sky airglow imagers, *Geophys. Res. Lett.*, 31, L15803, doi:10.1029/2004GL 020262, 2004.
- Otsuka, Y., T. Ogawa, and Effendy, VHF radar observations of nighttime F-region field-aligned irregularities over Kototabang, Indonesia, *Earth, Planets Space*, 61, 431-437, 2009.
- Saito, A., M. Nishimura, M. Yamamoto, S. Fukao, T. Tsugawa, Y. Otsuka, S. Miyazaki, and M. C. Kelley, Observations of traveling ionospheric disturbances and 3-m scale irregularities in the nighttime F-region ionosphere with the MU radar and a GPS network, *Earth, Planets and Space*, 54, 31-44, 2002.
- Shiokawa, K., Y. Otsuka, C. Ihara, T. Ogawa, and F. J. Rich, Ground and satellite observations of nighttime medium-scale traveling ionospheric disturbance at midlatitude, *J. Geophys. Res.*, 108, 1145, doi:10.1029/2002JA009639, 2003.
- Woodman, R. F., and C. LaHoz, Radar observations of F-region equatorial irregularities, *J. Geophys. Res.*, 81, 5447-5466, 1976.

MULTI-FREQUENCY RADAR STUDIES OF THE EQUATORIAL 150-KM REGION

J. L. Chau¹, M. A. Milla^{1,2}, and E. Kudeki²

¹Radio Observatorio de Jicamarca, Instituto Geofísico del Perú, Lima

²Electrical and Computer Engineering, University of Illinois, Urbana-Champaign, IL, USA

1. Introduction

Relatively strong radar echoes are being observed everyday between 140 and 170 km above the Jicamarca Radio Observatory. The phenomenon has been known at Jicamarca since 1964, and more recently similar echoes have also been observed at other equatorial (magnetically) stations (e.g., Pohnpei, Brazil, Africa) and even at latitudes outside the equatorial electrojet belt (Gadanki in India, EAR in Indonesia). Contrary to other ionospheric echoes (equatorial electrojet, spread F), these so-called 150-km radar echoes have not been yet explained by any plausible physical model that has been put forward.

The main characteristics of 150-km radar echoes can be found in *Chau et al.* [2009] and references therein. There are basically two types of reported echoes, i.e., those observed when the probing radar is pointed perpendicular/off-perpendicular to the magnetic field (**B**) (Perpendicular/Oblique). The perpendicular echoes were discovered first and have been subjected to extensive studies. They have also been observed with relatively small radar systems in the aforementioned places. The oblique echoes, on the other hand, have been discovered only recently over Jicamarca [*Chau, 2005*]. In both cases, the total backscattered power is stronger than the expected incoherent scatter echoes at these altitudes by up to 10-20 dB.

So far the 150-km echoes appear as an exclusively radar phenomenon. A handful of rockets have been launched to the 150-km region, but none of them has shown a clear in-situ signature related to these echoes (existence of 3-m irregularities or strange density profiles). There are very few satellites that can observe this region, and again none has reported observations that can be related to 150-km echoes. In this work we report the simultaneous observations of the echoes detected with the Jicamarca VHF radar and in high resolution ionograms (in both time and altitude) observed with a newly deployed digital ionosonde named VIPIR. Although not concurrent, we also present previous high-resolution electron density measurements performed in the region with the incoherent scatter radar at Jicamarca. Our results indicate that the electron density of this region may be highly structure in altitude and time, and the observed structuring might be related to neutral wind dynamics, particularly the meridional component, in this region.

2. Jicamarca Incoherent and Coherent Scatter Observations

As in the case of other radars, 150-km echoes are always observed at Jicamarca during daytime hours when the radar beams are pointed perpendicular to **B**. In Figure 1 we show an example of daytime coherent echoes taken in January 2009 using a combined MST and Incoherent Scatter radar mode (MST-ISR). From this figure can identify the following echoes: (a) mesospheric (below 90 km), (c) equatorial electrojet (EEJ) and meteors between 90 and 120 km), and (c) around 150-km. Note that the 150-km echoes are not affected by the almost zero electric that causes the disappearance of the EEJ echoes around 1230 LT. The characteristic features distinguishing the perpendicular echoes, e.g., necklace shape, layering, periodicities [e.g., *Kudeki and Fawcett, 1993*], are clearly observed in this plot.

In Figure 2 we show a pair of altitude-time density plots for the region obtained with a high-resolution incoherent scatter mode, similar to the one used by *Chau and Woodman* [2005]. The top panel shows the electron density estimates obtained from Faraday rotation, which is independent of the scattering process. The bottom panel, by contrast, shows the density estimates obtained from the absolute power under the assumption that scattering originates from thermal level fluctuations (i.e., incoherent scatter). Each profile has been obtained after 3 minutes of integration. The two figures attribute different density levels to the same layer near 170 km altitude, which rules out the possibility of attributing the layer to incoherent scattering, that is, to a density enhancement. On the other hand, although noisier, the density maps from Faraday measurements indicate depleted regions surrounding the echoing layer, which vary in both altitude and time. A similar altitudinal structure was also presented in Figure 1 of *Chau and Woodman* [2005].

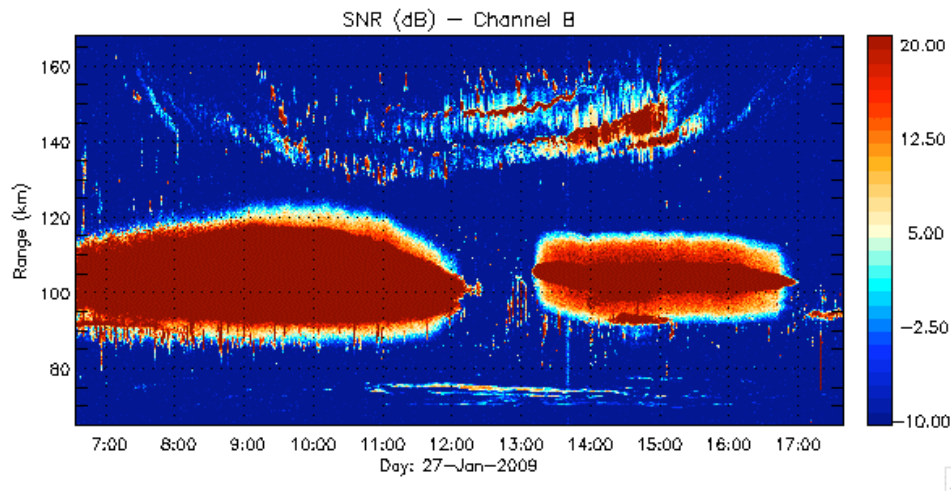


Figure 1. Range-time intensity map of daytime coherent echoes over Jicamarca. Range is equivalent to altitude for the pointing direction used.

3. Ionosonde Observations

The ionosonde observations reported in this work have been obtained with a new digital sounder named VIPIR (Vertical Incidence Pulsed Ionospheric Radar). This system is a component of the Low-latitude Ionospheric Network (LISN) project operating from Jicamarca. The VIPIR is a fully digital instrument and very flexible to configure. Among its features, one can change: the operation frequency table, the pulse width and inter-pulse period, the number of antennas for reception, etc. In our case, we have synchronized the system with the main Jicamarca system using a 1 pulse-per-second signal from a GPS system and obtained high-resolution ionograms every 2 minutes focused on the valley region, i.e., between 2 and 5 MHz and between 90 and 400 km above Jicamarca. Even higher time- and altitude-resolutions are possible with the system.

In Figure 3 we show an ionogram example from VIPIR for the day of Figure 1, with the red and blue traces corresponding to O and X mode virtual heights around 1230 LT. Consistent with Jicamarca radar results for this period, the observed virtual height traces are not cluttered by EEJ activity. This makes it easier to interpret the ionogram traces, and attribute the observed dips and cusps above foE and fxE (i.e., E-region peak densities in O and X modes, respectively) to a structuring in the valley region above the E-region density maximum. In this particular example, we can see that the valley region is very structured in both frequency and range. This structuring represents different peaks and therefore small enhancements and depletions in range.

In order to compare the VIPIR and Jicamarca radar results, we have produced in Figure 4 range-time plots of VIPIR (a) peak power (top), (b) peak frequency (bottom), for both O (left) and X (right) modes. These values have been obtained for each ionogram, i.e., for a given range and ionogram we have calculated the largest power and its corresponding frequency. Recall that frequency is proportional to the square root of electron density. Moreover 140-170 km in altitude corresponds to ~ 150 -220 km in virtual height, depending on the ionospheric conditions.

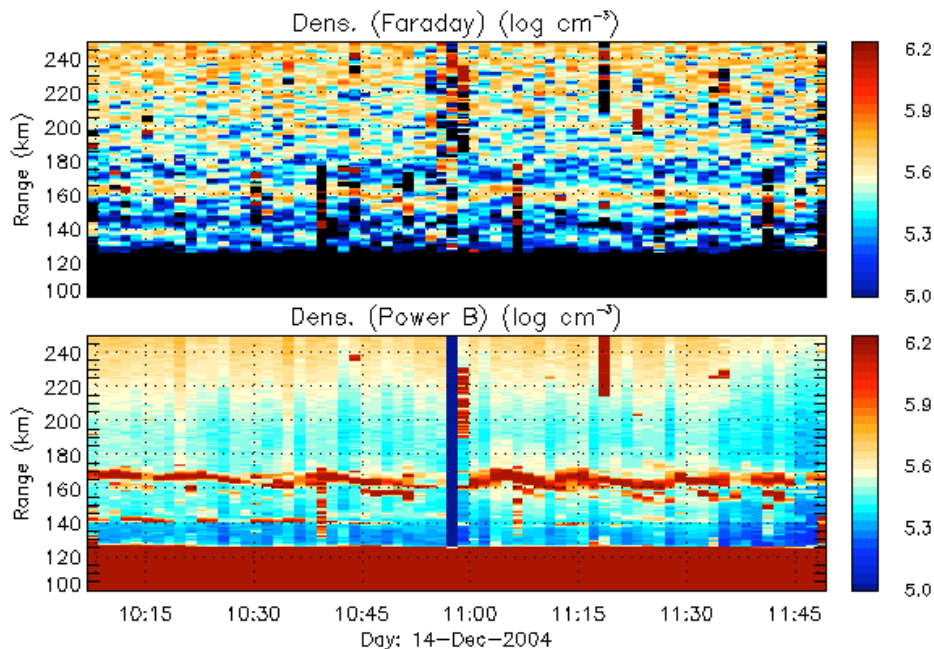


Figure 2. Range-time electron density maps from: (a) Faraday rotation (top), and (b) absolute power (bottom).

Comparing Figures 1 and 4, we can observe a close correlation between the 150-km echoes, particularly if the altitude of 150-km echoes is roughly converted to the expected virtual height. In both cases, we observe the necklace shape and more importantly similar time and range modulation.

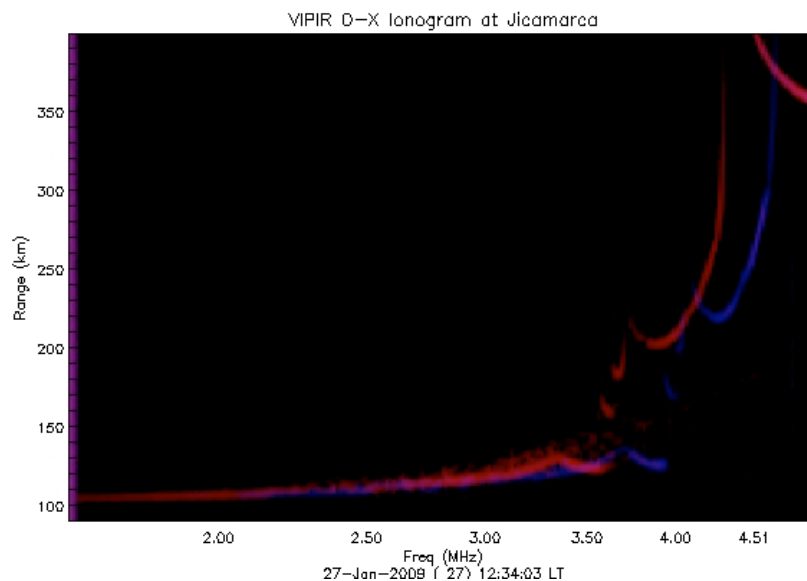


Figure 3. An example of VIPIR ionogram showing both O (red) and X (blue) modes. In this case range represents virtual height.

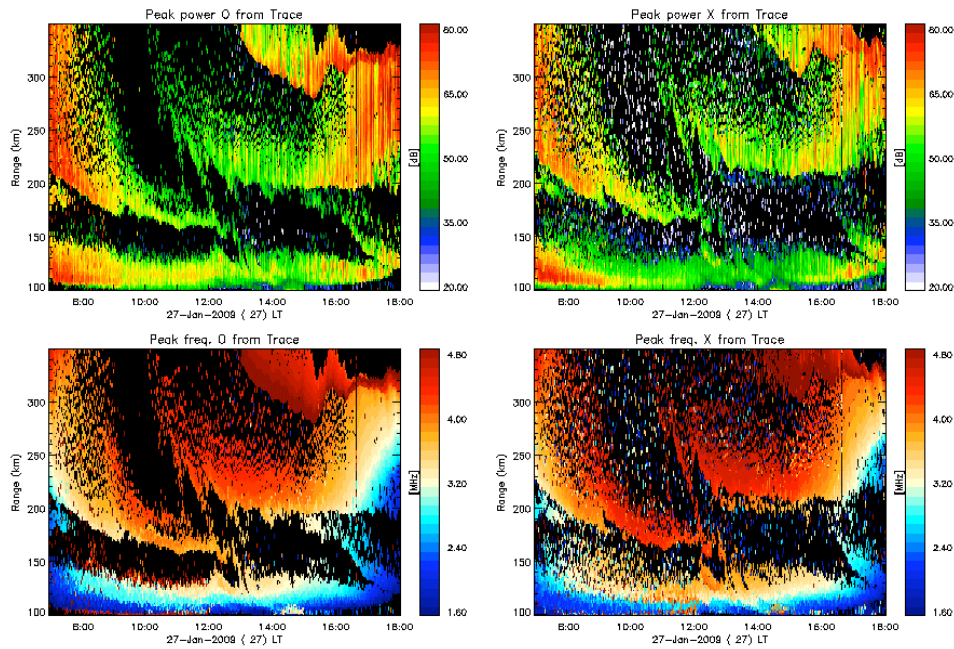


Figure 4. Range-time plots of (a) peak power (top), (b) peak frequency for both O (left) and X (right) modes.

4. Concluding Remarks

In this work we have added another piece to the so-called 150-km puzzle. The electron density structure (time and 3D space) is highly structured and we think that may prove important in the understanding of the production of these echoes. Moreover, such electron density structuring might be in turn related to the neutral dynamics of the region. It is known that in this region the meridional winds present large shears and variability. We plan to improve the experiments, for example, by combining VIPIR observations with high-resolution incoherent scatter experiments for better inversions of the valley-region densities, determining the spatial location of the scattering echo to determine its zonal and meridional dependence, improve the time and altitude resolution of VIPIR experiments.

Acknowledgements. The Jicamarca Radio Observatory is a facility of the Instituto Geofísico del Perú (IGP) operated with support from the NSF Cooperative Agreement ATM-0432565 through Cornell University. LISN is a Boston College project in collaboration with IGP.

Bibliography

- Chau, J. L., Unexpected Spectral Characteristics of VHF Radar Signals from 150-km Region over Jicamarca, *Geophys. Res. Lett.*, 31, L23803, doi:10.1029/2004GL021620, 2004.
- Chau, J. L. and R. F. Woodman, Daytime Vertical and Zonal Velocities from 150-Km Echoes: Their Relevance to F-Region Dynamics, *Geophys. Res. Lett.*, 31, L17801, doi:10.1029/2004GL020800, 2004.
- Chau, J. L. and R. F. Woodman, D- and E-Region Incoherent Scatter Radar Density Measurements over Jicamarca, *J. Geophys. Res.*, 110, A12314, doi:10.1029/2005JA011438, 2005.
- Chau, J. L., R. F. Woodman, M. A. Milla, and E. Kudeki, Naturally enhanced ion-line spectra around the equatorial 150-km region, *Ann. Geophys.*, 27, 933-942, 2009.
- Kudeki, E. and C. D. Fawcett, High resolution observations of 150 km echoes at Jicamarca, *Geophys. Res. Lett.*, 20, 1987-1990, 1993.

HYDROXYL OPTICAL EMISSIONS BY HIGH-POWER RADIOWAVES

Ludmila Kagan

University of Western Ontario, London ON, Canada

1. Introduction.

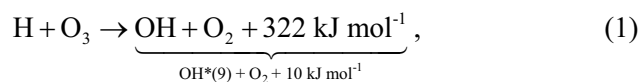
Vibrational excitation of OH^{*}(9-6) could naturally happen in the mesosphere under conditions of the secondary mesospheric maximum of ozone and dissociation of proton clusters caused by electrons brought down by such atmospheric processes as, for example, atmospheric buoyancy waves, called gravity waves. Manmade hydroxyl optical emissions OH^{*}(9,3) were observed during the multi-instrument optical-heating-backscatter campaign at the Sura facility in Russia in August 2004 (Kagan et al., 2005; Kagan et al., 2006). These are the only observations of radiowave-induced hydroxyl optical emissions. Their importance for tracking global warming and climate change have stimulated a special interest in understanding the OH^{*}(9,3) mechanisms and in developing a technique for their generation by high-power radiowaves. In Section 2 below we give the observational summary from the 2004 Sura campaign followed by discussion of atmospheric chemistry in Section 3. We outline the OH^{*}(9,3) production scenario and its important sequences in Section 4.

2. Observational Summary.

Kagan et al. [2005] and *Kagan* [2008] showed that OH^{*}(9,3) was vibrationally excited within 2 s after turn-on high-power radiowaves (practically instantaneously following the heater ‘on’ times) and was observed in the presence of low-altitude weak sporadic ionization layers near 80-85 km (most probably associated with mesospheric summer echoes, MSE) detected by the so-called artificial periodic irregularities (API) technique (e.g. Belikovich et al., 2002; Kagan et al., 2002). Though the radar echoes were detected from 30-meter irregularities and technically, perhaps could not be called MSE (which are usually related to 3-m and smaller irregularities), the extensive observations at the Sura facility of the mesospheric echoes in the HF range showed that they are the part of the same MSE phenomena (e.g. Karashtin et al., 1997; Karashtin et al., 2006). Hydroxyl optical emissions were observed in between ionization clouds with their maximum emission intensity reaching 40-50 Rayleighs. The emissions disappeared with the pump turn-off. All the observations of OH^{*}(9,3) were after local midnight.

3. Atmospheric Chemistry.

The main uncertainty in understanding the mechanism of OH^{*}(9) production came from the atmospheric chemistry. Although observation of OH^{*}(9,3) clearly pointed to the only reaction producing OH at the 9th vibrational level [Brasseur and Solomon, 2005; Wayne, 2000]:



until very recently we knew the answer to only the first of three major questions of $\text{OH}^*(9,3)$ generation by power radio transmissions [Kagan, 2008]. These questions are

- what was the source of O_3 ?
- what was the origin of H?
- how do radiowaves misbalance the H – O_3 equilibrium?

3.1. Ozone.

We show that ozone, essential for producing excited hydroxyl, was most probably due to the mesospheric ozone maximum (also called secondary ozone maximum) that forms between 85 and 90 km altitude and is due to the balance between chemical reaction producing and destroying ozone. The ozone production is due to the three-body reaction between atomic and molecular oxygen with a very temperature-sensitive reaction coefficient. The dominating reaction of ozone destruction during night is the one producing excited hydroxyl $\text{OH}^*(9-6)$ (Eq. 1). The property of the mesospheric ozone maximum can be summarized as follows (Smith and Marsh, 2005; Sonnemann and Grygalashvily, 2005; Sonnemann et al., 2006):

- The altitude of O_3 maximum is defined by the minimum in mesopause temperature (the lower temperature, the higher ozone concentration) and the maximum in atomic oxygen density.
- In equilibrium the ozone production through the 3-body reaction is balanced by its destruction which is in the nighttime is predominantly by hydrogen (Eq. 1) generating OH^* at the 9th vibrational level;
- It is influenced by transport effects of diffusion and advection (lifetime of O is ~ a month near 95 km and molecular and eddy diffusion, i.e. diffusion of atomic oxygen and hydrogen down from the thermosphere, and upward transport of water vapor by advection and diffusion (primary source of atomic hydrogen);
- The secondary ozone maximum disappeared near sunset and re-appear after midnight.

3.2. Origin of free atomic hydrogen and its relation to high-power radiowave transmission.

The breakthrough in understanding the two other puzzles of $\text{OH}^*(9,3)$ production: the origin of free hydrogen and the mechanism for misbalancing the H- O_3 equilibrium by high-power radiowaves, comes with recent extensive work on noctilucent clouds and mesospheric summer echoes by *Lübken et al* [2009] and other papers in the JASTPh-2009 special issues 3-4.

Analysis of simultaneous measurements of polar mesosphere summer echoes (PMSE) by a VHF radar and temperatures in the mesopause region by a potassium lidar performed on Spitsbergen by *Lübken et al* [2009] showed that

- In the presence of PMSE temperatures were practically always lower than the frost point which confirms the importance of ice particles for PMSE;
- Around the mesopause approximately 80% of the observations showed very low temperatures but no PMSE;
- PMSE intensity rapidly decreased above 83–89 km (the maximum signal), and the radar very seldom detected PMSE above 92 km, although it was persistently cold these higher altitudes and ice particles presumably existed (explained by importance of sufficiently strong turbulence increasing with height where increasing viscosity destroyed small-scale fluctuations). The lowest temperatures were around 90 km \cong 110K from mid June to mid July and were \cong 130-140K in mid August (time of our observations by *Kagan et al.*, 2005).
- The absence of PMSE could not be taken as a proof for the absence of ice particles and the freeze-drying effect may not be as important as previously anticipated.

- The observed temperatures assumed huge degrees of saturation (up to 10^6 – 10^8) which allowed for homogeneous nucleation. In the altitude range of their best data coverage (~88–93 km) the contribution of $S > 100$ and $S > 10,000$ to all cases of super saturation was approximately 40–50% and 10–20% respectively, where $S = P(H_2O)/P_{sat}$ ($P(H_2O)$ is the partial pressure of water vapor and P_{sat} is the saturation pressure of water vapor over ice; $S=1$ is called a frost point: ice particle can exist or grow at $S > 1$ and sublimate at $S < 1$).

4. $OH^*(9,3)$ production scenario and its important sequences.

Important sequences of the abovementioned recent work by *Lübken et al* [2009] for the $OH^*(9,3)$ production scenario are that (1) the presence of mesospheric summer echoes near 80–85 km (observed by the API technique) indicated very cold mesospheric temperatures, supposedly ~ 20–30K lower than predicted by the MSIS model shown in Fig. 1; (2) an extended altitude range (~86–94 km in mid August) for minimum temperature of ~130–140 K; and (3) presence of high concentration of super-saturated water vapor, ice particles and proton hydrates up to 95 km.

Such an extended altitude range of very cold temperature would result in a higher concentration of ozone well above its mesospheric maximum (up to ~95 km) (see Eq. 1), while presence of high concentration of super-saturated water vapor, ice particles and proton hydrates at these altitudes would allow liberation of free atomic hydrogen by dissociative recombination of proton hydrates and by dissociation of water vapor by electrons accelerated by high-power radiowaves.

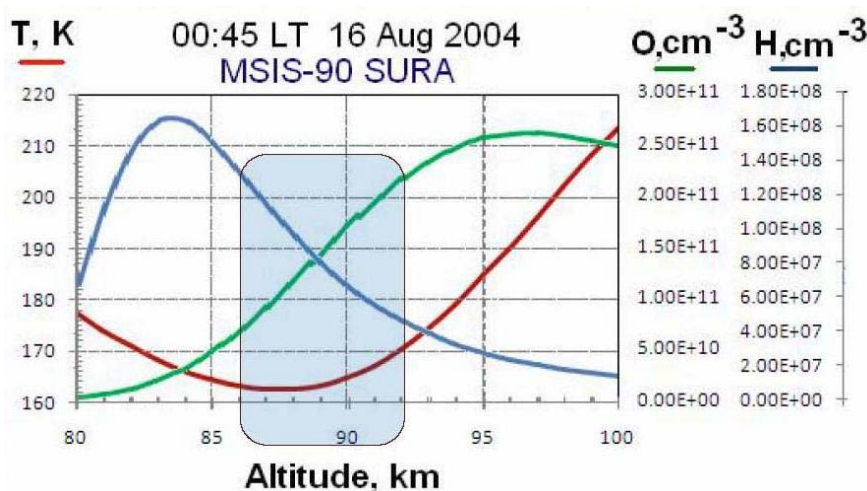


Figure 1. MSIS-modeled temperature profiles of atomic hydrogen and oxygen as function of altitude for the *Kagan et al.* [2005] $OH^*(9,3)$ observations at the Sura facility.

We have shown that generation of hydroxyl optical emissions by high-power radiowaves is intimately related to the mesopause (secondary) ozone maximum and one of manifestations of the complex phenomena known as noctilucent (or mesospheric) clouds and mesospheric summer echoes. To induce hydroxyl optical emissions by high-power radiowave transmissions the observations should be carried out in the season of the coldest temperatures (the season of PMSE) after local midnight. Excited hydroxyl observations at two wavelengths would allow measuring of mesospheric temperature (also could be observed by lidars) and water vapor content (about which is not much known) and estimating ozone

concentration (is not much known either) at the altitudes where global warming and climate change would show up first.

Acknowledgement: This work has been supported by Canadian Space Agency for the ePOP/Cassiope mission.

Bibliography

- Belikovich, V. V. , E. A. Benediktov, A. V. Tolmacheva, N. V. Bakhmet'eva, *Ionospheric Research by Means of Artificial Periodic Irregularities*, Copernicus, ISBN: 978-3-936586-03-9, 2002.
- Brasseur, G.P. and S. Solomon, *Aeronomy of the Middle Atmosphere: Chemistry and Physics of the Stratosphere and Mesosphere*, 3d edition, Dordrecht : Springer, 2005.
- Kagan, L.M., N.V. Bakhmet'eva, V.V. Belikovich, A.V. Tolmacheva, and M.C. Kelley, Structure and dynamics of sporadic E layers, *Radio Sci.*, **37**(6), 1106-1118, 2002.
- Kagan, L.M., M.J. Nicolls, M.C. Kelley, H.C. Carlson, V.V. Belikovich, N.V. Bakhmet'eva, G.P. Komrakov, T.S. Trondsen, and E. Donovan, Observation of Radiowave-Induced Red Hydroxyl Emission at Low Altitude in the Ionosphere, *Phys. Rev. Lett.*, **94**(9), 095004, 2005.
- Kagan, L.M., M.J. Nicolls, M.C. Kelley, V.L. Frolov, V.V. Belikovich, N.V. Bakhmet'eva, G.P. Komrakov, D.I. Nedzvetski, V.P. Uryadov, Yu. M. Yampolski, A.V. Koloskov, A.V. Zalizovski, V.L. Galushko, S.B. Kasheev, N.F. Blagoveshenskaya, V.A. Kornienko, T.D. Borisova, A.V. Gurevich, G.G. Vertogradov, V.G. Vertogradov, T.S. Trondsen, and E. Donovan, Optical and RF diagnostics of the ionosphere over the Sura facility. Review of Results, *J. of Radiophysics and Radio Astronomy*, **11**(3), 221-242, 2006.
- Kagan, L.M., Auroral lights created by high-power radiowaves in the ionospheric E region, *Plasma Phys. Control. Fusion* **50** 074001 (9pp) doi: 10.1088/0741-3335/50/7/074001, 2008.
- Karashtin, A. N. , Y. V. Shlugaev, I. V. Berezin and G. P. Komrakov, Seasonal behavior of middle-latitude short-wave mesospheric radio echoes, *Radiophys. and Quantum Electronics*, **41**(10), DOI 10.1007/BF02676453, 842-849, 1998.
- Karashtin, A. N. , Yu. V. Shlyugaev, V. I. Abramov, V. V. Bychkov and G. P. Komrakov, Angles of arrival of HF mesosphere radar echoes, *Geomagnetism and Aeronomy*, **47**(2), DOI 10.1134/S0016793207020132, 244-250, 2007.
- Lübken, F.-J., J. Lautenbach, J. Höffner, M. Rapp, M. Zeche, First continuous temperature measurements within polar mesosphere summer echoes, *J. Atmos. Sol.-Terr. Phys.*, **71**, 453-463, 2009.
- Smith, A. K., and D. R. Marsh, Processes that account for the ozone maximum at the mesopause, *J. Geophys. Res.*, **110**, D23305, doi:10.1029/2005JD006298, 2005.
- Sonnemann, G., M. Grygalashvyly, and U. Berger, *Atmos. Sol.-Terr. Phys.*, **68**, 2012-2025, 2006.
- Sonnemann, G. and M. Grygalashvyly, *Atmos. Sol.-Terr. Phys.*, **67**, 177-190, 2005.
- Wayne, R.P., *Chemistry of atmospheres: an introduction to the chemistry of the atmospheres of earth, the planets, and their satellites*, 3rd ed., Oxford [England]; New York: Oxford University Press, 2000.

ON THE RELATION BETWEEN MF RADAR SCATTERERS AND EQUATORIAL SPORADIC E

R. Dhanya, S. Gurubaran and K. Emperumal

Equatorial Geophysical Research Laboratory, IIG, Tirunelveli - 627 011

1. Abstract

Nature of the MF radar scatterers and the physical parameters influencing them are not known completely. Our current understanding of the physical processes comes from VHF observations and MF radar studies can help in providing more insight. Signatures of equatorial electrojet (EEJ) have been observed in Medium frequency (MF) radar echoes over Tirunelveli (8.7°N, 77.8°E, geographic; 1.34°N, magnetic dip). The MF radar echoes at EEJ heights exhibit complex behaviour during various electrodynamical conditions. This work aims to understand the possible linkage of MF radar echoes with the EEJ and the mechanisms that influence the geometrical parameters and their relation to electrodynamical processes to get more insights of the nature of the scatterers under various geophysical conditions. A case study of the behaviour of MF radar echoes during different electrodynamical conditions is performed using supporting data from co-located digital magnetometer and a vertical incidence ionosonde, to understand the nature of scatterers responsible for the MF radar echoes. Specific echo character can be associated with a particular state of E_{Sq} provided the electric field direction is known from the magnetogram.

2. Results and discussion

Characteristics of MF radar echoes under different electrojet conditions

Case-I: Quiet CEJ day marked with no E_{sb} – 26 June 2007 ($A_p = 9$).

CEJ- No Blanketing (NBCEJ)

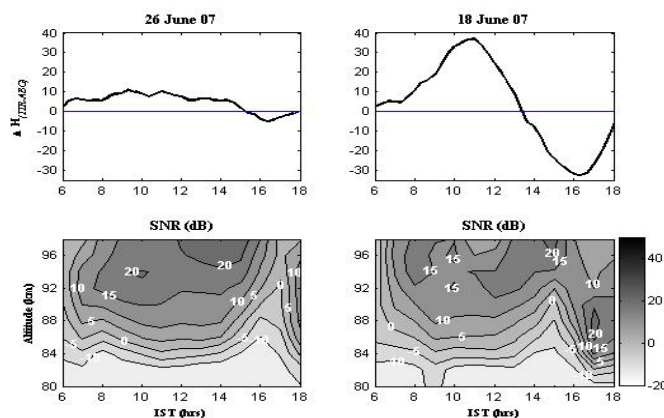


Figure 1: SNR as on 26 & 18 June 2007.

This day serves as a classical example for representing the behaviour of MF radar echoes during the times of CEJ without blanketing. The behaviour of MF radar scatterers during different phases of E_{Sq} (growth, decay) can be studied from this day signified by the absence of E_{sb} .

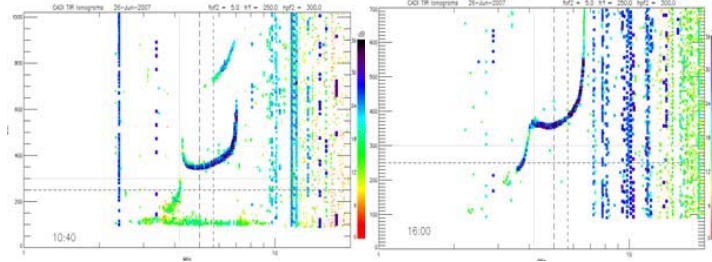


Figure 2: Sample ionograms for 26 June 2007.

This day is characterized by a weak EEJ that is followed by partial/weak CEJ as seen in top panel on the left, in Figure 1. The EEJ magnitude on this day is very weak compared to the other selected day ($\Delta H \approx 11$ nT) and so is the Partial CEJ ($\Delta H \approx -5$ nT) that followed it and lasts roughly from 15:20-18:00 IST. CEJ max occurs around 16:15 IST.

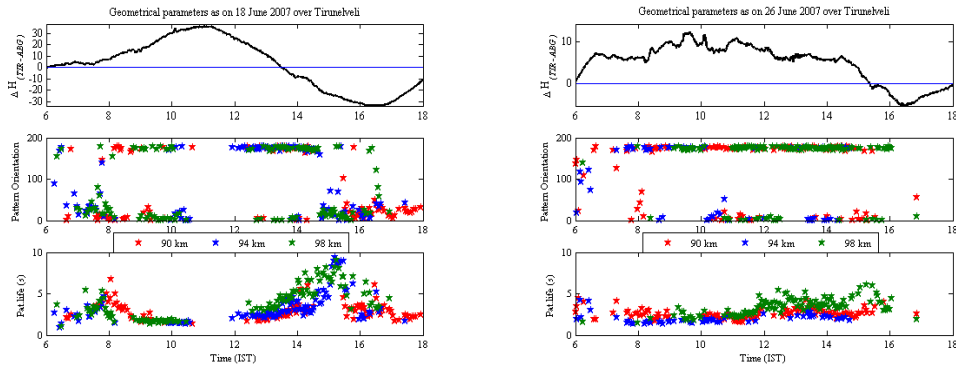


Figure 3: Geometrical parameters as on 18 & 26 June 2007.

The ionograms show the presence of E_{Sq} from 07:30 - 16:00 IST (Two sample ionograms are shown in Figure 2). E_{Sq} starts weakening from the time of ΔH reversal and vanished just before the time of CEJ max. It is noted in general, that on a quiet day marked by normal afternoon CEJ without blanketing and presence of E_s , SNR follows ΔH (Figure 1 bottom panel on the left) and Pattern life (Figure 3, right) seems to have an inverse relation with ΔH . This is evident from the observations that in the absence of any disturbance, SNR builds up gradually with E_{Sq} and remains high till E_{Sq} is stronger and goes below the threshold when E_{Sq} disappears. On the other hand, the Pattern life is smaller when E_{Sq} is fully developed and remains small till the weakening of E_{Sq} indicating the presence of turbulence and hence shorter life time owing to the randomness of the medium. In general, lower Pattern life and strong north south orientation are expected during the times of strong EEJ (Figure 3, right).

Whenever ΔH reverses, E_{Sq} weakens as seen in the ionogram (sample is shown in Figure 2) and vanishes completely just before the time of CEJ maximum. SNR falls below the threshold at all the three heights and the antenna parameters are rejected due to low SNR (Briggs, 1984) due to the non-availability of conditions supporting the presence of type II irregularities.

**Case-II: Very Quiet day marked with occurrence of strong E_{sb} – 18 June 2007 ($A_p=2$).
CEJ- Blanketing (BCEJ)**

Top panel of Figure 1 (right) shows $[\Delta H_{TIR} - \Delta H_{ABG}]$ representing the day time electrojet strength. This is a good example for a CEJ day marked by a characteristic increase in electrojet strength ($\Delta H \approx 40$ nT), and is followed by an afternoon strong depression in ΔH ($\Delta H \approx -30$ nT) from 13:15-18:15 IST with a peak around 16:15 IST. Among the two selected days this is the strongest both in terms of CEJ and EEJ.

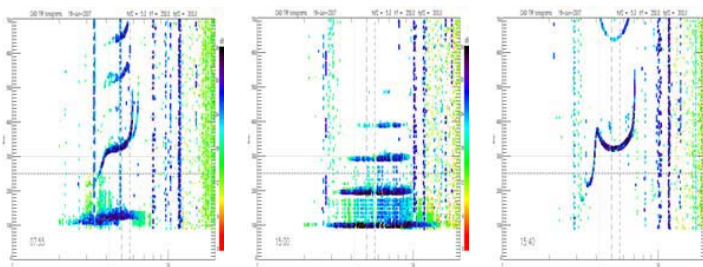


Figure 4: Sample ionograms for 18 June 2007.

The presence of strong E_{Sq} as seen by the ionosonde from 07:45 - 08:00 IST (Ionograms on bottom left in Figure 4) is characterized by increase in SNR, high Pattern life time and gradual alignment towards the field (Figure 3, left). However the lower height of 90 km is marked by a drop in SNR, probably, due to height variations in current structures (Devasia and Reddy, 1995) and hence the dataset for 90 km is rejected.

E_{Sq} persists in the ionogram upto 14:30 IST. E_{Sq} layer slowly turns into E_{sb} , as evident from the multiple reflection observed beyond 14:35 IST. E_{sb} lasts for ~ 45 minutes (14:40-15:25 IST) with a peak around 15:00 IST. On the other hand, the magnetogram shows the presence of CEJ from 13:15-18:15 IST with a maximum around 16:15 IST.

On this day the blanketing occurs well before the maximum of CEJ. E_{sb} weakens and vanishes completely around 15:35 IST and does not appear again. The behaviour of geometrical parameters on this day is strikingly different from that reported earlier during CEJ times (Ramkumar et al., 2002; Gurubaran et al., 2007), wherein the geometrical parameters randomize and SNR drops to low values, soon after ΔH reverses and the electric field control is lost. Most of the earlier cases reported, are probably during CEJ conditions not accompanied by blanketing.

For CEJ accompanied by blanketing, the scenario is quite different. Figure 4) represents a sample ionogram of E_{sb} in its peak marked by characteristic increase in SNR (Figure 1, bottom right panel), high Pattern life time and randomization of Pattern orientation (Figure 3, left). The SNR continues to remain high at 98 km alone, whereas the lower heights

of 90 km and 94 km are marked by a drop in SNR, following a raise around 16:00 IST could not be accounted for. This day stands as an observational evidence for the proposed height dependent structures present in the Electrojet region.

MF radar scatterers during the blanketing CEJ are characterized by anomalous increase in the Pattern life time and randomization of orientation.

3. Conclusion

This study is one of the first reports on behaviour of MF radar geometrical parameters during blanketing conditions. An interesting and significant outcome of this study is the clear height variation as reported for the first time with MF radar. Sometimes, even during the times of well behaved echoes (preferred orientation in the North-South direction and no randomization), the ionograms do not show the presence of E region irregularities. This could either be due to the differences in sensitivity between the MF radar and the ionosonde to distinct echoing regions, or, the irregularities responsible for the echoes received by the two instruments are not the same but due to a common origin. In general, the Pattern life time and Pattern orientation respond quickly to the blanketing conditions than the other geometrical parameters. Invariably of the electrodynamical condition, blanketing as recorded by the ionosonde is accompanied by large Pattern life time and randomization of Pattern orientation. In case of strong E_{sq} , the echoes are sensitive only at times. This could be due to the dependence of echoes on occurrence height of E_{sq} , that influence the SNR and other geometrical parameters resulting in lower sensitivity of echoes. Some times drifts motions at 90 km do not appear to be driven by the electric field, though other parameters reveal strong linkage to electrodynamical conditions associated with EEJ (Tsunoda et al., 1999). Further studies involving simultaneous measurements using MF and VHF radar, magnetometers and ionosonde can bring out better insights of the problems stated.

4. References

1. Briggs, B. H.: The analysis of spaced sensor records by correlation techniques, Handbook for MAP., 13, 166-186, 1984.
2. Devasia C.V., Reddy C.A.: Retrieval of east-west wind in the equatorial electrojet from the local wind-generated electric field, J. Atmos. Terr. Phys., 57, 1233-1239, 1995.
3. Gurubaran, S., Dhanya, R., Sathishkumar, S., Paramasivan, B. : On the electric field control of the MF radar scatterers in the lower E region over the magnetic equator, Geophys. Res. Lett., 34, L06105, doi:10.1029/2006GL028748, 2007.
4. Ramkumar, T. K., Gurubaran, S., and Rajaram R.: Lower E-region MF radar spaced antenna measurements over magnetic equator, J. Atmos. Solar-Terr. Phys., 64, 1445-1453, 2002.
5. Tsunoda, R. T., and Ecklund, W. L.: On the nature of radar echoes below 95 km during counter streaming in the equatorial electrojet, Geophys. Res. Lett., 26, 2717-2720, 1999.

**Session 5:
Meteorology, Forecasting
and Nowcasting**

PROGRESS REPORT ON THE O-QNET, A NEW CANADIAN WINDPROFILER NETWORK.

W. K. Hocking¹, P. Taylor², N. Swarnalingam, P. S. Argall¹, D. Tarasick⁴, I. Zawadzki³, F. Fabry³, J. Barron¹, R. Mercer¹, G. Klaassen², G. McBean¹, R. Sica¹, H. Hangan¹.

1. University of Western Ontario, London, Ont., Canada.
2. York University, Toronto, Canada.
3. McGill University, Montreal, Canada.
4. Environment Canada.

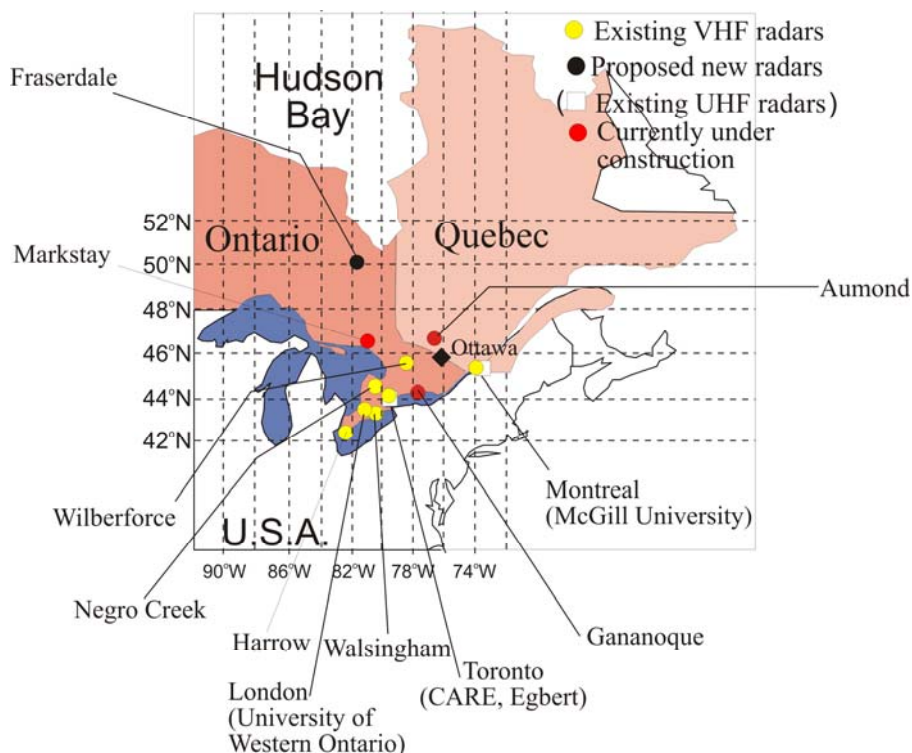
Introduction.

The O-Qnet was introduced to the MST community in Hocking et al., (2007). The basic design features were discussed there, and progress to date was described. In this paper, we provide an update on progress since 2006, highlighting any changes in direction and describing the current status of the system.

New Sites. General Progress.

One of the main changes since the last report has been development of new sites, in some cases at new locations. New locations have often been necessitated for logistical reasons.

Fig. 1. Revised locations of sites for the O-QNet.



The revised sites are shown in fig. 1. Locations are close to the previous distribution, but are not all identical. Five sites are now complete, and giving data on an hourly basis. The data from the sites are updated at <http://www.yorku.ca/oqnet/>

Design updates.

The radars consist of dual sub-radars, comprising a large Doppler radar for upper level wind determinations and a smaller sub-system for wind measurements between 400m and 2000m altitude. The Doppler system is well established, and reliable. The boundary-layer mode has required some extra development. During the period leading up to MST11, extensive investigations of methods to measure boundary layer winds were discussed (Hocking, 2006; 2007). In contrast to other systems, our system was limited by lack of available bandwidth, so use of short pulses was not permitted. Pulse lengths were limited to typically 300m and more, but it was our intent to measure winds down to altitudes of 400m and lower. This required new approaches to antenna placement and software design. A bistatic antenna arrangement, with separate transmitter and receiver antennas was mandated by this requirement, and a design was required that limited direct ground-wave pick-up of the transmitter signal by the antennas. As discussed by Hocking (2007), a variety of approaches were applied, including the use of loop antennas. A view of some loop antennas is shown in fig. 2.

Fig. 2. View of loop antennas through the boundary-layer transmitter antennas



Loop antennas were considered good candidates because, when properly aligned, they were considered to have superior rejection of ground-level pickup from the transmitter. However, measurements also showed that they had narrow bandwidth (600 kHz) and were 10-15 dB less efficient than a 2-element Yagi. In order to improve the efficiency, a design was developed that involved not a single loop but a closely-wound double loop made from semi-rigid coaxial cable, which improved efficiency, but it suffered from an unexpected characteristic – even a small amount of water between the coils caused the resonant frequency to shift by several hundred kHz, so the loops would not work during rain! Eventually the loop antennas were replaced by 3-element Yagi antennas, as discussed in Hocking (2007), Hocking et al., (2007). Examples of the 3-element Yagis are shown in fig. 3.

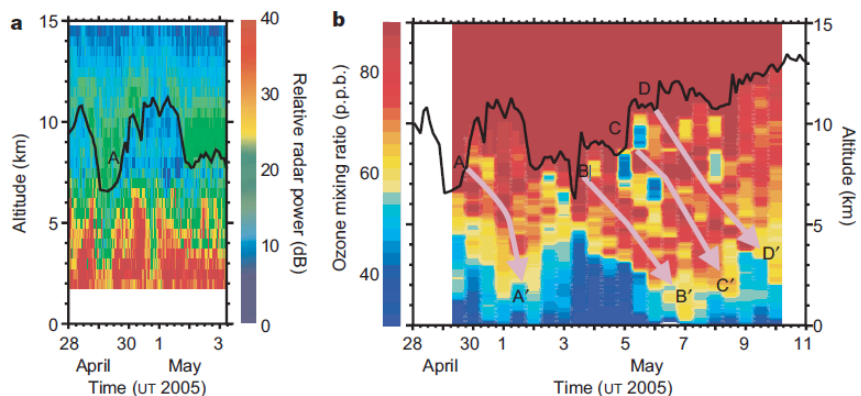
Another important characteristic required for good boundary-layer operation is a wide bandwidth for the transmitter antennas. Even if the antennas are tuned so that the VSWR at the central frequency is 1.0, the VSWR will become more than 1.0 as the frequency moves away from the central frequency. The transmitted pulse contains a range of Fourier components, and if the VSWR is different from unity at any of these Fourier components, some of the pulse (at these frequencies) will be reflected back to the transmitter. In order to reduce the effect, the VSWR needs to be as close to unity over as wide a band as possible. Reflected parts of the pulse may then reflect further from the transmitter, and so bounce back and forth between the

antenna and transmitter. Hence remnants of the pulse may persist even for delays of several times the pulse length, and if these signals are collected by the space antenna receivers as ground-waves, they will complicate the extraction of true atmospheric signal. These multiple reflections occur in almost all radars, and are often confused with “ground echoes”. Hence a wide bandwidth, and good suppression of direct pickup between the receiver antennas and the transmitter antennas, are crucial to the correct operation of boundary-layer system. More detail about the extraction process in boundary-layer mode can be found in Hocking and Hocking, 2010 (this issue). The new design optimizes these factors.

Fig. 3. Three-element Yagi antennas used for spaced-antenna reception at the Harrow site are seen in the foreground, just beyond the fence.



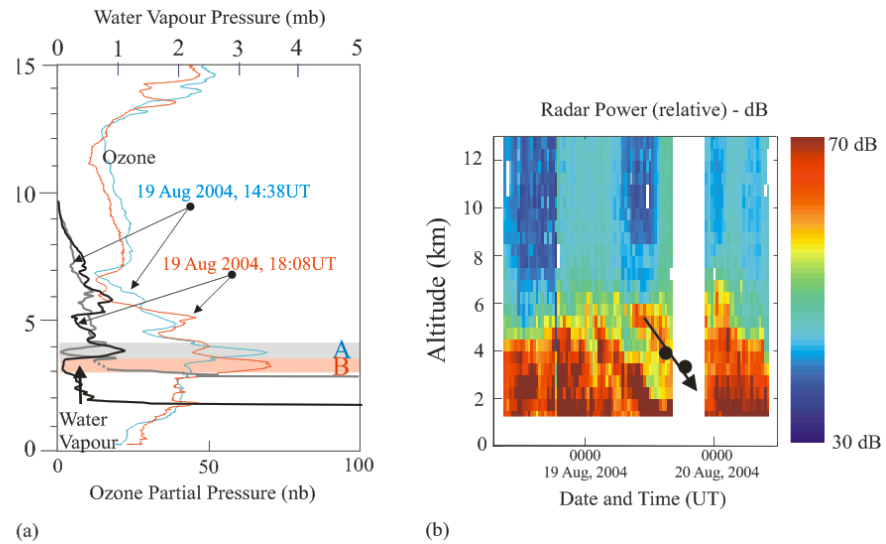
Fig. 4. Tracking the tropopause via radar (left), and (right) ozone intrusions seen using ozonesonde measurements. (from Hocking et al., 2007)



Significant recent Results.

The network has already proved useful for a variety of studies, including demonstration of the capability of windprofilers to forecast ozone intrusions from the stratosphere (Hocking et al., 2007). However, another result of that study is that it is sometimes possible to detect and track layers of ozone which have entered the troposphere from the stratosphere above. Fig. 5 shows ozone peaks observed using two successive ozonesonde measurements made only 4 hours apart. The peaks A and B not only have high ozone but also normally have low water vapour, and also steep gradients in water vapour content at their edges. These water vapour gradients help to produce enhanced radio backscatter, and the radar-signal enhancement shown in fig. 1(b) by the downward sloping arrow in fact tracks the ozone maximum. The two black dots in that figure show the height of the peaks in ozone density for events A and B (although unfortunately the radar was not operational for case B).

Fig. 5. Descending ozone layer (left) and corresponding radar backscatter (right) observed with the Clovar radar.



Future plans.

Unquestionably the major objective in the coming years is to integrate the windprofiler data into numerical forecast models. The output of the radars has been modified to produce bufr format as a standard output, and bufr files are sent to the forecast centre in Dorval (Quebec) every hour from all sites. Integration and testing of the usefulness of the profiler data in improving forecasting skill is currently underway, and results should be available by MST13.

References

- Hocking, W.K., "Comparison of IDI and FCA analyses for Boundary Layer VHF wind measurements", Paper I.3-27, MST11, the 11th International Workshop on Technical and Scientific aspects of Mesosphere-Stratosphere-Troposphere Radars, Gadanki/Tirupati, India, Dec 11-15, 2006.
- Hocking, W.K., P. Taylor, I. Zawadzki, S. Argall, F. Fabry, G. McBean, R. Sica, H. Hangan, G. Klassen, J. Barron and R. Mercer, "A New 40-55 MHz Windprofiler Network in Ontario and Quebec, Canada—The O-Qnet," Proceedings of the 11th International Workshop on Technical and Scientific Aspects of MST Radar, Gadanki, India, Dec 11-15, 2006, ed. V.K. Anandan, pp 377-380, publ. Macmillan India Inc., 2007.
- Hocking, W.K. "Boundary Layer Winds with 50 MHz Radars—Comparison of Different Approaches," Proceedings of the 11th International Workshop on Technical and Scientific Aspects of MST Radar, Gadanki, India, Dec 11-15, 2006, ed. V.K. Anandan, pp 284-287, publ. Macmillan India Inc., 2007.
- Hocking, W.K., T. Carey-Smith, D. Tarasick, S. Argall, K. Strong, Y. Rochon, I. Zawadzki, P. Taylor, "Detection of Stratospheric Ozone Intrusions by Windprofiler Radars", *Nature*, 450, 281-284, 2007.
- Hocking, W.K. and A. Hocking, "Procedure to extract Boundary-layer Wind Measurements using relatively long pulses", this issue, 2010.

REFINEMENT OF 3D DOPPLER VELOCITY USING 3D WINDPROFILER DATA

Yong Zhang, John L. Barron, Robert E. Mercer

`{yzhan433,barron,merc} @csd.uwo.ca`

Dept. of Computer Science, University of Western Ontario

London, Ontario, Canada, N6A 5B7

Abstract: We present a preliminary report on combining the data from a Windprofiler radar and a NEXRADII Doppler radar to compute 3D optical flow. Previously, we computed 3D optical flow from 3D Doppler radar radial velocity data only. Windprofiler data improves the recovery of the velocity component in the upwards direction, where Windprofiler data is believed to be more accurate.

Keywords: Doppler Radial Velocity, 3D Optical Flow, Doppler Radial Velocity, Windprofiler Velocity, Least Square Optical Flow, Regularized Optical Flow

1 Introduction

Doppler radar is an important meteorological observation tool. In order to gain knowledge of how storms move over time, much research have been devoted to retrieving 3D full velocity from the observed radial velocity (for example, Lhermitte and Atlas [LA61], Easterbrook [Eas75] and Waldteufel and Corbin [WC79]). Rather than using the traditional methods provided by meteorologists, our research group is solving this problem using the 3D Optical Flow framework [BRCJ05], which is a technology widely applied in the Computer Vision area. In this paper, we “refine” 3D Doppler optical flow by integrating Windprofiler data into the calculation. We illustrate this refinement using data from the Detroit NCDC Doppler and the Harrow Windprofiler radars.

We use a right-handed coordinate system where the x and y axes describe a plane and the z axis the height of the data. Optical flow is a 3D vector field, (U, V, W) , and is the 3D motion of water precipitation over time. At lower elevation angles in the data, we note that the W velocity component is almost orthogonal to the radial velocities: in the presence of even small amounts of noise, radial velocity contains little W information and is difficult to recover.

2 The Optical Flow Calculation

We have devised a 3D regularization solution based on an extension of Horn and Schunck’s 2D optical flow regularization algorithm [HS81]. That is, a number of constraint terms on 3D velocity are minimized (regularized) over the 3D domain.

The 1st term we use is the 3D **Radial Velocity Constraint**, which requires that the full velocity projected in the radial direction be the radial velocity:

$$\vec{V} \cdot \hat{r} = V_r, \quad (1)$$

where $\vec{V} = (U, V, W)$ is the local 3D velocity (which we want to compute), \hat{r} is the local unit radial velocity direction (which we know precisely from the structure of the radar data) and V_r is the measured local radial velocity magnitude.

The 2nd constraint is a 3D Horn and Schunck like **Velocity Smoothness Constraint**, which requires that velocity vary smoothly everywhere by keeping velocity component derivatives in the 3 dimensions as small as possible.

A 3rd constraint is based on an extension of the 2D Lucas and Kanade least squares optical flow algorithm [LK81] into 3D. This algorithm assumes that 3D velocity is locally constant in local neighbourhoods but that the local radial velocity varies in these $N \times N \times N$ neighbourhoods. A least squares calculation is then performed for each neighbourhood:

$$\underbrace{\begin{bmatrix} r_{X1} & r_{Y1} & r_{Z1} \\ r_{X2} & r_{Y2} & r_{Z2} \\ \dots & \dots & \dots \\ \dots & \dots & \dots \\ r_{XN} & r_{YN} & r_{ZN} \end{bmatrix}}_A \begin{bmatrix} U_{ls} \\ V_{ls} \\ W_{ls} \end{bmatrix} = \begin{bmatrix} V_{r1} \\ V_{r2} \\ \dots \\ \dots \\ V_{rN} \end{bmatrix}. \quad (2)$$

If matrix $A^T A$ can be reliably inverted the least squares velocity $\vec{V}_{ls} = (U_{ls}, V_{ls}, W_{ls})$ can be recovered. This allows us to use a **Least Squares Velocity Consistency Constraint**, which requires computed velocities to be consistent with local least squares velocities.

A 4th **Windprofiler Velocity Consistency Constraint** incorporates the Windprofiler velocity estimates, \vec{V}_{wp} , into the regularization, again by requiring local values of \vec{V}_{wp} and \vec{V} be consistent.

The complete regularization functional is the sum of these constraints:

$$\begin{aligned} & \int \int \int \left(\underbrace{(\vec{V} \cdot \hat{r} - V_r)^2}_{\text{Radial Velocity Constraint}} + \right. \\ & \underbrace{\alpha^2 (U_X^2 + U_Y^2 + U_Z^2 + V_X^2 + V_Y^2 + V_Z^2 + W_X^2 + W_Y^2 + W_Z^2)}_{\text{Velocity Smoothness Constraint}} + \\ & \underbrace{\beta^2 ((U - U_{ls})^2 + (V - V_{ls})^2 + (W - W_{ls})^2)}_{\text{Least Squares Velocity Consistency Constraint}} + \\ & \left. \sum_{i=1}^n \gamma_i^2 \underbrace{((U - U_{wpi})^2 + (V - V_{wpi})^2 + (W - W_{wpi})^2)}_{\text{Windprofiler Velocity Consistency Constraint}} \right) \partial X \partial Y \partial Z, \quad (3) \end{aligned}$$

where γ is the Lagrange multiplier for this additional constraint. The value of γ_i at each voxel is calculated from a 3D Gaussian function based on the distance between it and the location of the i^{th} point of the Windprofiler radar:

$$\gamma_i = \frac{\Gamma}{(2\pi)^{\frac{3}{2}} \prod_{k=1}^3 \sigma_k} e^{-\left(\frac{(x-x_{wpi})^2}{2\sigma_1^2} + \frac{(y-y_{wpi})^2}{2\sigma_2^2} + \frac{(z-z_{wpi})^2}{2\sigma_3^2}\right)}. \quad (4)$$

$\sigma_1, \sigma_2, \sigma_3$ are the three standard deviations that specify the shape of the 3D Gaussian distribution according to the distance between the points where \vec{V} and \vec{V}_{wpi} are measured in each of the 3 dimensions, while $\Gamma = 1000$ is a preset constant value. For our experiments, σ_1 and σ_2 have the value 20.0, reflecting the large x and y range of values, while $\sigma_3 = 0.4$, reflecting the much smaller range in the z values. The ‘‘goodness’’ of these parameter values are confirmed by synthetic and real data experiments.

We use Gauss-Seidel iterations on the Euler-Lagrange equations derived from Equation (3) to compute the flow. At the start of the iterations, \vec{V}^0 is set to zero. Until a fixed number of iterations (150) or while the difference between the k^{th} and $(k + 1)^{th}$ velocity fields remains greater than a threshold $\tau = 10^{-3}$, the iterative calculation continues. At the end, the velocity field is set to the last iteration's velocity field. We refer to this as the **refined** optical flow while the original optical flow without the Windprofiler constraint is referred to the **unrefined** optical flow [BRCJ05].

3 Experimental Results

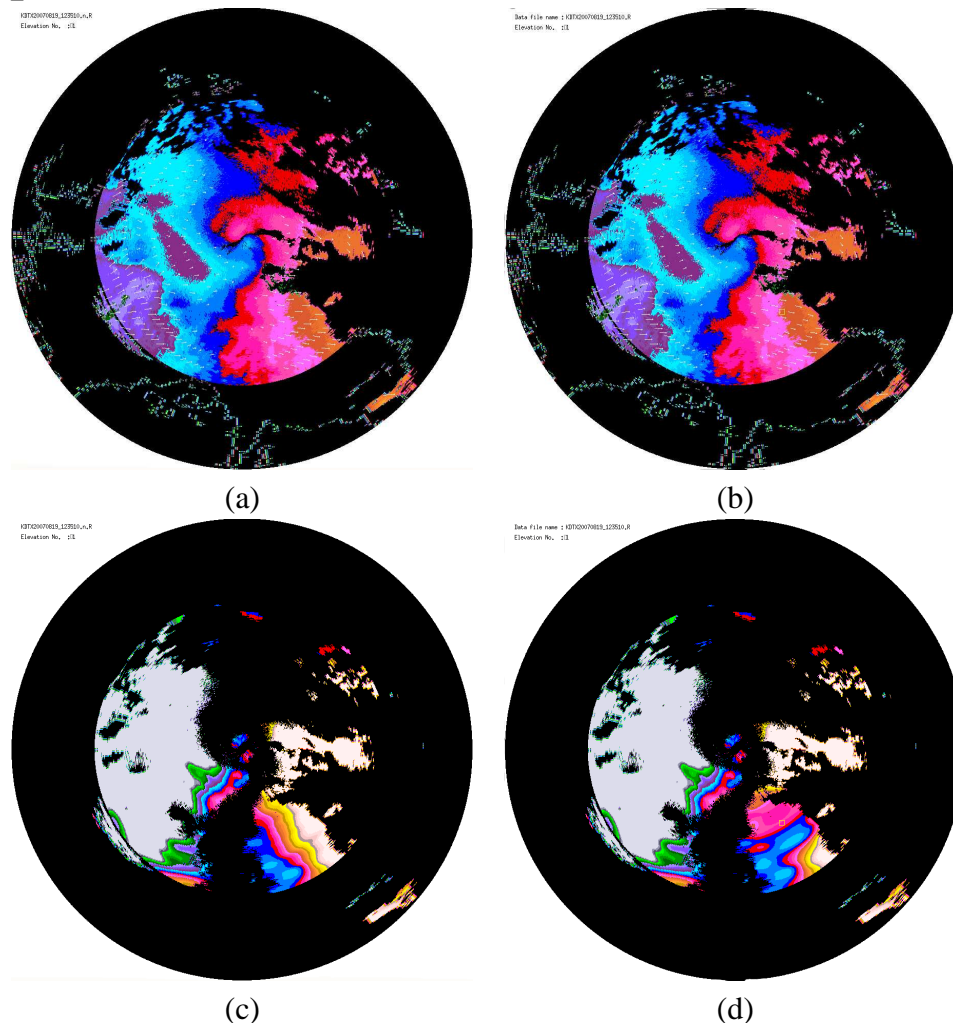


Figure 1: Full velocity retrieved from the Detroit Doppler (and the Harrow Windprofiler) data on August 19th, 2007 at 12:35:10: (a) the unrefined UV optical flow, (b) the refined UV optical flow, (c) the W component of the unrefined optical flow and (d) the W component of the refined optical flow.

We present some preliminary results for our measured Doppler and Windprofiler data. Figures 1a and 1b show the unrefined and refined UV optical flow fields for the Detroit Doppler data at 12 : 35 : 10 of August 19th, 2007. The yellow square in the bottom-right quadrant (near the origin) in these Figures indicates the position of the Harrow Windprofiler radar relative to the Detroit Doppler radar. We also show the W component of optical flow along the z (height) axis in Figures 1c and 1d. Component velocities in these figures are shown as coloured pixels,

whose correspondence with numerical values is the standard used for NEXRADII data. Note that these component colours have replaced the radial velocity magnitude colours in Figures 1a and 1b.

It is clear from the z component flow field images that the refined method significantly changes the flow field around the Windprofiler radar. Figure 1a has the unrefined flow going north while Figure 1c has the refined flow going south. We see a significant change in the recovery of component velocity W in the z direction. In the unrefined component flow shown in Figure 1c, there is a large area where the component velocities have reached their maximum value (yellow). However, in the component flow shown in Figure 1h, it is obvious that a more reasonable result has been obtained in the area surrounding the Windprofiler radar. We observe a major upward velocity component in the areas not overlapped by the Windprofiler radar but a significant downward velocity component in outer area around the Windprofiler radar. This is due to the fact that the Windprofiler constraint adopted different velocity values for the Doppler voxels according to their actual distances from the Doppler radar points.

4 Conclusions and Future Work

In this paper we briefly described how Windprofiler data at the Harrow radar station could be combined with NEXRADII Doppler data from Detroit to produce arguably more accurate optical flow field in the vicinity of the Windprofiler radar. We showed that qualitatively, more accurate and detailed information could be recovered along the z (depth) dimension and sometimes in the x and y dimensions. However, it is noted that a Windprofiler radar only covers a small overlapping area compared to a Doppler radar. This limits its application. Our framework can handle more Windprofiler radars but we do not yet have data for more than one overlapping Windprofiler and Doppler radars. Using multiple Doppler and Windprofiler radars over time is one current area of research. We are also currently constructing “realistic” Doppler and Windprofiler synthetic data and performing a quantitative analysis to determine the actual accuracy improvements of refined flow over unrefined flow.

References

- [BRCJ05] J.L. Barron, R.E. Mercer, X. Chen, and P. Joe. 3d velocity from 3d doppler radial velocity. *Intl. Journal of Imaging Systems and Technology*, 15:189–198, 2005.
- [Eas75] C. C. Easterbrook. Estimating horizontal wind fields by two-dimensional curve fitting of single doppler radar measurements. In *16th Radar Meteorology Conference*, pages 214–219, 1975.
- [HS81] B.K.P. Horn and B.G. Schunck. Determining optical flow. *Artificial Intelligence*, 17:185–204, 1981.
- [LA61] R. M. Lhermitte and D. Atlas. Precipitation motion by pulse doppler. In *Ninth Weather Radar Conference*, pages 218–223, 1961.
- [LK81] B.D. Lucas and T. Kanade. An iterative image-registration technique with an application to stereo vision. In *DARPA Image Understanding Workshop*, pages 121–130, 1981.
- [WC79] P. Waldteufel and H. Corbin. On the analysis of single-doppler radar data. *Journal of Applied Meteorology*, 18:532–542, 1979.

DYNAMICAL STRUCTURE OF TROPICAL CYCLONES REVEALED BY ATMOSPHERIC RADARS

Shoichiro Fukao¹, Michihiro Teshiba², and Yoshiaki Shibagaki³

¹Fukui University of Technology, Fukui, Japan,

²Weathernews Inc., Chiba, Japan, and

³Osaka Electro-Communication University, Osaka, Japan

1. Introduction

Tropical cyclone (TC) is known by different names in different parts of the world; hurricane in the North America, cyclone in Bangladesh, Pakistan, India and Australia, and typhoon in the western Pacific and Japan Archipelago.

Typhoon is born in the western Pacific, approaches to Japan Archipelago, and becomes typhoon when the wind speed exceeds 17 m/s. It grows, becomes matured, and decays to subtropical cyclone (e.g., Jorgensen, 1984a, b). A typhoon in mature stage typically has a warm and dry “eye” and clear spiral shape of clouds (e.g., Jordan, 1961; Franklin et al., 1988). As the TC decays, the atmosphere within the eye becomes moist and both eye and spiral structure decay (Kossin and Eastin, 2001). In this paper, we review the dynamical structure of the eye and eyewall of typhoons revealed with single atmospheric radar (wind profiler) or a part of its operational network in Japan.

2. Observations of TC eye structure

TC eye used to be considered to have the structure where warm and dry air descends from the lower stratosphere, and is stable with a remarkable inversion level in the lower troposphere. As the TC weakens, the inversion level ascends and the air within the eye becomes moist. The atmospheric radar (wind profiler) is one of the most suitable tools for observations of TC eye, since the air is too dry to observe with weather radar. We utilized the data from the MU radar of Kyoto University (Shibagaki et al., 2003), and WINDAS, a wind profiler network operated by Japan Meteorological Agency (JMA), composing of thirty-one 1.3-GHz wind profilers deployed all over Japan (Teshiba et al., 2004, 2005).

3. TC eye structure at the mature stage

On August 7-8, 2003, a mature Typhoon 0310 (Etau) passed right above the WINDAS profiler at Naze, Okinawa (28.38°N, 129.5°E; Teshiba et al., 2005). The closest approach to the profiler was about 3 km at 2130 LT. The central pressure was 950 hPa at 2100 LT. The horizontal distribution of precipitations was monitored by the operational weather radar of JMA. A circular eyewall was formed with about 50 km radius. The eye diameter decreased and eyewall developed as the TC approached. Even after the TC passed the profiler, the TC eye still

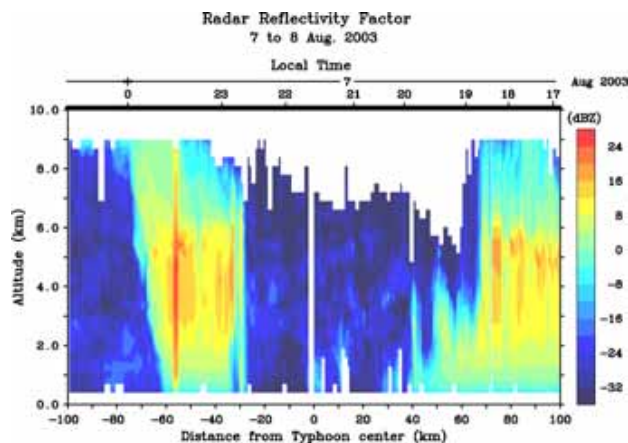


Figure 1. Radius-height cross section of radar reflectivity factor observed with the vertical beam of the Naze wind profiler (Teshiba et al., 2005).

remained in almost circular shape (Teshiba et al., 2005).

It is assumed that typhoon shape does not change significantly while translation and that the translation velocity is approximated by the mean velocity of TC eye and does not change with height. Then, the wind velocity associated with TC structure is estimated by subtracting translation velocity of TC from the observed wind, and separated into tangential and radial wind components. By assuming that typhoon shape does not change much, we can read the time axis as the horizontal distance along the TC path. No echo was found within 40 km in distance as shown in Figure 1. On the other hand, strong echo regions associated with the eyewall and the spiral rainbands were asymmetric, located at more than 30 km on the front side and from 40 to 70 km on the rear side. The cloud tops in the eyewall went up to 17 km according to the satellite observation. Echo top in the eye was a minimum of 6 km on the front side and a maximum of 9 km on the rear side. This weak echo region should be associated with the dry-air region.

Strong cyclonic wind was observed in the eyewall, especially, on the front side as shown in Figure 2. Inside the eyewall, the cyclonic wind suddenly weakened, preserving a clear cylindrical wind structure of the eyewall. In Figure 3, Doppler velocity observed with the vertical beam in the TC eye is indicated. Alternating relatively large (about 1 m/s) updraft and downdraft were dominated above 2 km height within the eye. The updraft did not form clouds and precipitation.

According to the upper-soundings made twice near the wind profiler, relatively unstable and saturated layers existed below 3 km height when the TC approached at 1530 LT. On the other hand, stable and dry air was found above them at 2100 LT when the TC was right above the profiler. The average vertical velocity and the radial wind component were more or less on naught inside the eyewall.

This result shows that the relatively stable layers where the level of free convection was high existed above 3 km height in the eye. Therefore, strong updrafts did not create clouds and rainfall in the eye. Regarding the no-echo region with the wind profiler above 6 km in height seems to be associated with the dry air. Dry air is considered to come from the upper troposphere and the lower stratosphere. If the dry air was located close to the precipitating clouds, the atmosphere around the clouds became unstable because it was cooled by the evaporation of rain. Since the dry air was provided to the lower layer on the front side,

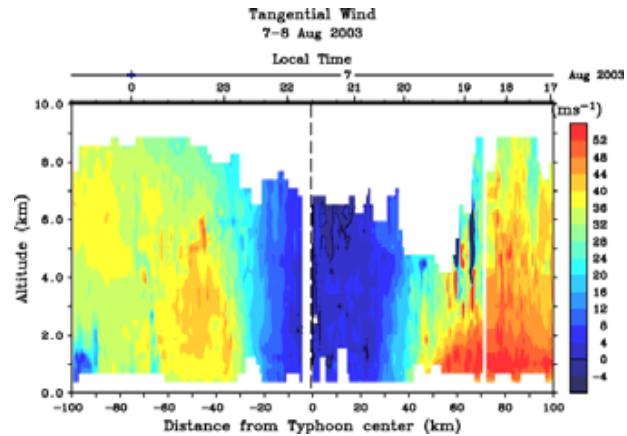


Figure 2. Same as Figure 1 except for the tangential wind component. Positive (negative) wind indicates cyclonic (anti-cyclonic) wind relative to the TC center (Teshiba et al., 2005).

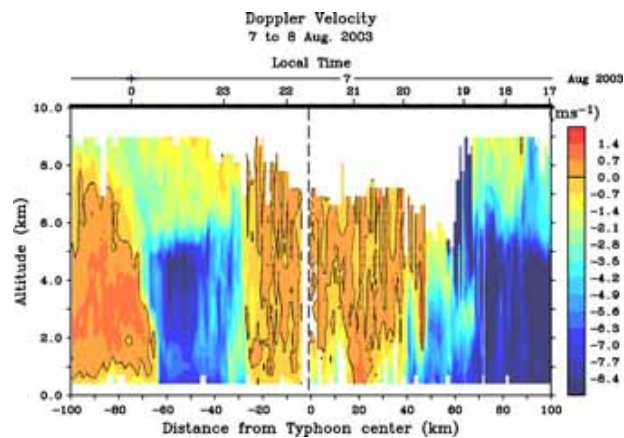


Figure 3. Same as Figure 1 except for the vertical wind component. Positive (negative) value indicates leaving (approaching) the wind profiler (Teshiba et al., 2005).

precipitation would develop on the front side as a result. The reason for the difference between the front and rear sides of the TC needs to be examined further. Figure 4 schematically shows the typhoon eye in the mature stage.

4. TC eye structure in the decay stage

Passage of Typhoon 9426 in the decay stage was observed above the MU radar in September 1994 (Shibagaki et al., 2003). In the last 25 years since its completion, it was indeed only one golden opportunity for the MU radar to observe the TC eye right overhead.

The equivalent potential temperature had a funnel-shaped structure near the TC eye that was typical of warm cores but the structure was limited only to the middle and upper troposphere. The TC was already decayed considerably. The T_{BB} of GMS IR data associated with this TC clearly illustrated that active cloud regions were located near the TC eye and on the southeastern side of the typhoon. The horizontal wind vector beautifully changes from southeast to west or southwest with time (Figure 5). However, no clear eye was seen.

There are several points worth mentioning about the decaying typhoon. First as expected, counter-clockwise rotation was dominant in the troposphere, while clockwise rotation was

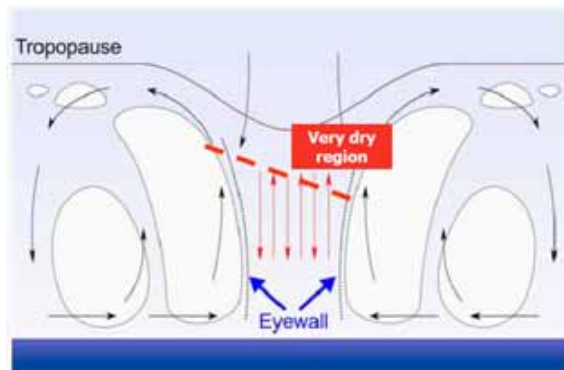


Figure 4. Schematic for wind structure of TC in the mature stage.

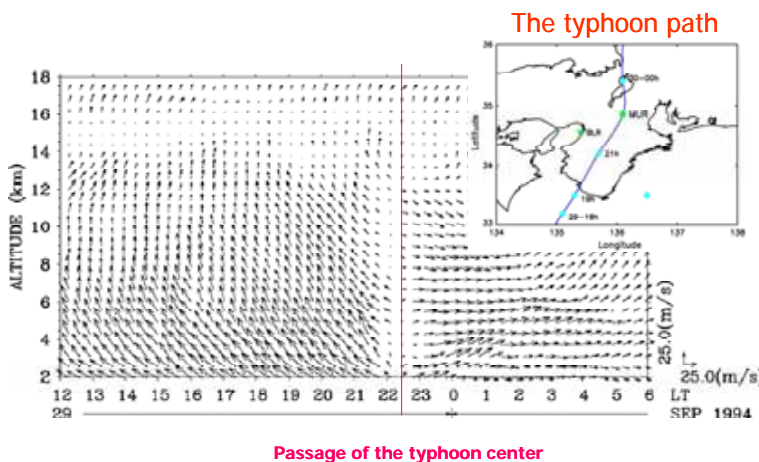


Figure 5. Height-time cross section of horizontal wind vector observed during passage of Typhoon 9426 over the MU radar on 29-30 September 1994.

5. Secondary circulation near the eye of TC decaying to an extra-tropical cyclone

Finally, a TC was observed by five profilers of the WINDAS network near Tokyo on October 1, 2002 (Teshiba et al., 2004). The minimum central pressure was 960 hPa. The composite of tangential wind averaged from the five profiler data showed that the cyclonic wind was prominent at 150 km distance and 2 km height. On the other hand, the radial wind became axi-symmetric; a strong inflow was prominent below 2 km height on the front side and an outflow above 3 km height. Both the outflow and inflow resulted from the secondary circulation of a tropical cyclone caused by the friction of the surface. On the rear side outflow was predominant in almost all heights. This asymmetric circulation is considered typical for

observed near the tropopause heights. Second, the structure was asymmetric between the front and rear sides. However, it will be most interesting to note that the tangential wind profile near the TC eye became winding or in a spiral shape with height. This suggests that the typhoon eye became winding in the decay stage as schematically illustrated in Figure 6.

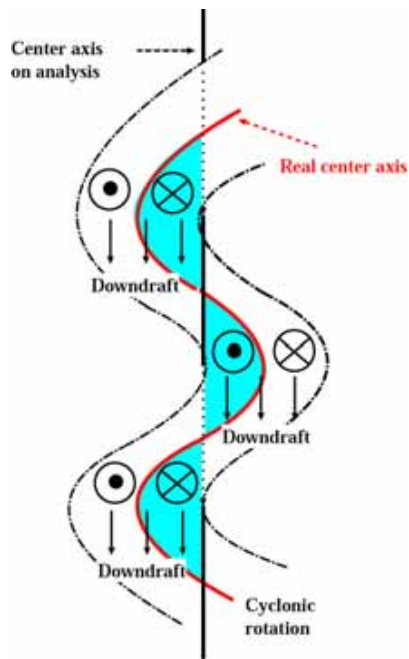


Figure 6. A schematic of winding eyewall of TC in the decay stage.

TC in the decay stage to an extratropical cyclone.

6. Conclusions

Detailed wind behavior in and near TC eyes has been studied with atmospheric radars (wind profilers) and the following results have been obtained: First, alternating updraft/downdraft existed in the dry and stable middle troposphere in the mature stage but no precipitation was accompanied. Secondly, a very dry air existed above the middle troposphere on its front side at the mature stage, possibly intensifying the rainfall. Thirdly, the tangential wind near decaying TC eye had a vertical spiral structure. Finally, the secondary radial circulation with an axi-asymmetric radial structure was detected with strong inflow in the lower height region and outflow above it.

Readers are referred to Teshiba et al. (2004, 2005) and Shibagaki et al. (2003) for more details.

REFERENCES

- Franklin, J. L., S. J. Lord, and F. D. Marks Jr., Dropwindsonde and radar observations of the eye of Hurricane Gloria, *Mon. Weather Rev.*, *116*, 1237-1244, 1988.
- Jordan, C. L., Marked changes in the characteristics of the eye of intense typhoons between the deepening and filling stages, *J. Meteorol.*, *18*, 779-789, 1961.
- Jorgensen, D. P., Mesoscale and convective-scale characteristics of mature hurricanes, Part I: General observations by research aircraft, *J. Atmos. Sci.*, *41*, 1268-1285, 1984a.
- Jorgensen, D. P., Mesoscale and convective-scale characteristics of mature hurricanes, Part II: Inner core structure of hurricane Allen (1980), *J. Atmos. Sci.*, *41*, 1287-1311, 1984b.
- Kossin, J. P., and M. D. Eastin, Two distinct regimes in the kinematic and thermodynamics structure of the Hurricane eye and eyewall, *J. Atmos. Sci.*, *58*, 1079-1090, 2001.
- Shibagaki, Y., M. D. Yamanaka, M. Kita-Fukase, H. Hashiguchi, Y. Maekawa, and S. Fukao, Meso- α -scale wind field and precipitating clouds in Typhoon 9426 (Orchid) Observed by the MU Radar, *J. Meteor. Soc. Japan*, *81*, 211-228, 2003.
- Teshiba, M., M. D. Yamanaka, H. Hashiguchi, Y. Shibagaki, Y. Ohno, and S. Fukao, Secondary circulation within a tropical cyclone observed with L-band wind profilers, *Ann. Geophys.*, *22*, 3951-3958, 2004.
- Teshiba, T., H. Fujita, H. Hashiguchi, Y. Shibagaki, M. D. Yamanaka, and S. Fukao, Detailed structure within a tropical cyclone "eye," *Geophys. Res. Lett.*, *32*, L24805, doi:10.1029/2005GL023242, 2005.

DETECTING AND TRACKING SEVERE STORMS IN 3D DOPPLER RADAR IMAGES

Robert E. Mercer, John L. Barron
 {mercero,barron}@csd.uwo.ca
 Dept. of Computer Science
 University of Western Ontario
 London, Ontario, Canada, N6A 5B7

Paul Joe
 Paul.Joe@ec.gc.ca
 King City Radar Station
 Meteorological Service of Canada
 Toronto, Ontario, Canada, M3H 5T4

Abstract: We describe our project for detecting and tracking severe weather in Doppler radar datasets. This 3D detection and tracking algorithm is posed in a relaxation labelling framework using compatibility functions that are based on the notions of fuzzy storms and fuzzy algebra using 3D reflectivity and radial velocity data: (1) the Doppler reflectivity data is used to detect and track storms as deformable 3D objects and (2) the Doppler radial velocity data to compute 3D optical flow to predict a 3D storm’s inter-frame motion.

Keywords: Severe Weather Storm Detection and Tracking, 3D Doppler Reflectivity (Precipitation Density), 3D Radial Velocity, Relaxation Labelling, 3D Fuzzy Algebra, 3D Optical Flow via Least Squares and Regularization

1 Introduction

We use both 3D Doppler reflectivity (precipitation density) [MBCB02] and radial velocity [BMCJ05] data to detect and track storms in a relaxation labelling framework using a “fuzzy” algebra [MBCB02]. We first present fuzzy algebra and fuzzy storms in Section 2, then present the calculation of 3D optical flow from radial velocities in Section 3, next present the relaxation labelling algorithm that integrates this data via compatibility factors in Section 4 and finally present some experimental results in Section 5.

2 3D Fuzzy Storms

Severe weather storms are not rigid and therefore can’t be tracked using their center of masses or contour outlines. Our tracking algorithm uses the notion of “fuzzy” storms to capture the uncertainty in a storm’s location.

Our storm detection program groups connected sets of precipitation reflectivity voxels above a threshold (30dBZ here) into potential storms using a floodfill algorithm. Each voxel has coordinates denoted as (x_1, x_2, x_3) with (μ_1, μ_2, μ_3) denoting the center of mass of a storm. We treat each set of 3D Doppler storm voxels as a 3D multivariate normal distribution [DHS02] and compute a 3×3 covariance matrix Σ (symmetric positive and semi-definite), where the $(i, j)^{th}$ element, σ_{ij} , is computed as:

$$\sigma_{ij} = \sqrt{\frac{\sum_{x_i, x_j \in R} (x_i - \mu_i)(x_j - \mu_j)}{|R| - 1}}, \quad (1)$$

where $|R|$ is the number of storm voxels in the ellipsoid. We compute the eigenvalues, λ_i , and the corresponding eigenvectors, \hat{e}_i of Σ and use each eigenvector as one of the ellipsoid axes and $\sqrt{\lambda_i}$ as the corresponding radii. We use these ellipsoids to represent hypothesised fuzzy storms in the 3D Doppler precipitation reflectivity data.

The definitions for ellipsoidal fuzzy algebra are basically the same as for spherical fuzzy algebra [MBCB02], except where changes are needed when ellipsoids instead of spheres are used.

Definition 1. A **3D fuzzy point** $E\langle c, r \rangle$ is defined as an ellipsoid with center $c = (x, y, z)$, three radii $r = (r_x, r_y, r_z)$ and three mutually orthogonal direction vectors $e = (\hat{e}_x, \hat{e}_y, \hat{e}_z)$.

The point can be anywhere in the ellipsoid including the center. Two fuzzy points $E_1\langle c_1, r_1, e_1 \rangle$ and $E_2\langle c_2, r_2, e_2 \rangle$ are identical if and only if $c_1 = c_2, r_{x_1} = r_{x_2}, r_{y_1} = r_{y_2}, r_{z_1} = r_{z_2}, e_{x_1} = e_{x_2}, e_{y_1} = e_{y_2}$ and $e_{z_1} = e_{z_2}$.

Definition 2. A **fuzzy vector** from a fuzzy point E_1 to another fuzzy point E_2 is defined as the infinite set of all displacement vectors from points in E_1 to points in E_2 , see [MBCB02].

Definition 3. The **fuzzy length** or **fuzzy magnitude** of a fuzzy vector \vec{E} is a set of lengths or magnitudes of all vectors in \vec{E} and is defined as $\|\vec{E}\|$.

Consider two fuzzy points E_1 and $E_2 \in \mathbf{E}$ (the set of all fuzzy vectors). The displacement vector from a point in E_1 to any point in E_2 can be defined as $\overrightarrow{E_1 E_2}$ since a fuzzy point is only a set of the Euclidean points in three dimensions. The set of all such vectors is the fuzzy vector from E_1 to E_2 , i.e.

$$\overrightarrow{E_1 E_2} = \{ \overrightarrow{e_1 e_2} \mid e_1 \in E_1 \text{ and } e_2 \in E_2 \}. \quad (2)$$

with fuzzy magnitude:

$$\|\overrightarrow{E_1 E_2}\| = \{ \|\overrightarrow{e_1 e_2}\| \mid \overrightarrow{e_1 e_2} \in \overrightarrow{E_1 E_2} \}. \quad (3)$$

We can express d_{min} and d_{max} given by the variables c_1, r_1, e_1 and c_2, r_2, e_2 as:

$$d_{min} = \min \{ \|\overrightarrow{e_1 e_2}\| \mid \overrightarrow{e_1 e_2} \in \overrightarrow{E_1 E_2} \} \text{ and} \quad (4)$$

$$d_{max} = \max \{ \|\overrightarrow{e_1 e_2}\| \mid \overrightarrow{e_1 e_2} \in \overrightarrow{E_1 E_2} \}. \quad (5)$$

A fuzzy magnitude is then the interval $[d_{min}, d_{max}]$.

Definition 4. The **fuzzy angle** subtended by a non-zero fuzzy vector \vec{Q} relative to another non-zero fuzzy vector \vec{P} is defined as the set of angles subtended by any displacement vector \vec{q} in \vec{Q} relative to another displacement vector \vec{p} in \vec{P} having a touching head and tail, respectively. The set can be denoted as $\langle \vec{P}, \vec{Q} \rangle_\theta$.

Consider the three fuzzy points: $E_1 = \langle c_1, r_1, e_1 \rangle, E_2 = \langle c_2, r_2, e_2 \rangle$ and $E_3 = \langle c_3, r_3, e_3 \rangle$. We can pick any point e_1 in E_1, e_2 in E_2 and e_3 in E_3 to form a pair of displacement vectors $\overrightarrow{e_1 e_2}$ and $\overrightarrow{e_2 e_3}$. The angle between these two vectors can be calculated by the dot product of the two vectors:

$$\cos \theta = \frac{\overrightarrow{e_1 e_2} \cdot \overrightarrow{e_2 e_3}}{\|\overrightarrow{e_1 e_2}\|_2 \|\overrightarrow{e_2 e_3}\|_2}. \quad (6)$$

We can define the minimum and maximum angles as: $\theta_{min} = \min \langle \overrightarrow{E_1 E_2}, \overrightarrow{E_2 E_3} \rangle_\theta$ and $\theta_{max} = \max \langle \overrightarrow{E_1 E_2}, \overrightarrow{E_2 E_3} \rangle_\theta$. The fuzzy angle is then the interval $[\theta_{min}, \theta_{max}]$.

We currently compute the fuzzy distances and angles by brute force; we just enumerate all distances and angles between the voxels in the ellipsoids.

3 3D Optical Flow

Our approach for computing 3D Least Squares and 3D Regularized optic flow follow the 2D optical flow methods proposed by Lucas and Kanade and Horn and Schunck [BFB94].

We use a 3D Lucas and Kanade like least squares calculation by using a radial velocity constraint equation $\vec{V} \cdot \hat{r} = V_r$ (the radial velocity is the projected 3D velocity $\vec{V} = (U, V, W)$ in the radial direction at each voxel) and assuming constant local velocity, to obtain a $n \times n \times n$ linear system of equations (at each voxel \hat{r} and V_r are usually different but \vec{V} is always the same) to compute the least square velocity, \vec{V}_{ls} at each voxel [BMCJ05].

We then use a 3H Horn and Schunck like regularization to obtain a smooth full velocity field that is close to the true full velocity and roughly satisfies the radial motion constraint at each voxel and is similar to the least squares \vec{V}_{ls} at that voxel. The regularization term is:

$$\int \int \int \underbrace{(\vec{V} \cdot \hat{r} - V_r)^2}_{\text{Radial Velocity Constraint}} + \alpha^2 \underbrace{(U_X^2 + U_Y^2 + U_Z^2 + V_X^2 + V_Y^2 + V_Z^2 + W_X^2 + W_Y^2 + W_Z^2)}_{\text{Smoothness Constraint}} + \underbrace{\beta^2((U - U_{ls})^2 + (V - V_{ls})^2 + (W - W_{ls})^2)}_{\text{Least Squares Velocity Consistency Constraint}} \partial X \partial Y \partial Z, \quad (7)$$

where $U_X, U_Y, U_Z, V_X, V_Y, V_Z, W_X, W_Y$ and W_Z are the 1st order velocity derivatives along the X, Y and Z dimensions. We used the Gauss Seidel method on the Euler-Lagrange equations of Equation (7) to minimal this functional [BMCJ05].

4 3D Tracking via Relaxation Labelling

Fuzzy storms are then tracked over time using an incremental relaxation labelling algorithm with compatibility factors that use fuzzy storm quantities and 3D optical flow. We used a modified version of Barnard and Thompson's relaxation labelling algorithm [BT80], that uses spatio-temporal smoothness constraints. We added *property coherence* to the algorithm which allows multiple properties of a storm (and not just disparities) to be tracked over times [MBCB02]. The storm properties used are: **size, magnitude displacement, angle, orientation** and **velocity**. Given hypothesized storms along a potential storm track we defined functions (using our fuzzy algebra) to specify how similar a storm's size, displacement magnitude, displacement angles (in 3 adjacent frames), ellipsoid orientation and center of mass velocity are to other storms. The total compatibility between two adjacent potential storms is computed using a weighted sum of these factors. These weight values are determined empirically. Two adjacent disparities are connected together if their compatibility value is greater than a threshold. When all qualified adjacent disparities have been linked together, the certainty of each disparity is refined iteratively by a relaxation labelling algorithm [BT80] that uses both supporting and contradictory evidence provided by the overall compatibility among its adjacent disparities [MBCB02].

5 Experimental Results

Each NEXRADI dataset consists of 15 elevations of precipitation density (reflectivity) and radial velocity of moving precipitation reflectivity data. At each elevation the data consists of 360 rays of reflectivity/radial velocity data (1 ray for each degree of a circle) and each

ray consists of 600 individual reflectivity and radial velocity values. We present results for detecting and tracking storms in the 3D Doppler reflectivity data that was collected at the Kurnell Radar Station in Australia at intervals of 10 minutes on 1999 September 16. The name of each image file gives the date and time of the image. Figure 1 shows an oblong storm, represented as ellipsoidal fuzzy storms tracked in 4 images from this dataset. The vectors are the optical flow vectors at the storm’s center of mass. We show that the predicted storm (via the center of mass velocity) and the actual storm in the next image overlapped by 90% or more [BMCJ05].

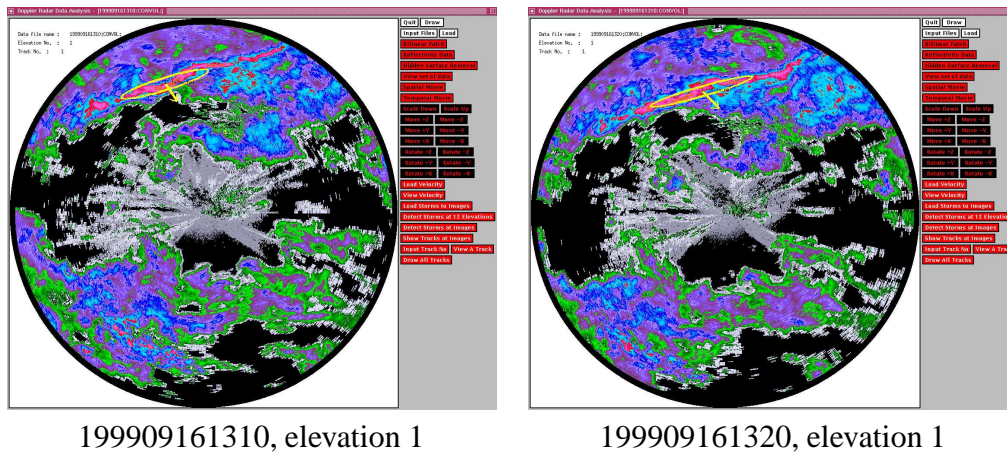


Figure 1: Velocity vectors (in yellow) at the center of mass of the second storm in 2 adjacent reflectivity images.

Figure 1 shows that the center of mass velocity points the direction of the storm’s displacement between 2 adjacent storm. Similar tracking results show that the other properties (even without velocity) produce correct tracking results for all the data we have [MBCB02].

6 Conclusions and Future Work

We have shown an effective tracking algorithm that uses relaxation labelling to track a number of storm properties, including size, length, angle, orientation and velocity displacement. Current work includes tracking storms among overlapping Doppler radars, integrating Wind-profiler and overlapping Doppler data together and detecting hook echoes (maybe indicating tornadoes) in severe weather events.

References

- [BFB94] J.L. Barron, D.J. Fleet, and S.S. Beauchemin. Performance of optical flow techniques. *Int. Journal of Computer Vision*, 12:43–77, 1994.
- [BMCJ05] J.L. Barron, R.E. Mercer, X. Chen, and P. Joe. 3d velocity fields from 3d doppler radial velocity. *Intl. Journal of Imaging Systems and Technology*, 15(3):189–198, 2005.
- [BT80] S. T. Barnard and W. B. Thompson. “Disparity analysis of images”. *IEEE Trans. Pattern Analysis and Machine Analysis*, 2(4):333–340, 1980.
- [DHS02] R.O. Duda, P.E. Hart, and D.G. Stork. *Pattern Classification*. John Wiley and Sons, 2nd edition, 2002.
- [MBCB02] R.E. Mercer, J.L. Barron, D. Cheng, and A. Bruen. Fuzzy points: Algebra and application. *Pattern Recognition (PR2002)*, 35(5):1153–1166, May 2002.

Identifying Monsoon Dynamics Using Wind Profiler

Srinivasa Rao Vanukuru¹, M. P. Rao² and M. C. R. Kalapureddy³

¹ Department of Physics, Govt. College (A), Rajahmundry-533105. (draoavs@gmail.com)

² Department of Physics, Andhra University, Visakhapatnam-530003. (raomp17@rediffmail.com)

³ Indian Institute of Tropical Meteorology, Pune (madhuchandra@tropmet.res.in)

1. Introduction

Monsoon is a synoptic phenomenon, which needs proper understanding for predicting the variability of the Indian monsoon rainfall. The monsoon is strongly coupled to the warm oceans surrounding the subcontinent. There are monsoon related phenomena whose associations are very much prominent in deciding the vigor of monsoon. Two such phenomena are Low-Level Jet (LLJ) and Tropical Easterly Jet (TEJ). TEJ is a strong cross-equatorial, synoptic-scale boreal summer monsoon induced atmospheric jet streams at 150 hPa over tropical India [Mokashi, 1974]. The other jet stream (LLJ) occurs at 850hPa. LLJ is another strong cross-equatorial, synoptic-scale boreal-summer SW monsoon induced atmospheric jet stream [Joseph and Raman, 1966; Findlater, 1966, 1967; Desai et al., 1976].

Onset of the summer monsoon has been defined by various methods. Using rain gauge data, Ananthkrishnan and Soman [1988] defined the onset of ISM based on Kerala rainfall during which the rainfall amounts increase to over 15 mm per day. Fasullo and Webster [2003] defined the ISM onset and withdrawal by vertically integrated moisture transport over the Arabian Sea. Flatau et al. [2001] defined double onset or bogus onset of ISM based on a conceptual model. Prasad and Hayashi [2005] studied onset in terms of Zonal asymmetric temperature anomaly between 850 hPa and 200 hPa with NCEP/NCAR reanalysis data. Taniguchi and Koike [2006] defined onset based on wind speed exceeding 8 ms⁻¹ at 850 hPa using NCEP/NCAR reanalysis data. Several investigators found interesting features during evolution of numerous parameters related to the monsoon activity. Wind profiler's Observations reveals the potential of wind profiling radars in identifying the various phases associated with monsoon (onset, active, weak, break and withdrawal) rather solely. In the present study UHF wind profiler (UWP) enables us to observe monsoon progress using the wind and other radar parameters.

2. EXPERIMENTAL TECHNIQUE

In India the only 400 MHz wind profiler system now available was developed by Society for Applied Microwave Electronics Engineering & Research (SAMEER) in 2001 under sponsorship of Department of Science and Technology, Government of India. The system is situated at Pashan campus of India Meteorology Department (IMD) in Pune and is being regularly operated as an R & D unit since June 2003. The Pune UWP configured has a typical height coverage up to 6-10 km (depending on the weather conditions) with a resolution of 300 m for wind and 2-3 km for temperature measurement. The system consists of a dual polarized coaxial collinear antenna array made out of low loss dielectric RF coaxial cable of 7/8" size, operating at 404.37 MHz with a peak power aperture product of 3.6×10^4 W-m² [Pant et al., 2005]. The two polarized arrays are aligned along true N-S and E-W directions respectively. The receiver is a heterodyne type and consists of a blanking switch, Low Noise Amplifier (LNA), RF

amplifier chain, Mixer and band pass filters. Local Oscillator (LO) signals required for the receiver operation are derived from exciter subsystem. During first stage the LO frequency (404.37-IF) is mixed to get IF (Intermediate frequency) output which is filtered and amplified using IF amplifier. In second stage a quadrature mixer is used to recover the base band in I and Q channels. This is subsequently passed through a low pass filter and Video amplifier and then fed to two independent ADC channels. Output of ADC goes to processor where time domain processing takes place. Coded signal is first decoded in the processor and then subjected to coherent integrations. The pre-processed data is then given to FFT processor and the host computer for further frequency domain analysis. More details of the hardware are described by [Chande et al. 2000].

3. Results and Discussion

The UWP observation on all three wind components in the height region, 1.05-6.45 km, has been used for the period May 2004 to May 2006. This data has processed to ensure its quality and continuity. Moreover, only clear air observations are chosen for the present study. The figure 1. shows the Height Time Intensity (HTI) maps on observed dynamical parameters, zonal, meridional and vertical wind, wind speed and direction. Nearly every 6 minutes interval height profiles in each hour are averaged and hourly profiles of all dynamical parameters for all clear air period are used. It can be seen strong zonal wind (U) of magnitude around 15 m/s observed during monsoon, June-September.

These strong positive zonal winds indicate they are originating from west of the observation site. During the rest of the seasons zonal winds magnitudes are weak i.e., ± 5 m/s. These low level strong zonal winds in the height region of 2-4 km and its magnitude falls either side of the height region named as Low Level Jet (LLJ) [Joseph and Raman, 1969]. It is also observed that during monsoon season itself, there are strong and weak spells in observed zonal winds, zonal wind magnitudes respectively around 15 m/s and ± 5 m/s. These strong positive zonal winds indicate they are originating from west of the observation site. During the rest of the seasons zonal winds magnitudes are weak i.e., ± 5 m/s. These low level strong zonal winds in the height region of 2-4 km and its magnitude falls either side of the height region named as Low Level Jet (LLJ) [Joseph and Raman, 1969]:

It is also observed that during monsoon season itself, there are strong and weak spells in observed zonal winds, zonal wind magnitudes respectively around 15 m/s and ± 5 m/s. In general, the meridional wind (V) is noticed to be meager and southerly (positive). During winter and pre-monsoon southerlies are observed in the lower levels, below 2 km. whereas, during monsoon, meridional winds are scanty whenever zonal winds are strong. The vertical wind (W) shows strong updrafts (positive) in the lower level, below 2 km, indicating convective activity associated with atmospheric boundary layer (ABL). This convective activity is observed to be strong and frequent during around monsoon season. The wind speed (WS) has arrived from zonal and meridional wind. During monsoon, WS essentially shows the same features as zonal wind do. It indicates the dominance of zonal wind over meridional wind during monsoon. Few couple of strong WS spells observed during June and July 2004 and July and August 2005 have been observed to be correlated with active monsoon spells. The weak spells in between are indication of break monsoon spells.

The wind direction (WD) shows clear westerlies/north westerlies during monsoon and rest of the seasons it is easterly. It is observed that winds are easterlies during break monsoon. In order to identify the active and break monsoon spells solely from UWP, zonal winds and wind direction has examined. It is well aware that monsoon winds are westerly, i.e., dominance of zonal wind, around 15 m/s, with wind direction around 270° [Joseph and Sijikumar, 2004]. Hence, daily mean zonal wind and wind direction during monsoon has plotted for the years 2004 and 2005 in figure 2.

Daily average zonal wind speed shows above 20 m/s with wind direction around 270° , westerly, identified as active monsoon spell. Whereas during break monsoon spell is identified when zonal wind speed less than 5 m/s and wind direction around 90° , easterly.

This criterion has been checked with IMD reported monsoon breaks for the years 2004 and 2005 [Thapliyal *et al.*, 2005; 2006] and found good correlation as well. Hence, the UWP can identify active and break monsoon spells, which are presented in table 1.

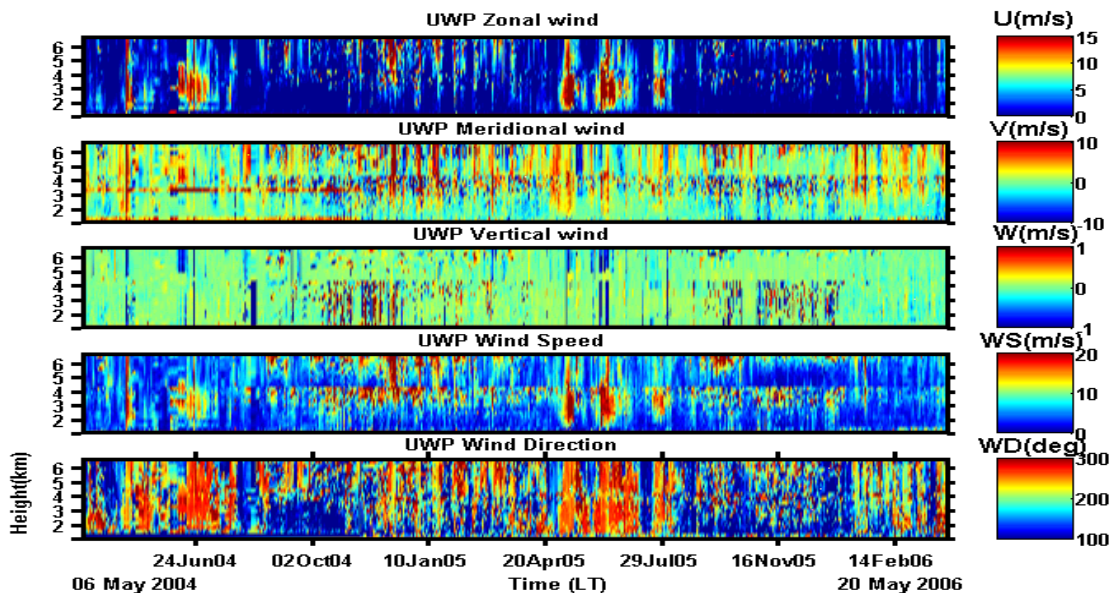


Figure 1. HTI map of Zonal, Meridional, Vertical wind, Wind Speed and Wind Direction

S. No.	Monsoon	2004		2005	
		UWP	IMD	UWP	IMD
1		---	18 July	---	30 June
2	Active	7 August	---	2 July & 26 July	---
3	Break	24 -26 July	19 – 27 July	14 August 23 August	11 – 12 August 24 – 27 August
4	Withdrawal	---	22 September	---	22 September

Table: 1 Details of monsoon periods for the years 2004 and 2005

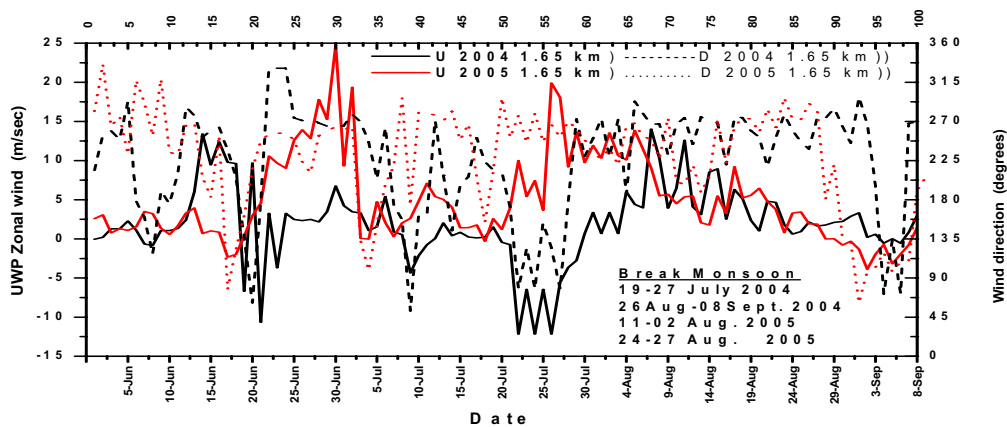


Figure 2. Daily mean zonal wind and wind direction during monsoon for 2004 and 2005

4. Conclusions:

- UWP observations during two monsoon years able to identify the various monsoon phases such as onset, active/break phases and withdrawal of Indian Summer Monsoon over observational site.
- Identified active and break spells shows significant difference in wind magnitude and direction.
- Correlating all these findings with OLR and Radar reflectivity/SNR is under investigation.

4. References

- Ananthkrishnan, R., and M. K. Soman (1988), The onset of the southwest monsoon over Kerala, *Int. J. Climatol.*, 8, 283–296.
- Chande, J.V., et. al., UHF wind profiler and radio acoustic sounding system development at SAMEER, Mumbai. 9th International Workshop on Technical and Scientific Aspects of MST Radar and MST 9 Combined with Cost 76 Final Profiler Workshop, Toulouse, France, 13-17 March 2000.
- Desai, B.N., Rangachari, N. and Subramanian, S.K., Structure of low-level jet stream over the Arabian Sea and the Peninsula as revealed by observations in June and July during the monsoon experiment (MONEX) 1973 and its probable origin. *Indian J. Meteorol. Hydrol. Geophys.*, 27, 263–274, 1976.
- Fasullo, J., and P. J. Webster (2003), A hydrological definition of Indian monsoon onset and withdrawal, *J. Clim.*, 16, 3200–3211.
- Findlater, J., Some further evidence of cross-equatorial jet streams at low level over Kenya. *Meteorological Magazine*, 95, 353–364, 1966 & 96, 216–219, 1967.
- Flatau, M. K., P. J. Flatau, and D. Rudnick (2001), The dynamics of double monsoon onsets, *J. Clim.*, 14, 4130–4146.
- Joseph, P.V. and Raman, P.L., Existence of low-level westerly jet stream over peninsular India during July. *Ind. J. Met. Geophys.*, 17, 407–410, 1966.
- Joseph, P.V. and Sijkumar, S., Intra-seasonal variability of the Low-Level Jet stream of the Asian summer monsoon. *J. Climate*, 17, 1449–1458, 2004.
- Mokashi, R.Y., The axis of the tropical easterly jet stream over India and Ceylone. *Indian J. Met. Geophys.*, 25(1), 55–68, 1974.
- Thapliyal, V., Desai, D. S. and Krishnan, V., Weather in India-Monsoon season (June-September, 2004). *Mausam*, 56 (3), pp.739, 2005.
- Thapliyal, V., Desai, D. S. and Krishnan, V., Weather in India-Monsoon season (June-September, 2005). *Mausam*, 57 (3), pp.546, 2006.

MESO- γ -SCALE CONVECTIVE SYSTEMS OBSERVED BY A 443 MHz WIND-PROFILING RADAR WITH RASS IN THE OKINAWA SUBTROPICAL REGIONS

Aya Mikami¹, Jun-ichi Furumoto¹, Toshitaka Tsuda¹,
Shinsuke Satoh², Seiji Nagai², Yasuhiro Murayama²,
Takuya Kawabata³

¹ Research Institute for Sustainable Humanosphere, Kyoto University, JAPAN

² National Institute of Information and Communications Technology, JAPAN

³ Meteorological Research Institute, Japan Meteorological Agency, JAPAN

1. Introduction.

In the atmospheric disturbances in connection with a cyclic process of water and energy, perturbations with different horizontal scales are mutually related, and they make a hierarchic structure. A meso-scale convective system (hereafter, abbreviated as MCS) is a typical example of the hierarchical meteorological phenomenon. Around Japan the MCS appears in a Baiu front, winter cloud bands over the Japan Sea, a small low pressure and a summer thunderstorm. Ninomiya and Akiyama (1992) clarified the hierarchic structure of the multiplex scales of the precipitation system in the Baiu front. They pointed out that the cloud cluster has a hierarchic structure ranging from meso- α to meso- γ scales, further, interaction between two or more scales plays an important role for development and maintenance of a precipitation system.

Okinawa is situated under a subtropical oceanic climate, and a warm ocean current flow through the surrounding ocean. The climate of Okinawa is characterized by high temperature and high humidity throughout a year. The behavior of MCS over Okinawa under a relatively quiet condition has been studied by several studies. For example, Akaeda et al. (1991) showed the evolution process and the fine structure during the formative to mature stages of the meso- β -scale convective system, on the basis of observations with a Doppler radar in Naha on June 6, 1987. Chuan et al. (1991) performed a two-dimensional numerical simulation about the convective system for the case observed in Akaeda et al. (1991), and showed the key generating factor of a convective system, and motion of the system.

This paper reports a case study of the MCS with its scale smaller than those treated in the aforesaid studies focused on MCS generated over the Okinawa Island on 23 and 25 July 2007 when the area was covered with a high pressure in summer season.

This study used the high temporal and height resolution data of virtual temperature and wind velocity observed with the 443MHz wind-profiling radar (443MHz WPR) with RASS (radio acoustic sounding system), as well as the Non-Hydrostatic model (NHM) results. By taking advantage of continuous virtual temperature data with RASS, the atmospheric stability and the thermodynamics structure related to generation of a convective system are investigated. Data from surface weather chart, weather radar echo map and sounding data of the Japan Meteorological Agency (JMA) are also used in this study.

2. Outline of Rain Clouds Over the Okinawa Island.

A surface weather chart indicates that a Baiu-front existed in a wide area of Japan extending from Tohoku to northern Kyushu. However, the Okinawa area was covered by the Pacific high throughout 21-26 July 2007 with its center located south of Okinawa. On 23 July and 25 July, a developed cloud passed through the radar site located in the northern Okinawa.

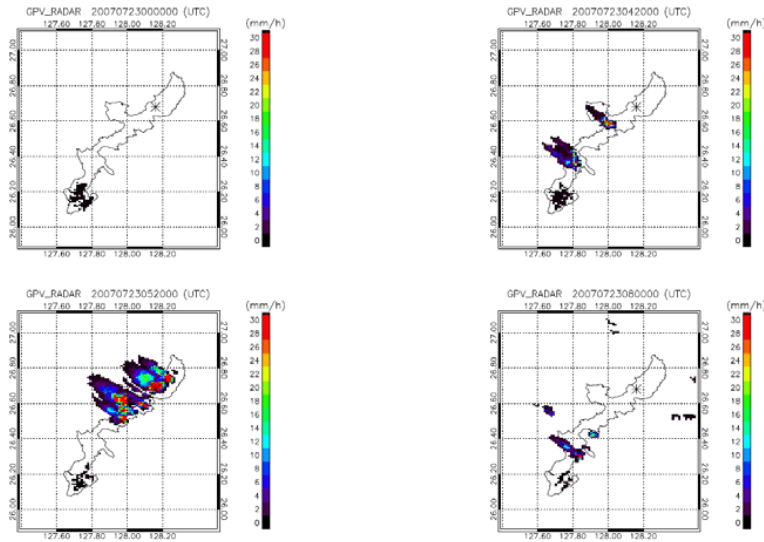


Figure 1. Precipitation rate from an operational weather radar by JMA on 23 July 2007. The asterisk indicates the location of the Ogimi radar site.

These two cases on 23 and 25 July show an overall similarity. A weak rain cloud first occurred in the southern Okinawa during the morning. During the daytime, many convective systems were generated in all over Okinawa island. All rain cloud disappeared at night after 19:00 LT.

Here, the characteristics of convective clouds appeared on 23 July are described in detail. The weak rain cloud with the precipitation rate of 1.0 mm/hr was generated only near Naha at 0700 - 1050 LT. During 1100 - 1730 LT the convective system with more than 30.0 mm/hr with the horizontal and temporal scale of 10 km and 40 - 60 minutes, respectively was generated all over the Okinawa island (Figure 1).

Using the data of NHM forecast at the radar site, Lifting Condensation Level (LCL), Level of Free Convection (LFC), Convective Available Potential Energy (CAPE), and Convective Inhibition (CIN) are estimated to 194.4 m and 1110.0 m, 1245.2 J/kg, and 2.0 J/kg, respectively. These values suggest that the background condition tended to generate convections easily.

3. Static Stability Structure before the Development of Convective System

Variations of the detailed time-height structure of atmospheric static stability were investigated during generation and development process of a convective system on 23 and 25 July 2007 over the Ogimi radar site. For the precise estimation of Brunt-Väisälä frequency squared in moist but unsaturated air, the virtual temperature (T_v) should be used instead of T^2 . This study used N^2 calculated from T_v profile observed with 443MHz WPR-RASS. The forecast of NHM model are also used to compare characteristics of N^2 between the RASS and NHM results. Because no significant convective system is not seen in the NHM forecast at the radar site on 23 and 25 July, a direct comparison is not available. However, NHM forecast shows a strong convective system appeared by 15 km southwest from the radar site. Since a convective system shown in the NHM forecast has a similar precipitation characteristics to the actual convective system on 23 and 25 July, such event is compared with the observed convective system at the radar site. The NHM data at the point, where convection did not appear, are also compared to that where a convection appears.

Left panel of Figure 2 show the time height distribution of N^2 observed with RASS on 25 July, respectively. Precipitation was observed during 15:50-17:40 LT at the radar site. N^2 at the 1.3 km altitude was relatively large during 14:00 LT to 15:28 LT, but it suddenly decreased to 0.86 rad/s² at 15:28-15:32 LT, then N^2 increased again.

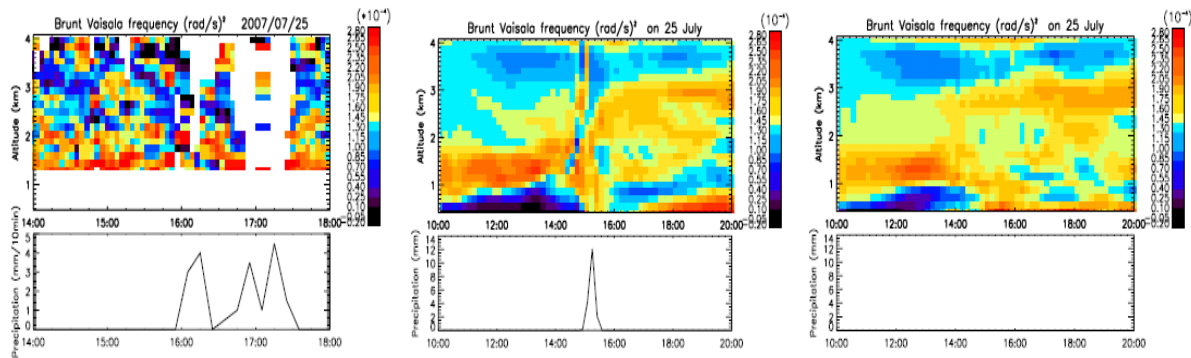


Figure 2. Time-height section of N^2 on 25 July 2007 (top panels), and time variation of precipitation rate every ten minutes (bottom panels). Left, middle and right panels show the results observed with 443MHz WPR-RASS and rain-gauge and data of NHM forecast at the place where a convective system appeared and does not appeared on 25 July, respectively.

The time-height structure of N^2 shows that the small N^2 extended toward higher altitude up to 2.0 km during 15:32-15:56 LT, which coincided with start timing of the precipitation at 15:56 LT. It is noteworthy that the similar time-height structure of N^2 was commonly seen on both 23 and 25 July, which coincided with the start of precipitation at the radar site.

Data of NHM forecast on 25 July was also investigated to generalize the relation between the structure of the static stability and the development of a convective system. Middle panel of Figure 2 shows the time height distribution of N^2 at the place where a precipitation event appeared in the NHM forecast at 14:55-15:35 LT. The negative N^2 below about 0.8 km was continuously seen from 10:00 LT to 14:30 LT, when the precipitation started. On the other hand, a stable layer at the altitude of 1.2-2.2 km was overlaid on a statically unstable layer below 0.8 km. The low static stability region sharply moves toward higher altitudes with time. This behavior in the model agrees very well with the observed one. Right panel of Figure 2 shows the time height distribution of N^2 at the point, where convection does not appeared. The general layered structure is similar to the case in the middle panel with convection. But, the development of the low stability region, which moved upward, did not appear. The decrease of the static stability and its extension along altitude is generally recognized before precipitation, and this fact strongly suggests this upward propagation of low stability region is important characteristics in the development of a convective system. Since this structure coincides with the cloud top in the NHM forecast data, we consider that decreases of the static stability near a cloud top is caused by the increase of T_v inside of the cloud. Moreover, a cloud develops up to high altitude because of unstable condition near the cloud top.

4. Generation Mechanism of a Convective Systems

Figure 3 shows the time height distribution of the perturbations of T_v and vertical wind velocity (w) observed with the 443MHz WPR-RASS on 25 July. Surface temperature at the radar site (T_s) is also plotted. T_s increased during 0600LT and 1000LT due to solar insolation. Although after 1000LT decrease of T_v was observed at 1.0-2.5 km, T_s did not show a decrease below the daily mean temperature, but short time scale perturbations are recognized. T_v in the lowest height region gradually increased, which is generally consistent with the T_s increase after a sunrise. However, after 1000LT, T_v decreased in the lowest layer at 1.0 - 2.5 km altitude.

Before the precipitation, w was violently fluctuated with short time scales, which seemed to occur by an inflow of the air with low T_v from southeast. During 1000-1400 LT, the upward winds became suppressed near the top of low T_v atmosphere. However, after

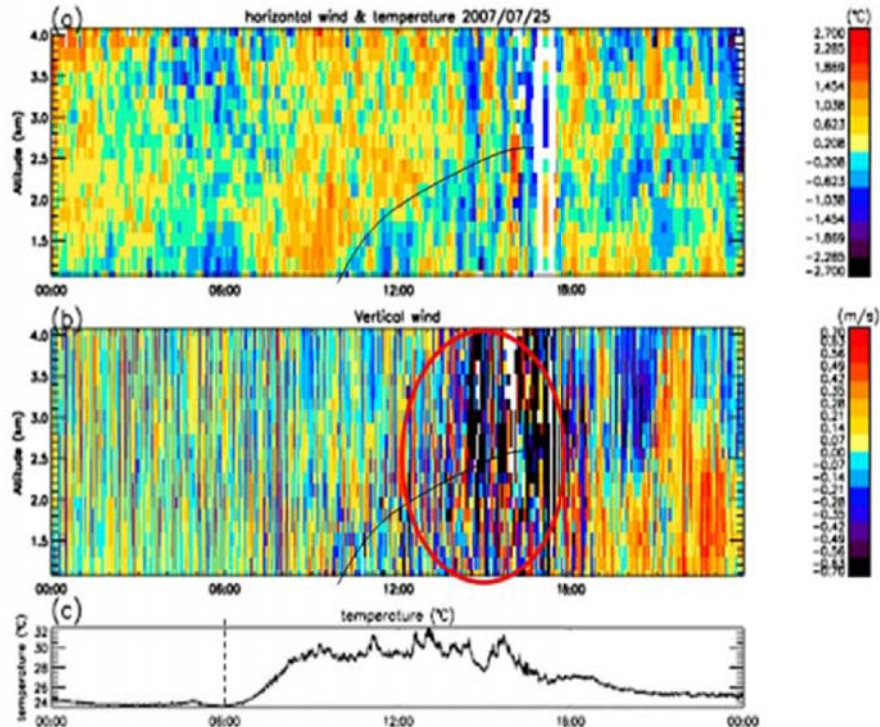


Figure 3. Time-height distribution of (a) the perturbation of T_v and (b) the vertical wind velocity observed by the 443MHz WPR, respectively, and (c) the temporal variation of the temperature observed on the ground at the radar site on 25 July.

1400LT the w fluctuations became stronger and it reached over the top height of low T_v atmosphere.

Sea Breeze Circulation (SBC) was examined through the analysis of NHM forecast. The sea breeze flowed into a surface layer from the neighboring sea on both sides of the island, and SBC already began earlier on the east coast from 1000LT. After 1100LT, SBC also started at the west coast, and convergence began to appear in a lower layer at the same time. As the sea breeze on the west coast invaded deeply, a convergence region moves toward the inland side. After 1130 LT, because of the sea breeze from both coasts collided on the land, the value of convergence became large, and the vertical wind also became stronger. The air with high temperature and high-humidity in the lower layer was lifted by the upward wind caused by the convergence. The large convective clouds seem to be generated after this air mass reached LCL. The synergetic effect of low static stability and the convergence triggered the generation of convective systems, which eventually grew up to 11 km over the radar site.

Bibliography

Akaeda, K., T. Yokoyama, A. Tabata, M. Ishihara, and H. Sakakibara: Evolution of kinematic structure within a meso- β -scale convective system in the growing and mature stages, *Mon. Wea. Rev.*, 119, 2664-2676, 1991.

Chang, C.Y., and M. Yoshizaki: Numerical study of the mesoscale convective system observed over the Okinawa island in June 1987, *Mon. Wea. Rev.*, 119, 2724-2733, 1991.

Ninomiya, K., and T. Akiyama: Multi-scale features of Baiu, the summer monsoon over Japan and the East Asia, *J. Meteor. Soc. Jpn.*, 70, No.1B 467-495, 1992.

MODELLING THE OUTER SCALE OF TURBULENCE TO IMPROVE TEMPERATURE PROFILE MEASUREMENTS WITH A VHF RADAR

Vladislav Klaus

Météo-France, CNRM-GAME, Toulouse, France

1. Abstract

VHF-radar echo power allows an estimation of the square of the Brunt-Vaisala frequency (N^2) in layers where humidity is small, typically above 4 km height in middle latitudes (Hooper et al. 2004). By integrating N^2 , the temperature (T) profile can be derived, provided a reference point is available (Revathy et al., 1996, Klaus, 2008). To solve the equations, the value of the outer scale of turbulence (L_0) must be known.

L_0 has been diversely estimated: As a nearly constant value (VanZandt et al., 1978, Fukao et al., 1994), with large time and height variations (Muschinski, 1997, Eaton and Nastrom, 1998), depending on N^2 (Gage et al., 1980), and deduced from the statistical model of Cn^2 by VanZandt et al. [1981]. Here we investigate the model of L_0 which improves the best the T profile determination with the VHF radar.

The two-month MAP Campaign data set, including continuous working of the INSU/Météo 45 MHz radar and daily radio soundings has been used to validate the technique.

2. Introduction

There exist various methods to extract temperature information from ST radar measurements. They can be summarized in Fig. 1.

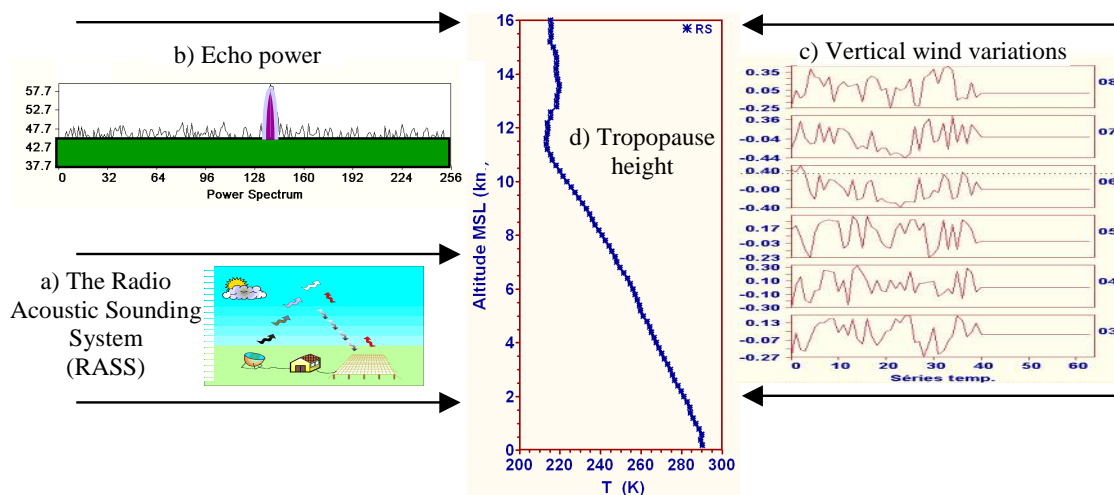


Figure 1. The various methods to extract temperature information from ST radar measurements.

The Radio Acoustic Sounding System (RASS) (Fig. 1a) capabilities to measure virtual temperature profiles using a wind profiler have already been widely attested (Adachi et al. 1993, Angevine et al. 1994, May et al. 1989, Peters, 2000, Klaus et al. 1998). This technology, involving acoustic transmission in the atmosphere is quite accurate and efficient

in all weather conditions. Its limitations are the noise pollution and the height coverage reduction due to the advection of the acoustic waves by the wind.

To complement the temperature profile above the range covered by the RASS, other possibilities can be exploited with VHF radars by evaluating the Brunt-Väisälä frequency (N) and integrating the equation provided a reference value is known at a given altitude inside the radar range.

When humidity is negligible, in the upper troposphere, one simple way consists in extracting these data directly from the echo spectral power (Fig. 1b). The dry term of the refractive index gradient M is calculated from the signal-to-noise ratio of the radar (VanZandt et al. 1978, Gage and Balsley 1980) and temperature is deduced from the general equation relating M to atmospheric parameters.

Provided the horizontal wind is not too strong, the B-V frequency can be deduced by measuring the variations of the vertical wind velocity (W) at high time resolution of about 1 min, as has already been attested (Ecklund et al. 1985, Röttger 1985, Revathy et al. 1996) (Fig. 1c). However, longer series of vertical profiles are needed, which prevent during this time a normal functioning as a wind profiler.

Finally, the tropopause height has been investigated by comparing several methods (Sweezy and Westwater, 1986) (Fig. 1d). This is also an important information for determining accurate temperature profile around 10 km height.

In this study, the echo power technique (b) will be brought into focus. In order to evaluate the practical capabilities and limits of this technique, tests have been conducted with the INSU/Météo 45 MHz instrument during the Mesoscale Alpine Project (MAP) cooperative campaign in the region of Milano (Italy) in 1999 (Bougeault et al. 2001). A two-month data set of controlled VHF radar measurements were available, completed with around one hundred radio soundings (RS).

3. Theoretical background

The radar reflectivity η includes information on temperature and humidity, mainly their gradients. In altitudes where humidity is present, these informations are mixed, which prevents any possibility to extract any of these two parameters if no further information is available. Assuming temperature profile is known, humidity can be derived in lower troposphere, as has been demonstrated in various experiments (Tsuda et al., 2001, Stankov et al., 2003, Klaus et al., 2006). By contrast, in the upper troposphere where humidity gets negligible, temperature factors predominate.

The radar backscatter η is related to the structure constant of refractive index Cn^2 and the radar wave length λ as follows:

$$\eta = 0.38 \lambda^{-1/3} C_n^2 \quad (1)$$

Cn^2 is related to the outer scale of turbulence L_0 , and the gradient of the refractive index M (VanZandt et al., 1978): $C_n^2 = 2.8 L_0^{4/3} M^2$ (2)

where L_0 is the outer scale length of the turbulence spectrum, η is the radar reflectivity extracted from the echo power intensity (VanZandt et al. 1978, Gage and Balsley 1980), and λ is the radar wavelength..

Eq. 1 and 2 allows to express M directly from radar reflectivity η as:

$$|M| = 0.97 L_0^{-2/3} \lambda^{1/6} \eta^{1/2} \quad (3)$$

M is related to atmospheric parameters, pressure P , Temperature T , specific humidity q , its vertical gradient dq/dz , the Brunt-Vaisala frequency N , and to the gravity acceleration g :

with
$$M = -77.6 \times 10^{-6} \frac{P}{T} \left[\frac{N^2}{g} \left(1 + 15600 \frac{q}{T} \right) - \frac{7800}{T} \frac{dq}{dz} \right] \quad (4)$$

which reduces to the dry term when humidity is negligible:
$$M_D \approx -77.6 \times 10^{-6} \frac{P}{T} \frac{N^2}{g} \quad (5)$$

Then, N^2 is deduced from the combination of Eq. 3 and 5:

$$N^2 = 1.25 \times 10^4 g \frac{T}{P} L_0^{-2/3} \lambda^{1/6} \eta^{1/2} \quad (6)$$

Capability to deduce by this way N from ST radar measurements has already been assessed (Hooper et al., 2004). In this study, we focus on the possibility to extract temperature information from the upper troposphere where humidity is negligible.

From N^2 , temperature profile can be obtained, provided a reference point is known, as has already been applied for example by Revathy et al. [1996] and Klaus [2008].

Knowing that:
$$N^2 = g \frac{d \ln \theta}{dz} = \frac{g}{\theta} \frac{d\theta}{dz} = \frac{g}{T} \left(\frac{dT}{dz} + \Gamma \right) \quad (7)$$

potential temperature θ can easily be calculated:

$$\theta(z) = \theta(z_0) \exp \left[\int_{z_0}^z \frac{N^2(z')}{g} dz' \right] \quad (8)$$

In the same way, absolute temperature can be integrated after removing g and multiplying the second and third members in Eq. 7 by T/θ :

$$\frac{1}{\theta} \frac{dT}{dz} - \frac{T}{\theta^2} \frac{d\theta}{dz} = \frac{dT/\theta}{dz} = -\frac{\Gamma}{\theta} \quad (9)$$

which gives:
$$T(z) = \theta(z) \left[\frac{T(z_0)}{\theta(z_0)} - \Gamma \int_{z_0}^z \frac{dz'}{\theta(z')} \right] \quad (10)$$

In conclusion, a good estimation of N^2 allows retrieval of the potential temperature and then of the absolute temperature profile, provided a reference point is available.

4. Discussion

Eq. 6 shows that 3 terms must be correctly evaluated for an accurate estimation of N^2 vis T/P , L_0 , and η .

4.1 - T/P is inversely proportional to density and may be approximated as (Hooper et al. (2004),

$$\frac{T}{P} = \frac{T_0}{P_0} \exp \left(\frac{(z - z_0)}{\bar{H}} \right) \quad (11)$$

where P_0 and T_0 are the pressure and temperature respectively at the reference level z_0 , and \bar{H} is the mean scale height across the whole altitude range. Slight variations of \bar{H} between troposphere and stratosphere will need to implement a statistical curve. Experiment has shown that variations are sufficiently small above 5 km height, allowing a single function model to be used for all cases with a fair accuracy (Klaus, 2008).

If P profile is known, a mathematical algorithm could be implemented by including T as the variable to solve. In such a case, the temperature is deduced from the resolution of a different equation:

Writing :

$$T = \theta \left(\frac{P}{1000} \right)^{Ra/Cpa} \quad (12)$$

Eq. 6 and 7 finally gives:

$$\frac{1}{\theta^2} \frac{d\theta}{dz} = 1737 P^{Ra/Cpa-1} L_0^{-2/3} \lambda^{1/6} \eta^{1/2} \quad (13)$$

and by integration:

$$\frac{1}{\theta} = \frac{1}{\theta_0} - 1737 \lambda^{1/6} \int_{z_0}^z P^{Ra/Cpa-1} L_0^{-2/3} \eta^{1/2} dz \quad (14)$$

Then absolute temperature can easily be computed from Eq. 12.

4.2 - η may not be correctly estimated due to difficulties to calibrate the radar properly and the possible fluctuations of the radar performances with time. Consequently, η is only estimated through a multiplication constant to be evaluated from validation with radio soundings or by using two temperature reference points.

4.3 - L_0 needs a particular investigation as no consensus has been found in the literature about its value. A review on the subject has been made (Hooper et al., 2004) and the few specific measurements of this parameter which have been performed have confirmed large variations both in time and altitude, based on the classical expression relating turbulence dissipation rate ε to the wind shear S and L_0 (Tatarskii, 1971).

$$\varepsilon = L_0^2 S^3 \quad (15)$$

Fig. 2a: shows a 4-year statistics with a 49.5 MHz radar using Eq. 15 with data extracted from the radar (Eaton and Nastrom, 1998). Fig. 2b and 3c gives the details of L_0 profile extracted from Eq. 2 with Cn^2 measured with the 53.5 MHz SOUSY radar and M with radio soundings (Muschinski, 1997). Moreover, in this last study, a possible correlation with N^2 (Gage et al., 1980) has been confirmed from experience as shown on Fig. 2c.

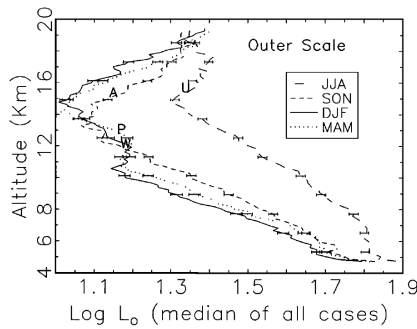


Figure 2a: 5-year statistics of L_0 profile using the 49.5 MHz radar at Missile Range and Eq. 13 (Eaton and Nastrom, 1998).

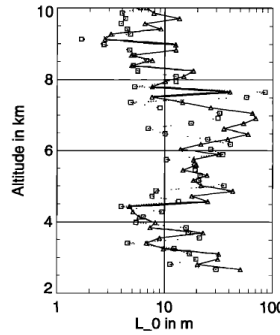


Figure 2b - L_0 profile during a warm front using the SOUSY radar and Eq. 14 with Cn^2 (radar) and M^2 (RS) (Muschinski, 1997)

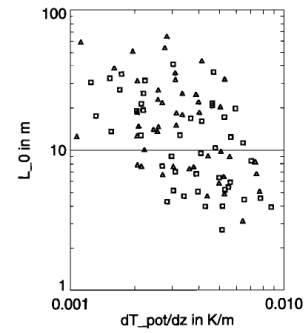


Figure 2c - Scatterplot of L_0 versus N^2 (Muschinski, 1997)

In this study, we investigate, which model of L_0 is best suited for the extraction of the temperature profile. Due to limited space, we shall focus on the extraction of the potential temperature (Eq. 8) by using 4 models of L_0 :

- L_0 constant, for example 10 m, as suggested by VanZandt et al. [1978]
- L_0 extracted from Eq. 15
- Climatologic L_0 , representing the mean value of all the L_0 profiles giving the same N^2 as the radio sounding (Eq. 11) where η is deduced from the radar and all other parameters from the radio soundings.
- Climatologic $L_0 N^2$, same as above, after multiplying L_0 by N^2 .

In all these cases, Eq. 6 will be used with P/T extracted directly from the radio soundings. In a second step, the same calculations will be performed, first by modeling P/T as mentioned above (4.1) and then by assuming P to be known, and using consequently Eq. 14 instead of Eq. 6.

In order to remove any calibration uncertainty of the radar, a multiplication variable α will be introduced in Eq. 6. Consequently two temperature reference points will be used, one for integrating Eq. 6, the second one for solving this variable. In practical application, this assumption may be based on the availability of temperature data at the top of the RASS profile at about 5 km height and at higher altitudes provided by the commercial aircrafts in the AMDAR network (Klaus, 2008).

$$\text{Eq. 6 thus becomes: } N^2 = K g \frac{T}{P} L_0^{-2/3} (\alpha \eta)^{1/2} \quad (16)$$

$$\text{with } K = 1.25 \times 10^4 \lambda^{1/6} \alpha^{1/2} \quad (17)$$

Assuming potential temperatures θ_0 and θ_1 are known at heights z_0 and z_1 respectively,

$$\text{Eq. 8 can be solved: } \ln \theta = \ln \theta_0 + K \int_{z_0}^z \frac{T}{P} L_0^{-2/3} \eta^{1/2} dz' \quad (18)$$

$$\text{with: } K = \frac{\ln \theta_1 - \ln \theta_0}{\int_{z_0}^{z_1} \frac{T}{P} L_0^{-2/3} \eta^{1/2} dz'} \quad (19)$$

Then absolute temperature is calculated from Eq. 12.

5. Experimental results

5.1 Statistical values of L_0

Fig. 3 shows the statistical values of L_0 in each of the 4 cases mentioned above, computed by reference to nearly one hundred radio soundings during the MAP campaign: If every case, the standard deviation (left) and the median value (right) are shown.

Fig. 3a is just a reminder of using a constant L_0 . In this case, its value can be merged into K in Eq. 18 and 19.

Fig. 3b represents L_0 calculated from wind shear and turbulent dissipation rate (Eq. 15). Two important points can be noted:

- Confirming previous long-term studies with VHF (Easton and Nastrom, 1998), the outer scale is far from being statistically constant in altitude.

- The median values profiles are decreasing with altitude up to around 12 km height, which is located above the tropopause. This confirms previous results (Fig. 2a). However, large standard deviations show that such profile may vary considerable and as such will be a source of inaccuracies in the temperature determination.

Fig. 3c shows the value of L_0 in Eq. 6 which provides N^2 identical to the RS measurements (Eq. 7). To this purpose, T and P have been taken from RS and λ and ε from the radar data using the same data set. Here the decrease of L_0 with altitude is even more pronounced in the lower stratosphere. The standard deviation stays quite high with a relatively lower value after 12 km height.

Fig 3d shows the climatologic value of $L_0 N^2$ (with a multiplication coefficient of 10000), under the same condition as in the above case. By multiplying both members by $(N^2)^{-2/3}$, Eq. 6 becomes:

$$(N^2)^{1/3} = 1.25 \times 10^4 g \frac{T}{P} (L_0 N^2)^{-2/3} \lambda^{1/6} \eta^{1/2} \quad (20)$$

It is interesting to note that standard deviation of $L_0 N^2$ is significantly lower than in the two previous cases. The median value also shows a different pattern with practically a constant up to 6 km height, a regular gradient between 6 and 9 km and then a nearly stable level increasing very slightly in the stratosphere.

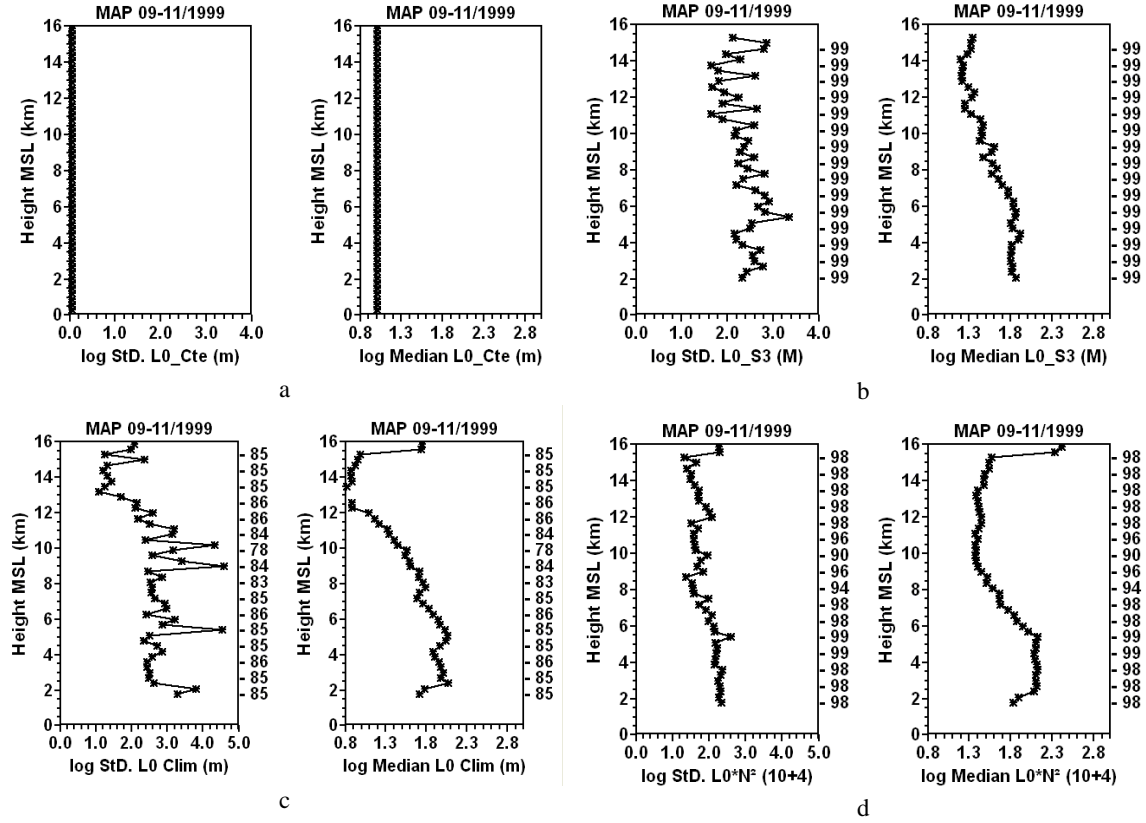


Figure 3: Standard deviation (left) and median value of L_0 (right) in log for each of the 4 cases under study: 3a: Constant value (as just a reminder), 3b: Using the Tatarskii expression with ε and S (Eq. 15), 3c: climatologic value giving for each profile N^2 identical to the radio sounding (Eq. 6), 3d: Climatologic value of $L_0 N^2$ giving for each profile $(N^2)^{1/3}$ identical to the radio sounding (Eq. 20). On the right column of each figure are indicated the total number of cases used for the statistics..

5.2 Temperature retrieval

Having obtained the 4 types of L_0 profiles through the methods above-mentioned, it was now possible to test the validity of the temperature retrieval deduced from Eq. 6 by reference to the radio soundings. The two selected reference point for temperature were located at 5 and 11 km height respectively.

A general observation for all the cases is a standard deviation between 2 and 4 K between the reference points and quite bigger values above 11 km. It may be mentioned that a previous study has shown a standard deviation of 3 K by using simple interpolation between the 2 reference points (Klaus, 2008). The bias is generally restricted under 2 K with important variations according to the case.

As already computed in the previous study a constant L_0 (Fig. 4a) brings a standard deviation of 2K and a bias reaching 2K (Fig. 4a). The bias is much more reduced by using the classical relation (Eq. 15) (Fig. 4b) and the climatologic value (Fig. 4c). In this last case, the standard deviation is the lowest. The climatologic $L_0 N^2$ does not bring any improvement,

probably due to the fact a third power expression (Eq. 20) may considerably increase inaccuracies.

Consequently, the case c) using climatologic value of L_0 provides the best estimation of temperature profile even if above the second reference point (11 km), large deviations remain.

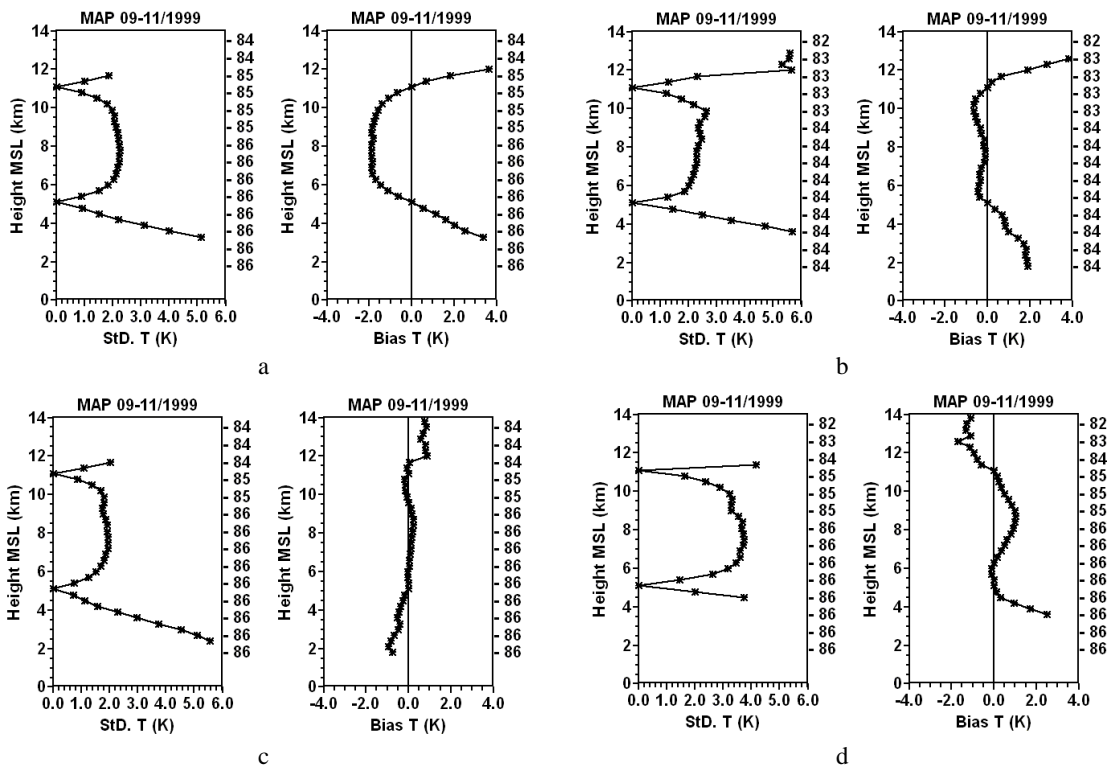


Figure 4: Standard deviation (left) and median value of T (right) using L_0 for each of the 4 cases under study: 4a: Constant L_0 , 4b: With L_0 extracted from the Tatarskii expression with ε and S (Eq. 15), 4c: climatologic value of L_0 , 4d: Climatologic value of $L_0 N^2$. On the right column of each figure are indicated the total number of cases used for the statistics..

At this point, it may be noted the relatively low performances of method b) using L_0 directly computed from radar data. In a further step, we shall crosscheck the techniques used to extract the signal width on the spectra, which serves as a basis for the calculation of the turbulence dissipation rate.

Due to large vertical variations of N^2 , the climatologic $L_0 N^2$ appears as a poor choice in spite of its relatively good time and height coherency both in standard deviation and in absolute value (Fig. 3d). In fact, the power index of the radar reflectivity η in the expression of N^2 to be integrated in Eq. 20 is $3/2$ instead of $1/2$, which implies significant rise of any inaccuracy involved in the calculation of the signal-to-noise ratio, at the basis of the calculation of η . As in the previous case, particular attention will be focused on the methodology used to extract the zeroth moment of the signal on the spectra.

At this point, climatologic value of L_0 (case c) appears as the best choice for improving the temperature measurement, at least between two reference points in the upper troposphere and stratosphere. The improvement observed by comparison with the results obtained with a constant value of L_0 (case a) is quite encouraging. However, high sensitivity in the measurement quality will need to fine-tune the accuracy of the 3 moments of the radar signal.

5.2 Examples of temperature profiles

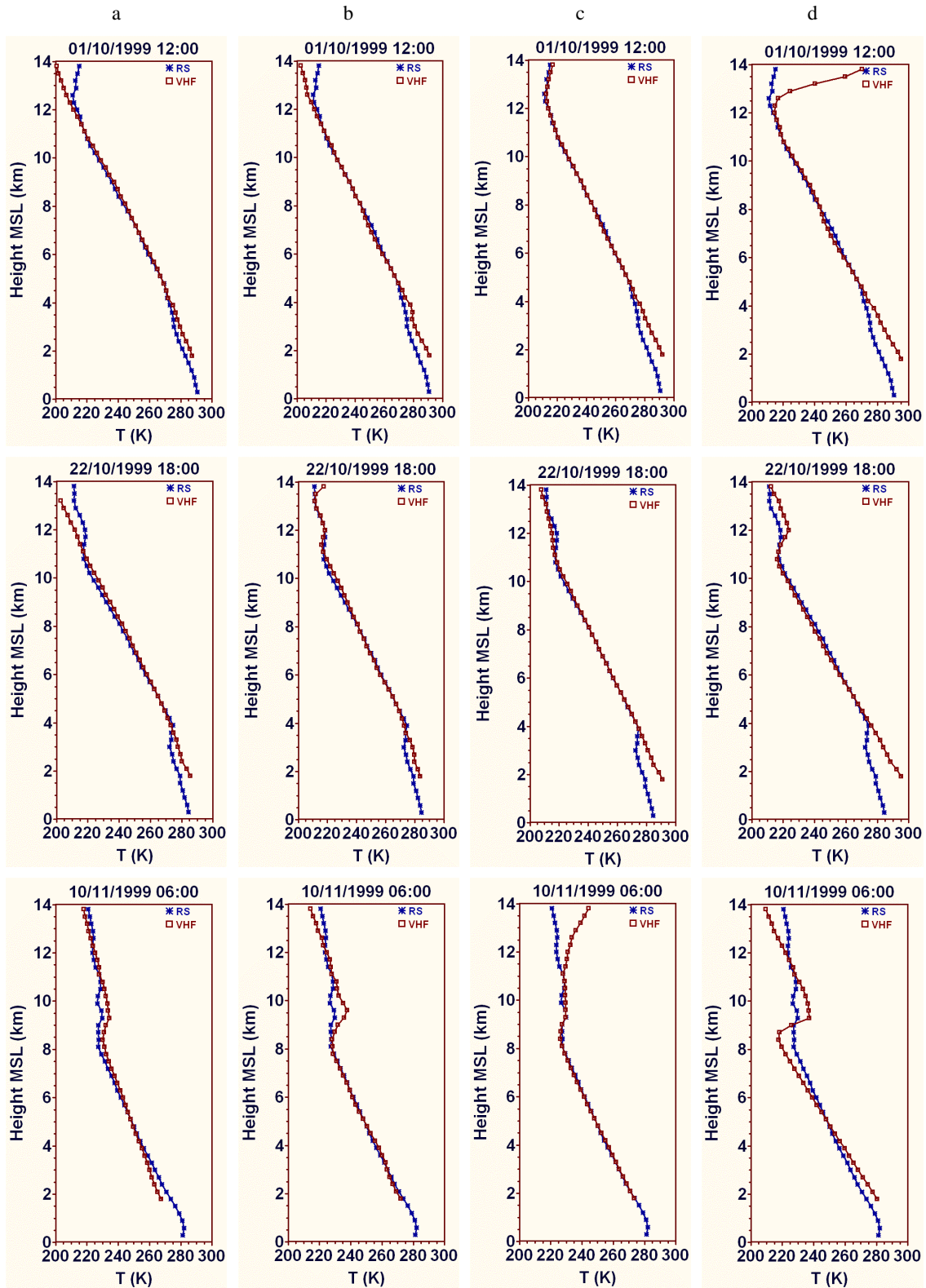


Figure 5: Examples of temperature profiles obtained by each of the above mentioned methods by comparison with radio soundings: 4a: Constant L_0 , 4b: L_0 extracted from the Tatarskii expression using ε and S (Eq. 15), 4c: climatologic value of L_0 , 4d: Climatologic value of $L_0 N^2$.

Few examples of the temperature profile retrievals using all the 4 methods are illustrated on Fig. 5 in the same order as previously with reference points at 5 and 11 km respectively. Completing the statistical results (Fig. 4), they show that even in the stratosphere, above the upper reference point, good estimation can be obtained, essentially with the b) and the c) methods.

Conclusion

In this preliminary study, several methods have been tested to improve Brunt-Vaisala frequency calculation, and consequently temperature profile retrieval at altitudes where humidity becomes negligible, using the VHF radar echo power measurements. To this purpose, attention has been focused on the time and height variations of the outer scale L_0 . Several methods have been tested, showing that improvements could be made, compared to the results obtained by just assuming a constant L_0 value in time and height.

The results have encouraged us to continue the study mainly toward the quality of the measurement of the zeroth and second moments of the signal on the radar spectra. The large sensitivity of these calculations may need higher accuracy in order to improve some of the involved methods.

Bibliography

- Adachi, T., T. Tsuda, Y. Masuda, T. Takami, S. Kato, and S. Fukao. Effects of the acoustic and radar pulse length ratio on the accuracy of Radio Acoustic Sounding System (RASS). Temperature measurements with monochromatic acoustic pulses. *Radio Sci.*, 28, 571-583, 1993.
- Angevine, W. M., W. L. Ecklund, D. A. Carter, K. S. Gage, and K. P. Moran. Improved radio acoustic sounding techniques. *J. Atmos. Oceanic Technol.*, 11, Part 1, 1994.
- Bougeault, P., P. Binder, A. Buzzi, R. Dirks, R. Houze, J. Kuettner, R. B. Smith, R. Steinacker, H. Volkert. et al.: The MAP Special Observing Period. *Bull. Amer. Meteor. Soc.*, 82, 433-462, 2001.
- Ecklund, W. L., B. B. Balsley, D. A. Carter, A. C. Riddle, M. Crochet, and R. Garello: Observations of vertical motions in the troposphere and lower stratosphere using three closely spaced ST radars. *Radio Sci.*, 20, 1196-1206, 1985.
- Eaton, F. D., and G. D. Nastrom. Preliminary estimates of the vertical profiles of inner and outer scales from White Sands Missile Range, New Mexico, VHF radar observations, *Radio Sci.*, 33(4), 895-903, 1998.
- Fukao, S., M.D. Yamanaka, N. Ao, W.K. Hocking, T. Sato, M. Yamamoto, T. Nakamura, T. Tsuda, and S. Kato. "Seasonal Variability of Vertical Eddy Diffusivity in the Middle Atmosphere 1. Three-Year Observations by the Middle and Upper Atmosphere Radar." *J. Geophys. Res.* 99, no. D9, 18973-87, 1994.
- Gage, K. S. and B. B. Balsley: On the scattering and reflection mechanisms contributing to clear air radar echoes from troposphere, stratosphere and mesosphere. *Radio Sci.*, 15, 243-257, 1980.
- Hooper, D. A., J. Arvelius, and K. Stebel: Retrieval of atmospheric static stability from MST radar return signal power. *Ann. Geophysicae*, 22, 3781-3788, 2004.
- Klaus, V., J.-P. Aubagnac, J. v. Baelen, G. Chérel, R. Durbe, and A. Frappier: New developments with the INSU/Météo VHF radar at CNRM/Toulouse: RASS, FDI and upgraded processing techniques. *Meteor. Zeit.*, NF7, 355-365, 1998.
- Klaus, V., L. Bianco, C. Gaffard, and T. Hewison: Combining UHF radar wind profiler and microwave radiometer for the estimation of atmospheric humidity profiles. *Meteor. Zeitsch.*, 15, 87-97, 2006.

- Klaus, V.,: Temperature Retrieval With VHF Radar Using Combined Techniques. *Ann. Geophys.*, 26, 3805-3817, Klaus, V., 2008.
- May, P. T., R. G. Strauch, K. P. Moran, and W. L. Ecklund: temperature soundings by RASS with wind profiler radars. *IEEE Trans. Geosci. Remote Sens.*, 28, 19-28, 1990.
- Muschinski, A., 1997: Turbulence and gravity waves in the vicinity of a midtropospheric warm front: A case study using VHF echo-intensity measurements and radiosonde data. *Radio Sci.*, 32, 1161-1178.
- Peters, G., H. Timmerman, and H. Hinzpeter: Temperature sounding in the planetary boundary layer by RASS – System analysis and results. *Int. J. Remote Sens.*, 4, 49, 63, 1983.
- Revathy, K., S. R. P. Nair, and B. V. K. Murthy: Deduction of temperature profile from MST radar observations of vertical wind. *Geophys. Res. Lett.*, 23, 285-288, 1996.
- Röttger, J.: Determination of the Brunt-Vaisala frequency from vertical velocity spectra. *Handbook for MAP*, 20, 168-172, 1985.
- Stankov, B. B., E. E. Gossard, B. L. Weber, R. J. Latatits, A. B. White, D. E. Wolfe, and D. C. Welsh: Humidity Gradient Profiles from Wind Profiling Radars Using the NOAA/ETL Advanced Signal Processing System (SPS). *J. Atmos. Oceanic Technol.*, 20, 3-22, 2003.
- Sweezy, W. B., and E. R. Westwater: A comparison of methods for determining tropopause height from VHF radar observations. *J. Atmos. Oceanic Technol.*, 3, 324-332, 1986.
- Tatarskii, V. I., Wave propagation in a turbulent medium. McGraw-Hill, 1961.
- Tatarskii, V. I. The effects of the turbulent atmosphere on wave propagation. *Israel Program for Scientific Translations*, Jerusalem, 472 p., , 1971.
- Tsuda, T., M. Miyamoto, and J. Furumoto: Estimation of a Humidity Profile Using Turbulence Echo Characteristics. *J. Atmos. Ocean. Technol.*, 18, 1214-1222, 2001.
- VanZandt, T. E., J. L. Green, K. S. Gage, and W. L. Clark: Vertical profiles of refractivity turbulence structure constant: Comparison of observation by the Sunset radar with a new theoretical model. *Radio Sci.*, 13, 819-829, 1978.
- VanZandt, T.E., K.S. Gage, and J.M. Warnock. An Improved Model for the Calculation of Profiles of C_n^2 and Epsilon in the Free Atmosphere from Background Profiles of Wind, Temperature and Humidity. *Paper presented at the 20th Radar Meteor. Conf.* 1981.

MU RADAR AND LIDAR OBSERVATIONS OF CLEAR-AIR TURBULENCE AND MAMMATUS UNDERNEATH CIRRUS

Hubert Luce, Takuji Nakamura¹, Masayuki K. Yamamoto², Mamoru Yamamoto² and Shoichiro Fukao³

LSEET, Université du Sud-Toulon Var, La Garde, France

¹Space and Upper Atmosphere Science Group, NIPR, Tokyo, Japan

²Research Institute for Sustainable Humanosphere, Kyoto University, Uji, Japan

³Department of Space Information Science and Engineering, Fukui University of Technology, Fukui, Japan

1. Introduction

In 07-08 June 2006, the MU radar (MUR) was operated in range imaging mode and monitored 0.5- to 2-km-deep turbulent layers with roll-like appearance below the altitude of 8.0 km. Coincident observations with a co-located Rayleigh/Mie/Raman (RMR) lidar showed a 4-km-deep layer of cirrus above 8.0 km. The turbulent layers were likely the result of convective currents due to cooling by sublimation of ice crystals beneath the cirrus cloud base. The RMR lidar also detected downward protruding structures at the cloud base. Downward and upward air motions measured by MUR were generated by the convective instability and very likely contributed to their formation. The cloudy protuberances can be cirrus mamma (e.g., Schultz et al., 2006). Mamma are “smooth lobe-like hanging protuberances extending downward from the base of cumulonimbus anvils and stratiform clouds like cirrus” (Glossary of Meteorology).

2. Instrumental set up

MUR was operated in Frequency radar Interferometric Imaging (FII) observational mode using the Capon method with five equally spaced frequencies from 46.0 MHz to 47.0 MHz (e.g. Hassenpflug et al., 2008). Range sampling was performed from 1.32 km up to 20.37 km ASL with a step of 5 m (the initial range resolution was 150 m). The number of coherent integrations was set equal to 32 times. One profile is calculated every ~ 10 s and the time resolution is ~ 20 s. The radar beam was steered into five positions: one vertical and four oblique directions at zenith angle of 10° off zenith toward North, East, South and West. In the present work, high resolution time-height cross sections of radar reflectivity and vertical wind velocity are described. The other parameters are shown at the initial range resolution of 150 m.

The RMR lidar was originally installed at Shigaraki MU Observatory in 2000. The system has been upgraded to have pure rotational Raman scatter detection in order to lower the observational height for temperature down to 1-2 km (Behrendt et al., 2004). The transmitter is an injection-seeded pulsed Nd:YAG laser with 532.25 nm output of 600 mJ/pulse at 50 Hz repetition frequency. The receiving telescope is a Cassegrainian telescope with a diameter of 82 cm. Received signal is divided into 5 channels, two-elastic channels for Rayleigh and Mie scatter detection, water vapor vibrational Raman channel, and two pure rotational Raman channels, and recorded by both photon counting and A/D recording. In the current study, observations were carried out with an integration time of 15 sec and a height resolution of 18 m. A Raman reference signal, i.e., a temperature independent signal proportional to molecular density, was obtained from two rotational channels, and then

backscatter ratio was calculated with signal intensities of low sensitivity elastic channel and Raman reference signal. The backscatter ratio is used as an index of clouds.

In the present work, we will show radar and lidar observation results from 2206 LT 07 June 2006 to 0236 LT 08 June 2006.

3. Results of observations

The top panel of Fig. 1 shows the time-height cross-section of RMR lidar backscatter ratio (dB). A cirrus layer was present above 8.0 km. Despite the optical attenuation, it can be seen that the cirrus cloud extended up to the altitude of 12.5 km (i.e., the tropopause), around 2205 LT and 0030 LT. Infrared (IR1) satellite images at 0200 LT 08 June 2006 over Japan confirm the presence of cirrus (not shown).

The bottom panel of Fig. 1 shows an expanded view of the backscatter ratio between 0036 LT and 0206 LT from 7.0 km to 9.0 km. Protuberances at the cloud base are particularly noticeable between 0100 LT and 0140 LT. The vertical extent of the protuberances is $\sim 0.2\text{--}0.8$ km around 0136 LT. Assuming that these structures are advected by the wind at the same speed as the cloud base (i.e., of the order of 20 m s^{-1} according to the MUR measurements and those made by a Vaisala RS90G balloon launched at 2357 LT on 07 June 2006, not shown), the horizontal extent of each protuberance is 1.0–4.0 km.

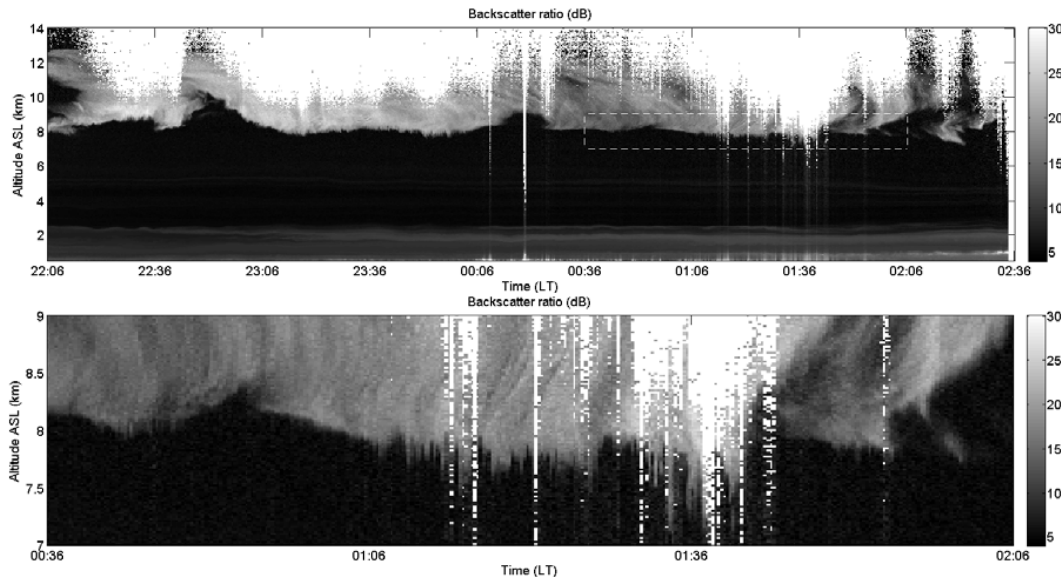


Figure 1: (Top) Time-height cross-section of RMR lidar backscatter ratio (dB) from 2206 LT 07 June 2006 to 0236 LT 08 June 2006. Optical attenuation was strong enough to cause range-limiting effects at some periods and altitudes. (Bottom) the inset in the top panel is expanded, white box in the top panel indicates inset in the bottom panel.

Figure 2 shows the time-height cross sections of radar reflectivity (dB) in arbitrary units after doing the Capon processing and after correcting the range attenuation effects using the vertical and South beams between 2200 LT and 0230 LT in the height range 6.0–9.0 km. Superimposed is the cloud base contour arbitrarily defined as the 9.54-dB level (9 in linear scale) of the lidar backscatter ratio. This level enables us to nicely delineate the cloud base irregularities. The contour also shows that the presence of cirrus affects the radar returns. Since a VHF radar is not sensitive to (small) hydrometeors but to clear air refractive index fluctuations, the effects of cirrus on radar backscattering only result from the refractive index perturbations associated with these clouds.

Figure 2 shows non aspect sensitive turbulent layers developing within and underneath the protruding structures. Their morphology suggests that they develop near the cloud base around 8 km.

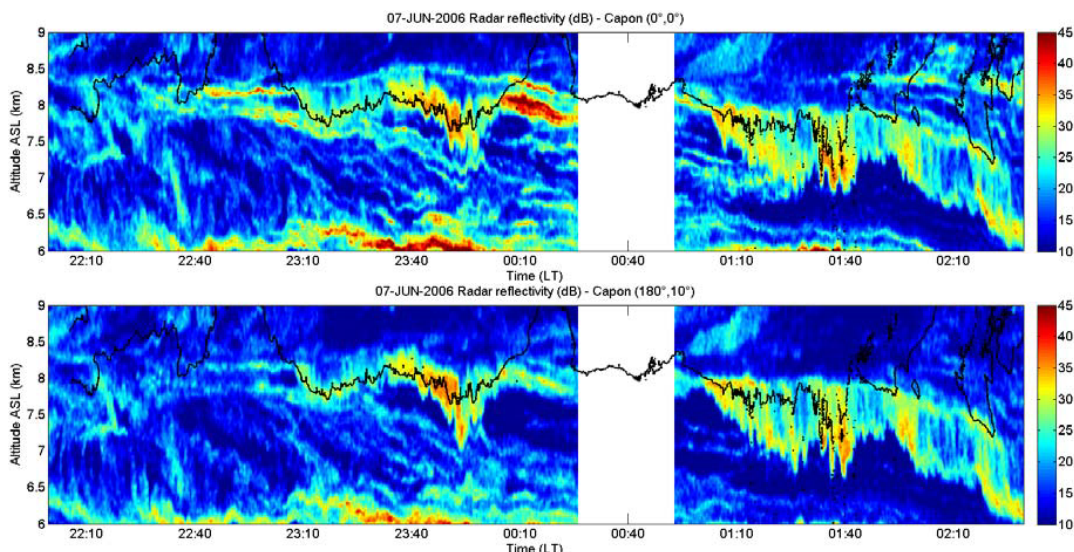


Figure 2: Time-height cross section of radar reflectivity (dB) after correcting the range attenuation effects for the period of lidar observations using the vertical beam (top) and the oblique ($180^\circ, 10^\circ$) beam (bottom). The black contour shows the cirrus cloud edges.

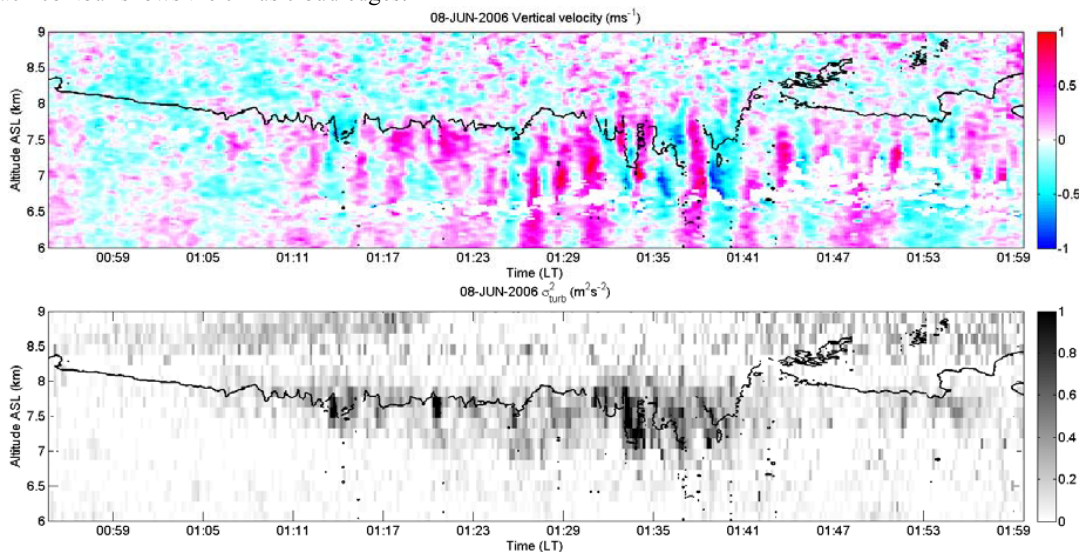


Figure 3: Expanded views of the time-height cross-section of vertical wind (ms^{-1}) (top) and σ_{turb}^2 (m^2s^{-2}) (bottom) from 0055 to 0200 LT 08 June 2006 between 6.0 km and 9.0 km. The black line contour shows the cirrus edges arbitrarily defined in the same way as defined in Fig. 2.

The bottom panel of Fig. 3 displays time-height cross sections of variance σ_{turb}^2 of Doppler spectrum from the vertical beam after correcting the non turbulent effects at a range resolution of 150 m from 0055 LT to 0200 LT. Negative values due to statistical errors have been put to zero and values for signal to noise ratios < -5 dB removed. Values of σ_{turb}^2 are maximum within the protuberances and can exceed $1 \text{ m}^2\text{s}^{-2}$.

The corresponding height-time cross-section of vertical air velocity is shown in the top panel of Fig. 3. Rapid oscillatory vertical wind disturbances are observed in the vicinity of the cloudy protuberances down to the altitude of 6.0 km (but not inside the cloud). The

downward-penetrating lobes are associated with downward air motions while updrafts of similar intensity as the downdrafts are observed between the lobes and might be associated with dry air intrusions into the cloud base.

4. Interpretation and possible mechanisms

The balloon data (not shown) revealed a differential advection of cloudy air above the subcloud layer. The wind shear was maximum at the cloud base and weak in the range of the turbulent layer indicating that a dynamical shear instability was likely not the source of the turbulent layers. The subcloud layer was very dry and weakly stable. According to e.g. Schultz et al. (2006), these conditions are conducive to an “upside-down” convective instability generated by cooling due to sublimation of ice at the cloud base. The coherent structures in the reflectivity patterns can be due to some sort of convective cells and the observed downdrafts and updrafts are likely to be a signature of convective currents spawned by the convective instability. The downdrafts may have pushed down the cloudy air and the updrafts may have pushed up the clear and dry air to form the cloud base protuberances which are possibly mamma.

Cooling by sublimation can be responsible for the convective instability (subcloud evaporation /sublimation mechanism). Sublimation can occur when ice crystals precipitate into the dry subcloud layer. When the particles begin to sublime, they cool the unsaturated layer, steepening the lapse rate. A statically unstable layer can be generated if the cooling is enough so that the clear air becomes negatively buoyant. The persistence of the turbulent layer (Figure 2) for about 90 min may indicate that the cooling of the air just underneath the cloud base was likely sufficient for sustaining the superadiabatic lapse rate and then the convective instability.

Mixing of the dry and cloudy air at the cloud base is an alternative mechanism. Mixing can result from turbulence spawn by Kelvin-Helmholtz instability or by cloud-base detrainment instability (CDI). Proposed by Emanuel (1981) in analogy with the cloud-top entrainment instability (CEI), CDI differs from the subcloud evaporation mechanism in that the ice crystals are introduced into the dry layer by spontaneous mixing at the cloud base. By mixing subsaturated and cloudy airs, sublimation takes place, air parcels become negatively buoyant and a convective instability is generated much the same way as the subcloud evaporation mechanism. CDI is relevant when cloudy air is advected over clear air because this condition is favorable to the criterion for CDI, i.e. a decrease of the liquid (ice) water static energy across the cloud base. From a practical point of view, the vertical gradient of ice- (liquid-) water virtual potential temperature θ_{iv} should be negative at the cloudy interface. Using standard values of ice crystal content for cirrus, we found that the CDI criterion ($d\theta_{iv}/dz < 0$) can be satisfied at the cloud base. CDI can thus be an alternative to subcloud sublimation mechanism and KH instability.

Bibliography

- Behrendt, A., T. Nakamura, and T. Tsuda, Combined temperature lidar for measurements in the troposphere, stratosphere, and mesosphere, *Appl. Optics*, 43, 2930-2939, 2004.
- Emanuel, K. A., A similarity theory for unsaturated downdrafts within clouds, *J. Atmos. Sci.*, 38, 1541-1557, 1981.
- Hassenpflug, G., M. Yamamoto, H. Luce, and S. Fukao, Description and demonstration of the new Middle and Upper atmosphere Radar imaging system: 1-D, 2-D, and 3-D imaging of troposphere and stratosphere, *Radio Sci*, 43, RS2013, doi:10.1029/2006RS003603, 2008
- Schultz, D. M., and Co-authors, The mysteries of mammatus clouds: Observations and formation mechanisms, *J. Atmos. Sci.*, 63, 2409-2435, 2006.

EXCHANGE PROCESSES OF ENERGY AND MATTER BETWEEN THE SURFACE AND THE ATMOSPHERE

Andrei Serafimovich¹, Stephanie Schier¹, Franz X. Meixner^{2,3}, Thomas Foken¹

¹ University of Bayreuth, Department of Micrometeorology, Bayreuth, Germany

² Max Planck Institute for Chemistry, Biogeochemistry Department, Mainz, Germany

³ University of Zimbabwe, Physics Department, Harare, Zimbabwe

1. Introduction

In a forested ecosystem low frequency coherent events contribute significantly to the transport of energy and matter and originate from dynamical instabilities of the inflected mean horizontal velocity profile (Raupach et al., 1996; Finnigan, 2000). In the frame of the EGER (ExchanGE processes in mountainous Regions) project the detailed quantification of coherent exchange between the surface and the atmosphere was investigated. To observe coherent structures, in most measuring campaigns eddy covariance systems consisting of sonic anemometer and fast response gas analyzer are used. Here micrometeorological measurements were supplemented by individual soundings by radar system to extend spatial information about the processes and to improve representativeness of the data. The other aim of this study was the observation of local wind phenomena at the site, the determination of their frequency and their relation to surrounding meteorological circumstances.

2. Experiment setup

To observe diurnal and annual cycles of energy, water and trace gases two Intensive Observation Periods (IOP) were carried out in North-Eastern Bavaria (Germany) at the Waldstein/Weidenbrunnen FLUXNET site DE-Bay in the Fichtelgebirge mountains (50° 08'N, 11° 52'E, 775 m a.s.l.). IOP1 was conducted in September and October 2007, IOP2 in June and July 2008. The experiment site is described in detail in Gerstberger et al. [2004], and a summary of background data can be found in Staudt and Foken [2007].

Observations of turbulent flows of energy and matter and their dynamics in the vegetation and lower part of the roughness sub layer were obtained by a vertical profile of ultrasonic anemometers equipped with fast carbon dioxide and water vapor analyzers installed on the 36 m tall tower. The atmospheric boundary layer was profiled with an acoustic and radioacoustic radar remote sensing system SODAR-RASS. The measurements were performed with a system consisting of a phase array Doppler SODAR DSDPA.90-64 with a 1290-MHz- RASS extension by Metek GmbH. The acoustic sounding system was located at a distance of approximately 250 m from the tower in a forest clearing. Two operating modes were used. To observe coherent structures in the vertical wind speed and temperature the sounding parameters were selected with a sufficient resolution in time (Thomas et al., 2006). The antennas were limited to the vertical and radio magnetic antennas only. The acoustic sounding frequency was chosen as 1650 Hz. The resulting mean sampling frequency of the time series was determined to be 0.4 Hz, i.e. single soundings could be performed every 2.5 s. The vertical range of measurements was from 20 m to 200 m a.g.l. Height resolution was 10 m. A 25-min interval of measurements with the settings described above was followed by the profiling of the atmospheric boundary layer for a period of 5 min up to an observation

level of 900 m, using a vertical resolution of 20 m. This gave a mean profile of the wind vector and the acoustic temperature. In contrast to IOP1, during IOP2 additionally a second SODAR (referred to as miniSODAR) without a RASS-extension was used consisting of a phased array of 64 speakers. The measurements were performed in a multi-frequency mode in which ten pulses of different frequencies from 2550 to 4850 Hz in a sequence were transmitted. The data were obtained with 5 m vertical resolution from 10 to 300 m above ground averaged for five or ten minutes. The 482 MHz UHF wind profiler (WPR) at Bayreuth operated by the German Meteorological Service (DWD) provided an averaged wind vector over the first 26 minutes of each half-hour interval up to 16500 m above ground with vertical resolution of 500 m (high mode) or up to 7560 m with vertical resolution of 250 meters (low mode). In this study only the low mode was used. The virtual temperature was measured with vertical resolution of 250 m up to 4200 m above ground.

3. Results

To derive characteristics of coherent structures from SODAR/RASS individual soundings data preparation and the wavelet analysis were used. In order to compensate for the effect of environmental noise in measurements and the discarding of erroneous data, gap filling and de-noising were applied (Miller and Rochwarger, 1970; Neff and Colter, 1986; Crescenti, 1998). In a first step, the data were filtered using the error flag output of the SODAR/RASS system. As a next step, a quality control described in Thomas et al. [2006] was applied. An example of resulting time-height cross-section of the vertical wind is presented in Figure 1 for 25-min period. The measurements show consistent updrafts and downdrafts across all observation levels.

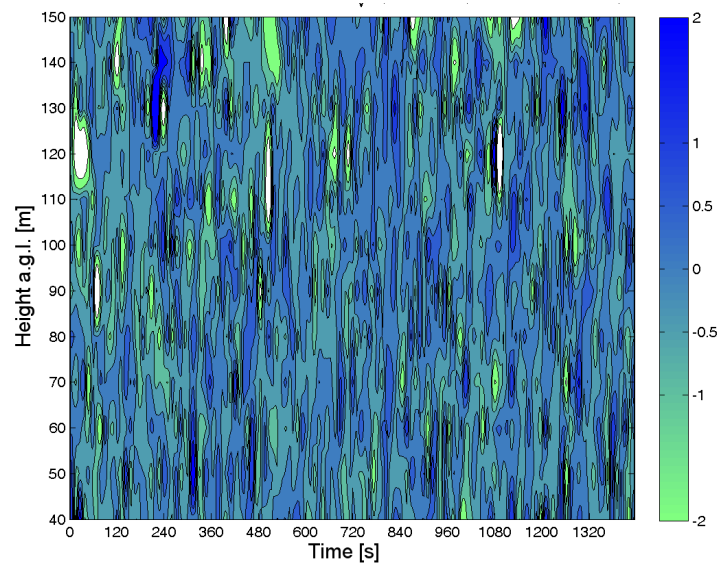


Figure 1. Time-height cross-section of the low-pass filtered and normalized vertical wind speed w_z/σ_{wz} during IOP1 September 14, 2007 00:00 – 00:25 CET.

Wavelet analysis yields the wavelet spectrum and its peak frequencies. A detailed description of the method applied is given in Thomas and Foken [2005]. The transform was performed on wavelet dilation scales a representing event durations D [Collineau and Brunet, 1993]. Corresponding to Fig. 1, an example of the spectra of wavelet variance for different observation levels is presented in Fig. 2. The data for the lower observations heights exhibit the first maximum at ~ 30 sec, whereas the observation levels above show the stronger maximum at ~ 50 -60 sec.

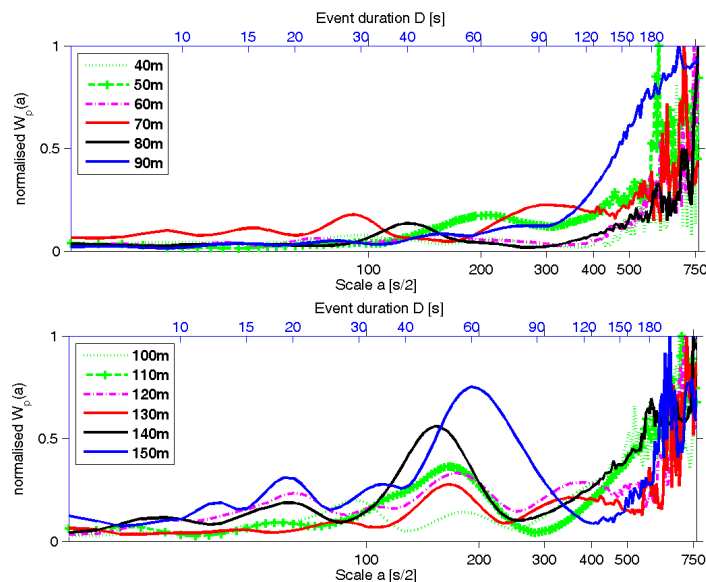


Figure 2. Spectra of the wavelet variance for different observation levels for the vertical wind during IOP1 September 14, 2007 00:00 – 00:25 CET corresponding to the cross-section presented in Fig. 1.

In contrast to temporal scales of coherent structures observed with sonic anemometers at the canopy level (Fig. 3) time scales of coherent events in the roughness sublayer observed by the SODAR/RASS system are larger and increase with height.

During both IOPs some nocturnal low-level jets (LLJ) with a duration time of several hours were observed (Fig. 4). Maximum horizontal wind speed v_{hmax} was in the range from 11.5 to 12.3 m/s for IOP1 and in the range from 8.0 to 11.6 m/s for IOP2. The height of v_{hmax} varied between 100 and 230 m a.g.l. Most of the LLJ events were characterized by an approaching flow from south-easterly directions.

Another phenomenon was observed in the profile of the wind vector. It showed a strong turn of the wind direction with increasing height (Fig. 5). At night times and during the morning hours flows above the canopy came from the east while the geostrophic wind approached from the south-westerly directions. The topography and resulting canalising effects seem to be the reason for the generation of LLJ as well as for the turn of the wind direction.

4. Conclusions

Wavelet analysis of SODAR/RASS data shows that single soundings allow observation of coherent structures in the roughness sublayer. The characteristic time scales of coherent events are larger than those in the proximity to tall plant canopies and increase with height in the roughness sublayer. Due to the influence of topography on the local wind field LLJs are observed at the measuring site, and lead to generation of shear and turbulence in the layer below. Expected influence on the concentration and mixing processes of environmentally relevant substances such as CO₂ and ozone will be a subject of future studies.

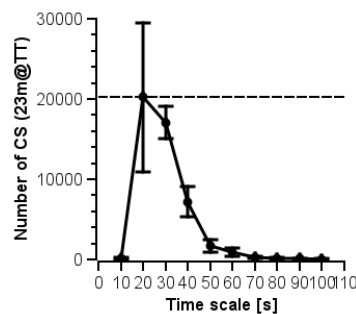


Figure 3. Temporal scales of coherent structures detected from 14.09.2007 until 08.10.2007 at 23m height.

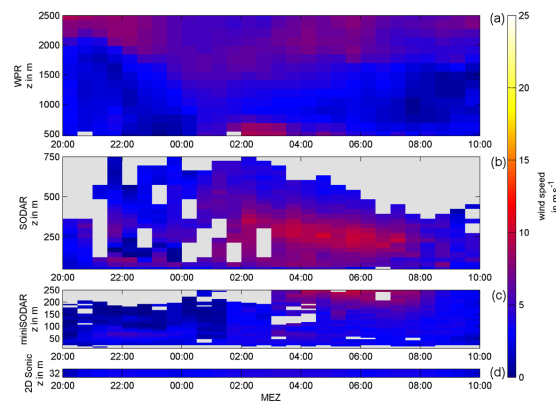


Figure 4. Time-height cross-sections of wind speed on 30.06.08 - 01.07.2008 observed with wind profiler (a), SODAR/RASS (b), miniSODAR (c) and 2D sonic anemometer installed at 32 m (d).

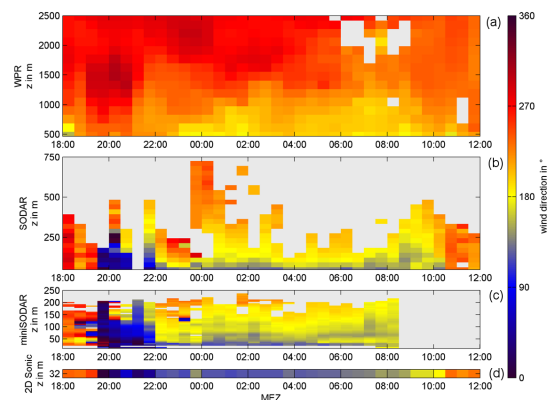


Figure 5. Time-height cross-sections of wind direction on 24.06.2008 - 25.06.2008 derived from wind profiler (a), SODAR/RASS (b), miniSODAR (c) and 2D sonic anemometer installed at 32 m (d).

5. Acknowledgment

The project is funded by the German Science Foundation (FO~226/16-1, ME2100/4-1, ZE~792/4-1). The authors wish to acknowledge the technical support performed by the staff of the Bayreuth Center for Ecology and Environmental Research (BayCEER) of the University of Bayreuth. The authors also wish to gratefully acknowledge all those who supported the field measurements, especially Lukas Siebicke, Katharina Staudt, Johannes Lüers, Johannes Olesch and Volker Lehmann for advice, comments and technical assistance.

Bibliography

- Collineau, S. and Y. Brunet, Detection of turbulent coherent motions in a forest canopy. Part I: Wavelet analysis, *Boundary-Layer Meteorol.*, 65, 357-379, 1993.
- Crescenti, G., The degradation of Doppler sodar performance due to noise: A review, *Atmos. Environ.*, 32, 1499-1509, 1998.
- Finnigan, J., Turbulence in plant canopies, *Ann. Rev. Fluid Mech.*, 32, 519-571, 2000.
- Gerstberger, P., T. Foken, and K. Kalbitz, The Lehstenbach and Steinkreuz catchments in NE Bavaria, Germany, in E. Matzner (ed.), *Biogeochemistry of Forested Catchments in a Changing Environment. Ecological Studies*, 172, Springer, Heidelberg, 15-41, 2004.
- Miller, K. and M. Rochwarger, On estimates of spectral moments in the presence of colored noise', *IEEE Trans. Inf. Theory IT-16*, pp. 303-308, 1970.
- Neff, W. and R. Coulter, Acoustic Remote Sensing, in D. Lenschow (ed.), *Probing the atmospheric boundary layer*, American Meteorological Society, Boston, pp. 201-239, 1986.
- Raupach, M. R., J. J. Finnigan and Y. Brunet, Coherent eddies and turbulence in vegetation canopies: The mixing-layer analogy', *Boundary-Layer Meteorol.* 78, 351-382., 1996.
- Thomas, C. and T. Foken, Detection of long-term coherent exchange over spruce forest using wavelet analysis, *Theoretical and Applied Climatology*, 80, 91-104, 2005.
- Thomas, C., J. C. Mayer, F. X. Meixner, and T. Foken, Analysis of low-frequency turbulence above tall vegetation using a Doppler sodar, *Boundary-Layer Meteorology*, 119, 563-587, 2006.
- Staudt, K. and T. Foken, Documentation of reference data for the experimental areas of the Bayreuth Centre for Ecology and Environmental Research (BayCEER) at the Waldstein site, Print, *Arbeitsergebnisse 35*, University of Bayreuth, Department of Micrometeorology, ISSN 1614-8916, 2007.

BOUNDARY LAYER WIND PROFILER OBSERVATIONS OVER THE NORTH ATLANTIC GULF STREAM.

William Brown¹, James Edson², and Heather McIntyre¹

¹ National Center for Atmospheric Research / Earth Observing Lab, Boulder, CO, USA

² University of Connecticut / Dept of Marine Sciences, Groton, CT, USA

1. Introduction

The National Center for Atmospheric Research (NCAR) operated an Integrated Sounding System (ISS) on the R/V Knorr (figure 1) in the North Atlantic in early 2007 in support of the CLIMODE project. The CLIMODE (CLIVar Mode Water Dynamic Experiment) project (Marshall et.al. , 2009), lead by PIs from the Woods Hole Oceanographic Institute (WHOI), MIT, the University of Connecticut, and other groups, is a large multi-year oceanographic study of warm waters in the North Atlantic Gulf Stream. WHOI's R/V Knorr made multiple traverses of the northwestern boundary of the Gulf Stream off the northeast coast of the U.S. The ISS consisted of a UHF wind profiler radar and radiosonde sounding system (Parsons et.al., 1994). The radiosondes and wind profiler were deployed to examine the response of the atmospheric boundary layer in this region of very strong air-sea exchange. The radiosondes were typically launched at three to six hourly intervals, whereas the wind profiler operated continuously. One of the three-week cruise tracks is shown in figure 1.

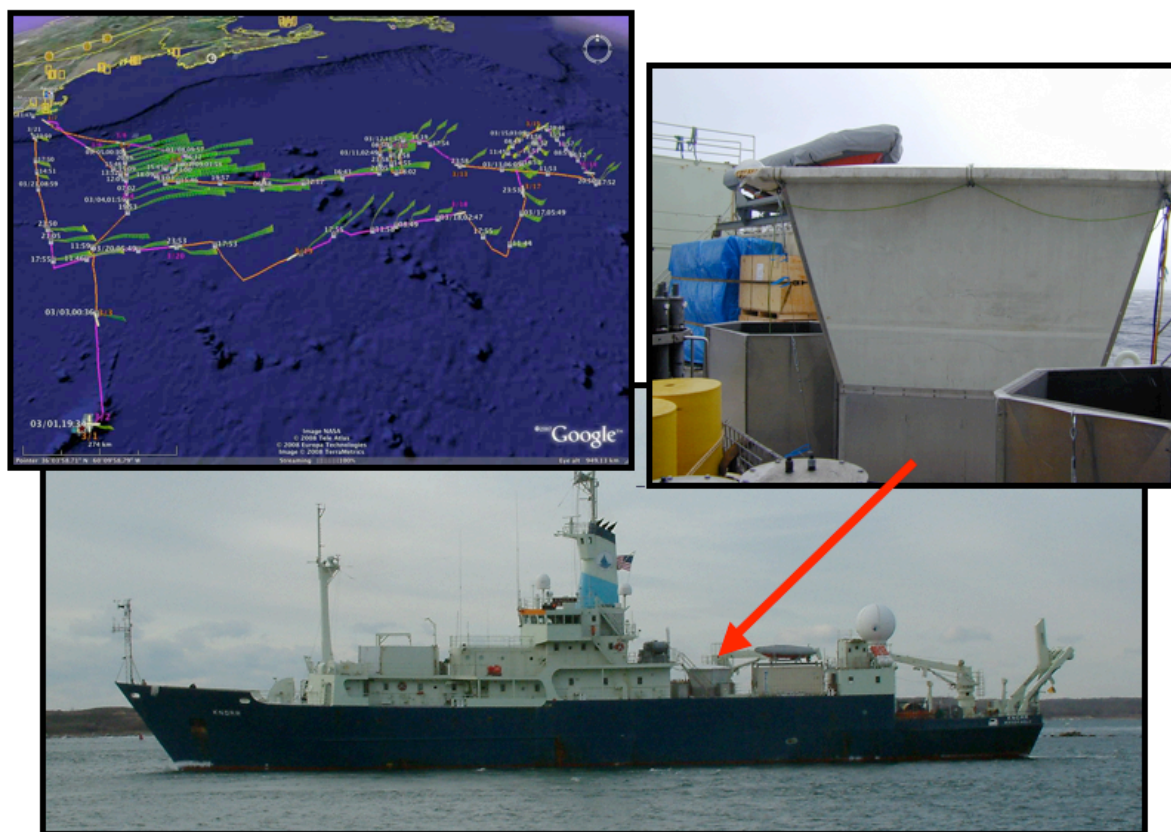


Figure 1. A cruise track with sounding trajectories overlaid (upper left) and photos of the wind profiler on the R/V Knorr. This cruise began in Bermuda 1 March 2007 and ended 3 weeks later in Woods Hole, Massachusetts.

2. Wind Profiler

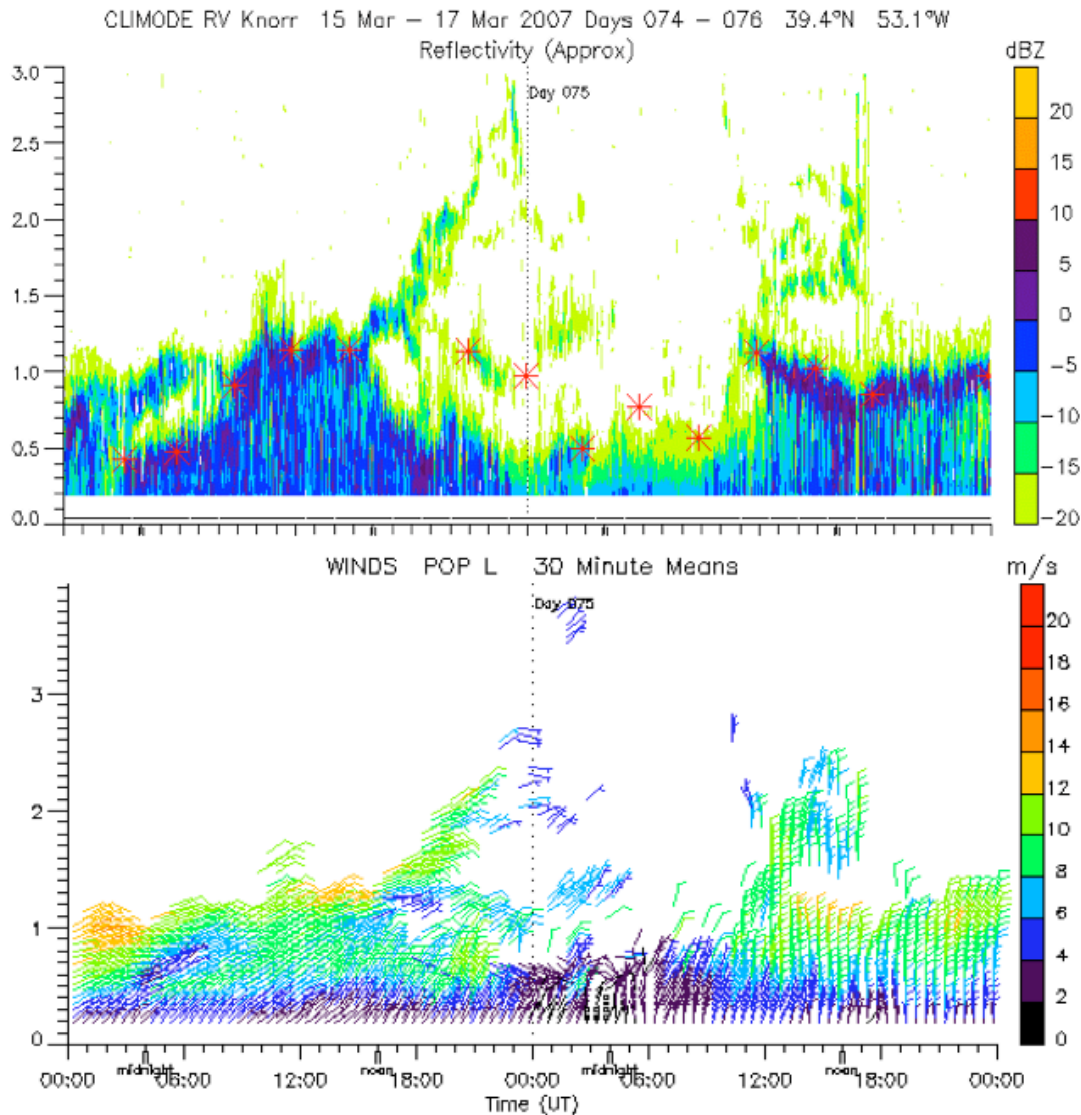


Figure 2. Time-height (km) plot of wind profiler observations from 0Z on March 15 to 0Z March 17. The upper panel shows SNR (Signal to Noise Ratio) with boundary layer depth (asterisks) and the lower panel shows wind barbs (30 minute averages, color coded by speed) as functions of altitude.

The wind profiler was a 915 MHz boundary-layer Doppler Beam Swinging (DBS) Boundary Layer profiler mounted on a gyroscopically stabilized platform (figure 1). Wind measurements from the profiler were compared with radiosondes wind measurements and agreed to within about 2 m/s (standard deviation), which is a reasonable agreement given active weather conditions and that the radiosondes and ship drift some distance apart during the observations.

Figure 2 shows a 48-hour example of observations made by the wind profiler near the eastern leg of the cruise shown in figure 1. Reflectivity is shown in the upper panel and wind measurements are shown in the lower panel. The top panel shows radar reflectivity. The red asterisks mark boundary layer top derived from radiosonde soundings and as can be seen, the radiosondes boundary layer depth generally correspond well with increased reflectivity as seen by the wind profiler. Other reflective layers originate from inversions generated as the atmosphere interacted with the varying sea surface in the region. The lower panel shows wind measurements corrected for ship motion.

3. RASS

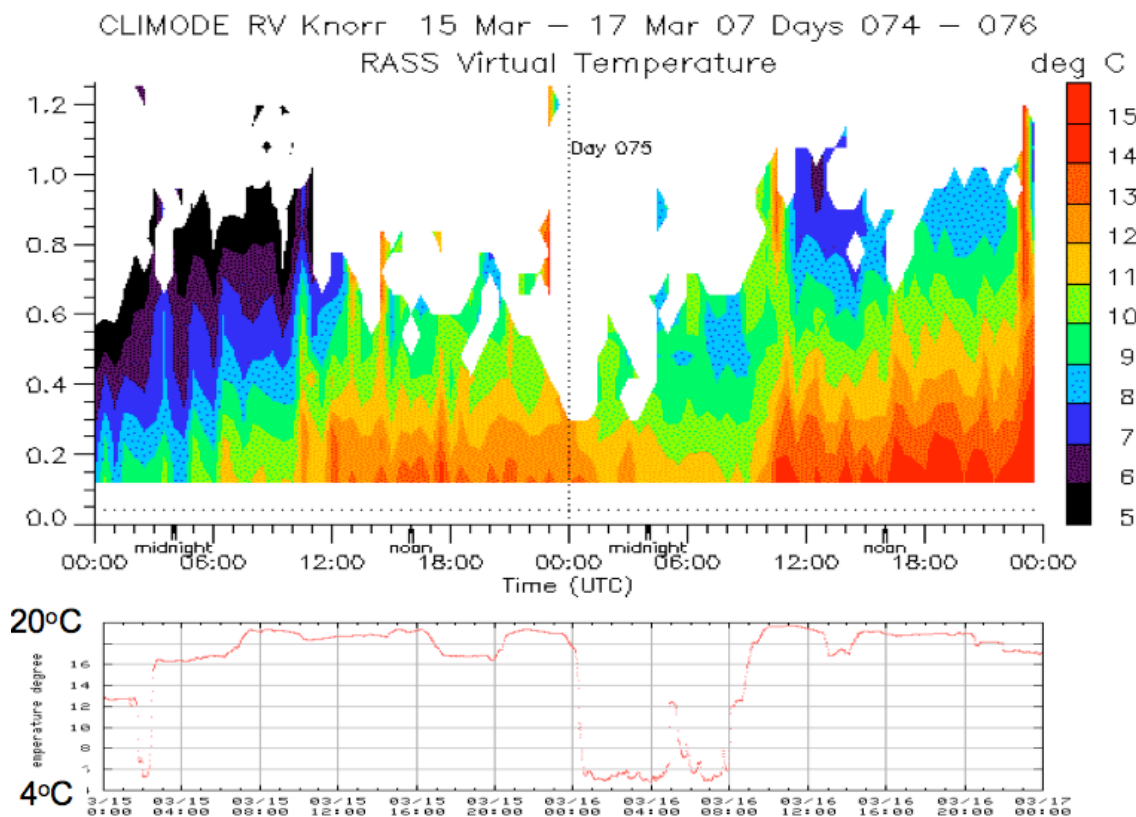


Figure 3. RASS Virtual temperature (upper panel) and sea surface temperature (lower panel) for the same 48-hour period as figure 2.

In addition to measuring the wind and atmospheric reflectivity, the profiler included a Radio Acoustic Sounding System (RASS) to measure virtual temperature aloft. RASS virtual temperatures for the same period as figure 2, along with corresponding sea surface temperatures as measured by an in-situ probe are given in figure 3. Notice that when the sea surface temperature drops (0 UTC on March 16) as the R/V Knorr moved out of the Gulf Stream, the temperature measured by RASS also drops. The radar reflectivity (figure 2) also is reduced and the boundary depth is shallower. Approximately 8 hours later, the Knorr moved back into warm waters, and RASS temperatures and radar reflectivity recovers and the boundary layer depth grows.

4. Boundary Layer Depth

Boundary layer depth derived from the radiosondes and wind profiler reflectivity for the entire three-week cruise is shown in figure 4. Also plotted is the sea surface temperature. There are many factors that affect marine boundary layer depth including advection, surface flux, precipitation, the synoptic situation and others (e.g. Edson et.al., 2007), however it can be seen that the boundary layer was generally deepened over, or near, the warm seas of the Gulf Stream.

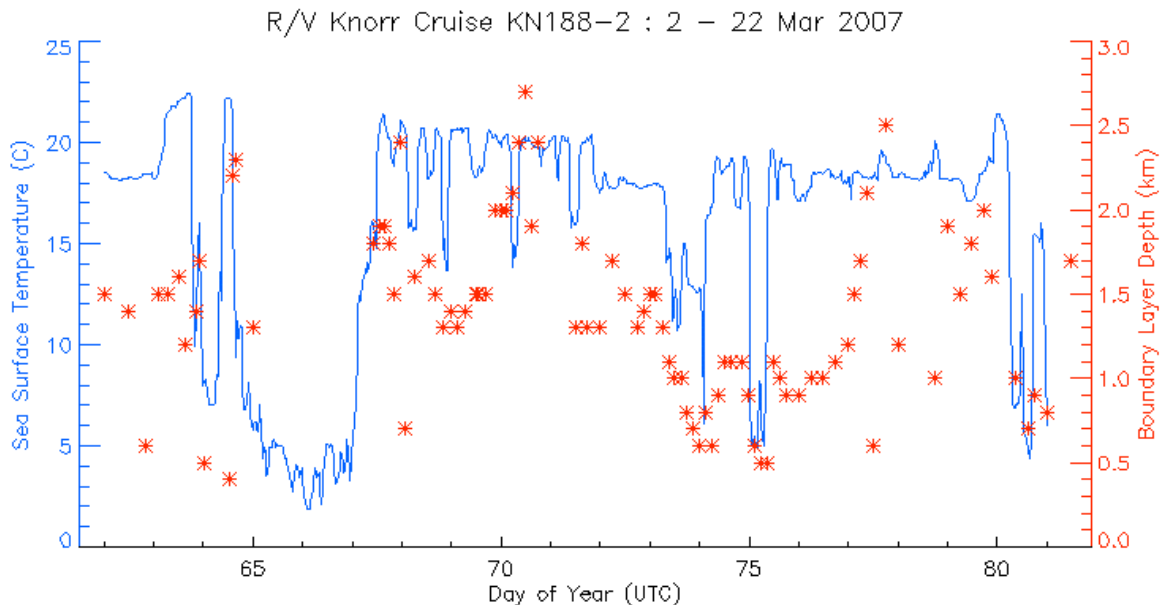


Figure 4. Time-series plots of sea surface temperature (blue line) and atmospheric boundary layer depth (asterisks) derived from the radiosonde soundings and wind profiler reflectivity.

Acknowledgements: The CLIMODE cruises and Jim Edson were funded by the U.S. National Science Foundation (NSF). NCAR is operated by the University Corporation for Atmospheric Research (UCAR) and sponsored by NSF. Thanks to NCAR staff, Jim Edson's team and the Knorr crew for assistance with balloon launches. Also thanks to Heather McIntyre and Kate Young for sounding analysis.

Bibliography

Edson J, Crawford T, Crescenti J, and co-Authors: The coupled boundary layers and air-sea transfer experiment in low winds, *Bull. Amer. Meteor. Soc.*, 88(3), 341-356, 2007.

Marshall, J., A. Andersson, N. Bates, W. Dewar, S. Doney, J. Edson, R. Ferrari, G. Forget, D. Fratantoni, M. Gregg, T. Joyce, K. Kelly, S. Lozier, R. Lumpkin, G. Maze, J. Palter, R. Samelson, K. Silverthorne, E. Skillingstad, F. Straneo, L. Talley, L. Thomas, J. Toole, and R. Weller: Observing the cycle of convection and restratification over the Gulf Stream system and the subtropical gyre of the North Atlantic ocean: preliminary results from the CLIMODE field campaign. *Bull. Amer. Meteor. Soc.*, 90 (9), 1337-1350, 2009.

Parsons, D. B., and Co-Authors: The Integrated Sounding System – Description and preliminary observations from Toga-COARE, *Bull. Amer. Meteor. Soc.*, 75, 553-567, 1994.

SKELETON BASED HOOK ECHO DETECTION IN RADAR REFLECTIVITY DATA

Hongkai Wang, John L. Barron, Robert E. Mercer

{barron,merc} @csd.uwo.ca

Dept. of Computer Science
University of Western Ontario
London, Ontario, Canada, N6A 5B7

Paul Joe

Paul.Joe@ec.gc.ca

King City Radar Station
Meteorological Service of Canada
Toronto, Ontario, Canada, M3H 5T4

Abstract: Automatic detection of severe weather events is of great interest to meteorologists. In this paper, we describe and evaluate a method to identify hook echoes automatically in radar reflectivity data. The method is based on the skeletonization of 2D shapes which are used to describe the shape of storms. We use 4 skeleton shape features: curvature, curve orientation, thickness variation and boundary proximity, and two shape features of the 2D object: southwest localization and size to detect hook echoes. We use these features to design a hook echo algorithm. We evaluate this algorithm on hook echoes detected in several radar datasets, which are verified against those manually identified by a human expert.

Keywords: Hook Echo Modelling, Tornadoes, Skeletonization, FAR/POD/CSI Analysis.

1 Introduction

This paper describes an automatic hook echo detection algorithm. Figure 1 shows a hook echo that was part of the May 3rd, 1999 Oklahoma severe weather outbreak.

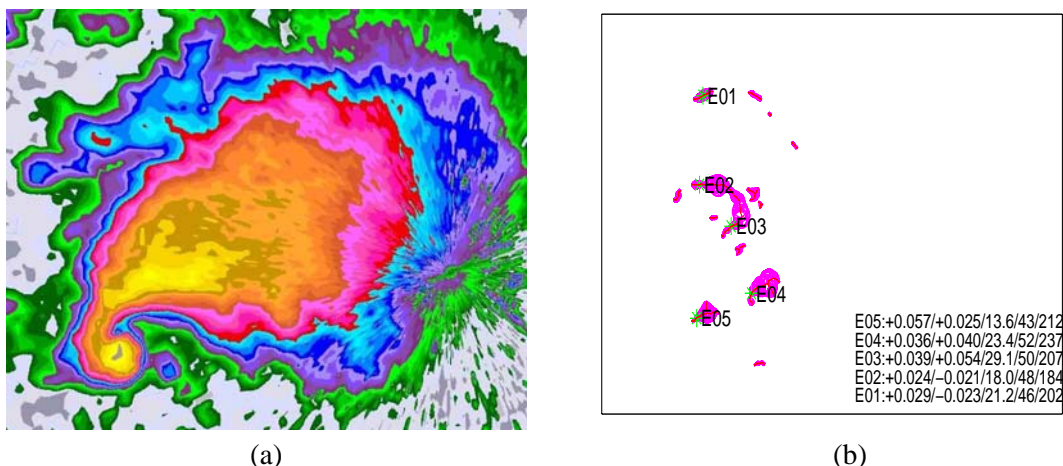


Figure 1: (a) A classic hook echo (coloured yellow and orange), with the colour table shown on the right hand side and (b) hook echoes detected for the May 3rd 1999, reflectivity data.

Storms are represented as skeletons. A skeleton is an interior contour of a region whose points are the locus of the centers of all maximally inscribed disks. We use the Hierarchic Voronoi Skeleton (HVS) algorithm [OK95] to perform skeletonization because it has a flexible tunable multi-hierarchical capability which is appropriate for finding small scale features (like hooks) embedded in a larger feature (the storm). A skeleton computed by the HVS algorithm for the storm in Figure 1 is shown in Figure 2a.

2 Hook Echo Modelling Methods

The basic idea is to employ skeletons as shape descriptors of storms and then to detect pieces of the storm skeletons that match the properties of the hook echo model. The basics are outlined in the subsections below.

2.1 Image Segmentation

The data set for the lowest elevation in the NEXRADII data is used since the hook echo is expected to be seen only at low levels. The segmentation steps are:

1. Bilinear interpolation is used to “fill-in” the data to have 125m pixel resolution to have smooth images.
2. Binary storm images are computed using the same threshold suggested by Johnson et al. [JMW⁺98] of 35dBZ on the reflectivity values.
3. Two passes of a 3×3 median filter further eliminates small storms and smooth storm boundaries.
4. Lastly, we eliminate “hole” artifacts in the image data using floodfilling [Wan05, WMBJ07].

2.2 Skeletonization

The parameters of the HVS algorithm are tuned to effectively capture the backbone and the hook-like shapes near the storm boundary. These parameters control the detection and clustering of skeleton branches and are described elsewhere [Wan05, WMBJ07]. Skeletonization converts the 2-D storm into a “backbone” skeleton represented by a (possible bifurcated) polyline.

2.3 Basic Features of the Hook Echo Model

The next task is to detect hooks in the skeleton representation. We extract:

1. **Curvature:** the curvature of the hook portion of the skeleton has a large absolute value. As shown in Figure 2b, along the skeleton branch, the position of the hook (indicated as A) has a relatively high curvature value.
2. **Orientation:** the orientation of the hook correlates strongly to hemispheric rotation: counter-clockwise is dominant in the northern hemisphere and clockwise is dominant in the southern hemisphere. In Figure 2b, the rotating arrow labelled C indicates the orientation of this hook as counter-clockwise (from the inner side to the endpoint). Detecting the orientation of hook echoes can help to rule out false positives.
3. **Thickness Variation:** the hook portion of the skeleton has a distinctive fat-thin-fat (bottle-neck) thickness variation between its surrounding boundary in close proximity to the region of high skeleton curvature. Figure 2c shows the result of straightening the curved skeleton in Figure 2a. This straightening suppresses the curvature property and only the thickness variation along the skeleton is illustrated. In Figure 2d, a hook (its high curvature region is indicated as B) can be seen that exhibits the fat-thin-fat property.
4. **Boundary Proximity:** the hook is near (touching or almost touching) the ends of the protruding parts of the storm shapes. As shown in Figure 2d, if a certain distance threshold value for being near such boundaries is set, for example, in the range M and N marked in the figure, then hook echoes are detected in those ranges. The endpoints of skeletons (boundaries of the topology) approximate the protruding storm boundaries in the hook echo model.
5. **Southwest Localization:** hook echoes tend to exhibit themselves in the southwest quadrant of the main storm region in the northern hemisphere (to the northwest in the southern hemisphere). A direction vector is used to capture this feature in the hook echo model.

6. **Storm Size:** the hook echo is associated with relatively large storms. The length of the skeleton (the maximum arclength distance marked on the skeleton distance map) provides an estimate of the actual storm size.

The actual computations that are used to compute these features are given elsewhere [Wan05, WMBJ07].

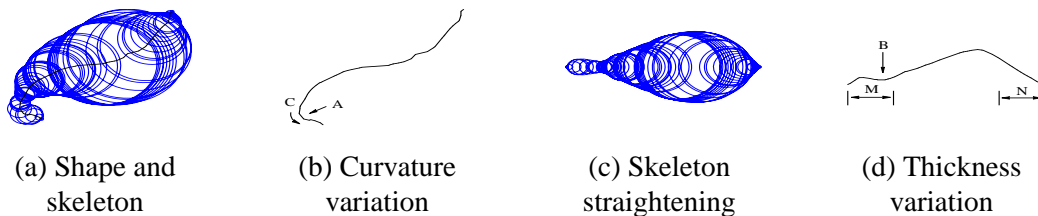


Figure 2: (a) The skeleton of an actual storm shape and its disk reconstruction, (b) the curvature variation along the skeleton (A indicates a high curvature location and C indicates the hook's orientation), (c) straightening the skeleton to eliminate its curvature property and only show its thickness variation property and (d) the thickness variation along the skeleton (B indicates the fat-thin-fat location).

3 Experimental Results

The six criteria introduced in the previous section are used to compute the values for the hook echo features. These feature are logically ANDed to detect hooks. That is, to be a hook, it must satisfy every feature criteria, otherwise it is rejected.

In order to evaluate the performance of our detection algorithm, an expert (the last author) independently provided the ground truth for three cases. Following Forbes [For81], definite hook echoes were labelled as 'well-formed' and possible hook echoes were labelled 'marginal'.

The detection results were compared with the ground truth and classify the results into three categories:

- **hits:** correct detection, that is, our detection matches with the estimated ground truth;
- **misses:** false negative, that is, the estimated ground truth indicates it is a hook, while the detection algorithm indicates that it is not;
- **false alarms:** false positive, that is, the estimated groundtruth indicates it is not a hook, while our detection result reports it is.

Note that we cannot count correct negatives.

The experimental results for the radar time of 23:56:21 of dataset KTLX19990503 are shown in Figure 1b. These two times at a moment when there were well-formed hook echoes.

Hook echo detection results are marked on the skeletons and the relevant numbers are printed in the legends of the figures. For each detected location, its curvature, orientation, thickness variation, boundary proximity, reflectivity and direction angle values are printed in the legend (lower right corner of the image). The format of a legend item is: Ex: $y/z/m/n/p$ where x is the detected hook echo number, y is the absolute value of the curvature value, the sign of y shows the orientation (+ for counter-clockwise and - for clockwise), z is the thickness variation value, m is the boundary proximity value, n is reflectivity value and p is the direction angle value (in degrees).

Detection results have been evaluated statistically using the Critical Success Index. The first score that we compute is the **False Alarm Ratio (FAR)**. It is the number of false alarms divided

Datasets	Well-formed Hooks Detected (POD score)	Marginal Hooks Detected (POD score)	False Alarms	POD Score	FAR Score	CSI Score
KTLX19990503 whole, 86 frames	102/126=81.0%	72/119=60.5%	270	71.0%	60.8%	33.8%
KTLX19990503 1 st half, 43 frames	57/66=86.4%	30/46=65.2%	68	77.7%	43.9%	48.3%
KTLX19990503 2 nd half, 43 frames	45/60=75.0%	42/73=57.5%	202	65.4%	69.9%	26.0%

Table 1: CSI analysis for a radar dataset using our Hook Echo detection algorithm.

by the number of total positive forecasts. The second score is the **Probability of Detection** (*POD*). It is the number of hits divided by the number of total observed ‘yes’ events. The third score is the **Threat Score** (*TS*) or the **Critical Success Index** (*CSI*). It is the numbers of hits divided by the number of hits, misses and false alarms. This score used to balance *POD* and *FAR* scores, and provides a measure of overall skill for verification purpose.

The experimental results for one datasets is shown in Table 1. These results show that our algorithm has considerable skill for well-formed hook echoes. For marginal hooks, the detection ratio is lower, but still show good skill, than that of well-formed hooks.

The KTLX19990503 dataset was split in half and analyzed separately. As shown in the 2nd and 3rd rows in Table 1, such differences exist even in the same dataset. The algorithm works better with well separated individual storms rather than with embedded storms.

4 Conclusions

In this paper, an automatic method to detect hook echoes is presented. This is the first report of such an algorithm. The output of the hook echo algorithm should not be used in isolation but combined with the other algorithm outputs to provide additional reliability in the storm rankings. The experimental results successfully demonstrate that this technique is effective for the hook echo detection task.

Future work includes using supervised learning techniques to tune the algorithm automatically to improve detection performance.

References

- [For81] G.S. Forbes. On the reliability of hook echoes as tornado indicators. *Monthly Weather Review*, 109:1457–1466, 1981.
- [JMW⁺98] J.T. Johnson, P.L. Mackeen, A. Witt, E.D. Mitchell, G.J. Stumpf, M.D. Eilts, and K. W. Thomas. The storm cell identification and tracking algorithm: an enhanced wsr-88d algorithm. *AMS Weather and Forecasting*, 13(2):263–276, 1998.
- [OK95] R.L. Ogniewicz and O. Kuebler. Hierarchic voronoi skeletons. *Pattern Recognition*, 28(3):343–359, 1995.
- [Wan05] H. Wang. Skeleton-based hook echo detection in doppler radar precipitation density imagery. Master’s thesis, The Dept. of Computer Science, The University of Western Ontario, December 2005.
- [WMBJ07] H. Wang, R. E. Mercer, J.L. Barron, and P. Joe. Skeleton-based tornado hook echo detection. In 14th *IEEE Intl. Conf. on Image Processing*, volume VI, pages 361–364, 2007.

MAMMATUS AND TURBULENCE OBSERVATIONS WITH THE VHF MU RADAR AND A Ka-BAND RADAR DURING THE TANUKI 2008 CAMPAIGN

Hubert Luce, Masayuki K. Yamamoto¹, Tomoaki Mega¹, Mamoru Yamamoto¹, Hiroyuki Hashiguchi¹, Shoichiro Fukao², Takuya Tajiri³, Masahisa Nakazato³, Takashi Ichiyama⁴, and Yuji Ohigashi⁴

LSEET, Université du Sud-Toulon Var, La Garde, France

¹Research Institute for Sustainable Humanosphere, Kyoto University, Uji, Japan

²Department of Space Information Science and Engineering, Fukui University of Technology, Fukui, Japan

³Meteorological Research Institute, Tsukuba, Japan

⁴Mitsubishi Electric TOKKI Systems Corporation, Tokyo, Japan

1. Introduction

In a companion work showing the results of concurrent lidar and MU radar observations (Luce et al, this issue), we described turbulent layers developing underneath cirrus clouds. These layers were likely generated by an “upside-down” convective instability due to evaporative cooling at the top of the dry subcloud layer. Mammatus-like downward protuberances were also observed on the underside of the cirrus and were found to be associated with clear air updrafts and downdrafts produced by the convective currents. In the present work, we report other events of convective and dynamical instabilities developing at cloud bases from data collected during the Turbulent Atmosphere observatioNs Using K-band and other Imaging radars (TANUKI¹) campaign. This campaign has been conducted for about one month in October-November 2008 at Shigaraki Observatory (34.85°N, 136.10°E) mainly with the MU radar (MUR), and a Ka-band (35 GHz) cloud-sensing FMCW radar and was devoted to study turbulence and clouds.

2. Instrumental set up

MUR was operated in Frequency radar Interferometric Imaging (FII) observational mode using the Capon method with five equally spaced frequencies from 46.0 MHz to 47.0 MHz (e.g. Hassenpflug et al., 2008). Range sampling was performed from 1.32 km up to 20.37 km ASL with a step of 5 m (the initial range resolution was 150 m). One profile is calculated every ~6.1 s and the time resolution is ~24.4 s. The radar beam was steered into three positions: one vertical and two oblique directions (0°,10°), (90°,10°).

The Ka-band radar is a newly developed Frequency Modulated-Continuous Wave (FM-CW) radar operating at 8.6 mm. It is mainly sensitive to Rayleigh or Mie scattering from condensation particles. The range resolution is 50 m. The acquisition time is 0.175 s and one profile is obtained every 20 s. The radar beam was directed vertically during the experiment.

3. Results of observations

Case 1: The top panel of Fig. 1 shows the time-height cross-section of equivalent reflectivity factor (dBZ) measured by the Ka-band radar from 1230 LT until 1600 LT on 12 October 2008. Deep protuberances can be noted at the cloud base around 1315 LT and from ~1350 LT. They were visually identified as mamma by one of the co-authors. The middle panel shows the corresponding cross-sections of reflectivity (dB in arbitrary units) measured

¹ TANUKI means « raccoon dog » in Japanese and is a symbol of Shigaraki...

by MUR at vertical incidence. The cloudy protuberances perfectly coincides with intense reflectivity layers developing from the cloud base from ~ 1305 LT and ~ 1345 LT. They grow downward and the depth reaches ~ 2.0 km around 1400 LT. Intense echoes persisted until the dissipation of the clouds or their disappearance above the radars. These observations strongly suggest that the clouds are the source of turbulent layers via a convective instability due to evaporative cooling at the cloud base. Turbulent mixing seems to be responsible for layer splitting from ~ 1330 LT and ~ 1435 LT due to homogenization. The bottom panel of Fig. 1 shows strong perturbations of vertical velocities exceeding ± 3 ms^{-1} associated with the cloudy protuberances. These protuberances likely result from the downdrafts and updrafts generated by the convective instability.

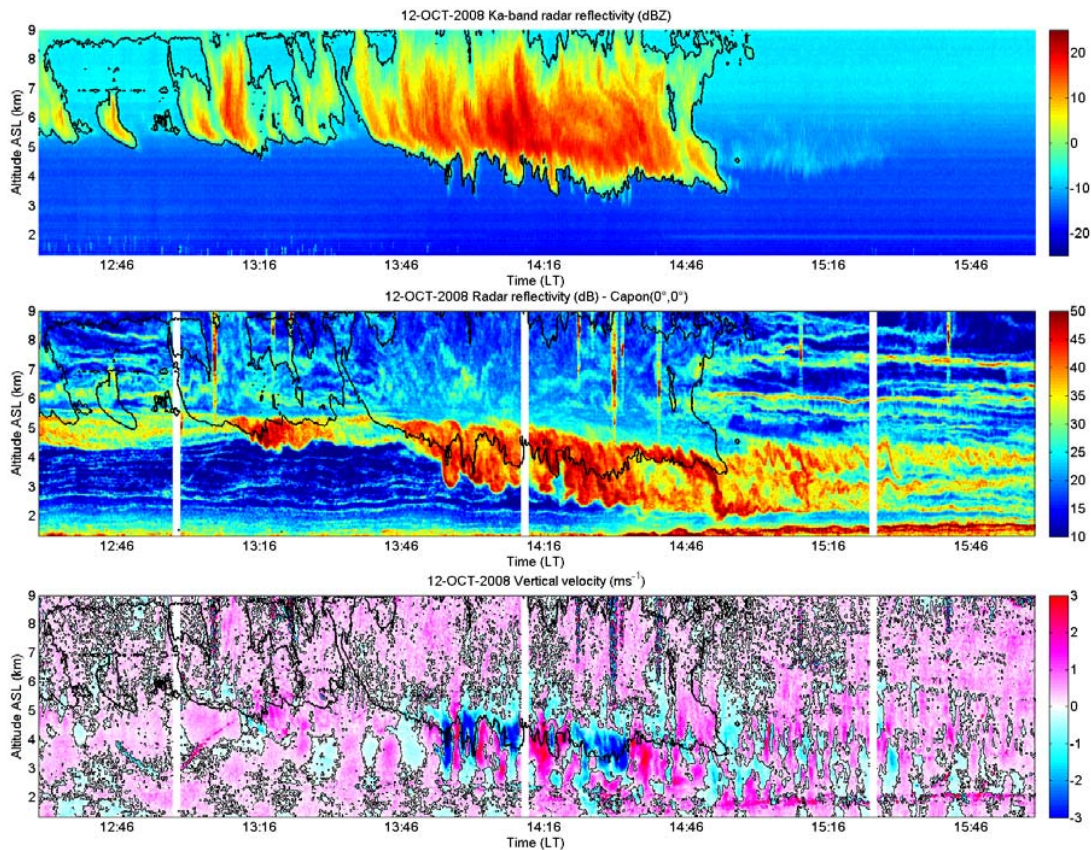


Figure 1: (Top) Time-height cross-section of equivalent reflectivity factor (dBZ) from 1230 LT to 1600 LT on 12 October 2008. The black contour is used as an index of the cloud contour. (Middle) The corresponding MUR reflectivity (dB in arbitrary units) at vertical incidence. (Bottom) The vertical velocity measured by MUR.

Figure 2 shows averaged profiles of zonal and meridional winds (ms^{-1}), wind shear and ($\text{ms}^{-1}\text{km}^{-1}$) and reflectivity (dB) measured with the three beams. The wind profiles are estimated from radar data collected just before the development of the deep turbulent layer. The zonal wind component strongly increased above ~ 5.5 km and the wind shear exceeded 30 $\text{ms}^{-1}\text{km}^{-1}$. Consequently, the cloudy air was advected above the subsaturated clear air. The wind shear is observed at the top of the ~ 2 -km deep turbulent layer, confirming that a dynamical shear instability is not the source of the observed turbulence. However, Kelvin-Helmholtz (KH) billows or braids can be seen at ~ 1340 LT and after ~ 1500 LT at the altitude of the strong wind shear. Thus, mixing at the cloud base by shear instability is here an alternative to Cloud Detrainment Instability for explaining evaporative cooling at the cloud base (see Luce et al., this issue, 2009).

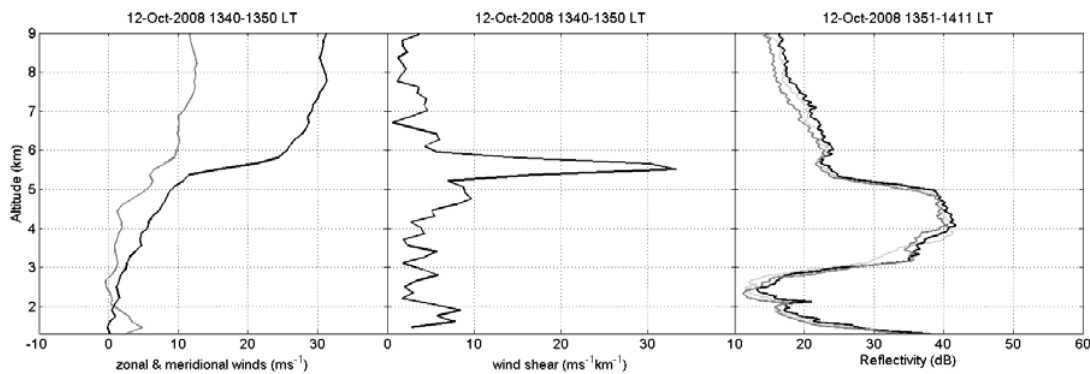


Figure 2: (Left) 10-min averaged vertical profiles of zonal and meridional winds just before the development of the deep turbulent layer. (Center) The corresponding wind shear. (Right) MUR reflectivity profiles at vertical incidence (black line), in the Northward beam (light gray line) and in the Eastward beam (heavy gray line).

Case 2: The top panel of Figure 3 shows height-time cross section of equivalent reflectivity factor (dBZ) from 0345 LT until 0445 LT on 08 October 2008. A cloud was detected above 3.5 km at 0345 LT and its depth gradually decreased with time. Downward protuberances appear approximately 4.5-6.0 km along the cloud base gradually rising with time and persisted for about 15 min in the radar image. They can be some sort of mamma or wave clouds. The vertical extent of the structures is about 0.3-1.0 km. Their time spacing is 2 min 13 s in average, corresponding to a mean horizontal separation of about 3.2 km (the mean wind speed was ~ 24 km, not shown). This mean value agrees well with the horizontal wavelength of the KH braids (~ 3.6 km) which can be seen in MUR reflectivity image (Figure 3, bottom panel). Indeed, the cloudy protuberances perfectly coincide with a large-amplitude (up to ~ 1000 m) KH instability released at the cloud base. After 0420 LT in absence of clouds, KH braided-like structures are still observed around 5.5 km but their periods are smaller and they become progressively shallower. The KH billows strongly affected the wind field in their vicinity and it is impossible to estimate the background wind and wind shear. However, a speed shear of $15\text{-}20\text{ ms}^{-1}\text{km}^{-1}$ could be identified in their altitude range before and after their occurrence (not shown).

Figure 4 shows the height-time cross section of vertical wind velocity W measured by MUR between 0355 LT and 0430 LT and in the height range 3.0-7.0 km. The thick black contours indicate the contours of the KH braids. Large oscillations ($> \pm 3\text{ ms}^{-1}$) extend from about 3.0 km to 7.0 km. All the characteristics of W are consistent with the development of a KH shear instability. In particular, the image presents a striking resemblance with the image described by Petre and Verlinde (2004) using a 95-GHz cloud radar. The KH braid at 0412 LT is associated with a shearing zone as depicted by Peter and Verlinde in their Figure 1: W vanishes along a line following approximately the slope of the braid and $W > 3\text{ ms}^{-1}$ and $W < -3\text{ ms}^{-1}$ above and below, respectively. The yellow arrows schematically represent the direction of the air velocity vectors relative to the mean wind as proposed by Petre and Verlinde.

The presence of the cloud was likely conducive to the onset of the KH instability by reducing the static stability near the cloud base because of air saturation or/and evaporative cooling.

Bibliography

Hassenpflug, G., M. Yamamoto, H. Luce, and S. Fukao, Description and demonstration of the new Middle and Upper atmosphere Radar imaging system: 1-D, 2-D, and 3-D imaging of troposphere and stratosphere, *Radio Sci*, 43, RS2013, doi:10.1029/2006RS003603, 2008

Luce, H. and co-authors, MU radar and lidar observations of clear-air turbulence and mammatus underneath cirrus, this issue, 2009.

Petre, J. M., and J. Verlinde, Cloud radar observations of Kelvin-Helmholtz instability in a Florida anvil, *Monthly Weather Rev.*, **132**, 2520-2523, 2004.

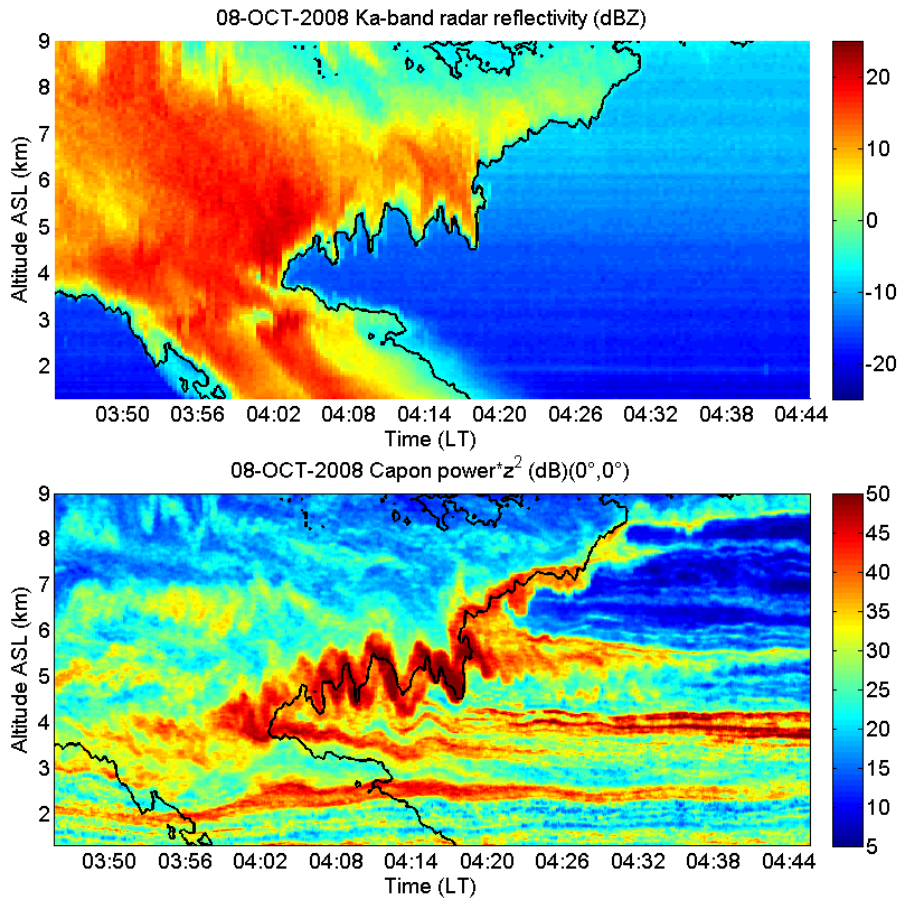


Figure 3: (Top) Time-height cross-section of equivalent radar reflectivity factor Z (dBZ) measured by the Ka-band FMCW radar from 0345 LT to 0445 LT on 08 October 2008. The black lines shows the $Z=-6$ dBZ level contour. (Bottom) The corresponding cross-section of MUR radar reflectivity (dB).

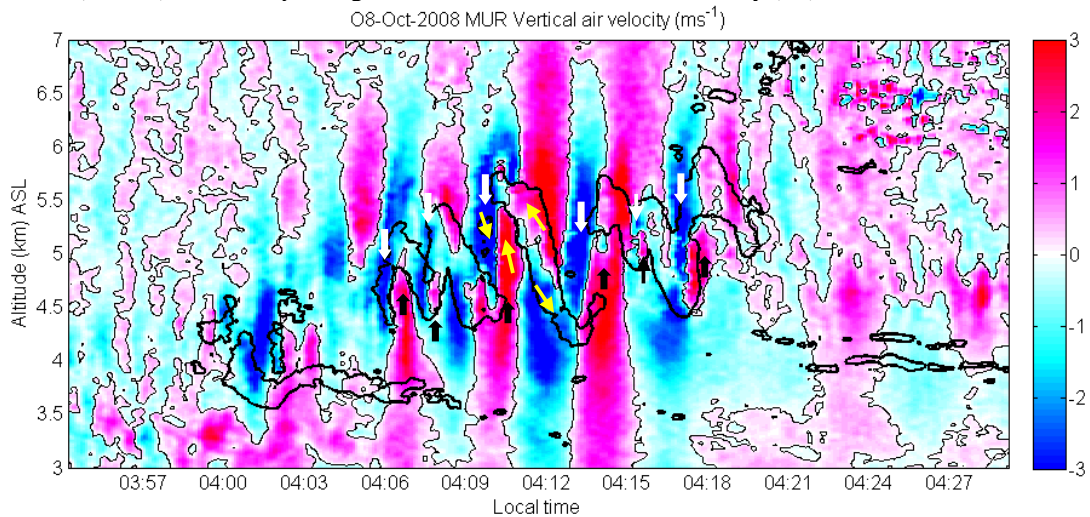


Figure 4: Height-time cross-section of vertical velocity measured by MUR. The thick contours are used as indicators of the KH braids.

Acknowledgment: This study is partially supported by the Ministry of Education, Culture, Sports, Science and Technology of Japan under the program of Special Coordination Funds for Promoting Science and Technology, “Japanese Cloud Seeding Experiments for Precipitation Augmentation (JCSEPA)”.

CHARACTERISTICS OF KELVIN-HELMHOLTZ INSTABILITIES IN THE TROPOSPHERE (UP TO 11 KM) SEEN BY THE MU RADAR IN RANGE IMAGING MODE

Hubert Luce, Shoichiro Fukao¹, Masayuki K. Yamamoto², Tomoaki Mega², Mamoru Yamamoto², Hiroyuki Hashiguchi², Takuya Tajiri³, Masahisa Nakazato³, Takashi Ichiyama⁴, and Yuji Ohigashi⁴

LSEET, Université du Sud-Toulon Var, La Garde, France

¹Department of Space Information Science and Engineering, Fukui University of Technology, Fukui, Japan

²Research Institute for Sustainable Humanosphere, Kyoto University, Uji, Japan

³Meteorological Research Institute, Tsukuba, Japan

⁴Mitsubishi Electric TOKKI Systems Corporation, Tokyo, Japan

1. Introduction

Small-scale turbulence in the lower atmosphere can be generated by various dynamical and convective instabilities and contributes to mixing and vertical transport even in strongly stratified conditions. Kelvin-Helmholtz (KH) shear instability is believed to be a common process in the stable troposphere and stratosphere but very little is still known about their occurrence and characteristics. In the present work, some cases of KH instability observed up to 11 km by the MU radar (MUR) are described. Statistics of KH instabilities based on radar data collected in range imaging (FII) mode for about 25 days during the Turbulent Atmosphere observations Using K-band and other Imaging radars (TANUKI) campaign (October / November 2008) are given. We also took advantage of concurrent observations from a Ka-band (35 GHz) radar for studying their possible interactions with clouds.

2. Instrumental set-up

MUR was operated in Frequency radar Interferometric Imaging (FII) observational mode using the Capon method with five equally spaced frequencies from 46.0 MHz to 47.0 MHz (e.g. Hassenpflug et al., 2008). Range sampling was performed from 1.32 km up to 20.37 km ASL with a step of 5 m (the initial range resolution was 150 m). One profile is calculated every ~ 6.1 s and the time resolution is ~ 24.4 s. The radar beam was steered into three positions: one vertical and two oblique directions ($0^\circ, 10^\circ$), ($90^\circ, 10^\circ$).

The Ka-band radar is a newly developed Frequency Modulated-Continuous Wave (FM-CW) radar operating at 8.6 mm. It is mainly sensitive to Rayleigh or Mie scattering from condensation particles. The range resolution is 50 m. The acquisition time is 0.175 s and one profile is obtained every 20 s. The radar beam was directed vertically during the experiment

3. Results of observations

Figure 1 shows a remarkable and unique sequence of KH vortices from their development to their decay for about 30 min. Each number indicates a different stage of evolution of the billows. Initially (stage 1), a ~ 300 -m deep non aspect sensitive reflectivity layer is seen at 1.5 km until ~ 0031 LT. Importantly, the isotropy of the radar echoes indicates that small-scale turbulence (smaller-scale KH billows) developed before the formation of the observed large-amplitude KH billows. A distortion of the layer due to the development of a KH billow starts from ~ 0032 LT (stage 2). Then, two well-developed vortices with a crest-to-trough amplitude of ~ 400 m can be noted from ~ 0036 LT until ~ 0043 LT (stage 3). They then decay, become shallower and less intense at 00:45, 00:48 and 00:51 LT (stage 4). They finally flatten and form a double layer from 00:52 LT, likely due to mixing (stage 5). The upper layer is less intense but is visible until $\sim 01:02$ LT. Such a KHI event has never been observed with MUR before. *It is the only case where it was possible to follow the evolution from the billow development to layer splitting.* The KHI pattern is also very clear in the Eastward beam (and

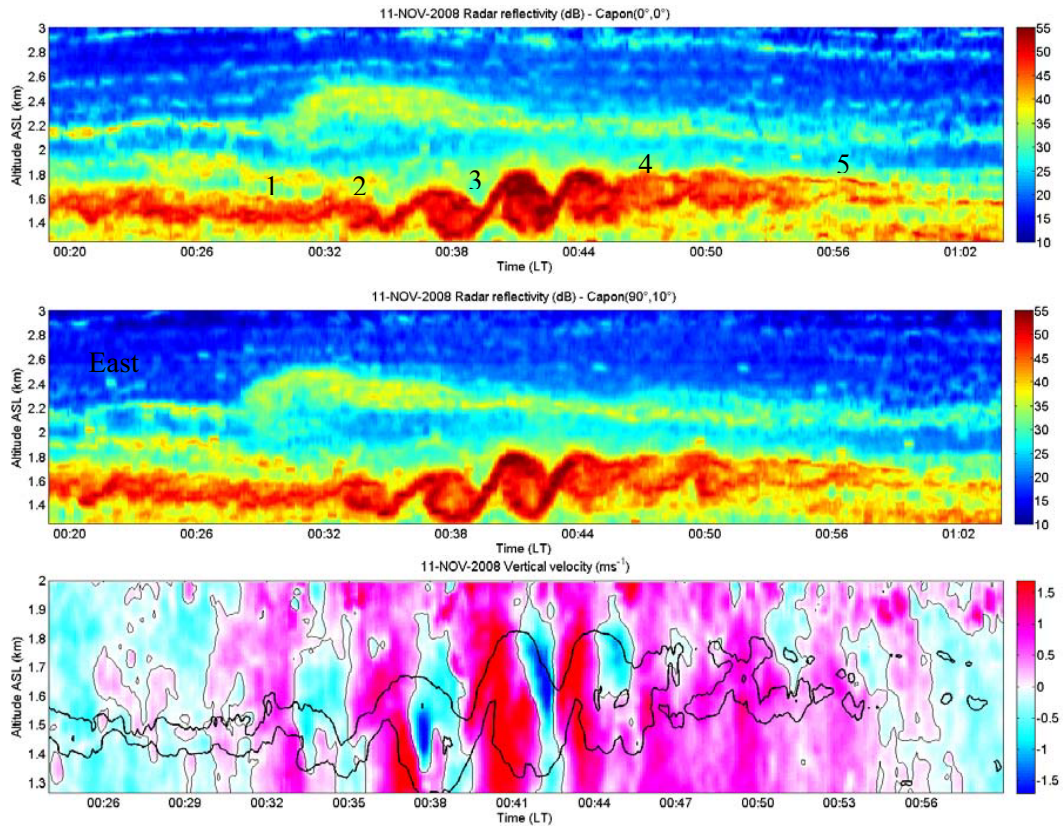


Figure 1 : (Top) Height-time cross-section of radar reflectivity (dB) between 1.245 km and 3.0 km at vertical incidence. (Center) Same as the top frame for the Eastward beam. (Bottom) The corresponding height-time cross-section of vertical velocity (ms⁻¹). Thick black lines show KH billow contours.

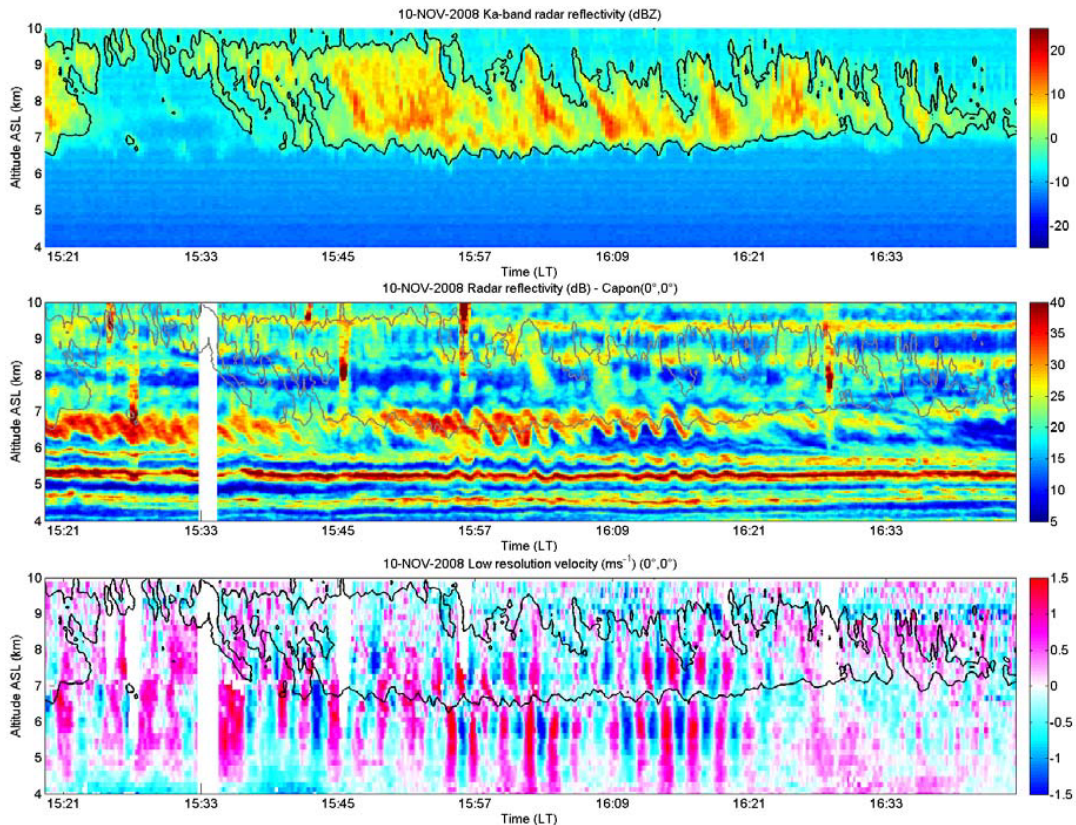


Figure 2: (Top) Height-time cross-section of equivalent reflectivity factor (dBZ). (Center) The corresponding MUR reflectivity (dB). (Bottom) The corresponding vertical velocity measured by MUR. The black lines show the cloud contour.

in the Northward beam, not shown). It is worth noting that the braids between ~ 0036 LT and ~ 0044 LT are not aspect sensitive but the echoes are more intense (likely due to the compression of the isentropes intensifying the irregularities at the Bragg scale). Figure 1c shows the vertical wind perturbations associated with the billows. As expected downward and upward motions occur at the right and left of the billows, respectively. Their amplitude exceeds $\pm 1.5 \text{ ms}^{-1}$.

Figure 2 shows a more representative example of observations made by MUR of a KH instability in the troposphere. Braided structures are seen between 6.0 km and 7.0 km (Figure 2a). They sometimes suddenly fade away (e.g. at ~ 1540 LT) or become shallower and progressively disappear without evidence of breaking, mixing and layer splitting (after 1620 LT). Their period is about 2 min. Large vertical wind oscillations are seen up to 8.0 km and down to 4.0 km likely due to the emission of gravity waves, as already shown by Klostemeyer and Ruster (1980), for example. They are responsible for the wavy perturbations of the thin stable layers between 4.0 km and 6.0 km (Figure 2a). A sudden phase shift of the perturbations of about 90° can also be noted at the critical level around 6.6 km.

Figure 2a shows the corresponding height-time cross-section of equivalent reflectivity factor Z (dBZ) measured with the Ka-band radar. A 1- to 2-km thick cloud is seen above ~ 6.5 km and the cloud base (stressed by the black contour) perfectly coincides with the altitude of KH instability. The downward protuberances at the cloud base (which can be some sort of wave clouds) are associated with the downdrafts (especially between ~ 1610 LT and 1620 LT) indicating that they can be the result of cloudy air entrainment by the KH billows. The Z distribution in the cloud also varies with time. This observation suggests that the KH instability may also affect the distribution of the ice particles inside the cloud.

The KHI event shown in Figure 2 has persisted for about 63 hours at cloud base around ~ 6.0 km. As shown in Figure 3, they sometimes reveal more complex patterns. After ~ 2200 LT, a train of billows (thickness ~ 1000 m, period ~ 4 min 30 s) is superimposed to smaller scale braids of period ~ 45 s. They might be an experimental observation of secondary spanwise billows already shown by Metcalf (1975).

Including the 63-hour event, we found that 46% of the detected KH events in the troposphere (52% in time) were found at cloud base suggesting that cloud base is a location favorable to their generation. They occur when there is a differential advection of cloudy air over dry air. This condition may be conducive to sublimation or evaporative cooling near the cloudy air-dry air interface which, in turn, reduces the static stability (and thus the Richardson number) in the region of the cloud base. The same mechanism may also produce convective instabilities if cooling is enough for generating a static instability (e.g. Luce et al., 2009, this issue).

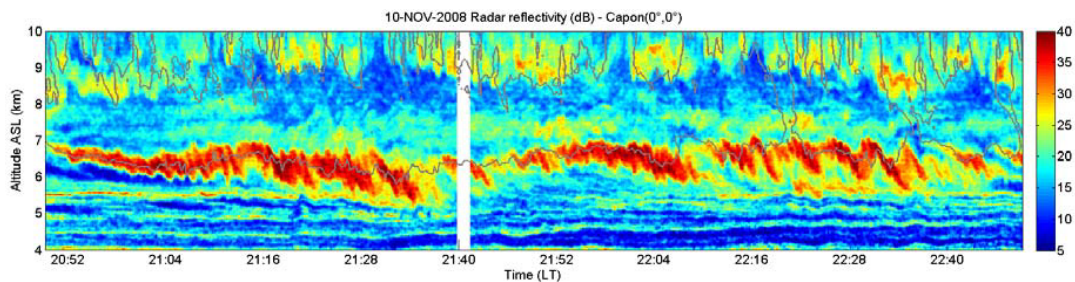


Figure 3: Height-time cross-section of MUR reflectivity (dB) at vertical incidence. The gray lines show the cloud contour.

4. Statistics

A statistical analysis of KH instabilities was carried out using the radar dataset collected during the TANUKI campaign between 1.32 km and 11.0 km. The statistics has been limited to the altitude of 11.0 km due to the lack of reliability of the wind and shear estimates at higher altitudes. KH billows have been identified visually and their characteristics estimated manually.

188 events of KH billows were listed. Some events may have been missed in regions where signal to noise ratios were too low for distinguishing the structures. Some could be confused with other types of instabilities but we think that errors did not affect too much the statistics. KH billows were observed 1.7% of the time and height. Because the statistics only cover a relatively short period in October and November 2008, the representativeness may be questionable. Browning (1971) found that KH billows were observed 5% of the time, but into a limited fraction of heights.

It is well-known that sheared regions of jet-streams in the middle troposphere are conducive to turbulence generated by KH instability. Since the jet-stream intensity and location strongly depends on season, we can expect strong seasonal variations of KHI events. From the present dataset and after rejecting the 63-hour event, it was found that 67% of KHI events occurred in the height range 7.0-11.0 km in accordance with the presence of the jet-stream.

As also reported by Browning (1971), we found that 66 % of the KH billows have a duration shorter than 30 min (typically 10-15 min). The longest « billow event » (composed of several consecutive billows, as defined by Browning) was about 97 min if we exclude the 63-hour event composed of many short-time billow events as shown in Figure 2.

77% of the KH wave periods do not exceed 90 s and tend to become shorter with altitude when approaching the jet-stream maximum. This property can be expected since the billows are advected by the wind which becomes stronger with height. Almost all the cases are associated with a speed shear indicating that turning shear may not often contribute to KH instability generation in the troposphere. The wind shear has been estimated from wind profiles averaged over 10 min. Almost all the billows are associated with a maximum of wind shear, i.e. with an inflexion point in the wind profiles, as expected by the theory. 55 % of the billows are associated with a wind shear between 15 and 30 $\text{ms}^{-1}\text{km}^{-1}$ and 14% with a shear smaller than 15 $\text{ms}^{-1}\text{km}^{-1}$.

The period of the billows can be converted into horizontal wavelength by multiplying by the wind speed. 67 % have a horizontal wavelength between 1500 m and 3000 m. Contrary to the period, there is no height dependence in wavelength.

66 % of the billows have a maximum depth between 200 m and 700 m. The maximum depth does not exceed 1500 m. 75 % of the billows have a ratio of crest-to-trough amplitude to wavelength between 0.1 and 0.2667. From Browning (1971), the proportion is 70%. Our statistics are, on the whole, similar to those proposed Browning from UHF scanning radar data.

Bibliography

Browning K. A., Structure of the atmosphere in the vicinity of large-amplitude Kelvin-Helmholtz billows, *Q. J. R. Met. Soc.*, 97, 283-290, 1971.

Hassenpflug, G., M. Yamamoto, H. Luce, and S. Fukao, Description and demonstration of the new Middle and Upper atmosphere Radar imaging system: 1-D, 2-D, and 3-D imaging of troposphere and stratosphere, *Radio Sci*, 43, RS2013, doi:10.1029/2006RS003603, 2008.

Klostermeyer, J., and R. Rüster, Radar observations and model computation of a jet stream-generated Kelvin-Helmholtz instability, *J. Geophys. Res.*, 85, 2841-2846, 1980.

Luce, H. and co-authors, MU radar and lidar observations of clear-air turbulence and mammatus underneath cirrus, this issue, 2009.

Metcalf, Microstructure of radar echo layers in the clear atmosphere, *J. Atmos. Sci.*, 32, 362-370, 1975.

Acknowledgment: This study is partially supported by the Ministry of Education, Culture, Sports, Science and Technology of Japan under the program of Special Coordination Funds for Promoting Science and Technology, “Japanese Cloud Seeding Experiments for Precipitation Augmentation (JCSEPA)”.

Session 6:
Middle Atmosphere
Dynamics and Structure

INTRASEASONAL VARIATIONS OF 6-DAY WAVE IN THE TROPICAL MIDDLE ATMOSPHERE

R. Kondala Rao¹, S. Gurubaran¹, S. Sathishkumar¹, S. Sridharan², T. Nakamura³, T. Tsuda³, H. Takahashi⁴, P. P. Batista⁴, R. A. Buriti⁵, D. Riggin⁶, D. V. Pancheva⁷ and N. J. Mitchell⁸

1 Equatorial Geophysical Research Laboratory, IIG, Tirunelveli, India

2 National Atmospheric Research Laboratory, Gadanki, India

3 Research Institute for Sustainable Humanosphere, Kyoto University, Kyoto, Japan

4 Instituto Nacional de Pesquisas Espaciais, Sao Jose dos Campos, Brazil

5 Departamento de Fisica, Universidade Federal de Campina Grande, Campina Grande, Brazil

6 Colorado Research Associates, Boulder, USA

7 Geophysical Institute, Bulgarian Academy of Sciences, Sofia, Bulgaria

8 Centre for Space Atmospheric and Oceanic Science, Department of Electronic and Electrical Engineering, University of Bath, Bath, UK

Introduction:

The 6.5-day westward propagating zonal wave number 1 ($s=1$) planetary wave is a prominent feature in the equinoctial mesosphere and lower thermosphere (MLT). Global observations showed that while the latitudinal structure identifies this wave as a $(s, n-s) = (1, 1)$ Rossby mode, the longer period and definite phase progression with altitude distinguish it from the free mode solution i.e., the “5-day wave” [Geisler and Dickinson, 1976; Salby, 1981]. These studies found that the 5-day wave amplitudes are magnified within the regions of westward zonal mean winds. [Meyer and Forbes, 1997] suggested that baroclinic instability in the mid-latitude mesosphere is assumed to be the forcing mechanism. However, global satellite observations in the MLT show no sign of midlatitude forcing [Talaat et al., 2001]. The study of Lieberman et al. [2003] provided an observational support for the 6.5 day wave as an unstable wave. The wave source, mean wind structure, instability, and the critical layers of the wave can all affect the wave response in the MLT region and can have strong seasonal dependence [Liu et al., 2004].

Data and analysis:

Simultaneous data obtained from the network of radars situated at the tropical latitude sites Tirunelveli (TIR) (8.7°N, 77.8°E), Hawaii (HAW) (21° N, 157° W), Cariri (CAR) (7.4°S, 36.5°W) and Ascension Island (ASC) (7.9°S, 14.4°W), during the period from June 2004 to December 2005 are made use of in this work to study the behavior of 6.5 day wave in the MLT region. The zonal

wind data provided by the United Kingdom Meteorological Office (Met Office data) are used to study the behavior of eastward propagating and westward propagating waves in zonal wind in the stratosphere. Temporal variations in radar winds are examined using the S-transform method, a technique for temporal localization of the Fourier transform [Stockwell and Lowe, 2001]. A two dimensional spectral analysis is used to retrieve the amplitudes of the waves from the MetO zonal wind fields.

Results and Discussion:

An S-transform method is applied to daily mean zonal winds at 88 km to find out the temporal behavior of the 5-6 day wave at all the four locations. Figure 1 shows the S-transform spectra of the zonal wind at 88 km over the four radar stations. The amplitudes of the time variations of the zonal winds peak at periods around 5-7 days at all the locations. The amplitudes of the 5-7 day wave become maxima at day numbers around 260, 450 and 620 (around Equinox periods September-2004, March-2005 and September-2005) over all the four locations. In addition to this, the amplitudes of the 5-7 days wave over CAR and ASC become strong at other periods (around day number 210, 330, 570 and 690 etc.) also.

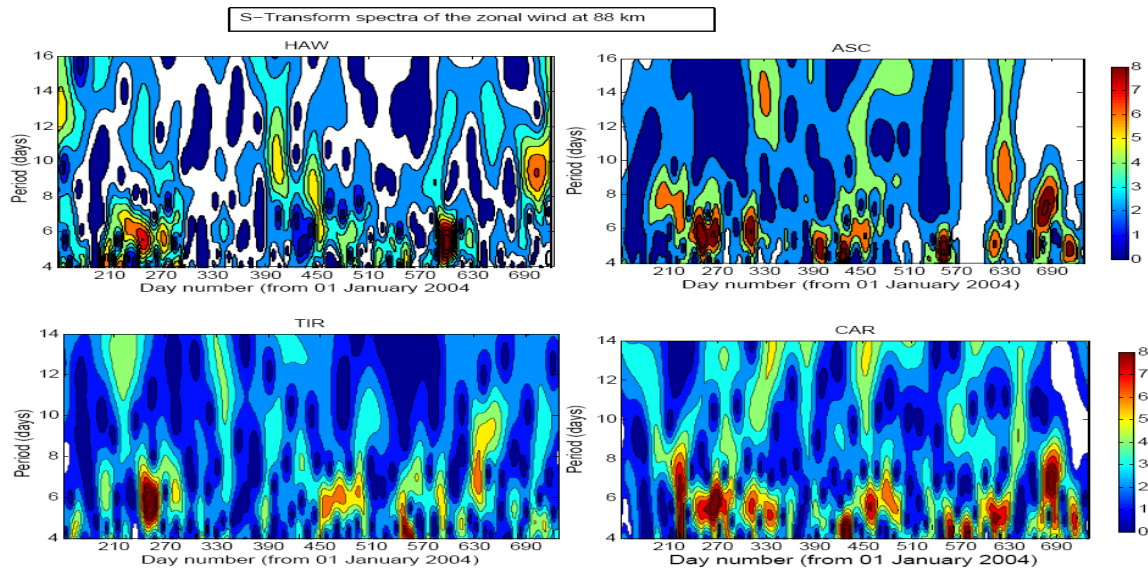


Fig.1. S-transform of zonal wind at 88 km for four tropical stations

It shows that the amplitudes of the 5-7 day in zonal wind at 88 km wave are undergoing temporal variabilities at intraseasonal time scale.

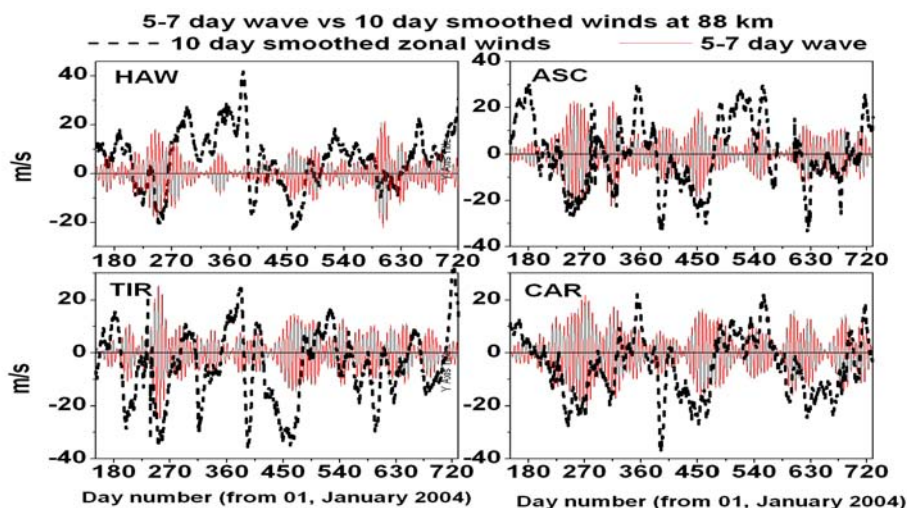


Fig.2. 5-7 day filtered zonal winds at 88 km and 10 day running mean at 88 km for four stations.

It can be easily observed from the Figure 3 that the mean zonal winds show variabilities at intraseasonal scale and the amplitudes of the 5-7 day wave become maxima during the westward phase of the mean zonal winds over all the four locations. These results reveal the dependence of the amplitudes of the 6 day wave on the background wind (not only on the seasonal but also) on the intraseasonal time scale. Before trying to understand the reasons for this intraseasonal variability of 6 day wave, one should understand the source mechanisms and vertical, latitudinal and horizontal propagation characteristics of this wave. Here, it has to be noticed that the zonal wind variations at period range 5-7 days observed in Figure 3 may contain features of both eastward propagating 6-day fast Kelvin and westward propagating 6-day Rossby wave. The comparison of the phases of the 6 day wave at different stations revealed that the wave contains both the features of 6 day Kelvin wave and 6 day Rossby wave.

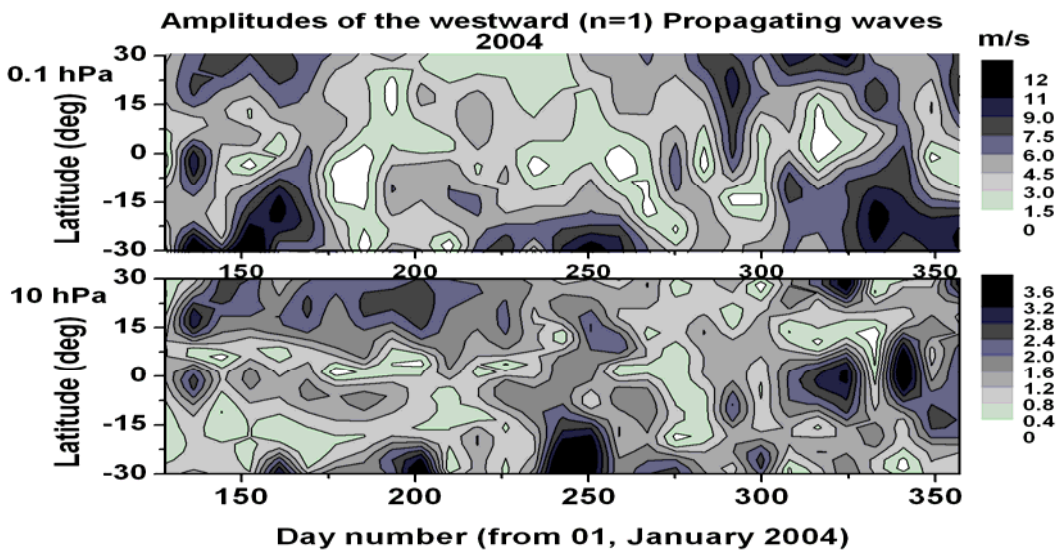


Fig.3. Time-latitude cross section of amplitude spectrum of zonal wind with westward at $n=1$ for two pressure level 10 and 0.1hPa during 2004

The latitude-time structures of the amplitudes of the eastward and westward propagating wave number 1 ($n=1$) components at two pressure levels 10 hPa and 0.1 hPa are shown in Figures 3. The 6 day Kelvin wave and 6 day Rossby wave are distributed nearly symmetric around the equator at 10 hPa where as it is very weak around the equator at 0.1 hPa. It seems that that some other wave components from mid latitude enters into the tropical region.

The observation of the latitude-time structures of the amplitudes at other pressure levels (Figures not shown) reveals that 6 day Kelvin and 6 day Rossby wave distributed symmetrically around the equator at lower heights (10 hPa) and their amplitudes start diminishing as height increases and they almost disappear at 0.1 hPa. From these results one can understand that these are equatorially trapped waves. One important thing to be noticed here is that the other mid latitude generated westward propagating waves enter into the tropical region as height increases. The wave source, mean wind structure, instability, and the critical layers of the wave can all affect the wave response in the MLT region [Liu et al., 2004]. The westward propagating planetary waves with period around 6-day generated in mid and high latitude lower atmosphere propagate upward and equatorward and they reach the mesopause level over and around the equator.

The convectively generated equatorial Kelvin and Rossby-gravity waves with period around 6-day in the tropical region propagate up to stratospheric heights and dissipate most of the times in the upper stratosphere itself without propagating up to mesopause level.

References:

1. Andrews, D. G., J. R. Holton, and C. B. Leovy (1987), *Middle Atmosphere Dynamics*, 1st ed., pp. 5 – 6, Elsevier, New York..
2. Geisler, J. E., and R. E. Dickinson (1976), The 5-day wave on a sphere with realistic zonal winds, *J. Atmos. Sci.*, 33, 632– 641.
3. Meyer, C. K., and J. M. Forbes (1997), A 6.5-day westward propagating planetary wave: Origin and characteristics, *J. Geophys. Res.*, 102, 26,173–26,178.
4. Lieberman, R. S., D. M. Riggan, S. J. Franke, A. H. Manson, C. Meek, T. Nakamura, T. Tsuda, R. A. Vincent, and I. Reid (2003), The 6.5-day wave in the mesosphere and lower thermosphere: Evidence for baroclinic/ barotropic instability, *J. Geophys. Res.*, 108(D20), 4640, doi: 10.1029/ 2002JD003349.
5. Talaat, E. R., J. H. Yee, and X. Zhu (2001), Observations of the 6.5-day wave in the mesosphere and lower thermosphere, *J. Geophys. Res.*, 106, 20,715– 20,723.
6. Talaat, E. R., J.-H. Yee, and X. Zhu (2002), The 6.5-day wave in the tropical stratosphere and mesosphere, *J. Geophys. Res.*, 107(D12), 4133, doi:10.1029/2001JD000822.
7. Liu, H.-L., Talaat, E.R., Roble, R.G., Lieberman, R.S., Riggan, D.M., Yee, J.-H. (2004), The 6.5-day wave and its seasonal variability in the middle and upper atmosphere, *J. Geophys. Res.*, 109, D21112 doi:10.1029/2004JD004795.
8. D.V. Pancheva, P.J. Mukhtarov, N.J. Mitchell, D.C. Fritts, D.M. Riggan, H. Takahashi, P.P. Batista, B.R. Clemesha, S. Gurubaran, G. Ramkumar. (2008), Planetary wave coupling (5–6-day waves) in the low-latitude atmosphere–Ionosphere system, *J. Atmos. Sol Terr. Phys.*, 70, 101-122.

THE AXONMET – A POLE TO POLE CHAIN OF ATMOSPHERIC METEOR RADARS.

Hocking, W. K.^a, A. Hocking^b, N. Mitchell^c, P. Batista^d, B. Clemesha^d, R. Buriti^e, A.H. Manson^f, C.E. Meek^f, M. Taylor^g, D. Janches^h, D. Riggin^h, D.C. Fritts^h, J. Drummondⁱ, and R.E. Hibbins^j.

(a)University of Western Ontario, London, Ont., N6A 3K7 Canada; (b) Mardoc Inc., London, Ont., Canada; (c) Bath University, United Kingdom (d) Instituto Nacional de Pesquisas Espaciais (INPE), CP 515, São José dos Campos, SP 12201-970, Brazil; (e) Universidade Federal da Paraíba, Campina Grande, Paraíba, Brazil; (f) Institute for Space and Atmospheric Science, Saskatoon, Canada; (g) Space Dynamics Laboratory and Physics Department, Utah State University, Logan, UT, USA; (h) Colorado Research Associates, Boulder, Co., USA.; (i) Dalhousie University, Halifax, Canada;.(j) British Antarctic Survey, UK.

1. Introduction

The AxonMet is a chain of SKiYMET meteor radars in the American longitudinal sector, owned and operated by a consortium of different scientists and organizations. AxonMet stands for Cross (X) Americas Observing Network for METeor Studies and the X (for “cross”) and A (in Americas) are interchanged in order. The title also borrows from the concept of a nerve Axon, since all the radars are interconnected to a central service centre.

SKiYMET radars (Hocking et al., 2001) are used for astronomical studies of meteor flux, shower radiant, orbit calculations and atmospheric meteor entrance speeds. The website concentrates on atmospheric parameters, especially upper atmosphere winds and temperatures. Count rates seen by the radars are also shown. SKiYMET radars are used exclusively because they are all of similar design, making comparisons between sites more reliable. The reliability of SKiYMET radars has been established in several publications (e.g., Jones et al., 2003; Franke et al., 2005, among others).

The data from the radars in this network are updated on a web site several times per day (typically every 4 hours). This is our normal update rate, but at some sites it is more frequent.

For still other sites, with poorer connectivity, the data may be updated less frequently (e.g., daily), so that some data-sets lag by one day compared to the normal

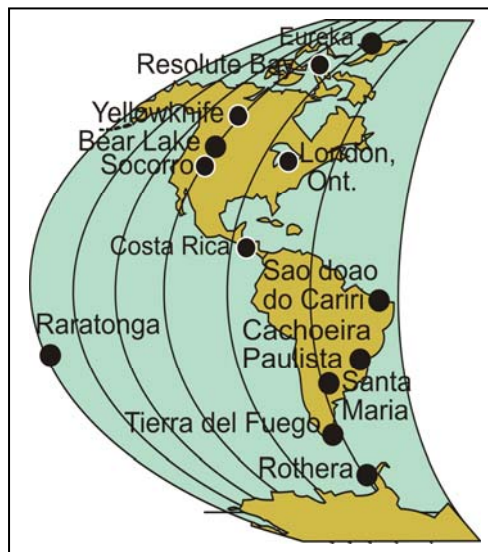


Fig.1. Sites of the Axonmet radars in 2010

situation. In this short overview, we guide the reader through the products of the web site.

Purpose:

The data represent a good resource for general interest, for real-time back-up to projects like rocket launches and campaign-mode studies, and even for guidance in the planning of real-time design of experiments. However, for more detailed studies, viewers should contact the radar owners directly. There may be multiple reasons for this. Researchers may want to contact one or two of the radar owners for data to supplement studies of their own; e.g., Smith et al. (2003) used data from the Socorro radar to provide background winds to a study of a bore-wave seen over Southern USA. Alternatively, a researcher may want to perform a global study of seasonal characteristics to compare with a model. The user should then contact each of the radar owners individually, describe the intended project, and seek data for the required time-frame. Radar owners may then provide data at their discretion; if, for example, the intended project conflicts with an existing project within their own group, data may be denied, but generally good cooperation can be expected. Data should be used only for the intended project. No central data-server exists – data must be obtained from each radar-user individually.

The Web Site:

The Axonmet web site can be found at:

<http://www.physics.uwo.ca/~whocking/axonmet/>

The cover page of the website shows a map of the sites, something similar to fig. 1 above. The user may then click on any of the sites on the map, or use a table on the left-hand side. This will bring the viewer to a page that looks something like fig. 2 below, which uses Google maps. The user may zoom in to take a closer look at the sites.

The page also contains a contact person for the site, and in the top right hand corner, there is a table referring to “Meteor Flux”, “Decay time/temperature” and “wind speed”. Clicking on any of these three options produces graphs pertaining to the relevant titles. Data cover the period from midnight UT on the previous day to the time of last data transfer.

Fig 3 shows an example for the meteor fluxes, in this case recorded on January 29, 2010. The colour coding is chosen to be different to that used on the web site in order to optimize the paper-presentation in this book. The top graph shows meteor counts per hour.

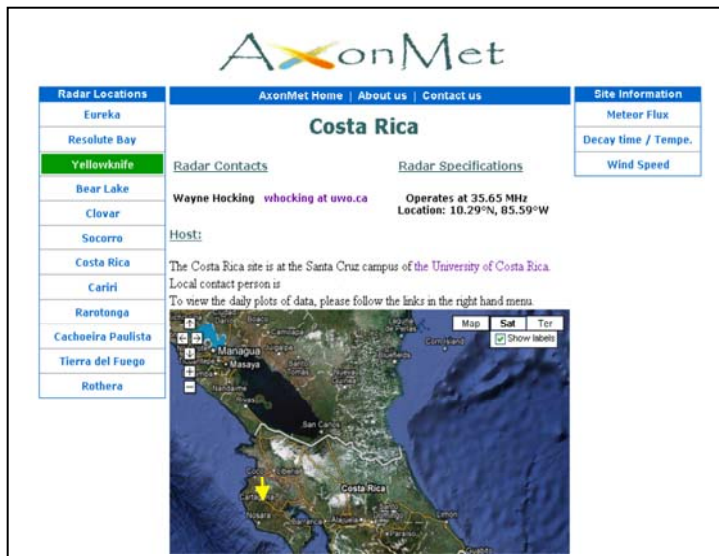


Fig. 2. A sample page from the Axomet Web site.

The blue colour refers to so-called “unambiguous” meteors. These are ones with locations that are known without doubt.

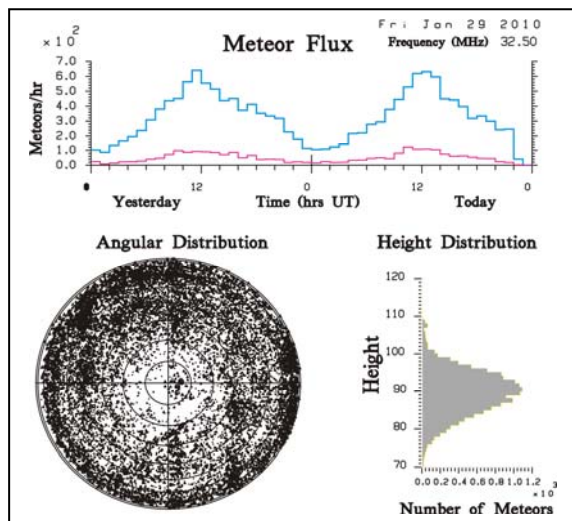


Fig. 3. Example of the “flux” plots on the Axonmet web sites.

The red colours show “ambiguous meteors” – these are meteors for which the range is aliased or the directional determination is ambiguous. Taking account of phase uncertainties, there may be two or more positions in the sky that could correspond to the phase differences recorded on each receiver, so the exact location is uncertain.

The graph at the lower left shows the locations of all meteors detected in the time frame defined by the upper curves. In this case we have used only a black and white presentation, but the web site plots are colour-coded to indicate the level of ambiguity.

As in the upper curves, blue/cyan indicates unambiguous detections, while red indicates 2-level ambiguity. Other colours are used for the rarer events of 3 or 4-level ambiguity or higher. The bottom right-hand graph shows the number of meteors detected per 1-kilometre-wide height interval as a function of altitude.

Fig. 4 shows examples of the wind plots. Again, colours are modified from those used on the web site to optimize presentation on paper. Winds are shown as zonal (eastwards)

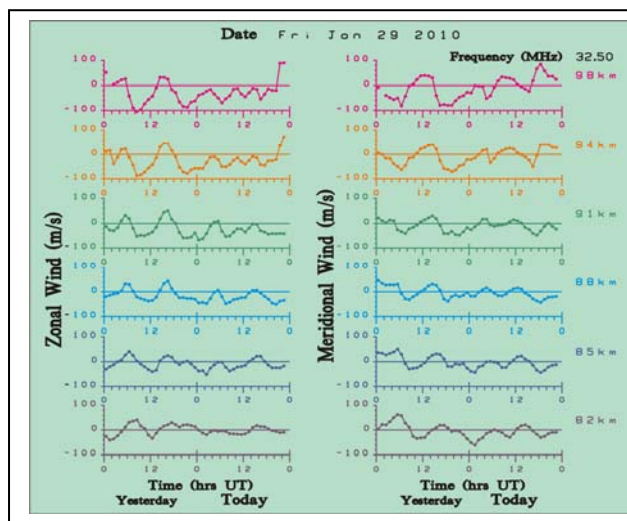


Fig.4. Winds recorded for Jan 28 and 29, 2010 at an Axonmet site.

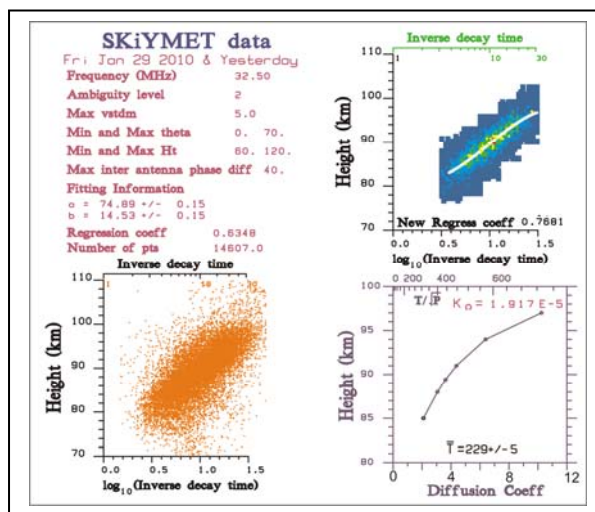


Fig. 5. Plots relating to decay times, ambipolar diffusion and temperatures.

and meridional (northwards), and, as in the earlier figures, are given for the current and previous days. Fig.5 shows data related to decay times and temperatures. Parameters used in the data-extraction are summarized in the top left of the figure, as well as correlation coefficients for the fitting of the log(inverse-decay times) vs. height.

It should be noted that the correlation coefficients will be less for lower temperatures (smaller scale heights) – this is a geophysical effect, as described by Hocking (2004). The lower left panel shows inverse decay times plotted as scatter plots as a function of height, and the top right-hand corner shows the same data but plotted as a colour-coded density plot. A best-fit polynomial is also fitted to the data (white line).

A straight-line fit is also performed. The coefficients are indicated in the table at left, with a revised regression coefficient, calculated after outliers are removed, shown above the abscissa in the top right-hand figure. At the bottom right, a graph of the mean diffusion coefficient is plotted as a function of height. This is also related to T^2/P (top axis).

T^2/P can be used to deduce the temperature if the pressure is known e.g., Hocking et al., (1997). Usually the pressure is not well known, and the temperature is found from the slope of the best-fit line, following Hocking, (1999); Hocking et al., (2004). The temperature deduced in this way is shown at the bottom of the right-hand lower figure, written just above the abscissa. Fig. 6 shows a sample of winds measured across the globe at 90 km altitude for June 17-18, 2008.

References:

- Franke et al., *J. Geophys. Res.*, **110**, D09S02, doi:10.1029/2003JD004486, 2005
 Hocking, W.,K., et al., *Geophys. Res. Lett.*, **24**, 2977-2980, 1997.
 Hocking, W.K., *Geophys. Res. Letts.*, **26**, 3297-3300, 1999.
 Hocking, W.K., et al., *J. Atmos. Solar-Terr. Physics*, **63**, 155-169, 2001.
 Hocking et al., *J. Atmos. Solar-Terr. Phys.*, **66**, 585-593, 2004.
 Hocking, W. K., *Annales Geophysicae*, **22**, 3805-3814, 2004.
 Jones et al., *Geophys. Res. Letts.*, **30**, 1743-1746, 2003.
 Smith, S.M, et al., *J. Geophys. Res.*, **108**(A2), 1083 doi:10.1029/2002JA009500, 2003.

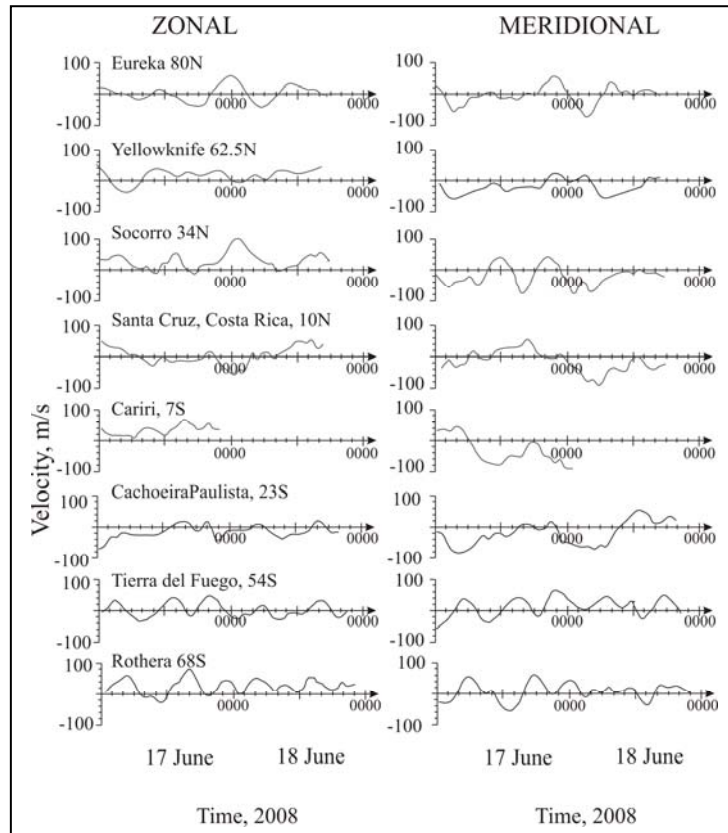


Fig. 6. Plots of winds at multiple sites from the far north to the far south for 90 km altitude for June 17-18, 2008.

LONG-TERM VARIATIONS OF LOW LATITUDE MESOSPHERIC MEAN WINDS OBSERVED USING INDIAN MST RADAR, MF RADAR, M-100 ROCKETSONDES AND HRDI MEASUREMENTS

G. Kishore Kumar¹, M. Venkat Ratnam², A. K. Patra², K. Kishore Kumar³, Geeta Ramkumar³,
S. Gurubaran⁴ and S. Vijaya Bhaskara Rao⁵

¹Department of Physics and astronomy, University of Western Ontario, London, Canada.

²National Atmospheric Research Laboratory, Tirupati, India.

³Space Physics Laboratory, Vikram Sarabhai Space Centre, Trivandrum, India.

⁴Equatorial Geophysical Research Laboratory, Indian Institute of Geomagnetism, Tirunelveli, India.

⁵Department of Physics, Sri Venkateshwara University, Tirupati, India.

1. Introduction

The mesosphere is the least explored region compared to other regions on earth atmosphere. In particular, the equatorial and low-latitude mesosphere shows different behavior, due to relatively less Coriolis force, quasi-biannual oscillation (QBO) and semiannual oscillation (SAO) in the zonal wind [Hirota, 1978; Andrews *et al.*, 1987]. In the present extended abstract we mentioned the details of the mean wind flow and the long-term variations of the mesospheric QBO and SAO using ground based (M100 rocket, MF radar and MST radar) and space borne observations (HRDI\UARS). More details about the mean winds and mesospheric QBO (MQBO) and SAO (MSAO) can be found in *Kishorekumar et al.*[2008], *Ratnam et al.*[2008].

2. Data Base

To investigate the background wind structure of the mesosphere and long-term variations in mesosphere like MQBO and MSAO, long term data base available over different low latitude stations have been used. The data base contains both ground based and space borne observations. The selected data included M-100 rocket (1971-1990) observations from Thumba (8.5°N, 77°E), Medium Frequency (MF) radar (1993-2001) observations from Tirunelveli (8.7°N, 77.8° E), and Mesosphere-Stratosphere-Troposphere (MST) radar (1994-2006) observations from Gadanki (13.5°N, 79.2°E). High Resolution Doppler Imager (HRDI) aboard Upper Atmosphere Research Satellite (UARS) (1991-2000) winds between the grids 8.5°N to 18.5° N and 69°E to 89°E are also used. The observed mean winds are also compared with Horizontal wind model 93 (HWM93).

3. Results and Discussion

3.1. Mean wind structure

The MST radar observations from mesosphere are mainly due to fluctuations in electron density which will be less during nighttime and hence daytime observations are only available to get reliable signals for wind estimation. So we restricted our analysis to daytime observations (1000 to 1600 local time (LT)) in the 65–85 km height region.

Figure 1 shows the composite monthly behavior of zonal (left panels) and meridional (right panels) winds obtained from different techniques. Clear eastward and westward flow in zonal wind is noticed during solstices and equinoxes, respectively. A clear SAO is observed in zonal wind in between 70 and 85 km with peak westward wind during the equinoxial months. Although all observations show similar behavior of SAO, there exists difference between the heights and intensity of SAO among different techniques. However, notable feature in all the observations is that the first peak of the SAO is stronger than the second peak, nearly twice of the second peak. From MST radar composite monthly wind, note that westward flow during the

fall equinox (~ 20 m/s) is much weaker than the spring equinox (~ 40 m/s). It is interesting to note that the first peak of SAO is observed relatively at higher heights than the second peak of SAO. The seasonal asymmetry of SAO can be ascribed to inter-hemispheric differences in planetary wave activity which is source for the SAO [Garcia *et al.*, 1997].

The eastward flow during winter period can be related to the mesospheric westerly jet of winter hemisphere. The eastward wind prevailing in winter decreases with increasing height, which is consistent with that reported elsewhere. Inspection of the composite monthly variations of M-100 rocket, HRDI, and MST radar observations, which belongs to different time spans, imposes a surprising result that the eastward flow during winter months decreases with time. It is clearly noticed that the wind reversal height also decreases similar to the winter eastward flow.

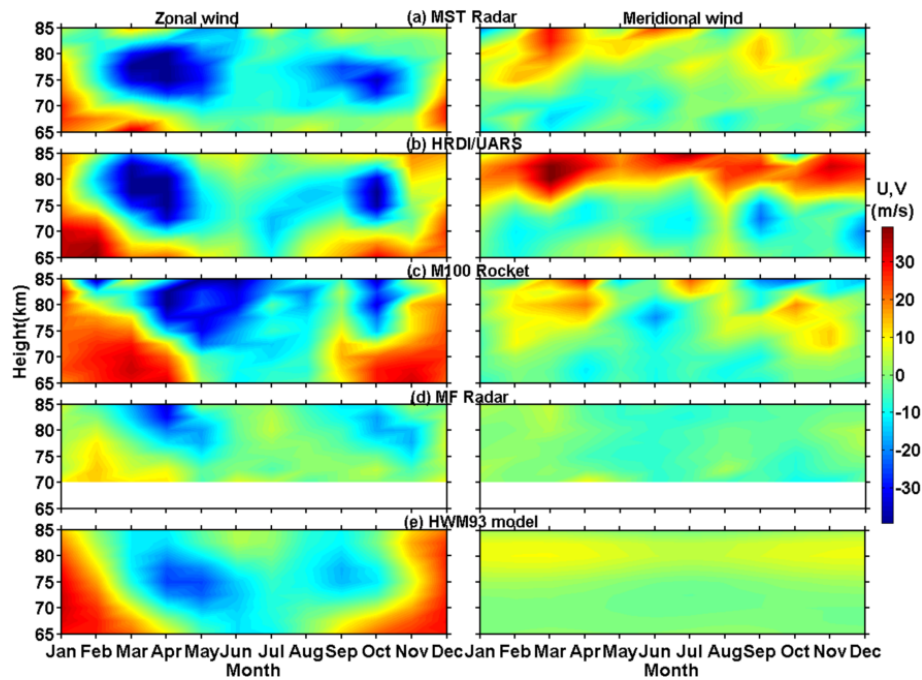


Figure 1. Composite monthly variation of zonal wind and meridional wind observed by (a) MST radar (1995–2006), (b) HRDI/UARS (1991–2000), (c) M100 rocket (1977–1991), (d) MF radar (1993–2000), and (e) HWM93 [Kishorekumar *et al.*, 2008].

Figure 1 (right) illustrates the meridional flow observed with different techniques. These panels clearly reveal the trans-equatorial flow of meridional winds: equatorward (southward) flow below 75 km and poleward (northward) flow above 75 km. There are large discrepancies between the magnitudes and the same can be attributed to the difference in data sampling methods as mentioned above. Figure 1b (right) reveals a strong poleward flow in HRDI meridional wind at and above 80 km and the same is due to diurnal tide signature, which cannot be nullified by the simple average of the wind profiles. The diurnal tide signature is maximum during equinoctial months. The MST radar meridional winds also show semiannual oscillation, although not clear like zonal winds: first maxima during March–April and second maxima during September–October. It is also to be noted that the second maxima (~ 10 m/s) is much weaker than the first maxima (~ 20 m/s). Similar to that observed in zonal wind the first maximum occurs at higher heights compared to second maxima. Similar SAO structure is also observed in the M-100 rocket observations. This signature is not clear in MF radar and HWM93 model winds.

3.2. Long term variation of MQBO and MSAO

From the comparison it is clear that most of the techniques are providing reliable wind information in the altitude range of 70–80 km except the MF radar. Thus, we used the M-100, HRDI and MST radar observations to generate the monthly mean winds for the period 1977–2006. Monthly mean winds are used for the extraction of MSAO and MQBO. To get reliable signal of MSAO and MQBO, the monthly mean winds between 70–75 km and 75–80 km have been averaged and taken as representative for 72.5 km and 77.5 km, respectively. To study the time evolution of MSAO and MQBO, a second order Butter-worth band pass filter with a pass band of 5–8 months and 23–36 months, respectively, was used.

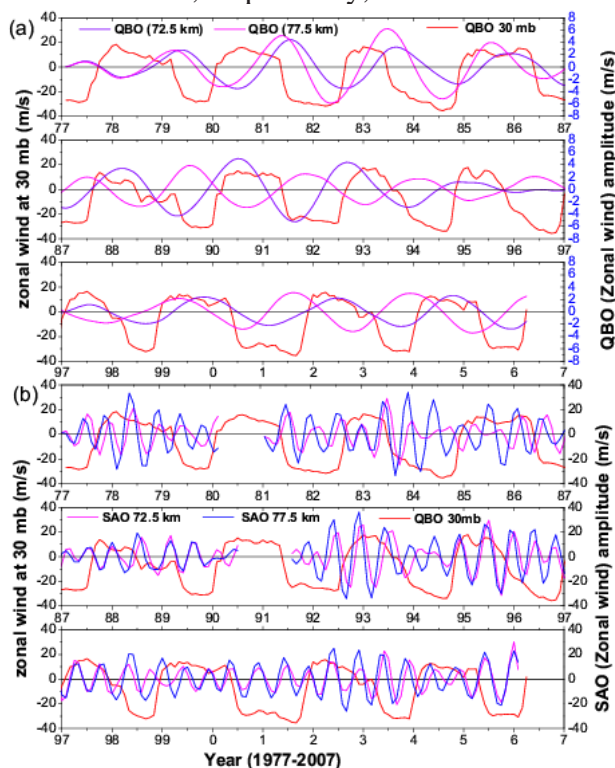


Figure 2. (a) Long-term variation of stratospheric mean zonal wind 30 mb observed at Singapore and superimposed lines are the amplitudes of MQBO at 72.5 km and 77.5 km with axis on right side. (b) Same as Figure 2(a) but for amplitudes of MSAO at 72.5 km and 77.5 km with axis on right side [Ratnam *et al.*, 2008].

Figure 2a shows the variation of MQBO at 72.5 km and 77.5 km with superposed Singapore stratospheric winds at 30 mb showing SQBO. The stratospheric winds clearly showed the QBO with period ranging from 25–35 months. Nearly 12 SQBO cycles are observed during 1977–2006 and out of them three long period SQBO cycles have been observed with more than 32 months periodicity during 1983–86, 1988–91, and 2000–03. In general, Figure 2a reveals that the MQBO at 72.5 km and 77.5 km are out-of-phase with SQBO, consistent with the earlier observations by *Burrage et al.* [1996]. However, during a few QBO cycles, this phase difference is nearly absent. From 1977–2006, in general, westward phase of MQBO at 77.5 km occurs during the eastward phase of SQBO. Except during 1982–1987 and 1999–2001 where this relation is completely opposite. It is seen that during these years, SQBO period is quite long being >32 months. Even though the 1988–1991 SQBO has 35 months period, it is not strong like the other two long SQBOs (note that the strength of QBO is defined based on the amplitude of

the winds). This indicates that the out-of-phase relation between SQBO at 30 mb level and MQBO at 77.5 km fails during long and strong SQBO. The phase relation may not change for long and weak SQBO.

Figure 2b reveals the variation of MSAO at 72.5 km and 77.5 km and its relation to SQBO. The MSAO at 72.5 km follows MSAO at 77.5 km, clearly showing the downward phase progression both in eastward and westward phases. The downward phase progression varies from 1–5 km/month. In a few cycles (for example, during 1985, 1992, 1994), the progression is rapid enough to cause phase reversal between SAO at 77.5 and 72.5 km. The amplitude of the MSAO varies from 10–35 m/s. The observed amplitudes of MSAO are in general smaller than those reported for Christmas Island from rocket and HRDI [Burrage *et al.*, 1996] and meteor radar observations [Palo and Avery, 1993]. This difference in the amplitudes can be attributed to the fact that Christmas Island results correspond to a higher height and lower latitude compared to the present results. It is also clear that the first peak of SAO (spring equinox) is stronger than the second peak of SAO (fall equinox). The difference in the spring and fall equinox SAO amplitudes is discussed by Garcia *et al.* [1997] in the light of hemispheric asymmetry in wave forcing. Bispectrum analysis shows that MSAO and MQBO interact non-linearly and produce side bands in MSAO. Present results show that the modulations of MSAO would not only occur during the eastward phase of SQBO but also in westward phase (relatively with fewer chances). This phenomenon is observed to be prominent at 77.5 km.

References :

- Andrews, D. G., J. R. Holton, and C. B. Leovy, Middle Atmosphere Dynamics, 489 pp, *Academic Press*, Orlando, FL, 1987.
- Burrage, M. D., R. A. Vincent, H. G. Mayr, W. R. Skinner, N. F. Arnold, and P. B. Hays, Long-term variability of the equatorial middle atmosphere zonal wind, *J. Geophys. Res.*, 101, 12,847– 12,854, 1996.
- Garcia, R. R., T. J. Dunkerton, R. S. Lieberman, and R. A. Vincent, Climatology of the semiannual oscillation of the tropical middle atmosphere, *J. Geophys. Res.*, 102(D22), 26,019– 26, 032, 1997.
- Hirota, I., Equatorial waves in the upper stratosphere and mesosphere in relation to the semiannual oscillation of the zonal wind, *J. Atmos. Sci.*, 35, 714, 1978.
- Kishore Kumar, G., M. Venkat Ratnam, A. K. Patra, V. V. M. Jagannadha Rao, S. Vijaya Bhaskar Rao, K. Kishore Kumar, S. Gurubaran, G. Ramkumar, and D. Narayana Rao, Low-latitude mesospheric mean winds observed by Gadanki mesosphere-stratosphere-troposphere (MST) radar and comparison with rocket, High Resolution Doppler Imager (HRDI), and MF radar measurements and HWM93, *J. Geophys. Res.*, 113, D19117, doi:10.1029/2008JD009862, 2008.
- Palo, S. E., and S. K. Avery, Mean winds and the semiannual oscillation in the mesosphere and lower thermosphere at Christmas Island, *J. Geophys. Res.*, 98(D11), 20,385–20,400, 1993.
- Ratnam, M. V., G. K. Kumar, B. V. K. Murthy, A. K. Patra, V. V. M. J. Rao, S. V. B. Rao, K. K. Kumar, and G. Ramkumar, Long-term variability of the low latitude mesospheric SAO and QBO and their relation with stratospheric QBO, *Geophys. Res. Lett.*, 35, L21809, doi:10.1029/2008GL035390, 2008.

TIDAL AND PLANETARY WAVE COUPLING OF THE LOW LATITUDE MESOSPHERE-LOWER THERMOSPHERE-IONOSPHERE (MLTI) REGION

S. Gurubaran¹, R. Dhanya¹, S Sathiskumar¹ and P. T. Patil²

¹ Equatorial Geophysical research Laboratory, Indian Institute of Geomagnetism, Tirunelveli, India

² MF Radar, Indian Institute of Geomagnetism, Shivaji University Campus, Kolhapur, India

1. Abstract

Planetary-scale waves like tides, global-scale normal modes and equatorial Kelvin waves play an important role in the dynamics of the mesosphere-lower thermosphere (MLT) region. It has been hypothesized in the past that if a global-scale wave with large amplitude and fairly long vertical wavelength propagates into the ionosphere from below, it should drive an electric current system through the dynamo action with a period of the global-scale wave. This wave-like perturbation causes perturbations in geomagnetic field that could be recorded on ground. Part of these variabilities during magnetically quiet times could very well be due to the variabilities of tides and other planetary-scale waves but what conditions exist in the MLT region that permit these large-scale waves to reach the dynamo heights and have an influence on the ionospheric variabilities there and higher above are not known. Aiming to resolve this issue, we recently initiated an analysis of simultaneous observations of MLT winds from the two low latitude MF radar sites, Tirunelveli (8.7°N) and Kolhapur (16.8°N), available for about an year (2008-2009) in the Indian sector. Results from this exercise will be presented and discussed in the current context of our understanding of the role of tides and planetary waves in the ionospheric variabilities at low latitudes.

2. Introduction

Electric fields at E and F region heights show a considerable day-to-day variability even during magnetically undisturbed conditions and this variability is still one of the less understood aspects of ionospheric physics. The propagation of planetary waves, tides and gravity waves into the ionosphere may play an important role in this day-to-day ionospheric variability.

Planetary scale waves like tides, global-scale normal modes and equatorial Kelvin wave play an important role in the dynamics of the mesosphere-lower thermosphere (MLT) region. Earlier it has been hypothesized that if a global-scale wave with large amplitude and fairly long vertical wavelength propagates into the ionosphere from below, it should drive an electric current system through the dynamo action with a period of the global-scale wave. This wave-like perturbation causes perturbation in the geomagnetic field that could be recorded on the ground. We look for a wave that has its origin in the lower atmosphere and that travels up to E region heights and even above and drive the electric fields at ionospheric heights. We intend to identify waves having those periodicities and study them in detail.

This work aims to identify the role of wave dynamical processes in causing the observed variabilities in winds in the mesosphere-lower thermosphere region at low latitudes and the wave signatures in quiet-time ionospheric current systems (Sq and Equatorial Electrojet (EEJ)) using ground magnetic records.

MF radar data available from the low latitude Indian sector for the specified period were subjected to traditional FFT, focusing on 90, 92 and 94 km heights. The FFT analysis performed separately for zonal and meridional winds shows the presence of 5-8 and 10-13 day wave periodicities in meridional wind and 5, 6.5, 10, 16 day periodicities in zonal wind for the period Feb-Apr 2008 (Figure 1). Besides FFT, wavelet and band pass filtering techniques were used to identify the time of occurrence of these bursts.

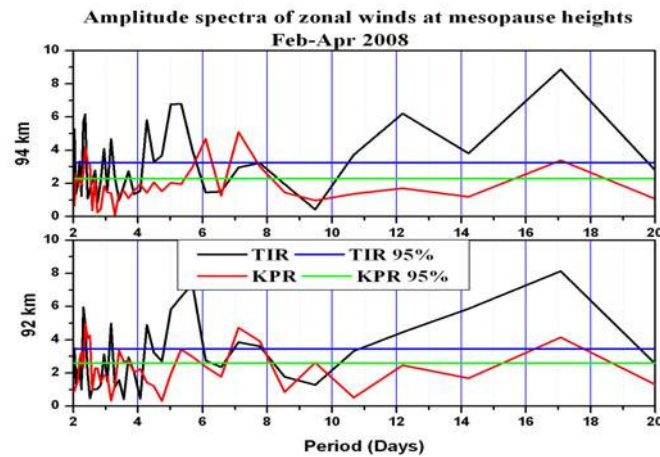


Fig 1: FFT amplitude spectra of radar zonal winds

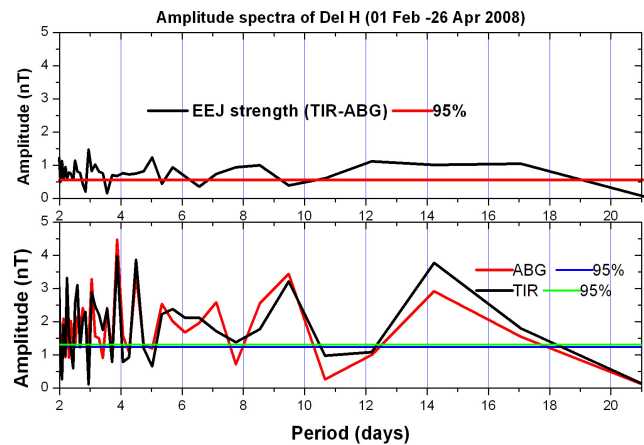


Fig 2: FFT amplitude spectra of geomagnetic field

Hourly values of magnetometer data from the equatorial station, Tirunelveli and an off equatorial station, Alibag, were used to determine the strength of the EEJ given by the difference between the horizontal field variations at Tirunelveli and Alibag.

It was evident that 5 day and 16 day periodicities were strong in both radar (zonal wind) and magnetometer data (Figure 2). We anticipate that the planetary waves that are responsible for these variabilities are either in-situ generated or they are of lower atmospheric origin propagating through the middle atmosphere.

To ascertain this we examined the zonal and meridional wind data obtained from UKMO assimilations. UKMO zonal winds show the presence of 16 day wave at 5 hPa (~ 37 km) (Figures 3 and 4) confirming that these waves were generated in the lower atmosphere and propagated to ionospheric heights and modulated the E-region electric field there.

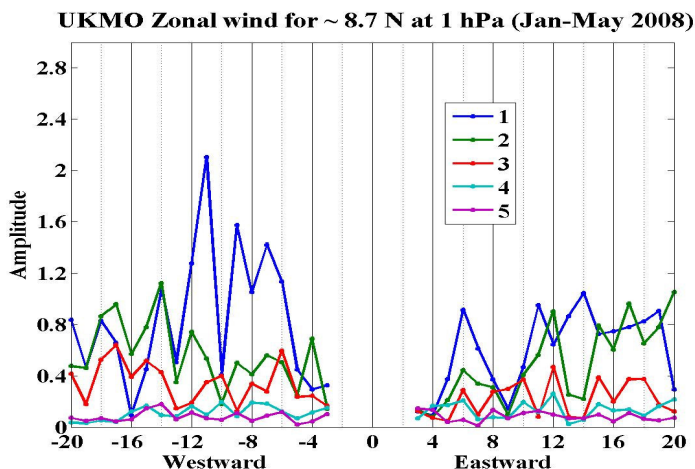


Fig 3: Wavenumber frequency spectra of UKMO zonal wind for $\sim 8.7^\circ\text{N}$ at 5 hPa

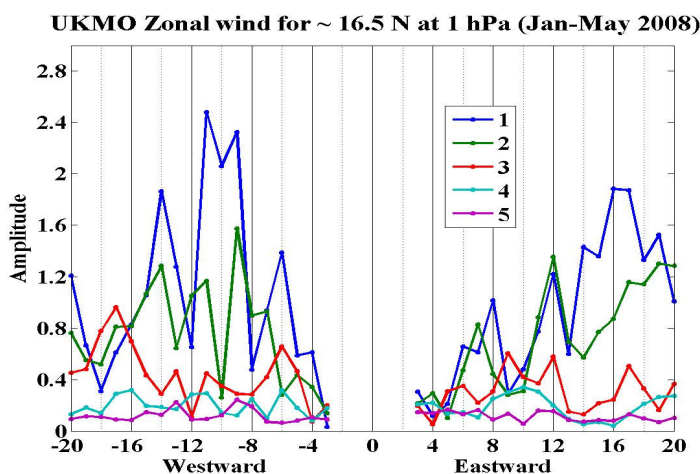


Fig 4: Wavenumber frequency spectra of UKMO zonal wind for $\sim 16.5^\circ\text{N}$ at 5 hPa

Wave number spectral analysis similar to one described by *Pancheva et al.* [2008] has been performed. This analysis shows that most of the energy of the 16 day wave was in westward wave number 1.

Tidal winds over Tirunelveli and Kolhapur exhibit rich spatio-temporal behavior during summer 2008 (Figure 5). A detailed study is being carried out on this aspect and the results will be presented in a future meeting.

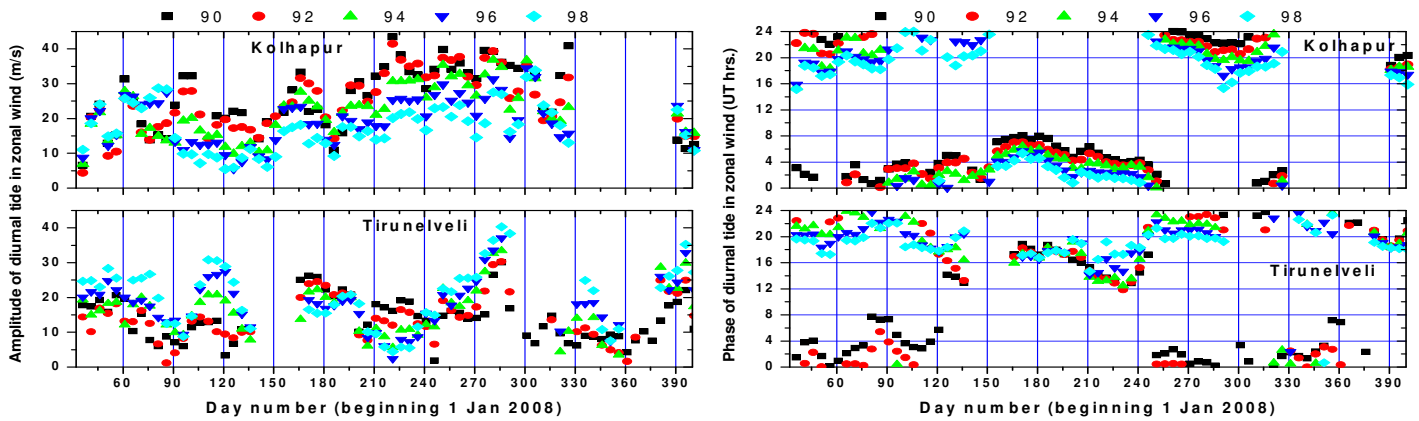


Fig 5: Amplitude and phase of diurnal tide over Tirunelveli and Kolhapur for the heights 90-98 km in 2km interval

3. References

Pancheva, D., et al., Planetary waves in coupling the stratosphere and mesosphere during the major stratospheric warming in 2003/2004, *J. Geophys. Res.*, 113, D12105, doi:10.1029/2007JD009011, 2008.

DIURNAL AND SEASONAL VARIABILITY OF D-REGION ELECTRON DENSITIES AT 69°N

W. Singer¹, R. Latteck¹, and M. Friedrich²

¹ Leibniz Institute of Atmospheric Physics, Kühlungsborn, Germany

² Technical University of Graz, Graz, Austria

1. Introduction

The availability of electron densities in the lower ionosphere (50-90 km) is relatively limited, partly because of observational limitations and partly because of difficulties in interpreting the observed ground-based data. The relatively high neutral air densities make measurements with sounding rockets difficult and seldom. The partial reflection experiment utilizes partial reflection of radio waves with ordinary and extraordinary polarisation from scatterers in the altitude range 50-90 km to estimate electron densities. The 3-MHz narrow-beam Doppler radar installed in Saura close to the Andøya Rocket Range in Andenes, Norway (16.3°E, 69.0°N) provides electron densities using the differential absorption experiment (DAE) as well as the differential phase experiment (DPE) at 3.17 MHz since summer 2003.

2. Measurement principle

Pulses of medium or high frequency (2–6 MHz) are vertically radiated with circular polarisation corresponding to the two characteristic components, the ordinary (o) and extraordinary (x) mode. Their returns from ionospheric scatterers below the E-region are received and the amplitude ratio A_x/A_o (phase difference $\varphi_x - \varphi_o$) is measured as function of height (for an overview of the technique see Manson and Meek, 1984). The ratio of the amplitudes A_x/A_o (equation 1) is related to the ratio of the reflection coefficients R_x/R_o (assumed to be independent from the electron number density)

$$\frac{A_x}{A_o} = \frac{R_x}{R_o} \exp \left\{ -2 \int_0^h (k_x - k_o) dh \right\} \quad (1) \quad N(h) = \frac{\Delta(\ln R_x / R_o) - \Delta(\ln A_x - A_o)}{2(k_x - k_o)\Delta h} \quad (2)$$

For the differential absorption experiment (DAE) the electron density $N(h)$ is obtained from the amplitude ratios at adjacent heights according to equation (2) where $(k_x - k_o)$ is the normalized differential absorption $(\chi_x - \chi_o)\omega/c$ and ω is the wave frequency, and $\chi_{x,o}$ the imaginary part of the generalized Sen-Wyller complex refractive index $(\mu - j\chi)$.

A monoenergetic collision frequency profile $\nu_m(h)$ is required for equations (1) and (2). It is obtained from atmospheric pressure profiles $p(h)$ of a model atmosphere, e.g. CIRA, or in-situ observations by falling sphere soundings are used.

$$\nu_m(h) = K \cdot p(h) \quad \text{with} \quad K = 6.4 \cdot 10^{-5} \frac{2}{m} \frac{s^{-2}}{N^{-1}} \quad (3)$$

3. The DAE/DPE experiment

The narrow beam transmitting/receiving antenna of the Saura MF radar consists of 29 crossed 3.17-MHz half-wave dipoles and is arranged as a Mills Cross. The positions of the crossed dipoles are shown in Fig. 1 (left part). Each dipole is fed by its own transceiver unit with a peak power of 2 kW which is individually controlled in phase on transmission and reception.

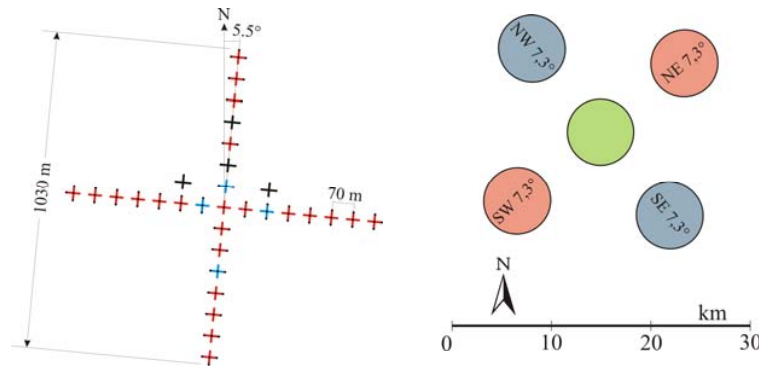


Figure 1. Mills Cross antenna of the Saura MF radar and illuminated areas by the vertical and oblique beams (7.3° off-zenith) in 85 km.

Antenna and transceiver system provide high flexibility in beam forming and pointing as well as the capability forming right and left circular polarization (ordinary and extraordinary magneto-ionic component). Interleaved transmission of the ordinary and extraordinary polarisation with a change of the polarisation from data point to data point allows differential absorption (DAE) and differential phase (DPE) measurements to estimate electron densities. The system is operated with a peak power of 116 kW and has a best height resolution of 1 km. Normally pulses of 10 μ s width at a pulse repetition frequency of 80 Hz and two coherent integrations only are applied. The small number of coherent integrations results in a wide spectral range of ± 10 Hz. Frequency aliasing of interfering signals into the frequency band (± 0.5 Hz) of the atmospheric signal is considerably reduced. With a sequence of tilted and vertically directed beams (right part of Fig. 1) horizontal winds and turbulence from spectral width data can be derived (Singer et al., 2008).

4. Results

The Saura MF radar continuously provides in standard mode of operation electron density profiles each 9 minutes in height steps of 1 km. We present hourly mean height profiles formed as average of the electron densities estimated from the DAE and DPE experiments with the constraint that DAE/DPE electron number densities do not differ by more than a factor of two. The height profiles cover an altitude range 60-85 km under undisturbed ionospheric conditions, reliable data down to 55 km are obtained under disturbed conditions (geomagnetic disturbances and/or solar activity storms). The height coverage is some times reduced by an enhanced background noise level due to external interference (other transmitters or long distance HF propagation at night-time) as shown in Fig. 2 for observations under polar night conditions. The background noise level is determined as mean value of the echo power measured at the heights 40-45 km.

The electron density profiles derived from DAE and DPE measurements are in remarkable good agreement between 55 - 85 km (Fig. 3).

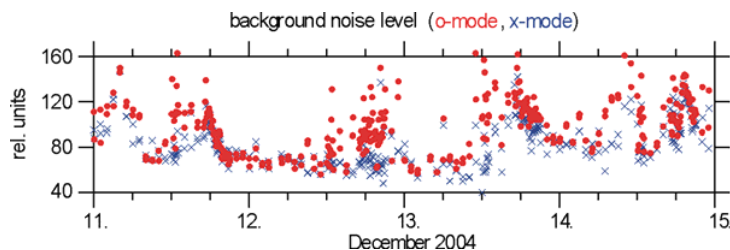


Figure 2. Diurnal variation of the background noise level of o- and x-mode on December 11-15, 2004.

General agreement was also found with electron densities from rocket-borne radio wave propagation measurements (Faraday rotation; Jacobsen and Friedrich, 1979) at Andenes as shown in Figure 4 by co-located and simultaneously measured electron density profiles.

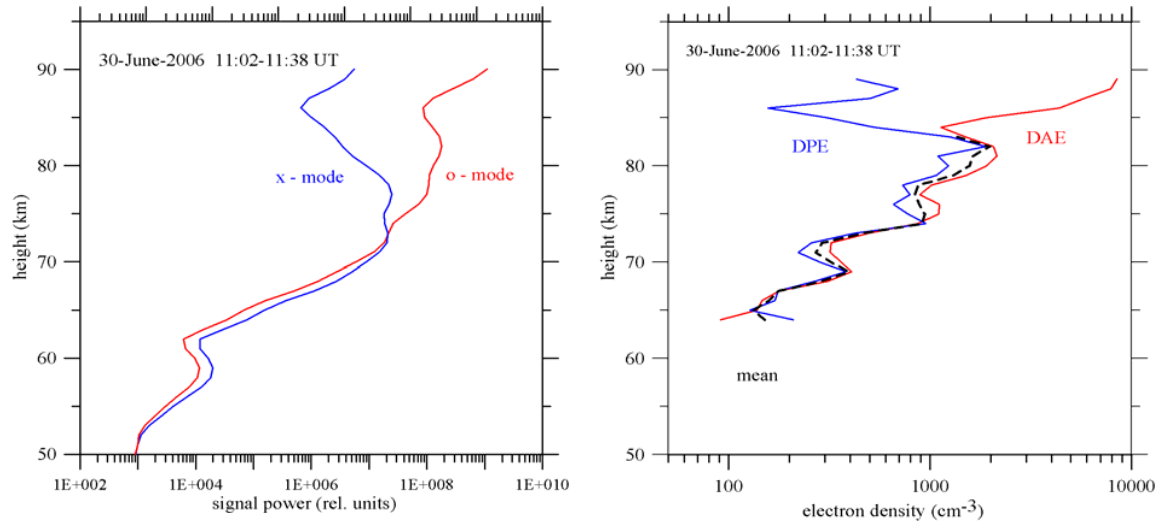


Figure 3. Echo power of the ordinary and extra-ordinary mode and corresponding electron densities after DAE and DPE measurements (dashed: mean profile).

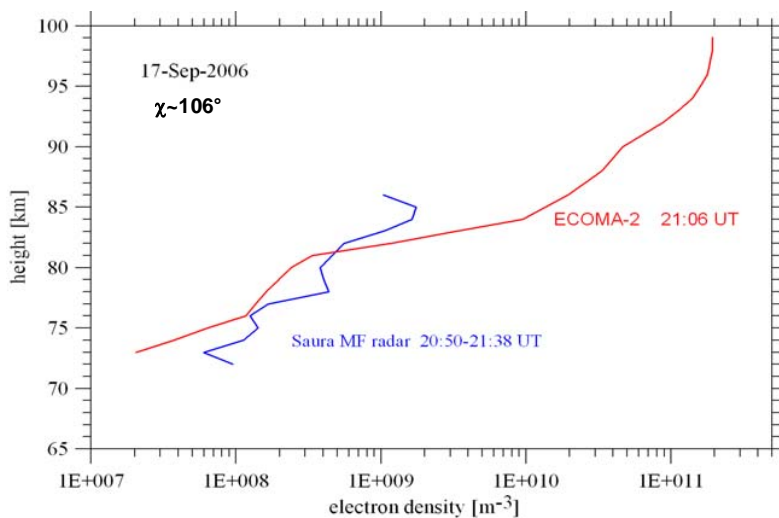


Figure 4. Ground-based and rocket-borne electron density measurements.

The derived electron densities are characterised by well expressed solar zenith angle dependence under undisturbed conditions (ionization by solar EUV) with increasing electron density for decreasing solar zenith angle (Fig. 5). Figure 6 depicts the seasonal variation of electron density basing on monthly mean profiles at a constant solar zenith angle ($SZA=80^\circ$) for February, April, and June show a weak seasonal variation with the lowest electron density values in April (Fig. 6, left panel). The deep minimum of electron density (bite out) in June 2008 around 83 km (also present on July 7, 2004 in Figure 5) is related to appearance of nanometer-sized ice particles in the cold polar summer mesopause region capturing free background electrons. At moderate solar activity ($SZA=50^\circ$) electron densities are enhanced at altitudes above about 65 km due to increase of solar UV and Ly- α radiation whereas ionization by galactic cosmic rays dominates below 65 km at low solar activity (Fig. 6, right panel). During solar activity storms enhanced electron densities by one order of magnitude are observed down to about 55 km (Fig. 7).

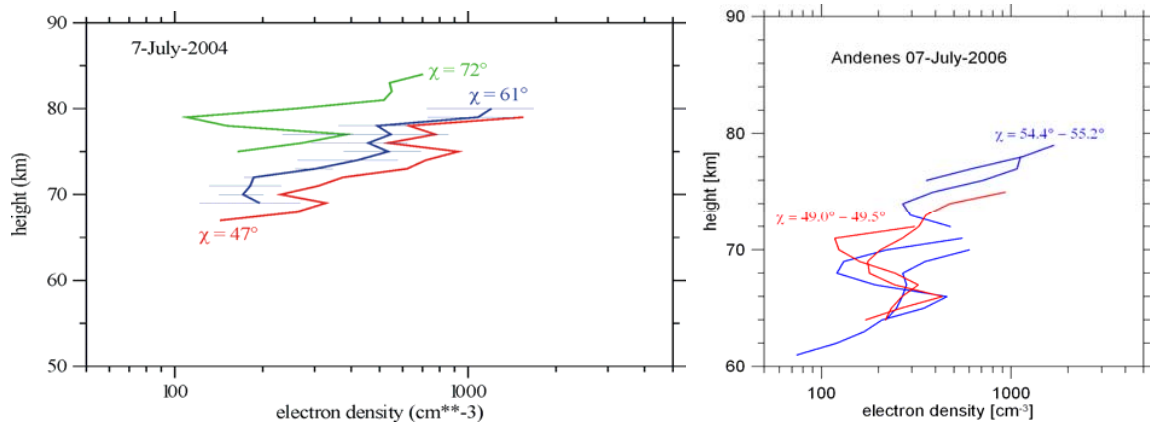


Figure 5. Diurnal variation of electron density in summer.

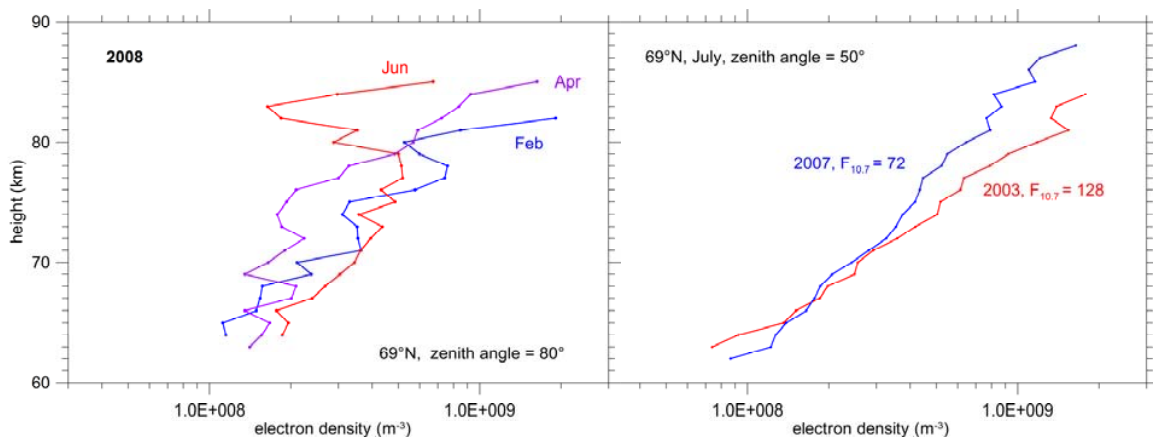


Figure 6. Seasonal and solar activity variation of electron density.

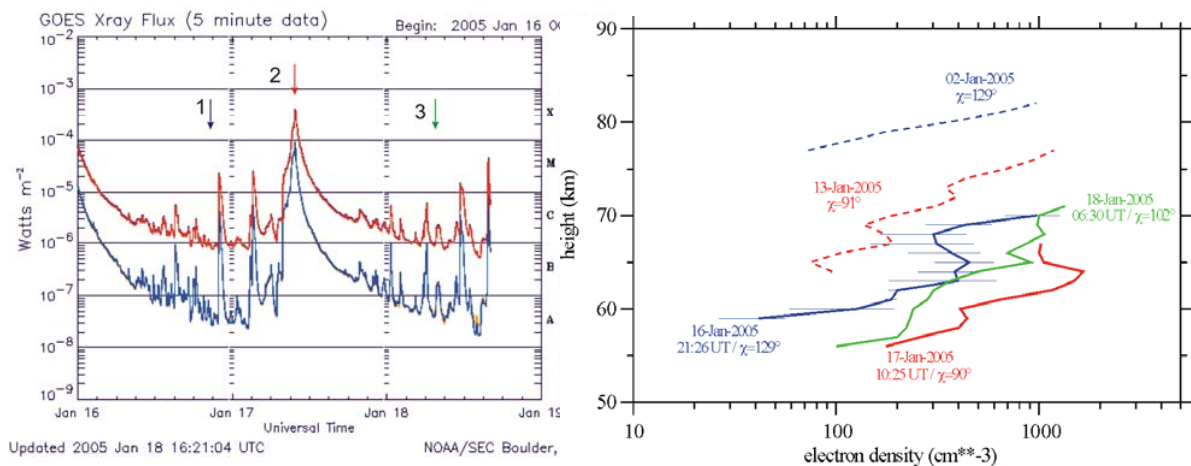


Figure 7. Electron density profiles before (16-Jan), during (17-Jan) and after (18-Jan) the solar activity storm on January 17, 2005 together with solar proton fluxes (left panel).

References

- Manson, A.H., and C.E. Meek, *MAP Handbook*, **13**, 113-123, 1984.
 Jacobsen, T.A. and M. Friedrich, *J. atmos. terr. Phys.*, **41** (12), 1195-1200, 1979.
 Singer, W., R. Latteck, and D.A. Holdsworth, *Adv. Space Res.*, **41**, 1487-1493, 2008.

ON THE VIABILITY OF LAGRANGIAN THEORIES OF INTERNAL WAVE SPECTRA: IMPLICATIONS FOR DOPPLER-SPREAD THEORY AND RADAR MEASUREMENTS

Gary P. Klaassen

Dept. of Earth & Space Science & Engineering, York University, Canada

1. Introduction.

This paper addresses a recent controversy regarding the mechanisms responsible for saturated internal wave fields in the middle atmosphere. Key assumptions made in the kinematic advection theories of Allen and Joseph (1989, hereafter AJ89), Hines (2001, hereafter H01) and Chunchuzov (2002, hereafter C02) are tested, and the consequences for the Doppler-spread theory (Hines 1991, hereafter H91) and its associated parameterization (Hines 1997, hereafter H97) are discussed. Further implications for middle atmosphere measurements are considered.

2. The Debate Over the Nature of the Saturated Gravity Wave Spectrum.

H91 proposed that conservative wave-wave Doppler spreading processes are the dominant mechanism for the formation of the universal saturated spectrum found (on average) in measurements of atmospheric fluctuations (e.g. Smith et al. 1987). According to Hines, the advective nonlinearity “has the effect of Doppler shifting the local intrinsic frequency of any given wave in the wind field imposed by all waves.” Waves with vertical wavenumbers m exceeding a characteristic value m_c (comparable to $N/2\sigma$, where N is the buoyancy frequency and σ is the rms wind speed) are “spread” predominantly toward larger vertical wavenumbers where they would assume m^{-3} form. During these wave-wave Doppler-spreading interactions, no momentum would be transferred to the mean background flow unless the tail extended to sufficiently large m , say m_M . At $m > m_M$, waves were expected to “enter into critical-layer interactions as they approached heights where their intrinsic frequencies were Doppler shifted toward zero”; these interactions would obliterate the short-scale waves and deposit their momentum to the background flow. Thus, in this picture, gravity-wave momentum deposition is an indirect consequence of conservative wave-wave Doppler spreading, and is confined to the shortest scales.

As stated by H91, the Doppler-spread analysis treats each individual wave as if it “were propagating (without reflections) through a stationary, non-wave system of horizontal winds having the same statistical characteristics as the irregular wind field”. Eckermann (1997, hereafter E97) tested the validity of this key assumption with a ray tracing model. He presented examples which demonstrated that H91’s stationary-wave assumption led to significant overestimates of short-wave refraction; he also found no evidence for critical-layer events of the sort envisaged by H91. Hines (1999, hereafter H99) argued that E97’s use of eikonal methods (which require sufficient scale separation) was inappropriate for the broad spectrum of waves envisaged by H91, and that E97’s calculations contained too few waves (less than or equal to 8) to be considered a “broad” spectrum. H99, however, offered no calculations to support his claims; instead, he appealed to earlier results of AJ89, who had derived wave spectra similar to H91’s without neglecting horizontal and temporal variations.

AJ89 advocated the calculation of Eulerian wave properties by transforming weakly-interacting (i.e. quasilinear) superpositions of Lagrangian waves into the Eulerian frame, a lengthy mathematical procedure which yielded an asymptotic Eulerian spectral tail of universal m^{-3} form. Both Hines (2001) and Chunchuzov (2002) have published variations on the AJ89 theory. A key assumption in all three versions is that the Jacobian of the Lagrangian to Eulerian transformation remain near unity (i.e. that changes in parcel

volume remain small). This condition is required to maintain the tractability of the Lagrangian to Eulerian transformation; it is also needed in order to approximate the Lagrangian spectrum by quasilinear (i.e. weakly- or non-interacting) waves.

Hines (2002a, hereafter H02a) noted that the theories for gravity-wave interactions and spectra advanced by Weinstock (1976, hereafter W76) and Medvedev and Klaassen (1995, hereafter MK95) were fundamentally incompatible with the quasilinear Lagrangian theories of AJ89, H01 and C02. Although H02a raised many issues, the basic argument concerned the mechanisms responsible for producing the saturated Eulerian tail in the vertical wavenumber range $m_c \leq m \leq m_M$. In H02a's view, this feature was produced by conservative kinematic advection processes (or wave-wave Doppler spreading), while in the view of W76 and MK95, saturation was produced by wave-wave interactions (and associated instabilities) that could be parameterized by a Taylor-type diffusion. In DSP, wave momentum deposition was confined to the components undergoing critical-level obliteration beyond the end of the tail ($m \geq m_M$). In the MK95 gravity wave drag parameterization, it is the momentum deposition at each wavenumber that produces the average m^{-3} form of the Eulerian tail. H02a claimed to have found mathematical errors in W76, which were supposed to resolve the disagreement in favour of AJ89, H01 and C02. Weinstock, Klaassen and Medvedev (2007, hereafter WKM07) showed that H02a's claim rested on a gross misinterpretation of W76's mathematical methods. [Incidentally, publication of WKM07 was delayed by an extended editorial exchange and review process, in which Dr. Hines eventually withdrew his response.]

3. Testing Hines' Prototype Quasilinear Lagrangian Spectrum.

Hines (2002b, hereafter H02b) derived criteria for Lagrangian quasilinearity and presented a prototype spectrum that was professed to satisfy these criteria. Vertical wavelengths ranged from 3.5 km to 14 km, while horizontal wavelengths ranged from 350 to 1400 km; the vertical displacement amplitude given by H02b was $\langle \zeta \rangle = 500$ m, where the angle brackets indicate a root-mean-square (rms) average, and N was taken to be 0.02 s^{-1} . These specifications are all representative of gravity waves in the Earth's middle atmosphere.

Using a kinematic advection model similar to that of Eckermann (1999, hereafter E99), it is a straightforward matter to specify the Lagrangian horizontal and vertical displacement fields (χ, ζ) as a sum of sinusoidal waves, to transform them to the Eulerian frame, and to calculate the corresponding average vertical wave number spectra. As a supplement to E99's model, I evaluate the range of parcel volumes in the wave field, using the Lagrangian continuity equation $J = V/V_0$, where J is the Jacobian, V_0 is the equilibrium parcel volume in the absence of waves, and V is the instantaneous parcel volume. These values may be compared to the range of parcel volumes expected for adiabatic wave fields; the latter are given by $J_{\text{ad}} = \exp[\zeta/\gamma H]$, where H is the isothermal scale height and $\gamma = c_p/c_v$ is the ratio of specific heats (Klaassen 2009a/b, hereafter K09a/b).

The present study examines cases with 21 Lagrangian waves, which individually obey the internal wave dispersion and polarization relations. The components are assigned one of 3 different horizontal wavenumbers $|k_j| = k_h/2, k_h, 2k_h$, and one of 7 different vertical wavenumbers $m_i = -[i + 1]m_c/8$, $i = 1, 2, \dots, 7$. The choices $k_h = 2\pi/(700\text{km})$ and $m_c = 2\pi/(3.5\text{km})$ correspond to H02b's prototype quasilinear Lagrangian spectrum.

The rms vertical displacement $\langle \zeta \rangle$ of the Lagrangian spectrum is chosen to produce values of α in the measured range for saturated atmospheric waves, $0.1 \leq \alpha \leq 0.5$. After the Lagrangian wave fields at a given instant are transformed to an Eulerian grid, vertical profiles are extracted at different horizontal locations. Eulerian power spectral densities

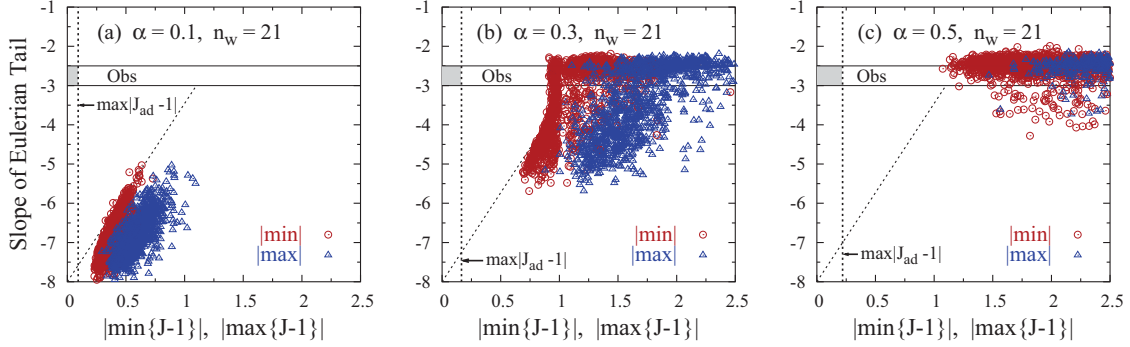


Figure 1: Scatter plots of Eulerian tail slope s vs. $|\min\{J-1\}|$ and $|\max\{J-1\}|$ for H02b-type fields with 21 waves and $\alpha =$ (a) 0.1, (b) 0.3, (c) 0.5. The data for a saturated atmospheric wave field would cluster within the shaded rectangle; H02’s prototype spectrum instead clusters around and to the right of the slanted dashed reference line. Note that $|J-1| \geq 1$ represents a singular Lagrangian to Eulerian transformation. For $\alpha = 0.5$, $|J-1|$ values extend far beyond the edge of the graph, to $|J-1| \sim 4$.

(PSD) of vertical displacement ζ are computed for each profile and then averaged. The PSD at $m > m_c$ is then fit to the empirical form αm^s . I also sample the same realizations of the wave field in order to calculate extreme values of both the volume ratio J and the vertical displacement ζ ; the latter are used to compute the expected adiabatic range of J -values, $J_{\text{ad}}(\pm\zeta_{\text{max}})$.

Fig. 1 shows scatter plots of average Eulerian tail slope s vs. the magnitude of the extreme values of $J-1$ for the cases $\alpha = 0.1, 0.3$ and 0.5 . Each point represents the values for a given instantaneous realization of the wave field, in a domain of vertical extent $8\pi/m_c = 14$ km and horizontal extent $4\pi/k_h = 1400$ km. The evolving fields are sampled 1280 times over a temporal record equal to 20 times the longest wave period present. If one plotted atmospheric measurements of saturated waves, the data would fall within the shaded boxes which are bounded by $|J-1| \leq \max|J_{\text{ad}}-1|$ and $-3 \leq s \leq -2.5$. If the theories and methods of AJ89, H01, H02b and C02 are correct for saturated waves, the kinematic advection model should produce an asymptotic Eulerian spectrum with “tail slope” near $s = -3$, while J values should remain near unity; such results should also cluster within the “observational box”. In contrast, one can see that not even a single realization of H02’s prototype spectrum comes close to the observational box.

The reason for this gross departure from physical behaviour becomes clear upon inspection of the J -values: not a single sample is anywhere near the value unity ($J-1 = 0$) required for Lagrangian quasilinearity. Moreover, those that are closest to unity [see Fig. 1(a), $\alpha = 0.1$] have corresponding tail slopes in the range of $s = -6.5$ to -8 , while still exceeding adiabatic J -values by a wide margin. Tail slopes only approach the saturated atmospheric range of -3 to -2.5 when the values of $|\min\{J-1\}|$ and $|\max\{J-1\}|$ are both $\gtrsim 1$. The latter case, however, corresponds to volume ratios, that are less than or equal to zero, a patently unphysical situation which indicates that some Lagrangian to Eulerian parcel transformations are singular. [Note that for $\alpha = 0.5$, all realizations of the wave field contain parcels with negative volumes. Any profile containing a parcel with negative volume has been excluded from the computation of Eulerian tail slopes.]

Fig. 2 graphically illustrates the consequences of imposing (as AJ89, H01 and C02 have done) a spectrum of sinusoidal internal waves in the Lagrangian frame. Since the transformation from Lagrangian to Eulerian coordinates is purely kinematic in the present model, for certain locations and wave fields, it blithely produces vertical profiles of the

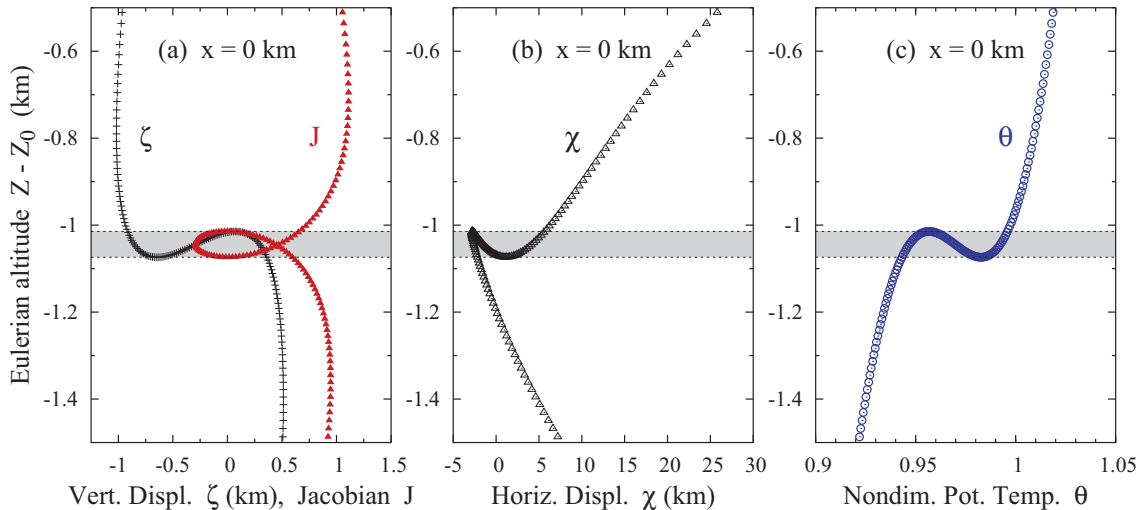


Figure 2: Vertical Eulerian profiles (at $x = 0$ and $t = 7854$ s) of horizontal and vertical displacements (χ, ζ), Jacobian J and nondimensional potential temperature θ ; for the Lagrangian ensemble ($n_w = 21, \alpha = 0.3$) of Fig. 1. Drawing (horizontal) lines at fixed Eulerian z demonstrates that for altitudes where one parcel has $J \leq 0$ (shaded region), a second or third parcel occupies the same position (x, z) .

peculiar form shown. In the shaded region $J \leq 0$, and the transformation is mathematically singular: for every level where $J \leq 0$ multiple parcels have been moved into the same physical (x, z) location. Similar unphysical behaviour is seen in profiles of horizontal and vertical displacement, as well as other fields such as the nondimensional potential temperature $\theta = \exp[N^2(z - \zeta)/g]$, where $N^2 = g(\gamma - 1)/\gamma H$ and g is the gravitational acceleration. This happens because the imposed Lagrangian wave field is not a valid solution of the dynamical equations of motion. Note that for every nonsingular altitude, the potential temperature profile has $d\theta/dz > 0$, indicating static stability, and that θ increases across the singular layer. Owing to the multivalued profile, $d\theta/dz$ takes on both positive and negative values at each level within the singular region; this is a mathematical oddity which serves to illustrate the bizarre consequences of the assumptions made by AJ89, H01 and C02.

In summary, when amplitudes are consistent with the measured range for saturated waves, H02b's prototype Lagrangian spectrum contains parcels with J -values that exceed adiabatic constraints by a considerable margin. The conclusion is inescapable: H02b's prototype Lagrangian spectrum does not even approximately satisfy the linearized Lagrangian continuity equation ($J \approx 1$), and therefore cannot be regarded as quasilinear. Furthermore, since the Lagrangian to Eulerian transformation is often singular (or nearly so), it does not produce physically plausible Eulerian wave fields. Ironically, H02b's proposed amplitude of $\langle \zeta \rangle = 500$ m corresponds to $\alpha = 1.1$, a value which exceeds the atmospheric range considered in Fig. 1 and produces even stronger and more extensive singularities than those shown here.

4. Implications for the Lagrangian Wave Theories of AJ89, H01, C02 and Hines' Doppler-spread Theory (DST) and Parameterization (DSP).

Klaassen (K09a/b) has conducted a thorough examination of wave fields with parameters other than those suggested by H02, and has been unable to find any superposition of Lagrangian waves which simultaneously satisfies adiabatic constraints on parcel volumes

and produces Eulerian tail slopes in the measured atmospheric range. For amplitudes consistent with saturated wave fields, both extreme and RMS values of $J - 1$ are found to exceed adiabatic constraints. Furthermore, Fig. 1 and its counterparts in K09a/b demonstrate that there is a firm correlation between J -values and Eulerian vertical wavenumber spectra: the latter only match atmospheric measurements of saturated waves (i.e. produce tail slopes in the range $-3 \leq s \leq -2.5$) when the postulated Lagrangian wave field contains singular parcel volumes.

These tests demonstrate unambiguously that saturated atmospheric wave fields cannot consist of superpositions of quasilinear Lagrangian waves, a fact that undermines the central tenets and calculations of AJ89, H01 and C02. [Recall that AJ89, H01 and C02 all assume $J \approx 1$ during the course of their calculations.] Clearly, these kinematic advection theories cannot provide a physically plausible explanation of Eulerian wave spectra. The collapse of these theories undermines H99's only defense for key assumptions made in the course of his Doppler-spread theory of gravity wave interactions (e.g. representing the irregular wave field by an equivalent steady horizontal wind). Consequently, E97's critique of DST stands unchallenged. This should be of concern to climate modellers who have adopted Hines' Doppler-spread parameterization of gravity wave drag (H97).

It has been asked by J. Alexander (personal communication), that if DST is based on incorrect physics then why does DSP work as well as it does in middle atmosphere models? There are several reasons. The key parameter for momentum deposition in the DSP is the maximum permissible vertical wavenumber m_M . DST provides no means of determining a precise value for this parameter – it may be “tuned” by a factor of 4 or perhaps more (H97). Uncertainties in the source spectrum for $m \leq m_c$ provide additional opportunities for tuning. In addition, DSP includes Doppler shifting and critical level dissipation induced by the background wind (effects which are not considered in DST). Critical levels induced by the background wind have been shown to account for a significant portion of the wave drag in practical applications (Medvedev and Klaassen, 2000).

Although DSP has been used in several middle atmosphere GCMs, there have been relatively few studies which demonstrate how “well” DSP works in GCMs in comparison to other schemes, such as MK (MK95), WM (Warner and McIntyre 2001) or AD (Alexander and Dunkerton 1999). The comparison of DSP, WM and AD by McLandress and Scinocca (2005) found that the 3 schemes could be tuned to produce similar results. A study by Manson et. al (2002) found that the MK scheme produced better overall agreement with radar-based wind observations in the altitude range (60-87 km) compared to DSP. It is worth mentioning that the MK scheme produced a very good representation of the semi-annual oscillation (Medvedev and Klaassen 2001) in the Canadian Middle Atmosphere Model (CMAM); unfortunately, there was no corresponding publication based on CMAM simulations with DSP. For what it is worth, around the year 2000, DSP in the extended CMAM tended to produce much colder temperatures than those observed in the altitude range 60 to to 100 km, while MK produced considerably closer agreement with observations. These comparisons were, to the best of my knowledge, never published.

In any case, the results of E97, the present work and K09a/b, demonstrate there is no theoretical support for Doppler spreading as a significant mechanism for wave momentum deposition. It therefore seems unwise to invest in further expensive climate simulations using DSP, or further attempts to “tune” or otherwise modify the scheme.

5. Implications for Radar Measurements.

The singular layers found in the kinematic model tend to be relatively thin (only 60 m deep for the case shown in Fig. 2). As shown in K09a, such thin layers are produced by

deformation fields, which push parcels from widely differing locations into a given region by means of opposing displacements. Such deformation fields are known to produce instabilities which allow parcels to deform and either split or slip around each other without experiencing large changes in net volume. As discussed in more detail in K09a/b, these deformation instabilities are known to be associated with the production of turbulence in thin layers, e.g. in Kelvin-Helmholtz billows (Klaassen and Peltier 1991). The picture presented here and in K09a/b strongly suggests that saturated wave fields should contain thin layers of turbulence, and provides an attractive alternative explanation for radar measurements of so-called specular reflectors (e.g. Hocking et al. 1991, Dalaudier et al. 1994, E99).

AJ89 and H01 maintain that the Eulerian tail spectra are “purely a kinematic consequence of what might be termed looking at the waves in the wrong coordinate system” (H01), that nonlinear wave-wave interactions in the Eulerian frame “are mere mathematical artefacts and have no import” (H01), that “experiments which focus upon this decaying Eulerian tail cannot yield information about fundamental dynamical processes” (AJ89), and that “the advective nonlinearity is a kinematic effect” (AJ89). These authors clearly state that measurements of disturbance fields in the Earth-based Eulerian frame are incapable of revealing anything about the underlying dynamical processes. In fact, AJ89 specifically argue for the necessity of Lagrangian measurements, which would be extremely difficult to accomplish with radar or other available equipment.

The conclusions I draw from the results presented here and in K09a/b are entirely opposite to the notions expressed by AJ89 and H01: wave saturation is directly produced by advective nonlinearities, which induce instabilities at sufficiently large amplitudes over a broad range of vertical wavenumbers. One candidate is the wave-wave-induced deformation instability discussed here and in K09a/b; other instabilities (e.g., Sonmor and Klaassen 1997) and critical layer interactions with the background wind must also play prominent roles. Consequently I see considerable motivation for Earth-based measurement programs of disturbance fields in the middle atmosphere.

There is, however, an additional caveat. The present results suggest that saturated wave fields in the middle atmosphere consist of a mixture of instabilities, turbulence and vertically propagating waves. In such situations, it can be difficult to identify the relative contributions of each to the mix, so one must exercise caution when invoking wave-like properties such as dispersion and polarization relations.

Acknowledgements: The author gratefully acknowledges helpful suggestions from L. Sonmor, S. Eckermann, A. Medvedev, and critical commentary from I. Chunchuzov.

6. References.

- Alexander, M.J. and T.J. Dunkerton, 1999: A spectral parameterization of mean-flow forcing due to breaking gravity waves. *J. Atmos. Sci.* 56, 4167–4182.
- Allen K.R., and Joseph, R.I., A canonical statistical theory of oceanic internal waves. *J. Fluid Mech.* 204, 185–228, 1989.
- Chunchuzov, I., On the High-Wavenumber Form of the Eulerian Internal Wave Spectrum in the Atmosphere. *J. Atmos. Sci.* 59, 1753–1774, 2002.
- Dalaudier F., Sidi C., Crochet M., Vernin J., Direct evidence of sheets in the atmospheric-temperature field. *J. Atmos. Sci.* 51, 237–248, 1994.
- Eckermann, S.D., Influence of Wave Propagation on the Doppler Spreading of Atmospheric Gravity Waves. *J. Atmos. Sci.* 54, 2554–2573, 1997.
- Eckermann, S.D., Isentropic Advection by Gravity Waves: Quasi-Universal M^{-3} Vertical Wavenumber Spectra Near the Onset of Instability. *Geophys. Res. Lett.* 26, 201–204, 1991.

- Hines, C.O., The saturation of gravity waves in the middle atmosphere, 2, Development of Doppler-spread theory. *J. Atmos. Sci.* 48, 1360–1379, 1991.
- Hines, C.O., Doppler-spread parameterization of gravity-wave momentum deposition in the middle atmosphere. Part 1: Basic formulation. *J. Atmos. Solar-Terr. Phys.* 59, 371–386, 1997.
- Hines, C.O., Comments on “Influence of Wave Propagation on the Doppler Spreading of Atmospheric Gravity Waves”. *J. Atmos. Sci.* 56, 1094–1098, 1999.
- Hines, C.O., Theory of the Eulerian tail in the spectra of atmospheric and oceanic internal gravity waves. *J. Fluid Mech.* 448, 289–313, 2001.
- Hines, C.O., Comments on the Gravity-Wave Theory of J. Weinstock Concerning Dissipation Induced by Nonlinear Effects. *J. Atmos. Sci.* 59, 2024 – 2030, 2002a.
- Hines, C.O., Nonlinearities and linearities in internal gravity waves of the atmosphere and oceans. *Geophys. Astrophys. Fluid Dyn.* 96, 1–30, 2002b.
- Hocking, W.K, S. Fukao, M. Yamamoto, T. Tsuda, and S. Kato, Viscosity waves and thermal-conduction waves as a cause of “specular” reflectors in radar studies of the atmosphere. *Rad. Sci.* 26, 1281–1303, 1991.
- Klaassen, G.P. and Peltier, W.R., The influence of stratification on secondary instabilities in free shear layers. *J. Fluid Mech.*, 227, pp. 71-106, 1991.
- Klaassen, G.P., Testing Lagrangian Theories of Internal Wave Spectra, Part I. Varying the Amplitude and Wavenumbers. *J. Atmos. Sci.* 66 1077-1100, 2009a.
- Klaassen, G.P., Testing Lagrangian Theories of Internal Wave Spectra, Part II. Varying the Number of Waves. *J. Atmos. Sci.* 66 1101-1125, 2009b.
- Manson, A.H., C.E. Meek, J. Koshyk and coauthors, Gravity wave activity and dynamical effects in the middle atmosphere (60-90 km): observations from an MF/MLT radar network, and results from the Canadian Middle Atmosphere Model (CMAM). *J. Atmos. Solar-Terr. Physics* 64, 65–90, 2002.
- McLandress, C. and Scinocca, J.F., The GCM Response to Current Parameterizations of Nonorographic Gravity Wave Drag *J. Atmos. Sci.* 62, 2394–2413, 2005.
- Medvedev, A.S. and Klaassen, G.P., Vertical evolution of gravity wave spectra and the parameterization of associated wave drag. *J. Geophys. Res.* 100, 25,841–25,853, 1995.
- Medvedev, A.S. and Klaassen, G.P., Parameterization of gravity momentum deposition based on a nonlinear theory of wave spectra. *J. Atmos. Solar-Terr. Physics* 62, 1015–1033, 2000.
- Medvedev, A.S. and Klaassen, G.P., Realistic semiannual oscillation simulated in a middle atmosphere general circulation model. *Geophys. Res. Lett.* 28, 733–736, 2001.
- Smith, S.A., Fritts, D.C., VanZandt, T.E., Evidence for a saturated spectrum of atmospheric gravity waves. *J. Atmos. Sci.* 44, 1404–1410, 1987.
- Sonmor L.J. and Klaassen, G.P., Toward a unified theory of gravity-wave stability. *J. Atmos. Sci.* 54, 2655-2680, 1997.
- Warner, C.D. and M.E. McIntyre, An Ultrasimple Spectral Parameterization for Nonorographic Gravity Waves *Journal of the Atmospheric Sciences* *J. Atmos. Sci.* 58, 1837–1857, 2001.
- Weinstock, J., Nonlinear theory of acoustic-gravity waves: 1. Saturation and enhanced diffusion, *J. Geophys. Res.* 81, 633–652, 1976.
- Weinstock, J., G.P. Klaassen and A.S. Medvedev, Reply to Comments on the gravity-wave theory of J. Weinstock concerning dissipation induced by nonlinear effects”. *J. Atmos. Sci.* 64 1027–1041, 2007.

MESOSPHERE – LOWER THERMOSPHERE TURBULENCE OVER BEAR LAKE, UTAH, 1999-2002

R. G. Roper^a and F. T. Berkey^b

^a105 Silverwood Road NE, Atlanta, Georgia, U.S.A.

^bP.O. Box 477, White Salmon, Washington, U.S.A.

Bear Lake Observatory (41.9°N, 111.4°W) dynasonde IDI data for the years 1999 through 2000 are analyzed to produce not only mesospheric – lower thermospheric (MLT) mean winds, tides and gravity waves, but also estimates of turbulence parameters – characteristic velocities, energy dissipation rates, eddy diffusion coefficients and buoyancy scale lengths.

1. The mean flow

The zonal and meridional monthly mean winds and tides throughout the 75 to 114 km height range analyzed are characteristic of winds measurements at mid latitudes. The diurnal tidal amplitude is less than 20 ms^{-1} below 100 km, with peaks at 105 km of 70, 65, and 50 ms^{-1} in February-March, June-July and September, respectively. The semidiurnal tide shows distinct differences between the mesosphere and lower thermosphere.

2. Gravity waves.

The gravity wave vertical velocities presented here are analyzed using the method described in Roper and Brosnahan (2005). Figure 1 is a plot of the monthly mean variations of the gravity wave velocity v_g . In all years, from February through October, v_g in the upper mesosphere at 85 km increases from 4 ms^{-1} to 5 ms^{-1} , decreasing to 4.5 ms^{-1} in December. From a minimum of 4 ms^{-1} in October at the mesopause at 87 km, v_g increases to 4.5 ms^{-1} at 100 km and spreads upwards to 114 km.

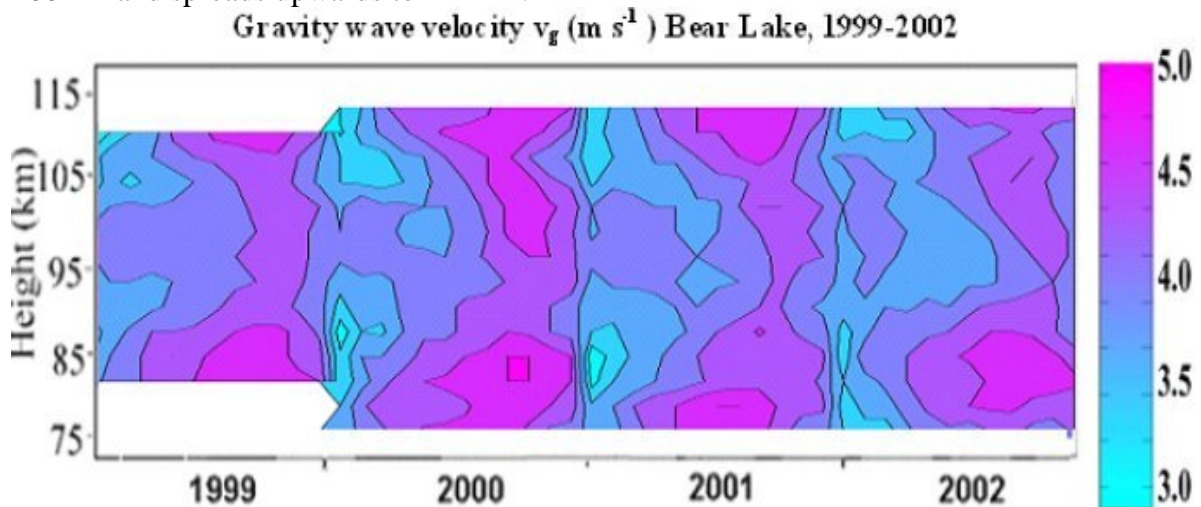


Figure 1. Gravity wave vertical velocity for the years 1999 to 2000. Note that in 1999 data was collected between 82 and 107 km. The mesopause is well delineated and the inter-annual variability surprisingly small.

3. Turbulent velocities

The turbulent velocity σ is obtained by subtracting the gravity wave vertical velocity v_g from the residual resulting from the subtraction of the mean line of sight velocity component from the measured velocity (Roper and Brosnahan, 2005). The monthly mean velocity σ for the years 1999 - 2000 appear in Figure 2. These results are somewhat surprising (as with those presented later) in that they show coherence from month to month at certain altitudes, particularly in the delineation of the mesopause at around 87 km. The coherence between the gravity wave and turbulence velocities ($R = 0.8 + 0.1$) confirms gravity waves as the source of the turbulent energy.

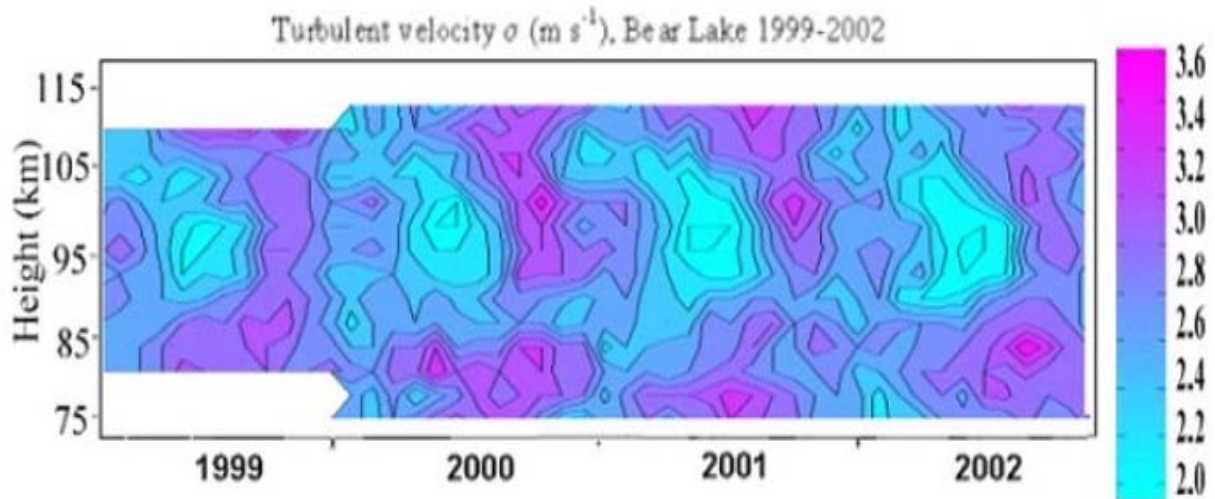


Figure 2. The rms turbulent velocity σ

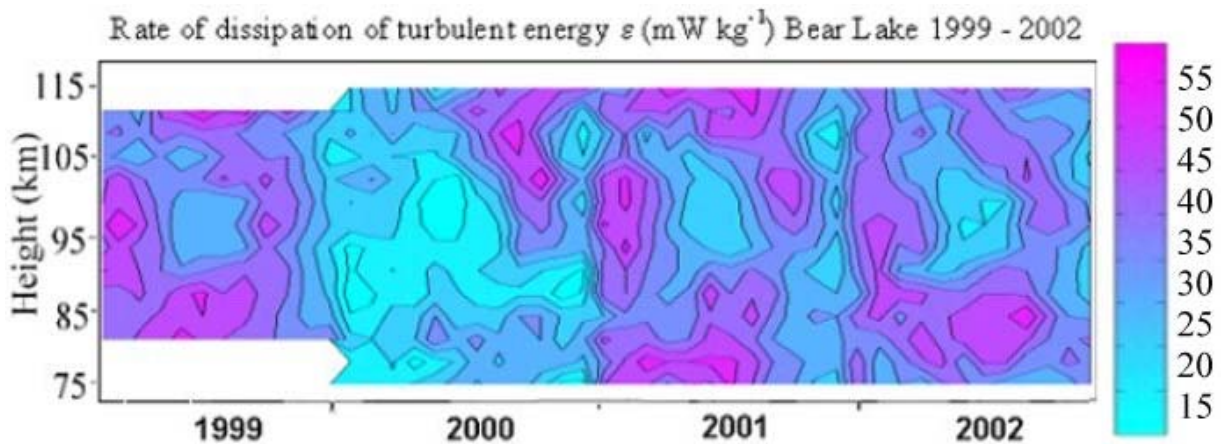


Figure 3. The turbulent energy dissipation rate ϵ for the years 1999 to 2000.

4. Turbulent energy dissipation rate.

The rate of dissipation of turbulent energy $\epsilon = 0.16\sigma^2\omega$, where σ is estimated from the line of sight residuals remaining after the line of sight component of the mean wind has been subtracted (Roper, 2000) and ω is the Brunt Vaisala frequency. In the upper mesosphere, the turbulent dissipation rate ϵ (see Figure 3) increases from some 20 mWkg^{-1} in January to peaks of 30 mWkg^{-1} in May, July and September-October, decreasing to 25 mWkg^{-1} in December. The major feature is an increase from a background at 105 km of some

25 mWkg⁻¹ to a peak of 55 mWkg⁻¹ in August-September, which descends to around 95 km in October. The 1999 through 2002 series shows a surprisingly small interannual variability. If the international ionosonde network were to be upgraded to utilize the IDI technique, a truly global mesosphere – lower thermosphere wind measuring system would be created.

5. Acknowledgments.

At USU, the operation of the Bear Lake ionosonde was facilitated under NSF grant ATM02-18206. The authors further acknowledge the contributions to aeronomy by Dr. G.O.L. (Owen) Jones, formerly of the British Antarctic Survey, whose group, with the installation at the Halley Research Station, Antarctica, was the first to adapt the IDI technique for the synoptic measurement of mesospheric winds with the NOAA digital ionosonde.

6. References

Roper, R.G., and J.W. Brosnahan, Diurnal Variations in the rate of dissipation of turbulent energy in the equatorial upper mesosphere lower thermosphere, *Radio Sci.*, 40, 1029-1044, 2005.

Roper, R.G., On the radar estimation of turbulence parameters in a stably stratified atmosphere, *Radio Sci.*, 35, 999-1008, 2000.

Pertinent papers referenced in the published version.

Adams, G.W., D.P. Edwards, and J.W. Brosnahan, The imaging Doppler interferometer: Data Analysis, *Radio Sci.*, 20, 1481-1492, 1985.

Adams, G. W., J. W. Brosnahan, D. C. Walden, and S. F. Nerney, Mesospheric observations using a 2.66 MHz radar as an imaging Doppler interferometer: description and first results, *J. Geophys. Res.*, 91, 1671-1683, 1986.

Berkey, F.T., C.S. Fish and G.O.L. Jones, Initial Observations of Mesospheric Winds Using IDI Radar Measurements at the Bear Lake Observatory, *Geophys. Res. Lett.*, 28, (1), 135-138, 2001.

Jones, G. O. L., K. Charles and M. J. Jarvis, 1997, First mesospheric observations using an imaging Doppler interferometer adaptation of the dynasonde at Halley, Antarctica, *Radio Sci.*, 3, 2109-2122.

HI-RESOLUTION RADAR OBSERVATIONS OF KH-BILLOWS AT UPPER-TROPOSPHERIC HEIGHTS

R.F. Woodman and F. Villanueva R.

Jicamarca Radio Observatory, Instituto Geofisico del Peru

At the previous MST11 workshop, we presented first hi-resolution results (Roettger et al., 2006, Woodman et al, 2006) obtained with the SOUSY MST radar at its new location, at the Jicamarca Radio Observatory. The latter paper reported some clear observations of billows, or cat eyes, at an altitude of 8.5 km, and with a resolution of 37.5 meters. This and other interesting features had been obtained a short time earlier, but only Range-Time-Intensity (RTI) plots were reported. In this occasion we present the velocity field as well as spectral widths of such features. In addition we are now in the position of comparing them with numerical simulations of comparable phenomena which were presented, also for the first time (Fritts et al, 2006), at the same conference.

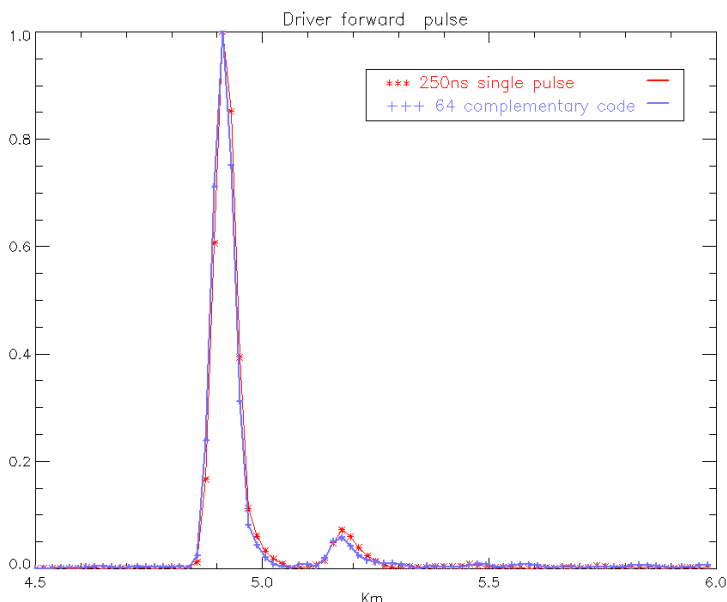


Figure 1 Instrument function showing the system altitude resolution

The control and processing system of the SOUSY radar has been modernized. A description of the system, as it now stands, and the configuration parameters of the radar for the results presented here are described in the Proceedings of the MST11 workshop (Woodman, et al., 2006). It is sufficient to mention here, that we used the 60mx60m Yagi array of the radar pointing vertically. The power level was limited to the 20kW maximum peak level of the transmitter driver in order to obtain better resolution than what could have been achieved using the final stage. A 64 Baud complementary code was used with 250 nsec Baud-width at a 5% duty cycle. The resolution is best described showing the instrument function, including the effect of the receiver bandwidth (4 MHz), depicted in Figure 1.

Three events of interest were observed on the Dec 4, 2006, run, reported previously. They are reproduced in Figure 2. The most conspicuous events are the cat eyes seen at the 214 minutes mark at 8.5 km altitude. The second event of interest is the layer splitting starting at 9.7 km altitude. This occurs after a not very clear billows event shortly before. The third event is an inverted S shape event at 7 km altitude right underneath the billows at the 214 minute mark. Its interest will become clear when we see it in context with other radar observations and numerical results. None of these features would have shown this clear with the usual 500 m resolution used in MST radars in their hi-resolution mode.

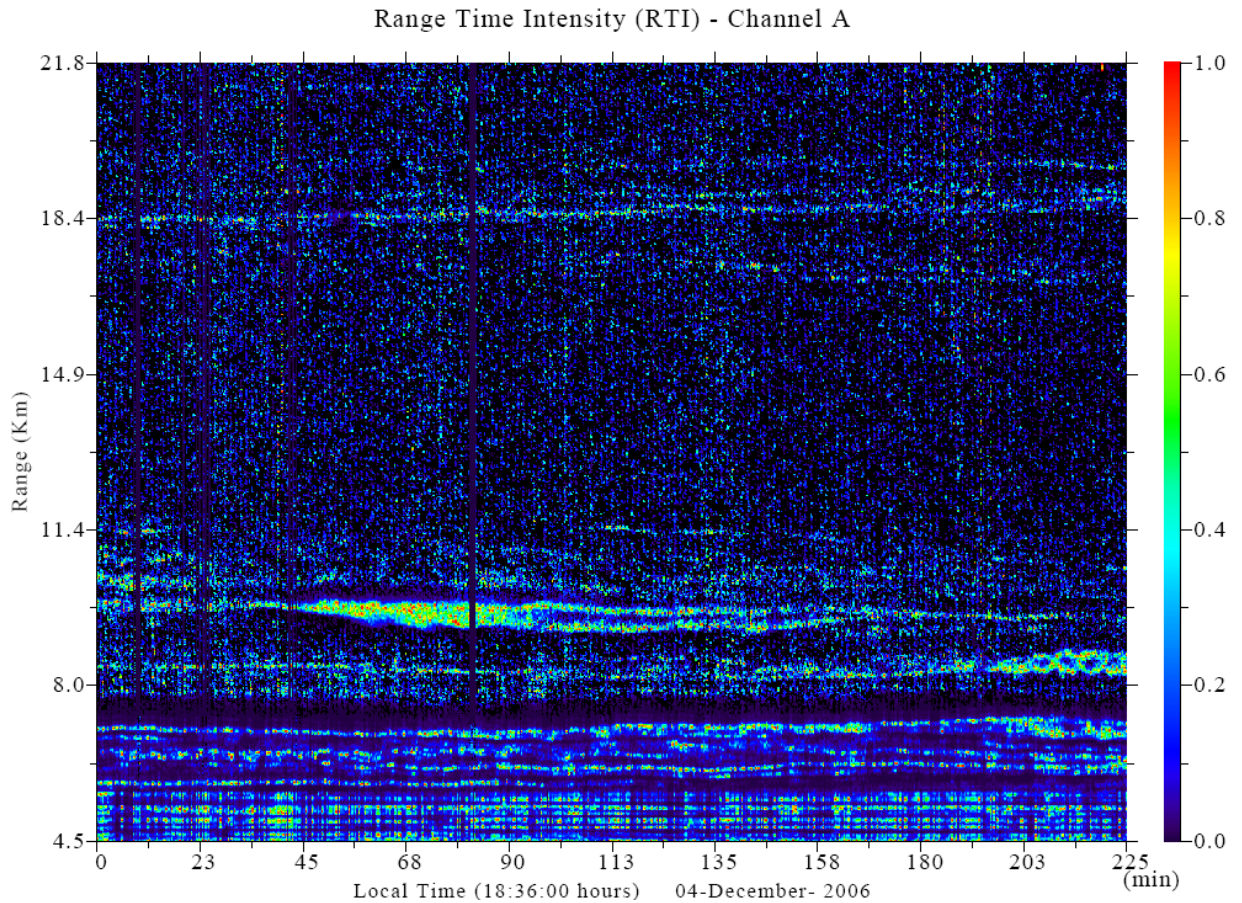


Figure 2 RTI plot showing in context the three features discussed in the text

Figure 3 shows the three first moments corresponding to two of the features mentioned above. The top left panel shows signal intensity of the KH billows and it is used as a mask to the two panels below. The panel just below shows the velocity field within the billows. Note the periodicity of the up down pattern. The left side of every CAT eye moves up, and the other side down. The lowest panel is a measure of the spectral width, but, without information available about the horizontal wind velocity, it does not lend itself to discussion, since we cannot deconvolve beam-widening effects (We can get this information from the Jicamarca main radar in the future). The right hand panel shows the same information but for the layer splitting feature. The first half of the picture shows a late turbulent stage. The remaining periodicity of the billows is partially evident in the velocity field, where we can still see the red- blue-red repetitive pattern. We would like to interpret these features as experimental evidence of the two states of the KH billows generation and its final decay shown by two instantaneous frames of Fritts et al., 2006, numerical simulation shown in Figure 4.

As mentioned in the caption of Figure 4 the blue tone palette is a good proxy of the regions where we expect the strongest radar echo returns. If we repeat periodically the one CAT eye shown on the left panels of Figure 4, periodic and tilted inverted S shapes of the blue traces appear. The third detail identified in Figure 1, just under the billows, is a weak evidence of this feature shown in the numerical simulation. In fact, a subsequent run of the radar in the hi-resolution mode, not reproduced here, shows that the periodic S shapes are a common occurrence.

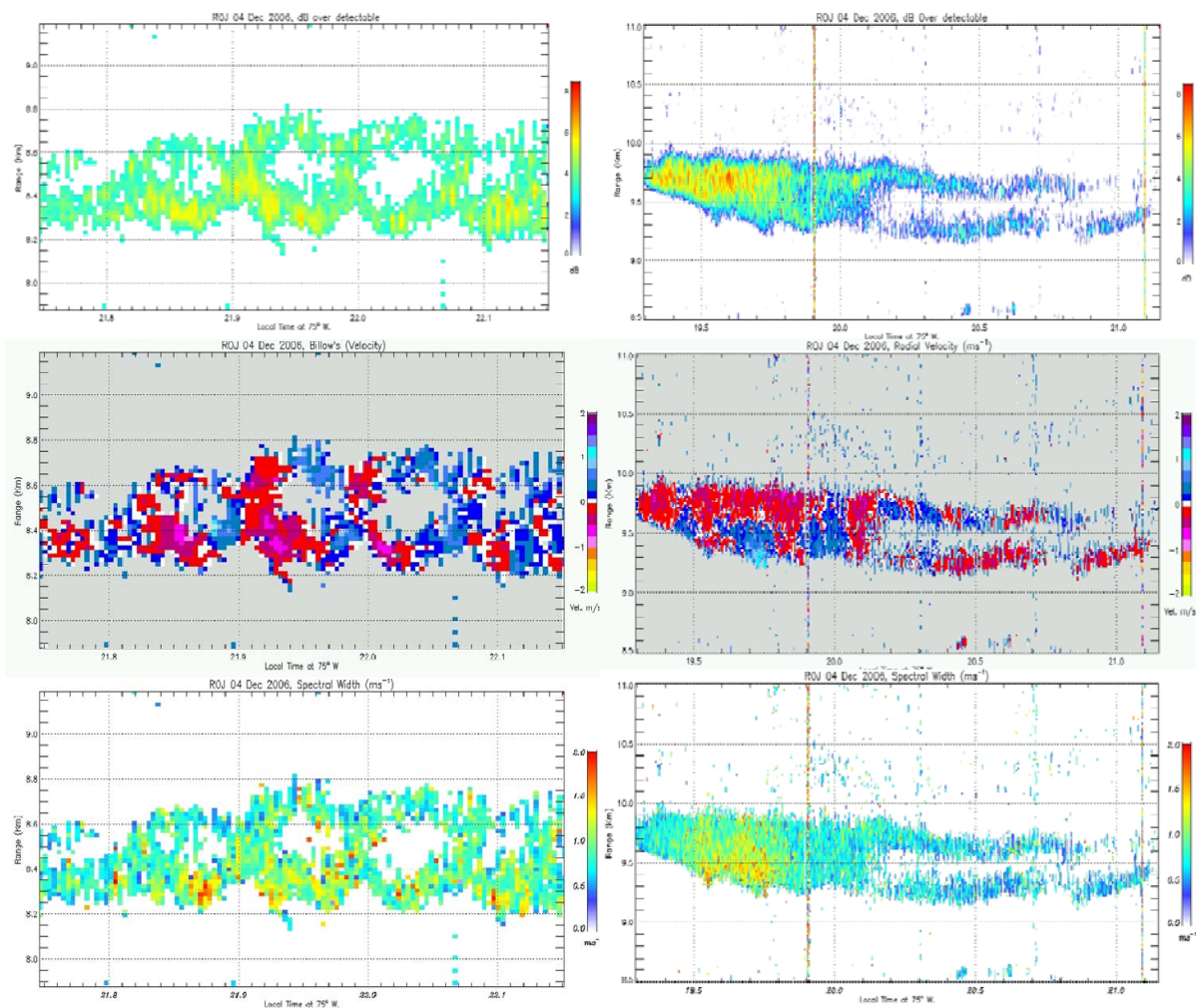


Figure 3. Left: First three moments of the KH billows shown in Figure 2 . Right: the same for the layer split shown at 9.5 km altitude

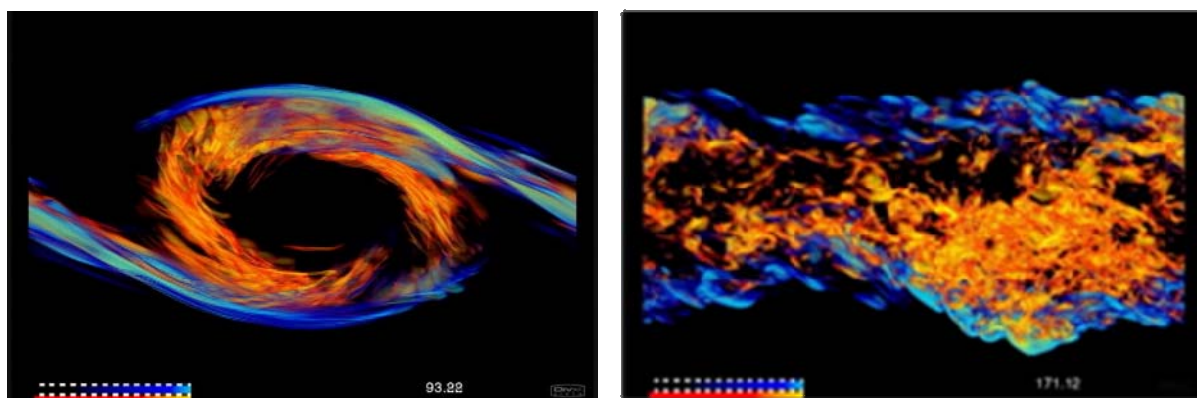


Figure 4. Two states of the development of a KH billow taken from Frits et al (2006) numerical simulation movie. The blue palette shows the thermal dissipation rate, a good proxy of the region where scattering is strongest, and the orange shows the viscous dissipation rate

In Figure 5, taken from Fritts et al., 2009, columns 1 and 2 show a radar simulation of the power and Doppler velocity backscattered from a numerical simulation of a KH billow similar to the ones shown above, corresponding to different stages of the formation and decay of the unstable layer. Columns 3 and 4 correspond to the “true” velocities and to their difference with respect to the radar velocities (column 2), respectively. By true velocity, is meant the average of the Eulerian velocities corresponding to each numerical resolution pixel, averaged throughout a radar resolution volume.

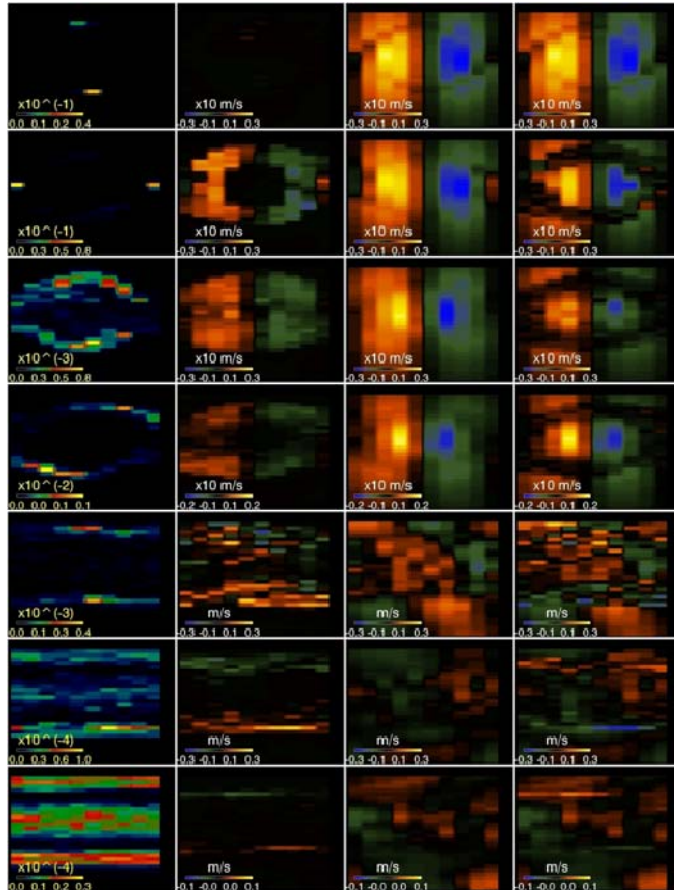


Figure 5. Simulation of radar results that would be obtained from the numerically simulated KH billows. See text (After Fritts et al., 2009)

correlated velocities occur. The lower resolution radars would give velocities biased toward these values.

References.

Woodman R.F., G. Michhue, J. Röttger and O. Castillo, The MPI-SOUSY-VHF Radar at Jicamarca: High Altitude-Resolution Capabilities. Extended Abstracts, MST11, 2006, Gadanki India

Fritts D.C, P.M. Franke, K.Wan¹, T.Lund¹, and J.Werne,¹ 2009, Computation of radar backscatter from realistic turbulence volumes, I: Radar backscatter computations and measurement biases, *J. Geophys. Res.*, submitted.

Fritts D.C., 2006, Numerical simulation video presented at the MST11 workshop, Gadanki India. Personal communication,

Notice also the similarity of the third line in Figure 5 with the red-blue pattern in the experimental radar results. and the lack of echoes coming from the center of the billows,

What the numerical simulations show, and depicted in the last column of Figure 5, is that the radar velocity does not always measure the true velocity. The radar weights the different small scale contributions within a resolution volume with the signal intensity associated to them, and if there is a correlation between the two, as it seems to be the case, it leads to a consistent bias. This is also seen in our results, but at a larger scale, provided we imagine a radar with a poorer resolution than the one we used. We see for instance the consistence of the S shapes in intensity favoring a region in the billows in which consistent and

CHARACTERISTICS OF ATMOSPHERIC WAVES IN THE UPPER TROPOSPHERE OBSERVED WITH THE GADANKI MST RADAR – RASS

T. V. Chandrasekhar Sarma¹, Toshitaka Tsuda²

¹National Atmospheric Research Laboratory, Gadanki 517112 AP, India

²Research Institute for Sustainable Humanosphere, Kyoto University, Kyoto 611 0011, Japan.

Introduction

VHF Radio acoustic sounding system (RASS) has been established as a reliable technique for simultaneous ground-based remote profiling of vector winds and atmospheric virtual temperature in the troposphere and lower stratosphere on a continuous basis. RASS is the only technique that can operate during day and night times in all weather conditions. The dynamical behaviour of the atmosphere consisting of the waves, tides and stability stratification structure can be well elucidated from these observations.

It is well established that long and short period atmospheric gravity waves and tides that are generated in the tropics have a defining role in driving global general circulation. Using a RASS system, profiling of atmospheric dynamical structure parameters upto lower stratospheric altitudes has been demonstrated (Alexander & Tsuda 2007, Alexander & Tsuda 2008).

Radio Acoustic Sounding System (RASS) developed at Gadanki (13.46°N, 79.17°E) (Sarma et al., 2008) was augmented and operated during 2007 and during a few days in 2008. During 22-25 August 2007 continuous operation was conducted for about 69 hours. The RASS system was operated in temperature profiler mode and wind profiler modes alternately. Backscattered echo was received from altitudes upto ~14km and ~20km respectively from acoustic wavefronts and background turbulence. Data was analysed to derive altitude profiles of virtual temperature and zonal, meridional and vertical components of the wind. Perturbations in the wind and temperature fields from the background were computed and further band-pass filtering of these results was done to reveal inertial gravity wave activity. The dominant periods of gravity waves were found to be at ~8hours and ~15hours. Further, signatures of diurnal tide were also observed and the phase maxima in observations were found to exhibit a close match with the global-scale wave-model-generated phase maxima of zonal and meridional winds and temperature. From the virtual temperature profiles, Brunt-Vaisala frequency was computed to deduce the background atmospheric stability during the observation period. Hodograph analysis of zonal and meridional winds was used along with TRMM precipitation data to deduce the location of the source of the inertial gravity wave activity.

Experimental set up of RASS

Figure 1 shows the location of the RASS acoustic transmitters in and around the MST Radar antenna array. Four additional acoustic exciters were added along the periphery of the radar antenna array as shown, to augment the existing two exciters that are located at the center.

Radar observation scheme & Simultaneous radiosonde soundings

The RASS system was operated during 22-25 August 2007 for about 69 hours. The observations started at around 1000LT and were continued in three modes viz., acoustic mode, correction wind mode and background wind mode in a cyclic fashion. The radar experimental specifications used for this experiment are shown in table 1. Simultaneous GPS radiosonde flights were launched at an interval of about 6 hours starting at 1130LT on 22nd August 2007. Echoes from the acoustic excitation were received upto an altitude of about 14km and those from background turbulence were obtained upto an altitude of about 20km.

Table 1. Experimental parameters of MST radar- RASS

Parameter	Acoustic mode	Correction wind mode	Background wind mode
Pulse Width (μs)	16	16	16
Coding used	16-bit, 1 μs baud ,Biphase Complementary	16-bit, 1 μs baud, Biphase Complementary	16-bit, 1 μs baud, Biphase Complementary
Range resolution (m)	150	150	150
Inter Pulse Period (μs)	1000	1000	1000
Beam sequence	10° E, 9°E, 8°E, Zy	10°E, 9°E, 8°E, Zy	10°E, 10°W, Zy, Zx*, 10°N, 10°S
No. of coherent integrations	24	64	64
No. of FFT points	256	512	512
No. of online incoherent integrations	4	1	4
Start of observation range window (km)	3.6	3.6	3.6
No. of range bins	150	150	150
Second LO offset frequency (Hz)	-110	0	0
Time duration (minutes)	2	8	7

*Zx and Zy – Zenith beams formed using N-S and E-W dipoles, respectively.

Data analysis procedure

The radar computed the power spectrum online at each of the range bins. First three central moments viz., power, mean Doppler shift and spectral width (Woodman, 1985) were computed at each range bin after subtracting noise (Petitdidier et.al, 1995) and by Gaussian fitting. The Doppler shift of the acoustic mode observations was corrected, by subtracting from it, the Doppler shift of the correction wind mode in the same beam direction. True speed of sound Ca was computed from the corrected Doppler shift. Virtual temperature was computed at each altitude using the following relation.

$$Ca = 20.047\sqrt{T_v}$$

Figure 2 shows the average T_v profile over the entire observation duration from RASS compared with the mean T_v computed from the radiosonde observations.

Using the data from Background wind mode, zonal, meridional and vertical winds were computed. A median profile over the entire observation period was generated for each of the zonal, meridional and virtual temperature profiles; contour plots of perturbations from this median profile are shown in figures 3, 4 and 5 respectively. Bandpass filtering of the perturbations was done to reveal gravity wave activity at periodicities of ~8 hours and ~15 hours. Signature of diurnal tide was also deduced by a bandpass filter centered at 24 hours. Virtual Brunt-Vaisala frequency (N) was computed from the T_v profiles and a contour plot of N^2 is shown in figure 6. Downward tilted layered structures of stability are seen to descend from about 9km in altitude on 22nd August to 4km on 25th August.

Conclusions

As it is well known, wave and tidal activities govern the momentum and energy transport whereas stability structure delineates the transport and mixing processes thereby impacting the chemical composition and minor constituents. RASS is a powerful technique for profiling the atmospheric winds and temperature and thereby to study the momentum and energy transport.

Continuous profiling of atmospheric virtual temperature along with the winds has been done using the Gadanki MST Radar-RASS system. Further analysis of the data has revealed various dynamical structures and features of waves and diurnal tide. Hodograph analysis has been applied to the winds and temperature data for locating the source of the waves and TRMM satellite precipitation radar data was used to corroborate the direction of the source of the wave activity. This work demonstrates the utility of MST Radar-RASS observations along with complementary ground-based, satellite-based and *in situ* sounding techniques for elucidation of tropical atmospheric processes.

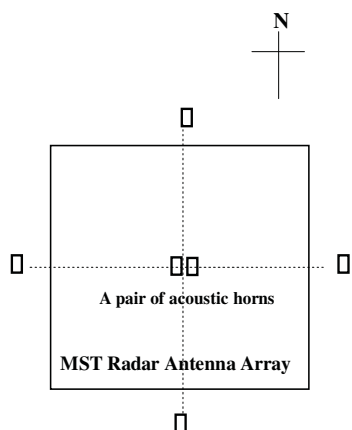


Figure 1: Location of acoustic exciters in the MST Radar antenna array

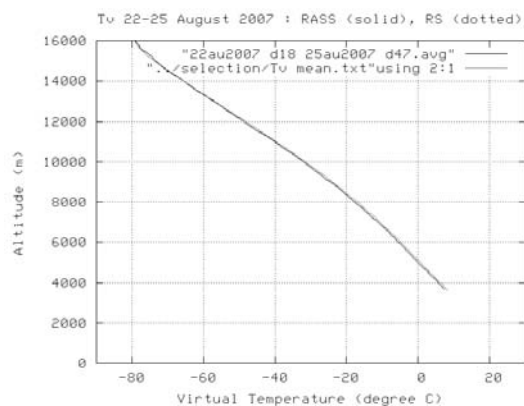


Figure 2: Mean virtual temperature profile from RASS (solid) and mean virtual temperature profile from radiosonde (dotted).

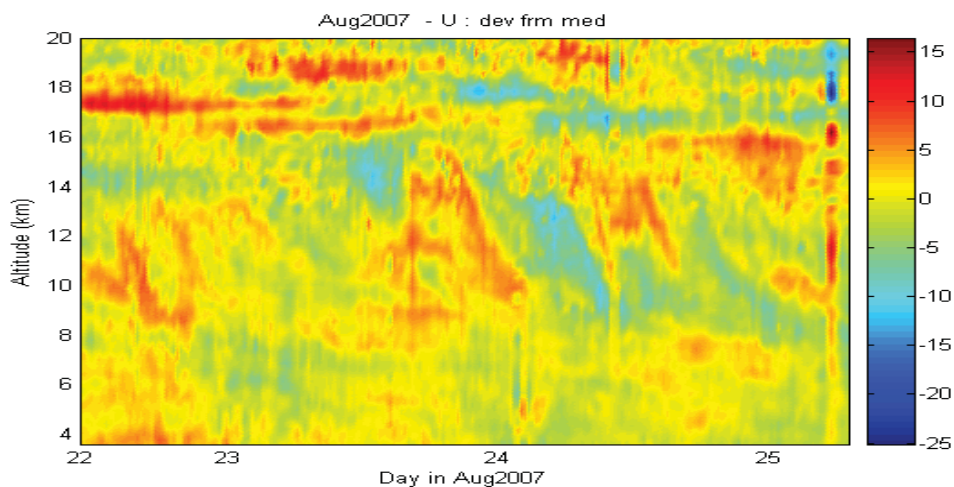


Figure 3: Contour plot of perturbations of zonal wind speed. Colour code units are ms^{-1} .

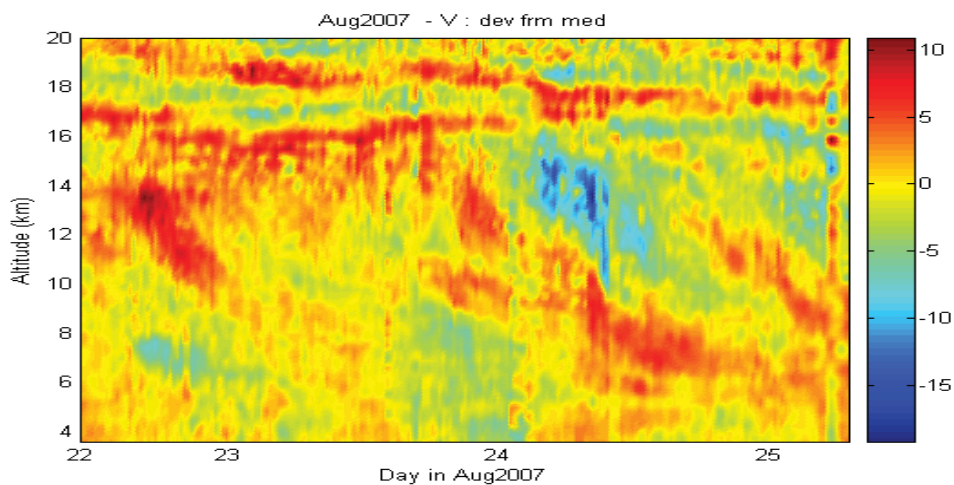


Figure 4: Contour plot of perturbations of meridional wind speed. Colour code units are ms^{-1} .

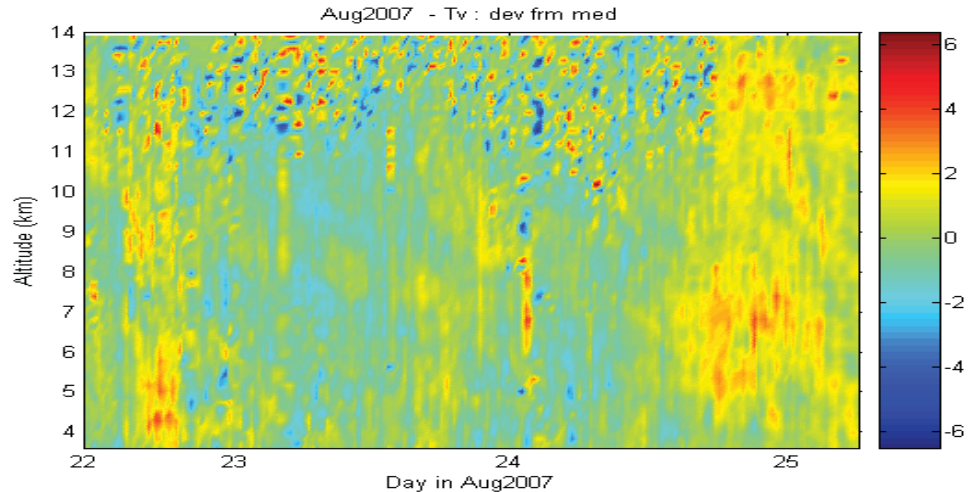


Figure 5: Contour plot of perturbations of virtual temperature. Colour code units are $^{\circ}\text{C}$.

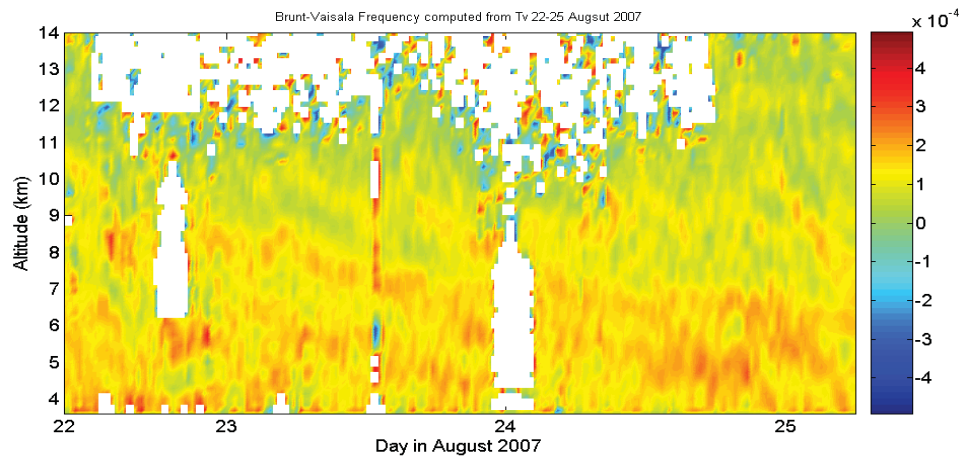


Figure 6: Contour plot of square of Brunt-Vaisala frequency (N^2). Colour code units are $\text{rad}^2 \text{s}^{-2}$.

References

Alexander, Simon P, Toshitaka Tsuda and Junichi Furumoto, Effects of Atmospheric Stability on Wave and Energy Propagation in the Troposphere, *Journal of Atmospheric and Oceanic Technology*, 24, 602–615, 2007.

Alexander, Simon P. and Toshitaka Tsuda, High-Resolution Radio Acoustic Sounding System Observations and Analysis up to 20 km, *Journal of Atmospheric and Oceanic Technology*, 25(8), 1383–1396, 2008.

Petitdidier, M., A. Sy, A. Garrouste, and J. Delcourt (1997), Statistical characteristics of the noise power spectral density in UHF and VHF wind profilers, *Radio Sci.*, 32(3), 1229-1247.

Sarma, T.V. Chandrasekhar, D. Narayana Rao, J. Furumoto, T. Tsuda, “Development of radio acoustic sounding system (RASS) with Gadanki MST radar – first results”, *Annales Geophysicae*, 26(9), 2531-2542, 2008.

Woodman, R. (1985), Spectral moment estimation in MST radars, *Radio Sci.*, 20(6), 1185-1195.

LATITUDINAL VARIABILITY IN THE MIDDLE ATMOSPHERE (30-90 KM)
WINDS DURING THE MAJOR STRATOSPHERIC WARMING EVENT IN
2005/2006

S. Sathishkumar¹, R. Kondala Rao¹, S. Gurubaran¹, Dennis M. Riggin², W. Singer³,
Alan. H. Manson⁴ and Christopher.E. Meek⁴

1. Equatorial Geophysical Research Laboratory, Indian Institute of Geomagnetism, Tirunelveli, India
2. Colorado Research Associates Division, Northwest Research Associates, Boulder, Colorado, USA
3. Leibniz-Institute of Atmospheric physics, Schloss-Street6, 18225 Kuehnhangsborn, Germany
4. Institute of Space and Atmospheric Studies, University of Saskatchewan, 116 Science place, Saskatoon, SK, Canada

Email: sathish_egrl@rediffmail.com

1. Introduction:

The dynamics of the middle atmosphere is characterized by a strong variability during the winter months. Possible causes are planetary wave activity and sudden stratospheric warming events. The Sudden stratospheric Warming (SSW) is one of the large scale dynamics phenomena in the winter polar region which strongly affects entire middle atmosphere. It causing significant variations in the mesosphere and lower thermosphere (MLT) as well and it involves considerable changes in the background wind, temperature, planetary wave and gravity activity in the high latitude. This event is discovered by *Scherhag* [1952]. A spectrum of waves are exciting in the atmosphere which are including more than one normal mode and commonly observed modes are those with periods around 2,5,10 and 16 days. The SSW event can be identified as major mid-winter warming when the zonal-mean temperature increases poleward from 60°N at 10hPa or below with an associated circulation reversal and hence a breakdown or splitting of the polar vortex [*Labitzke and Naujo kat*, 2000]. In contrast, during minor warming the temperature increases with lesser extent during the period of a week or less but the zonal mean zonal wind does not change its direction.

The key mechanism behind the SSW initially proposed by *Matsuno* [1971] and now widely accepted that growth of upward propagating planetary waves and their non linear interaction with the zonal mean flow. The interaction decelerates and/or reverses the eastward winter winds also induces a downward circulation in the stratosphere causing adiabatic heating and an upward circulation in the mesosphere causing adiabatic cooling [*Liu and Roble*, 2002]

The present work is focused on the circulation changes observed in the stratosphere and mesosphere and lower thermosphere during the Arctic winter of 2005/2006. Period of time between November 2005 and February 2006 is investigated thoroughly.

2. Observation and Data analysis:

The UKMO data is used to examine the features of circulation changes and study the global planetary scale oscillation present in the winter of 2005/2006 stratosphere of the Northern Hemisphere (NH). The daily data fields have global coverage with 2.5° and 3.75° steps in latitude and longitude respectively. Simultaneous data obtained from the network of radars situated from tropical latitude to high latitude during 01 December 2005-28 February 2006 in the Northern Hemisphere. These radars are situated at Tirunelveli (8.7°N , 77.8°E), Kauai (21°N , 159°W), Platteville (40°N , 105°W), Saskatoon (52°N , 107°W) and Andenes (69°N , 16°E). The planetary waves are transient phenomena and they are studied by a wavelet transform method. To determine the predominant periods of the planetary waves, we use a spectral analysis method that is a two-dimensional analogue of the Lomb-Scargle periodogram method [Lomb, 1975; Scargle, 1982] based on a least-squares fitting procedure applied to the entire time series.

3. Results and Discussion:

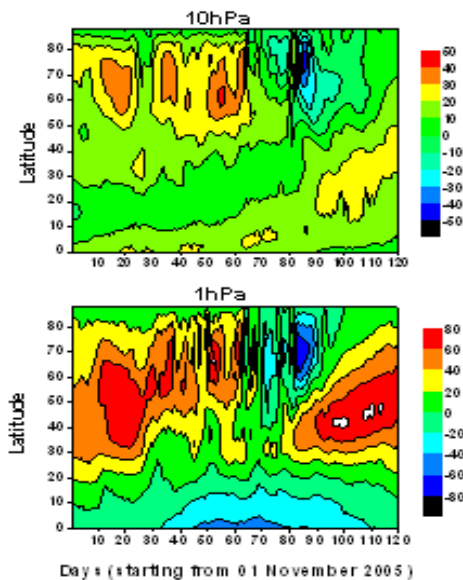


Fig.1 Time-latitude cross section of zonal mean zonal wind at 10 and 1 hPa

Figure.1 depicts the time-latitude cross section of zonal mean zonal wind during the period from 01 November 2005 to 28 February 2006 for two pressure level namely 10hPa (top panel) and 1hPa (bottom panel) respectively. As can be seen in both panels shows the strong westward wind regime of ~ 50 m/s on day numbers between 71 and 91 at $50\text{-}80^\circ\text{N}$. This disturbance has been seen in the low latitude region as well in the sense that strengthened eastward of 25 m/s at 10hPa and strengthened in westward directed winds of 50 m/s at 1hPa associated with high latitude westward wind regime.

Fig.2 shows the latitude amplitude spectrum of zonal wind for three different pressure levels say 10hPa, (left column) 1hPa (middle column) and 0.3hPa (right column) respectively. Top panel represents the eastward wave propagation and bottom panel represents the westward planetary wave propagation at wavenumber 1. The spectrum has been obtained from 01 October 2005 to 31 March 2006. A careful inspection of the spectra of each row reveals those different periods are present in the eastward and westward wave direction. They indicate that 5-6, 11 and 15-17 days in the eastward wave direction and 11, 15-17 and 22-25 day periods present in the westward direction. There are two latitudinal amplifications of the eastward wave in the zonal wind that the main amplification is centered at around $40\text{-}55^\circ\text{N}$ and the other one is around $75\text{-}80^\circ\text{N}$. 11 day wave is the strongest among the planetary waves. However, there are three latitudinal

amplification of the westward propagating wave in the zonal wind that main amplification is observed at 40-50°N and other two are 70-80°N and 10-20°N. The low latitude branch is weak in amplitude comparative with mid and high latitude but it is not seen in the eastward wave propagating planetary waves.

There are two strong wave periods observed in the westward wave that 15-17 day and 22-25 day period which has shown in the bottom panel of figure. The ~ 10-11 days wave are peak in eastward propagating wave than the analogous ones for westward propagating waves. It is evident that in most cases the westward peaks are stronger than the eastward one.

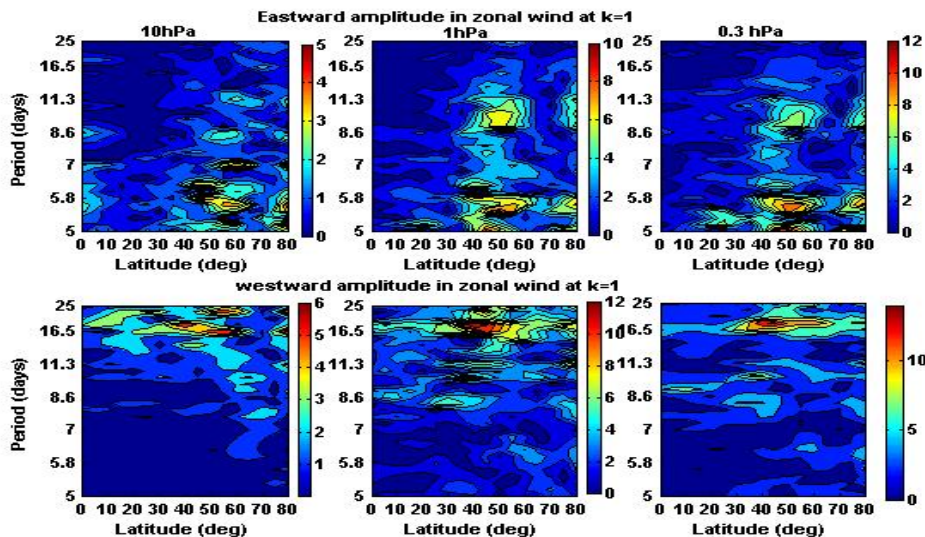


Fig.2. Latitudinal amplitude spectra of zonal wind of wavenumber 1 at three pressure level of 10, 1 and 0.3hPa during 01 October 2005-31 March 2006

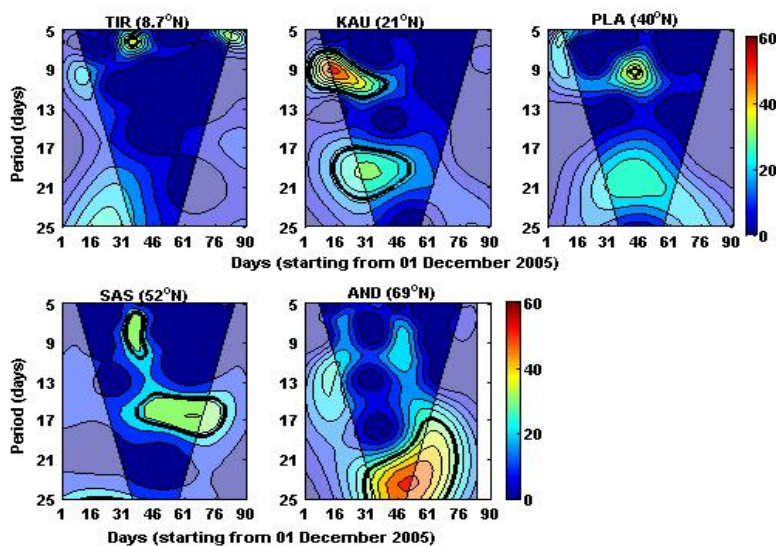


Figure 3 shows the wavelet amplitude spectra of zonal wind at 86 km for five stations from low latitude to high latitude region. 9-11 day wave activity was observed prior to the SSW events in the low latitude regions. Similar period was seen during onset of SSW in the mid and high latitude region.

Fig 3. Wavelet amplitude spectra of zonal wind at 86 km during 01 December 2005-28 February 2006 over Tirunelveli, Kauai, Plattville, Saskatoon and Andenes.

The strong 22 day wave burst was noticed during SSW over Andenes which has not observed over Tirunelveli. The 16 day wave activity was found during onset of SSW over Saskatoon which is noticed prior to the SSW over Kauai.

The main problem addressed in this study is related to the circulation changes in the tropical to high latitude in the stratosphere and mesosphere and lower thermosphere region during major SSW in the Arctic winter of 2005/2006. It was found that the latitudinal relationship between variability of zonal mean winds at mid latitude slightly preceded that at high latitude but it reached the highest westward regime. High and low latitude mesosphere is very similar to that in the stratosphere which could be generated by zonally symmetric waves. Planetary wave signatures during SSW with different latitude were investigated, strong 10 day wave activity is noticed before to the SSW and ~20 day oscillations were noticed onset of the SSW. This result is good agreement with earlier observations from stratosphere and mesosphere and lower thermosphere.

References:

1. Cho, Y.-M., G. G. Shepherd, Y.-I. Won, S. Sargoytchev, S. Brown, and B. Solheim (2004), MLT cooling during stratospheric warming events, *Geophys. Res. Lett.*, 31, L10104, doi:10.1029/2004GL019552.
2. Dowdy, A. J., R. A. Vincent, D. J. Murphy, M. Tsutsumi, D. M. Riggin, and M. J. Jarvis (2004), The large-scale dynamics of the mesosphere-lower thermosphere during the Southern Hemisphere stratospheric warming of 2002, *Geophys. Res. Lett.*, 31, L14102, doi:10.1029/2004GL020282.
3. Gregory, J. B., Manson, A. H. (1975), Wind and waves to 110 km at mid-latitudes. III. Response of mesospheric and lower thermospheric winds to major stratospheric warmings. *J. Atmos. Sci.*, 32, 1676-1681.
4. Hoffmann, P., W. Singer, and D. Keuer (2002), Variability of the mesospheric wind field at middle and Arctic latitudes in winter and its relation to stratospheric circulation disturbances, *J. Atmos. Sol. Terr. Phys.*, 64, 1229–1240.
5. Labitzke, K., Naujokat, B (2000), The lower arctic stratosphere mid winter warmings since 1952, *SPARC Newsletters* 15, 11-14.
6. Liu, H.-L., and R. G. Roble (2002), A study of a self-generated stratospheric sudden warming and its mesospheric-lower thermospheric impacts using the coupled TIME-GCM/CCM3, *J. Geophys. Res.*, 107, 4695, doi:10.1029/2001JD001533.
7. Manney, G. L., Lahoz, W. A., Swinbank, R., O'Neill, A., Connell, P. M., and Zurek, R. W (1999), Simulation of the December 1998 stratospheric major warming, *Geophys. Res. Lett.*, 26, 2733–2736.
8. Matsuno, T. (1971), A dynamical model of the stratospheric sudden warming. *J. Atmos. Sci.*, 28, 1479-1494.
9. Scherhag, R. (1960), Stratospheric temperature changes and the associated changes in pressure distribution. *Journal of Meteorology* 17, 572-585.
10. Schoeberl, M.R. (1978), Stratospheric warmings: observations and theory. *Review of Geophysics and Space Physics* 16, 521-537.

GRAVITY WAVE MOMENTUM FLUXES IN THE MESOSPHERE / LOWER THERMOSPHERE AT HIGH- AND MID-LATITUDES

Manja Placke¹, Ch. Jacobi², P. Hoffmann¹, W. Singer¹, E. Becker¹, M. Rapp¹, and G. Stober¹

¹ Leibniz-Institute of Atmospheric Physics, Kühlungsborn, Germany

² Institute for Meteorology, University of Leipzig, Leipzig, Germany

1. Introduction

Gravity waves (GWs) propagating upward in the atmosphere can break in the mesosphere / lower thermosphere region (MLT, 82–98 km) due to their exponential growth, thereby impose their momentum and energy on the general circulation, and hence play a major role in the dynamics of the middle atmosphere. Applying a method presented by *Hocking* [2005] to the data of all-sky interferometric (SKiYMET) meteor radars, wind variances and GW momentum fluxes are provided in the MLT region considering waves and variances with periods less than 2 hours. A comparative study for high- and mid-latitudes has been made for the meteor radars at Andenes (69.3°N, 16.0°E) and Collm (51.3°N, 13.0°E). For both sites the seasonal cycles of variances and momentum fluxes have been examined. The coupling processes between breaking GWs and the general circulation are clearly revealed by the seasonal variation of the vertical flux of zonal momentum and the mean zonal wind.

2. Observation and data analysis

Meteor radars transmit short electromagnetic pulses circumpolar into the atmosphere. These pulses are reflected at ionization trails of incoming meteoroids if they are perpendicular to the radar beam. For every ionization trail moving with the wind the location, echo amplitude, and radial wind velocity can be determined by interferometric analysis of the meteor echoes. Using the analysis by *Hocking et al.* [2001] mean winds can be determined continuously in the height region between 80 and 100 km. For the present study all-sky meteor radars positioned at the polar location Andenes and the mid-latitudinal location Collm have been used. Their technical characteristics are given in Table 1.

Table 1. Technical parameters of the meteor radars at Andenes and Collm.

Technical parameters	Andenes	Collm
Transmitter antenna	1 crossed 3-elements Yagi	1 single 3-elements Yagi
Receiver antenna	5 crossed 2-elements Yagi	5 single 2-elements Yagi
Frequency	32.55 MHz	36.2 MHz
Peak power	12 kW	6 kW
Pulse width (height resolution)	13.3 μ s (2 km)	
PRF	2144 Hz	
Reference	<i>Singer et al.</i> [2004]	<i>Jacobi et al.</i> [2007]

For GW analysis the meteor method presented by *Hocking* [2005] has been applied. It allows the simultaneous determination of wind variances (u'^2 , v'^2 , w'^2) and momentum fluxes ($u'v'$, $u'w'$, $v'w'$) based on the assumption that GWs cause wind fluctuations that appear in the

variation between the measured radial wind velocity v_{rad} and the mean radial wind velocity v_{radm} assuming a constant background wind. Here u' , v' , and w' are the fluctuating eastward, northward, and vertical winds. Minimizing the quantity $\Lambda = \sum ((v'_{rad})^2 - (v'_{radm})^2)^2$ leads to a matrix equation for estimating the wind variance and flux parameters (see *Hocking, 2005*). The data analysis has been carried out in four height gates, each of 3 km vertical extent, between 83.5 and 95.5 km. Meteors with zenith angles between 10 and 50° are regarded if their distance to the radar is smaller than 400 km and if the amount of the radial drift velocity does not exceed 200 m/s. The averaging time interval for the evaluation is 2 h in which a minimum number of 30 meteors is required.

3. Results and conclusions

The 4-year mean annual variation and vertical structure of GW variances for Andenes and Collm is displayed in Fig. 1. The data consists each of 14-days averages, and a 4-year mean annual cycle has been constructed using the variances from August 2004 to July 2008. In the lowermost panel the 4-year mean number of meteors fulfilling all previously described selection criteria is shown with a time step of 2 h. The annual cycle of the meteor rates displays the typical maximum in early summer and lower count rates during the other seasons (e.g. *Singer et al., 2004*). As the meteor radar at Andenes consists of crossed antenna elements in contrast to Collm where single elements are used, Andenes has higher meteor counts with maximum more than 500 meteors per 2 hours in summer and a minimum average of about 200 during most of the other seasons. At Collm the values vary between about 100 and 300 meteors per 2 hours within the selected 12 km altitude range. Several peaks in-between the diagrams appear due to meteor showers.

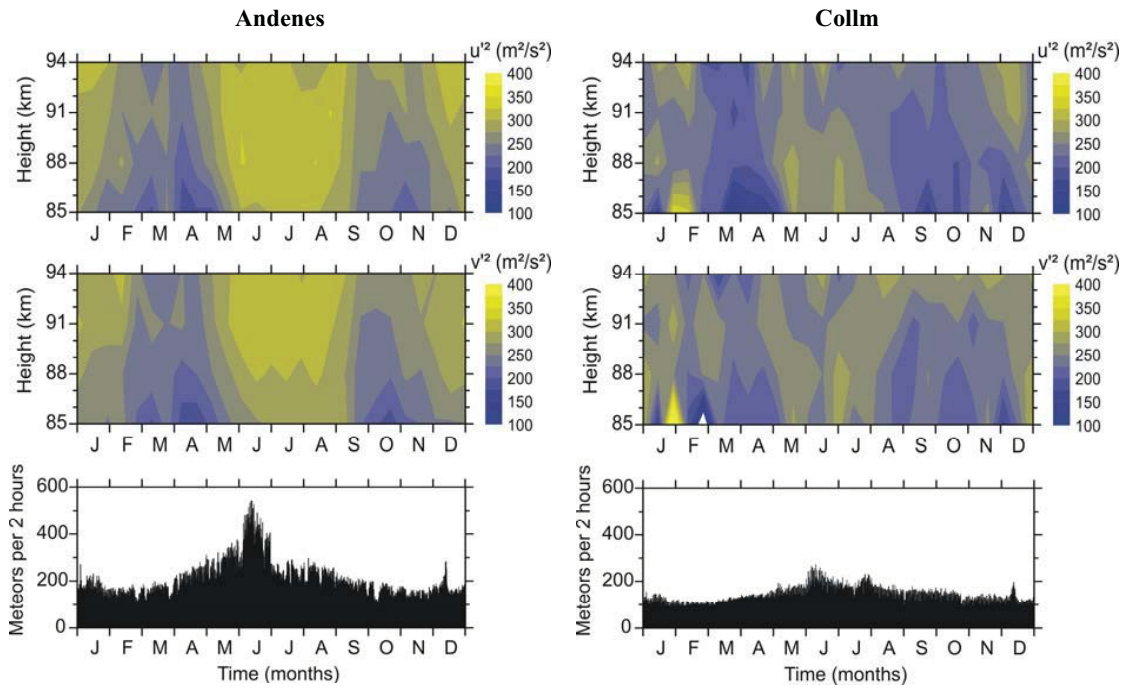


Figure 1. Height-time cross-sections for the zonal (upper panels) and meridional (middle panels) wind variance at Andenes (left) and Collm (right). Running averages over 14 days have each been averaged within the period of four years (August 2004 to July 2008). The 4-year mean number of meteors per 2 h summed for the altitude range between 83.5 and 95.5 km is shown in the lowermost panels.

The zonal and the meridional wind variance at Andenes and Collm show both a semi-annual variation having a maximum in summer and a secondary weaker maximum in winter as well as two minima around the equinoxes. This variation is stronger pronounced for Andenes with values between 200 and 400 m^2/s^2 . At Collm the wind variances are about 100 m^2/s^2 lower and the annual meridional wind variance fluctuation is less pronounced. The different amounts of variances at the two locations may be partly due to the different meteor count rates. As horizontal wind variances are associated with GW activity the meteor analysis gives a semi-annual oscillation of the GW activity in the MLT for both the high- and the mid-latitude site.

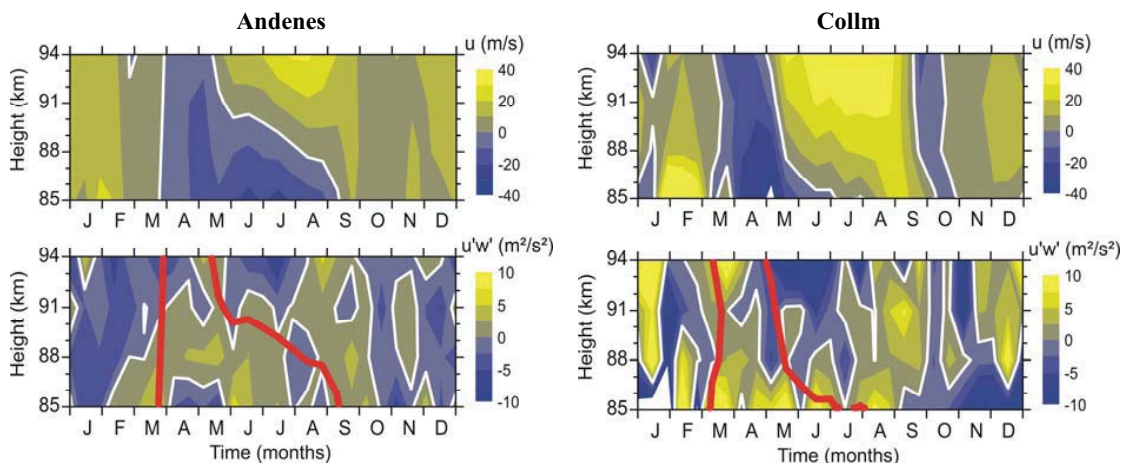


Figure 2. Height-time cross-sections for the mean zonal wind (upper panels) and the vertical flux of zonal momentum (lower panels) at Andenes (left) and Collm (right). Running averages over 14 days have each been averaged within the period of four years (August 2004 to July 2008). The red lines in the lower panels indicate the zonal zero-wind line.

Another interesting point is the comparison of the variation of the mean zonal wind u and the vertical flux of zonal momentum $u'w'$ which clearly reveals the coupling between GWs and the background circulation. Fig. 2 shows the 4-year mean annual cycles that have been constructed like in Fig. 1. In the upper panels the mean zonal wind is displayed which is eastward directed in summer and predominantly westward directed in winter (e.g. *Jacobi et al.*, 2007). The measured maxima are about 40 m/s in both directions, but the occurrence of high values at Collm is temporally longer than at Andenes. During summer the zonal wind reversal can be seen shifting from higher to lower altitudes. This reversal occurs at high-latitudes in greater heights than at mid-latitudes as it is also reflected by e.g. the new Horizontal Wind Model (HWM07) in *Drob et al.* [2008]. Thus the zero-wind line lies e.g. in June at about 90 km for Andenes, but at about 85 km for Collm.

The lower panels of Fig. 2 show the vertical flux of zonal momentum. Positive values (yellow) characterize vertical transport of eastward directed momentum and negative values (blue) westward directed momentum flux, respectively. It is noticeable that at high-latitudes the momentum flux is weaker than at mid-latitudes. Eastward directed vertical momentum flux occurs mainly where approximately westward zonal wind is prevailing and vice versa. This shows that $u'w'$ and u are directly coupled, because in general a vertical propagation of GWs occurs only when the waves move against the background wind. In case of wave breaking due to the exponential increase with height the momentum of the GWs is imposed on the background flow. Hereby a force is induced which can lead to a reversal of the wind.

This effect can be seen in Fig. 2 as the summer zonal wind reversal indicated by the red lines in the lower panels occurs at Andenes and at Collm above the region of positive values of the GW momentum flux. These results confirm that GWs have a significant influence on the atmospheric circulation patterns.

Bibliography

- Drob, D.P., J.T. Emmert, G. Crowley, J.M. Picone, G.G. Shepherd, W. Skinner, P. Hays, R.J. Niecejewski, M. Larsen, C.Y. She, J.W. Meriwether, G. Hernandez, M.J. Jarvis, D.P. Sipler, C.A. Tepley, M.S. O'Brien, J.R. Bowman, Q. Wu, Y. Murayama, S. Kawamura, I.M. Reid, and R.A. Vincent, An empirical model of the Earth's horizontal wind fields: HWM07, *J. Geophys. Res.*, *113*, doi:10.1029/2008JA013668, 2008.
- Hocking, W.K., B. Fuller, and B. Vandeppeer, Real-time determination of meteor-related parameters utilizing modern digital technology, *J. Atmos. Solar-Terr. Phys.*, *63*, 155-169, 2001.
- Hocking, W.K., A new approach to momentum flux determinations using SKiYMET meteor radars, *Ann. Geophys.*, *23*, 2433-2439, 2005.
- Jacobi, Ch., K. Fröhlich, C. Viehweg, G. Stober, and D. Kürschner, Midlatitude mesosphere / lower thermosphere meridional winds and temperatures measured with meteor radar, *Adv. Space Res.*, *39*, 1278-1283, 2007.
- Singer, W., J. Weiß, U. von Zahn, Diurnal and annual variations of meteor rates at the arctic circle, *Atmos. Chem. Phys.*, *4*, 1355-1363, 2004.

CAWSES – INDIA: AN OVERVIEW

P. B. Rao¹, R. Sridharan², S.C. Chakravarty³, Kusuma G. Rao³, G. Beig⁴,
R. S. Dabas⁵, S. Gurubaran⁶, P. K. Manoharan⁷, T. K. Pant² and Sudha Ravindran²

1. National Remote Sensing Centre, Hyderabad, India
2. Space Physics Laboratory, VSSC, Trivandrum, India
3. ISRO HQ, Bangalore, India,
4. Indian Institute of Tropical Meteorology, Pune, India,
5. Radio and Atmospheric Sciences Division, NPL, New Delhi, India,
6. Equatorial Geophysical Research Laboratory, IIG, Tirunelveli, India
7. Radio Astronomy Centre, NCRA, TIFR, Ooty, India,

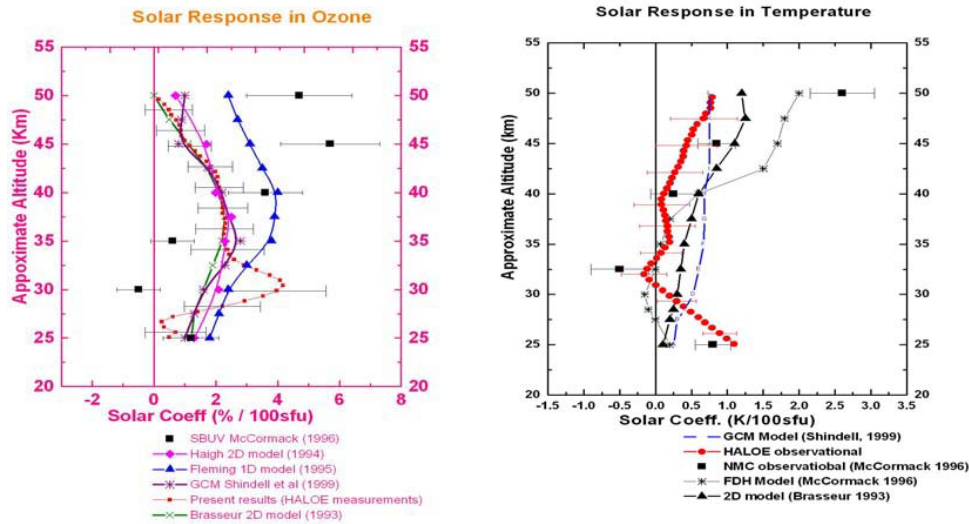
Introduction:

The Climate and Weather of the Sun – Earth System (CAWSES) is an international program initiated by SCOSTEP. The program, drawn up for a period of four years (2004 – 2008), has been formulated under four themes: 1. Solar Influence on Climate, 2. Space Weather: Science and Applications, 3. Atmospheric Coupling Processes and 4. Space Climate. The CAWSES-India program was formulated along the same thematic lines as the international program. The program was designed to focus on phenomena unique to equatorial and low latitude region with special emphasis on coupling processes. Under theme 1, a study was undertaken on solar variability in middle atmosphere chemical climate using satellite data and two-dimensional (2D) model simulations. Two campaigns were conducted during March – April 2006, one each under ‘space weather: science and applications’ (theme 2) and ‘atmospheric coupling processes’ (theme 3). The campaign under theme 2 was to study the day-to-day variability of the equatorial ionosphere – thermosphere system with special emphasis on the generation and evolution of equatorial spread-F (ESF). The theme 3 campaign was mainly to characterize tropical atmospheric tides as they propagate from troposphere, the source region, to thermosphere, where they manifest in a variety of ionospheric phenomena. The development of equatorial and low latitude ionospheric models was taken up as one of the prime activities under ‘space climate’ (theme 4). The paper presents some highlights of the results from phase 1 of the program

Some Highlights of the Results:

Solar Influence on Climate: Figure 1 shows observational and model profiles of solar response in ozone and temperature over a height range of 25 – 50 km. The solar response of ozone from satellite observations shows a peak value of 4% /100 sfu at about 32 km. The results are found to be in fairly good agreement with the 2D and GCM models. The satellite observations of solar response of temperature shows that it starts to fall from 1.2⁰ K /100sfu at 25 km to become negligible over the range of ~ 30 – 40 km; it starts to increase again with height to reach a value of 1⁰ K / 100sfu at the stratopause level. The observational and model profiles are found to be in qualitative agreement; there are significant differences, however, like that seen between the HALOE observational and FDH model profiles at heights above 40 km.

Space Weather - Science and Applications: The results generated under ‘space weather’ and ‘atmospheric coupling processes’ were due mainly to the two multi-institutional, multi-instrument campaigns. Figure 2 shows mesopause temperature from the day-glow photometer observations made during March 17 – 21, 2006, a period that started on a quiet day and lasted through a moderate geomagnetic storm. The observations show a significant fall in mesopause temperature in the afternoon



Figures 1: observational and Model profiles of solar response in ozone and temperature.

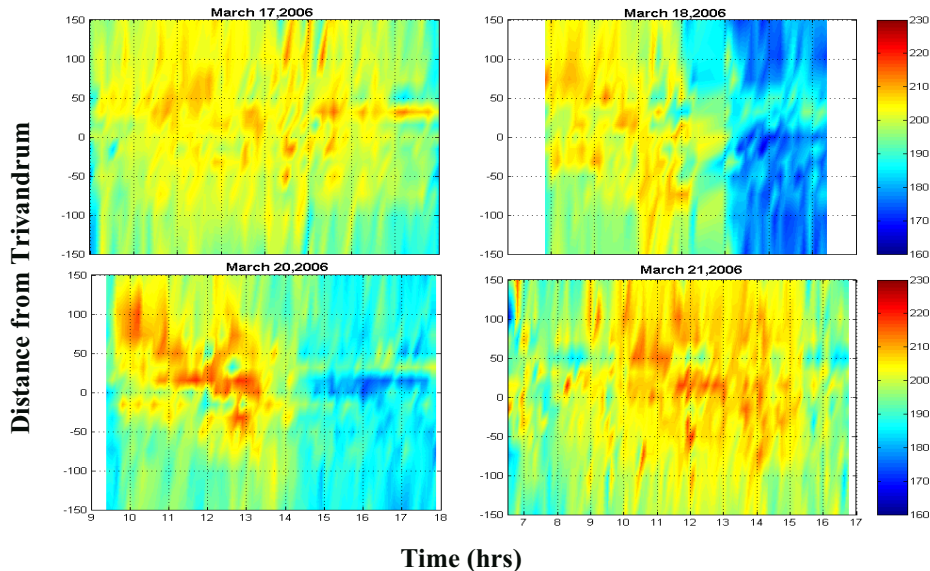


Figure 2: Day glow photometer observations of mesopause temperature during March 17 – 21, 2006; a moderate geomagnetic storm occurred on 18 March.

hours on March 18, which is in clear association with the geomagnetic storm. Other highlights of the campaign include: improved prediction of equatorial spread-F (ESF) based on a new factor combining the strength and asymmetry of the equatorial ionospheric anomaly (EIA); simultaneous detection of quasi-2-day and 5-day waves at both EEJ and F-region heights; tomographic image showing TID in association with an unusual depletion of thermospheric airglow intensity at 630 nm and the occurrence of a counter electrojet event seen in ΔH . In addition to the above, some other important contributions from theme 2 are: a comprehensive study on CRIs, CMEs and solar wind in the acceleration region and the associated space weather effects; the response of the equatorial ionosphere-thermosphere system to geomagnetic storms, in particular the distinctly different effects of the prompt penetration and disturbance dynamo fields on the occurrence of ESF.

Atmospheric Coupling Processes: The important results from the tidal campaign conducted under ‘atmospheric coupling processes’ (theme 3) are: the diurnal tide shows a peak amplitude of 35 m/s at 45 km in zonal wind and a significantly lower amplitude (< 15 m/s) in the meridional wind; a comparison of the diurnal tide observed at 88 km using meteor radar at Trivandrum and MF radar at Tirunelveli shows that while the zonal component is of the same order, the meridional component at Trivandrum (~ 40 m/s) is about twice that observed at Tirunelveli; the MF radar observations at Tirunelveli indicate the presence of 15 – 20 day modulation of diurnal tide at MLT heights. The most significant result from the campaign is the clear evidence linking the convective activity in the lower atmosphere to the tidal variability in the MLT region, as shown in figure 3. The similarity between the variations in the OLR field and the amplitude of the diurnal tide suggests a possible link between the MLT tidal variations and the variations in the tropical convection through the non-migrating tides it generates. The other important contributions made under theme 3 include: the multi-institutional coordinated measurements for understanding “Tropical Tropopause Dynamics”; extensive collocated measurements from MST Radar, Lidar, GP Sondes, combined with satellite data, for characterization of cirrus clouds; Tropical Tropopause Layer (TTL) characterization in terms of the MST radar observed major convective outflow and studying the variations in TTL during METEOSAT observed clear sky and convective conditions.

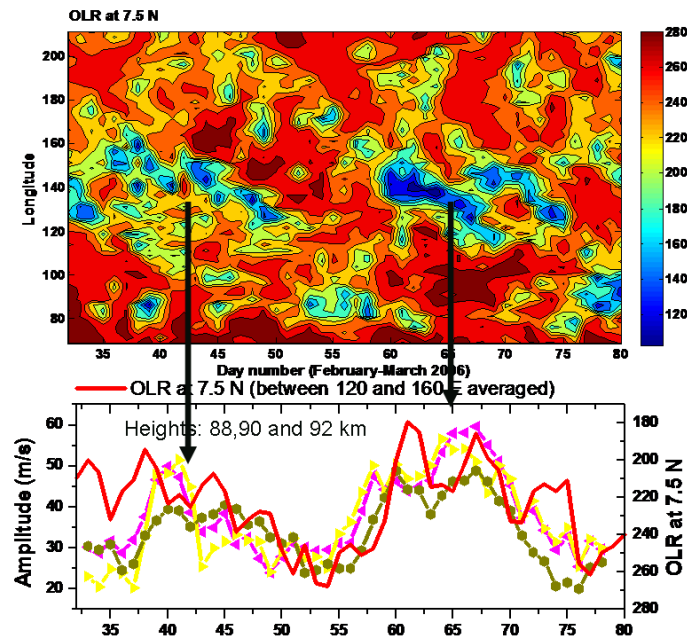


Figure 3: The contour plot of OLR observed over $70^{\circ} - 210^{\circ}\text{E}$ at 7.5°N for the period February – March 2006, and the amplitude of the diurnal tide at MLT heights and the variation of OLR averaged over $120^{\circ} - 160^{\circ}\text{E}$

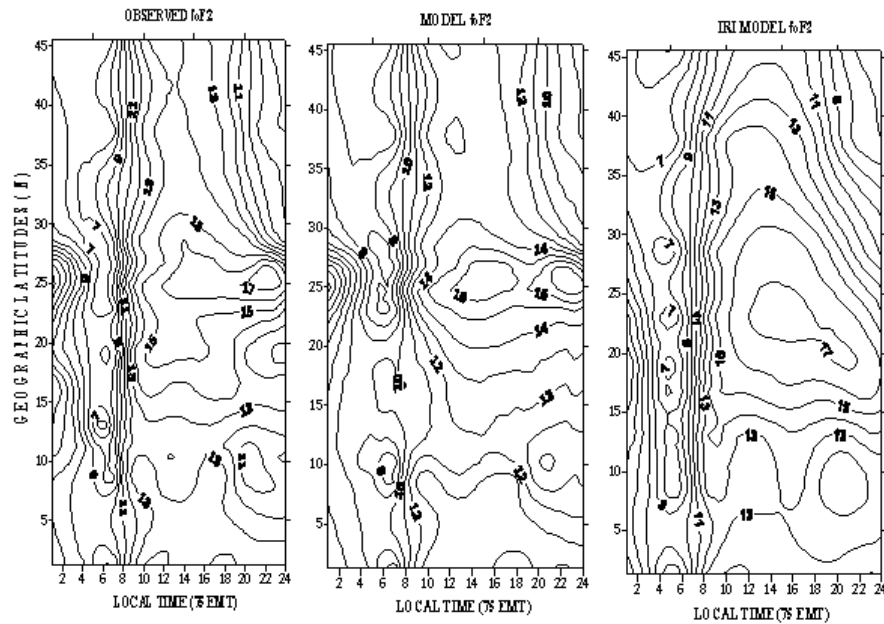


Figure 4: The observed and model contour plots of foF2 for high solar activity month of March 1958; observed data (first panel) SD-model (second panel) and IRI model (third panel).

Space Climate: A comprehensive study has been made of the climatology of the equatorial and low latitude ionosphere-thermosphere system using long series of data from Indian ionosonde network and the multi-frequency radio beacon observations of total electron content (TEC) and ionospheric scintillations. The development of application oriented ionospheric models for short and long term predictions of the F-region parameters over Indian zone has been a significant accomplishment of the studies carried out under space climatology. Two types of models have been developed, one based on second degree (SD) empirical relationships of F_0F_2 and $M(3000)F_2$ to the monthly mean sunspot number and the other based on multi-regression analysis (MRA) involving expressions relating F_0F_2 and $M(3000)F_2$ to $S_{10.7}$ and A_p indices, representing the solar and geomagnetic activities, respectively. Figure 4 shows a comparison of the SD model contour plot of F_0F_2 for March 1958, representing high solar activity, with the corresponding observed and International Reference Ionosphere (IRI) model plots. The comparison clearly shows that the SD model is a significantly better representation of the ionosphere over $0 - 45^\circ\text{N}$ in the Indian sector compared to the IRI model. The MRA model developed for Delhi was also found to do fairly well in representing the storm-time behavior of F_0F_2 and h_mF_2 , not only in terms of gross variations but short term fluctuations as well. Thus, the SD and MRA models developed for the Indian sector have the potential to contribute significantly towards refining the IRI model to overcome its current limitations in representing the equatorial and low latitude ionosphere.

Acknowledgements: The work reported in this paper is based on the Climate and Weather of the Sun-Earth System (CAWSES – India) program supported by the Department of Space, Government of India.

Session 7:
Tropopause Processes and
Stratospheric/Tropospheric
Exchange

Stratospheric–Tropospheric Exchange of Ozone during February – April 2008, Eureka

M. Osman¹, W. K. Hocking¹, D.W. Tarasick², H. He², J. Drummond³

¹*University of Western Ontario, Dept. of Physics & Astronomy, London, ON, N6A 3K7, Canada.*

²*Environment Canada, 4905 Dufferin St., Downsview, ON, M3H 5T4, Canada.*

³*University of Dalhousie, Dept. of Physics & Atmos. Sci., Halifax, N S, B3H 3J5, Canada.*

1. INTRODUCTION

Stratospheric ozone prevents life on Earth against harmful ultraviolet radiation and also it heats the region by strongly absorbing thermal radiation (WMO, 1999). Ozone in the troposphere has the capacity to oxidize and remove atmospheric pollutants via the formation of hydroxyl radicals (WMO, 1999). The change in atmospheric ozone concentration both in the stratosphere and troposphere has different impacts on climate, human life and the ecosystem. For example, high concentrations of ozone in the lower tropopause result in atmospheric pollution via formation of photochemical smog and global warming (as it is a greenhouse gas) (WMO, 1999) and these have a direct impact both on human life as well as the ecosystem.

The stratosphere-troposphere exchange of ozone is critical for understanding of tropospheric ozone climatology budget as well as long term trends (Lin et al., 2000). The major source of tropospheric ozone in the lower troposphere is photochemistry (Altshuller and Lefohn, 1996), but in addition it is believed that ozone intrusions from the stratosphere to the troposphere happen as part of the Brewer–Dobson circulation (Stohl et al., 2003). However the details of the process are not well understood yet.

This study examines the detection of stratospheric ozone leakage from the stratosphere to the troposphere, as revealed by a continuous ozonesonde campaign made by Environment Canada at Eureka from February 24 up to April 18, 2008. Furthermore, we employed windprofiler radars simultaneously with the ozonesonde launches in order to investigate the ozone intrusion thoroughly. Low atmospheric relative humidity is used as a sign that the ozone originated from stratosphere. This paper reveals the stratospheric-tropospheric exchange of ozone and discusses the results that we obtained from our experimental campaign. We particularly highlight noticeable differences between February-March and April.

2. METHODOLOGIES

Simultaneous measurement of atmospheric information (such as wind velocity and turbulence strengths) and ozone concentration were taken by using windprofiler radars combined with frequent launches of ozonesonde, respectively. Windprofilers (Roettger and Larsen, 1990) are ground-based radars that can help study the atmosphere from regions close to ground-level up to altitudes of 16 km (depending on power output). A radar transmitter sends out successive signals of radio wave into the atmosphere and receives the backscattered signals which will then be recorded for further analysis (Hocking et al., 2007). The wind and turbulence strengths are then deduced from the returned signals (Hocking et al., 2007).

EN-SCI ozonesondes with ground based receiver were employed to measure atmospheric ozone concentration. The ozonesondes were accompanied by Vaisala RS-92 radiosondes for pressure, humidity and temperature measurements. On-board GPS receivers were used to track the sonde positions and allow wind velocity determination. Helium filled balloons of mass either 1200 g or 800 g were used in the campaign. The work was also supported by a theoretical computer

simulation program called FLEXPART (Stohl et al., 2005), a Lagrangian particle dispersion model which simulates ozone movement in the atmosphere. FLEXPART can be run both forward and backward in time to simulate the dispersion of ozone from their sources and track the potential source of it, respectively.

The radar used was located at Eureka, Nunavut (79.99°N, 85.94°W) with an operating frequency of 51.00 MHz. A steerable beam of one-way beam half-power half-width 2.75° was used either pointing vertically or off-vertical at 10.9° with different azimuth angles. The radar height resolution was 500 m. The ozonesonde balloons were launched in close proximity to the radar site to take daily measurements of the aforementioned atmospheric parameters. The synchronized measurements using radar and ozonesonde were later compared to FLEXPART simulation.

3. RESULTS

The ozonesonde launches campaigns were made from 24 February – 18 April 2008 but we split the data into two because of the existence of many missing sonde data between 12 and 31 March 2008. Figure 1 reveals the result we obtained from the ozonesonde and radiosonde.

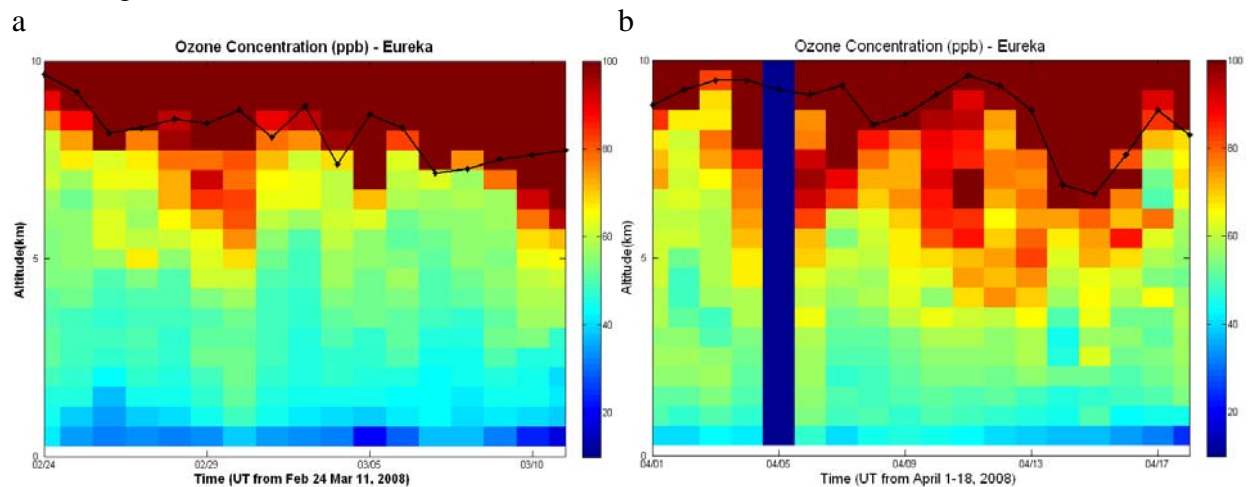


Figure 1| Eureka Ozonesonde Measurements Campaign February - April 2008. a and b are the plots of ozone densities (measured in parts per billion) as a function of height and time for the periods 24 February – 11 March 2008 and 1 – 18 April 2008, respectively. Each vertical column of colored boxes represents a different launch. The solid black line is the estimated thermal tropopause height as determined from the temperature profiles.

As can be seen from Figure 1a there is a noticeable red transition to softer colour that indicates in general a high gradient of ozone concentration (i.e. sharp cut off) during the February-March period. On the other hand, a smeared out ozone concentration can be seen in the middle and upper troposphere during the April period (see Figure 1b), indicating high ozone concentration just below the tropopause. A weaker gradient of ozone concentration just below the tropopause is observed in April as compared to February-March. Therefore, we focus in this paper on the difference in ozone concentration in the lower and upper troposphere between February-March and April.

We examined if this difference was due to ozone concentration just above the tropopause and turbulence strengths but we obtained no noticeable differences between the two periods. We used

low relative humidity as a partial indicator of ozone originating in the stratosphere and we found that the high ozone concentration in April to be stratospheric ozone. Furthermore, we diagnosed if the tropopause during that period was poorly defined (as it is a possible indicator if stratosphere-troposphere exchange takes place); however the gradient of temperature around tropopause was not that weak which implies that the tropopause is well defined.

As a proxy for gravity wave intensity we looked at the standard deviation of the hourly mean vertical component of the wind but nothing was distinct statistically between the two periods. No obvious difference between the two periods was observed with regard to vertical component of wind velocity. The horizontal components of wind velocity are shown in Figure 2.

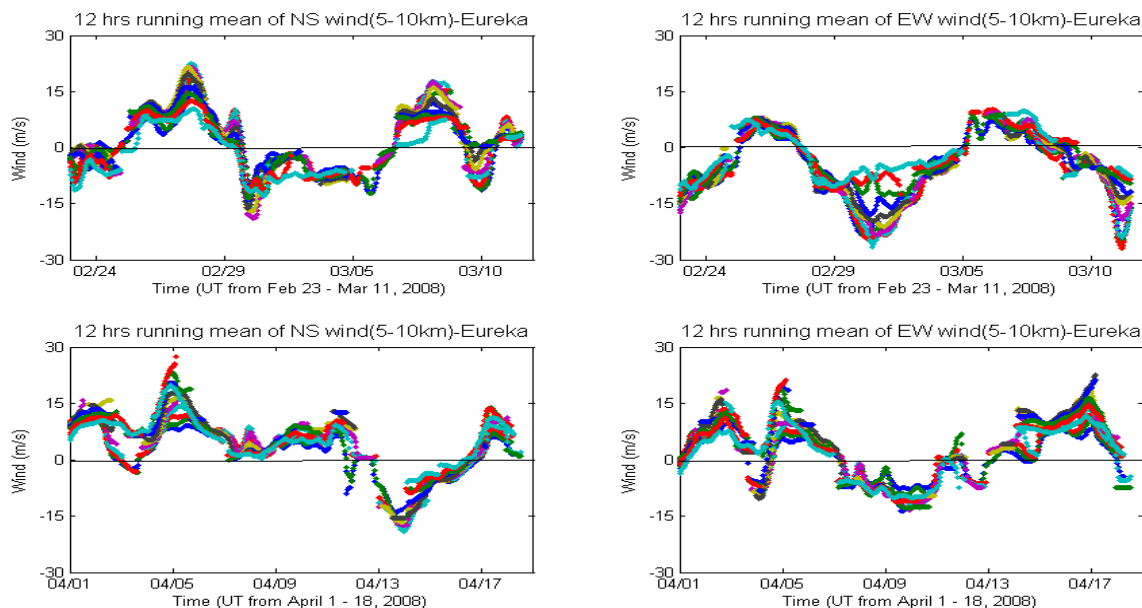


Figure 2| Eureka Radar Measurements of Horizontal Wind Velocity February - April 2008.

The plot of 12 hours running hourly mean of horizontal component of wind velocity (measured in ms^{-1}) versus time for the periods of 23 February – 11 March 2008 and 1 – 18 April 2008. The first and second columns show 12 hours running mean north-south and east-west wind velocities of February-March and April 2008 periods, respectively, for height range between 5 and 10 km.

Figure 2 shows the results of radar measurements of wind velocity from 5 km up to 10 km for every 0.5 km interval. Different colors depict the wind velocity at different height. From Figure 2 one can see that from 1 to 13 April 2008 the wind was dominantly blowing northward which suggests the high ozone concentration at Eureka may have been the result of ozone which came from the south of Eureka. The average wind speed during this period is approximately 7 m/s (~ 605 km/day). Therefore, in 10 days the air would move 6050 km (i.e. the air as far south as 25°N could get to Eureka during this time.).

This work was supported by a theoretical computer simulation for modeling ozone movement using FLEXPART to see if the above observation has any correlation with the result from the model.

The results of a numerical simulation using FLEXPART is shown in Figure 3. The computer simulation evidently points out that there is a significant downward motion that results a deep stratospheric ozone influx to the south of Eureka on both the 5th and 7th of April 2008.

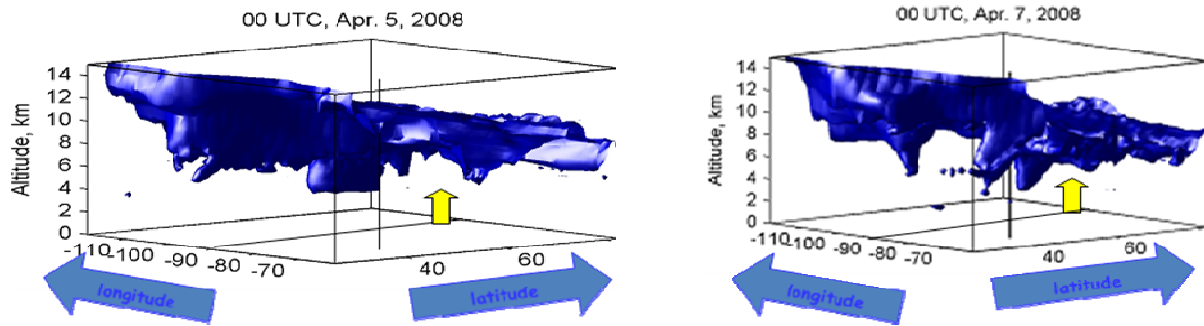


Figure 3 | Three-dimensional image of the 80 ppb ozone surface during the events of 5th (at 00:00 UTC) & 7th (at 00:00 UTC) of April 2008, as determined by the FLEXPART model. The location of the ozonesonde launches site is shown (vertical yellow line).

The numerical FLEXPART model for 5th and 7th of April 2008 (generally in April 2008) clearly shows the occurrence of stratospheric ozone intrusion events in the south of Eureka. This result is found to be in full agreement with the results that we obtained from radar measurements of the horizontal component of wind velocity.

4. CONCLUSIONS

Stratospheric-Tropospheric Exchange of ozone was observed in April even though the ozone intrusion events occurred in the south of Eureka. This stratospheric ozone was steadily blown northward with the wind for approximately successive 13 days that resulted in ozone rich air with low relative humidity in the middle and higher troposphere of Eureka.

ACKNOWLEDGEMENT: We would like to thank Environment Canada and the Canadian Network for the Detection of Atmospheric Change (CANDAC) for logistic and financial support of this work.

5. REFERENCES

- Altshuller, A. P. & Lefohn, A. S., 1996. Background ozone in the planetary boundary layer over the United States. *J. Air Waste Manage. Assoc.* 46, 134–141.
- Hocking, W.K., Carey-Smith, T., Tarasick, D. W., Argall, P.S., Strong, K., Rochon, Y., Zawadzki, I., Taylor, P. A., 2007. Detection of Stratospheric Ozone Intrusions by Windprofiler Radars, *Nature*, 450, pp. 281-284.
- Lin, C.-Y. C., Jacob, D. J., Munger, J. W. & Fiore, A. M., 2000. Increasing background ozone in surface air over the United States. *Geophys. Res. Lett.* 27, 3465–3468.
- Roettger, J. & Larsen, M. F., 1990. In *Radar in Meteorology* (ed. Atlas, D.) 235–281 (American Meteorology Society, Boston, Massachusetts).
- Stohl, A., Forster, C., Frank, A., Seibert, P., Wotawa, G., 2005. Technical note: The Lagrangian particle dispersion model FLEXPART version 6.2. *Atmos. Chem. Phys.* 5, 2461–2474.
- Stohl, A., Wernli, H, James, P, Bourqui, M, Forster, C, Liniger, M.A., Seibert, P, Sprenger, M., 2003. A new perspective on stratosphere-troposphere exchange. *Bull. Am. Meteorol. Soc.* 84, 1565–1573.
- World Meteorological Organization. *Scientific Assessment of Ozone Depletion 1998. Global Ozone Research Monitoring Project Report 44* (WMO, Geneva, 1999).

HIGH RESOLUTION MEASUREMENTS OF STRATOSPHERE-TROPOSPHERE EXCHANGE USING RADAR WINDPROFILERS AND BALLOON-BORNE OZONESONDES

D.W. Tarasick¹, T.K. Carey-Smith², W.K. Hocking³, S. Argall³, O. Cooper⁴, H. He¹, G. Liu¹, Y. Rochon¹

¹Air Quality Research Division, Environment Canada, Downsview, ON, Canada M3H 5T4

²National Institute of Water and Atmospheric Research Ltd., Private Bag 14901, Kilbirnie, Wellington, New Zealand

³Department of Physics and Astronomy, University of Western Ontario, London, Ontario, Canada N6A 3K7

⁴Cooperative Institute for Research in Environmental Sciences, University of Colorado, Boulder, Colorado, USA

1. Introduction

Previous work [Hocking *et al.*, 2007] demonstrated, using windprofiling radar and multiple ozone soundings, that intrusions of stratospheric ozone into the troposphere can be predicted by rapid changes in tropopause height, and that intrusion events are (surprisingly) frequent at midlatitudes in Canada.

Intrusion events identified in ozone soundings were confirmed by model results (Figure 1), using the Lagrangian particle dispersion model FLEXPART [Stohl *et al.*, 2005] with (hourly) meteorological input at from version 3.2.0 of GEM, the Canadian operational forecast model, with 58 vertical levels on the standard regional domain covering North America.

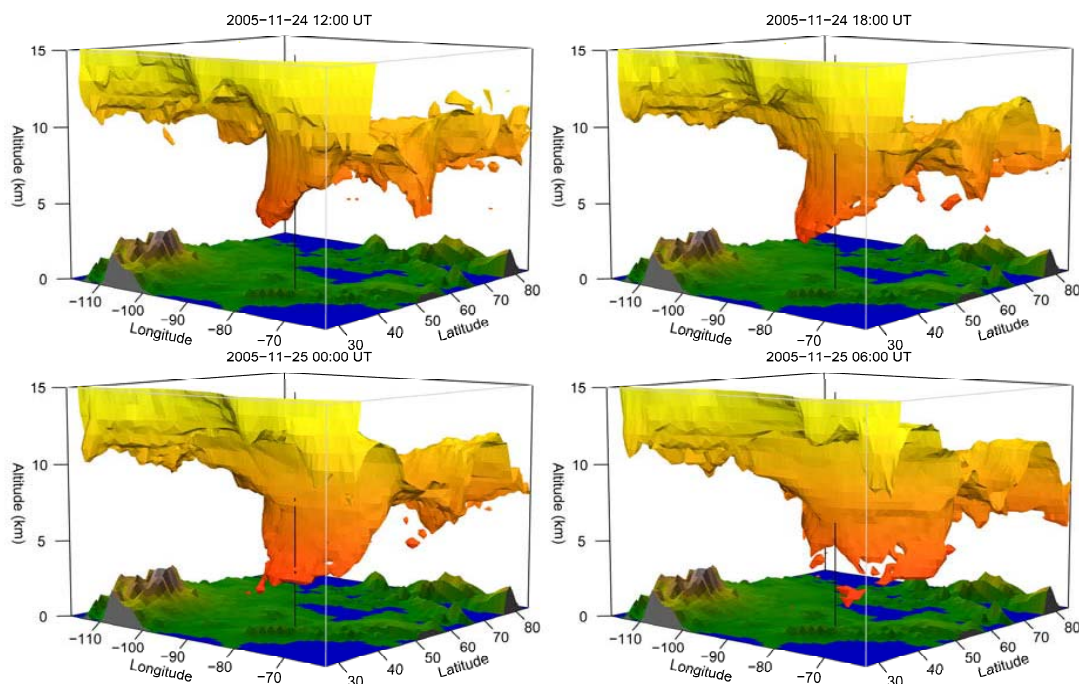


Figure 1. FLEXPART output showing the 80 ppb ozone mixing ratio iso-surface at 6-hour intervals from 12UT on 24 November to 6UT on 25 November, 2005. The black line shows the location of the wind-profiling radar at Walsingham, Ontario.

The balloon-borne instruments used were GPS-equipped EN-SCI 2Z ECC ozonesondes and Vaisala RS80 radiosondes, providing vertical profiles of ozone concentration, temperature, humidity, wind speed and wind direction. They were released approximately twice daily near the radar sites located at Montreal (45.4 N, 73.9 W), and Walsingham, ON (42.6 N, 80.6 W).

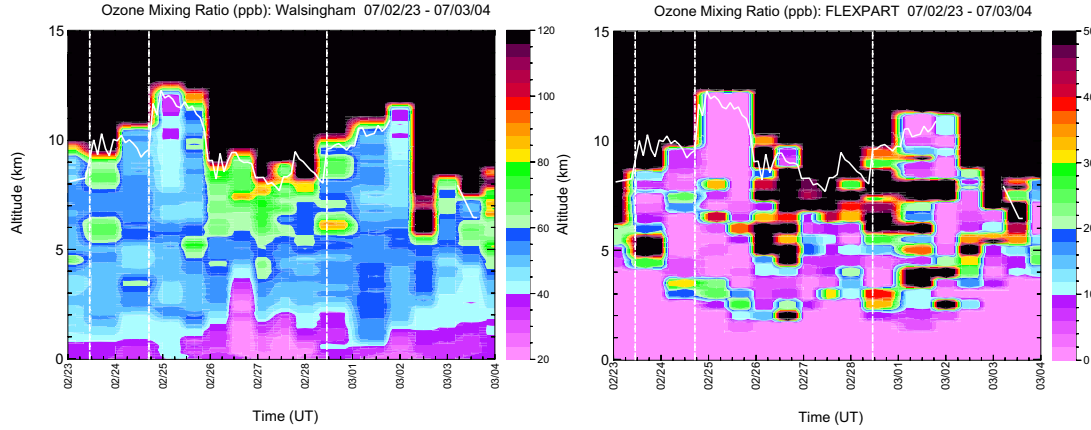


Figure 2. Left: Vertical profiles of ozone mixing ratio for the April-May 2006 Walsingham campaign. The solid line shows the tropopause height derived from the radar data. The dashed lines indicate times when the tropopause undergoes a rapid ascent. Right: A similar plot of ozone mixing ratio values from a GEM-FLEXPART simulation. The values were extracted from the FLEXPART output grid at locations along the sonde flight paths. Note the change in colour scale. Much of the lower part of the figure is featureless (with zero ozone) as the FLEXPART simulation does not include background tropospheric ozone.

2. Recent results

Several recent radar-ozonesonde campaigns have extended the data set of *Hocking et al.* [2007], and confirmed the close correspondence between ozone intrusions and rapid tropopause height changes [*Carey-Smith et al.*, 2010]. FLEXPART modeling of ozone transport indicates that much of the observed variability of ozone in the upper troposphere is due to the stratospheric source (Figure 2). In general, stratospheric intrusions appear to follow the passage of upper level cyclones which temporarily force the mid-latitude jet stream south of the observing locations. Since total ozone variations at extratropical latitudes are well-correlated with synoptic scale meteorological disturbances [*Dobson and Harrison*, 1926; *Dobson et al.*, 1946], particularly tropopause height [*Ohring and Muench*, 1960; *Schubert and Munteanu*, 1988], this suggests that it may be possible to relate rapid changes in total ozone to the occurrence of ozone intrusions.

While the tropopause height determined by the radar is typically identical to that using the standard lapse rate definition (*WMO*, 1966), this is not always the case. The backscattered power for a VHF radar is approximately proportional to M^2/r^2 , where r is the range from the radar and M is the vertical gradient of the potential refractive index

$$M = -7.76 \times 10^{-5} \left(\frac{p}{T} \right) \left(\frac{\partial \ln \theta}{\partial z} \right) \left[1 + \frac{15500q}{T} \left(1 - \frac{\frac{\partial \ln q}{\partial z}}{2 \frac{\partial \ln \theta}{\partial z}} \right) \right]$$

where θ (K) is potential temperature, T is temperature, p (hPa) is pressure, z (m) is altitude, and q is specific humidity [*Vanzandt et al.*, 1978]. The term in square brackets is generally ignored, as q is small above the lower troposphere. The radar usually detects a maximum in

backscatter at the abrupt change in the gradient of potential temperature at the tropopause. However, in some cases an increase in $\partial \ln \theta / \partial z$ at a lower altitude, often coincident with a sharp negative gradient of water vapour, can produce a larger maximum. In these cases soundings show dynamically disturbed profiles of temperature, ozone and water vapour, and it appears that the radar is in fact detecting the sharp increase in potential temperature and decrease in water vapour associated with an intrusion of stratospheric air. In the cases shown in Figure 3, the sharp negative gradients of water vapour actually contribute significantly to the backscatter, as $\partial \ln q$ is much larger than $\partial \ln \theta$, and the factor in square brackets is about 1.2 even though q is very small.

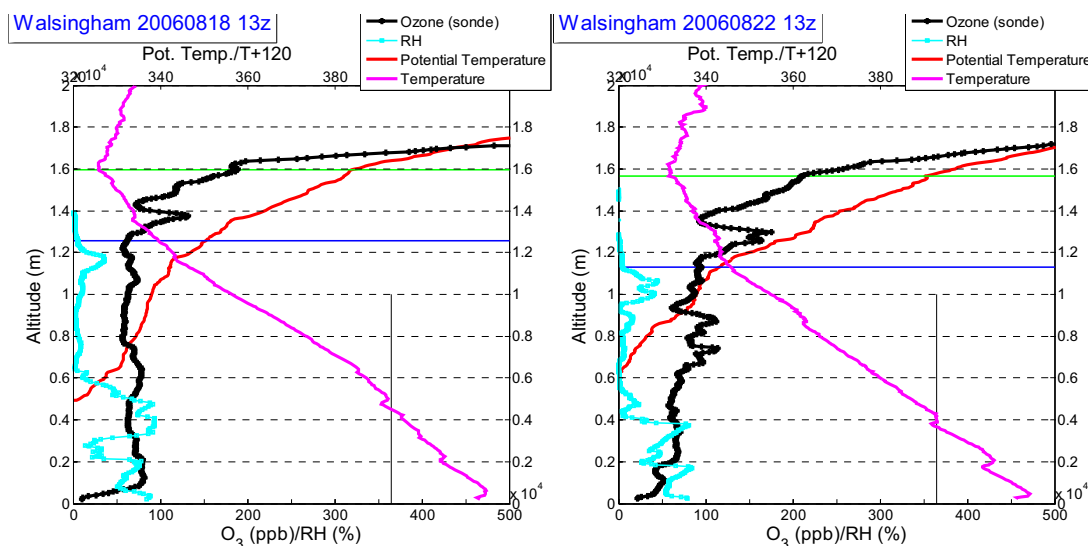


Figure 3. Ozone and water-vapour pressure profiles taken at Walsingham. The green line indicates the WMO (temperature lapse rate) tropopause; the blue line the radar tropopause.

In the lower troposphere, where q is larger, gradients of humidity can dominate the radar signal. Figure 4 shows successive ozone and humidity profiles and simultaneous observations with the radar near London, ON. It is apparent that the radar can track the descent of the dry layer of high ozone.

3. Conclusions

Twice daily ozonesondes were launched during six 10-day campaigns, incorporating nearby windprofiler measurements, in Ontario and Quebec between 2005 and 2007. This novel combination of observations has demonstrated the existence of a strong relationship between discontinuities in the tropopause and stratosphere-troposphere exchange (STE). Since windprofilers can routinely measure the height of the tropopause, this may be useful for tropospheric air quality forecasts. GEM-FLEXPART modeling is able to reproduce much of the observed variability of ozone in the upper troposphere, confirming its stratospheric origin, and also indicating that GEM is representing tropospheric dynamics quite well.

Further examination shows that where the radar-determined tropopause differs from the WMO thermal tropopause, the radar is typically responding to the sharp gradients of potential temperature and humidity at the lower edge of a stratospheric intrusion. Radar appears to be a particularly good intrusion detector. In addition to explaining the radar's success at finding STE events, this fact can potentially be used to follow the descent of layers of stratospheric origin in the troposphere.

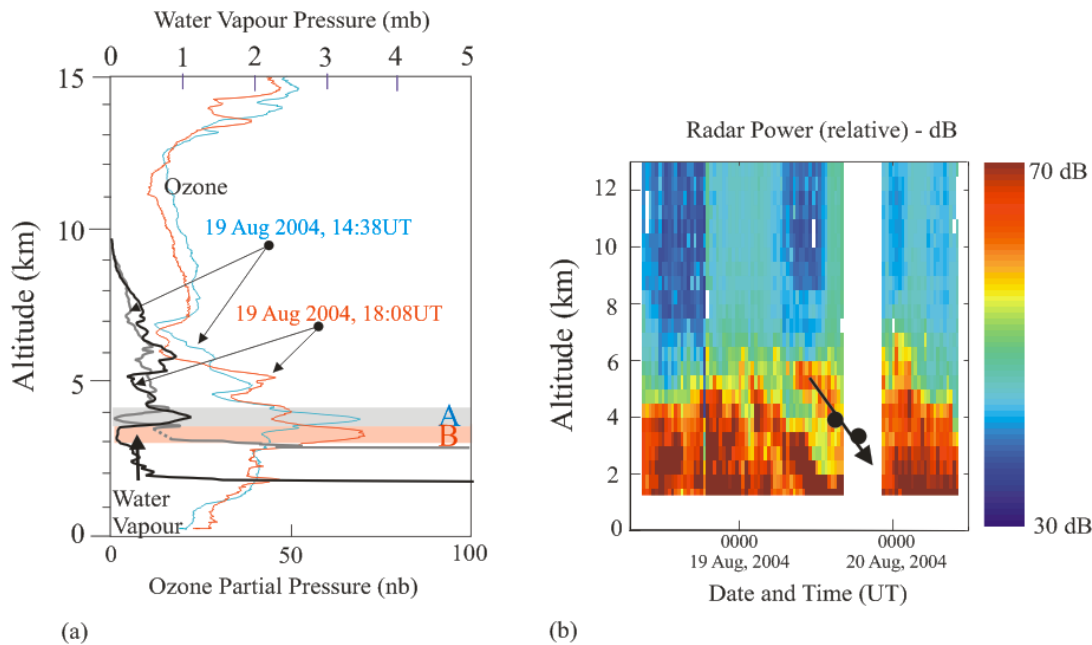


Figure 4. (a) Successive ozone and water-vapour pressure profiles taken only four hours apart on 19 August, 2004. Movement can be seen, as peak A moves to peak B. Graph (b) shows radar backscattered power as a function of time and height from 18 to 20 August, 2004. The peaks A and B have high ozone but low water vapour, and steep gradients in water vapour at their edges. These water vapour gradients produce enhanced radio backscatter, and the radar signal enhancement shown in 1b by the downward sloping arrow in fact tracks the ozone maximum. The two black dots in that figure show the height of the peaks in ozone density for events A and B (although unfortunately the radar was not operational for case B).

4. References

- Carey-Smith, T.K., D.W. Tarasick, W.K. Hocking, O.R. Cooper, G. Liu, P.S. Argall and Y. Rochon, High resolution measurements of stratosphere-troposphere exchange using radar windprofilers and balloon-borne ozonesondes, *J. Geophys. Res.*, to be submitted, 2010.
- Hocking, W. K., T. K. Carey-Smith, D. W. Tarasick, P. S. Argall, K. Strong, Y. Rochon, I. Zawadzki and P. A. Taylor, Detection of stratospheric ozone intrusions by windprofiler radars, *Nature*, 450(7167), 281–284, doi:10.1038/nature06312, 2007.
- Stohl, A., C. Forster, A. Frank, P. Seibert, and G. Wotawa, Technical note: The Lagrangian particle dispersion model FLEXPART version 6.2, *Atmos. Chem. Phys.*, 5, 2461–2474, 2005.
- Vanzandt, T.E., J.L. Green, K.S. Gage, and W.L. Clark, Vertical profiles of refractivity turbulence structure constant: Comparison of observations by the Sunset Radar with a new theoretical model, *Rad. Sci.*, 13(5), 819–829, 1978.
- Dobson, G.M.B., and D.N. Harrison, Measurements of the amount of O₃ in the earth's atmosphere and its relation to other geophysical conditions: Part I. *Proc. Roy. Soc. London*, A110, 660–693, 1926.
- Dobson, G.M.B., A.W. Brewer and B.M. Cwiling, Meteorology of the lower stratosphere. *Proc. Roy. Soc. London*, A185, 144–175, 1946.
- Ohring, G., and H.S. Muench, Relationships between ozone and meteorological parameters in the lower stratosphere. *J. Meteor.* 17, 195–206, 1959.
- Schubert, S.D., and M.J. Munteanu, An analysis of tropopause pressure and total ozone correlations. *Mon. Weather Rev.*, 116, 569–582, 1988.
- WMO, *International Meteorological Vocabulary*. WMO, No. 182. TP. 91. Geneva (Secretariat of the World Meteorological Organization), 1966. pp. xvi, 276.

A STUDY OF TROPICAL TROPOPAUSE VARIATION AT GADANKI (13.46°N, 79.17°E) USING A LONG-TERM MST RADAR DATA-BASE

T. V. Chandrasekhar Sarma¹, Toshitaka Tsuda²

¹National Atmospheric Research Laboratory, Gadanki 517112 AP, India

²Research Institute for Sustainable Humanosphere, Kyoto University, Kyoto 611 0011,
Japan.

Introduction

Consequent to the realisation in the later half of the 20th century that unbridled anthropogenic forcings of the atmosphere have driven irreversible climate change, there has been a search for conclusive evidence within atmospheric observational data sets. Data and results from observational techniques (e.g. radiosonde) (Highwood et.al, 2000; Seidel et.al., 2001) and numerical weather forecasts based on reanalyses (Highwood and Hoskins 1998; Randel et.al., 2000) and in climate models forced by combined natural and anthropogenic effects have indicated the changes in atmospheric parameters. One of the important indicators of climate change has been established to be the altitude of the tropopause. Several studies have indicated this parameter to be a reliable indicator of climate change brought about by forcings – both natural and anthropogenic. Global-scale studies of tropopause height based on radiosonde data recorded over several decades and computations using climate models based on estimated natural forcings (solar irradiance, volcanic aerosols) and anthropogenic forcings (changes in well mixed green-house gases, direct scattering effects of sulphate aerosols, tropospheric and stratospheric ozone) have established the linkage of human activities over climate change (Santer et.al., 2003). The present study was motivated by the desire to explore if such changes in the tropopause height could be detected in an atmospheric radar data located at a tropical station.

Data Set

The MST Radar at Gadanki in southern part of India was established in 1993 and has been operated since then for several observations studies. The radar was operated in three main operational programmes. They are campaign mode (national and international), user scientist experiments (special experiments proposed by individual groups) and common mode experiments (routine operations to create a long-term data-base). The data used for present study was recorded under the common-mode programme between 2001 and 2008. The radar was operated in 5 or 6-beam (off zenith along E,W,N and S and vertical) operational mode mainly covering altitudes between 3.6 and 26.1 km though useful signals often existed only upto about 22km in altitude. GPS radiosondes were launched coinciding with radar operation between 2006 and 2008 on most occasions.

Analysis Procedure

It is well known that the vertically pointed radar beams can return strong echoes from stably stratified regions of the atmosphere. Stable stratification near the tropopause results in strong echoes. The method proposed by *Gage and Green* (1982) was used to determine the altitude of the lapse rate tropopause(LRT) as per WMO definition. Radiosonde data of 2006-2008 was analysed to generate a normalised power (S , watt) profile as per the relation of *Gage & Green* (1982) adapted to Gadanki radar.

$$S = 2.96 \times 10^{10} P_i \left[\frac{\Delta r}{10^3} \right]^2 \left[\frac{P}{T} \frac{\partial \ln \theta}{\partial z} \right]^2 \quad \text{-----(1)}$$

Here Δr is the range resolution, P is pressure, T absolute temperature, θ the potential temperature and z is the altitude.

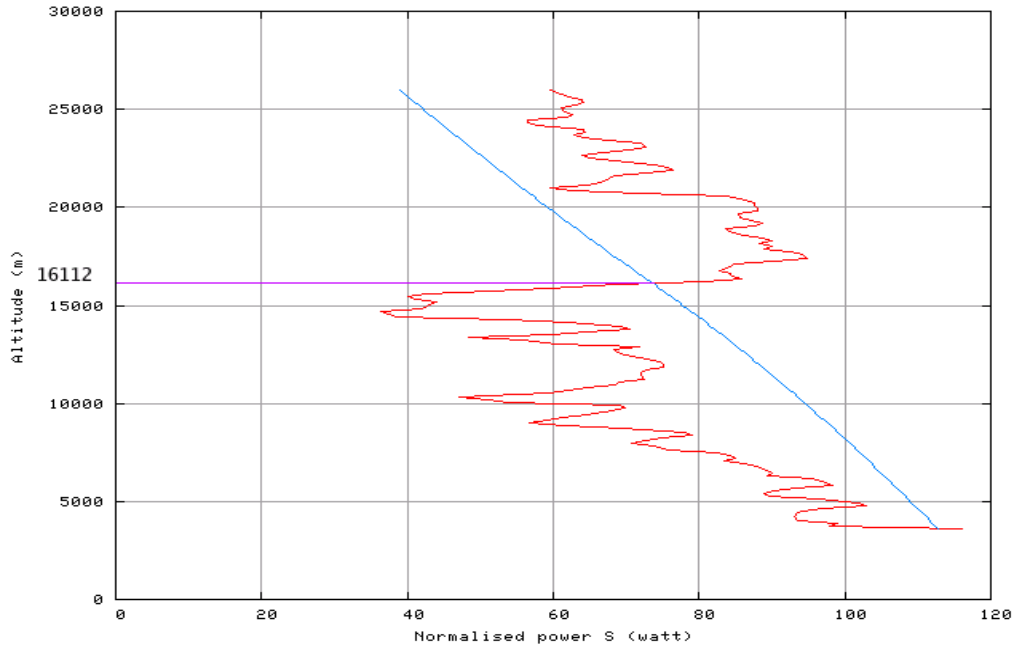


Figure 1: Normalised power S (in red) computed using radiosonde data of 19June2008 and using 2K/km model (blue). The intersection at 16.1km is taken as the height of the LRT.

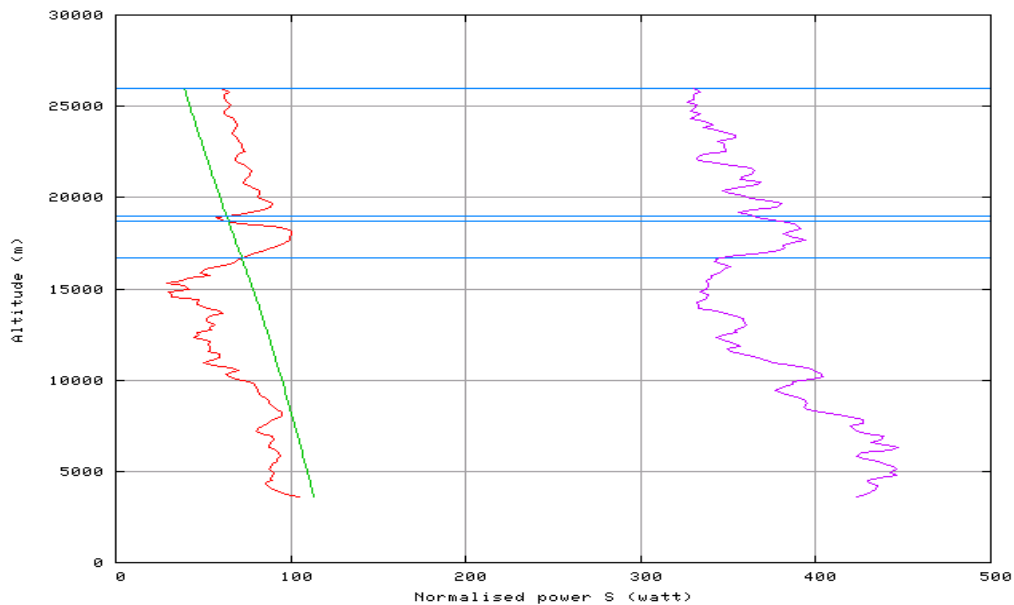


Figure 2: Normalised powers S_{rs} (in red), S_{mod} (green) and S_{radar} (magenta) computed using data of 30th May 2007.

Identification of Tropopause altitude

The WMO definition that the tropopause is located at the lowest altitude (above the 500mb level) above which the temperature lapse rate does not exceed 2K km^{-1} for at least two kilometers, was used. Using the radiosonde measured P and T , a profile of S_{rs} was computed. Similarly a model profile of S_{mod} was computed using (1) and 2K km^{-1} lapse rate. The altitude of intersection of S_{mod} with S_{rs} designated as the tropopause height. This is shown in figure 1. Similarly a profile of S for radar S_{radar} was computed

for each month during 2006-2008 when the radiosonde data was available and intersections were found as shown in figure 2. Using this data, the correction in the numerical constant in (1) was computed for each month so that the profiles of *Sradar* coincide with those of *Srs*. Now, using these new constants, the *Sradar* profiles were computed between 2001 and 2008 for all available months and radar tropopause was detected as the intersection altitude with the *Smod*. These radar tropopause altitudes are shown in figure 3. Further, studies on the interpretation of the tropopause altitude are being done using this data-base.

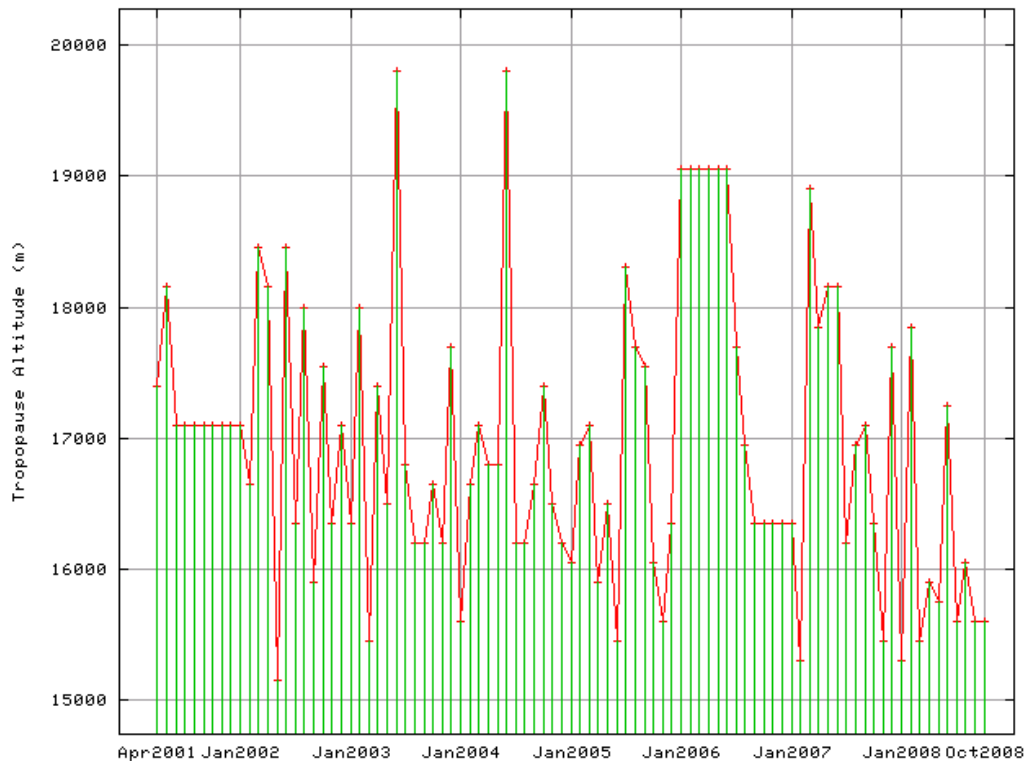


Figure 3: Radar tropopause altitudes between 2001 and 2008.

References

Gage, K. and J. Green, An objective method for the determination of tropopause height from VHF radar observations, *J. Appl. Met.*, 21,1150-1154, 1982.

Highwood,E. and B. Hoskins, The tropical tropopause, *Q.J.R. Met.Soc.*,124, 1579-1604, 1998.

Highwood,E., B. Hoskins and P. Berrisford, Properties of the arctic tropopause, *Q.J.R.Met. Soc.*, 126, 1515-1532, 2000.

Randel, W., F. Wu, and D. Gaffen, Interannual variability of the tropical tropopause derived from radiosonde data and NCEP reanalyses, *J. Geophys. Res.*, 105(D12), 15509-15523, 2000.

Santer, B., M. Wehner, T. Wigley, R. Sausen, G. Meehl, K. Taylor, C. Ammann, J. Arblaster, W. Washington, J. Boyle and W. Bruggmann, Contributions of anthropogenic and natural Forcing to recent tropopause height changes, *Science*, 301, 479-483, 2003.

Seidel, D., R. Ross, J. Angell, and G. Reid, Climatological characteristics of the tropical tropopause as revealed by radiosondes, *J. Geophys. Res.*, 106(D8), 7857-7878, 2003.

RANGE-IMAGING OBSERVATION OF TURBULENCE AROUND TROPICAL TROPOPAUSE BY EQUATORIAL ATMOSPHERE RADAR

Tomoaki Mega¹, Masayuki K. Yamamoto¹, Matoko Abo², Hubert Luce³, Hiroyuki Hashiguchi¹, Yoshikazu Tabata¹, Manabu D. Yamanaka⁴, Shoichiro Fukao⁵

1. Research Institute for Sustainable Humanosphere, Kyoto University, Japan.
2. Tokyo Metropolitan University, Japan
3. LSEET, Université du Sud-Toulon Var, La Garde, France
4. Japan Agency for Marine-Earth Science and Technology (JAMSTEC), Japan
- 5 Fukui University of Technology, Japan

1. INTRODUCTION

Observations of temperature, winds, and atmospheric trace gases suggest that the transition from the troposphere to the stratosphere occurs in a layer, rather than at a sharp tropopause. In the tropics, this layer is often called the tropical tropopause layer (hereafter TTL). TTL has a bottom at 150 hPa, 355 K, 14 km (pressure, potential temperature, and altitude) and has a top at 70 hPa, 425 K, 18.5 km. TTL acts in many ways as a gate to the stratosphere, and understanding all relevant processes is of great importance for reliable predictions of future climate (Fueglistaler, et al. 2009).

By receiving echoes from refractive index irregularities, VHF wind profilers typically operated near 50-MHz frequency (6-m wavelength) have the capability to continuously observe vertical profiles of vertical and horizontal air winds both in clear and cloud regions. In the equatorial Indonesia, a 47-MHz Doppler radar referred to as the Equatorial Atmosphere Radar (hereafter EAR) has been operated at the Equatorial Atmosphere Observatory, Kototabang (hereafter KT), West Sumatra (0.2°S, 100.32°E). Using observational results of wind and turbulence around the TTL observed by the EAR,

turbulence features in TTL, which are expected to contribute air mass mixing there, have been shown (Fujiwara et al. 2003; Yamamoto et al. 2003). Using frequency diversity of transmitted radar signals, atmospheric radars are able to attain higher range resolution (up to several tens of m) than one determined by the transmitted pulse width. The technique is called Frequency-domain interferometry imaging (hereafter FDI) or range imaging. FDI has been used to reveal turbulent features around the tropopause in the midlatitude region (e.g., Luce et al. 2006). In the report, preliminary observational results of turbulence in TTL are shown using the FDI observation mode of the EAR.

2. Data

The EAR has a circular antenna array, approximately 110 m in diameter, which consists of 560 three-element Yagi antennas. To produce total peak output power of 100 kW, each antenna is driven by a solid-state transmitter-receiver module with 180-W peak output power. For the detailed description of the EAR, see Fukao et al. (2003). In December 2009, we carried out the observation campaign named the Cloud experiment by Lidar and the Equatorial Atmosphere Radar (hereafter CLEAR). During the CLEAR campaign, the EAR was operated with a FDI mode to observe fine time and altitude variations of turbulence. On pulse-to-pulse basis, the EAR changed transmitted frequencies from 46.50 to 47.50 MHz

with 250 kHz spacing (five frequencies). In the FDI mode, the radar beam was pointed to vertical direction (0° , 0°). Amplitude and phase information of received signals obtained using five frequencies were used for Capon processing method (Luce et al., 2001) to derive altitude profiles of clear-air echoes with high vertical resolutions. Altitude profiles of clear-air echoes were computed with 5-m vertical intervals.

3. Results

Figure 1a shows a time-altitude plot of intensity of received (echo) signals observed by the EAR from 0145 to 0215 LT 18 December 2008. The intensity of echo signals is expressed in arbitrary unit. Wavy echoes, which reached to about 15.6 km and had a period of about 7 min, were observed. Figure 1b shows a time series of Doppler velocity observed by the vertically-pointed radar beam of the EAR at 15.22 km. Upward wind of about 1 m s^{-1} or larger was observed when upward lifts of enhanced echoes (up to 15.2 km or higher) were observed (around 0146-0148LT, 0153-0155 LT, and 0159-0202 LT). At the lower altitude (14.77 km), this tendency was still observed, though it was not clear as compared with one at 15.22 km.

Figure 2 shows observational results of the radiosonde located at 14.0-15.5 km from 0029 to 0032 LT 18 December 2008 (about 90 min earlier than the EAR observations). The profiles in Figure 2 are computed with the interval of 50 m. At 14.60-14.65 km, potential temperature (hereafter Θ) and square of Brunt-Väisälä frequency (hereafter N^2) showed rapid increase with altitude (Figures 2a and b). Above 14.65 km, Θ was quite uniform (Figure 2a). The increase of Θ just above 14.60 km and uniform Θ above 14.65 km indicates the presence of the airmass mixing. Vertical horizontal wind shear exceeded $25 \text{ m s}^{-1} \text{ km}^{-1}$ at 14.55-14.75 km (Figure 2c). This large wind shear was caused by the eastward vertical wind shear (not shown). Owing to the large vertical horizontal wind shear and decreased N^2 , Richardson number (hereafter Ri) was dominantly less than 0.25 around 14.7-14.9 km (Figures 2b, c, and d). The small Ri less than 0.25 indicates that shear instability (or Kelvin-Helmholtz instability) was easy to occur at the altitudes, and also suggests that the observed wavy echoes and large Doppler velocity observed by the EAR were produced by shear instability. The wavy enhanced echoes observed by the EAR suggest that the isentropic surface with large vertical gradient of Θ , which was the part of billow of shear instability, was lifted. Uniform Θ above 14.65 km also suggests the presence of airmass mixing by shear instability. Previous study has shown that shear instability frequently occurs around the tropical tropopause due to large eastward vertical wind shear (Yamamoto et al. 2003). However, their results were based on observational data with the time resolution of 1 h. The wavy echoes and Doppler velocity as shown in the Figure 1 provide detailed information on observed scales of shear instability which occurs in TTL.

4. SUMMARY

In the report, preliminary observational results of turbulence in TTL have been shown using the FDI observation of the EAR. The range-imaging technique (FDI) would be important for exploring turbulence processes associated with cloud and precipitation. Further, FDI enables the high-resolution observation of vertical and horizontal winds, though this report does not show this capability. We are now carrying out the analyses of data observed by the EAR and lidar installed at KT, and the results will be reported in forthcoming studies.

ACKNOWLEDGMENTS

The 47-MHz wind profiler belongs to Research Institute for Sustainable Humanosphere (RISH), Kyoto University and is operated by RISH and National Institute of Aeronautics and Space (LAPAN), Indonesia. The work was supported by Hydrometeorological Array for Isv-Monsoon AUTomonitoring (HARIMAU) project of the Japan EOS Promotion Program (JEPP).

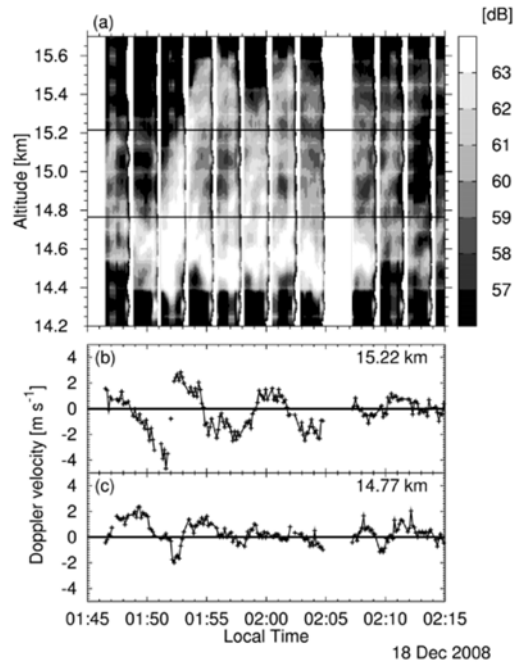


Figure 1. Time-altitude plots of (a) intensity of received (echo) signals observed by the EAR from 0145 to 0215 LT 18 December 2008. Time series of Doppler velocity observed by the vertically-pointed radar beam of the EAR at (b) 15.06 km and 14.61 km. Thin black lines in (a) show the altitude of 15.06 km and 14.61 km, respectively.

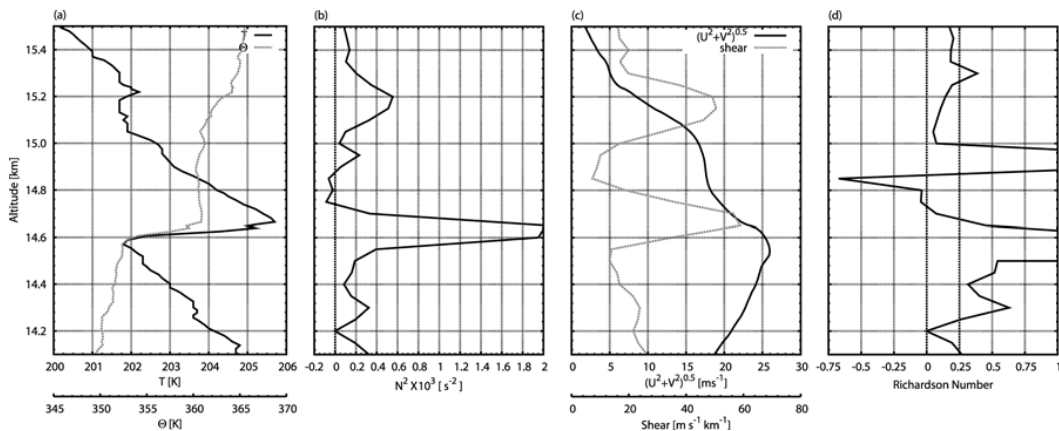


Figure 2. Altitude profiles of (a) T (black) and Θ (gray), (b) square of Brunt-Väisälä frequency (N^2), (c) amplitude of horizontal wind (black) and its vertical shear (gray), and (d) Richardson number (Ri) observed by the radiosonde located at 14.0-15.5 km from 0029 to 0032 LT 18 December 2008.

Bibliography

- Fueglistaler, S., A. E. Dessler, T. J. Dunkerton, I. Folkins, Q. Fu, and P. W. Mote, Tropical tropopause layer, *Rev. Geophys.*, 47, RG1004, doi:10.1029/2008RG000267, 2009.
- Fujiwara, M., M. K. Yamamoto, H. Hashiguchi, T. Horinouchi, and S. Fukao, Turbulence at the tropopause due to breaking Kelvin waves observed by the Equatorial Atmosphere Radar, *Geophys. Res. Lett.*, 30(4), 1171, doi:10.1029/2002GL016278, 2003.
- Fukao, S., H. Hashiguchi, M. Yamamoto, T. Tsuda, T. Nakamura, M. K. Yamamoto, T. Sato, M. Hagio and Y. Yabugaki, Equatorial Atmosphere Radar (EAR): System description and first results, *Radio Sci.*, 38(3), 1053, doi:10.1029/2002RS002767, 2003.
- Luce, H., G. Hassenpflug, M. Yamamoto, and S. Fukao, High-resolution vertical imaging of the troposphere and lower stratosphere using the new MU radar system, *Ann. Geophys.*, 24, 791-804, 2006.
- Luce, H., M. Yamamoto, S. Fukao, D. H elal, and M. Crochet, A frequency domain radar Interferometric imaging (FII) technique based on high-resolution methods, *J. Atmos. Sol. Terr. Phys.*, 63(2-3), 221-234, doi:10.1016/S1364-6826(00)00147-4, 2001.
- Yamamoto, M. K., M. Fujiwara, T. Horinouchi, H. Hashiguchi, and S. Fukao, Kelvin-Helmholtz instability around the tropical tropopause observed with the Equatorial Atmosphere Radar, *Geophys. Res. Lett.*, 30(9), 1476, doi:10.1029/2002GL016685, 2003.

LARGE-SCALE STUDIES OF STE USING TRAJECTORY MODELING, SATELLITE AND OZONESONDE MEASUREMENTS

H. He¹, D.W. Tarasick², T.K. Carey-Smith³, W.K. Hocking¹, Y. Rochon²,
M. Moran², P.S. Argall¹, K. Strawbridge², J. McConnell⁴, D. Jones⁵ and M. Bourqui⁶

¹ Dept. of Physics and Astronomy, University of Western Ontario, Canada

² Environment Canada, Downsview, Canada.

³ National Institute of Water and Atmospheric Research Ltd., New Zealand

⁴ Dept. of Earth and Space Science and Engineering, York University, Canada

⁵ Dept. of Physics, University of Toronto, Canada

⁶ Dept. of Chemistry and Atmospheric and Oceanic Sciences, McGill University, Canada

1 Introduction

We explore the temporal and spatial evolution of stratosphere ozone intrusion events over North America, with GEM-FLEXPART model simulations and TES observations, during the spring and summer ARC-IONS ozonesonde campaigns in 2008, when numerous stratospheric ozone intrusions are indicated by ozonesonde observations. TES observations and GEM-FLEXPART results together provide a continental-scale three-dimensional picture of stratosphere-troposphere exchange (STE), capturing the vertical and horizontal structure as well as the time-evolution of STE.

2 Data

Balloon-born ozonesondes with fine vertical resolution (~ 100 - 150 m) from the ground to the stratosphere, and high temporal resolution (*e.g.* twice a day) during campaigns, are important tools to study STE at specific locations and times (*e.g.* Wakamatsu *et al.*, 1989; Hocking *et al.*, 2007). The ozonesonde data used in this study come from the ARCTAS Intensive Ozonesonde Network Study (ARC-IONS) 2008, which cooperated with the NASA project Arctic Research of the composition of the Troposphere Aircraft and Satellites (ARCTAS) in spring and summer 2008 over Northern America.

Observations by the Tropospheric Emission Spectrometer (TES) on board NASA's Aura satellite (Beer *et al.*, 2001; Beer *et al.*, 2006) are useful for studying the dynamic change of ozone profiles globally, although they have limited vertical resolution. This study uses version 3 (V003) of the TES level 2 data products by nadir viewing. The data used here were obtained from 16-orbit global surveys during ARC-IONS campaigns with observation footprint $5 \text{ km} \times 8 \text{ km}$. Initial validation studies have shown that the TES ozone profiles show a 5-15% high bias in the troposphere compared to ozonesondes (Nassar *et al.*, 2008).

3 Methodology

3.1 GEM-FLEXPART Model Simulation

The Lagrangian particle dispersion model FLEXPART has become one of the most popular models to study stratospheric ozone intrusions (Stohl *et al.*, 2003; Stohl *et al.*, 2003; Cooper *et al.*, 2004; Cooper *et al.*, 2005; Hocking *et al.*, 2007). In this study, the hourly fields output from the Canadian operational weather forecast Global Environment Multiscale (GEM) model (based on 12-hour meteorological analysis)(Côté *et al.*, 1998), are used as the input to FLEXPART. The standard regional domain of GEM version 3.2.2 covering North America with fifty-eight vertical levels, is used. GEM output is interpolated onto a $0.5^\circ \times 0.5^\circ$ longitude-latitude grid and converted to GRIB format for input to FLEXPART. More details on how GEM-FLEXPART was set up for stratospheric ozone intrusion studies are given in Carey-Smith *et al.* [2009].

3.2 3-D Interpolation Methodology

TES ozone data is sparse in the horizontal (latitude-longitude) dimension. A two-step point-wise three-dimensional quadratic interpolation of TES ozone profiles can provide a more complete three-dimensional view of stratospheric and tropospheric ozone. In the initial step, vertical quadratic interpolations at determined altitude levels (the same as FLEXPART levels) are performed at each point (x, y) (latitude, longitude). In the second step, for each vertical level z (meters above sea level), two-dimensional quadratic interpolations are implemented at grid points $\{(x, y)\}$, using the closest N (e.g. 8) known neighbor points. The second order interpolation polynomial is of the form

$$f(x, y) = a_1x^2 + a_2y^2 + a_3xy + a_4x + a_5y + a_6,$$

where the coefficients $\{a_i\}_{i=1}^6$ are estimated under the least squared error criterion.

4 Observations

The campaign sites for ARC-IONS 2008 are shown in Figure 1. Campaigns sites for spring and summer 2008 are displayed in blue and black, respectively. Those active in both spring and summer are displayed in red. There were 12 sites operating in spring and 13 in summer.

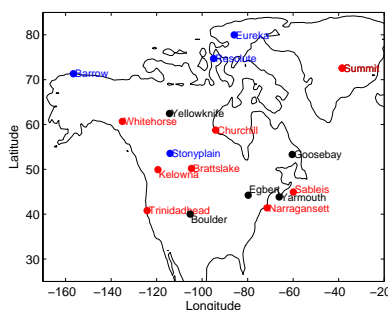


Figure 1: ARC-IONS campaign sites.

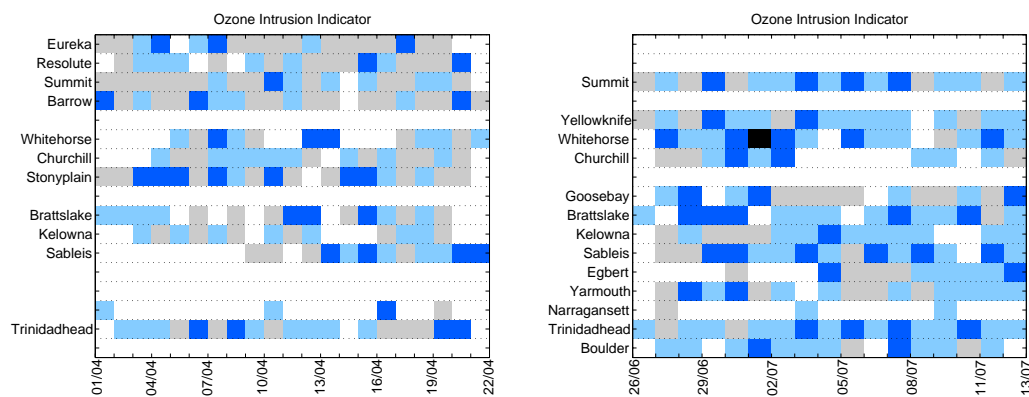


Figure 2: Stratospheric ozone intrusion indicator charts for ARC-IONS (left: spring 2008; right: summer).

Figure 2 shows the occurrence of stratospheric ozone intrusions at the sites in Figure 1 during ARC-IONS. Tropopause heights are estimated from the ozonesonde temperature profiles according to usual World Meteorological Organization (WMO) temperature lapse rate definition. The intrusion indicator $I(t)$ is computed following Hocking *et al.* (2007), $I(t) = M(t) - B(t)$,

where $M(t)$ is the the maximum ozone mixing ratio (in ppbv) between 3km altitude and the tropopause, and $B(t)$ (background) is the average of all nearby values of ozone mixing ratio before, after, above and below the point of the maximum. When $I(t)$ is larger than 25 ppbv, coincident with a local minimum in relative humidity, a dark-blue box is shown in Figure 2. Light blue boxes are used when $M(t)$ exceeds $B(t)$ by 15-25 ppbv, and grey boxes when the difference is less than 15 ppbv. White boxes indicate when no ozonesonde data are available. The single black box used in the right-hand plot denotes an occurrence of a strong intrusion with $I(t) > 25$ and deep downward below 5 km. More active stratospheric ozone intrusions were observed in the summer (June and July) of 2008 than in spring (April), especially at high latitudes. This is in contrast to what is commonly expected (e.g. Appenzeller *et al.*, 1996) but similar to the observations of Merrill *et al.* (1996) over the United States.

Since high tropospheric ozone concentrations can be formed by photochemical reactions involving precursors like nitrogen oxides (NOx) and volatile organic compounds (VOCs) generated by anthropogenic activities, especially in the hot summer season, it is necessary to validate their stratospheric origin by GEM-FLEXPART model simulations. Figure 3 shows observation and simulation results at Bratt's Lake in summer 2008. Ozonesonde profiles (every 24 hours at 21 UT), which suggest occurrences of ozone intrusions (on 28-30 June, July 7 and 10) as above in Figure 2, are shown in the upper left plot. The corresponding plot of ozone of stratospheric origin (also in ppbv) extracted from a GEM-FLEXPART simulation at this location is in the upper right. The lower two plots, although less detailed, give the large-scale picture: the 80-ppbv ozone mixing ratio iso-surface from the GEM-FLEXPART simulation, at 21 UT on June 27th and July 7th, clearly indicates in each case a deep influx of ozone from the stratosphere, resulting in a tongue of ozone penetrating to 4km and 6km, respectively. Ozone intrusions in Figure 2 were confirmed by GEM-FLEXPART simulation results.

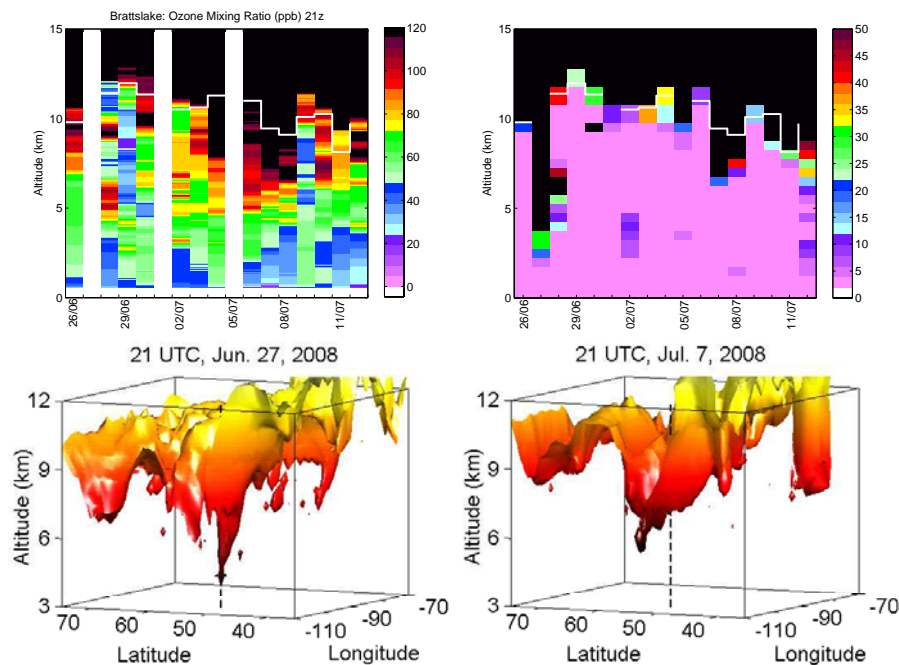


Figure 3: Observation and simulation results at Bratt's Lake ($50.20^{\circ}\text{N}, 104.70^{\circ}\text{W}$) in summer 2008 (see the text for details). The black dashed lines show the location of Bratt's Lake.

It can be observed from Figure 2 that strong stratospheric ozone intrusions occurred at five campaign sites (Whitehorse, Churchill, Bratt's Lake, Sable Island, and Yarmouth), on 30 June 2008. The GEM-FLEXPART 80-ppbv ozone mixing ratio iso-surface at 21 UT on June 30th is shown in the left-hand plot of Figure 4, clearly shows two deep influxes of ozone over northwest Canada (including Whitehorse and Churchill) and the northeast United States (including Sable Island and Yarmouth). The 90-ppbv ozone mixing ratio iso-surface produced by three-dimensional interpolation using TES and ozonesonde profiles for June 30th, shown in

the right-hand plot of Figure 4, shows good qualitative agreement with the FLEXPART picture. This suggests that when the scale of an ozone intrusion is larger than the distance between two TES tracks, three-dimensional interpolation of TES ozone profiles can show the topography of the ozone enhancement in the upper troposphere.

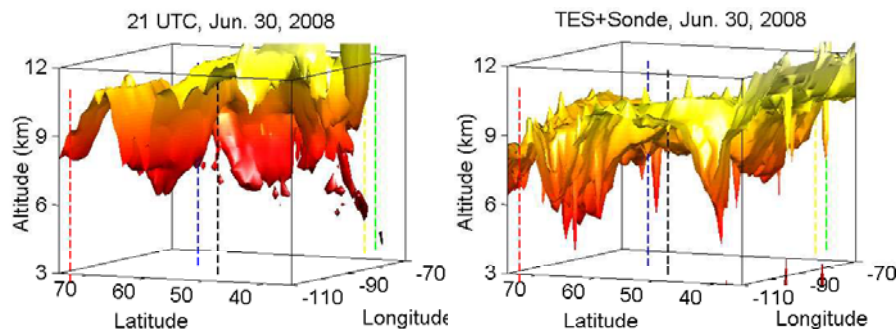


Figure 4: Comparison of TES interpolations and GEM-FLEXPART simulation results on June 30, 2008. The dashed lines shows the locations of Bratt's Lake (black), Whitehorse (red), Churchill (blue), Sable Island (green) and Yarmouth (yellow) Canada.

With three-dimensional interpolation, satellite data are able to provide a more complete three-dimensional view of stratospheric ozone intrusion events.

References

- [1] Appenzeller, C., J. R. Holton, and K. H. Rosenlof (1996), Seasonal variation of mass transport across the tropopause, *J. Geophys. Res.*, 101(D10), 15,071-15,078, doi:10.1029/96JD00821.
- [2] Beer, R., T. A. Glavich, and D. M. Rider (2001), Tropospheric Emission Spectrometer for the Earth Observing System Aura satellite, *Appl. Opt.*, 40, pp.2356-2367.
- [3] Beer, R. (2006), TES on the Aura mission: Scientific objectives, measurements, and analysis overview, *IEEE Trans. Geosci. Remote Sens.*, 44, 1102-1105.
- [4] Carey-Smith T.K., D.W. Tarasick, W.K. Hocking, O.R. Cooper, G. Liu, P.S. Argall, K. Strong, Y. Rochon, I. Zawadzki, and P.A. Taylor (2009), High resolution measurements of stratosphere-troposphere-exchange, to be submitted to *Journal of Geophysical Research*, personal communication.
- [5] Cooper, O. R., C. Forster, D. Parrish, E. Dunlea, G. Habler, F. Fehsenfeld, J. Holloway, S. Oltmans, B. Johnson, A. Wimmers, and L. Horowitz (2004), On the life-cycle of a stratospheric intrusion and its dispersion into polluted warm conveyor belts, *J. Geophys. Res.*, 109, doi:10.1029/2003JD004006, 2004.
- [6] Cooper, O. R., et al. (2005), Direct transport of midlatitude stratospheric ozone into the lower troposphere and marine boundary layer of the tropical Pacific Ocean, *J. Geophys. Res.*, 110, D23310, doi:10.1029/2005JD005783.
- [7] Côté, J., S. Gravel, A. Methot, A. Patoine, and M. Roch (1998), The operational CMC-MRB Global Environmental Multiscale (GEM) model, part I: Design considerations and formulation, *Mon. Weather Rev.*, 126(6), 1373-1395.
- [8] Hocking, W.K., T.K. Carey-Smith, D.W. Tarasick, P.S. Argall, K. Strong, Y. Rochon, I. Zawadzki, and P.A. Taylor (2007), Detection of stratospheric ozone intrusion by windprofiler radars, *Nature*, 450(7167), 281-284, doi:10.1038/nature06312.
Merrill, J. T., J. L. Moody, S. J. Oltmans, and H. Levy II (1996), Meteorological analysis of tropospheric ozone profiles at Bermuda, *J. Geophys. Res.*, 101(D22), 29,201-29,211, doi:10.1029/95JD03432.
- [9] Nassar, R., J.A. Logan, H.M. Worden, I.A. Megretskaja, K.W. Bowman, G.B. Osterman, A.M. Thompson, D.W. Tarasick, S. Austin, H. Claude, M.K. Dubey, W.K. Hocking, B.J. Johnson, E. Joseph, J. Merrill, G. Morris, M. Newchurch, et al. (2008), Validation of Tropospheric Emission Spectrometer (TES) nadir ozone profiles using ozonesonde measurements, *J. Geophys. Res.*, 113, D15S17, doi:10.1029/2007JD008819.
- [10] Stohl, A. H. Wernli, P. James, M. Bourqui, C. Forster, M.A. Liniger, P. Seibert, and M. Sprenger (2003c), A new perspective of stratosphere-troposphere exchange, *Bulletin of the American Meteorological Society*, 84(11), 1563-1573, doi:10.1175/BAMS-84-11-1565.
- [11] Stohl, A., C. Forster, A. Frank, P. Seibert, and G. Wotawa (2005), Technical note: The Lagrangian particle dispersion model FLEXPART version 6.2, *Atmos. Chem. Phys.*, 5, 2461-2474.
- [12] Wakamatsu S., Uno I., Ueda H., Uehara K., and Tateishi H. (1989), Observational study of stratospheric ozone intrusions into the lower troposphere. *Atmospheric Environment* 23, 1815-1826.

Appendices

Appendix A

MST-12 WORKSHOP SUBMISSIONS

The following appendix lists all papers submitted to the workshop. Unfortunately, not all could be presented because some participants could not attend due to the H1N1 virus, which was a major concern at the time. Nevertheless, we have listed all the papers for completeness. Papers which were not presented are marked by asterisk.

Section 1: Scattering, Calibration and Microscale processes session

Talks

- | | |
|----------------------------|--|
| Fritts et al. | Assessments of Radar Measurement Biases Using Numerical Simulations of Turbulence Dynamics and Radar Backscatter |
| Balsley and Woodman | Co-Locating High-Resolution Temperature and Velocity Profiles with a Radar Beam: An Opportunity to Study Fine-Scale Processes in the Troposphere |
| Balsley | On the Ubiquity of Small-Scale Turbulence in the Troposphere and Stratosphere |
| Cheinet | The spatial distribution of Cn2 in the Convective boundary layer: a LES analysis |

- Muschinski and Frasier** Vertical fluxes of clear-air radar reflectivity
- Lehmann** Intermittent clutter echoes in radar wind profilers: Signal characteristics and filtering
- Lee and Vaughan** Use of Wind Profilers to Quantify Atmospheric Turbulence
- Belova et al.** Fine structure of wintertime mesospheric radar echoes – a comparison between high and low latitudes
- Selvamurugan et al.** On first Lightning experiment using Indian MST radar over Gadanki (13.5N, 792.E)
- Beres et al.** Active and Passive Observations of Lightning
- Stober and Jacobi** Evaluation of Absolute Radar Calibration using Cosmic Noise (QDC) and Simulated Signals
- Li et al.** A derivation of microphysical parameters of mesospheric ice clouds from calibrated PMSE observations at 53.5 MHz and 500 MHz
- Singer et al.** Longitudinal differences of PMSE strength at high Arctic latitudes and their relation to precipitating particles.
- Swarnalingam and Hocking** A Decade-long aspect-sensitivity study of polar mesosphere summer echoes at Resolute Bay

Posters

Balsley and Woodman

The Use of Probability Density Functions to Examine High-Resolution Echoes Using the SOUSY Radar

Singh et al.

Scales sizes of turbulence and height coverage of wind profiling radars

Meek

MFR trends in angle of arrival: tilt vs. height vs. month

Housley and Vaughan

A statistical approach to modelling VHF radar echoes

Section 2: New Instruments, signal processing and quality control.

Talks

- | | |
|---------------------------------|---|
| Nishimura et al. | High-resolution 3D imaging of turbulence using the MU radar |
| Nicolls et al. | D-Region Observations with the Poker Flat Incoherent Scatter Radar |
| Latteck et al. | The new MST radar on Andøya/Norway |
| Bhattacharjee et al. | Design aspects of the antenna array for ST Radar in central Himalyan region at Nainital,India |
| Viswanathan et al.* | Compact ST Radar @ 206.5 MHz to study Atmospheric Dynamics over Himalayas |
| Cohn et al. | A proposed deployable Modular Profiling Network (MPN) |
| Anandan and Jagannatham* | An Autonomous Interference Filtering Approach Applied to Wind Profilers |
| Sato et al. | Program of the Antarctic Syowa MST/IS Radar. |
| Kuyeng et al. | Tropopause altitude detection at 78°N, 16°E, 2008: first results of the refurbished SOUSY radar |
| Hooper and Gaffard | What is the optimal level of time-averaging for radar-derived wind-profiles? |
| Chen and Chu | Beam Broadening Effect on Radial Velocity and Doppler Spectral Width of Wind Profiler |

- Scipion et al.** Quantification of horizontal shear of vertical velocity in DBS and SA mean estimates
- Dehghan and Hocking** Reliability of Turbulence Measurements by Radars
- Lakshmi Kantha et al.*** Turbulence Dissipation Rates from Radiosondes?
- Furumoto et al.** Application of the frequency- domain interferometric imaging to RASS measurements
- Shinoda et al.** Continuous observations of temperature profiles by 443 MHz wind profiling radar with RASS in Okinawa
- Urbina et al.** 50 MHz Software Defined Radar Receiver
- Sunderland et al.** Design of a Digital Pulsed Radar Receiver
- McLaughlin et al.** A Modern Radar Wind Profiler Using Electronic Beam Steering and a Digital Receiver
- Aryal et al.,** An Innovative and Versatile Dual-Channel Transceiver Module for Radar Beam Forming and Beam Steering Applications
- Li Chen et al.*** The design of MST based on signal beam forming Array Antenna.
- Srinivasulu et al.*** Development of UHF Wind Profiling Radar at NARL for Lower Atmospheric Research Applications.

Posters

- Kumar et al.** FPGA based implementation of DSP scheme for upcoming 206.5MHz ST Radar at ARIES Nainital, India
- Palo** Parameter Estimation and Error Analysis of Meteor Radar Signals
- Prakash et al.** Peak Power Aperture Calculation For Aries St Radar By Measuring Cn2 In Shivalik Range Of Himalaya At Nainital, India
- Pillai et al.*** FPGA based Timing Signal Generation, data acquisition and processing using LabVIEW for WP/RASS
- Jenn-Shyong Chen et al.*** A novel phase calibration method for multiple-frequency range imaging of VHF/UHF atmospheric radar
- Khandare et al.*** Monopulse Tracking System For Upper Air Atmosphere
- Eastment et al.** The effects of almost 20 years of operation on the performance of the Aberystwyth MST Radar
- Hooper et al.** The diagnosis of a range gating problem suffered by the Aberystwyth MST Radar
- Renkwitz et al.,** Multiple Beam Capability of An Array of 64 Yagi Antennas For Mesospheric Observations
- Viswanathan et al.*** ST Radar for studying Atmospheric Dynamics over Himalayas

- Lindseth et al.** Engineering aspects for the 449 MHz Modular Wind Profiling Network (MPN)
- Keuer et al.** Pulse Coding To Reduce The Influence Of Man-Made Noise On Mf Radar Observations Of Winds And Electron Densities
- Scipion et al.** Effects of vertical velocity shear on mean wind estimates using Doppler beam swinging and spaced antenna techniques
- Hocking and Hocking** A radar digitizer and encoder based on deconvolution procedures.
- Farag and Hocking** Determination of precise pointing angles of the O-QNet radars

Section 3: Meteors studied with MST Radar.

Talks

- | | |
|-----------------------------|--|
| Brown et al. | Application of an automated 3D wavelet algorithm for meteor shower identification using the Canadian Meteor Orbit Radar (CMOR) |
| Vaudrin and Palo | Overview and Initial Results of a FPGA Based Digital Receiver for Meteor Radar Applications |
| Chilson et al. | Are underdense meteor decay rates and PMSE influenced by the presence of charged aerosols? |
| Janches et al., | Direct Observation of micrometeor differential ablation |
| Younger et al., | A survey of meteor shower radiants and orbits using the Darwin and Davis Station VHF meteor radars |
| Meek and Manson | A curious feature in meteor trail 3-D wind analysis |
| Verbeeck and Ryabova | Calculation of the meteoroid flux density of the Geminid stream by radar observations |
| Selvamurugan et al.* | Observation On Simultaneous Occurrence Of Meteor Shower With E-Region Irregularities Over Gadanki (13.5° N, 79.2° E) |
| Hibit et al. | Seasonal and Diurnal Variability of Mid-Latitude Specular and Non-Specular Meteors |

- Fritts et al.** The Southern Argentina Agile Meteor Radar (SAAMER): Radar configuration and first results
- Chu and Cheng*** Observations of Inertial-gravity wave from long-lasting meteor trail echoes made with VHF radar
- Antonita et al.** Gravity wave and planetary wave interactions in the low latitude MLT region: A study using meteor radar observations
- Cheng et al.*** Mesosphere region temperature from meteor trail decay time
- Xiong et al.** Mean mesopause temperatures over Wuhan and Beijing

Posters

- Younger et al.** Evaporation, ionization, and deceleration of meteoric material in the upper atmosphere
- Galindo and Chau** Observations of sporadic and shower meteor-head echoes using narrow and wide beams at Jicamarca
- Younger et al.** Absorbing aerosols' impact on meteor diffusion coefficient estimates
- Reddy and Yellaiah*** A study on Perseid meteoroid stream from the Gadanki MST radar observations of the shower activity
- Selvamurugan*** VHF Radar Observations on Meteor Induced Turbulent Plasma Irregularity Layers

Selvamurugan*

Mesosphere-Lower Thermosphere Neutral Wind
Observations Using Meteor Trails as Tracers

Keuer et al.

Signatures of the ionization trail of a fireball
observed in the HF and VHF range above Middle-
Europe on January 17, 2009

Section 4: Plasma Irregularities.

Talks

- Fukao et al.** Coupling Processes in the Equatorial Atmosphere (CPEA): A new feature of plasma irregularities revealed over the Indonesian equator
- Chau et al.** Multi-frequency and multi-volume radar studies of the equatorial 150-km region
- Kudeki et al.** Calibrated radar observations of the equatorial mesosphere and ionosphere during an 11-day campaign
- Kuo-Feng Yang*** First measurement of tilted angle of echo layer structure in sporadic E region using Interferometry Technique
- Kagan** Hydroxyl optical emissions by high-power radiowaves
- Latteck and Rapp** Multi-Radar Studies Of PMSE: Implications For Mesospheric Large Scale Variability And Microphysical Processes
- La Hoz and Havnes** Recent Investigations of Polar Mesospheric Winter and Summer Echoes with the MORRO and EISCAT Radars
- Nicolls and Kelley** Characteristics of PMSE at 33 cm with the Poker Flat Incoherent
- Koustov** Characteristics of E region coherent echoes inferred from SuperDARN radar observations

Posters

Ramani and Guruburan

On the relationship between the MF radar scatterers and the equatorial sporadic E

Kuo-Feng Yang*

First measurement of tilted angle of echo layer structure in sporadic E region using Interferometry Technique

Patra*

Freshly generated F region irregularities after the post-midnight collapse of the F region observed by the Gadanki radar

N. V. Rao and Patra*

On the opposite nature of velocity reversal in the positive and negative sloped QP striations

Yuichi Otsuka*

Statistical study of daytime 150-km echoes observed with Equatorial Atmosphere Radar in Indonesia

Patra et al.*

Coordinated observations of 150-km echoes from Gadanki, India and Kototabang, Indonesia - A comparative study

Kirkwood et al.

Similarities and differences between Arctic and Antarctic PMSE - ESRAD, MARA and Davis

Section 5: Meteorology, Forecasting and Nowcasting

Talks

- | | |
|----------------------------------|--|
| Taylor and Hocking et al. | The Canadian O-QNet – implementation and impact on forecasting in Canada |
| Cohn et al. | Rotor and Wave Characteristics from a Network of Boundary Layer Wind Profilers |
| Williams. | Improved Vertical Air Motion Estimates using Combined 50- and 920-MHz Profiler Observations |
| Barron et al. | Refinement of 3D Doppler Velocity using 3D Windprofiler Data |
| Tsuda et al. | Meso-gamma-scale convective systems observed by a 443 MHz wind-profiling radar with RASS in the Okinawa subtropical region |
| White et al. | Observations and Forecast Tools to Help Detect and Monitor Storms Causing Dangerous Debris Flows |
| Fukao et al. | Dynamical structure of tropical cyclones revealed by atmospheric radars |
| Mercer et al. | Adding Value to Doppler Radar Data |
| Caccia et al. | A wind profiler network around the north-western Mediterranean sea for the future HyMeX-campaign |

- Gaffard et al.*** Integrated profiling station for High Resolution Numerical Weather Prediction
- Srinivasa Rao Vanukuru et al.** Identifying Monsoon Dynamics using Wind Profiler
- T. N. Rao et al.*** Multipeak Raindrop Size Distribution – Nature, Origin and Statistical Characteristics
- Kalia et al.** Some comparisons between OQ Net VHF wind profiler observations, various other measurements and model forecasts
- Campos et al.** Using UHF Wind Profiler for Weather Nowcasting during the 2010 Winter Games
- Chilson et al.** Combined Wind Profiler and Polarimetric Weather Radar Observations of Squall Lines
- Klaus.** Modeling the outer scale of turbulence to improve temperature profile measurements with a VHF radar
- Luce et al.** MU radar and lidar observations of clear-air turbulence and mammatus underneath cirrus
- Serafimovich et al.** Exchange processes of energy and matter between the surface and the atmosphere
- Yamamoto et al.** Vertical air motion in mid-level shallow-layer clouds observed by 47-MHz wind profiler and 532-nm Mie lidar
- Kusumma G. Rao et al.*** Northward propagation of Cold Point Tropopause patterns in Radio Occultation measurements during Indian monsoon

- Brown et al.** Boundary layer wind profiler observations over the North Atlantic Gulf Stream
- Kalapureddy and Campistron*** Onset of the West African Monsoon over Djougou (9.5°N, 1.5°E) using an Atmospheric Wind Profiler.
- Tabata et al.** Characteristics of Diurnal Variation in Indonesian Maritime Continent Based on Wind Profiler Observations.
- Barron et al.** Skeleton-Based Hook Echo Detection in Radar Reflectivity Data

Posters

- Satyanarayana et al.*** Characteristics of draft cores in wet and dry spells of the monsoon and their relation to the thermal structure of the atmosphere
- Kesarkar et al.** Validation of mesoscale model forecasts using Gadanki MST RADAR data
- Kusuma Rao and Ramakrishna** Numerical Simulation of Sharp Wind Shears observed by Indian MST radar using a Mesoscale Model during PRWONAM
- Jaiswal et al.*** A Different Approach to Find Z-R Relationship
- Barron et al.** Skeleton-Based Hook Echo Detection in Radar Reflectivity Data
- Uma et al.*** VHF radar observed characteristics of convectively generated gravity waves during wet and dry spells of Indian summer monsoon

- Kirkwood and Voelger** Mountain waves generated by the Scandinavian mountain chain –case studies using ESRAD and WRF
- Yamamoto et al.** Comparison study of lower-tropospheric horizontal wind over Sumatra, Indonesia using NCEP/NCAR reanalysis, operational radiosonde, and the Equatorial Atmosphere Radar
- Luce et al.** Mammatus and turbulence observations with the VHF MU radar, Ka-band and X-band radars during the TANUKI 2008 campaign
- Luce et al.** Characteristics of Kelvin-Helmholtz instabilities in the troposphere (up to ~16 km) seen by the MU radar in range imaging mode
- Argall et al.** Validation of ADM-Aeolus winds using wind profiler measurements
- Tabata et al.** Evaluation of Objective Reanalysis Data Accuracy over Indonesian Maritime Continent.

Section 6: Middle Atmosphere Dynamics and Structure

Talks

- Chris Meek** Motion of large scale velocity perturbations field across an array of MF radars
- Hocking et al.** The Axonmet - a new radar chain for Mesopause Science
- Kondala Rao et al.** Intraseasonal variations of 6 day wave in the low latitude middle atmosphere
- Cho** Comparison of SATI temperatures and radar wind measurements
- G. Kishore Kumar et al.** Long-term variations of Low latitude mesospheric mean winds observed using Indian MST radar, MF radar, M-100 rocketsondes and HRDI measurements
- Venkat Ratnam et al.*** New insights in understanding the low latitude mesospheric dynamics
- Morris et al.** Low latitude 2-day day planetary wave impact on austral polar mesopause temperatures: revealed by a January diminution in PMSE above Davis, Antarctica
- K. Kishore Kumar et al.,** Short-term variability of quasi 2-day waves and their interaction with tides in the MLT region using meteor radar observations

- Ward et al.,** Results from the CAWSES Global Tidal Campaigns
- Ward et al.,** Short term variations in equatorial tides:
Interference as an explanation?
- Gurubaran et al.** Tidal and planetary wave coupling of the low
latitude Mesosphere- Lower Thermosphere
Ionosphere (MLTI) region
- Ramkumar et al.** The Climatological Mean Wind Structure from the
Surface to 100 km at an Equatorial Station-
Trivandrum (8.5°N, 77°E)
- Singer et al.,** Diurnal and Seasonal Variability of D-Region
Electron Densities at 69°N
- Stober and Jacobi,** Ionospheric coupling from Cosmic Noise
Absorption and MLT winds observed with a
standard meteor radar
- Reid et al.** Temperature and wind measurements in the MLT
region using radar and airglow
- Snively et al.** Assessing gravity wave propagation characteristics
with simultaneous airglow image and meteor
radar wind data
- Mitchell and Beldon,** Climatologies of gravity waves observed by meteor
radar in the Arctic and Antarctic mesosphere.
- Klaassen** Testing Lagrangian theories of internal wave
spectra
- McCullough et al.** Lidar Measurements of Gravity Waves in the Arctic
Middle Atmosphere

- Ajay Kumar et al.*** Characteristics of high frequency gravity waves generated by tropical deep convection: Case studies
- Roper et al.** MLT Winds and Turbulence over Bear Lake, Utah, for the year 2000
- Lehmacher et al.** Kelvin-Helmholtz instabilities in the mesosphere observed by the Jicamarca radar
- Talaat et al.** Interannual variabilities in mesospheric waves as observed by the HF SuperDARN network
- Woodman and Villanueva** Hi-resolution radar billows observations at upper tropospheric heights
- Chandrasekhar et al.** RASS observations up to UTLS region at Gadanki (13.46°N, 79.17°E)
- Somayaji et al.*** Long term trend of Transition Height in D-Region – Implications to human induced perturbations
- Xiong et al.** The preliminary results of Tides in Beijing and Sanya observed by meteors

Posters

- Iain Reid and Jonathan Woithe** The long term variability of MLT winds, 730 nm OH and 558 nm OI nightglow intensity at Adelaide, Australia
- Aleem Basha et al.** High resolution observations of turbulence in the troposphere and lower stratosphere over Gadanki
- Suresh et al.** Seasonal Variation in the Momentum Flux of Planetary Waves in the MLT region at Trivandrum
- Sathishkumar et al.** Latitudinal variability in the middle atmosphere (30-90 km) winds during the major stratospheric warming event in 2005/2006
- Geetha Ramkumar et al.** Periodic Oscillations in the Middle Atmosphere at the Tropical region
- C. Bhuvanendran et al.** Signature of wave like fluctuations in the Equatorial F region vertical plasma drift during post- sunset and pre- sunrise hours
- Manja Placke et al.** Gravity wave momentum fluxes in the mesosphere / lower thermosphere at high- and mid-latitudes
- T. Maria Antonita et al.** Meteor Radar Observation of Gravity wave-Tidal Interaction in the MLT region over low latitude
- Klaassen and Sonmor** Nonlinearities of Lagrangian and Eulerian Internal Wave Ensembles
- Siddarth Shankar Das et al.** Comparison of mesospheric temperature measured by All-SKiYMET meteor radar with UARS/HALOE and TIMED/SABER observations at equatorial station Thumba

- K. Kishore Kumar et al.** Meteor radar observations of MLT region gravity wave variances during passage of deep convective systems
- Antonita and K. Kishore Kumar** Investigations on the MLT region horizontal structures within the radar volume using All-sky SKiYMET Meteor Wind Radar at Trivandrum (8.5N, 77E)
- P. B. Rao et al.** CAWSES - India: An Overview

Section 7: Tropopause processes and Stratospheric/Tropospheric exchange.

- Pan** Chemical Structure of the Extratropical Tropopause from New Satellite and Aircraft Observations
- Osman** Stratospheric–Tropospheric Exchange of Ozone during February – April 2008, Eureka
- Tarasick** High Resolution Measurements of Stratosphere-Troposphere Exchange Using Radar Windprofilers and Balloon-Borne Ozonesondes
- Bourqui** Descent of deep stratospheric intrusions in the troposphere
- Gjekaj*** The Role of Mixing to Upward Transport Across the Tropopause Layer
- Kusuma Rao*** Tropopause Altitudes from Indian MST Radar for Unlike Normal Cases of Cooling and Warming: Underlying Mechanisms
- Sarma and Tsuda** A study of tropical tropopause variation at Gadanki (13.46°N, 79.17°E) using a long-term MST radar data-base supplemented with radiosonde and RASS measurements
- Satheesh Kumar*** Diurnal variation of the tropical tropopause layer over Gadanki

Dutta et al., Seasonal variation of short-period (<2 h) gravity wave activity over Gadanki, India (13.5N, 79.2E)

Tomoaki Mega Range-imaging observation of turbulence around the tropical tropopause by Equatorial Atmosphere Radar

Posters

T. K. Ramkumar* MST radar observation of dissipation and generation of high frequency gravity waves

Srivastava et al. Lidar-radar probing of the atmosphere in the UTLS region: Implications on Troposphere-Stratosphere Exchange Processes

P. Vinay Kumar et al.* Measurements of short period gravity wave variances and momentum fluxes generated by deep tropical convective events using Gadanki MST radar

S. S. Das and K. Kishore Kumar Manifestation of inertia-gravity wave on tropopause height during the passage of tropical cyclone: Observations with Gadanki MST radar

K. Kishore Kumar et al. High temporal resolution VHF radar observations of stratospheric air intrusions in to the upper troposphere during the passage of a mesoscale convective system over Gadanki (13.50N , 79.20E)

Sanjay Kumar Mehta et al.* Study of stable layers in the UTLS region over Gadanki (13.5N, 79.2E) using Indian MST radar and high resolution GPS radiosonde measurements

Sreeletha et al.* Study Of Short Period Gravity Wave Spectrum In The Low Latitude Troposphere Using Indian Mst Radar

Shu Duan*

Stratosphere – Troposphere Interaction Process in
Mid-latitude Spring as Revealed by Xianghe VHF
Doppler Radar and Other Related Data

He et al.

Large-scale studies of stratosphere-troposphere
exchange using trajectory modelling, satellite and
ozonesonde measurements

Appendix B

MST-12 WORKSHOP PARTICIPANTS

<i>Name</i>	<i>Email Address</i>	<i>Country</i>
Antonita, M.	mariaspl@gmai.com	India
Aryal, P.	paryal@gsoft.com.au	Australia
Balsley, B.	balsley@cires.colorado.edu	USA
Barron, J.	barron@csd.uwo.ca	Canada
Belova, E.	belova@irf.se	Sweden
Beres, I.	iberes@uwo.ca	Canada
Bhattacharjee, S.	mr_tskumar@yahoo.com	India
Bhuvanendran, C.	c.bhuvanen@rediffmail.com	India
Bourqui, M.	michel.bourqui@mcgill.ca	Canada
Brown, P.	pbrown@uwo.ca	Canada
Brown, W.	wbrown@ucar.edu	USA
Caccia, J. -L.	caccia@lseet.univ-tln.fr	France
Campbell, W.	carroll.campbell@noaa.gov	USA
Campos, E.	Edwin.Campos@ec.gc.ca	Canada
Chao-Tuan, C.	966403008@cc.ncu.edu.tw	Taiwan
Cheinet, S.	cheinet@isl.tm.fr	France
Chilson, P	chilson@ou.edu	USA
Cho, Y. -M.	youngmin@yorku.ca	Canada
Chong Shing, J. C.	jchau@jro.igp.gob.pe	Peru
Cohn, S.	cohn@ucar.edu	USA
Dehghan, A.	adehghan@uwo.ca	Canada
Dutta, G.	gopadutta@yahoo.com	India
Farag, A.	ofarag@uwo.ca	Canada
Fournier, G.	gilles.fournier@ec.gc.ca	Canada
Fritts, D. C.	dave@cora.nwra.com	USA
Fukao, S.	s.fukao@kde.biglobe.ne.jp	Japan
Fuller, B	bfuller@gsoft.com.au	Australia
Furumoto, J. -I.	furumoto@rish.kyoto-u.ac.jp	Japan

<i>Name (continued)</i>	<i>Email Address</i>	<i>Country</i>
Garbanzo, M.	mac@fisica.ucr.ac.cr	Costa Rica
Guruburan, S.	gurubara@iigs.iigm.res.in	India
He, H.	huixia@mast.queensu.ca	Canada
Hibit, E.	ebh130@psu.edu	USA
Hocking, A.	mardoc-inc@rogers.com	Canada
Hocking, W. K.	whocking@uwo.ca	Canada
Hooper, D.	david.hooper@stfc.ac.uk	UK
Housley, D. -J.	djhousley@phsics.org	UK
Janches, D.	diego@cora.nwra.com	Canada
John, N.	john.neuschaefer@vaisala.com	Finland
Kagan, L.	lkagan@uwo.ca	Canada
Kalia, S.	ksshama@yorku.ca	Canada
Keuer, D.	keuer@iap-kborn.de	Germany
Kirkwood, S.	sheila.kirkwood@irf.se	Sweden
Kishore Kumar, G.	kishorekumargrandhi@gmail.com	India
Kishore Kumar, K.	kishorekumargrandhi@gmail.com	India
Klaassen, G.	gklaass@yorku.ca	Canada
Klaus, V.	vladislav.klaus@yahoo.fr	France
Koustov, A.	sasha.koustov@usask.ca	Canada
Kudeki, E.	erhan@illinois.edu	USA
Kumar, A	ashish@yahoo.com	India
Kuyeng Ruiz, K. M.	kkuyeng@jro.igp.gob.pe	Peru
Latteck, R.	latteck@iap-kborn.de	Germany
Lee, C.	christopher.lee@postgrad.manchester.ac.uk	UK
Lehmacher, G.	glehmac@clemson.edu	USA
Lehmann, V.	volker.lehmann@dwd.de	Germany
Li, Q.	liqiang@iap-kborn.de	Germany
Lindseth, B.	lindseth@ucar.edu	USA
Luce, H.	luce@lseet.univ-tln.fr	France
McCullough, E.	emccull2@uwo.ca	Canada
Meek, C.	chris.meek@usask.ca	Canada
Meng-Yuan, C.	s1643009@cc.ncu.edu.tw	Taiwan

<i>Name (continued)</i>	<i>Email Address</i>	<i>Country</i>
Mercer, R.	mercerc@csd.uwo.ca	Canada
Mitchell, N.	N.J.Mitchell@bath.ac.uk	UK
Mohammad, K.	afsarmoonstone@gmail.com	India
Mohammed, S.	salauddin.physics@gmail.com	India
Morris, R. J.	ray.morris@aad.gov.au	Australia
Murphy, A.	amurphy@gsoft.com.au	Australia
Muschinski, A.	muschinski@ecs.umass.edu	USA
Nicolls, M.	michael.nicolls@gmail.com	USA
Nie, Y.	ynie3@uwo.ca	Canada
Nishimura, K.	knish@nipr.ac.jp	Japan
Osman, M.	mosman4@uwo.ca	Canada
Otterbacher, S.	seotterb@mtu.edu	USA
Palo, S.	palo@colorado.edu	USA
Palomino, F. R. G.	fgalindo@jro.igp.gob.pe	Peru
Placke, M.	placke@iap-kborn.de	Germany
Prakash, C.	chandra@aries.ernet.in	India
Ramkumar, G.	geetha_ramkumar@vssc.gov.in	India
Reid, I.	iain.reid@adelaide.edu.au	Australia
Renkwitz, T.	renkwitz@iap-kborn.de	Germany
Ritter, C.	critter@awi-potsdam.de	Germany
Roper, R.	rgroper@bellsouth.net	USA
Serafimovich, A.	andrei.serafimovich@uni-bayreuth.de	Germany
Sica, R.	sica@uwo.ca	Canada
Singer, W.	singer@iap-kborn.de	Germany
Singh, N.	nelli.narendra@gmail.com	India
Snively, J.	jonathan.snively@usu.edu	USA
Srivastava, A. K.	atul@tropmet.res.in	India
Stober, G.	stober@uni-leipzig.de	Germany
Sunderland, M.	mds5000@psu.edu	USA
Swarnalingam, N.	nswarnal@uwo.ca	Canada
Tabata, Y.	yoshikazu-tabata@k7.dion.ne.jp	Japan
Talaat, E.	etalaat@yahoo.com	USA

<i>Name (continued)</i>	<i>Email Address</i>	<i>Country</i>
Tarasick, D.	david.tarasick@ec.gc.ca	Canada
Taylor, P.	pat@yorku.ca	Canada
Pan, L.	liwen@ucar.edu	USA
Tomoaki, M.	akmega@kawachi.zaq.ne.jp	Japan
Tsuda, T.	tsuda@rish.kyoto-u.ac.jp	Japan
Urbina, J.	jvu1@psu.edu	USA
Van Depeer, B.	bvandepe@gsoft.com.au	Australia
Vanukur, S. R.	drraovs@gmail.com	India
Vaudrin, C.	cody.vaudrin@colorado.edu	USA
Verbeeck, F.	cis.verbeeck@scarlet.be	Belgium
Ward, W.	wward@unb.ca	Canada
Williams, C.	Christopher.R.Williams@noaa.gov	USA
Wing, R.	rwing2@uwo.ca	Canada
Woodman, R.	acalle@jro.igp.gob.pe	Peru
Xiong, J.	xjg@mail.iggcas.ac.cn	China
Yamamoto, M.	m-yamamo@rish.kyoto-u.ac.jp	Japan
Younger, J.	joel.younger@adelaide.edu.au	Australia
Zhang, Y.	yzhan433@uwo.ca	Canada

Author Index

- Abo, M., 302–305
 Argall, S. P., 179–182, 295–298, 306–309
 Barron, J. L., 179–186, 191–194, 225–228
 Batista, P. P., 239–246
 Becker, E., 281–284
 Beig, G., 285–288
 Belova, E., 69–72
 Beres, I., 73–76
 Berkey, F. T., 266–268
 Bourqui, M., 306–309
 Bradford, J., 119–122
 Brown, W., 221–224
 Buriti, R. A., 239–246
 Carey-Smith, T. K., 295–298, 306–309
 Chakravarty, S. C., 285–288
 Chandrasekhar Sarma, T. V., 273–276, 299–301
 Chau, J. L., 165–168
 Clemesha, B., 243–246
 Cooper, O., 295–298
 Dabas, R. S., 285–288
 Davies, O., 123–126
 Davies, O. T., 119–122
 Dean, L., 119–122
 Dehghan, A., 103–106
 Dhanya, R., 173–176, 251–254
 Drummond, J., 85–88, 243–246, 291–294
 Eastment, J., 119–122
 Edson, J., 221–224
 Emperumal, K., 173–176
 Fabry, F., 179–182
 Farag, A., 139–142
 Foken, T., 217–220
 Friedrich, M., 255–258
 Fritts, D. C., 243–246
 Fukao, S., 161–164, 187–190, 213–216, 229–236, 302–305
 Furumoto, J. -I., 107–114, 199–202
 Gaffard, C., 99–102
 Gonzales, S., 115–118
 Gurubaran, S., 173–176, 239–242, 247–254, 277–280, 285–288
 Hangan, H., 179–182
 Hashiguchi, H., 229–236, 302–305
 He, H., 291–298, 306–309
 Hibbins, R. E., 243–246
 Hocking, A., 135–138, 243–246
 Hocking, W. K., 73–76, 85–92, 103–106, 135–142, 179–182, 243–246, 291–298, 306–309
 Hoffmann, P., 131–134, 281–284
 Hooper, D., 99–102, 119–126
 Ichiyama, T., 229–236

- Jacobi, C., 77–80, 281–284
Janches, D., 243–246
Joe, P., 191–194, 225–228
Jones, D., 306–309
Jones, G. O. L., 266–268
- Kagan, L. M., 169–172
Kalapureddy, M. C. R., 195–198
Kallenrode, M. -B., 85–88
Kawabata, T., 199–202
Keuer, D., 131–134, 154–157
Kirkwood, S., 69–72
Kishore Kumar, G., 247–250
Kishore Kumar, K., 247–250
Klaassen, G., 179–182, 259–265
Klaus, V., 203–212
Kondala Rao, R., 239–242, 277–280
Kudeki, E., 165–168
- Latteck, R., 85–88, 95–98, 127–130,
255–258
- Li, Q., 81–84
Liu, G., 295–298
Luce, H., 213–216, 229–236, 302–
305
- Manoharan, P. K., 285–288
Manson, A. H., 85–88, 150–153, 243–
246, 277–280
Matsugatani, A., 107–110
McBean, G., 179–182
McConnell, J., 306–309
McIntyre, H., 221–224
Meek, C., 85–88, 150–153, 243–246,
277–280
Mega, T., 229–236, 302–305
Meixner, F. X., 217–220
Mercer, R., 179–182
- Mercer, R. E., 183–186, 191–194,
225–228
Mikami, A., 199–202
Milla, M. A., 165–168
Mitchell, N. J., 239–246
Moran, M., 306–309
Murayama, Y., 111–114, 199–202
- Nagai, S., 199–202
Nakamura, T., 213–216, 239–242
Nakazato, M., 229–236
Narayana Rao, T., 69–72
Nash, J., 123–126
Nilsson, H., 69–72
- Oakley, T., 123–126
Ohigashi, Y., 229–236
Olewicz, Z., 119–122
Osman, M., 291–294
Otsuka, Y., 161–164
- Palo, S., 145–149
Pancheva, D. V., 239–242
Pant, T. K., 285–288
Patil, P. T., 251–254
Patra, A. K., 247–250
Placke, M., 281–284
- Röttger, J., 27–65, 81–84
Ramkumar, G., 247–250
Rao, K. G., 285–288
Rao, P. B., 285–288
Rao, P. M., 195–198
Rapp, M., 81–84, 95–98, 281–284
Ratnam, M. V., 247–250
Ravindran, S., 285–288
Renkowitz, T., 95–98, 127–130
Riggin, D. M., 239–246, 277–280

- Rochon, Y., 295–298, 306–309
Roper, R. G., 266–268
- Satheesh Kumar, S., 69–72
Sathishkumar, S., 239–242, 251–254,
277–280
- Satoh, S., 111–114, 199–202
Schier, S., 217–220
Serafimovich, A., 217–220
Sergienko, T., 69–72
Shibagaki, Y., 187–190
Shinoda, T., 107–114
Sica, R., 179–182
Singer, W., 77–80, 85–88, 95–98,
127–134, 154–157, 255–258,
277–284
Sridharan, R., 285–288
Sridharan, S., 239–242
Stober, G., 77–80, 154–157, 281–
284
Strawbridge, K., 306–309
Sultzer, M., 115–118
Sunderland, M., 115–118
Swarnalingam, N., 85–92, 179–182
- Tabata, Y., 302–305
Tajiri, T., 229–236
Takahashi, H., 239–242
Tarasick, D. W., 179–182, 291–298,
306–309
Taylor, M., 243–246
Taylor, P., 179–182
Teshiba, M., 187–190
Thomas, R., 73–76
Tsuda, T., 107–114, 199–202, 239–
242, 273–276, 299–301
Turp, M., 123–126
- Urbina, J., 115–118
- Vanukuru, S. R., 195–198
Vaudrin, C., 145–149
Vijaya Bhaskara Rao, S., 247–250
Villanueva R, F., 269–272
- Wang, H., 225–228
Wissing, J. M., 85–88
Woodman, R., 269–272
- Yamamoto, M., 161–164, 213–216,
229–236
Yamamoto, M. K., 213–216, 229–
236, 302–305
Yamanaka, M. D., 302–305
- Zawadzki, I., 179–182
Zecha, M., 81–84
Zhang, Y., 183–186



Canadian Association of Physicists
Suite 112, McDonald Building
University of Ottawa
Ottawa, Ontario
Canada K1N 6N5